EUM P 22 ISSN 1011-3932

PRE-PRINTS

American

Meteorological

Society

Société

Météorologique

de France

EUMETSAT

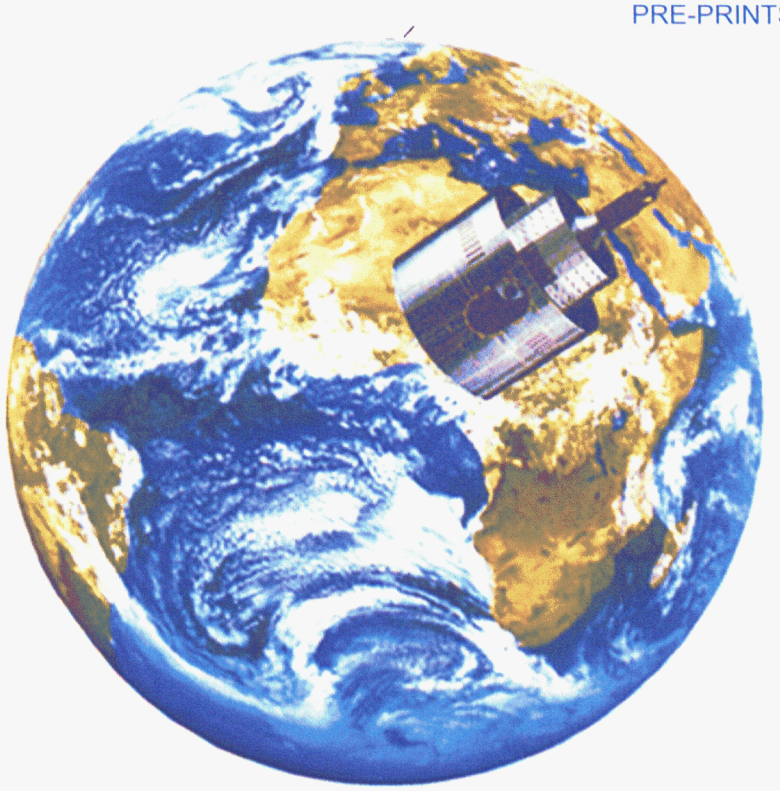

Vol. 1

9th conference on satellite meteorology and oceanography

PARIS
UNESCO

25th - 29th May

•1998•1998•1998•

Co-sponsors providing support to the Conference:

Intergovernmental Oceanographic Commission of UNESCO

World Meteorological Organization (WMO)

Météo-France

Centre National d'Etudes Spatiales (CNES)

Service Hydrographique et Océanographique de la Marine (SHOM)

Deutsche Meteorologische Gesellschaft (DMG)

Free Internet connection kindly provided by Cegetel

Icebreaker cocktail sponsored by Lockheed Martin

Reception offered by the Mayor of Paris

Pre-prints sponsored by EUMETSAT

ISBN 92-9110-000-5

TL
798
.M4
C61
9th
1998
V.1

NINTH CONFERENCE ON SATELLITE METEOROLOGY AND OCEANOGRAPHY

25–29 May 1998 UNESCO, Paris, France

Organizers/Sponsors
American Meteorological Society (AMS)
Societe Meteorologique de France (SMF)
European Organization for the Exploitation of Meteorological Satellites (EUMETSAT)

Front Cover: The Meteosat satellite superimposed over a Meteosat image, together with an artist's impression of the Eiffel Tower (from an idea by S3C/Production. Météo-France; illustration by Gérard Prat).

All Rights Reserved. No part of this publication may be reproduced or copied in any form or by any means – graphic, electronic, or mechanical, including photocopying, taping, or information storage and retrieval systems – without the prior written permission of the publisher. Contact AMS for permission pertaining to the overall collection. Authors retain their individual rights and should be contacted directly for permission to use their material separately. The manuscripts reproduced herein are unrefereed papers presented at the ***Ninth Conference on Satellite Meteorology and Oceanography***. Their appearance in this collection does not constitute formal publication.

AMERICAN METEOROLOGICAL SOCIETY
45 BEACON STREET, BOSTON, MASSACHUSETTS USA 02108-3693

National Oceanic and Atmospheric Administration
TIROS Satellites and Satellite Meteorology

ERRATA NOTICE

One or more conditions of the original document may affect the quality of the image, such as:

Discolored pages
Faded or light ink
Binding intrudes into the text

This has been a co-operative project between the NOAA Central Library and the Climate Database Modernization Program, National Climate Data Center (NCDC). To view the original document contact the NOAA Central Library in Silver Spring, MD at (301) 713-2607 x124 or Library.Reference@noaa.gov.

HOV Services
Imaging Contractor
12200 Kiln Court
Beltsville, MD 20704-1387
January 26, 2009

Blank page retained for pagination

FOREWORD

In early 1996, the Société Météorologique de France issued an invitation to the American Meteorological Society to hold the Ninth Conference on Satellite Meteorology and Oceanography in Paris, France in 1998. This is only the second time that this conference has convened outside of the United States, and is direct recognition of growing international commitments to remote sensing of the global environment, as evidenced by the conference sponsoring organizations, the American Meteorological Society, Société Météorologique de France, the European Organization for the Exploitation of Meteorological Satellites (EUMETSAT), Météo-France, the World Meteorological Organization, Intergovernmental Oceanographic Committee of UNESCO, Centre National d'Etudes Spatiales, Service Hydrographique et Océanographique de Marine, and Deutsche Meteorologische Gesellschaft.

Approximately 350 abstracts were received in response to the Call for Papers, which specified the following topics: (Meteorology from Space) (1) nowcasting and forecasting applications of satellite observations particularly including direct radiance assimilation, (2) fast and accurate forward radiative transfer modeling for global applications, (3) satellite wind observations, (4) long-term satellite data analysis studies for climatological applications, (5) ozone observations from satellites; (Oceanography from Space in support of the 1998 IOC Year of the Ocean) (6) ocean color, (7) circulation, (8) surface fluxes, (9) sea surface temperature, (10) surface phenomenology modeling; (Scientific Basis and Algorithms for Upcoming Technology) (11) GPS meteorology, (12) hyperspectral visible/infrared sensors, (13) advanced multichannel microwave imaging/sounding sensors, (14) calibration and validation techniques, and (15) experiments and issues. The conference program committee especially invited students to be an integral part of the conference. Therefore, posters identified as student submissions on the abstract were automatically entered in a student poster contest, with cash prizes and certificates provided by SeaSpace Corporation, USA, to be awarded at the conference.

The abstracts strongly reflected the degree with which satellite images and data are now integrated into meteorology and oceanography, and how evolved the data applications have become. Indeed, the papers indicate that a type of continuum has developed as sensor engineers, satellite data users, and modelers have become more sophisticated in their knowledge of the end-to-end processes and physics involved in environmental remote sensing, and data sets have gotten longer and more extensive. Five overlapping, daily themes were selected to show the range of this continuum, grouped into climatological, operational, and geostationary data applications, new technology, and prediction and monitoring capability. Also, a more overt attempt to balance the meteorological and oceanographic contributions was achieved by including a day on oceanographic data assimilation, in recognition of the Year of the Ocean. To foster interactions among the international attendees, a new format was adopted for the first time at this conference which included invited, oral plenary and state-of-the-art presentations to set the themes of each day, all supporting papers as posters, followed by poster discussion periods. The program committee hopes that this arrangement of consolidating themes, overview oral presentations, and extensive opportunity for personal interactions will contribute to an exceptional scientific experience for all attendees.

Program Committee: Marie Colton, Chairperson, Office of Naval Research, USA; Marc Gillet, Cochairperson, Météo-France, France; Johannes Schmetz, Cochairperson, EUMETSAT, Germany; Thomas F. Lee, Naval Reseach Laboratory, USA, Gary Jedlovec, NASA/MSFC, USA; Noelle Scott, LMD, France; and Robert Bernstein, SeaSpace Corporation, USA.

Blank page retained for pagination

TABLE OF CONTENTS

NINTH CONFERENCE ON SATELLITE METEOROLOGY AND OCEANOGRAPHY

PAGE

FOREWORD

XXIX AUTHOR INDEX

ORAL SESSION O1A: WELCOMING REMARKS AND AMS REMOTE SENSING LECTURE

* O1.1A WELCOMING REMARKS. Patricio Bernal, UNESCO/IOC, Paris, France

* O1.2A To Be Announced. Andre Lebeau, Societe Meteorologique de France, Paris, France

* O1.3A To Be Announced. Tillmann Mohr, Director, EUMETSAT, Darmstadt, Germany

* O1.4A FUTURE DIRECTIONS OF EUMETSAT. Alain Ratier, Technical Director, EUMETSAT, Darmstadt, Germany

* O1.5A U.S. SATELLITE PROGRAMS AND PERSPECTIVES. Robert Winokur, Director, National Oceanic and Atmospheric Administration (NOAA)/National Environmental Satellite Data Information Service (NESDIS), Silver Spring, MD, USA

1 O1.6A AMS REMOTE SENSING LECTURE: SATELLITE REMOTE SOUNDING—THE EVOLUTION OF A GLOBAL OBSERVING SYSTEM. William L. Smith, National Aeronautics and Space Administration (NASA)/Langley Research Center (LRC), Hampton, VA, USA

ORAL SESSION O1B: APPLICATIONS OF SATELLITE DATA FOR CLIMATOLOGY

5 O1.7B THE DATA SETS OF THE NOAA/NASA PATHFINDER PROGRAM. George Ohring, NOAA/NESDIS and NASA, Washington, DC, USA; and J. Dodge

9 O1.8B USE OF SATELLITE SOUNDING CLIMATE RESEARCH. John J. Bates, NOAA/Environmental Research Lab. (ERL)/Climate Diagnostics Center (CDC), Boulder, CO, USA

* O1.9B LONGTERM SATELLITE DATA SETS OF THE WORLD CLIMATE RESEARCH PROGRAM. Rolf Stuhlmann, World Climate Research Program, Geesthacht, Germany

13 O1.10B REANALYSIS OF TOVS DATA: LESSONS LEARNED FOR CLIMATE STUDIES OF THE EOS AND METOP ERA. A. Chedin, Laboratoire de Meteorologie Dynamique (LMD) du Centre National de la Recherche Scientifique (CNRS), Ecole Polytechnique, Palaiseau, France

POSTER SESSIONS P1A AND P1B: APPLICATIONS OF SATELLITE DATA FOR CLIMATOLOGY

15 P1.1A OBSERVED VARIABILITY OF TOTAL COLUMN WATER VAPOR RELATED TO ATMOSPHERIC TEMPERATURE. David L. Randel, Colorado State Univ., Ft. Collins, CO, USA; and T. H. Vonder Haar and M. A. Ringerud

18 P1.2B THE WCRP/GEWEX GLOBAL WATER VAPOR PROJECT. David L. Randel, Colorado State Univ., Ft. Collins, CO, USA; and T. H. Vonder Haar

22 P1.3A ANALYSIS OF UPPER TROPOSPHERIC WATER VAPOR BRIGHTNESS TEMPERATURES FROM SSM/T 2 AND HIRS. Wesley Berg, Cooperative Inst. for Research in the Environmental Sciences (CIRES)/Univ. of Colorado, Boulder, CO, USA; and J. J. Bates, D. L. Jackson, and M. Deeter

26 P1.4B INTERCOMPARISONS OF TOTAL PRECIPITABLE WATER FROM SATELLITE AND OTHER LONG TERM DATA SETS. Fong-Chiau Chang, Univ. of Alabama/Global Hydrology and Climate Center (GHCC), Huntsville, AL, USA; and G. J. Jedlovec, R. J. Suggs, and A. R. Guillory

30 P1.5A THE USE OF A SATELLITE CLIMATOLOGICAL DATA SET TO INFER LARGE SCALE THREE DIMENSIONAL FLOW CHARACTERISTICS. Jeffrey A. Lerner, Univ. of Alabama/GHCC, Huntsville, AL, USA; and G. J. Jedlovec and R. J. Atkinson

* Manuscript not available

TABLE OF CONTENTS

NINTH CONFERENCE ON SATELLITE METEOROLOGY AND OCEANOGRAPHY

PAGE		
34	P1.6B	1DVAR ANALYSIS OF GPS RADIO OCCULTATION MEASUREMENTS. P. I. Palmer, Oxford Univ., Oxford, UK; and J. J. Barnett and J. R. Eyre (Student Paper)
•	P1.7A	MONITORING THE SURFACE HYDROLOGY WITH THE SSM/I INSTRUMENT. Alan Basist, NOAA/NESDIS/National Climatic Data Center (NCDC), Asheville, NC, USA
*	P1.8B	COMPARISON OF RADIATIVE COMPONENTS DERIVED FROM METEOSAT DATA WITH GROUND MEASUREMENTS DURING SEVERAL EXPERIMENTS IN TROPICAL AND MEDITERRANEAN REGIONS. Heiner Billing, Inst. for Meteorology, Berlin, Germany
•	P1.9A	THE USE OF SATELLITE IMAGES TO MONITOR THE LATITUDINAL POSITION OF THE ITCZ OVER TROPICAL ATLANTIC BASIN. Antonio Ferreira, FUNCEME, CEP Fortaleza, CE, Brazil; and N. da Silva Mello, E. de Souza, and M. S. Sakamoto
38	P1.10B	DAILY EXTENDED 1-KM AVHRR DATA SETS OF THE MEDITERRANEAN. Dirk Koslowsky, Freie Univ., Berlin, Germany
42	P1.11A	ANALYSIS OF SRB DATA OVER THE MEDITERRANEAN BASIN AS A PRELIMINARY STUDY IN THE RESMEDES (REMOTE SENSING OF MEDITERRANEAN DESERTIFICATION AND ENVIRONMENTAL STABILITY) PROJECT CONTEXT. Gustavo Haba-Ejarque, Univ. of Valencia, Valencia, Spain; and E. Lopez-Baeza and J. M. Fuster-Escuder
46	P1.12B	CLOUD CLIMATOLOGY OF THE ALPINE REGION FROM LONG-TERM AVHRR DATA. Martina Kastner, Inst. fur Physik der Atmosphare (IPA), Deutsches Zentrum fur Luft-und Raumfahrt (DLR), Oberpfaffenhofen, Germany; and K. T. Kriebel
•	P1.13A	A CLOUD CLIMATOLOGY OF THE LOWER NORTH ISLAND OF NEW ZEALAND USING AVHRR DATA. James McGregor, Inst. of Geophysics, Wellington, New Zealand; and T. Hume
49	P1.14B	CYCLOGENETIC CLOUDINESS OVER SOUTH AMERICA. Natalia Fedorova, Federal Univ. of Pelotas, Rio Grande do Sul, Brazil; and G. da C. Pinheiro and D. Fedorov
53	P1.15A	COMPARISON OF MONTHLY MEAN SATELLITE ESTIMATES OF PRECIPITATION WITH GAUGES OVER AFRICA. Arnold Gruber, NOAA/NESDIS/Office of Research and Applications (ORA), Camp Springs, MD, USA; and J. R. McCollum and M. B. Ba
57	P1.16B	EXTENDED-RANGE TROPICAL FORECASTS BASED ON THE SLOW EVOLUTION OF THE MADDEN-JULIAN OSCILLATION USING THE SATELLITE OUTGOING LONGWAVE RADIATION. Duane E. Waliser, State Univ. of New York (SUNY), Stony Brook, NY, USA; and C. Jones and N. E. Graham
61	P1.17A	ESTIMATION OF OROGRAPHIC PRECIPITATION OVER WESTERN NORTH AMERICA USING GEOSTATIONARY SATELLITE OBSERVATIONS. Robert J. Joyce, NOAA/National Weather Service (NWS)/National Centers for Environmental Prediction (NCEP), Washington, DC, USA; and P. A. Arkin and W. Higgins
65	P1.18B	ANNUAL AND INTERANNUAL VARIABILITY IN GLOBAL PRECIPITATION FROM 1979–1996. Phillip A. Arkin, NOAA/NWS/NCEP, Washington, DC, USA; and P. Xie
69	P1.19A	RECONSTRUCTION OF 120 YEAR RAINFALL AND WIND SPEED FIELDS FOR THE EASTERN NORTH ATLANTIC. Malcolm Taberner, Univ. of Bristol, Bristol, UK; and D. R. Kniveton
73	P1.20B	QUALITY ASSESSMENT OF NEAR SURFACE TROPICAL WIND OBSERVATIONS. Willemien van Hoeve, Royal Netherlands Meteorological Inst. (KNMI), De Bilt, and Utrecht Univ., Utrecht, The Netherlands; and A. Stoffelen (Student Paper)

* Manuscript not available

TABLE OF CONTENTS

NINTH CONFERENCE ON SATELLITE METEOROLOGY AND OCEANOGRAPHY

PAGE		
74	P1.21A	COUPLED ANALYSIS OF ACTIVE AND PASSIVE MICROWAVE MEASUREMENTS. APPLICATION TO THE SEA-SURFACE WIND RETRIEVAL FROM TOPEX-POSEIDON. Sid-Ahmed Boukabara, Atmospheric Environmental Research, Inc. (AER), Cambridge, MA, USA; and L. Eymard (Student Paper)
*	P1.22B	SSM/I DERIVED RAINFALL CLIMATOLOGY USED FOR CLIMATE MONITORING IN CHINA. Songshan Gu, Nanjing Inst. of Meteorology, Nanjing, Jiangsu, China
78	P1.23A	A 10-YEAR CLIMATOLOGY OF AMAZONIAN RAINFALL DERIVED FROM PASSIVE MICROWAVE SATELLITE OBSERVATIONS. A. J. Negri, NASA/Goddard Space Flight Center (GSFC), Greenbelt, MD, USA; and E. N. Anagnostou and R. F. Adler
*	P1.24B	ASSIMILATION OF SSM/I PRECIPITATION AND TOTAL PRECIPITABLE WATER FOR IMPROVING CLIMATE SIGNALS IN THE GEOS ANALYSIS. Arthur Hou, NASA/GSFC, Greenbelt, MD, USA; and S. Zhang, A. da Silva, G. Huffman, and J. Joiner
82	P1.25A	ADVANCES IN APPLIED RESEARCH OF THE SATELLITE OBSERVATIONS ON THE GENERAL CIRCULATION AND CLIMATE VARIATION. Shangcheng Jiang, Peking Univ., Beijing, China
*	P1.26B	CHANGES IN STRATOSPHERIC OZONE: CONNECTIONS WITH VOLCANIC ERUPTIONS. Lucas Alados-Arboledas, Univ. of Granada, Granada, Spain; and J. Vida, I. Foyo-Moreno, and F. J. Olmo
84	P1.27A	NEURAL NETWORK APPROACH FOR TOTAL COLUMN OZONE RETRIEVAL FROM NOAA-TOVS DATA. Anton Kaifel, Center for Solar Energy and Hydrogen Research, Stuttgart, Germany
88	P1.28B	A ROTATED PRINCIPAL COMPONENT ANALYSIS OF TOTAL COLUMN OZONE DERIVED FROM TOMS (VERSION 7.0) FOR 1980-1992. Brian K. Eder, NOAA/Air Resources Lab. (ARL), Research Triangle Park, NC, USA
*	P1.29A	TOTAL OZONE AMOUNT DERIVATION FROM NOAA/TOVS DATA IN POLAND. Bozena Lapeta, Inst. of Meteorology and Water Management, Krakow, Poland
92	P1.30B	ASSIMILATION OF OZONE IN THE ECMWF MODEL. Elias V. Holm, European Centre for Medium-Range Weather Forecasts (ECMWF), Reading, Berks., UK; and A. Untch, A. Simmons, R. W. Saunders, and F. Bouttier
*	P1.31A	MONITORING EL NINO IMPACTS ON LAND ECOSYSTEMS FROM NOAA POLAR ORBITING SATELLITES. Felix Kogan, NOAA/NESDIS, Camp Springs, MD, USA
94	P1.32B	CHARACTERIZING SPATIAL AND TEMPORAL DISTRIBUTIONS OF BIOMASS BURNING USING MULTI-SPECTRAL GEOSTATIONARY SATELLITE DATA. Elaine M. Prins, NOAA/NESDIS/ORA and Univ. of Wisconsin, Madison, WI, USA; and W. P. Menzel and J. Feltz
98	P1.33A	CONFIRMATION OF HELMHOLTZ RECIPROCITY USING SCARAB SATELLITE DATA. Michel Capderou, LMD/CNRS, Palaiseau, France
102	P1.34B	SATELLITE DATA ANALYSIS FOR EARTH RADIATION BUDGET (ERB): 1. SIMULATION OF TIME SAMPLING ERRORS IN THE SHORTWAVE DOMAIN FOR VARIOUS SATELLITE ERB EXPERIMENTS. Michel Viollier, LMD/CNRS, Ecole Polytechnique, Palaiseau, France; and A. Rodelet and C. Standfuss
106	P1.35A	SATELLITE DATA ANALYSIS FOR EARTH RADIATION BUDGET (ERB): 2. SUPPORT OF THE SHORT-WAVE DIURNAL INTERPOLATION AND EXTRAPOLATION PROCEDURE (DIEP) USING MEASUREMENTS FROM GEOSTATIONARY SATELLITES. Carsten Standfuss, LMD/CNRS, Palaiseau, France; and M. Viollier

* Manuscript not available

TABLE OF CONTENTS

NINTH CONFERENCE ON SATELLITE METEOROLOGY AND OCEANOGRAPHY

PAGE		
110	P1.36B	REMOVING SATELLITE EQUATORIAL CROSSING TIME BIASES FROM THE DAILY GLOBAL OUTGOING LONGWAVE RADIATION DATASET. Lisanne E. Lucas, SUNY, Stony Brook, NY, USA; and D. E. Waliser, J. E. Janowiak, and B. Liebmann
114	P1.37A	APPLICATION OF BROADBAND FLUXES FROM SCARAB AND AVHRR NARROWBAND RADIANCES FOR BALTEX AND MAGS. Rainer Hollmann, GKSS Research Center, Geesthacht, Germany; and J. Feng, J. Mueller, H. G. Leighton, and R. Stuhlmann (Student Paper)
118	P1.38B	A NEW SATELLITE METHOD TO COMPUTE MONTHLY OCEAN AIR TEMPERATURE, SPECIFIC HUMIDITY AND LATENT HEAT FLUX. Catherine Gautier, Univ. of California, Santa Barbara, CA, USA; and C. Jones and P. Peterson
•	P1.39A	LONG TERM SURFACE ENERGY FLUX ESTIMATES BASED ON ISCCP CLOUDS AND GEOS DAS. Man-Li Wu, NASA/GSFC, Greenbelt, MD, USA; and S. Schubert, C. Lin, and R. Rood
•	P1.40B	AN EXPERIMENTAL TECHNIQUE TO ESTIMATE GLOBAL PRECIPITATION FROM THE ISCCP CLOUD PARAMETERS. Chandra R. Kondragunta, NOAA/NESDIS/ORA, Washington, DC, USA
122	P1.41A	CLOUDS AS SEEN BY SATELLITE SOUNDERS (3I) AND IMAGERS (ISCCP). C. J. Stubenrauch, LMD/CNRS, Ecole Polytechnique, Palaiseau, France; and W. B. Rossow, N. A. Scott, and A. Chedin
126	P1.42B	ANALYSIS OF A GLOBAL, SATELLITE-DERIVED CLIMATOLOGICAL DATA SET. Roberta DiPasquale, Analytical Services and Materials, Inc., Hampton, VA, USA; and P. Stackhouse
•	P1.43A	SATELLITE IDENTIFICATION OF SYSTEMS EVOLVING WITHIN THE MADDEN-JULIAN OSCILLATION. Jenni L. Evans, Penn State Univ., University Park, PA, USA
130	P1.44B	THE 16–YEAR AVHRR PATHFINDER GLOBAL DATASET: EVALUATING THE EFFECTS OF AEROSOL PARTICLES ON CLOUD RADIATIVE FORCING. Melanie A. Wetzel, Desert Research Inst. (DRI), Reno, NV, USA; and L. L. Stowe
134	P1.45A	THE NASA TOVS POLAR PATHFINDER: 18 YEARS OF ARCTIC DATA. Jennifer Francis, Rutgers Univ., New Brunswick, NJ, USA; and A. Schweiger and D. Groves
137	P1.46B	MODEL SIMULATED INTERANNUAL SST VARIABILITY IN NORTH INDIAN OCEAN. S. K. Behera, Inst. for Global Change Research, Tokyo, Japan; and P. S. Salvekar (Student Paper)
141	P1.47A	RELATIONSHIP BETWEEN SEA SURFACE TEMPERATURE, VERTICAL DYNAMICS, AND THE VERTICAL DISTRIBUTION OF ATMOSPHERIC WATER VAPOR, INFERRED FROM TOVS OBSERVATIONS. Jean-Pierre Chaboureau, LMD/CNRS, Ecole Polytechnique, Palaiseau, France; and A. Chedin and N. A. Scott
145	P1.48B	CLEAR SKY ATMOSPHERIC LONGWAVE COOLING WITH THE TOVS/PATH-B DATASET. F. Cheruy, LMD/CNRS, Palaiseau, France; and F. Chevallier and N. A. Scott
*	P1.49A	ASSIMILATING TOVS HUMIDITY INTO THE GEOS DATA ASSIMILATION SYSTEM. Minghang Chen, NASA/GSFC, Greenbelt, MD, USA
769	P1.50B	INTERANNUAL VARIABILITY OF OUTGOING LONGWAVE RADIATION, MOISTURE, AND CLOUDS OVER THE INDIAN OCEAN AS SEEN IN THE GLA-TOVS RETRIEVALS. Amita V. Mehta, General Sciences Corp. (GSC), Greenbelt, MD, USA; and J. Susskind
149	P1.51A	USE OF THE GLA TOVS PATHFINDER DATA SET FOR CLIMATE STUDIES. J. Susskind, NASA/GSFC, Greenbelt, MD, USA; and E. Anyamba, L. Iredell, A. Mehta, and P. Piraino
•	P1.52B	NOAA LONG-TERM POLAR ORBITER ARCHIVE FOR CLIMATOLOGICAL STUDIES. Lise D. Maring, NOAA, Satellite Active Archive/CSC, Suitland, MD, USA

* Manuscript not available

TABLE OF CONTENTS

NINTH CONFERENCE ON SATELLITE METEOROLOGY AND OCEANOGRAPHY

PAGE		
154	P1.53A	DIRECT RADIATIVE FORCING BY AEROSOLS AS OBSERVED FROM THE NOAA/AVHRR PATHFINDER ATMOSPHERE (PATMOS) MULTI-YEAR DATASET. Larry L. Stowe, NOAA/NESDIS/ORA, Washington, DC, USA; and H. Jacobowitz, C. Kondragunta, and G. Luo
•	P1.54B	IMPROVED STRATOSPHERIC SOUNDING UNIT (SSU) TEMPERATURE RETRIEVALS. Laurie Rokke, NASA/GSFC and UMBC, Greenbelt, MD, USA
156	P1.55A	A 3-DIMENSIONAL DAILY OZONE ANALYSIS USING SBUV/2 AND TOVS MEASUREMENTS: SMOBA. Shi-Keng Yang, Research and Data Systems Corp., Greenbelt, MD, USA; and S. Zhou and A. J. Miller
757	P1.56B	SEA-AIR TEMPERATURE DIFFERENCES DERIVED FROM THE GLA TOVS RETRIEVALS. E. Anyamba, GSC/NASA/GSFC, Greenbelt, MD, USA; and J. Susskind
761	P1.57A	GLOBAL WARMING ESTIMATION FROM MSU. C. Prabhakara, NASA/GSFC, Greenbelt, MD, USA; and R. Iacovazzi, Jr., J.-M. Yoo, and G. Dalu
766	P1.58B	SAMPLING ERROR ESTIMATION FOR SATELLITE/MICROWAVE RAINFALL CLIMATOLOGIES AND THEIR VARIATION WITH TYPES OF RAIN. Thomas L. Bell, NASA/GSFC, Greenbelt, MD, USA; and P. Kundu
	ORAL SESSIONS O2A AND O2B: SATELLITE APPLICATIONS: OCEAN, ATMOSPHERE, AND LAND	
*	O2.1A	THE SATELLITE APPLICATIONS FACILITY: A CONTRIBUTION TO OPERATIONAL OCEANOGRAPHY. Herve Roquet, Météo-France, Paris, France
160	O2.2A	WEATHER PRODUCTS VIA THE INTERNET. Thomas F. Lee, Naval Research Lab. (NRL), Monterey, CA, USA; and J. Hawkins, K. Richardson, and J. Turk
•	O2.3A	ASSIMILATION OF ALTIMETER SEA LEVEL DEVIATIONS FOR OPERATIONAL EL NINO FORECASTS. Robert Cheney, NOAA/NESDIS, Silver Spring, MD, USA
*	O2.4A	PROTECTION OF MICROWAVE FREQUENCIES FOR MICROWAVE REMOTE SENSING. Guy Rochard, Météo-France, Paris, France
162	O2.5B	SATELLITE RETRIEVALS OF SEA SURFACE TEMPERATURE FOR LONG-TERM CLIMATE MONITORING. Andrew R. Harris, UK Met Office, Bracknell, Berks., UK; and C. J. Merchant, B. Candy, C. A. Clayson, M. J. Murray, A. M. Zavody, and M. R. Allen
166	O2.6B	SEA ICE REMOTE SENSING FROM SPACE. Alain Cavanie, IFREMER, Centre de Brest, Plouzane, France
*	O2.7B	SATELLITE DATA FOR LAND APPLICATIONS. Michel M. Verstraete, Space Applications Inst., Ispra, Italy
	POSTER SESSIONS P2A AND P2B: SATELLITE APPLICATIONS: OCEAN, ATMOSPHERE, AND LAND	
169	P2.1A	THE EUMETSAT ATOVS AND AVHRR PROCESSING PACKAGE (AAPP), AN EXAMPLE FOR INTERNATIONAL CO-OPERATION. K. Dieter Klaes, EUMETSAT, Darmstadt, Germany; and M. Langevin
173	P2.2B	AN OPERATIONAL SOUNDING SCHEME FOR HRPT STATIONS. Lydie Lavanant, Météo-France/Centre de Météorologie Spatiale, Lannion, France; and G. Rochard, P. Brunel, and S. Levasseur

* Manuscript not available

TABLE OF CONTENTS

NINTH CONFERENCE ON SATELLITE METEOROLOGY AND OCEANOGRAPHY

PAGE		
177	P2.3A	USE OF TOVS OBSERVATIONS FOR THE IDENTIFICATION OF TROPOPAUSE-LEVEL THERMAL ANOMALIES. N. Fourrie, LMD/CNRS, Palaiseau, France; and C. Claud, R. Armante, B. Pouponneau, and J.-P. Cammas
181	P2.4B	SURFACE AND ATMOSPHERIC TEMPERATURE RETRIEVAL WITH THE HIGH RESOLUTION INTERFEROMETER IASI. Filipe Aires, LMD/CNRS, Palaiseau, France; and R. Armante, A. Chedin, and N. A. Scott (Student Paper)
187	P2.5A	ANALYSIS OF RADIANCE FLUCTUATIONS IN THE CO_2V3 BAND AROUND 4.3 UM: EFFECTS OF NONLOCAL THERMODYNAMIC EQUILIBRIUM FOR NADIR OBSERVATIONS. Gabriel Castelain, ONERA, Palaiseau, France; and P. Simoneau, V. Achard, B. Rozier, and J. C. Buriez
191	P2.6B	ADVCLD: AIR FORCE WEATHER AGENCY'S IMPROVED CLOUD FORECAST MODEL. Thomas J. Kopp, Headquarters Air Force Weather Agency, Offutt AFB, NE, USA; and M. M. Wonsick, L. E. Cantrell, and F. D. Bieker
193	P2.7A	COMPARISON BETWEEN GLOBALLY MAPPED, LAYERED CLOUD AMOUNT FROM CLAVR, ISCCP, AND RTNEPH. Gang Luo, Scientific Management & Applied Research Technologies, Inc., Silver Spring, MD, USA; and L. L. Stowe and K. A. Campana
*	P2.8B	PREDICTION OF CONVECTIVE PRECIPITATION FROM IR IMAGES USING A NEW CLOUD DETECTION ALGORITHM. Gianni Pedrizzetti, Univ. of Firenze, Firenze, Italy
197	P2.9B	A COMPARISON OF 15 GLOBAL, NON-PARAMETRIC, AUTOMATED THRESHOLD SELECTION PROCEDURES FOR CLOUD DETECTION. Larry Di Girolamo, Univ. of Arizona, Tucson, AZ, USA
	P2.10B	PAPER WITHDRAWN
201	P2.11A	MULTI-CHANNEL IR OBSERVATIONS OF CLOUDS AND COLLOCATED MICROWAVE RADIOMETER OBSERVATIONS. Toshiro Inoue, Meteorological Research Inst. (MRI), Tsukuba, Ibaraki, Japan
204	P2.12B	THE APPLICATION OF CLOUD-FREE RADIANCES TO THE RETRIEVAL OF CLOUD TOP PRESSURES FROM HIRS DATA. Hung-Lung Huang, Cooperative Inst. for Meteorological Satellite Studies (CIMSS)/Univ. of Wisconsin, Madison, WI, USA; and K. D. Hutchison
208	P2.13A	COMBINING IMAGER DATA AND SOUNDER DATA TO DERIVE CLOUD PRODUCTS. Dongsoo Kim, CIRES/Univ. of Colorado and NOAA/FSL, Boulder, CO, USA
212	P2.14B	COMBINED SATELLITE- AND SURFACE- BASED OBSERVATIONS OF CLOUDS. Bryan C. Weare, Univ. of California, Davis, CA, USA
214	P2.15A	SIMULTANEOUS OBSERVATION OF SNOWING CLOUDS BY MULTICHANNEL AIRBORNE MICROWAVE RADIOMETER AND X-BAND DOPPLER RADAR. Masaki Katsumata, Hokkaido Univ., Sapporo, Japan; and H. Uyeda, K. Iwanami, and G. Liu (Student Paper)
218	P2.16B	RETRIEVAL OF CIRRUS MICROPHYSICAL AND BULK PROPERTIES USING RADIANCE DATA FROM THE ALONG TRACK SCANNING RADIOMETER (ATSR-2). Anthony J. Baran, UK Met Office, Bracknell, Berks., UK; and P. D. Watts and P. N. Francis
*	P2.17A	REMOTE SENSING OF SNOW FIELDS AND CLOUDS FROM SPACE. Alexander A. Kokhanovsky, Clausthal Technical Univ., Clausthal-Zellerfeld, Germany
*	P2.18B	INTEGRATION OF PASSIVE MICROWAVE AND INFRARED DATA FOR SHORT-TERM GLOBAL RAINFALL ESTIMATES. Chris Kidd, Universities Space Research Association (USRA), Greenbelt, MD, USA

* Manuscript not available

TABLE OF CONTENTS

NINTH CONFERENCE ON SATELLITE METEOROLOGY AND OCEANOGRAPHY

PAGE		
222	P2.19A	DETERMINATION OF THE CLOUD DROPLET EFFECTIVE RADIUS BY USING SSM/I DATA. Constantin A. Pontikis, Météo France/Univ. des Antilles et de la Guyane, Pointe a Pitre, Guadeloupe, French West Indies; and E. M. Hicks
*	P2.20B	COMPARISONS OF PRECIPITATION ESTIMATES FROM MICROWAVE AND INFRARED SATELLITE IMAGERY AND METEOROLOGICAL RADAR FOR SAO PAULO STATE, BRAZIL. Jonas T. Nery, Inst. Nacional de Pesquisas Espaciais (INPE), SP, Brazil
*	P2.21A	USE OF SATELLITE DERIVED MOISTURE FIELDS IN A LAPS-MM5 LINKAGE FOR PRECIPITATION FORECASTING. Robert Bornstein, San Jose State Univ., San Jose, CA, USA
226	P2.22B	USING SSM/I DATA AND COMPUTER VISION TO ESTIMATE TROPICAL CYCLONE INTENSITY. Richard L. Bankert, NRL, Monterey, CA, USA; and P. M. Tag
230	P2.23A	SSM/I-BASED TROPICAL CYCLONE STRUCTURAL OBSERVATIONS. Jeffrey D. Hawkins, NRL, Monterey, CA, USA; and D. A. May, J. Sandidge, R. Holyer, and M. J. Helveston
234	P2.24B	TOTAL WATER VAPOR FROM DMSP SSM/I AND NOAA TOVS: NORTH PACIFIC HIGH AND ITS INFLUENCES ON THE EAST ASIAN SUMMER MONSOON. Byung-Ju Sohn, Seoul National Univ., Seoul, Korea; and D.-H. Kim and H.-S. Chung
236	P2.25A	VARIABILITY IN ATMOSPHERIC MOISTURE OVER THE TROPICAL EAST PACIFIC FROM MULTISPECTRAL SATELLITE OBSERVATIONS. Wesley Berg, CIRES/Univ. of Colorado, Boulder, CO, USA; and M. Deeter and D. Anderson
*	P2.26B	RESULTS: DETERMINATION OF INTEGRATED WATER VAPOR OVER ANTARCTICA UTILIZING SPECIAL SENSOR MICROWAVE TEMPERATURE-2 (SSM/T-2) DATA. Stephen L. Moore, Texas A&M Univ., College Station, TX, USA
240	P2.27A	ABSOLUTE LIMITS FOR UPPER-TROPOSPHERIC HUMIDITY IN SUBTROPICAL HIGHS BASED ON SSM/T-2 OBSERVATIONS. Clay B. Blankenship, Texas A&M Univ., College Station, TX, USA; and T. T. Wilheit
242	P2.28B	CLOUD SENSITIVITY OF PASSIVE MICROWAVE OBSERVATIONS. Gerald W. Felde, Space Vehicles Directorate, Air Force Research Lab., Hanscom AFB, MA, USA
244	P2.29A	CLOUD BASE HEIGHT RETRIEVAL FROM DMSP MICROWAVE DATA AND *A PRIORI* CLOUD TOP TEMPERATURES. Thomas T. Wilheit, Texas A&M Univ., College Station, TX, USA; and K. D. Hutchison
246	P2.30B	DEVELOPMENTS ON SST RETRIEVAL OVER THE ATLANTIC USING GEOSTATIONARY AND POLAR ORBITER SATELLITE DATA IN THE FRAME OF EUMETSAT OCEAN AND SEA ICE SATELLITE APPLICATION FACILITY. Soren Andersen, DMI, Copenhagen, Denmark; and A. Brisson, S. Eastwood, P. Le Borgne, and A. Marsouin
*	P2.31A	SST OBSERVATIONS FROM GOES-8 AND -9 GEOSTATIONARY SATELLITES. Richard Legeckis, NOAA/NESDIS, Washington, DC, USA
*	P2.32B	THE ALGORITHMS FOR DERIVING SEA SURFACE TEMPERATURES WITH GOMS AND NOAA/AVHRR DATA. Alexander B. Uspensky, SRC PLANETA, Roshydromet, Moscow, Russia
250	P2.33A	FIVE YEARS OF OPERATIONAL DERIVATION OF MULTICHANNEL SEA SURFACE TEMPERATURES AT THE GERMAN REMOTE SENSING DATA CENTER. Stefan W. Dech, DLR, Oberpfaffenhofen, Germany; and P. Tungalagsaikhan, A. Holz, and R. E. Meisner
*	P2.34B	SEA SURFACE TEMPERATURE MAPS OBTAINED AT THE ITALIAN METEOROLOGICAL SERVICE. L. DeLeonibus, Italian Meteorological Service, Rome, Italy

* Manuscript not available

TABLE OF CONTENTS

NINTH CONFERENCE ON SATELLITE METEOROLOGY AND OCEANOGRAPHY

PAGE		
254	P2.35A	HIGHLY ACCURATE RETRIEVAL OF SKIN SEA SURFACE TEMPERATURE. Christopher J. Merchant, Univ. College London, Dorking, Surrey, UK (Student Paper)
256	P2.36B	SENSOR DESIGN CONSIDERATIONS FOR THE RETRIEVAL OF SEA SURFACE TEMPERATURES IN THE NPOESS ERA. Keith D. Hutchison, Lockheed Martin Missiles & Space Center for Remote Environmental Sensing Technology (CREST), Sunnyvale, CA, USA; and S. Marusa, W. G. Uplinger, and J. A. Twomey
*	P2.37A	RELATIONSHIP BETWEEN CHLOROPHYLL CONCENTRATION AND SATELLITE MEASURED SST. Eugenio Lopez, Inst. de Meteorologia, Havana, Cuba
*	P2.38B	ADVANCED USE OF SATELLITE INFORMATION INCLUDING MULTISPECTRAL COLOUR COMPOSITIONS ON SYNERGIE WORKSTATIONS AT MÉTÉO-FRANCE. Patrick Benichou, Météo-France, Toulouse, France
260	P2.39A	DEVELOPMENT OF A MULTI-SENSOR ICE PRODUCT. Lars-Anders Breivik, Norwegian Meteorological Inst., Oslo, Norway; and O. Godoy, H. Schyberg, and S. Andersen
262	P2.40B	INTERPRETATION OF SAR IMAGERY OF VESTFJORDEN, NORWAY. E. G. Mitchelson-Jacob, Univ. of Wales, Bangor, Menai Bridge, Anglesey, UK; and B. Jones
266	P2.41A	CONTRAIL COVERAGE OVER WESTERN EUROPE DERIVED FROM 2 YEARS OF NOAA-AVHRR-DATA. Richard Meyer, DLR-IPA, Wessling, Bavaria, Germany; and H. Mannstein
270	P2.42B	FOG DETECTION AND FORECAST OF FOG DISSIPATION USING BOTH AVHRR AND METEOSAT DATA. A. I. Anthis, Hellenic National Meteorological Service, Athens, Greece; and A. P. Cracknell
274	P2.43A	FOG DETECTION IN OPERATIONAL MODE. Astrid Clausen, Univ. of Hannover, Hannover, Germany; and H. Roozekrans and P. Scheidgen
276	P2.44B	RETRIEVAL OF AEROSOL PROPERTIES FROM MERIS. Thomas Heinemann, Freie Univ., Berlin, Germany; and J. Fischer (Student Paper)
278	P2.45A	DIRECT RETRIEVAL OF SURFACE LATENT HEAT FLUX FROM SATELLITE DATA; COMPARISON TO LIU ET AL. (1984) METHOD ON DATA OF THE SEMAPHORE EXPERIMENT. Denis Bourras, Centre d'Etude des Environments Terrestre et Plainetaires, Velizy, France; and L. Eymard (Student Paper)
283	P2.46B	SOLAR RADIATION BUDGETS FOR MAGS AND BALTEX. J. Feng, McGill Univ., Montreal, PQ, Canada; and R. Hollmann, J. Muller, R. Stuhlmann, and H. G. Leighton (Student Paper)
*	P2.47A	ESTIMATION OF SURFACE RADIATION BUDGET FROM SATELLITE DATA OVER NATIVE VEGETATION. Eduardo de Brito Bastos, Inst. Nacional de Pesquisas Espaciais, Sao Jose dos Campos, SP, Brazil
*	P2.48B	THE ESTIMATE OF ATMOSPHERIC SOLAR RADIATION ABSORPTION OVER THE MOSCOW AREA USING DATA THE AVHRR/NOAA. V. V. Trembach, Inst. of Molecular Physics Russian Research Centre, Kurchatov Inst., Moscow, Russia (Student Paper)
287	P2.49A	A RADAR-SATELLITE RAINFALL ESTIMATION TECHNIQUE FOR HYDROLOGICAL APPLICATIONS. Federico Porcu, FISBAT-CNR, Bologna, Italy; and M. Borga and F. Prodi
*	P2.50B	SATELLITE IMAGES AND VORTICITY FIELDS IN THE ANALYSIS AND FORECAST OF MEDITERRANEAN CYCLOGENESIS. Natasa Strelec Mahovic, Meteorological and Hydrological Service, Zagreb, Croatia

* Manuscript not available

TABLE OF CONTENTS

NINTH CONFERENCE ON SATELLITE METEOROLOGY AND OCEANOGRAPHY

PAGE		
*	P2.51A	DEVELOPMENT OF A MODEL FOR ESTIMATING RAINFALL IN SPECIFIC AGRO-ECOLOGICAL ZONES AND A TOOL FOR EARLY WARNING PURPOSES. G. K. Munthali, Meteorological Dept., Chileka, Malawi
*	P2.52B	USE OF SATELLITE IMAGERIES IN WEATHER FORECASTING IN NIGERIA. S. Mangi Wilson, Central Forecast Office, Oshodi-Lagos, Nigeria
*	P2.53A	THE POTENTIAL OF SATELLITE IMAGERY IN DROUGHT MAPPING AND MONITORING. Filipe Lucio, National Inst. of Meteorology, Maputo, Mozambique
*	P2.54B	SATELLITE MONITORING OF SQUALL FIELDS OVER A MARINE SURFACE IN REGIONS WITH SYNOPTICAL PROCESSES. M. V. Bukharov, Hydrometcentre of Russia, Moscow, Russia
291	P2.55A	RAPID COLLAPSE OF A GULF WINTER SHEMAL. Joe Parsons, Dept. of Civil Aviation, Dubai, United Arab Emirates
*	P2.56B	USE OF METEOSAT DATA IN DISASTER PREVENTION DURING THE 1996 LONG-RAINY PERIOD OF ETHIOPIA. Zewdu Tessema, National Meteorological Services Agency, Addis Ababa, Ethiopia
*	P2.57A	USE OF SATELLITE IMAGES OF THE ARABIAN SEA, RED SEA AND INDIAN OCEAN FOR WEATHER PREDICTION ON DIFFERENT SEASONS OF ETHIOPIA. Teferi Dejene, National Meteorological Service Agency, Addis Ababa, Ethiopia
*	P2.58B	SATELLITE THERMAL INFRARED DERIVED CONVECTIVE CLOUDS ITS SPATIAL AND TEMPORAL ORGANIZATION IN ETHIOPIA AS DEPICTED BY EIGENVECTOR AND CLUSTER ANALYSIS. Abebe Yeshanew, National Meteorological Services Agency, Addis Ababa, Ethiopia
295	P2.59A	SATELLITE-BASED PRODUCTS FOR MONITORING OF WEATHER IN SOUTH AMERICA. J. C. Ceballos, INPE, Cachoeira Paulista, SP, Brazil; and L. A. T. Machado, J. Sakuragi, G. B. Franca, R. Hallak, R. C. G. Pereira, and C. A. Nobre
297	P2.60B	IDENTIFICATION OF WARM ADVECTION ON SATELLITE DATA. N. Fedorova, Federal Univ. of Pelotas, Rio Grande do Sul, Brazil; and L. Bakst
*	P2.61A	STUDY OF THE THERMAL REGIME OF CENTRAL ASIA LAKES AND RESERVOIRS USING REMOTE SENSING DATA. V. E. Chub, SANIGMI, Tashkent, Republic of Uzbekistan
*	P2.62B	USE OF DIGITAL SATELLITE REMOTELY SENSED INFORMATION FOR ESTIMATION OF THE AMUDARYA RIVER'S DELTA WATERING DYNAMICS. N. E. Gorelkin, SANIGMI, Tashkent, Republic of Uzbekistan
*	P2.63A	SURFACE OZONE TRENDS MONITORED USING THE U.V. PHOTOMETER OF THE OZONESONDE AT THE NAIROBI STATION. HOW DOES THIS COMPARE WITH SATELLITE DERIVED OZONE PROFILES? Stephen H. Mwandoto, Kenya Meteorological Dept., Nairobi, Kenya
*	P2.64B	AN OPERATIONAL SATELLITE RAINFALL ESTIMATE TECHNIQUE. Lu Naimeng, National Satellite Meteorology Center, Beijing, China
*	P2.65A	REMOTE SENSING DECISION TREE CLASSIFICATION BY MEANS OF SPECTRAL AND TEXTURAL INFORMATION. Miloud Bouazza, Free Univ. of Brussels, Brussels, Belgium (Student Paper)
*	P2.66B	COMPARISON OF TWO DIFFERENT METHODS FOR CALCULATING LAND SURFACE EMISSIVITY FROM NOAA/AVHRR IMAGES. Judit Kerényi, Hungarian Meteorological Service, Budapest, Hungary (Student Paper)

* Manuscript not available

TABLE OF CONTENTS

NINTH CONFERENCE ON SATELLITE METEOROLOGY AND OCEANOGRAPHY

PAGE		
301	P2.67A	GLOBAL LAND SURFACE PROPERTIES INFERRED FROM COMBINED PASSIVE MICROWAVE AND VISIBLE/NEAR-INFRARED SATELLITE DATA. Ralf Bennartz, Freie Univ., Berlin, Germany; and G. G. Gutman
*	P2.68B	A COMPARISON BETWEEN SNOW COVER PRODUCTS DERIVED FROM VISIBLE AND MICROWAVE SATELLITE OBSERVATIONS. Alan Basist, NOAA/NESDIS/NCDC, Asheville, NC, USA
304	P2.69A	LAND SURFACE TEMPERATURES AND LEAF AREA INDEX DERIVED FROM AVHRR/NDVI TIME SERIES. P. Tungalagsaikhan, DLR, Oberpfaffenhofen, Germany; and S. W. Dech, R. E. Meisner, and C. Preusser
*	P2.70B	CONTRIBUTION OF SATELLITE IMAGERY TO FORECASTING APPLICATIONS OF CLOUD BANDS IN SOUTHERN AFRICA. Tichaona Zinyemba, Zimbabwe Meteorological Services, Harare, Zimbabwe
*	P2.71A	RELATIONSHIP BETWEEN OUTGOING LONGWAVE RADIATION AND INTERANNUAL RAINFALL VARIABILITY OVER SOUTHERN AFRICA. W. Zhakata, Zimbabwe Meteorological Services, Harare, Zimbabwe
*	P2.72B	DEVELOPMENT OF A MODEL FOR ESTIMATING RAINFALL IN SPECIFIC AGRO-ECOLOGICAL ZONES AND A TOOL FOR EARLY WARNING PURPOSES. Gray Muthal, Meteorological Dept., Chileka, Malawi
*	P2.73A	HIGH LATITUDE GREENING TREND FROM THE NASA/NOAA AVHRR LAND PATHFINDER DATA FROM 1981-1994. Ranga Myneni, Boston Univ., Boston, MA, USA
*	P2.74B	PHOTOSATELLITE INFORMATION FOR A SHORT TERM WEATHER FORECAST ON TOGO. Koure M. Toure, Airport of Lome Togo, Asecna, Togo
308	P2.75A	MONITORING PHENOLOGICAL STAGES OF CULTIVATED CROPS BY REMOTE SENSING IN MALI. Mamadou Adam Diallo, Direction Nationale de la Meteorologie, Bamako, Mali and Fondation Univ. Luxembourgeoise, Arlon, Belgium; and B. Tychon
*	P2.76B	USE OF NDVI FOR BIOMASS PREDICTION IN ZIMBABWE. Veronica Mutikani, Dept. of Agricultural Technical and Extension Services, Harare, Zimbabwe
*	P2.77A	SPECTRAL REFLECTANCE MEASUREMENTS FOR THE RADIOMETRIC CALIBRATION SITE OF CHINA REMOTE SENSING SATELLITE SENSORS. Zhang Yuxiang, National Satellite Meteorological Center, Beijing, China
*	P2.78B	THE 1997 FLOOD IN POLAND USING METEOROLOGICAL SATELLITE IMAGES. Piotr Struzik, Inst. of Meteorology and Water Management, Krakow, Poland
*	P2.79A	DETERMINATION OF LAND SURFACE EMISSIVITIES AT FREQUENCIES FROM 1 TO 100 GHZ. Katja Paape, Freie Univ., Berlin, Germany
*	P2.80B	USE OF LOW RESOLUTION SATELLITE IMAGES AS METEOROLOGICAL FORECASTING TOOL IN A DEVELOPING COUNTRY. Dialle Boubacar Madina, Chef du Centre Meteorologique National, Conakry, Guinea
*	P2.81A	A BLENDED LAND SURFACE TEMPERATURE PRODUCT FROM SATELLITE AND INSITU MEASUREMENTS. Alan Basist, NOAA/NESDIS/NCDC, Asheville, NC, USA
311	P2.82B	LAND SURFACE RESPONSE TO NON-PERIODIC HYDROMETEOROLOGICAL EVENTS APPLYING WAVELET TRANSFORM ANALYSIS TO AVHRR AND SMMR TIME SERIES DATA. Saturnino Leguizamon, Univ. of Mendoza, Mendoza, Argentina; and M. Menenti and B. Choudhury

* Manuscript not available

TABLE OF CONTENTS

NINTH CONFERENCE ON SATELLITE METEOROLOGY AND OCEANOGRAPHY

PAGE		
*	P2.83A	THUNDERSTORM FREQUENCY AND RAINFALL ESTIMATION USING SATELLITE DATA OVER LAKE VICTORIA BASIN. Eliakim E. Matari, Directorate of Meteorology, Dar-es-salaam, Tanzania
313	P2.84B	IMPROVED LONG-TERM AVHRR REFLECTANCE AND NDVI TIME SERIES USING EMPIRICALLY DERIVED NADIR CORRECTION FACTORS. Dirk Koslowsky, Freie Univ., Berlin, Germany
*	P2.85A	SATELLITE DERIVED CLOUD PROPERTIES AND PRECIPITATION IN ZAMBIA. Gervas Muloshi, Zambian Meteorological Dept., Lusaka, Zambia
*	P2.86B	APPLICATION OF SATELLITE DATA RECEIVED AT THE ZAMBIAN METEOROLOGICAL DEPARTMENT. Slade M. Syakango, Zambian Meteorological Dept., Lusaka, Zambia
*	P2.87A	ASSESSMENT AND FORECAST OF CEREAL CROP YIELD USING SATELLITE INFORMATION. A. Kleschenko, Director of ARRIAM, Russian Federation
317	P2.88B	ANTARCTIC MESOCYCLONE EVENTS OVER THE SOUTHERN PACIFIC DURING FROST SOP1 AND SOP3: A MESO-SCALE ANALYSIS USING AVHRR, SSM/I, ERS-SCATTEROMETER AND NUMERICAL MODEL DATA. Michael Lieder, Univ. Bonn, Bonn, Germany; and G. Heinemann
*	P2.89A	DETERMINATION OF WIND VELOCITY NEAR WATER SURFACE IN THE TROPICAL CYCLONES ZONE WITH MICROWAVE RADIOMETRIC DATA. Milekhin Leonid, Scientific & Production Association "Typhoon", Inst. of Experimental Meteorology, Obninsk, Kaluga Region, Russia
319	P2.90B	THE SATELLITE APPLICATION FACILITY (SAF) OF EUMETSAT TO SUPPORT NOWCASTING: AN INTRODUCTION. Jose Miguel Fernandez, INM, Madrid, Spain; and H. Legleau, V. Zwatz-Meise, and A. Dybbroe
323	P2.91A	NEURAL NETWORK APPROACHES TO OCEAN PARAMETER RETRIEVALS: APPLICATION TO THE ERS1 SCATTEROMETER WIND AND TO PHYTOPLANCTON CONTENT FROM OCEAN COLOR MEASUREMENTS. M. Crepon, LODYC, UPMC, Paris, France; C. Mejia, S. Thiria, L. Gross, N. Tran, P. Richaume, H. Roquet, F. Badran, and R. Frouin
	ORAL SESSIONS O3A AND O3B: GEOSTATIONARY SATELLITES AND DATA APPLICATIONS	
*	O3.1A	RECENT SUCCESS IN THE DEVELOPMENT AND APPLICATION OF WINDS DERIVED FROM GEOSTATIONARY SATELLITES. Christopher Velden, Univ. of Wisconsin, Madison, WI, USA
*	O3.2A	IMPACT OF GEOSTATIONARY WINDS AND RADIANCES ON THE OPERATIONAL SYSTEM AT ECMWF. Anthony Hollingsworth, ECMWF, Reading, Berks., UK
327	O3.3A	INTENSE RAINFALL MONITORING FROM GEOSTATIONARY SATELLITES. Vincenzo Levizzani, Inst. FISBAT-CNR, Bologna, Italy and EUMETSAT, Darmstadt, Germany
331	O3.4A	GOES-8 AND BEYOND: SCIENCE ADVANCES AND FUTURE DIRECTIONS. James F. W. Purdom, NOAA/NESDIS, Washington, DC, USA
*	O3.5B	SATELLITE OBSERVATIONS FOR CLIMATOLOGICAL RESEARCH. Michel Desbois, LMD/CNRS, Palaiseau, France
335	O3.6B	FROM METEOSAT TO METEOSAT SECOND GENERATION (MSG). Johannes Schmetz, EUMETSAT, Darmstadt, Germany; and H. Woick, S. Tjemkes, and M. Rattenborg
	POSTER SESSIONS P3A AND P3B: GEOSTATIONARY SATELLITES AND DATA APPLICATIONS	
339	P3.1A	APPLICATION OF GOES-8/9 SOUNDINGS TO WEATHER FORECASTING AND NOWCASTING. Frances C. Holt, NOAA/NESDIS/ORA, Washington, DC, USA; and W. P. Menzel

* Manuscript not available

TABLE OF CONTENTS

NINTH CONFERENCE ON SATELLITE METEOROLOGY AND OCEANOGRAPHY

PAGE		
*	P3.2B	PAPER WITHDRAWN
343	P3.3A	CLOUD FIELD CHARACTERIZATION BASED ON METEOSAT IMAGERY AND NWP MODEL DATA. Paul de Valk, KNMI, De Bilt, The Netherlands; and A. Feijt and H. Roozekrans
345	P3.4B	EVOLUTION AND VELOCITY OF THE CYCLONIC CLOUD SYSTEMS FROM SATELLITE DATA. N. Fedorova, Federal Univ. of Pelotas, Rio Grande do Sul, Brazil; and L. Bakst and D. Fedorov
*	P3.5A	APPLICATION OF METEOSATA DATA FOR THE SHORT-TERM FORECAST OF MAXIMUM PRECIPITATION IN ACTIVE CONVECTIVE ZONES. A. A. Aleksseva, Hydrometcentre of Russia, Moscow, Russia
349	P3.6B	THE MARSHALL AUTOMATED WIND ALGORITHM FOR GEOSTATIONARY SATELLITE WIND APPLICATIONS. Gary J. Jedlovec, NASA/Marshall Space Flight Center (MSFC)/GHCC, Huntsville, AL, USA; and R. J. Atkinson
353	P3.7A	THE GENERATION, QUALITY CONTROL AND DISTRIBUTION OF HIGH RESOLUTION WATER VAPOUR WINDS FROM METEOSAT DATA. S. S. Elliott, EUMETSAT, Darmstadt, Germany
356	P3.8B	MEASURE OF DIVERGENCE AT THE TOP OF TROPICAL CONVECTIVE SYSTEMS USING WIND FIELDS DERIVED FROM WATER VAPOUR IMAGES. Meiry S. Sakamoto, FUNCEME, Fortaleza, CE, Brazil; and H. Laurent
773	P3.9A	A REAL TIME QUALITY ESTIMATE OF ATMOSPHERIC MOTION VECTORS. Kenneth Holmlund, EUMETSAT, Darmstadt, Germany; and S. Elliott and M. Rohn
360	P3.10B	USE AND IMPACT OF ATMOSPHERIC MOTION VECTORS AT ECMWF. Michael Rohn, ECMWF, Reading, Berks., UK; and G. Kelly and R. W. Saunders
*	P3.11A	IMPACT OF GEOSTATIONARY RADIANCE DATA ON THE 4DVAR ASSIMILATION SYSTEM AT ECMWF. Rosemary Munro, ECMWF, Reading, Berks., UK
364	P3.12B	THE IMPACT OF WATER VAPOR WINDS IN HIGH RESOLUTION PREDICTION OF HURRICANE OPAL (1995). Melinda S. Peng, NRL, Monterey, CA, USA; and S. W. Chang
*	P3.13A	IMPACT OF MULTISPECTRAL GOES WIND OBSERVATIONS ON GFDL HURRICANE MODEL FORECASTS. Brian J. Soden, NOAA/Geophysical Fluid Dynamics Lab. (GFDL), Princeton, NJ, USA
367	P3.14B	ASSIMILATION OF WATER VAPOUR MOTION WINDS IN THE GLOBAL MODEL OF DWD. M. Tomassini, Deutscher Wetterdienst, Offenbach, Germany; and H. Neumeister and G. Paul
*	P3.15A	GEOSTATIONARY OBSERVATIONS OF WINDS. Mark Abrams, ITT Aerospace, Ft. Wayne, IN, USA
370	P3.16B	DETECTION OF LOW CLOUDS IN METEOSAT IR NIGHT-TIME IMAGES BASED ON A CONTEXTUAL SPATIO-TEMPORAL LABELING APPROACH. Christophe Papin, IRISA/INRIA, Rennes, France; and P. Bouthemy and G. Rochard (Student Paper)
374	P3.17A	CLOUD FILTERING USING A BI-SPECTRAL SPATIAL COHERENCE APPROACH. Anthony R. Guillory, NASA/MSFC/GHCC, Huntsville, AL, USA; and J. M. Lecue, G. J. Jedlovec, and B. N. Whitworth
377	P3.18B	A FULLY AUTOMATED DETECTION AND TRACKING OF MESOSCALE CONVECTIVE SYSTEMS BASED ON THE METEOSAT INFRARED CHANNEL. Christophe Morel, CNRM/GMME, Météo-France, Toulouse, France; and S. Senesi (Student Paper)

* Manuscript not available

TABLE OF CONTENTS

NINTH CONFERENCE ON SATELLITE METEOROLOGY AND OCEANOGRAPHY

PAGE		
*	P3.19A	MESOSCALE CONVECTIVE SYSTEMS MONITORING BY AN OPERATIONAL APPLICATION AT THE ITALIAN METEOROLOGICAL SERVICE. L. DeLeonibus, Italian Meteorological Service, Rome, Italy
*	P3.21A	DETERMINATION OF THE INTENSITY OF LOCAL STORMS FROM GOES-IR. Eugenio Lopez, Inst. de Meteorologia, Havana, Cuba
381	P3.22B	INTERNALLY CALIBRATED, THERMAL-INFRARED FIELD RADIOMETER: CHARACTERIZATION AND COMPARISONS WITH OTHER FIELD INSTRUMENTS. Michael Sicard, CIMEL Electronique, Paris, France; and P. R. Spyak (Student Paper)
385	P3.23A	REMOVAL OF ANOMALOUS RADAR PROPAGATION WITH A NEURAL NETWORK PRECIPITATION CLASSIFIER TRAINED ON METEOSAT INFRARED IMAGERY. George S. Pankiewicz, UK Met Office, Bracknell, Berks., UK
*	P3.24B	A LAGRANGIAN STUDY OF UPPER TROPOSPHERIC WATER VAPOR. Brian J. Soden, NOAA/GFDL, Princeton, NJ, USA
389	P3.25A	USE OF WATER VAPOR DATA FROM NOMINAL AND ATLANTIC METEOSAT FOR TROPICAL CLIMATIC STUDIES. Laurence Picon, LMD/CNRS, Ecole Polytechnique, Palaiseau, France; and R. Roca
393	P3.26B	COMPARISON OF UPPER TROPOSPHERIC HUMIDITY RADIANCES FROM ECMWF OPERATIONAL ANALYSES AND THE METEOSAT WATER VAPOUR CHANNEL. Alan J. Geer, Imperial College, London, UK; and J. E. Harries (Student Paper)
397	P3.27A	ESTIMATION OF THE UPPER TROPOSPHERIC MOISTURE FIELD FROM VISSR/GMS-5 WATER VAPOR CHANNEL DATA. Naonori Osaki, Hokkaido Univ., Sapporo, Japan; and H. Uyeda (Student Paper)
401	P3.28B	ARCHIVED FIELDS DERIVED FROM GOES-8 AND GOES-9 DATA AT THE CMC. Louis Garand, Atmospheric Environment Service (AES), Dorval, PQ, Canada; and N. Wagneur
403	P3.29A	ASSIMILATION OF INFRARED DATA FROM METEOSAT TO RETRIEVE RAINFALL FIELDS. Olga V. Zhiltsova, Moscow State Univ., Moscow, Russia (Student Paper)
405	P3.30B	COMPARISON BETWEEN RAINGAUGE MEASUREMENTS AND ISOPLET MAPS FROM IR METEOSAT IMAGES. Ramon Tarruella, Univ. Politecnica de Catalunya, Manresa, Spain; and J. Jorge (Student Paper)
*	P3.31A	A GOES-9 STUDY OF HAWAIIAN RAINBANDS. David B. Johnson, National Center for Atmospheric Research (NCAR), Boulder, CO, USA
*	P3.32B	HEAVY RAINFALLS DO NOT LOOK ALWAYS EQUAL. Juan J. Rivera, Univ. Politecnica de Catalunya, Manresa, Barcelona, Spain (Student Paper)
*	P3.33A	METEOSAT RAIN MONITORING USING SSM/I RAIN-RATES FOR CALIBRATION. Daniel Taurat, Max-Planck-Inst. for Meteorologie, Hamburg, Germany
*	P3.34B	MULTICHANNEL RETRIEVAL OF CLOUD PROBABILITY DISTRIBUTION FUNCTIONS. Darren S. McKague, Univ. of Colorado, Boulder, CO, USA (Student Paper)
408	P3.35A	AVHRR MULTISPECTRAL DERIVED CLOUD PARAMETERS: RELATIONSHIPS TO MICROWAVE SCATTERING SIGNATURE AND TO CLOUD-TO-GROUND LIGHTNING. Mamoudou B. Ba, NOAA/NESDIS, Washington, DC, USA; and D. Rosenfeld and A. Gruber

* Manuscript not available

TABLE OF CONTENTS

NINTH CONFERENCE ON SATELLITE METEOROLOGY AND OCEANOGRAPHY

PAGE		
412	P3.36B	USE OF METEOSAT IMAGERY FOR AUTOMATIC TRACKING OF CONVECTIVE CLOUD SYSTEMS AND SYSTEM FEATURES MONITORING: APPLICATION FOR THE CASE OF TWO FLOOD INCIDENTS IN GREECE. Haralambos N. Feidas, Univ. of Athens, Athens, Greece; and C. Cartalis
416	P3.37A	EXTRACTION OF MONSOON WINDS AND DETERMINATION OF TRAJECTORIES OF CONVECTIVE CLOUD ELEMENTS OVER WEST AFRICA. Andre Szantai, LMD/CNRS, Ecole Polytechnique, Palaiseau, France; and F. Desalmand and M. Desbois
•	P3.38B	RELATIONSHIPS OF GEOSTATIONARY METEOSAT SATELLITE DERIVED CONVECTIVE CLOUD CHARACTERISTICS, RAINFALL AND OROGRAPHY IN ETHIOPIA. Abebe Yeshanew, National Meteorological Services Agency, Addis Ababa, Ethiopia
•	P3.39A	COMPARISON BETWEEN COLD CLOUD DURATIONS, CB AND RAINFALL. Sow Cheikh Sadibou, Ecole Africaine de la Meteorologie et de l'Aviation Civile (EAMAC), Niamey, Niger
•	P3.40B	DIURNAL CYCLE OF CONVECTION OVER WESTERN AFRICA. Diori Salley, EAMAC, Niamey, Niger (Student Paper)
420	P3.41A	CLIMATOLOGICAL ASPECTS OF AFRICAN WAVES BASED ON REMOTE SENSING AND MODEL DATA. Wassila Thiaw, NOAA/NWS/NCEP, Washington, DC, USA
424	P3.42B	DETERMINATION OF THE DIURNAL WAVE OF THE LAND SURFACE TEMPERATURE WITH METEOSAT. Stephan Schaedlich, Univ. of Karlsruhe, Karlsruhe, Germany; and H. Fischer
426	P3.43A	CHARACTERIZATION OF LAND-SURFACES BY MODELLING DIURNAL TEMPERATURE WAVES EXTRACTED FROM METEOSAT-IR DATA. Frank-M. Göttsche, Inst. fur Meteorologie und Klimaforschung, Forschungszentrum Karlsruhe, Germany; and F. S. Olesen
428	P3.44B	MAPPING OF RADIATION BALANCE COMPONENTS IN HUNGARY USING METEOSAT DATA. Aniko Rimoczi-Paal, Hungarian Meteorological Service, Budapest, Hungary; and J. Mika, T. Szentimrey, R. Randriamampianina, and I. Dobi
430	P3.45A	SOLAR RADIATION MONITORING USING A PHYSICAL MODEL AND GOES 8-VIS IMAGERY. Juan C. Ceballos, INPE, Cachoeira Paulista, SP, Brazil; and R. C. G. Periera, E. J. B. Bastos, and E. C. Moraes
432	P3.46B	USING METEOSAT IMAGES TO MAP THE SOLAR RADIATION: IMPROVEMENT OF THE HELIOSAT METHOD. C. Rigollier, Ecole des Mines de Paris, Sophia Antipolis, France; and L. Wald (Student Paper)
434	P3.47A	SATELLIGHT: A WWW SERVER WHICH PROVIDES HIGH QUALITY DAYLIGHT AND SOLAR RADIATION DATA FOR WESTERN AND CENTRAL EUROPE. Marc Fontoynont, Ecole Nationale des Travaux Publics de l'Etat, Vauix en Velin, France; and D. Dumortier, D. Heinemann, A. Hammer, J. A. Olseth, A. Skartveit, P. Ineichen, C. Reise, J. Page, L. Roche, H. G. Beyer, and L. Wald
438	P3.48B	NOAA'S GEOSTATIONARY OPERATIONAL ENVIRONMENTAL SATELLITE (GOES) PROGRAM —STATUS REPORT. Gerald J. Dittberner, NOAA/NESDIS, Suitland, MD, USA
•	P3.49A	GOESNET OBSERVATION DELIVERY SYSTEM. Benjamin Watkins, NOAA/NESDIS, Satellite Service Division, Washington, DC, USA
442	P3.50B	THE NATIONAL WEATHER SERVICE GOES-8/9 ASSESSMENT: UPDATED RESULTS ON OPERATIONAL UTILITY OF GOES DIGITAL DATA. James J. Gurka, NOAA/NWS, Silver Spring, MD, USA; and S. Lord and R. S. Gird
	P3.51A	PAPER WITHDRAWN

* Manuscript not available

TABLE OF CONTENTS

NINTH CONFERENCE ON SATELLITE METEOROLOGY AND OCEANOGRAPHY

PAGE		
446	P3.52B1	EPPREPMEX, AN OPERATIONALLY RAINFALL ESTIMATION SYSTEM FOR MEXICO, BASED ON *IR-GOES* IMAGERY. Jorge Sanchez-Sesma, Inst. Mexicano de Tecnologia del Agua (IMTA), Jiutepec, Morelos, Mexico; and M. A. Sosa-Chinas
450	P3.52B2	AUTOMATIC GEOGRAPHICAL LOCALIZATION OF TROPICAL CYCLONES USING *IR-GOES* IMAGERY. Jorge Sanchez-Sesma, IMTA, Jiutepec, Morelos, Mexico; and M. A. Sosa-Chinas
*	P3.53A	EUROMET DEMONSTRATION STAND. José Prieto, EUMETSAT, Darmstadt, Hessen, Germany
•	P3.54B	THE ANALOGUE TO DIGITAL CONVERSION, THE NEW LRPT/LRIT FORMATS. Donald E. Hinsman, World Meteorological Organization, Geneva, Switzerland
452	P3.55A	A NEW ADVANCED DIGITAL SIGNAL PROCESSING RECEIVER FOR RECEPTION OF METEOROLOGICAL AND HYDROLOGICAL DATA. John N. Thompson, Signal Engineering, Inc. for Handar, Inc., San Diego, CA, USA
*	P3.56B	OPERATIONAL USE OF THE GROUND BASED SATELLITE RECEIVING SYSTEMS AT THE NIGERIAN METEOROLOGICAL SERVICES. Francis Adefuye, Nigerian Meteorological Services, Oshodi, Lagos, Nigeria
777	P3.57A	USE OF METEOSAT WV CHANNEL DATA FOR DETECTION OF MODEL ANALYSIS AND FORECAST ERRORS OF POTENTIAL VORTICITY FIELDS. Christo Georgiev, National Inst. of Meteorology and Hydrology, Sofia, Bulgaria
*	P3.58B	ON THE ROLE OF TROPICAL AND EXTRATROPICAL VORTICES IN THE ASIAN SUMMER MONSOON CIRCULATION. Brij Bhushan, Satellite Meteorology Division, New Delhi, India
	P3.59A	PAPER WITHDRAWN
454	P3.60B	NEW SATELLITE PRODUCTS AND SERVICES FOR NATIONAL WEATHER SERVICE OPERATIONS. Ron S. Gird, NOAA/NWS, Washington, DC, USA; and J. Gurka and S. Lord
458	P3.61A	BISPECTRAL SATELLITE TECHNIQUE FOR DELINEATING INTENSE CONVECTION: APPLICATIONS TO TROPICAL CYCLONES. Christopher S. Velden, CIMSS/Univ. of Wisconsin, Madison, WI, USA; and T. L. Olander
462	P3.62B	COMBINING GEOSTATIONARY AND SSM/I DATA FOR RAPID RAIN RATE ESTIMATION AND ACCUMULATION. F. Joseph Turk, NRL, Monterey, CA; and F. S. Marzano and E. A. Smith
466	P3.63A	6.7 MICRON WATER VAPOR AND TOTAL PRECIPITABLE WATER CHARACTERISTICS OF WESTERN USA WINTER STORMS DURING THE 1997-1998 EL NINO. Rod A. Scofield, NOAA/NESDIS/ORA, Washington, DC, USA; and G. A. Vicente and B. Rabin
470	P3.64B	COMBINATION OF THE GOES-8/9 INFRARED CHANNEL AND RADAR DATA FOR REAL TIME, HIGH RESOLUTION RAINFALL RATE ESTIMATION. Gilberto A. Vicente, NOAA/NESDIS/ORA, Washington, DC, USA; and R. A. Scofield
	ORAL SESSIONS O4A AND O4B: NEW SENSORS AND TECHNOLOGY	
472	O4.1A	SATELLITE REMOTE SENSING IN THE 21ST CENTURY: LESSONS FROM ADEOS, TRMM AND SEAWIFS. Akimasa Sumi, Univ. of Tokyo, Tokyo, Japan
*	O4.2A	THE ADEOS PROGRAM AND ITS OUTREACH. Haruhisa Shimoda, NASDA, Tokyo, Japan
*	O4.3A	SCIENCE RESULTS FROM NSCAT. Timothy Liu, Jet Propulsion Lab., Pasadena, CA, USA
*	O4.4A	EARLY RESULTS FROM THE TROPICAL RAINFALL MEASURING MISSION. Christopher D. Kummerow, NASA/GSFC, Greenbelt, MD, USA

• Manuscript not available

TABLE OF CONTENTS

NINTH CONFERENCE ON SATELLITE METEOROLOGY AND OCEANOGRAPHY

PAGE

• O4.5B EARLY RESULTS FROM SEAWIFS. John Brock, NOAA Coastal Services Center, Charleston, SC, USA

• O4.6B GPS METEOROLOGY VIA RADIO OCCULTATION TECHNIQUES. Per Hoegh, Danish Meteorological Inst., Copenhagen, Denmark

476 O4.7B COMPARISONS BETWEEN AMSU AND DMSP MEASUREMENTS. Norman C. Grody, NOAA/NESDIS/ORA, Washington, DC, USA; and F. Weng and R. R. Ferraro

POSTER SESSIONS P4A AND P4B: NEW SENSORS AND TECHNOLOGY

480 P4.1A THE ERS SCATTEROMETER MISSIONS AFTER MORE THAN SEVEN YEARS OF OPERATIONS. Pascal Lecomte, European Space Agency (ESA)/ESRIN, Frascati, Italy

484 P4.2B A COMPARISON OF SURFACE WINDSPEED, DERIVED FROM SSM/I DATA BY MEANS OF A 1DVAR SCHEME, WITH ERS SCATTEROMETER MEASUREMENTS. Jeff Ridley, UK Met Office, Bracknell, Berks., UK

485 P4.3A TANDEM ERS SCATTEROMETER IMPACT ON HIRLAM FORECASTS. Ad Stoffelen, KNMI, De Bilt, The Netherlands; and P. Von Beukering

489 P4.3B1 OCEAN SURFACE WINDS: SATELLITE AND AIRCRAFT SCATTEROMETER MEASUREMENTS OF HURRICANE FRAN. James R. Carswell, Univ. of Massachusetts, Amherst, MA, USA; and W. J. Donnelly, P. S. Chang, and R. E. McIntosh

493 P4.4B AN ANALYSIS OF TROPICAL CYCLONE GENERATION BY ADEOS/NSCAT DATA. Tetsuo Nakazawa, MRI, Tsukuba, Ibaraki, Japan; and R. F. Milliff

497 P4.5A POLDER: A COMPREHENSIVE SET OF KEY GEOPHYSICAL PARAMETERS FOR OCEANOGRAPHY AND CLIMATE RESEARCH. Anne Lifermann, Centre National d'Etudes Spatiales, Toulouse, France

500 P4.6B COMPARISON OF THE POLDER CLOUD DETECTION OVER OCEAN WITH A METEOSAT CLOUD CLASSIFICATION. Genevieve Seze, LMD/CNRS, and Univ. P. et M. Curie, Paris, France; and C. Vanbauce, J.-C. Buriez, F. Parol, and P. Couvert

• P4.7A SEAWIFS VS. SHIPBOARD MEASUREMENTS: EARLY INTERCOMPARISON RESULTS FROM THE REGION OFFSHORE SOUTHERN CALIFORNIA. Kota S. Prasad, SeaSpace Corp., San Diego, CA, USA

• P4.8B SEAWIFS AND MOS, TWO NEW OCEAN COLOR SENSORS, PRODUCTS, PRESENTATION AND VALIDATION. Jean-Manuel Melinotte, ESA/ESRIN, Frascati, Italy

* P4.9A AN EXPERIMENTAL STUDY COMPARING PATTERNS IN SAR AND AVHRR IMAGERY AND IN OCEAN COLOR OVER THE SOUTHEAST BERING SEA. Bernie Walter, NorthWest Research Associates, Bellevue, WA, USA

* P4.10B RECENT IMPROVEMENTS IN GLOBAL MERGED PRECIPITATION ANALYSES RELATED TO THE GLOBAL PRECIPITATION CLIMATOLOGY PROJECT (GPCP) AND TO THE USE OF TRMM DATA. Robert F. Adler, NASA/GSFC, Greenbelt, MD, USA

505 P4.11A RETRIEVAL OF PRECIPITATION AND LATENT HEATING PROFILES FROM COMBINED TRMM TMI/PR/VIRS OBSERVATIONS. William S. Olson, Univ. of Maryland, Baltimore, MD, USA; and C. D. Kummerow, N. F. Viltard, and Y. Hong

509 P4.12B RETRIEVAL OF PRECIPITATION FROM SATELLITE PASSIVE MICROWAVE DATA USING A PHYSICAL/STATISTICAL APPROACH IN THE CONTEXT OF TRMM. Nicolas F. Viltard, USRA and NASA/GSFC, Greenbelt, MD, USA; and C. D. Kummerow, Y. Hong, and W. S. Olson

• Manuscript not available

TABLE OF CONTENTS

NINTH CONFERENCE ON SATELLITE METEOROLOGY AND OCEANOGRAPHY

PAGE		
*	P4.13A	PRELIMINARY INTERCOMPARISON RESULTS OF TRMM PRECIPITATION PROFILE ALGORITHMS. Song Yang, Florida State Univ., Tallahassee, FL, USA
*	P4.14B	INITIAL PERFORMANCE ASSESSMENT OF TRMM RADAR-RADIOMETER COMBINED PRECIPITATION RETRIEVAL ALGORITHMS. Eric A. Smith, Florida State Univ., Tallahassee, FL, USA
*	P4.15A	PRELIMINARY RESULTS FROM THE TRMM MICROWAVE IMAGER. Thomas T. Wilheit, Texas A&M Univ., College Station, TX, USA
*	P4.16B	A NEW SURFACE RAINFALL RETRIEVAL ALGORITHM FOR APPLICATION TO SSM/I DATA. Peter Bauer, DLR, DFD-US, Koeln, Germany
513	P4.17A	FUSION OF SURFACE RADAR AND SATELLITE RAINFALL DATA USING FEATURE CALIBRATION AND ALIGNMENT. Christopher Grassotti, AER Inc., Cambridge, MA, USA; and R. N. Hoffman and H. Iskenderian
517	P4.18B	ADJUSTMENT OF MONTHLY MICROWAVE RAINFALL ESTIMATES OVER AMAZONIA. E. N. Anagnostou, USRA, Greenbelt, MD, USA; and A. J. Negri and R. F. Adler
521	P4.19A	CHARACTERIZATION OF THE RADIO OCCULTATION MEASUREMENT AND DATA PROCESSING ERRORS FOR NWP. Juha-Pekka Luntama, UK Met Office, Bracknell, Berks., UK
522	P4.20B	COMPARING GPS RADIO OCCULTATION BENDING ANGLE MEASUREMENTS WITH VALUES SIMULATED BY A GEOMETRICAL OPTICS FORWARD OPERATOR USING NUMERICAL WEATHER PREDICTION ANALYSES. S. B. Healy, UK Met Office, Bracknell, Berks., UK; and D. Offiler and J. R. Eyre
523	P4.21A	GROUND-BASED GPS WATER VAPOUR ESTIMATION FOR METEOROLOGICAL FORECASTING. H. C. Baker, Univ. of Nottingham, Nottingham, UK; and A. H. Dodson, D. Jerrett, and D. Offiler
527	P4.22B	GPS PRECIPITABLE WATER MEASUREMENTS MADE DURING THE SALPEX'96 EXPERIMENT. Mark Falvey, Victoria Univ., Wellington, New Zealand; and J. Beavan and J. McGregor
*	P4.23A	METEOROLOGICAL APPLICATION FROM A EUROPEAN GROUND BASED GPS NETWORK. Eva Borbas, Hungarian Meteorological Service, Budapest, Hungary
531	P4.24B	SIMULATION OF FULL DATA ASSIMILATION CYCLE COMPARISON. Luis Kornblueh, Max-Planck-Inst. for Meteorology, Hamburg, Germany; and M. Gorbunov and L. Bengtsson
535	P4.25A	GPS/MET JAPAN SUMMER CAMPAIGN 1997 IN TSUKUBA. Yoshinori Shoji, MRI, Tsukuba, Ibaraki, Japan; and H. Seko, K. Aonashi, H. Nakamura, A. Ichiki and members of GPS/MET Japan Summer Campaign 1997 in Tsukuba
*	P4.26B	AN OVERVIEW OF NOAA/NESDIS DATA PROCESSING SYSTEMS AND DERIVED PRODUCTS FOR NOAA-K. Pam Taylor, NOAA/NESDIS, Washington, DC, USA
537	P4.27A	A CLOUD TOP PHASE CLASSIFICATION ALGORITHM FOR USE WITH NOAA-K DATA. Keith D. Hutchison, Lockheed Martin Missiles & Space, CREST, Sunnyvale, CA, USA
541	P4.28B	EXPECTED VERTICAL TEMPERATURE AND HUMIDITY SOUNDINGS FROM THE ADVANCED INSTRUMENTATION ONBOARD THE NOAA-K SERIES SATELLITES USING STATE OF THE ART RETRIEVAL ALGORITHMS. Hal J. Bloom, Raytheon-STX Corp., Lanham, MD, USA; and E. J. Kratz and A. H.-L. Huang
545	P4.29A	PROCESSING ATOVS: A NEW GENERATION OF SATELLITE SOUNDING DATA. B. R. Barwell, UK Met Office, Bracknell, Berks., UK; and S. J. English and J. R. Eyre

* Manuscript not available

TABLE OF CONTENTS

NINTH CONFERENCE ON SATELLITE METEOROLOGY AND OCEANOGRAPHY

PAGE		
547	P4.30B	THE RETRIEVAL OF TEMPERATURE AND WATER VAPOR PROFILES FROM ATOVS DATA: AN ADAPTATION OF THE 3I-SCHEME. M. Herveou, LMD/CNRS, Palaiseau, France; and N. A. Scott, R. Armante, and A. Chedin
*	P4.31A	THE FAST PENALIZED LIBRARY METHOD FOR IMPROVED AMSU WATER VAPOR RETRIEVALS. Hung-Lung Huang, CIMSS/Univ. of Wisconsin, Madison, WI, USA
551	P4.32B	THE AVHRR DATA ON AMSU-A/B FOOTPRINTS. Dongsoo Kim, CIRES/Univ. of Colorado and NOAA/FSL, Boulder, CO, USA
553	P4.33A	THE EFFECTS OF CLOUD AND PRECIPITATION ON AMSU BRIGHTNESS TEMPERATURES: SIMULATING THE DATA AND TESTING THE DATA PROCESSING SCHEME. Andrew J. Smith, UK Met Office, Bracknell, Berks., UK; and S. English and R. J. Renshaw
554	P4.34B	IMPROVED FORECASTING OF STORMS USING SATELLITE BORNE IR INTERFEROMETRY. D. Pick, UK Met Office, Farnborough, Hants, UK; and H. Mooney
555	P4.35A	A COMPARISON OF THE MODIS AND MISR CLOUD MASKS AS APPLIED TO GLOBAL AVHRR LAC DATA. Larry Di Girolamo, Univ. of Arizona, Tucson, AZ, USA; and S. Ackerman and E. Clothiaux
*	P4.36B	THE DEVELOPMENT OF THE EOS-PM ADVANCED MICROWAVE SCANNING RADIOMETER (AMSR) LAND RAIN RATE RETRIEVAL ALGORITHM. Yiping Wang, NOAA/NESDIS/Systems Engineering and Security, Inc., Camp Springs, MD, USA
*	P4.37A	LAND SURFACE PROCESSES AND INTERACTIONS MISSION. Jean-Yves Labandibar, Aerospatiale, Space and Defense, Cannes la Bocca, France
*	P4.38B	ENVIRONMENTAL DATA RECORD (EDR) SIMULATION TO EVALUATE THE MILITARY VALUE OF NPOESS. David J. Smalley, SenCom Corp., Bedford, MA, USA
557	P4.39A	THE EUMETSAT POLAR SYSTEM (EPS). M. Langevin, EUMETSAT, Darmstadt, Germany; and K. D. Klaes, B. Marcorelles, and J. Perez
561	P4.40B	THE MISSIONS OF THE EPS/METOP SYSTEM. K. Dieter Klaes, EUMETSAT, Darmstadt, Germany; and M. Langevin, B. Marcorelles, and E. Oriol-Pibernat
*	P4.41A	HYPERSPECTRAL IMAGING SPECTROMETERS FOR FUTURE EARTH OBSERVING SYSTEMS. Jeffery J. Puschell, Raytheon Systems Co., Goleta, CA, USA
*	P4.42B	COMPARATIVE ASSESSMENT OF SEMIEMPIRICAL ATMOSPHERIC CORRECTION METHODS FOR AVIRIS SPECTROMETRIC DATA. Corina Alecu, National Inst. of Meteorology and Hydrology, Bucharest, Romania
*	P4.43A	VERTICAL SOUNDING TECHNIQUE FOR HYPERSPECTRAL INFRARED MEASUREMENTS. Hung-Lung Huang, CIMSS/Univ. of Wisconsin, Madison, WI, USA
*	P4.44B	OBSERVATIONS OF ATMOSPHERIC VARIABILITY IN HYPERSPECTRAL IMAGERY. Mark Abrams, ITT Aerospace, Ft. Wayne, IN, USA
565	P4.45A	THE ATMOSPHERIC PROFILING EARTH WATCH MISSION—A TOOL FOR OPERATIONAL METEOROLOGY, CLIMATE AND SPACE WEATHER MONITORING AND PREDICTION. Paul Ingmann, European Space Research and Technology Center, Noordwijk, The Netherlands; and P. Silvestrin
569	P4.46B	RETRIEVAL OF COLUMNAR WATER VAPOUR PATH OVER LAND FROM ENVISAT'S MERIS. R. Bennartz, Freie Univ., Berlin, Germany; and J. Fischer

* Manuscript not available

TABLE OF CONTENTS

NINTH CONFERENCE ON SATELLITE METEOROLOGY AND OCEANOGRAPHY

PAGE		
571	P4.47A	RETRIEVAL OF ATMOSPHERIC PARAMETERS FROM ENVISAT'S MERIS. J. Fischer, Freie Univ., Berlin, Germany; and R. Bennartz, T. Heinemann, R. Preusker, and L. Schüller
•	P4.48B	MEDIUM RESOLUTION IMAGING SPECTROMETER (MERIS). G. Baudin, Aerospatiale, Space and Defense, Cannes la Bocca, France
574	P4.49A	RETRIEVAL OF CLOUD OPTICAL THICKNESS AND CLOUD ALBEDO FROM THE MEDIUM RESOLUTION IMAGING SPECTROMETER (MERIS). L. Schüller, Freie Univ., Berlin, Germany; and R. Preusker and J. Fischer
577	P4.50B	RETRIEVAL OF CLOUD TOP PRESSURE FROM MERIS. R. Preusker, Freie Univ., Berlin, Germany; and L. Schüller and J. Fischer
•	P4.51A	THE MICROWAVE HUMIDITY SOUNDER (MHS) QUASI-OPTICAL NETWORK. Laurent Costes, Matra Marconi Space, Toulouse, France
•	P4.52B	THE STRATOSPHERIC AEROSOL AND GAS EXPERIMENT III. Larry W. Thomason, NASA/LRC, Hampton, VA, USA
579	P4.53A	OPTIMIZATION OF SAGE III SPECTRAL CHANNELS FOR WATER VAPOR RETRIEVAL. Er-Woon Chiou, Science Applications International Corp. (SAIC), Hampton, VA, USA; and W. P. Chu and L. W. Thomason
583	P4.54B	COMPUTER SIMULATION OF THE STRATOSPHERIC AEROSOL AND GAS EXPERIMENT (SAGE III). Didier F. Rault, NASA/LRC, Hampton, VA, USA
587	P4.55A	SATELLITE REMOTE SENSING OF TEMPERATURE AND PRESSURE BY THE STRATOSPHERIC AEROSOL AND GAS EXPERIMENT III. Michael C. Pitts, SAIC, Hampton, VA, USA; and L. W. Thomason and W. P. Chu
591	P4.56B	INFORMATION CONTENT AND RETRIEVAL ERROR ANALYSIS FOR REMOTE SENSING OF ATMOSPHERIC TRACE GASES COLUMN AMOUNTS BY IASI. Alexander B. Uspensky, Scientific Research Center PLANETA, Moscow, Russia; and A. N. Trotsenko, A. N. Rublev, and S. V. Romanov
594	P4.57A	IASI DATA INFORMATION CONTENT: INSTRUMENT CHARACTERIZATION AND THE IMPACT OF A PRIORI INFORMATION. P. Prunet, CNRM, Météo-France, Toulouse, France; and V. Casse and J.-N. Thepaut
*	P4.58B	IASI: THE NEW GENERATION INFRARED SOUNDER OF METOP. C. Singer, Aerospatiale, Space and Defense, Cannes la Bocca, France
•	P4.59A	INCOHERENT WIND LIDARS AS A FUTURE OPERATIONAL SYSTEM: RECENT PROGRESS. Didier Morancais, Matra Marconi Space, Toulouse, France
598	P4.60B	4D VARIATIONAL ASSIMILATION OF OZONE AND DOPPLER WIND LIDAR DATA. J. Pailleux, CNRM, Météo-France, Toulouse, France; and A. Baverez, C. Cardinali, and J.-N. Thepaut
*	P4.61A	ALADIN: ATMOSPHERIC LASER DOPPLER WIND LIDAR INSTRUMENT FOR WIND VELOCITY MEASUREMENTS FROM SPACE. R. Krawczyk, Aerospatiale Space and Defense, Cannes la Bocca, France
*	P4.62B	WATER VAPOR AND WIND VELOCITY MEASUREMENTS FROM SPACE USING 2 MICRON LIDAR. J. H. Ghibaudo, Aerospatiale, Space and Defense, Cannes la Bocca, France
764	P4.63A	SATELLITE OCEANOGRAPHY IN ESA EARTH OBSERVATION PROGRAMS. Guy Duchossois, ESA, Paris, France; and E. Oriol-Pibernat

* Manuscript not available

TABLE OF CONTENTS

NINTH CONFERENCE ON SATELLITE METEOROLOGY AND OCEANOGRAPHY

PAGE

600 P4.64B NESDIS OPERATIONAL SOUNDING PRODUCT SYSTEMS FOR NOAA AND DMSP POLAR ORBITING SATELLITES. Anthony L. Reale, NOAA/NESDIS, Washington, DC, USA; and M. W. Chalfant and E. B. Brown

604 P4.65A A NEW PRECIPITATION ALGORITHM BASED ON TRMM SENSOR SYNERGY. Peter Bauer, DLR, Cologne, Germany; and L.-C. Schanz, J. Schulz, R. Bennartz, and J. Testud

ORAL SESSIONS O5A AND O5B: APPLICATION OF SATELLITE OBSERVATIONS FOR MONITORING AND PREDICTION OF OCEANIC AND ATMOSPHERIC VARIABILITY (UNESCO IOC Year of the Ocean)

• O5.1A SPACE OBSERVATIONS IN SUPPORT OF A GLOBAL OCEAN OBSERVING SYSTEM. Michel LeFebvre, Ocean Obs. Panel for Climate, Villeneuve, Tolosane, France

• O5.2A SST FRONTS IN THE WORLD OCEAN. Peter Comillon, Univ. of Rhode Island, Narragansett, RI, USA

• O5.3A SCIENTIFIC AND TECHNICAL MERITS OF OCEAN SURFACE SALINITY REMOTE SENSING BY SATELLITE. Gary Lagerloef, Earth and Space Research, Seattle, WA, USA

• O5.4A SSM/I: A DECADE LONG SATELLITE WIND PRODUCT. David Adamec, NASA/GSFC, Greenbelt, MD, USA

* O5.5B FOAM GOES OPERATIONAL. Mike Bell, UK Met Office, Bracknell, Berks., UK

* O5.6B OCEAN DATA ASSIMILATION FOR MERCATOR. Pierre De Mey, LEGOS/GRGS, Toulouse, France

* O5.7B THE GLOBAL OCEAN DATA ASSIMILATION EXPERIMENT (GODAE). Philippe Courtier, CNES, Toulouse, France

POSTER SESSIONS P5A AND P5B: APPLICATION OF SATELLITE OBSERVATIONS FOR MONITORING AND PREDICTION OF OCEANIC AND ATMOSPHERIC VARIABILITY (UNESCO IOC Year of the Ocean)

* P5.1A ON THE INITIALISATION OF A COUPLED OCEAN/ATMOSPHERE MODEL IN THE PRESENCE OF OCEAN DATA ASSIMILATION. Philippe Rogel, CERFACS, Toulouse, France

607 P5.2B ALTIMETER DATA ASSIMILATION FOR SEASONAL FORECASTING. J. Alves, ECMWF, Reading, Berks., UK; and J. Segschneider, K. Haines, D. Anderson, M. Balmaseda, and T. Stockdale

* P5.3A SEASONAL TO DECADAL CHANGES IN OCEAN TOPOGRAPHY AND CIRCULATION FROM SATELLITE ALTIMETRY. Chet Koblinsky, NASA/GSFC, Greenbelt, MD, USA

* P5.4B DATA ASSIMILATION OF REMOTE SENSED SEA SURFACE TEMPERATURE ON THE ATLANTIC BASIN AND A NESTED WINDOW VIA A HYDRODYNAMIC MODEL. M. Ouberdous, Joint Research Centre, Space Applications Inst., ISPRA, Varese, Italy

• P5.5A NON-SEASONAL SEA SURFACE TEMPERATURE AND SEA SURFACE HEIGHT ANOMALY CORRELATIONS. Kenneth S. Casey, USRA, Greenbelt, MD, USA

611 P5.6B REFORMATION TIME FOR THE THERMAL SKIN LAYER OF THE OCEAN. M. R. Mobasheri, Islamic Republic of Iran Meteorological Organization, Tehran, Iran

619 P5.7A INVESTIGATING THE THERMAL SKIN OF THE OCEAN BY SATELLITE. Brett Candy, UK Met Office, Bracknell, Berks., UK

620 P5.8B DIURNAL HEATING OF SEA SURFACE TEMPERATURE IN THE EASTERN PACIFIC OBSERVED USING SATELLITE DATA. Gary A. Wick, CIRES/Univ. of Colorado and NOAA/Climatic Diagnostics Center (CDC), Boulder, CO, USA; and J. J. Bates

• Manuscript not available

TABLE OF CONTENTS

NINTH CONFERENCE ON SATELLITE METEOROLOGY AND OCEANOGRAPHY

PAGE		
624	P5.9A	COMPARISON OF SKIN TEMPERATURES FROM THE MAPS/RUC FORECAST MODEL AND FROM GOES-8. Dongsoo Kim, CIRES/Univ. of Colorado and NOAA/FSL, Boulder, CO, USA; and S. Benjamin, T. Smirnova, and J. Brown
*	P5.10B	REMOTE SENSING OF TOPOGRAPHICALLY-INDUCED UPWELLING ALONG THE SOUTHERN COAST OF SICILY. Farid Askari, SACLANT Undersea Research Centre, La Spezia, Italy
*	P5.11A	TRANSPORT PATTERN OF BLACK SEA WATER INTO THE N AEGEAN SEA BASED ON NOAA-AVHRR AND CZCS. Lennart Jönsson, Dept. of Water Resources Engineering, Lund, Sweden
626	P5.12B	THE DISTRIBUTION AND DYNAMICS OF SUSPENDED PARTICULATE MATTER IN BELGIAN COASTAL WATERS DERIVED FROM AVHRR IMAGERY. Kevin Ruddick, Management Unit of the Mathematical Models of the North Sea and Scheldt Estuary (MUMM), Brussels, Belgium; and F. Ovidio, D. Van den Eynde, and A. Vasilkov
630	P5.13A	THE ATMOSPHERIC DYNAMICS MISSION—A TOOL FOR SATELLITE WIND OBSERVATIONS. P. Ingmann, ESRTC, Noordwijk, The Netherlands; and J. Fuchs
633	P5.14B	1997 ENSO FROM ADEOS/NSCAT DATA. Tetsuo Nakazawa, MRI, Tsukuba, Ibaraki, Japan
*	P5.15A	SEASONAL AND INTERANNUAL VARIABILITY IN THE TROPICAL PACIFIC OCEAN: ASSESSMENT OF REANALYSIS AND SSM/I SURFACE WINDS. Michele M. Rienecker, NASA/GSFC, Greenbelt, MD, USA
635	P5.16B	SSM/I ESTIMATION OF OCEAN SURFACE WIND SPEEDS IN LITTORAL ZONES. T. Bellerby, Univ. of Hull, Hull, UK; and M. Taberner and A. Wilmshurst
639	P5.17A	GLOBAL DISTRIBUTION OF SSM/I RAINFALL RETRIEVAL ERROR. Qihang Li, NOAA/NESDIS, Camp Springs, MD, USA; and R. Ferraro and N. C. Grody
643	P5.18B	EXPLAINING SOURCES OF DISCREPANCY BETWEEN SSM/I WATER VAPOR ALGORITHMS. B.-J. Sohn, Seoul National Univ., Seoul, Korea; and E. A. Smith
646	P5.19A1	CLOREVAL: SSM/I LIQUID WATER PATH VALIDATION. David Offiler, UK Met Office, Bracknell, Berks, UK; and L. Eymard, H. Gang, E. Gerard, and D. Kilham
650	P5.19A2	CLOREVAL: SSM/I LIQUID WATER PATH VALIDATION: RESULTS. David Kilham, Univ. of Bristol, Bristol, UK; and D. Offiler, H. Gang, L. Eymard, and E. Gerard
653	P5.20B	DIRECT ASSIMILATION OF MULTICHANNEL MICROWAVE BRIGHTNESS TEMPERATURES INTO A MESOSCALE NUMERICAL WEATHER PREDICTION MODEL. Kazumasa Aonashi, MRI, Tsukubai, Ibaraki, Japan; and G. Liu
656	P5.21A	A VARIATIONAL ASSIMILATION OF SSM/I RETRIEVED COLUMN INTEGRATED WATER VAPOR. Godelieve Deblonde, AES, Dorval, PQ, Canada
660	P5.22B	3/4DVAR ASSIMILATION OF SSM/I TOTAL COLUMN WATER VAPOUR IN THE ECMWF SYSTEM. Elisabeth Gerard, ECMWF, Reading, Berks., UK; and R. W. Saunders
664	P5.23A	ASSIMILATION OF SATELLITE DATA INTO US NAVY MODELS. R. L. Crout, Naval Meteorology and Oceanography Command, Stennis Space Center, MS, USA; and D. L. Durham, E. T. Petruncio, and J. B. Boatman
*	P5.24B	DYNAMIC AND THERMODYNAMIC REGULATION OF SEA SURFACE TEMPERATURES. Tianming Li, NRL, Monterey, CA, USA

* Manuscript not available

TABLE OF CONTENTS

NINTH CONFERENCE ON SATELLITE METEOROLOGY AND OCEANOGRAPHY

PAGE		
668	P5.25A	A PHYSICAL FORMULATION OF ATMOSPHERIC TRANSMITTANCES FOR THE OPERATIONAL ASSIMILATION OF SATELLITE INFRARED RADIANCES. Louis Garand, AES, Dorval, PQ, Canada; and D. S. Turner, C. Chouinard, and J. Halle
670	P5.26B	DMSP MICROWAVE SOUNDER MEASUREMENTS IN THE INITIALIZATION AND ASSIMILATION OF A REGIONAL WEATHER PREDICTION SYSTEM USING THE MM5 MODEL. Lei Shi, SeaSpace Corp., San Diego, CA, USA; and D. E. Waliser
672	P5.27A	RADIANCE ASSIMILATION OF POLAR AND GEOSTATIONARY SATELLITE DATA IN LAPS. Daniel Birkenheuer, NOAA/FSL, Boulder, CO, USA
*	P5.28B	THE USE OF SATELLITE WATER VAPOUR IMAGERY AND POTENTIAL VORTICITY CONCEPTS IN SHORT-RANGE WEATHER FORECASTING. Meral Demirtas, UK Met Office, Reading, Berks., UK
*	P5.29A	IMPLEMENTATION OF THE ASSIMILATION OF TOVS RADIANCES AT METEO-FRANCE. Philippe Caille, Météo-France, Toulouse, France
676	P5.30B	USE OF (A)TOVS RADIANCES IN 3DVAR. R. J. Renshaw, UK Met Office, Bracknell, Berks., UK; S. J. English, J. R. Eyre, and A. J. Smith
*	P5.31A	VARIATIONAL APPROACH TO CLOUD-CLEARING AS APPLIED TO TOVS OBSERVATIONS. Joanna Joiner, NASA/GSFC, Data Assimilation Office, Greenbelt, MD, USA
677	P5.32B	A "FAST" FORWARD MODEL FOR SSMIS: A NEURAL NETWORK APPLICATION. Barbara A. Burns, GenCorp Aerojet, Azusa, CA, USA; and A. P. Stogryn
*	P5.33A	GENERATION AND VALIDATION OF FAST FORWARD MODELS FOR ADVANCED INFRARED SOUNDERS. L. Larrabee Strow, Univ. of Maryland, Baltimore, MD, USA
678	P5.34B	A SIMPLE METHOD FOR PARAMETERIZING THE EFFECTS OF INHOMOGENEITY ON SOLAR RADIATIVE TRANSFER IN CLOUDS, WITH APPLICABILITY TO THE GLOBAL REMOTE SENSING OF CLOUD PROPERTIES. Grant W. Petty, Purdue Univ., W. Lafayette, IN, USA
682	P5.35A	THE 1997 SPECTROSCOPIC GEISA DATABASE SYSTEM AND THE SECOND GENERATION VERTICAL SOUNDERS RADIANCE SIMULATION. N. Jacquinet-Husson, LMD/CNRS, Palaiseau, France; and N. A. Scott, A. Chedin, A. Barbe, V. G. Tuyterev, J. P. Champion, M. Winnewisser, L. R. Brown, R. Gamache, V. F. Golovko, and A. A. Chursin
686	P5.36B	FAST RADIATIVE TRANSFER MODEL BASED ON THE LINE-BY-LINE CALCULATION LOOK-UP TABLES. Anatoly N. Trotsenko, Russian Research Center, Kurchatov Inst., Moscow, Russia; and A. V. Kopylov and A. B. Uspensky
690	P5.37A	A FAST AND ACCURATE NEURAL NETWORK-BASED COMPUTATION OF LONGWAVE RADIATIVE BUDGET: APPLICATION IN A GCM. F. Chevallier, LMD/CNRS, Ecole Polytechnique, Palaiseau, France; and F. Cheruy, Z. X. Li, and N. A. Scott
694	P5.38B	AN IMPROVED FAST RADIATIVE TRANSFER MODEL FOR ASSIMILATION OF SATELLITE RADIANCE OBSERVATIONS. R. W. Saunders, ECMWF, Reading, Berks., UK; and M. Matricardi and P. Brunel
698	P5.39A	TWO-STREAM APPROXIMATION FOR MICROWAVE RADIATIVE TRANSFER: APPLICATIONS FOR REMOTE SENSING OF ICE CLOUDS. Fuzhong Weng, NOAA/NESDIS/ORA, Washington, DC, USA; and N. C. Grody
*	P5.40B	NUMERICAL EXPERIMENTS WITH THE C4 MONTE CARLO BROADBAND RADIATIVE TRANSFER MODEL. I. A. Podgorny, Scripps Inst. of Oceanography, La Jolla, CA, USA

* Manuscript not available

TABLE OF CONTENTS

NINTH CONFERENCE ON SATELLITE METEOROLOGY AND OCEANOGRAPHY

PAGE		
702	P5.41A	A FAST RADIATIVE TRANSFER MODEL FOR IASI. Marco Matricardi, ECMWF, Reading, Berks., UK; and R. W. Saunders
706	P5.42B	USE OF A NEW, FAST RADIATIVE TRANSFER MODEL FOR DIRECT RADIANCE ASSIMILATION IN THE GLOBAL DATA ASSIMILATION SYSTEM AT NCEP. Thomas J. Kleespies, NOAA/NESDIS/ORA, Washington, DC, USA; and J. Derber
*	P5.43A	REFLECTANCE OF LIGHT FROM WHITECAPS. Alexander A. Kokhanovsky, IMVT/UVT, Clausthal Technical Univ., Clausthal-Zellerfeld, Germany
710	P5.44B	EFFECTIVE ACCURACY OF MODELS CONVERTING SATELLITE RADIANCES TO HOURLY SURFACE INSOLATION. Antoine Zelenka, Swiss Meteorological Inst., Zurich, Switzerland; and R. Perez, R. Seals, and D. Renne
714	P5.45A	INTERCALIBRATION OF GOES, METEOSAT, GMS, HIRS, AND AVHRR INFRARED RADIANCES. Steve Wanzong, CIMSS/Univ. of Wisconsin, Madison, WI, USA; and W. P. Menzel and G. Callan
718	P5.46B	CORRECTION FOR SPURIOUS TRENDS IN THE 3I REANALYSIS OF TOVS DATA. R. Armante, LMD/CNRS, Ecole Polytechnique, Palaiseau, France; and L. Crepeau, N. A. Scott, and A. Chedin
722	P5.47A	THE USE OF SATELLITE INFORMATION IN CORRECTING MODEL-PREDICTED CLOUDS. Dongsoo Kim, CIRES/Univ. of Colorado and NOAA/FSL, Boulder, CO, USA; and J. Brown, S. Benjamin, and T. Smirnova
*	P5.48B	USING MULTISENSOR SATELLITE CLOUD RETRIEVAL IN POLAR REGIONS FOR THE INITIALISATION OF NUMERICAL SIMULATIONS OF POLAR LOWS WITH A LIMITED AREA MODEL. Michael Lieder, Meteorologisches Inst. der Univ. Bonn, Bonn, Germany
*	P5.49A	ASSIMILATING CLOUD DATA FROM SATELLITE OBSERVATIONS INTO NCEP'S ETA MODEL TO IMPROVE CLOUD AND PRECIPITATION FORECASTS. Qingyun Zhao, GSC/EMC/NCEP, Camp Springs, MD, USA
*	P5.50B	ASSIMILATION OF SATELLITE CLOUD OBSERVATIONS USING 4DVAR TECHNIQUE AND A MESOSCALE FORECAST MODEL. Tomislava Vukicevic, NCAR, Boulder, CO, USA
724	P5.51A	SIMULATION OF TROPICAL CONVECTIVE RAINFALL IN THE U.K. MET OFFICE GLOBAL NWP MODEL. Mark A. Ringer, UK Met Office, Bracknell, Berks., UK
728	P5.52B	THE CLOUDS AND THE EARTH'S RADIANT ENERGY SYSTEM (CERES) EXPERIMENT. Gary G. Gibson, NASA/LRC, Hampton, VA, USA; and B. A. Wielicki and B. R. Barkstrom
*	P5.53A	EVALUATION OF NCEP GLOBAL FORECAST MODEL WITH CERES MEASUREMENTS. Shi-Keng Yang, Research & Data Systems Corp. and NOAA/NWS/NCEP, Washington, DC, USA
732	P5.54B	HIGH SPECTRAL RESOLUTION RADIATIVE TRANSFER MODEL FOR IR AND NIR ATMOSPHERIC AND CLOUD REMOTE SENSING APPLICATIONS. Catherine Gautier, Univ. of California, Santa Barbara, CA, USA; and Y. Shiren and P. Ricchiazzi
*	P5.55A	VARIABILITY OF OCEAN SURFACE CO2 AND AIR-SEA CO2 FLUX IN THE EQUATORIAL PACIFIC AND ATLANTIC OCEANS. Jacqueline Boutin, LODYC/UPMC, Paris, France
*	P5.56B	RADIATIVE HEATING AND CLOUD EFFECT AT THE OCEAN SURFACE DERIVED FROM TOGA COARE AND GMS MEASUREMENTS. Ming-Dah Chou, NASA/GSFC, Greenbelt, MD, USA
736	P5.57A	GEOSTATIONARY EARTH RADIATION BUDGET EXPERIMENT (GERB). R. Mossavati, Imperial College, London, UK; and J. Harries, S. Kellock, R. Wrigley, N. Fox, J. Mueller, M. Caldwell, E. Sawyer, and J. Delderfield

* Manuscript not available

TABLE OF CONTENTS

NINTH CONFERENCE ON SATELLITE METEOROLOGY AND OCEANOGRAPHY

PAGE		
739	P5.58B	THE EARTH RADIATION MISSION—A TOOL FOR IMPROVING CLIMATE PREDICTION. P. Ingmann, European Space Research and Technology Center, Noordwijk, The Netherlands; and W. Leibrandt
743	P5.59A	HIGH TEMPORAL AND SPATIAL VARIABILITY OF SURFACE RADIATION BUDGET COMPONENTS. Franz H. Berger, Dresden Univ. of Technology, Tharandt, Germany; and B. Rockel
747	P5.60B	DERIVATION OF DAYLIGHT AND SOLAR IRRADIANCE DATA FROM SATELLITE OBSERVATIONS. A. Hammer, Univ. of Oldenburg, Oldenburg, Germany; and D. Heinemann, A. Westerhellweg, P. Ineichen, J. A. Olseth, A. Skartveit, D. Dumortier, M. Fontoynont, L. Wald, H. G. Beyer, C. Reise, L. Roche, and J. Page
751	P5.61A	WAVE MODEL ANALYSIS IMPROVEMENT BY USING ALTIMETRIC WAVE HEIGHTS MEASUREMENTS. Jean Barckicke, CNES, Toulouse, France; and Y. Menard
755	P5.62B	IMPLEMENTATION OF WAVELET NETWORKS FOR THE PARAMETERISATION OF CLOUD RADIATIVE TRANSFER IN GENERAL CIRCULATION MODELS. Anne Fouilloux, LAMP, Clermont-Ferrand, France; and T. Faure and J. Iaquinta

• Manuscript not available

AUTHOR INDEX

NINTH CONFERENCE ON SATELLITE METEOROLOGY AND OCEANOGRAPHY

	PAPER #	PAGE
A		
Ababa, A.	P2.57A	•
Ababa, A.	P2.58B	•
Abrams, M.	P3.15A	•
Abrams, M.	P4.44B	•
Achard, V.	P2.5A	187
Ackerman, S.	P4.35A	555
Adamec, D.	O5.4A	•
Adefuye, F.	P3.56B	•
Adler, R. F.	P1.23A	78
Adler, R. F.	P4.10B	*
Adler, R. F.	P4.18B	517
Aires, F.	P2.4B	181
Alados-Arboledas, L.	P1.26B	*
Aleksseva, A. A.	P3.5A	•
Allen, M. R.	O2.5B	162
Alves, J.	P5.2B	607
Anagnostou, E. N.	P1.23A	78
Anagnostou, E. N.	P4.18B	517
Andersen, S.	P2.30B	246
Andersen, S.	P2.39A	260
Anderson, D.	P2.25A	236
Anderson, D.	P5.2B	607
Anthis, A. I.	P2.42B	270
Antipolis, S.	P3.46B	432
Anyamba, E.	P1.51A	149
Anyamba, E.	P1.56B	757
Aonashi, K.	P4.25A	535
Aonashi, K.	P5.20B	653
Arkin, P. A.	P1.17A	61
Arkin, P. A.	P1.18B	65
Armante, R.	P2.3A	177
Armante, R.	P2.4B	181
Armante, R.	P4.30B	547
Armante, R.	P5.46B	718
Askari, F.	P5.10B	*
Atkinson, R. J.	P1.5A	30
Atkinson, R. J.	P3.6B	349
B		
Ba, M. B.	P1.15A	53
Ba, M. B.	P3.35A	408
Badran, F.	P2.91A	323
Baker, H. C.	P4.21A	523
Bakst, L.	P2.60B	297
Bakst, L.	P3.4B	345
Balmaseda, M.	P5.2B	607
Bankert, R. L.	P2.22B	226
Baran, A.	P2.16B	218
Barbe, A.	P5.35A	682
Barckicke, J.	P5.61A	751
Barkstrom, B. R.	P5.52B	728
Barnett, J. J.	P1.6B	34
Barwell, B. R.	P4.29A	545
Basist, A.	P1.7A	•
Basist, A.	P2.68B	*
B (Continued)		
Basist, A.	P2.81A	•
Bastos, E. J. B.	P2.47A	•
Bastos, E. J. B.	P3.45A	430
Bates, J. J.	P1.3A	22
Bates, J. J.	O1.8B	9
Bates, J. J.	P5.8B	620
Baudin, G.	P4.48B	*
Bauer, P.	P4.16B	•
Bauer, P.	P4.65A	604
Baverez, A.	P4.60B	599
Beavan, J.	P4.22B	527
Behera, S. K.	P1.46B	137
Bell, M.	O5.5B	*
Bell, T. L.	P1.58B	766
Bellerby, T.	P5.16B	635
Bengtsson, L.	P4.24B	531
Benichou, P.	P2.38B	*
Benjamin, S.	P5.9A	624
Benjamin, S.	P5.47A	722
Bennartz, R.	P2.67A	301
Bennartz, R.	P4.46B	569
Bennartz, R.	P4.47A	571
Bennartz, R.	P4.65A	604
Berg, W.	P1.3A	22
Berg, W.	P2.25A	236
Berger, F. H.	P5.59A	743
Bernal, P.	O1.1A	*
Beyer, H. G.	P3.47A	434
Beyer, H. G.	P5.60B	747
Bhushan, B.	P3.58B	*
Bieker, F. D.	P2.6B	191
Billing, H.	P1.8B	*
Birkenheuer, D.	P5.27A	672
Blankenship, C. B.	P2.27A	240
Bloom, H. J.	P4.28B	541
Boatman, J. B.	P5.23A	664
Bocca, C. I.	P4.37A	*
Bocca, C. I.	P4.48B	•
Bocca, C. I.	P4.58B	•
Borbas, E.	P4.23A	•
Borga, M.	P2.49A	287
Bornstein, R.	P2.21A	•
Bouazza, M.	P2.65A	*
Boukabara, S.-A.	P1.21A	74
Bourras, D.	P2.45A	278
Bouthemy, P.	P3.16B	370
Boutin, J.	P5.55A	*
Bouttier, F.	P1.30B	92
Breivik, L.-A.	P2.39A	260
Brisson, A.	P2.30B	246
Brock, J.	O4.5B	*
Brown, E. B.	P4.64B	600
Brown, J.	P5.9A	624
Brown, J.	P5.47A	722
Brown, L. R.	P5.35A	682
Brunel, P.	P2.2B	173

AUTHOR INDEX

NINTH CONFERENCE ON SATELLITE METEOROLOGY AND OCEANOGRAPHY

	PAPER #	PAGE
B (Continued)		
Brunel, P.	P5.38B	694
Bukharov, M. V.	P2.54B	*
Buriez, J. C.	P2.5A	187
Buriez, J.-C.	P4.6B	500
Burns, B. A.	P5.32B	677
C		
Caille, P.	P5.29A	*
Caldwell, M.	P5.57A	736
Callan, G.	P5.45A	714
Cammas, J.-P.	P2.3A	177
Campana, K. A.	P2.7A	193
Candy, B.	O2.5B	162
Candy, B.	P5.7A	619
Cantrell, L. E.	P2.6B	191
Capderou, M.	P1.33A	98
Cardinali, C.	P4.60B	598
Carswell, J. R.	P4.3B1	489
Cartalis, C.	P3.36B	412
Casey, K. S.	P5.5A	*
Casse, V.	P4.57A	594
Castelain, G.	P2.5A	187
Cavanie, A.	O2.6B	166
Ceballos, J. C.	P2.59A	295
Ceballos, J. C.	P3.45A	430
Chaboureau, J. P.	P1.47A	141
Chalfant, M. W.	P4.64B	600
Champion, J. P.	P5.35A	682
Chang, F.-C.	P1.4B	26
Chang, P. S.	P4.3B1	489
Chang, S. W.	P3.12B	364
Chedin, A.	O1.10B	13
Chedin, A.	P1.41A	122
Chedin, A.	P1.47A	141
Chedin, A.	P2.4B	181
Chedin, A.	P4.30B	547
Chedin, A.	P5.35A	682
Chedin, A.	P5.46B	718
Chen, M.	P1.49A	*
Cheney, R.	O2.3A	*
Cheruy, F.	P1.48B	145
Cheruy, F.	P5.37A	690
Chevallier, F.	P1.48B	145
Chevallier, F.	P5.37A	690
Chiou, E.	P4.53A	579
Chou, M.	P5.56B	*
Choudhury, B.	P2.82B	311
Chouinard, C.	P5.25A	668
Chu, W. P.	P4.53A	579
Chu, W. P.	P4.55A	587
Chub, V. E.	P2.61A	*
Chung, H.-S.	P2.24B	234
Chursin, A. A.	P5.35A	682
Claud, C.	P2.3A	177
Clausen, A.	P2.43A	274
C (Continued)		
Clayson, C. A.	O2.5B	162
Clothiaux, E.	P4.35A	555
Cornillon, P.	O5.2A	*
Costes, L.	P4.51A	*
Courtier, P.	O5.7B	*
Couvert, P.	P4.6B	500
Cracknell, A. P.	P2.42B	270
Crepeau, L.	P5.46B	718
Crepon, M.	P2.91A	323
Crout, R. L.	P5.23A	664
D		
da C. Pinheiro, G.	P1.14B	49
Dalu, G.	P1.57A	761
da Silva, A.	P1.24B	*
da Silva Mello, N.	P1.9A	*
de Souza, E.	P1.9A	*
de Valk, P.	P3.3A	343
Deblonde, G.	P5.21A	656
Dech, S. W.	P2.33A	250
Dech, S. W.	P2.69A	304
Deeter, M.	P1.3A	22
Deeter, M.	P2.25A	236
Dejene, T.	P2.57A	*
Delderfield, J.	P5.57A	736
DeLeonibus, L.	P2.34B	*
DeLeonibus, L.	P3.19A	*
Demirtas, M.	P5.28B	*
Derber, J.	P5.42B	706
Desalmand, F.	P3.37A	416
Desbois, M.	O3.5B	*
Desbois, M.	P3.37A	416
Diallo, M. A.	P2.75A	308
DiGirolamo, L.	P2.9B	197
DiGirolamo, L.	P4.35A	555
DiPasquale, R.	P1.42B	126
Dittberner, G. J.	P3.48B	438
Dobi, I.	P3.44B	428
Dodge, J.	O1.7B	5
Dodson, A. H.	P4.21A	523
Donnelly, W. J.	P4.3B1	489
Duchossois, G.	P4.63A	764
Dumortier, D.	P3.47A	434
Dumortier, D.	P5.60B	747
Durham, D. L.	P5.23A	664
Dybbroe, A.	P2.90B	319
E		
Eastwood, S.	P2.30B	246
Eder, B.	P1.28B	88
Elliott, S. S.	P3.7A	353
Elliott, S. S.	P3.9A	773
English, S. J.	P4.29A	545
English, S. J.	P4.33A	553
English, S. J.	P5.30B	676

AUTHOR INDEX

NINTH CONFERENCE ON SATELLITE METEOROLOGY AND OCEANOGRAPHY

	PAPER #	PAGE
E (Continued)		
Evans, J. L.	P1.43A	*
Eymard, L.	P1.21A	74
Eymard, L.	P2.45A	278
Eymard, L.	P5.19A1	646
Eymard, L.	P5.19A2	650
Eyre, J. R.	P1.6B	34
Eyre, J. R.	P4.20B	522
Eyre, J. R.	P4.29A	545
Eyre, J. R.	P5.30B	676
F		
Falvey, M.	P4.22B	527
Faure, T.	P5.62B	755
Fedorov, D.	P1.14B	49
Fedorov, D.	P3.4B	345
Fedorova, N.	P1.14B	49
Fedorova, N.	P2.60B	297
Fedorova, N.	P3.4B	345
Feidas, H. N.	P3.36B	412
Feijt, A.	P3.3A	343
Felde, G. W.	P2.28B	242
Feltz, J.	P1.32B	94
Feng, J.	P1.37A	114
Feng, J.	P2.46B	283
Fernandez, J. M.	P2.90B	319
Ferraro, R. R.	O4.7B	476
Ferraro, R. R.	P5.17A	639
Ferreira, A.	P1.9A	*
Fischer, H.	P3.42B	424
Fischer, J.	P2.44B	276
Fischer, J.	P4.46B	569
Fischer, J.	P4.47A	571
Fischer, J.	P4.49A	574
Fischer, J.	P4.50B	577
Fontoynont, M.	P3.47A	434
Fontoynont, M.	P5.60B	747
Fouilloux, A.	P5.62B	755
Fourrie, N.	P2.3A	177
Fox, N.	P5.57A	736
Foyo-Moreno, I.	P1.26B	*
Franca, G. B.	P2.59A	295
Francis, J.	P1.45A	134
Francis, P.	P2.16B	217
Frouin, R.	P2.91A	323
Fuchs, J.	P5.13A	630
Fuster-Escuder, J. M.	P1.11A	42
G		
Gamache, R.	P5.35A	682
Gang, H.	P5.19A1	646
Gang, H.	P5.19A2	650
Garand, L.	P3.28B	401
Garand, L.	P5.25A	668
Gautier, C.	P1.38B	118
Gautier, C.	P5.54B	732

	PAPER #	PAGE
G (Continued)		
Geer, A. J.	P3.26B	393
Georgiev, C.	P3.57A	777
Gerard, E.	P5.19A1	646
Gerard, E.	P5.19A2	650
Gerard, E.	P5.22B	660
Ghibaudo, J. H.	P4.62B	*
Gibson, G. G.	P5.52B	728
Gird, R. S.	P3.50B	442
Gird, R. S.	P3.60B	454
Godoy, O.	P2.39A	260
Golovko, V. F.	P5.35A	682
Gorbunov, M.	P4.24B	531
Gorelkin, N. E.	P2.62B	*
Göttsche, F.-M.	P3.43A	426
Graham, N. E.	P1.16B	57
Grassotti, C.	P4.17A	513
Grody, N. C.	O4.7B	476
Grody, N. C.	P5.17A	639
Grody, N. C.	P5.39A	698
Gross, L.	P2.91A	323
Groves, D.	P1.45A	134
Gruber, A.	P1.15A	53
Gruber, A.	P3.35A	408
Gu, S.	P1.22B	*
Guillory, A. R.	P1.4B	26
Guillory, A. R.	P3.17A	374
Gurka, J. J.	P3.50B	442
Gurka, J. J.	P3.60B	454
Gutman, G. G.	P2.67A	301
H		
Haba-Ejarque, G.	P1.11A	42
Haines, K.	P5.2B	607
Hallak, R.	P2.59A	295
Halle, J.	P5.25A	668
Hammer, A.	P3.47A	434
Hammer, A.	P5.60B	747
Harries, J. E.	P3.26B	393
Harries, J. E.	P5.57A	736
Harris, A.	O2.5B	162
Hawkins, J. D.	O2.2A	160
Hawkins, J. D.	P2.23A	230
Healy, S. B.	P4.20B	522
Heinemann, D.	P3.47A	434
Heinemann, D.	P5.60B	747
Heinemann, G.	P2.88B	317
Heinemann, T.	P2.44B	276
Heinemann, T.	P4.47A	571
Helveston, M. J.	P2.23A	230
Herveou, M.	P4.30B	547
Hicks, E. M.	P2.19A	222
Higgins, W.	P1.17A	61
Hinsman, D. E.	P3.54B	*
Hoegh, P.	O4.6B	*
Hoffman, R. N.	P4.17A	513

AUTHOR INDEX

NINTH CONFERENCE ON SATELLITE METEOROLOGY AND OCEANOGRAPHY

	PAPER #	PAGE
H (Continued)		
Hollingsworth, A.	O3.2A	*
Hollmann, R.	P1.37A	114
Hollmann, R.	P2.46B	283
Holm, E. V.	P1.30B	92
Holmlund, K.	P3.9A	773
Holt, F. C.	P3.1A	339
Holyer, R.	P2.23A	230
Holz, A.	P2.33A	250
Hong, Y.	P4.11A	505
Hong, Y.	P4.12B	509
Hou, A.	P1.24B	*
Huang, A. H.-L.	P4.28B	541
Huang, H.-L.	P2.12B	204
Huang, H.-L	P4.31A	*
Huang, H.-L	P4.43A	*
Huffman, G.	P1.24B	*
Hume, T.	P1.13A	*
Hutchison, K. D.	P2.12B	204
Hutchison, K. D.	P2.29A	244
Hutchison, K. D.	P2.36B	256
Hutchison, K. D.	P4.27A	537
I		
Iacovazzi, R., Jr.	P1.57A	761
Iaquinta, J.	P5.62B	755
Ichiki, A.	P4.25A	535
Ineichen, P.	P3.47A	434
Ineichen, P.	P5.60B	747
Ingmann, P.	P4.45A	565
Ingmann, P.	P5.13A	630
Ingmann, P.	P5.58B	739
Inoue, T.	P2.11A	201
Iredell, L.	P1.51A	149
Iskenderian, H.	P4.17A	513
Iwanami, K.	P2.15A	214
J		
Jackson, D. L.	P1.3A	22
Jacobowitz, H.	P1.53A	154
Jacquinet-Husson, N.	P5.35A	682
Janowiak, J. E.	P1.36B	110
Jedlovec, G. J.	P1.4B	26
Jedlovec, G. J.	P1.5A	30
Jedlovec, G. J.	P3.6B	349
Jedlovec, G. J.	P3.17A	374
Jerrett, D.	P4.21A	523
Jiang, S.	P1.25A	82
Johnson, D. B.	P3.31A	*
Joiner, J.	P1.24B	*
Joiner, J.	P5.31A	*
Jones, B.	P2.40B	262
Jones, C.	P1.16B	57
Jones, C.	P1.38B	118
Jönsson, L.	P5.11A	*
Jorge, J.	P3.30B	405

	PAPER #	PAGE
J (Continued)		
Joyce, R. J.	P1.17A	61
K		
Kaifel, A.	P1.27A	84
Kastner, M.	P1.12B	46
Katsumata, M.	P2.15A	214
Kellock, S.	P5.57A	736
Kelly, G.	P3.10B	360
Kerényi, J.	P2.66B	*
Kidd, C.	P2.18B	*
Kilham, D.	P5.19A1	646
Kilham, D.	P5.19A2	650
Kim, D.	P2.13A	208
Kim, D.	P3.2B	*
Kim, D.	P4.32B	551
Kim, D.	P5.47A	722
Kim, D.	P5.9A	624
Kim, D.-H.	P2.24B	234
Klaes, K. D.	P2.1A	169
Klaes, K. D.	P4.39A	557
Klaes, K. D.	P4.40B	561
Kleespies, T. J.	P5.42B	706
Kleschenko, A.	P2.87A	*
Kniveton, D. R.	P1.19A	69
Koblinsky, C.	P5.3A	*
Kogan, F.	P1.31A	*
Kokhanovsky, A. A.	P2.17A	*
Kokhanovsky, A. A.	P5.43A	*
Kondragunta, C.	P1.40B	*
Kondragunta, C.	P1.53A	154
Kopp, T. J.	P2.6B	191
Kopylov, N. V.	P5.36B	686
Kornblueh, L.	P4.24B	531
Koslowsky, D.	P1.10B	38
Koslowsky, D.	P2.84B	313
Kratz, E. J.	P4.28B	541
Krawczyk, R.	P4.61A	*
Kriebel, K. T.	P1.12B	46
Kummerow, C. D.	O4.4A	*
Kummerow, C. D.	P4.11A	505
Kummerow, C. D.	P4.12B	509
Kundu, P.	P1.58B	766
L		
Labandibar, J.	P4.37A	*
Lagerloef, G.	O5.3A	*
Langevin, M.	P2.1A	169
Langevin, M.	P4.39A	557
Langevin, M.	P4.40B	561
Lapeta, B.	P1.29A	*
Laurent, H.	P3.8B	356
Lavanant, L.	P2.2B	173
LeBorgne, P.	P2.30B	246
Lecomte, P.	P4.1A	480

AUTHOR INDEX

NINTH CONFERENCE ON SATELLITE METEOROLOGY AND OCEANOGRAPHY

	PAPER #	PAGE
L (Continued)		
Lecue, J. M.	P3.17A	374
Lee, T. F.	O2.2A	160
LeFebvre, M.	O5.1A	*
Legeckis, R.	P2.31A	*
Legleau, H.	P2.90B	319
Leguizamon, S.	P2.82B	311
Leibrandt, W.	P5.58B	739
Leighton, H. G.	P1.37A	114
Leighton, H. G.	P2.46B	283
Leonid, M.	P2.89A	*
Lerner, J. A.	P1.5A	30
Levasseur, S.	P2.2B	173
Levizzani, V.	O3.3A	327
Li, Q.	P5.17A	639
Li, T.	P5.24B	*
Li, Z. X.	P5.37A	690
Liebmann, B.	P1.36B	110
Lieder, M.	P2.88B	317
Lieder, M.	P5.48B	*
Lifermann, A.	P4.5A	497
Lin, C.	P1.39A	*
Liu, G.	P2.15A	214
Liu, G.	P5.20B	653
Liu, T.	O4.3A	*
Lopez, E.	P2.37A	*
Lopez, E.	P3.21A	*
Lopez-Baeza, E.	P1.11A	42
Lord, S.	P3.50B	442
Lord, S.	P3.60B	454
Lucas, L. E.	P1.36B	110
Lucio, F.	P2.53A	*
Luntama, J.-P.	P4.19A	521
Luo, G.	P1.53A	154
Luo, G.	P2.7A	193
M		
Machaado, L. A. T.	P2.59A	295
Madina, D. B.	P2.80B	*
Mahovic, N. S.	P2.50B	*
Mannstein, H.	P2.41A	266
Marcorelles, B.	P4.39A	557
Marcorelles, B.	P4.40B	561
Maring, L. D.	P1.52B	*
Marsouin, A.	P2.30B	246
Marusa, S.	P2.36B	256
Marzano, F. S.	P3.62B	462
Matari, E. E.	P2.83A	*
Matricardi, M.	P5.38B	694
Matricardi, M.	P5.41A	702
May, D. A.	P2.23A	230
McCollum, J. R.	P1.15A	53
McGregor, J.	P1.13A	*
McGregor, J.	P4.22B	527
McIntosh, R. E.	P4.3B1	489
McKague, D. S.	P3.34B	*

	PAPER #	PAGE
M (Continued)		
Mehta, A. V.	P1.50B	769
Mehta, A. V.	P1.51A	149
Meisner, R. E.	P2.33A	250
Meisner, R. E.	P2.69A	304
Mejia, C.	P2.91A	323
Melinotte, J.	P4.8B	*
Menard, Y.	P5.61A	751
Menenti, M.	P2.82B	311
Menzel, W. P.	P1.32B	94
Menzel, W. P.	P3.1A	339
Menzel, W. P.	P5.45A	714
Merchant, C. J.	O2.5B	162
Merchant, C. J.	P2.35A	254
Mey, P. D.	O5.6B	*
Meyer, R.	P2.41A	266
Mika, J.	P3.44B	428
Miller, A. J.	P1.55A	156
Milliff, R. F.	P4.4B	493
Mitchelson-Jacob, E. G.	P2.40B	262
Mobasheri, M. R.	P5.6B	611
Mohr, T.	O1.3A	*
Mooney, H.	P4.34B	554
Moore, S. L.	P2.26B	*
Moraes, E. C.	P3.45A	430
Morancais, D.	P4.59A	*
Morel, C.	P3.18B	377
Mossavati, R.	P5.57A	736
Mueller, J.	P1.37A	114
Mueller, J.	P5.57A	736
Muller, J.	P2.46B	283
Muloshi, G.	P2.85A	*
Munro, R.	P3.11A	*
Munthali, G. K.	P2.51A	*
Murray, M. J.	O2.5B	162
Muthal, G.	P2.72B	*
Mutikani, V.	P2.76B	*
Mwandoto, S. H.	P2.63A	*
Myneni, R.	P2.73A	*
N		
Naimeng, L.	P2.64B	*
Nakamura, H.	P4.25A	535
Nakazawa, T.	P4.4B	493
Nakazawa, T.	P5.14B	633
Negri, A. J.	P1.23A	78
Negri, A. J.	P4.18B	517
Nery, J. T.	P2.20B	*
Neumeister, H.	P3.14B	367
Nobre, C. A.	P2.59A	295
O		
Offiler, D.	P4.20B	522
Offiler, D.	P4.21A	523
Offiler, D.	P5.19A1	646
Offiler, D.	P5.19A2	650

	PAPER #	PAGE
O (Continued)		
Ohring, G.	O1.7B	5
Olander, T. L.	P3.61A	458
Olesen, F. S.	P3.43A	426
Olmo, F. J.	P1.26B	*
Olseth, J. A.	P3.47A	434
Olseth, J. A.	P5.60B	747
Olson, W. S.	P4.11A	505
Olson, W. S.	P4.12B	509
Oriol-Pibernat, E.	P4.40B	561
Oriol-Pibernat, E.	P4.63A	764
Osaki, N.	P3.27A	397
Ouberdous, M.	P5.4B	*
Ovidio, F.	P5.12B	626
P		
Paape, K.	P2.79A	*
Page, J.	P3.47A	434
Page, J.	P5.60B	747
Pailleux, J.	P4.60B	598
Palmer, P. I.	P1.6B	34
Pankiewicz, G. S.	P3.23A	385
Papin, C.	P3.16B	370
Parol, F.	P4.6B	500
Parsons, J.	P2.55A	291
Paul, G.	P3.14B	367
Pedrizzetti, G.	P2.8B	*
Peng, M. S.	P3.12B	364
Pereira, R. C. G.	P2.59A	295
Pereira, R. C. G.	P3.45A	430
Perez, J.	P4.39A	557
Perez, R.	P5.44B	710
Peterson, P.	P1.38B	118
Petruncio, E. T.	P5.23A	664
Petty, G. W.	P5.34B	678
Pick, D.	P4.34B	554
Picon, L.	P3.25A	389
Piraino, P.	P1.51A	149
Pitts, M. C.	P4.55A	587
Podgorny, I. A.	P5.40B	*
Pontikis, C. A.	P2.19A	222
Porcu, F.	P2.49A	287
Pouponneau, B.	P2.3A	177
Prabhakara, C.	P1.57A	761
Prasad, K. S.	P4.7A	*
Preusker, R.	P4.47A	571
Preusker, R.	P4.49A	574
Preusker, R.	P4.50B	577
Preusser, C.	P2.69A	304
Prieto, J.	P3.53A	*
Prins, E. M.	P1.32B	94
Prodi, F.	P2.49A	287
Prunet, P.	P4.57A	594
Purdom, J. F. W.	O3.4A	331
Puschell, J. J.	P4.41A	*
R		
Rabin, B.	P3.63A	466
Randel, D. L.	P1.1A	15
Randel, D. L.	P1.2B	18
Randriamampianina, R.	P3.44B	428
Ratier, A.	O1.4A	*
Rattenborg, M.	O3.6B	335
Rault, D. F.	P4.54B	583
Reale, A. L.	P4.64B	600
Region, K.	P2.89A	*
Reise, C.	P3.47A	434
Reise, C.	P5.60B	747
Renne, D.	P5.44B	710
Renshaw, R. J.	P4.33A	553
Renshaw, R. J.	P5.30B	676
Ricchiazzi, P.	P5.54B	732
Rchardson, K.	O2.2A	160
Richaume, P.	P2.91A	323
Ridley, J.	P4.2B	484
Rienecker, M. M.	P5.15A	*
Rigollier, C.	P3.46B	432
Rimoczi-Paal, A.	P3.44B	428
Ringer, M. A.	P5.51A	724
Ringerud, M. A.	P1.1A	15
Rivera, J. J.	P3.32B	*
Roca, R.	P3.25A	389
Rochard, G.	P2.2B	173
Rochard, G.	O2.4A	*
Rochard, G.	P3.16B	370
Roche, L.	P3.47A	434
Roche, L.	P5.60B	747
Rockel, B.	P5.59A	743
Rodelet, A.	P1.34B	102
Rogel, P.	P5.1A	*
Rohn, M.	P3.9A	773
Rohn, M.	P3.10B	360
Rokke, L.	P1.54B	*
Romanov, S. V.	P4.56B	591
Rood, R.	P1.39A	*
Roozekrans, H.	P2.43A	274
Roozekrans, H.	P3.3A	343
Roquet, H.	O2.1A	*
Roquet, H.	P2.91A	323
Rosenfeld, D.	P3.35A	408
Rossow, W. B.	P1.41A	122
Rozier, B.	P2.5A	187
Rublev, A. N.	P4.56B	591
Ruddick, K.	P5.12B	626
S		
Sadibou, S. C.	P3.39A	*
Sakamoto, M. S.	P1.9A	*
Sakamoto, M. S.	P3.8B	356
Sakuragi, J.	P2.59A	295
Salley, D.	P3.40B	*
Salvekar, P. S.	P1.46B	137

AUTHOR INDEX

NINTH CONFERENCE ON SATELLITE METEOROLOGY AND OCEANOGRAPHY

	PAPER #	PAGE
S(Continued)		
Sanchez-Sesma, J.	P3.52B1	446
Sanchez-Sesma, J.	P3.52B2	450
Sandidge, J.	P2.23A	230
Saunders, R. W.	P1.30B	92
Saunders, R. W.	P3.10B	360
Saunders, R. W.	P5.22B	660
Saunders, R. W.	P5.38B	694
Saunders, R. W.	P5.41A	702
Sawyer, E.	P5.57A	736
Schaedlich, S.	P3.42B	424
Schanz, L.-C.	P4.65A	604
Scheidgen, P.	P2.43A	274
Schmetz, J.	O3.6B	335
Schüller, L.	P4.47A	571
Schüller, L.	P4.50B	577
Schüller, L.	P4.49A	574
Schulz, J.	P4.65A	604
Schweiger, A.	P1.45A	134
Schyberg, H.	P2.39A	260
Scofield, R. A.	P3.63A	466
Scofield, R. A.	P3.64B	470
Scott, N. A.	P1.41A	122
Scott, N. A.	P1.47A	141
Scott, N. A.	P1.48B	145
Scott, N. A.	P2.4B	181
Scott, N. A.	P4.30B	547
Scott, N. A.	P5.35A	682
Scott, N. A.	P5.37A	690
Scott, N. A.	P5.46B	718
Seals, R.	P5.44B	710
Segschneider, J.	P5.2B	607
Seko, H.	P4.25A	535
Senesi, S.	P3.18B	377
Seze, G.	P4.6B	500
Shi, L.	P5.26B	670
Shimoda, H.	O4.2A	*
Shiren, Y.	P5.54B	732
Shoji, Y.	P4.25A	535
Sicard, M.	P3.22B	381
Silvestrin, P.	P4.45A	565
Simmons, A.	P1.30B	92
Simoneau, P.	P2.5A	187
Singer, C.	P4.58B	*
Skartveit, A.	P3.47A	434
Skartveit, A.	P5.60B	747
Smalley, D. J.	P4.38B	*
Smirnova, T.	P5.9A	624
Smirnova, T.	P5.47A	722
Smith, A. J.	P4.33A	553
Smith, A. J.	P5.30B	676
Smith, E. A.	P3.62B	462
Smith, E. A.	P4.14B	*
Smith, E. A.	P5.18B	643
Smith, W. L.	O1.6A	1
Soden, B. J.	P3.13A	*
Soden, B. J.	P3.24B	*

	PAPER #	PAGE
S(Continued)		
Sohn, B.-J.	P5.18B	643
Sohn, B.-J.	P2.24B	234
Sosa-Chinas, M. A.	P3.52B1	446
Sosa-Chinas, M. A.	P3.52B2	450
Space, M. M.	P4.59A	*
Spezia, L.	P5.10B	*
Spyak, P. R.	P3.22B	381
Stackhouse, P.	P1.42B	126
Standfuss, C.	P1.34B	102
Standfuss, C.	P1.35A	106
Stockdale, T.	P5.2B	607
Stoffelen, A.	P1.20B	73
Stoffelen, A.	P4.3A	485
Stogryn, A. P.	P5.32B	677
Stowe, L. L.	P1.44B	130
Stowe, L. L.	P1.53A	154
Stowe, L. L.	P2.7A	193
Strow, L. L.	P5.33A	*
Struzik, P.	P2.78B	*
Stubenrauch, C. J.	P1.41A	122
Stuhlmann, R.	O1.9B	*
Stuhlmann, R.	P1.37A	114
Stuhlmann, R.	P2.46B	283
Suggs, R. J.	P1.4B	26
Sumi, A.	O4.1A	472
Susskind, J.	P1.50B	769
Susskind, J.	P1.51A	149
Susskind, J.	P1.56B	757
Syakango, S. M.	P2.86B	*
Szantai, A.	P3.37A	416
Szentimrey, T.	P3.44B	428
T		
Taberner, M.	P1.19A	69
Taberner, M.	P5.16B	635
Tag, P. M.	P2.22B	226
Tarruella, R.	P3.30B	405
Taurat, D.	P3.33A	*
Taylor, P.	P4.26B	*
Tessema, Z.	P2.56B	*
Testud, J.	P4.65A	604
Thepaut, J.-N.	P4.57A	594
Thepaut, J.-N.	P4.60B	598
Thiaw, W.	P3.41A	420
Thiria, S.	P2.91A	323
Thomason, L. W.	P4.52B	*
Thomason, L. W.	P4.53A	579
Thomason, L. W.	P4.55A	587
Thompson, J. N.	P3.55A	452
Tjemkes, S.	O3.6B	335
Tomassini, M.	P3.14B	367
Toure, K. M.	P2.74B	*
Tran, N.	P2.91A	323
Trembach, V. V.	P2.48B	*
Trotsenko, A. N.	P4.56B	591

AUTHOR INDEX

NINTH CONFERENCE ON SATELLITE METEOROLOGY AND OCEANOGRAPHY

	PAPER #	PAGE
T (Continued)		
Trotsenko, A. N.	P5.36B	686
Tungalagsaikhan, P.	P2.33A	250
Tungalagsaikhan, P.	P2.69A	304
Turk, F. J.	O2.2A	160
Turk, F. J.	P3.62B	462
Turner, D. S.	P5.25A	668
Tuyterev, V. G.	P5.35A	682
Twomey, J. A.	P2.36B	256
Tychon, B.	P2.75A	308
U		
Untch, A.	P1.30B	92
Uplinger, W. G.	P2.36B	256
Uspensky, A. B.	P2.32B	*
Uspensky, A. B.	P4.56B	591
Uspensky, A. B.	P5.36B	686
Uyeda, H.	P2.15A	214
Uyeda, H.	P3.27A	397
V		
van Hoeve, W.	P1.20B	73
Vanbauce, C.	P4.6B	500
van Beukering	P4.3A	485
Van den Eynde, D. V.	P5.12B	626
Vasilkov, A.	P5.12B	626
Velden, C.	O3.1A	*
Velden, C.	P3.61A	458
Verstraete, M. M.	O2.7B	*
Vicente, G. A.	P3.63A	466
Vicente, G. A.	P3.64B	470
Vida, J.	P1.26B	*
Viltard, N. F.	P4.11A	505
Viltard, N. F.	P4.12B	509
Viollier, M.	P1.34B	102
Viollier, M.	P1.35A	106
Vonder Haar, T. H.	P1.1A	15
Vonder Haar, T. H.	P1.2B	18
Vukicevic, T.	P5.50B	*
W		
Wagneur, N.	P3.28B	401
Wald, L.	P3.46B	432
Wald, L.	P3.47A	434
Wald, L.	P5.60B	747
Waliser, D. E.	P1.16B	57
Waliser, D. E.	P1.36B	110
Waliser, D. E.	P5.26B	670
Walter, B.	P4.9A	*
Wang, Y.	P4.36B	*
Wanzong, S.	P5.45A	714
Watkins, B.	P3.49A	*
Watts, P. D.	P2.16B	218
Weare, B. C.	P2.14B	212
Weng, F.	O4.7B	476

	PAPER #	PAGE
W (Continued)		
Weng, F.	P5.39A	698
Westerhellweg, A.	P5.60B	747
Wetzel, M. A.	P1.44B	130
Whitworth, B. N.	P3.17A	374
Wick, G. A.	P5.8B	620
Wielicki, B. A.	P5.52B	728
Wilheit, T. T.	P2.27A	240
Wilheit, T. T.	P2.29A	244
Wilheit, T. T.	P4.15A	*
Wilmshurst, A.	P5.16B	635
Wilson, S. M.	P2.52B	*
Winnewisser, M.	P5.35A	682
Winokur, R.	O1.5A	*
Woick, H.	O3.6B	335
Wonsick, M. M.	P2.6B	191
Wrigley, R.	P5.57A	736
Wu, M.	P1.39A	*
X		
Xie, P.	P1.18B	65
Y		
Yang, S.	P1.55A	156
Yang, S.	P4.13A	*
Yang, S.	P5.53A	*
Yeshanew, A.	P2.58B	*
Yeshanew, A.	P3.38B	*
Yoo, J.-M.	P1.57A	761
Yuxiang, Z.	P2.77A	*
Z		
Zavody, A. M.	O2.5B	162
Zelenka, A.	P5.44B	710
Zhakata, W.	P2.71A	*
Zhang, S.	P1.24B	*
Zhao, Q.	P5.49A	*
Zhiltsova, O.	P3.29A	403
Zhou, S.	P1.55A	156
Zinyemba, T.	P2.70B	*
Zwatz-Meise, V.	P2.90B	319

O1.6A

SATELLITE REMOTE SOUNDING – THE EVOLUTION OF A GLOBAL OBSERVING SYSTEM

REMOTE SENSING LECTURE OF THE AMERICAN METEOROLOGICAL SOCIETY

William L. Smith*
NASA Langley Research Center, Hampton, Virginia

1 INTRODUCTION

Today's global weather observing system is made possible by an international system of polar orbiting and geostationary satellites. The origins of the observations now provided by satellites can be traced to the pioneering rocket measurements of Robert H. Goddard (1929) who launched a payload consisting of a barometer, a thermometer, and a camera. Rocket technology, developed during World War II, provided the first pictures of clouds from high altitudes in the late 1940's. The first quantitative measurements of the atmosphere were provided in 1959 by Suomi's radiation measurement system aboard the Explorer VII satellite (Soumi, 1958). The evolution of satellite meteorology can be traced from these beginnings through the launch of the first weather satellite, TIROS-I, on April 1, 1960, into the current era of highly sophisticated Earth Observing System (EOS) satellites designed to observe the state of the Earth's environment. During the past 30 year evolutionary period, the emphasis has shifted from qualitative analyses of cloud patterns provided by imaging devices to quantitative contributions provided by multispectral atmospheric sounding radiometers, including input to numerical weather forecast and climate prediction models. Technology development has permitted a steady improvement in the spectral coverage, spectral resolution, spatial resolution, and the temporal frequency of measurement. We are now on the verge of a giant leap forward in observing capability as a result of focal plane detector arrays consisting of a million or more detector elements enabling continuous quantitative measurement of atmospheric composition and dynamics from geostationary satellites. Lidars, capable of providing high vertical resolution thermodynamic sounding and wind measurements, will be implemented from low Earth orbiters during the next decade.

The intent of this paper is to trace the evolution of satellite atmospheric sounding capabilities to the current state-of-the-art, as represented by the EOS, and into the foreseeable future as made possible by technology now emerging from the missile defense program. Results from computer simulations and satellite and aircraft instrument systems are used to demonstrate current and future global observing capabilities.

2 ATMOSPHERIC SOUNDING (1969–1998)

The use of Earth orbiting satellites for global sounding of the Earth's atmosphere was recognized in the historical papers of King (1958) and Kaplan (1959). The world's first atmospheric sounding instruments were flown on the polar orbiting Nimbus 3 satellite, launched April 14, 1969: (1) a Michelson interferometer, the Infrared Radiation Interferometer Spectrometer (IRIS) (Conrath et al., 1970), which measured the spectrum of infrared radiation emitted to space by the Earth's surface and atmosphere; and (2) a grating spectrometer, Satellite Infrared Radiation Spectrometer (SIRS) (Wark and Hilleary, 1969), which measured the radiation to space in eight distinct spectral bands selected specifically for temperature sounding. Although these two types of spectral selection (i.e., Michelson Interferometry and Grating Spectrometry) are the measurement techniques chosen for future high vertical resolution sounding instruments (Smith et al., 1990 and Chahine et al., 1990), the early versions of these instruments were replaced by a combination of broad band filter wheel infrared radiometers and microwave radiometers in order to achieve high spatial resolution and to cope with the interference of the sounding procedure by clouds (Smith et al., 1974). Today we fly a system of infrared and microwave sounding radiometers on the National Oceanic and Atmospheric Administration (NOAA) polar orbiting satellites and a high spatial resolution filter wheel infrared sounding radiometer of two U.S. geostationary satellites.

*Corresponding author address: William L. Smith, MS-401, NASA Langley Research Center, Hampton, VA 23681-2199

2.1 Polar vs Geostationary Observing Capabilities

It is important to recognize the importance of using both polar orbiting and geostationary satellites for sounding the atmosphere. The polar orbiting satellite provides: (1) global coverage, (2) high spatial resolution infrared measurement, (3) microwave sounding through clouds, and (4) the potential for high vertical resolution soundings using active lidar.

The geostationary satellite provides: (1) high temporal resolution, (2) quasi-synoptic sampling, (3) observation of weather dynamics, and (4) the ability to synergize with ground based observations.

Today's operational sounding system consists of two polar orbiters providing locally four soundings per day with global coverage and two geostationary satellites providing hourly sounding coverage over the Western hemisphere. Ultimately, the international system of geostationary satellites (i.e., the U.S., Europe, Japan, India, Russia, and China) will carry sounding instruments to provide a quasi-global and quasi-continuous coverage as needed for improved global weather predication.

3 FUTURE SATELLITE SOUNDING CAPABILITIES (1998–2010)

We are now on the verge of revolutionary improvements in the vertical resolution and accuracy of satellite sounding observations. These improvements will result from new instrument technologies. Improved technologies, enabling revolutionary improvement in upper air observations, include the large focal plane detector array. This will be used to provide a large number of spectral channels for improving vertical resolution (e.g., the EOS-AIRS grating spectrometer to fly on the EOS PM–platform) and/or to provide for a large number of simultaneously observed earth field of views to improve sampling efficiency and system signal to noise from geostationary orbit (e.g., the Advanced Geosynchronous Sounder, AGS). Longer lifetime lasers and lightweight telescopes may soon enable water vapor profiling with differential absorption lidar systems aboard satellites.

The first use of a large focal plane array for atmospheric sounding will be conducted with the EOS PM–platform Atmospheric Infrared Radiation Sounder (AIRS). AIRS is a grating spectrometer and the detector array is used to provide simultaneous high spectral resolution radiance measurements for a large number of spectral channels. Figures 1 and 2 show the temperature and moisture sounding accuracy, respectively, expected from the AIRS as compared to that achieved with the Advanced TIROS Operational Vertical Sounder (ATOVS) system aboard the U.S. polar orbiting NOAA satellites.

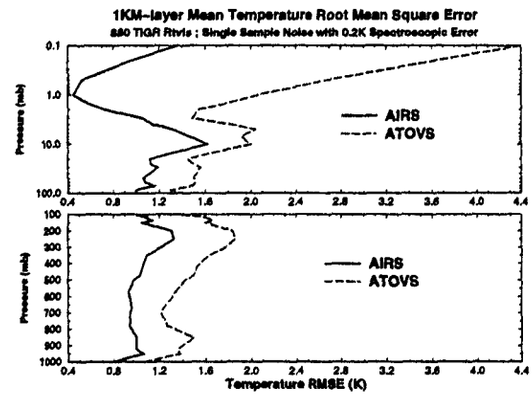

Figure 1: Comparison of temperature sounding accuracy expected for the EOS-AIRS with that to be achieved with the ATOVS flying on NOAA operational satellites.

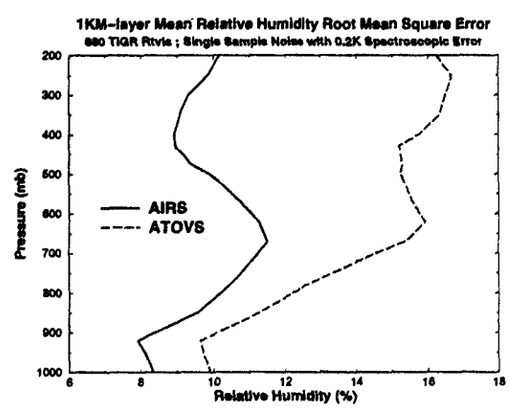

Figure 2: Refer to caption for Fig. 1, but for water vapor.

One new system which provides greatly improved vertical resolution has been demonstrated from aircraft and experimental satellites; it is the high spectral resolution radiance spectrum measurement system. Improvements using High-resolution Interferometer Sounder (HIS) are clearly shown in Figures 3 and 4 which show vertical cross-sections of temperature and water vapor comparisons with those achieved from operational TOVS and GOES sounders respectively. (The erroneously cold atmospheric regions below 500 mb of the HIS cross-section shown in Figure 3 are due to cloud attenuation, which was intentionally included for this presentation in order to illustrate the detail of the retrievable thermodynamic structure.)

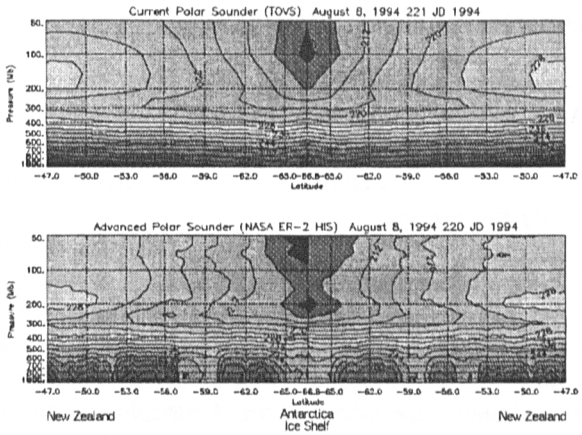

Figure 3: Comparison of a vertical cross-section of temperature obtained by HIS aboard the NASA ER-2 flying between New Zealand and Antarctica with observations along the flight track by the TIROS Operational Vertical Sounder (TOVS).

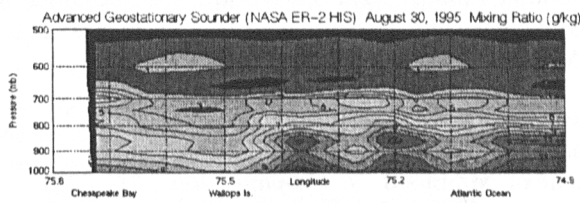

Figure 4: A vertical cross-section of lower tropospheric water vapor obtained by HIS aboard the NASA ER-2 flying a 50 km east to west leg over Wallops Island, VA.

It should also be mentioned that Europe is developing a Fourier Transform Spectrometer (FTS) equivalent of AIRS, called IASI (Interferometer Atmospheric Sounding Instrument), for the METOP satellite to the launched in 2002. Also, the U.S. is developing a Cross-track Interferometer Sounder (CrIS) to the part of the payload of the National Polar orbiting Operational Satellite System (NPOESS) to begin operation in the latter half of the next decade. The advantage of the FTS is that the entire spectrum is observed with a single detector element. Large focal plane arrays can be used with an FTS to provide simultaneous viewing of large geographical areas with high spatial and spectral resolution.

Differential Absorption Lidar (DIAL) has also been shown to provide high vertical resolution water vapor profiles. New lightweight composite technology will soon permit a DIAL system to be feasible for implementation on low earth orbiting satellites. Figure 5 shows a vertical water vapor cross-section obtained from the NASA ER-2 flying at an altitude of 20 km using the Lidar Atmospheric Sounding Experiment (LASE) developed by Browell, et al. (1996).

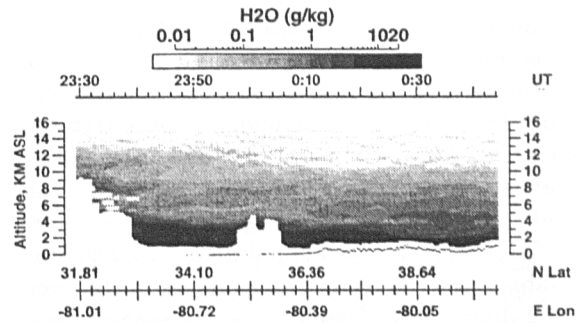

Figure 5: Demonstration of DIAL water vapor cross-section measured by LASE instrument for data acquired 26 September 1995.

A synergism of active and passive systems will permit very high vertical resolution temperature and water vapor profiles of the troposphere to be obtained by near nadir viewing. DIAL combined with a high spectral resolution FTS will permit a global coverage of high spatial resolution profiles to be achieved with a spatially scanning system aboard polar orbiting spacecraft. In this case the DIAL provides the high vertical resolution measure of the water vapor profile, while the high vertical resolution temperature profile is obtained from simultaneous water vapor thermal radiance measurements using an FTS. Since water vapor usually decreases at an increasing rate with increasing altitude, the thermal emission by water vapor arises from much narrower layers than does the thermal emission from a uniformly mixed gas (e.g., CO_2, traditionally observed for the temperature profiling application). Figure 6 shows, from theoretical simulation, a comparison of the FTS-DIAL temperature profiling accuracy as compared to an FTS alone and current low spectral resolution radiometers as represented by the ATOVS.

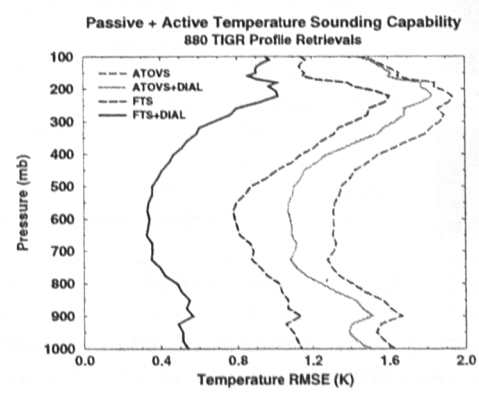

Figure 6: A comparison of RMS Temperature Profiler Error for three different systems.

Finally, an exciting new instrument development is the imaging FTS. As mentioned earlier, using a

large focal plane array in a Michelson interferometer enables simultaneous viewing of large geographical areas with high spatial resolution. One such instrument built by Utah State University's Space Dynamics Laboratory consists of a 128 x 128 InSb detector array within an FTS possessing 0.5 cm^{-1} unapodized spectral resolution. Figure 7 shows an example of the FTS imagers capability demonstrated in the laboratory. Shown is the data in 2 different types of 2-dimensional formats: (a) an image format for a selected spectral channel, and (b) a spectral format for a selected detector element. The images are for two different spectral channels; one where the atmosphere is transparent, and the other where atmospheric CO_2 is a strong absorber and emitter of radiant energy. As can be seen, the high intensity peaks in the spectrum of the person's breath correspond to the warm water vapor (2000 cm^{-1}) and CO_2 (2314 cm^{-1}) emissions. In fact, if one looks closely at the complete image for the CO_2 emitting wavelength (i.e., 2314 cm^{-1}), one can see the CO_2 being exhaled. Such instrumentation aboard a Geostationary Satellite would permit the observation of the transport of tropospheric molecules (e.g., H_2O, O_3, CO_2, CO, and CH_4) as well as provide a synoptic coverage of thermodynamic soundings with high spectral and spatial resolution. This capability, now possible using imaging FTS instruments, is currently being considered by the NASA/NOAA Advanced Geosynchronous Studies (AGS) program. The objectives of AGS are: (1) to enhance NASA's Earth System Science (ESS) observations, and (2) to infuse new technology into the NOAA GOES operational satellite program.

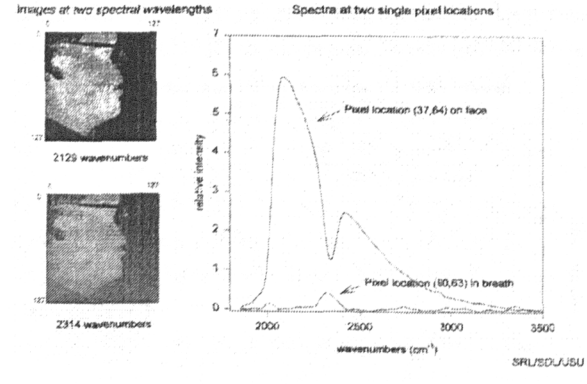

Figure 7: Images for two spectral channels and spectra for two different detectors of a focal plane array imaging interferometer (Suppi and Bingham, Utah State University, personal communication).

4 ACKNOWLEDGEMENTS

My appreciation to Dan DeSlover, from UW CIMSS at NASA LaRC, for preparing this manuscript for publication.

5 REFERENCES

Browell, E. V., S. Ismail, W. M. Hall, A. S. Moore, Jr., S. A. Kooi, V. G. Brackett, M. B. Clayton, J. D. W. Barrick, F. J. Schmidlin, N. S. Higdon, S. H. Melfi, and D. N. Whiteman (1996): LASE validation experiment. In *Advances in Atmospheric Remote Sensing with Lidar*, A. Ansmann, R. Neuber, P. Rairoux, and U. Wandinger, eds. Springer-Verlag, New York, pp. 289–295.

Chahine, M. T., F. G. O'Callaghan, H. H. Aumann, R. W. Capps, R. D. Haskins, R. J. Pagano, and R. A. Schindler (1990): Atmospheric Infrared Sounder (AIRS)–Science and Measurement Requirements. NASA-TM-104977, 36 pp.

Conrath, B. J., R. A. Hanel, V. G. Kunde, and C. Prabharkara (1970): The infrared interferometer experiment of Nimbus-3. *J. Geophys. Res.*, **75**, 5831–5857.

Goddard, R. H. (1919). *Smithson. Misc. Collect.*, **71**.

Kaplan, L. D. (1959): Inferences of atmospheric structures from satellite remote radiation measurements. *J. Opt. Soc. Am.*, **49**, 1004.

King, J. I. F. (1958): The radiative heat transfer of planet earth. In *Scientific uses of Earth Satellites*, Second Revised Ed., University of Michigan Press, Ann Arbor.

Smith, W. L., D. T. Hilleary, J. C. Fischer, H. B. Howell, and H. M. Woolf (1974): The Nimbus-5 ITPR experiment. *Appl. Opt.*, **13**, 449.

Smith, W. L., H. E. Revercomb, D. D. Laporte, L. A. Sromovsky, S. Silverman, H. M. Woolf, H. B. Howell, R. O. Knuteson, and H.-L. Huang (1990): GHIS–the GOES High-Resolution Interferometer Sounder. *J. Appl. Meteor.*, **29**, 1189–1204.

Suomi, V. E. (1958): The radiation balance of the earth from a satellite. *Ann. IGY*, **1**, 331–340.

Wark, D. Q. and D. T. Hilleary (1969): Atmospheric temperature: a successful test of remote probing. *Science*, **165**, 1256–1258.

O1.7B

THE DATA SETS OF THE NOAA/NASA PATHFINDER PROGRAM

George Ohring* and James Dodge
NOAA/NESDIS, Washington, DC and NASA, Washington, DC

1. INTRODUCTION/BACKGROUND

In the early 1990s, NOAA and NASA initiated a joint program to generate "research/climate quality" data sets from the archived operational satellite data and make these available to the global change research and earth science communities. Initial instruments selected for reprocessing included the AVHRR, TOVS, SSM/I, and GOES VAS. The program included the establishment of Science Working Groups (SWGs) to guide the projects, transcription of the archived satellite data to high density, easily accessible media for processing, development of instrument calibration histories and satellite to satellite intercalibration, selection of community consensus processing algorithms, writing/checkout of processing code, generation of products at distributed sites, validation of products, and provision of easy access to users. NASA later expanded its Pathfinder activities with a set of grants and projects for generation of data sets from additional satellite sensors, including RADARSAT, LANDSAT, and high-resolution AVHRR observations.

Table 1 shows the NOAA/NASA Pathfinder Projects and responsible organization. For TOVS, Path A uses a forecast temperature profile as a first guess for the retrieved profile, path B uses a library search technique to obtain a first guess, Path C deep-layer mean temperatures are independent of a priori information, and Path P represents polar soundings.

A major initial effort was the transcription of the archived data to accessible staging media for processing. Table 2 shows the volumes of data involved and the reduction in the number of storage units after transcription.

2. AVHRR, TOVS, GOES AND SSM/I DATA SETS

The AVHRR visible and near-infrared sensors are calibrated prior to flight but have no onboard calibration and tend to degrade in orbit. The AVHRR Pathfinder Calibration Working Group developed a stable calibration history of the Pathfinder AVHRRs using the Libyan desert as a stable calibration source (Rao and Chen, 1995). The WG also developed an improved treatment of the non-linearity of the IR channels (Walton et al., 1998).

Table 1. NOAA/NASA PATHFINDER PROJECTS

Project	Responsible Organization
AVHRR Calibration Corrections	NOAA/NESDIS
AVHRR Land	NASA/GSFC
AVHRR Sea Surface Temperature	NASA/JPL
AVHRR Atmosphere	NOAA/NESDIS
TOVS Path A Soundings	NASA/GSFC
TOVS Path B Soundings	CNRS
TOVS Path P Soundings	U. of Washington
TOVS Path C Deep Layer Mean Temp - 1	NASA/MSFC
TOVS Path C Deep Layer Mean Temp - 2	NOAA/NESDIS
GOES Reduced Resolution	U. of Wisconsin
SSM/I Full-Resolution Data and Products	NASA/MSFC
SSM/I Gridded Products	NASA/NSIDC

CNRS-National Center for Scientific Research
GSFC-Goddard Space Flight Center
JPL-Jet Propulsion Laboratory
MSFC-Marshall Space Flight Center
NESDIS-National Environmental Satellite, Data, and Information Service
NSIDC-National Snow and Ice Data Center

Table 2. PATHFINDER VOLUMES AND MEDIA

	TOVS	AVHRR	GOES	SSM/I
Period of Record	1979 to Date	1981 to Date	1978 to Date	1987 to Date
Archive Volume (TB)	0.8	3.9	145	0.4
Archive Units	15000	50000	33000	2500
Archive Medium	Cart. Tape	Round Tape	Sony U-Matic Cart.	Cart. Tape
Pathfinder Units	126	595	1350	80
Pathfinder Medium	Sony 12" Optical	Sony 12" Optical	Exa-byte	Exa-byte

*George Ohring, NOAA/NESDIS, E/RA1, 4700 Silver Hill Road, Stop 9910, Washington, DC 20233; e-mail: gohring@nesdis.noaa.gov

The main product of the AVHRR Land Pathfinder data set is the Normalized Difference Vegetation Index (NDVI). The NDVI is corrected for Rayleigh scattering and presented as 10 day composites, at 8 km and 1 deg resolution, for the time period July 1981 to September 1994.

The AVHRR Ocean Pathfinder data set consists of daily and monthly sea surface temperatures for both day and night at 9, 18, and 54 km resolutions. The data set processed with the Version 1 algorithm extends from January 1987 to December 1993. The data are currently being processed using the Version 4 algorithm and products are available for 1985-1996.

The AVHRR Atmosphere Pathfinder data set includes cloud amount, oceanic aerosol optical depth, and the ERB products of OLR and planetary albedo, including their clear-sky values. The data set is available as day and night, daily, pentad, and monthly 1 deg equal area grids from 1981 to the present. Fig. 1 is a time series of aerosol optical thickness for the operational zone 25N-25S.

The TOVS Path A data set consists of mean temperature at four pressure layers, total effective cloud fraction, cloud fractions at seven pressure layers, longwave cloud radiative forcing, outgoing long-wave radiation, cloud top pressure, precipitation estimate, precipitable water vapor above the surface and four pressure levels, surface pressure, cloud top temperature, and surface skin temperature. The data set is available as day and night daily, pentad, and monthly 1 deg equal area grids from 1985 to 1993. TOVS Path B has a similar set of products processed using the algorithm of Chedin et al. (1985). The products include temperature and moisture profiles, surface temperatures and sea ice presence, physical cloud properties, and profiles of upward and downward IR fluxes. Data are currently available from 1987 through April 1994. The TOVS Path C1 MSU data set consists of tropospheric and stratospheric deep layer temperatures (Spencer and Christy, 1990), and oceanic precipitation (Spencer, 1993), on daily and monthly 2.5 deg grids, for the time period 1979 to present. The tropospheric temperature data are being used to monitor greenhouse warming. The TOVS Path C2 data set contains mean temperatures for seven deep atmospheric layers generated by suitably combing MSU channel observations (Goldberg and Fleming, 1995). The data set

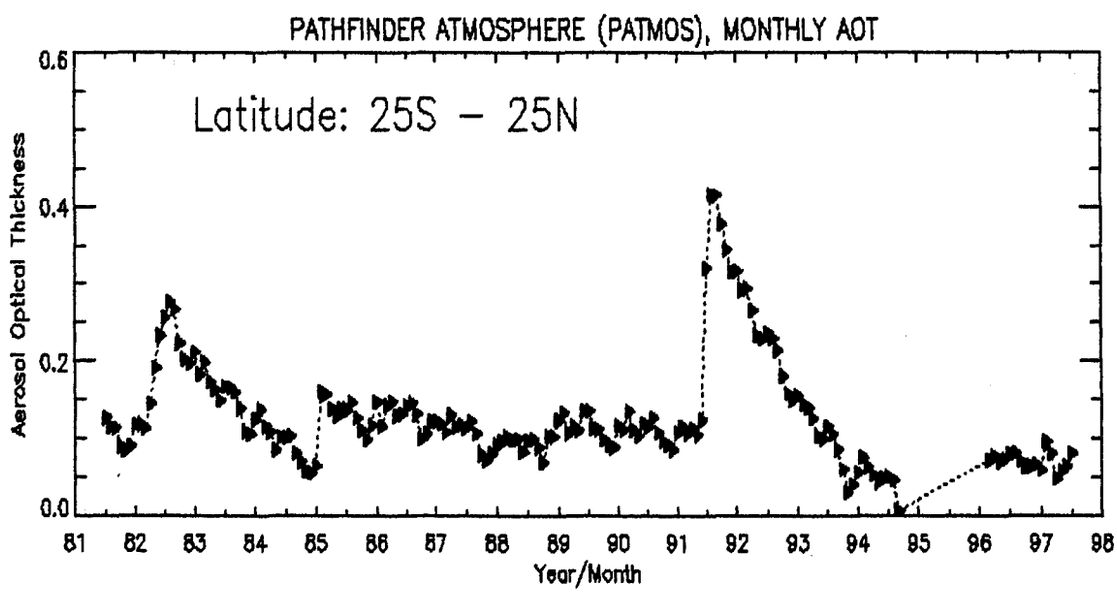

Fig. 1 Monthly aerosol optical depths over the oceans, 25N-25S, from the AVHRR Atmosphere Pathfinder project.

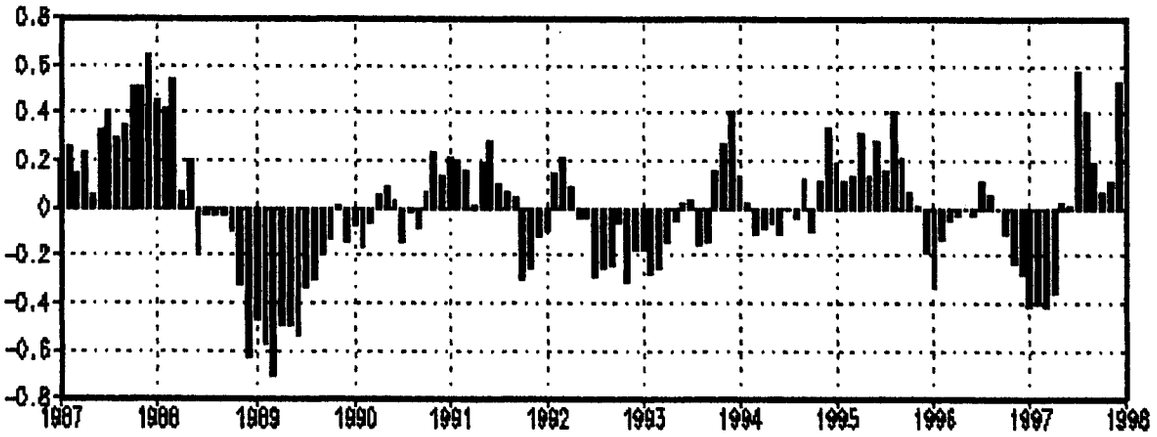

Fig. 2 TOVS C2 MSU lower troposphere temperature anomalies (K), 20N-20S

currently is available from 1987 to present, on a 2.5 deg, monthly grid. Fig. 2 is a time series of equatorial, monthly, lower troposphere temperatures from the TOVS C2 data set.

The GOES Pathfinder data set consists of hourly, 8 km visible, water vapor, and IR radiances and 70 km equal area statistics of the 8 km data for the Pathfinder Benchmark Period of April 1987 to November 1988.

The SSM/I Pathfinder products include precipitation; precipitable water, column liquid water, and surface wind speed over the ocean; sea ice; land surface properties; and snow and ice cover starting from the launch of the first SSM/I in August 1987. Fig. 3 is a time series from 1979 to 1997 of monthly anomalies of Northern Hemisphere snow cover area that is a blend of SSMR and SSM/I Pathfinder data (Armstrong, 1998).

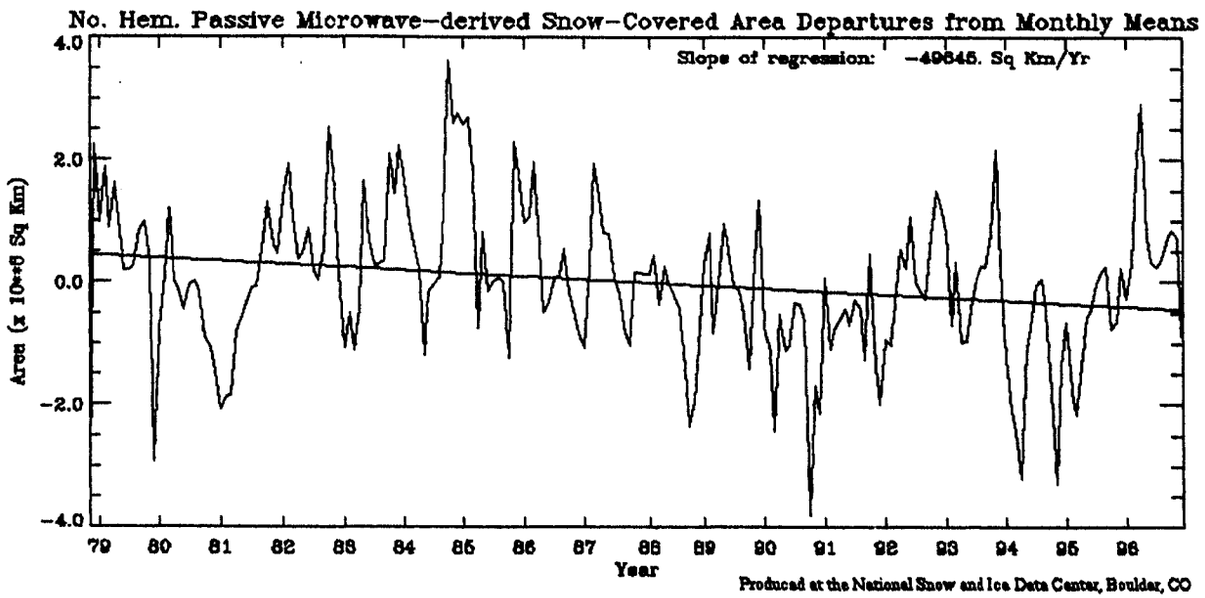

Fig. 3. Northern Hemisphere monthly snow cover area anomalies from SSMR and SSM/I.

3. LANDSAT AND OTHER DATA SETS

In 1995, NASA issued a Research Announcement requesting proposals from the scientific community to continue and expand the original NOAA/NASA Pathfinder Program. As a result of this Announcement, a number of new data sets are being produced as well as some studies to analyze satellite data sets. These projects include, among others, a LANDSAT data set with repeated mapping of multiple sites, production of a global land 1-km AVHRR data set, reprocessing of satellite altimeter data for oceanography, mapping of the Antarctic continent with RADARSAT data, and continuation of WCRP ISCCP and Surface Radiation Budget data sets, improved ozone data sets from combining data from IR and UV sensors, and global precipitation analyses from a merged SSM/I, Geosynchronous IR, and raingauge data set.

4. FUTURE DIRECTIONS AND WHERE TO OBTAIN DATA

These data sets are finding application in a number of climate related areas ranging from understanding to predicting climate and from seasonal-Interannual to decadal time scales. In most cases, the data sets begun under the NOAA/NASA Pathfinder program will continue into the future. The basic premise--that the operational environmental satellites provide the continuous, global observations needed to monitor global climate variations--remains valid. The operationalization of satellite climate observations will occur with the implementation of the NPOESS.

Data sets are available from NOAA and NASA. Good starting points are (for NASA) http://xtreme.gsfc.nasa.gov/pathfinder/Pathfinder_Prog.html and (for NOAA) http://aries.nesdis.noaa.gov

5. REFERENCES

Armstrong, R., 1998: Personal communication.

Chedin, A., N.A. Scott, C. Wahiche and P. Moulinier, 1985: The improved initialization inversion method: A high resolution physical method for temperature retrievals from satellites of the TIROS-N series. *J. Climate and Appl. Meteorology*, **24**, 128-143.

Goldberg, M. and H. Fleming, 1985: An algorithm to generate deep-layer temperatures from microwave satellite observations for the purpose of monitoring climate change. *J. Climate*, **8**, 993-1004.

Rao, N. and J. Chen, 1995: Inter-satellite calibration linkages for the visible and near-infrared channels of the AVHRR on the NOAA-7, -9, -11 spacecraft. *Intl. J. Remote Sensing*, **16**, 1931-1942.

Spencer, R.W., 1993: Global oceanic precipitation from the MSU during 1979-91 and comparisons to other climatologies. *J. Climate*, **6**, 1301-1326.

Spencer, R.W. and J.R. Christy, 1990: Precise monitoring of global temperature trends from satellites. *Science*, **247**, 1558-15.

Walton, C., J. Sullivan, N. Rao, and M. Weinreb, 1998: Corrections for detector non-linearities and calibration in consistencies of the IR channels of the AVHRR. *J. Geophys. Res.*, in press.

01.8B

USE OF SATELLITE SOUNDING CLIMATE RESEARCH

John J. Bates*
NOAA/ERL Climate Diagnostic Center, Boulder, CO

1. INTRODUCTION

As we come to the 20th year anniversary of the TOVS satellites, we should pause to reflect on how TOVS data have been used in climate studies, what are its strengths and weaknesses in climate studies, in what can we do in the future to make better use these data. The complex process of using satellite data for climate applications is illustrated schematically in figure 1. The ultimate goal of this process is to better understand the satellite data and then apply this knowledge to process studies of climate applications leading ultimately to improve climate predictions. There are, in general, two paths to reaching this goal, the forward problem and the inverse problem. In the forward problem, sampled geophysical variables are run through a forward radiative transfer model, along with specific information about the satellite instrument such as the instrument error characteristics and spectral response functions, and the outputs are simulated radiances. This process gives us an idea of what performance we might anticipate from a given instrument. The inverse problem begins with the actual satellite observations. These observations are then used with an inverse radiative transfer model to produce a retrieval of geophysical variables. In this process, additional constraints are often applied to the satellite observations such as use of the forecast first guess, other a priori data such as clustered radiosonde observations, and radiance bias corrections. Observed radiances are compared to simulated radiances and retrieved geophysical variables are compared to observed geophysical variables and this knowledge is then applied to process studies of climate.

2. WHAT IS CLIMATE?

What is climate is a question not easily answered. A formal definition for climate has been offered by the World Meteorological Organization to be the thirty-year mean of the daily averages for only surface variables. There is no definition of a climate average for upper air variables or for any satellite products. For satellite observations, the periods of record have been so short that one typically uses the entire record for the climate mean. Now that the TOVS record of observations is reaching twenty years, we can begin to think of climate periods for satellite sounding observations. This has already happened de facto for some model comparison studies and for reanalysis. The start of the satellite sounding climate period, then, should be defined as January 1, 1979. Logical periods of record for averaging would be five years, 10 years, and 20 years.

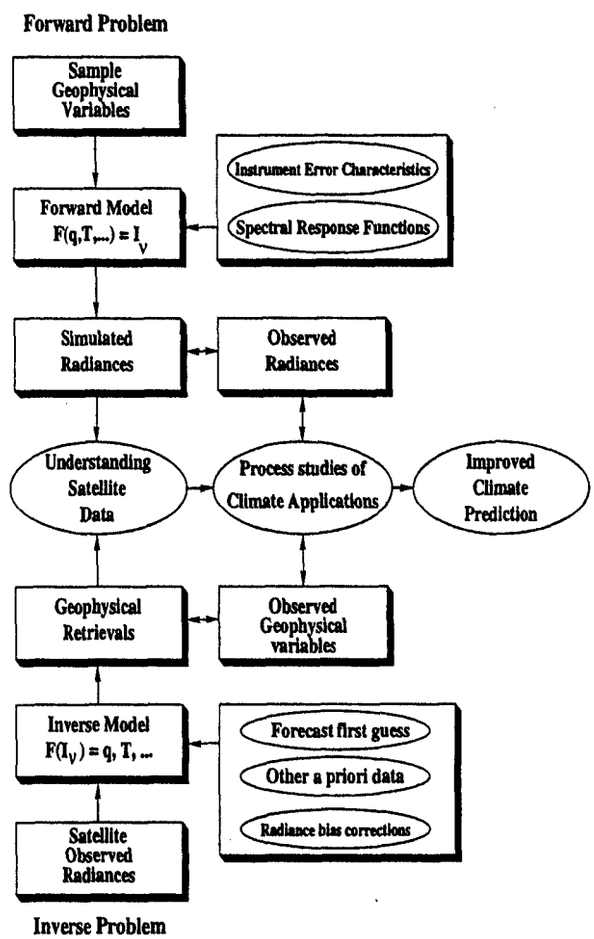

Figure 1: Schematic of the forward and inverse radiative transfer processes as applied to the use of satellite observations for climate monitoring and prediction.

*Corresponding author address: John J. Bates, NOAA/ERL Climate Diagnostic Center, Boulder, CO 80303; e-mail: bates@cdc.noaa.gov

3. APPLICATION OF SATELLITE SOUNDING DATA TO CLIMATE AND GLOBAL CHANGE

3.1 *Detection of Global Warming*

The network of global surface observations has shown that the global mean surface air temperature has increased by between 0.3° and 0.6° C since the late 19th-century. This network, however, is highly irregular in space and includes large data voids. Could we obtain more accurate and homogeneous observations of global temperature using satellite observations? This was the question that Roy Spencer and John Christy asked in the early 1990s (Spencer and Christy, 1992a; Spencer and Christy, 1992b). They examined the record of observations from the microwave sounding unit (MSU) using data from channel 2. They found that data from MSU channel 2 was very stable over time and that inter-satellite differences could be corrected to a common baseline using periods of satellite overlap. For climate studies, a seamless time series of observations is critical in order to perform time series analysis so that instrumental changes are not misinterpreted as climate changes. Because the Spencer and Christy MSU channel 2 index was so carefully constructed and provided a relatively long continuous time series, this index has been widely used in climate studies. This includes studies of the tropospheric temperature response to El Niño and to volcanic aerosol. Spencer and Christy, however, soon realized that the MSU channel 2 weighting function extended over too wide a depth of the troposphere so they looked for a better method that would isolate lower troposphere temperature from that of the upper troposphere and lower stratosphere. This improved method convolved a new weighting function using observations at differing angles along a scanline. Figure 2 shows global, monthly mean anomalies of the MSU lower troposphere and mid-stratospheric indices of Spencer and Christy from the mean of 1979-1995. Variability in stratospheric mean temperature is dominated by warming during volcanic aerosol episodes following the eruptions of El Chichon in 1982 and Mt. Pinatubo in 1991. Variability in the lower tropospheric temperature record is more complex: the peak in 1983 occurs during an El Niño warm event as does the peak in 1988 and in 1991, the dip in 1992 is likely due to Mt. Pinatubo aerosols. The most strident criticism of this index, however, is that the trend in global lower tropospheric temperature is just slightly negative over the period of record and is inconsistent with other global temperature records (Hurrell and Trenberth, 1998).

3.2 *Water Vapor Feedback in the Upper Tropospheric*

The water vapor feedback refers to a several step process initiated when the atmospheric concentration of

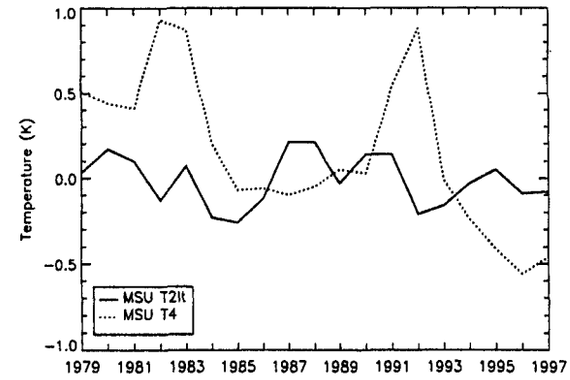

Figure 2: 17-yr time series of MSU lower tropospheric channel 2 (T2lt) and mid-stratospheric channel 4 (T4) temperature anomalies.

greenhouse gases is increased by man-made emissions. This initial perturbation causes a surface temperature increase which leads to increased in surface evaporation that provides an increase water vapor to the atmosphere. This increase in water vapor traps more outgoing longwave radiation and substantially increases the original temperature perturbation. This chain of events is referred to as a positive water vapor feedback. This positive water vapor feedback substantially increases model simulated global temperatures. The notion that the water vapor feedback is always positive was challenged by Lindzen (1990) who argued that deeper convection in the tropics could lead to a net drying or a negative feedback. This controversy renewed interest in the history of satellite water vapor observations, in particular, data from the HIRS water vapor channels. Previously, these data had not been used extensively because of uncertainties in the radiative transfer in the water vapor bands and continuum and due to the poor quality of radiosonde observations of water vapor in the middle and upper troposphere.

As with the MSU, in order to use data over a long time it is necessary to perform a careful inter-calibration of the HIRS instruments on different spacecraft. A priori estimates of the instrument to instrument change expected can be computed by using the pre-launch spectral response functions, a forward radiative transfer model, and a set of sample atmosphere profiles. However, because the HIRS instruments were not calibrated in a vacuum, the pre-launch spectral response functions for the water vapor channels appear to be correlated with the atmosphere in the test chamber. Thus, we used empirical technique to perform the inter-satellite calibration (Bates et al., 1996).

Anomaly time series of tropical aerial average upper tropospheric humidity index and clear-sky

outgoing longwave radiation (Figure 3) are significantly correlated. These time series, however, are not significantly correlated with typical El Niño indices. Nevertheless, these tropical aerial average time series appear to be bounded by the most extreme El Niño warm and cold events. During the 1982-83 El Niño warm event, the upper tropospheric humidity index shows a dramatic decrease and the clear-sky greenhouse increases by over 2 Wm^{-2}. There are only minor changes in the upper tropospheric humidity index and clear-sky greenhouse during 1986-87 in 1991-92 warm events. The other notable feature of the clear-sky greenhouse time series is the large decrease during 1988-89. This minimum slightly lags the minimum in sea surface temperature anomaly during the strong 1988-89 cold event. This has led me to the hypothesis that the response of the tropical water and energy cycles to extreme El Niño events is a negative water vapor feedback as nature tries to restore the current climate balance.

Using satellite data to form a single global average is a risky proposition for many reasons. First, the broad weighting function of the MSU channel 2 and HIRS 12 are inconsistent with measurements at a specific elevation. Second, the inter-satellite calibration must not have any errors that are correlated in time and space because these will show up as a source of systematic error when computing global means. Finally, there can be no systematic errors in the radiative transfer and, particularly, no errors in our understanding a microwave limb effects. Although the work of Spencer and Christy is most famous for this global thermometer use of MSU channel two, this is the most difficult and controversial of use of this data set.

3.3 *Fingerprint Approach to Climate Change Detection using Observations and Models*

Although global time series are important, a better use of the satellite data is to compare the observed spatial and temporal variability with that stimulated by models. This class of techniques, where spatial pattern matching is used to compare observations to simulations, has been called a fingerprinting approach (Santor et al., 1996). We are now only seeing the first attempts at applying these techniques to the TOVS observations. Figure 4 shows the leading mode of the inter-annual variability in the tropics for a variety of long-term satellite observations. Interannual variability of tropical sea surface temperature is dominated by El Niño events and a shift in deep tropical convection from the Western Pacific to the Central and Eastern Pacific. The MSU data show that the entire tropics warms during El Niño warm events particularly in the Eastern Pacific. The upper tropospheric humidity pattern shows strong drying in the subtropics in the Eastern Pacific. Although we have found large discrepancies in the absolute values of upper tropospheric humidity between

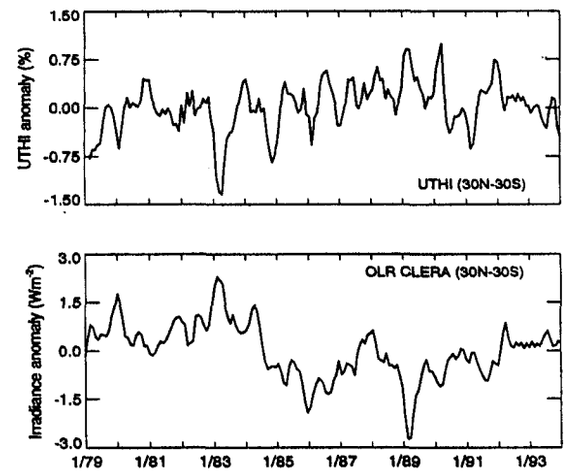

Figure 3: Anomaly time series of tropical areal average upper tropopsheric humidity index (UTHI) (a), and clear-sky longwave radiation (b).

observations and models, we have found better agreement with the pattern evolution (Bates and Jackson, 1997).

4. THE TOVS RADIANCE PATHFINDER

The TOVS radiance Pathfinder project is designed to produce an easy-to-use, high-quality, intercalibrated data set for a variety of uses. We will produce all-sky and clear-sky radiance data sets on a variety of time and space scales. Applications include climate process studies, future reanalysis projects, and validation studies of atmospheric general circulation models. We have just completed a first complete pass through the entire data set from 1979 through 1997 in a data-mining mode. We expect to release the first data sets by the end of 1998 (see web site www.cdc.noaa.gov/~climsat).

5. CONCLUSIONS

I have proposed periods and methods of averaging for climate means using TOVS sounding data. I suggest averaging periods of 5, 10, and 20 years where the averaging is the average of the daily mean quantities. The start of the TOVS climatology should be Jan. 1, 1979. Agreement on a common time period for satellite sounding climatologies will facilitate intercomparison of different studies because those studies will have common time periods.

TOVS data have been highly useful in studies of climate and global change, even though results remain controversial. Studies of lower tropospheric temperature trends from MSU indicate little or no increase in global temperatures during the past twenty years. Studies of the upper tropospheric water vapor feedback suggest that the water vapor feedback can

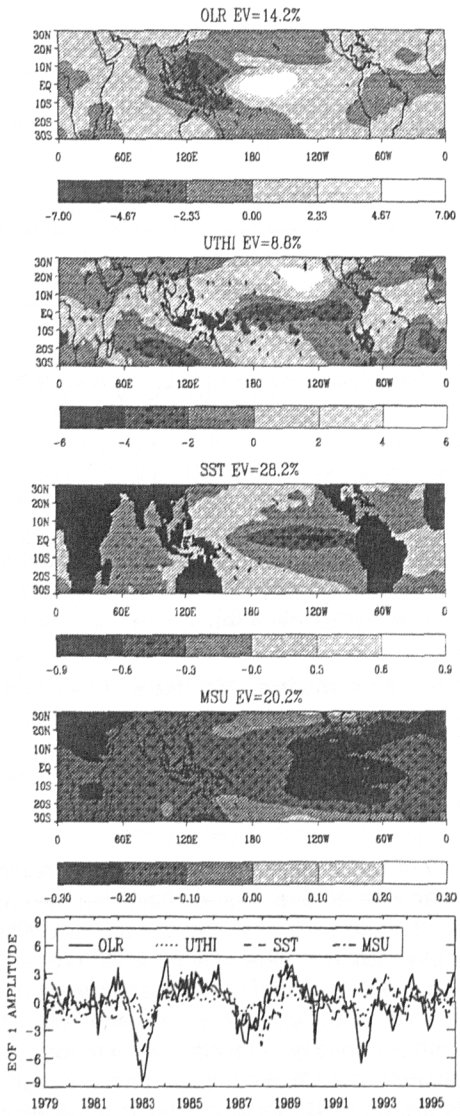

Figure 4: Leading EOF of interannual variability of SST, all-sky OLR, UTHI, and MSU T2.

sometimes be negative. Both of the studies however, rely upon extensive procedures for inter-satellite calibration. As such, the inter-satellite calibration remains the Achilles heel for long-term climate studies using satellite data. Much additional work remains to be done on the issue of inter-satellite calibration.

The preferred method for comparison of satellite observations with model simulations is the use of pattern correlation techniques, or fingerprint identification. This can be done using either satellite retrievals or satellite radiances. The TOVS radiance Pathfinder project will be producing a set of all-sky and clear-sky radiances suitable for such comparisons. We look forward to working with a variety of groups to make best use of this important observational data set for studies of climate global change. In the near future, we will be applying fingerprint techniques to the entire suite of TOVS sounding channels and believe that the TOVS data set will be the most powerful tool for validation of model simulations of climate and global change.

6. REFERENCES

Bates, J. J., and D. L. Jackson, 1997: A comparison of water vapor observations with AMIP I simulations. *J. Geophys. Res.*, **102**, 21 837-21 852.

Bates, J.J., X. Wu, and D.L. Jackson, 1996: Interannual variability of upper-tropospheric water vapor band brightness temperature. *J. Climate*, **9**, 427-438.

Hurrell, J. W., and K. E. Trenberth, 1998: Difficulties in obtaining reliable temperature trends: Reconciling the surface and satellite MSU records. *J. Climate*, in press.

Lindzen, R. S. , 1990. Some coolness concerning global warming. *Bull. Amer. Meteor. Soc.*, **71**, 288-299.

Santor, B. D., and colleagues, 1996: A search for human influences on the thermal structure of the atmosphere. *Nature*, **382**, 39-46.

Spencer, R. W., and J. R. Christy, 1992a: Precision and radiosonde validation of satellite gridpoint temperature anomalies. Part I: MSU channel 2. *J. Climate* , **5**, 847-857.

Spencer, R. W., and J. R. Christy, 1992b: Precision and radiosonde validation of satellite gridpoint temperature anomalies. Part II: A tropospheric retrieval and trends during 1979-90. *J. Climate*, **5**, 858-866.

O1.10B

REANALYSIS OF TOVS DATA: LESSONS LEARNED FOR CLIMATE STUDIES OF THE EOS AND METOP ERA

A. CHEDIN
Laboratoire de Météorologie Dynamique du CNRS
Ecole Polytechnique, RD36
91128 Palaiseau Cedex, France
chedin@ara01.polytechnique.fr

1. INTRODUCTION

Accurate soundings of atmospheric and surface parameters are fundamental to improving our understanding of the earth's atmosphere circulation, of the earth's climate, and the detecting/predicting of the possible climate changes.
Several on going international projects to study atmospheric and surface processes like Pathfinder, GEWEX heavily rely on satellite observations.
The Pathfinder data set concept was initiated in response to the question « What can be done now for further global change research? ». The answer of NOAA and NASA was 1) to take advantage of currently archived satellite data to elaborate an enhanced analysis of the real Earth climate driving forces and 2) to give immediate accessibility of new results to other researchers who can make use of them by integration into new products or process studies.

2. THE REANALYSIS OF A MULTI-YEAR TOVS DATA

Eventually, with space observation like the NOAA/TIROS-N series, started in 1979 and still in operation for the coming years an unique opportunity is offered, and in particular with the TOVS, to study the most relevant climate variables, globally and over long time series.
In our community, considerable research has been performed with regard to the development of the algorithms suite (forward and inverse) to derive accurate and spatially/temporally robust products using the presently available infrared and microwave radiometric soundings of the TOVS.
The result has been the elaboration of comprehensive long term validated datasets of atmospheric and surface variables (temperature, water vapor, clouds, surface characteristics, ...) associated with flux components (spectral, vertical, surface) and radiative cooling or heating rates.

There is now a consensus on the following points:
a) to make this elaboration successful requires expertise in:
- spectroscopy
- forward and inverse modeling
- data reduction and estimation theory

b) to make the dataset a useful tool for climatology requires:
- products quality assessment:
- use and developments of structural and statistical algorithms.

So far, a lot of work has been devoted to identify, acquire, handle a huge amount of auxiliary validation data sets , to organize the multiple interfaces of inputs/outputs and to elaborate the error description. Also, automatic decision algorithms have been implemented in order to maintain the product integrity by a control of the errors (random, systematic, « unplanned »).
A list of such products is given below. The spatial resolution is approximately 100x100km2. The temporal resolution is on the basis of daily, pentad and monthly means am and pm.

Units	Description
K	Temperature between 1000 mb and 850 mb
K	Temperature between 850 mb and 700 mb
K	Temperature between 700 mb and 500 mb
K	Temperature between 500 mb and 300 mb
K	Temperature between 300 mb and 100 mb
K	Temperature between 100 mb and 70 mb
K	Temperature between 70 mb and 50 mb
K	Temperature between 50 mb and 30 mb
K	same as above for 9 virtual temperatures
K	Temperature between 30 mb and 10 mb
K	Mean temperature surface to 500 mb
K	Mean temperature 500 mb to 300 mb
K	Mean temperature 300 mb to 100 mb
K	Mean temperature 100 mb to 30 mb
cm	Precipitable water vapor above surface
cm	Precipitable water vapor above 850 mb
cm	Precipitable water vapor above 700 mb

cm	Precipitable water vapor above 500 mb
cm	Precipitable water vapor above 300 mb
cm	Surface skin temperature
%	Total effective cloud amount
%	Effective cloud amount above 180 mb
%	Effective cloud amount between 310 and 180 mb
%	Effective cloud amount between 440 and 310 mb
%	Effective cloud amount between 560 and 440 mb
%	Effective cloud amount between 680 and 560 mb
	Effective cloud amount between 800 and 680 mb
v	Effective cloud amount below 800 mb
mb	Cloud top pressure
K	top temperature
deg	HIRS/2 satellite zenith angle
hrs	Local time of the day
N/A	Quality flag
%	microwave surface emissivity
N/A	air mass flag (from 1 to 5)

Level 4 products such as multi-layer upward and downward longwave fluxes are also generated.

3. THE SENSORS OF SECOND GENERATION

We have seen, during the reanalysis of the multi-year TOVS data, that even though the TOVS sensors provide so much data, some crucial features of the environment have been « hidden » or « distorted »: some examples are the retrievals of water vapor profiles under heavy cloudiness (more than 60%) or land surface temperatures. This may be due to the inherent limitations of the sounder (number and spectral or spatial characteristics of the channels) or some inability of the algorithms to correctly handle the information.
The coming microwave sounders (AMSU A and B) and the high spectral resolution infrared sounders (IASI/METOP or AIRS/EOS) are expected to provide improved measurements of clouds, atmosphere, land and oceans parameters with the accuracy, vertical resolution and coverage required by future weather and climate models (e.g. 1degreex1km for temperature, ...).
Work is in progress to extend the retrieval (pre-processing, processing) algorithms to this so-called second generation sounders which will « offer » some thousands of sounding channels in the 645-2800cm-1 spectral range with a 1200 resolution power- to be compared to the 20 channels of the TOVS !-.
No need to say that improvements in spectroscopy, as well as in the fields of classification, estimation, data compression are fully recurrent.

With TOVS, we have demonstrated that we can handle fuzzy, noisy and sometimes inconsistent data in a way that is possible only if we are able to analyze these data in detail.
We have learnt how to use selective perception to focus on processing certain features or how to define « agents » to successfully interact with such a complex environment (global surface - atmosphere system).

The coupling of forward and inverse modeling (both good but not yet optimal) associated with the already available information (good but to be improved) on the global surface-atmosphere system gives us an unparalleled way to make these « agents » as intelligent as possible in order to perform some tasks as:

- check of plausibility (with respect to first guess fields, climatological values, dynamic range simulations from forward modeling),
- check for contradictions (analysis of two or more parameters at the same location),
- check for consistency and spatial continuity (values of a variable at adjacent points usually are slightly different from each other),
- diagnostic equations (study of the residuals against "reference" values)

automatically followed by « reward » and « penalty » actions.
We have demonstrated that the reanalysis products allow for a successful description of some climate processes: so far, this has been done, to the best of our knowledge, in a supervised way (we were expecting finding some sea surface temperature anomalies associated with El Nino or La Nina).
The problem we have started to work on is: how possible will it be (with the new sensors / perceptors) and with what kind of tools (supervised, unsupervised or reinforced learning, ...) to reduce the number of hidden states and increase the feature detection of our environment for climate studies?

ACKNOWLEDGMENTS

This contribution emerges from many useful discussions within the frame of the NOAA/NASA Pathfinder Program, the GEWEX-GVap Program, the AIRS and IASI science team meetings, the WMO/IRC working groups (ITRA, ITSC). This presentation was also greatly helped by constructive discussions and questions with and from my colleagues and students of the ARA/LMD group.

P1.1A

OBSERVED VARIABILITY OF TOTAL COLUMN WATER VAPOR RELATED TO ATMOSPHERIC TEMPERATURE

David L. Randel* and Thomas H. Vonder Haar
Colorado State University, Ft. Collins, Colorado

Mark A. Ringerud
Science and Technology Corporation - METSAT

1. INTRODUCTION

The total column water vapor in the Earth's atmosphere is directly related to the atmospheric temperature through the evaporation and precipitation processes. The simple concept that warmer air can hold more water is known by every beginning meteorologist. However, the Clausius-Clapeyron equation, which defines this relationship at the saturation point is not applied at sub-saturated levels. So why does warmer air in general hold more water vapor? A simplistic response is that both evaporation and precipitation are processes at saturation and the magnitude of each defines the total water vapor content of the atmosphere. From the interaction of global temperature and water vapor, it is believed that the climate system follows a constant relative humidity rather than a constant absolute humidity (e.g., Stephens 1990; Gitowski et al. 1995).

The Earth-atmosphere system is controlled by both direct and indirect feedbacks mechanisms that affect the water vapor content and temperature. For example, water vapor has a direct radiative effect on the outgoing longwave radiation by "blocking" surface radiation, and increasing the lower layer temperature. In this case, water vapor is said to have a positive feedback on the temperature. An example of an indirect effect would be increasing cloudiness due to an increase in water vapor, thus raising the short-wave albedo of the cloud and resulting in atmospheric cooling. This produces a negative feedback on temperature. There are many of these feedbacks mechanisms, and as a science, we have varying success at both understanding and modeling their effects.

The purpose of the intercomparison presented here is not to improve our understanding of the individual feedbacks, but to observe their ensemble effect on the global atmosphere. This combined effect defines the response of our climate system to changes in atmospheric temperature. These results may also be used as a surrogate for future global warming since the amplitude of the observed temperature anomalies (1.0°C) is similar to that forecast for man-induced warming over the next 50 years (IPCC, 1996).

2. SATELLITE DATA SETS

Eight years of measurements of lower tropospheric temperature (LTT) and total column water vapor including the years 1988 – 1995 were used. The LTT data obtained is the 2R product created by Christy and Spencer (Christy et al. 1995) from the Microwave Sounding Unit (MSU) on board the NOAA series of operational satellites. The discussion of the differences between this dataset and others (Hurrell and Trenberth 1996) concerns the sign of the temperature trend over the entire NOAA time series. The temperature anomalies used here are an order of magnitude greater than the trend, and thus the discussion of the sign of the trend is not relevant.

The total column water vapor (WV) anomalies were produced from the NVAP dataset (Randel et al. 1996). This dataset merged water vapor retrievals from TIROS Operational Vertical Sounder (TOVS), Special Sensor Microwave / Imager (SSM/I), and global radiosondes, and is independent from the MSU temperature retrievals. The impetus of developing the NVAP dataset was to develop a global water vapor product in all sky conditions as a pilot dataset for the WCRP/GEWEX Global Water Vapor Project (GVaP).

The water vapor anomalies were calculated from the 8-year monthly means, while the LTT anomalies were calculated from the entire 16-year dataset.

* *Corresponding author address*: David L. Randel, Cooperative Institute for Research in the Atmosphere (CIRA), Colorado State University, Ft. Collins, CO 80525. Email: randel@cira.colostate.edu

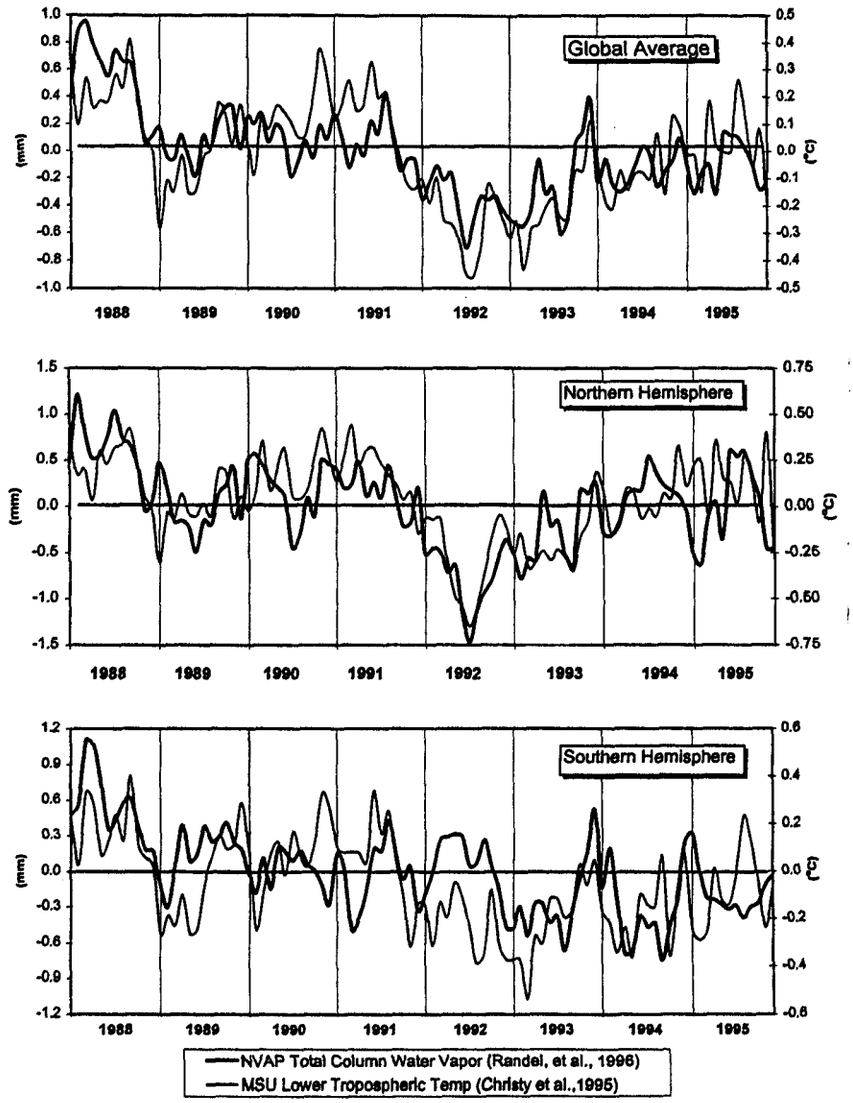

Figure 1. Time series of the anomalies of lower tropospheric temperatures (Christy et al. 1995) and total column water vapor (Randel et al. 1996). The large drop in global temperature and the associated drop in the water vapor in 1991-92 were due to the eruption of Mt. Pinatubo and stratospheric aerosol cooling.

2. ANOMALY INTERCOMPARISON

The time-series of the LTT and WV anomalies are presented in Fig. 1. The top chart uses the global averaged anomalies, and the hemispheric anomalies are shown below. The global temperature anomalies show the effect of stratospheric aerosol loading in 1991-1992 due to the eruption of Mt. Pinatubo. In this plot, the atmospheric cooling was 0.8°C, which was accompanied by a drop in WV of 1.3 mm. The response in the Northern Hemisphere was even greater with a 2 mm drop in WV and a 1°C drop in temperature. Overall, it can be noted from the respective scales on the plots, that the anomalies show a change in water vapor of approximately 1 mm for every 0.5°C temperature change.

Recent experiments (J.R. Garratt and G.L. Stephens, personal communication) used a number of general circulation models to study the atmospheric response to increasing CO_2. The results showed roughly the same temperature / water vapor response with a change of 1 mm in the total column water vapor for every 0.5 °C change in global temperature. These results are encouraging since they imply that the combined feedbacks and forcings in the models are of the

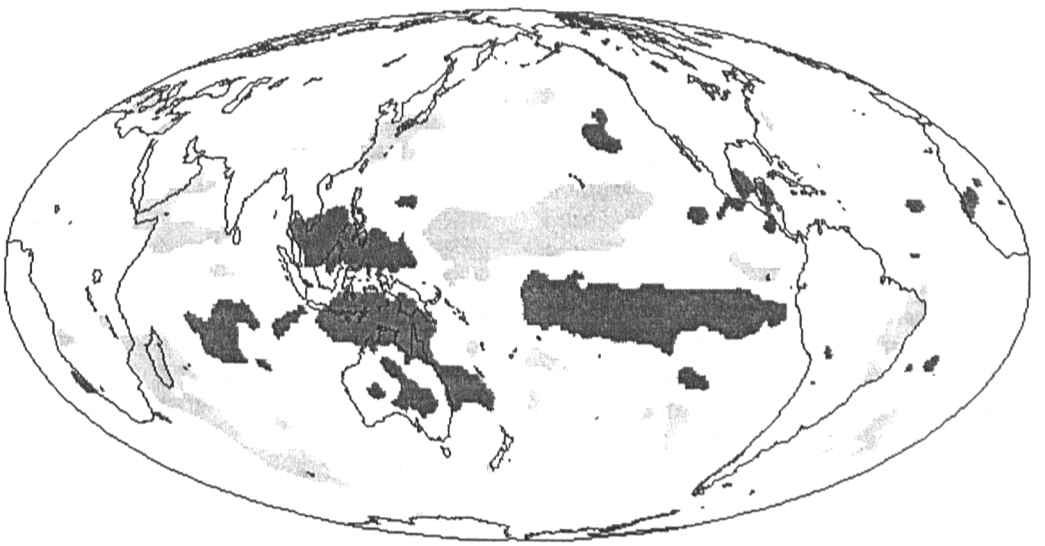

Figure 2. March 1991 anomaly of total column water vapor (mm). The dark shaded areas have less water vapor than the March average, while areas light shaded light have more. The threshold is anomalies greater or less than 3 mm.

same magnitude as those observed in the atmosphere.

Fig. 1 also shows that the relationship of the anomalies in the Southern Hemisphere (SH) is not as strong. While over the long-term the correlation still holds to the 1mm per 0.5°C, the short-term dependence is indistinct. Why doesn't the inter-dependence of water vapor and temperature always hold true? Certainly, there are many regional weather conditions where the temperature and water content of the atmosphere don't have a positive correlation. However, why does the relationship fail on these large global and hemispheric scales? Fig. 2 shows the water vapor anomalies for March 1991. This is an example when the sign of the temperature and water vapor anomalies did not agree, and the agreement in the SH was especially poor. During this month there were slightly warmer temperatures, yet the TCWV was less. In Fig. 2 we see the areas in the SH, as denoted by the dark shaded areas, which have less WV than normal. These areas tend to be the broad subsidence areas, the extent of which is controlled by the intensity of the ITCZ. The Australian desert also shows less than normal WV. The temperature/water vapor relationship will not hold in these two situations - increased subsidence warming over the ocean dries the atmosphere, as does continental heating with little soil moisture and evaporation.

3. SUMMARY

There is a strong correlation between the global and hemispheric anomalies of water vapor and temperature from 1988 - 1995. This relationship, from direct observations, may confirm the theory that periods of warmer global temperatures, will be accompanied by an increase in the total column water vapor.

References

Christy, J.R., R.W. Spencer, and R.T. McNider, 1995: Reducing noise in the MSU daily lower-tropospheric global temperature dataset. *J. Climate*, **8**, 888-896.

Gutowski, W.L., E.A. Lindemulder, and K. Jovaag, 1995: Temperature-dependent daily variability of precipitable water in special sensor microwave / imager observations. *J. Geophys. Res,* **100**, 22971-22980.

Hurrell, J. W., and K.E. Trenberth, 1996: Satellite versus surface estimates of air temperature since 1979. *J. Climate*, **9(9)**: 2222-2232.

IPCC (Intergovernmental Panel on Climate Change), 1996. Climate Change 1995: The Science of Climate Change. Eds. J.T. Houghton, F.G. Meira Filho, B.A. Callander, N. Harris, A. Kattenberg, and K. Maskell, Cambridge Univ. Press, Cambridge, U.K. 572 pp.

Randel, D.L., T.H. Vonder Haar, M.A. Ringerud, G.L. Stephens, T.J. Greenwald, and C.L. Combs, 1996: A new global water vapor dataset. *Bull. Amer. Meteor. Soc.,* **77**, 1233 – 1246.

Stephens, G.L., 1990: On the relationship between water vapor over the oceans and sea surface temperatures. *J. Climate*, **3**, 634-645.

Acknowledgements

This research was primarily sponsored by NASA grant NAG5 – 3449.

P1.2B

THE WCRP/GEWEX GLOBAL WATER VAPOR PROJECT

David L. Randel* and Thomas H. Vonder Haar
Colorado State University, Ft. Collins, Colorado

1. INTRODUCTION

After a successful 5-year pilot phase, the WCRP/GEWEX Global Water Vapor Project (GVaP) is planning a major startup within the next year. GVaP will concentrate its efforts, over the next 7 years, on improving the observations of atmospheric water vapor and investigating the variability, radiative effects, and its changes due to anthropogenic influences. A case can easily be made that water vapor is *the* critical component of the Earth-Atmospheric-Ocean system. It's importance lies in transporting water and energy around the globe without regard to continental boundaries, radiatively warming the Earth as our most important greenhouse gas, and providing the source of water for precipitating systems. The strength of the GVaP project is a unique focus on investigating the open scientific questions related to water vapor, with emphasis on improving the measurements through calibration, validation, and algorithm improvements. This will permit a new generation of global and regional datasets and climatologies to be developed and used effectively by each of the major WCRP efforts.

Over the previous 5 years, new ground-based water vapor verification systems have been developed including LIDAR, microwave radiometers, advanced radiosondes, and GPS. We now have, for the first time, the ability to accurately validate the global satellite retrievals of water vapor.

Understanding water vapor's role in our climate system has always been an important component of global climate research, therefore, why the emphases on water vapor now? *A program emphasizing water vapor is appropriate because the observations from the current and near-operational systems can finally meet the time and space resolution required to answer the important scientific questions which deal with water vapor.* Also, GVaP aims to assist each of the current WCRP projects by supplying accurate, validated water vapor data and provide the leadership for many of the water vapor related science issues.

In the past, water vapor studies have relied entirely on the ground launched, sparsely distributed network of global radiosondes. With the addition of satellite platforms for both infrared and microwave instrumentation, there is now a truly global observing system. The first significant advancement came in 1987 when the first of the Defense Meteorology Satellite Program (DMSP) satellites was launched with a multi-channel, duel polarization microwave instrument, the Special Sensor Microwave/Imager (SSM/I). For the first time, this allowed operational measurements, in all-sky conditions, of the total column water vapor over the world's oceans.

Essential to all of the major WCRP projects, is a historical data set of substantial length necessary to interpret the natural variability of the climate system. For measurements of atmospheric water vapor, we are finally reaching this threshold. Currently there are over 10 years of SSM/I measurements that, when combined with almost 20 years of infrared observations (from the NOAA series of operational satellites), provide a data record of significant extent. GVaP is strategically positioned to successfully combine this retrospective data with a number of new and innovative data collection systems that soon will produce a high percentage of the global observations of water vapor. These include retrievals from: Global Positioning System (GPS) (Bevis et al.,1992), the Advanced Microwave Sounding Unit (AMSU-B)(Vangasse et al.,1996), and the Water Vapor Sensing System (WVSS) component of the ACARS (the Aircraft Communications Addressing and Reporting System). In addition, considerable efforts are underway to standardize and improve the measurement technique and data processing of balloon observations in the global radiosonde network (Elliott and Gaffen, 1993).

Accompanying these innovative observing systems, is new instrumentation critical to the GVaP validation and calibration efforts. These include LIDAR systems, both DIAL and RAMAN, improved radiosonde sensor technology, ground-based microwave and infrared radiometers, and

* *Corresponding author address*: David L. Randel, Cooperative Institute for Research in the Atmosphere (CIRA), Colorado State University, Ft. Collins, CO 80525. Email: randel@cira.colostate.edu

GPS measurements. These new technologies are essential to GVaP since they allow the uncertainties in the satellite observations to be defined.

GVaP fits well with the other projects of the WCRP. These WCRP atmospheric research activities are currently underway and study the many other aspects of the Earth's climate system. They include:

- Arctic Climate System Study (ACSYS)
- Climate Variability and Predictability (CLIVAR)
- Global Energy and Water Cycle Experiment (GEWEX)
- Stratospheric Processes And their Role in Climate (SPARC)

Each of these projects, need the best available water vapor data in order to address their science issues, but often the incomplete spatial and temporal resolution, as well as the poorly-understood measurement uncertainties, have slowed the progress and limited the validity of the scientific conclusions.

Finally, GVaP has established a firm foundation upon which to build a successful international project. In the previous five years, GVaP has completed a successful pilot phase, including development of eight years of blended water vapor data currently used internationally by over 250 science groups (Randel et al., 1996). Also, there has recently been a large rise in scientific interest as evidenced by a surge of journal articles and the support shown during the AGU Chapman Conference on Water Vapor (Jekyll Island GA, October 1994) which had over 200 international participants.

2. GVaP's ROLE IN GEWEX

The Global Energy and Water Cycle Experiment (GEWEX) is a program initiated by the World Climate Research Programme (WCRP) to observe, understand and model the hydrological cycle and energy fluxes in the atmosphere, at the land surface and in the upper oceans. The goal of

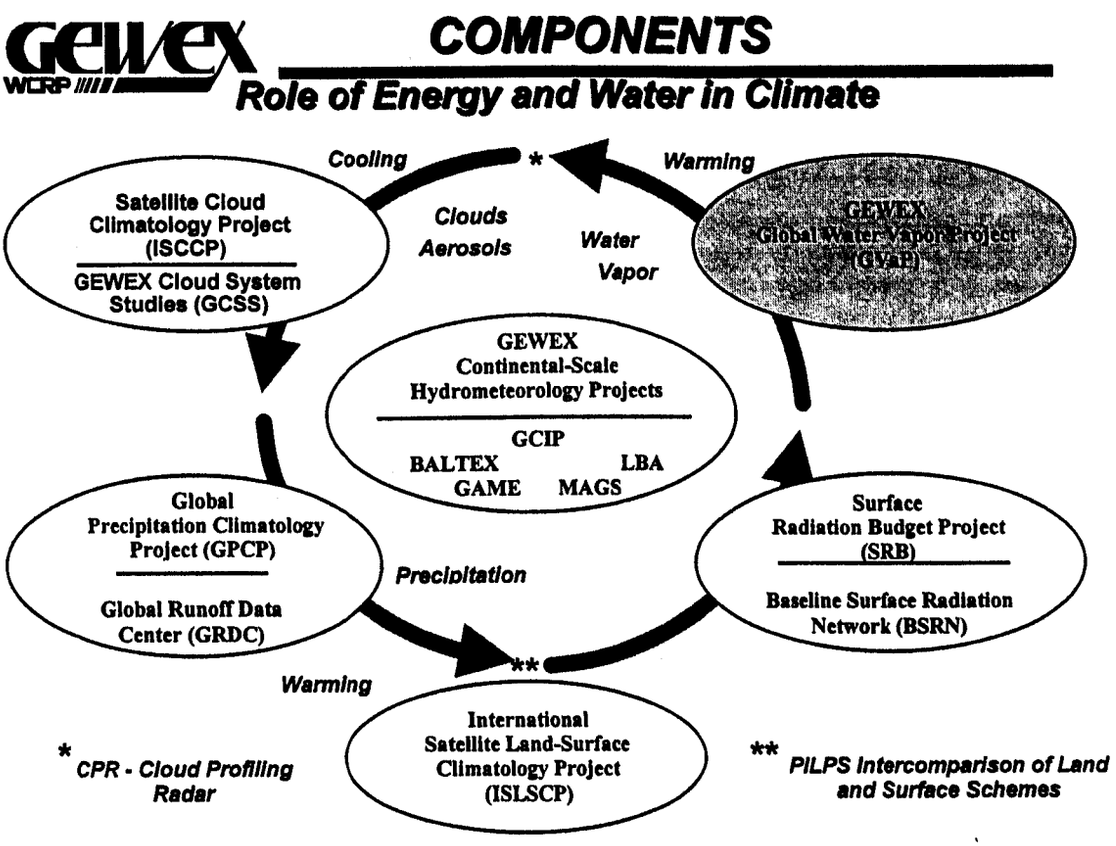

Fig 1. The importance of the GVaP project can easily been in this diagram of the various components of the hydrologic cycle that make up the Global Energy and Water Cycle Experiment (GEWEX).

the GEWEX Program is to reproduce and predict, by means of suitable models, the variations of the global hydrological regime, its impact on atmospheric and surface dynamics, and variations in regional hydrological processes and water resources and their response to changes in the environment, such as the increase in greenhouse gases. The essential role of water vapor in the hydrologic cycle can be seen in the unified view of the various GEWEX projects (Figure 1). Water vapor ties together the surface and atmosphere through the evaporation and condensation processes. Until this time, a project designed to concentrate on water vapor has been a missing component of the GEWEX Program.

3. GVaP PLAN & OBJECTIVES

The GVaP planning has from the beginning, included an international group of scientists, whom specialize in climate studies directly related to water vapor. Planning meetings included informal luncheons, gatherings at international scientific conferences, and two formal workshops in Geneva, Switzerland and Washington D.C. Rather than form a new program within the WCRP or GEWEX, it was decided that GVaP would be organized as a crosscutting effort within the WCRP, and administered by GEWEX. GVaP's charge is to both enhance and support the efforts of the current WCRP projects by: improving validation, reference, and calibration thus minimizing the uncertainties in the water vapor measurements, improving the global water vapor climatologies, using the new water vapor datasets to answer the pressing research questions related to water vapor, and developing new observing systems and strategies.

The original strategic plan for GVaP was developed in 1990 and stated in "The Role of Water Vapor in Climate" (1991). At that time, the overall goal of GVaP was:

To improve understanding of the role of water vapor in meteorological, hydrological, and climatological processes through improved knowledge of water vapor and its variability on all scales.

This goals statement was very broad, but it is still appropriate eight years later. Today, in the late '90s, additional emphasis is being placed on research that expounds the important role of water vapor in weather systems and the maintenance of

Overarching Science Goal of GVaP

Quantify and understand the role of water vapor in the meteorological, hydrological, and climatological processes by improving our knowledge of its variability, radiative effects, feedbacks, and change due to human activities.

GVaP Approach

Understand those mechanisms and processes responsible for the observed variability, at all time scales, in the global water vapor distribution.

Document the climatology of water vapor with respect to both the natural and anthropogenic forced variability.

GVaP Research Objectives

- Determine the horizontal and vertical transport, and the surface fluxes of water vapor on regional and global scales.
- Study the interannual and interseasonal variability of regional systems with emphasis on water vapor recycling through the monsoons.
- Investigate how the hydrologic cycle will change during periods of global warming.
- Characterize the role of clouds and other processes that maintain the vertical distribution of water vapor.
- Examine the direct and indirect water vapor feedbacks on the climate system.
- Document the 3-dimensional distribution of water vapor including interannual to short-term, daily variability.
- Investigate how water vapor and its variability relate to other climate variables such as sea surface temperature, precipitation, cloudiness and others.

the climate system. These studies include: forecasting severe weather events, water vapor radiative forcing and feedbacks, water vapors importance as the principal greenhouse gas, and water vapors significance in the hydrologic cycle related to biosphere changes. These additional research priorities are reflected in the updated overarching goal and objectives of GVaP.

To begin, GVaP will emphasize the calibration/validation issues, including algorithm development and intercomparison. Workshops are currently scheduled for comparison of upper and lower tropospheric water vapor retrievals. Preliminary intercomparison efforts are currently ongoing within various research groups, and their efforts will enable significant improvements to the pilot data sets once completed. The focus will then shift to the creation of new GVaP global data sets with additional data sources, and investigations into the GVaP science themes will commence. The GVaP plan includes migrating both the water vapor data sets and early scientific results to the research community using a combination of data distribution (this may be a NASA DAAC), workshops, symposia, reports, and individual scientific publications.

4. CALIBRATION AND VERIFICATION OF SATELLITE RETRIEVALS

In order to provide global coverage, the GVaP data sets of global water vapor distribution and derived products must be largely based on satellite remote sensing. A crucial requirement for GVaP will be the validation of these products in a structured and defensible manner using well-characterized ground-based remote and in situ sensing of the water vapor field. Therefore, such an effort requires the establishment of a network of ground stations strategically located to validate the accuracy of GVaP products over a wide range of climatic conditions, including significant structure in the vertical distribution of water vapor.

The GVaP calibration/validation plan calls for establishment of a global network of 5-6 sites fully instrumented sites with the most advanced water vapor sensors including: LIDAR, GPS receivers, ground based radiometers, and advances sondes. The deployment of these sites is already underway through sponsorship of the Department of Energy's Atmospheric Radiation Measurement (ARM) Program. In order to provide validation and verification under all meteorological and climatological situations, an additional 15-20 sites are needed to launch advanced radiosondes without the costly LIDAR systems.

5. SUMMARY

The WCRP/GEWEX Water Vapor Project (GVaP) is a 7-year project designed to improve the measurement of atmospheric water vapor, answer the most pressing research issues dealing with water vapor, and assist in development of new water vapor observing systems. In the coming months and years there will be many opportunities to contribute to the project by participation in working groups studying retrieval methodology, data intercomparison, instrument performance, and through basic research grants.

References

Bevis, M., S. Businger, and T.A. Herring, C. Rocken, R.A. Anthes, and R.H. Ware, 1992: GPS meteorology: Remote sensinf of atmospheric water vapor using the Global Positioning System. J. Geophy. Res., 97, 15787 – 15801.

Elliott, W.P., and D.J.Gaffen, 1993: Effects of conversion algorithms on reported upper-air dewpoint depressions. *Bull. Amer. Meteor. Soc.*, **74**, 1323-1325.

Randel, D.L., T.H. Vonder Haar, M.A. Ringerud, G.L. Stephens, T.J. Greenwald, and C.L. Combs, 1996: A new global water vapor dataset. *Bull. Amer. Meteor. Soc.*, **77**, 1233 – 1246.

The Role of Water Vapor in the Climate System: A strategic research plan for the proposed GEWEX Water Vapor Project (GVaP). 1991, NASA conference publication 3120. Ed: D.O'C.Starr and S.H. Melfi.

Vangasse, P., J. Charlton, and M. Jarrett, 1996: Characterisation of the Advanced Microwave Sounding Unit, AMSU-B. Advances in Space Research, Oxford, England, 17(1): 75-78.

Acknowledgements: Development of the GVaP plan and objectives has been an ongoing effort since the beginning of the decade. Literally hundreds of international scientists have participated in the research planning and drafting workshops providing both their time and significant efforts to GVaP. In addition, we thank Dr. Paul Try, Director of the International GEWEX Program Office for his GEWEX overview figure. Support has also been provided by the Cooperative Institute for Research in the Atmosphere (CIRA) for development of the formal GVaP Science and Implementation Plan, from which much of this paper is derived.

P1.3A

ANALYSIS OF UPPER TROPOSPHERIC WATER VAPOR BRIGHTNESS TEMPERATURES FROM SSM/T2 AND HIRS

Wesley Berg*[1], John J. Bates[2], Darren L. Jackson[1], Merritt Deeter[1]

[1]CIRES, University of Colorado, Boulder, CO
[2]NOAA/ERL Climate Diagnostic Center, Boulder, CO

1. INTRODUCTION

Upper-tropospheric water vapor is important for studies of weather and climate on a variety of time and space scales. Synoptic meteorologists have used infrared UTWV imagery from geostationary satellites in a qualitative manner for many years Tracking of UTWV features has long been used to derive water vapor drift winds for input to numerical weather prediction schemes. These data have been useful in providing improved initialization to numerical weather prediction (NWP) [*McNally and Vesperini*, 1996], and particularly, for improving hurricane track forecasting [*Velden et al.*, 1997]. More recently, these data have been used in direct one- and three-dimensional NWP assimilation schemes and have shown dramatic positive impact [McNally, personal communication].

Infrared UTWV data have also been used in a variety of climate studies. Recent interest was sparked by Lindzen [1990] who challenged the notion that UTWV would provide a strong positive feedback to increases in temperature initiated by increases in anthropogenic greenhouse gases. This stimulated a re-examination of the satellite record of infrared UTWV observations. The National Oceanographic and Atmospheric Administration (NOAA) polar-orbiting satellites have observed UTWV globally since 1979 using the up-welling radiance from the strong water vapor absorption line near 6.7μm. Initially these data were not used because of large uncertainties in the radiative transfer theory, specifically with regard to water vapor continuum effects, and because of disparities between these observations and in situ radiosonde observations. Recently, there has been considerable improvement in radiative transfer theory [*Clough et al.*, 1992] and in our understanding of radiosonde observations of UTWV. This has led to increased use of both polar-orbiting and geostationary satellite observations of UTWV, although infrared observations are limited to clear or cloud-cleared fields of view since clouds are opaque in the infrared. This leads to a systematic bias in sampling UTWV, although Soden and Lanzante [1996] suggest that this bias is rather small.

At microwave frequencies, up-welling atmospheric radiation penetrates through nonprecipitating clouds with relatively low water content, such as cirrus. Theoretical studies [*Rosenkranz et al.*, 1982; *Wilheit*, 1990] and aircraft measurements [*Wang et al.*, 1997] demonstrated that the water vapor resonance line at 183 GHz could be used to produce vertical profiles of water vapor by using measurements of several frequencies around the center of the line combined with information about the vertical temperature profile. Such an instrument, called the Special Sensor Microwave Water Vapor Sounder (SSM/T2), has now flown on the Defense Meteorological Satellite Program (DMSP) series of satellites for several years. A similar instrument will also fly on the NOAA polar-orbiting satellites as part of the Advanced Microwave Sounding Unit (AMSU) [*Diak et al.*, 1992]. Thus, there is a new opportunity for obtaining upper tropospheric moisture, even in the presence of nonprecipitating clouds, and to compare these measurements to those from infrared water vapor sounders to help quantify the extent of the cloud bias problem.

2. A CLOUD CLEARING ALGORITHM FOR SSM/T2

To compare observed brightness temperatures between the infrared HIRS and microwave SSM/T2 instruments a cloud detection algorithm was developed for the SSM/T2 data using the 92 and 150 GHz window channels. Visible observations over the west Pacific from the Japanese GMS-5 and over the east Pacific from the U.S. GOES-9 weather satellites were used to provide information on cloud coverage. In addition, comparisons with limited radiosonde profiles taken during the August 1997 PACS cruise and 1996 ETL Combined Sensor Program (CSP) cruise were used to help determine clear versus cloudy scenes.

The two window channels were chosen due to their differential sensitivity to cloud [*Liu and Curry*, 1996]. The 150 GHz channel is significantly more sensitive to cloud water and ice than the 90 GHz channel. Figure 1 shows the observed variations in fractional cloudiness derived from the GMS-5 visible channel as a function of the 92 and 150 GHz brightness temperatures (Tbs). Although it

* *Corresponding author address:* Wesley Berg, Cooperative Institute for Research in Environmental Sciences, University of Colorado, Campus Box 449, Boulder, CO 80309-0449;
e-mail:wkb@cdc.noaa.gov

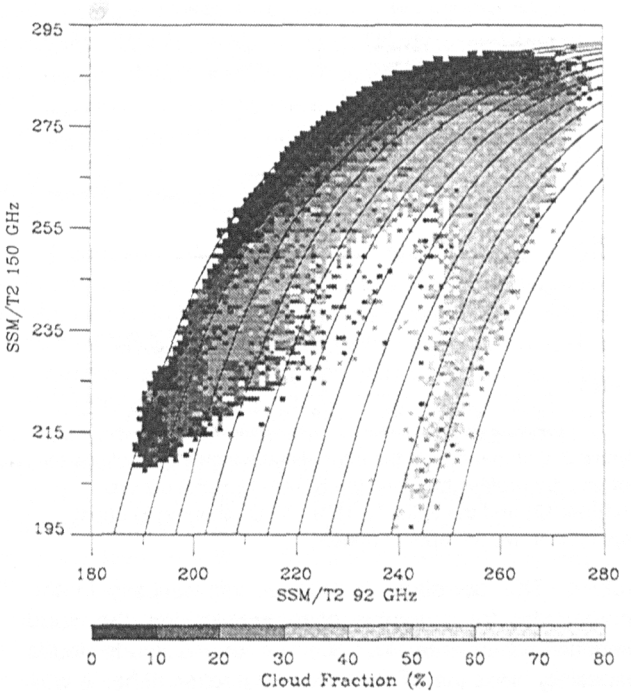

Figure 1: The cloud fraction within a T2 pixel as a function of both the 92 and 150 GHz window channels derived from GMS-5 visible data.

is apparent that the cloud fraction increases for increasing 92 GHz Tbs and decreasing 150 GHz Tbs, this relationship is highly nonlinear. The sharp boundary defined by the clear sky scenes can be approximated by a nonlinear exponential of the form:

$$Tb_{150} = a[b-e^{(Tb92-c)/d}] \qquad (1)$$

where a, b, c, and d are coefficients. Simulated Tbs from the 92 and 150 GHz T2 channels for cloudy conditions show similar variations in the 92 and 150 GHz Tbs with increasing cloud, although the actual magnitude of the values differs significantly due to the simplifying assumptions made in the model.

A simple equation for a cloud index was then developed by solving the nonlinear equation given above for the variable c. Figure 1 shows a series of lines for different values of c, which roughly approximate the variations in cloud fraction. The resulting equation for the cloud liquid water index (I_{CLW}) is as follows:

$$I_{CLW} = Tb_{92} - 170.57 + 23.94 \log[1.6725 - Tb_{150}/175.43] - 32.0 \qquad (2)$$

The coefficient 170.57 defines the upper boundary of the clear-sky scatter between the 92 and 150 GHz Tbs as shown in Figure 1.

To determine the cloud/no cloud threshold, or the threshold value below which the water vapor channel brightness temperatures are relatively insensitive to the presence of clouds, a comparison of simulated versus observed Tbs was used. Simulated Tbs were computed using radiosonde observations taken during a 1996 ETL combined sensor program cruise in the western and central Pacific and a 1997 cruise in the eastern Pacific in support of the Pan American Climate Studies (PACS) program. A plot of the mean difference between the observed and simulated values as well as the standard deviation of the differences is shown in Figure 2 for the 183±7 Ghz channel. Both of these statistics show a sharp increase for a threshold of about 20, indicating that for $I_{CLW} < 20$, the effect of clouds on the observed brightness temperatures is minimal. The 183±7 Ghz channel was used since it is more sensitive to cloud, especially at lower levels, although the same threshold applies for the 183±1 Ghz channel. Originally a subjectively chosen threshold value of 12 was used, so the actual threshold applied is 32.

Outside of the tropics the resulting Tbs decrease along the nonlinear path described by (1). For this reason, the nonlinear approach was necessary in order to account for differences in both surface and cloud characteristics at different latitudes. Although the validity of this technique is questionable outside of the tropics (30°S - 30°N), since limited observations from higher latitudes were used in its development, it appears to give reasonable results over tropical and midlatitude oceans when compared to cloud liquid water estimates from SSM/I.

3. INTERCOMPARISON OF SSM/T2 AND HIRS TBS

To understand the similarities and differences between the infrared HIRS channel 12 and the microwave SSM/T2 channel 2, a sensitivity analysis to changes in moisture and temperature was performed using radiative transfer model simulations from the TIGR-2 atmospheres,

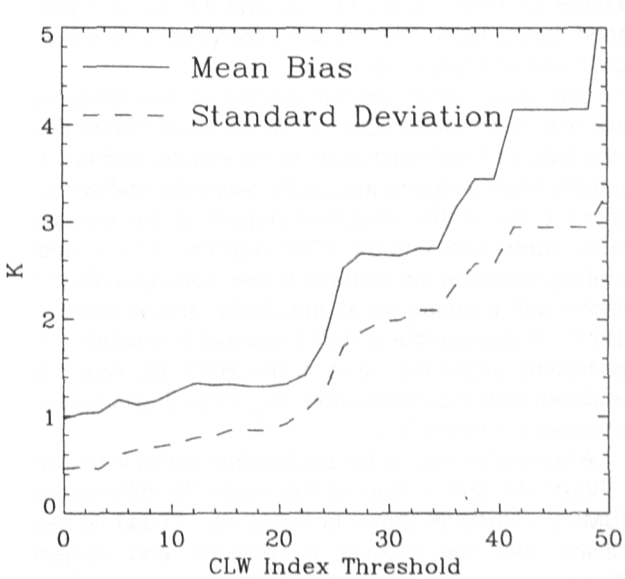

Figure 2: Mean bias and standard deviation of the differences between simulated and observed brightness temperatures versus I_{CLW} for the SSM/T2 183±7 GHz channel.

which is a set of 1761 radiosonde profiles clustered by air mass type [*Moine et al.*, 1987]. In addition, 5-day (pentad) averaged cloud-cleared Tbs from the two instruments were compared for an overlapping 1-year period during 1995.

3.1. *Sensitivity Analysis of modeled Tbs*

A comparison of the normalized weighting functions between the infrared NOAA-12 HIRS instrument and the microwave SSM/T2 are shown in Figure 3. Weighting functions from NOAA-11 and NOAA-14 HIRS were not included since they were found to be almost identical to the profiles computed for NOAA-12. Radiative transfer calculations of the transmission profile for both instruments were performed on two vastly different tropical profiles. One profile is characteristic of the intertropical convergence zone (ITCZ) with very warm temperatures and substantial moisture at all levels, while the second profile typifies the persistent subsidence regions in the tropics with warm temperature, but relatively little moisture. For the moist profile, shown in Figure 3b, HIRS channel 12 peaks at around 325 mb while SSM/T2 channel 2 peaks at around 375 mb. A comparison of a number of different profiles indicates that the weighting functions for SSM/T2 channel 2 generally peak lower in the troposphere. Figure 3a shows that for the dry profile, the peak occurs around 550 mb for HIRS channel 12 and around 600 mb for SSM/T2 channel 2. The HIRS IR instrument shows more sensitivity to a small maximum in moisture around 325 mb.

3.2. *Comparison of observed Tbs*

Cloud-cleared Tbs were computed for both the SSM/T2 channel 2 (from DMSP F11 and F12) and HIRS channel 12 (from NOAA-11, 12, and 14) for a 1-year period during 1995. The Tbs were composited over 2.5° x 2.5° bins and 5 days (pentads).

The mean cloud-cleared brightness temperatures have maximum values occurring in the cloud free region of the eastern Pacific just south of the equator and in the southern tropical regions just west of Australia and Africa. Minima occur in the convective regions of the western Pacific warm pool and the ITCZ regions. The largest variability occurs in the northern tropics corresponding to regions with a strong (large amplitude) annual cycle in UTWV. In general the SSM/T2 channel 2 variability is significantly larger than that of the HIRS-12, which is consistent with the results from the TIGR-2 simulations discussed in Section 3.1.

A correlation map of the pentad time series is shown in Figure 4a and a map of the mean Tb differences (SSM/T2 - HIRS) is shown in Figure 4b. These figures indicate that the highest correlations and largest differences occur along the northern tropical belt, corresponding to regions with a strong annual cycle in UTWV, and in the cloud free regions of the southern

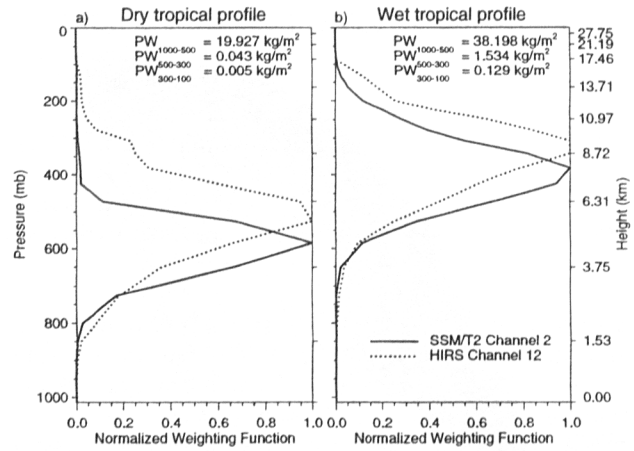

Figure 3: Comparison of the normalized weighting functions for wet and dry profiles between the NOAA-12 HIRS 6.7 μm (channel 12) and the SSM/T2 183±1 GHz (channel 2) upper tropospheric water vapor channels.

tropics. The correlations drop off dramatically in the midlatitudes for a number of reasons. First, the cloud detection schemes are less effective for midlatitude clouds especially since the SSM/T2 cloud detection scheme was developed from data over the western tropical Pacific. Second, the relative contribution of temperature versus moisture to changes in Tb increases at higher latitudes for HIRS channel 12 data. In the tropics not only are the temperature and moisture profiles highly correlated, but the moisture signal dominates the resulting Tbs. Unlike the SSM/T2, in the midlatitudes the lower moisture contents result in an increased sensitivity of the HIRS-12 to changes in temperature. As a result, the infrared HIRS

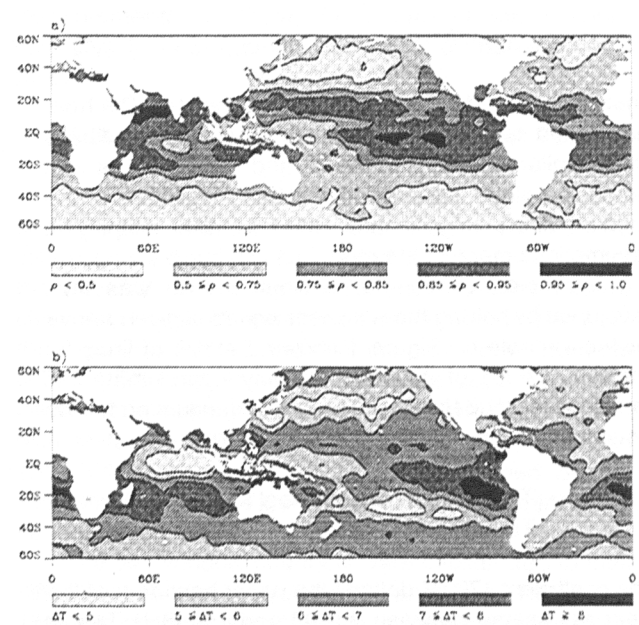

Figure 4: Spatial maps of the a) correlations and b) differences (SSM/T2-HIRS) between SSM/T2 183±1 Ghz (channel 2) and HIRS 6.7 μm (channel 12) clear-sky brightness temperatures. These statistics were computed from a time series of values averaged over 2.5° x 2.5° and five-day periods (pentads) during 1995.

and microwave SSM/T2 agree very well in the relatively cloud-free regions of the tropics, but that agreement falls off quickly at higher latitudes. A more detailed discussion of the intercomparison between SSM/T2 and HIRS UTWV brightness temperatures is given by Berg et al. [1998].

4. CONCLUSIONS

A comparison of cloud-cleared HIRS channel 12 Tbs with corresponding data from SSM/T2 channel 2 shows similar results in the tropics, but significant differences at higher latitudes. The observed differences are due to a combination of factors including differences in the level and depth of the atmospheric layer being observed, sensitivity to clouds and the resulting cloud detection algorithms used, and sampling differences.

The HIRS channel 12 is less sensitive overall to changes in UTWV, but it is more sensitive to moisture at very high levels due to the fact that the weighting function is centered slightly higher in the atmosphere. The HIRS and T2 channels are most highly correlated in relatively cloud clear regions such as the eastern tropical Pacific just south of the equator. Correlations are the highest, however, for regions with a strong annual cycle. The HIRS instrument also has significantly better sampling due to the availability of data from both am and pm satellites, wider swath coverage, and a greater percentage of clear-sky pixels. The relatively high correlations suggest that both instruments are seeing basically the same atmospheric signal in the tropics.

The upcoming launch of the Advanced Microwave Sounding Unit (AMSU) [*Diak et al.*, 1992] will provide higher resolution observations at frequencies at or very near the current HIRS and SSM/T2 channels. This will greatly simplify the task of intercomparing the microwave and infrared upper tropospheric water vapor channels. The availability of HIRS data beginning in 1979 and SSM/T2 data starting in 1993, however, will remain important for longer term climate studies, such as investigating the role of UTWV in the 1997-98 El Niño.

5. REFERENCES

Berg, W., J.J. Bates, and D.L. Jackson, 1998: Analysis of upper-tropospheric water vapor brightness temperatures from SSM/T2, HIRS, and GMS-5 VISSR, accepted pending revisions to *J. Appl. Meteor.*

Clough, S.A., M.J. Iacono, and J.-L. Moncet, 1992: Line-by-line calculations of atmospheric fluxes and cooling rates: Application to water vapor, *Journal of Geophysical Research*, ***97***, 15,761-15,785.

Diak, G.R., D. Kim, M.S. Whipple, and X. Wu, 1992: Preparing for the AMSU, *Bull. Amer. Meteor. Soc.*, ***73***, 1971-1984.

Lindzen, R.S., 1990: Some coolness concerning global warming, *Bulletin of the American Meteorological Society*, ***71***, 288-299.

Liu, G., and J.A. Curry, 1996: Large-scale cloud features during January 1993 in the North Atlantic Ocean as determined from SSM/I and SSM/T2 observations, *J. Geophys. Res.*, ***101***, 7019-7032.

McNally, A.P., and M. Vesperini, 1996: Variational analysis of humidity information from TOVS radiances, *Quarterly Journal of the Royal Meteorological Society*, ***122***, 1521-1544

Moine, P., A. Chedin, and N.A. Scott, 1987: Automatic classification of air mass type from satellite vertical sounding data. Application to NOAA-7 observations, *Ocean-Air Interactions*, ***1***, 95-108.

Rosenkranz, P.W., M.J. Komichak, and D.H. Staelin, 1982: A method for estimation of atmospheric water vapor profiles by microwave radiometry, *J. Appl. Meteor.*, ***2***, 1364-1370.

Soden, B.J., and J.R. Lanzante, 1996: An assessment of satellite and radiosonde climatologies of upper-tropospheric water vapor, *Journal of Climate*, ***9***, 1235-1250.

Velden, C.S., C.M. Hayden, S.J. Nieman, W.P. Menzel, S. Wanzong, and J.S. Goerss, 1997: Upper tropospheric winds derived from geostationary satellite water vapor observations, *Bull. Amer. Meteor. Soc.*, ***78***, 173-195.

Wang, J.R., J. Zhan, and P. Racette, 1997: Storm-associated microwave radiometric signatures in the frequency range of 90-220 Ghz, *J. Atmos. Oceanic Technol.*, ***14***, 13-31.

Wilheit, T.T., 1990: An algorithm for retrieving water vapor profiles in clear and cloudy atmospheres from 183 GHz radiometric measurements: simulation studies, *J. Appl. Meteor.*, ***29***, 508-515.SSSSSM,

P1.4B

INTERCOMPARISONS OF TOTAL PRECIPITABLE WATER FROM SATELLITE AND OTHER LONG TERM DATA SETS

Fong-Chiau Chang *
University of Alabama-Huntsville, GHCC, Huntsville, AL
and
Gary J. Jedlovec, Ronnie J. Suggs, Anthony R. Guillory
NASA/GHCC/MSFC, Huntsville, AL

1. INTRODUCTION

Observational studies on global water vapor distributions and their variations are necessary to the understanding of the hydrological and energy cycles of the Earth system. The success of these efforts depends on development of a comprehensive and accurate global water vapor data set. Recently, two types of global water vapor data sets have been produced to support this need. One is the NASA Water Vapor Project (NVAP) total and layered precipitable water (Randel et al., 1996). The NVAP data set blends the total precipitable water (TPW) retrievals from the Television and Infrared Operational Satellite (TIROS) Operational Vertical Sounder (TOVS) (Smith and Woolf 1984, Fleming et al. 1986 and Reale et al. 1989), Special Sensor Microwave/Imager (SSM/I) (Greenwald et al. 1993), and radiosonde (Ross and Elliot 1996) into a daily collage of TPW. The other type is the reanalysis that is derived from the four dimensional data assimilations (4DDA) and global forecast models (Bengtsson and Shukla 1988, Schubert et al. 1993, Kalnay et al. 1996). Several reanalyses produced by the National Centers for Environmental Prediction (NCEP), NASA Data Assimilation Office (DAO), European Centre for the Medium-Range Weather Forecast (ECMWF) and other data assimilation centers provide one of the most reliable long-term global data sets for the study of global atmospheric processes (Bengtsson and Shukla 1988).

TPW from the NVAP observations, NCEP and DAO reanalyses for a period from January 1988 to December 1992 were used by Jedlovec et al. (1998) in analyzing the variability of water vapor over the globe. Their analysis indicated global and regional variations of TPW differences among three data sets (see their Fig. 1). This paper is an extension of their study and focuses on regional analysis of the TPW between NVAP and NCEP, NVAP and DAO. This work describes research aimed at documenting the yearly, seasonal, monthly, intraseasonal and daily variability of total water vapor from the NVAP data set in the context of its accuracy and its ability to describe significant variations of water vapor. Time series of the global, hemispheric averaged TPWs and their anomalies will be presented as a continuation of the global analysis. Their relationship to the lower troposphere temperature (LTT) will be discussed also. We have performed preliminary regional analysis for several areas. However, this paper will focus on the regional analysis over the Eastern Tropical Pacific by analyzing time series of the area averaged regional TPW and their anomalies, and their relationship to sea surface temperature (SST), precipitation, and their corresponding anomalies.

* Corresponding author address: Fong-Chiau Chang, Global Hydrology and Climate Center, University of Alabama in Huntsville, 977 Explorer Blvd., Huntsville, AL 35806, 205-922-5766; e-mail fong-chiau.chang@msfc.nasa.gov

2. DATASETS

TPW data sets used in this study are the NVAP, NCEP and DAO reanalyses. The reader is referred to Jedlovec et al. (1998) for a brief summary of these three TPW data sets, and Higgins et al. (1996), Kalnay et al. (1996), Schubert et al. (1993) for more detail on the methodology. The Wentz's SSM/I TPW grids over the oceans are also included in this study (Wentz, 1986).

Precipitation, SST and LTT were also incorporated in this study. Data sources for precipitation are the Global Precipitation Climatology Project (GPCP) combined rain gauge and precipitation analysis (Huffman et al. 1997) and the Wentz's oceanic precipitation (Wentz, 1986). SST is available from NCEP optimal interpolation of

monthly mean sea surface temperature data (Reynolds and Smith 1994). LTT anomalies are derived from the Microwave Sounding Unit (MSU) on board the NOAA series of operational satellites (Christy et al. 1995).

3. INTERCOMPARISONS OF TPW

3.1 Time Series of Global and Hemispheric Averaged TPW

Global and hemispheric averaged TPW are computed for the NVAP, NCEP and DAO reanalyses for each month. In order to study temporal variations of the monthly mean TPWs, 5 year means were calculated for each individual calendar month for each data. Five year mean global TPW annual cycles show that NVAP is moister than either reanalyses. For the northern hemisphere annual cycle, the NVAP moist bias is not constant. In the winter months, the NVAP/NCEP difference is near zero. The DAO annual cycle is quite dry in both the global and hemispheric averages. For annual cycles over the southern hemisphere, NCEP is moister than NVAP and DAO from May to December.

The time series of the monthly global averaged TPW and their anomalies were analyzed. TPW anomalies were calculated using the 5 year mean for each individual calendar month. NVAP global averaged TPW is larger than NCEP and DAO reanalysis for all 60 months except for January and March 1991. The variations of the anomaly fields for the two reanalyses are greater than those of NVAP. Relatively large differences in the global averaged TPW anomalies occur in early 1989 and 1991. A similar analysis was performed for both the northern and southern hemispheric TPW. Relatively large differences between NVAP and the reanalyses in March 1989 and 1991 also appear in the southern hemispheric TPW anomalies. A good agreement exists between the global and hemispheric NVAP TPW and concurrent LTT anomalies (Randel et al. 1996) for all the 60 months except March 1991. During March 1991 the southern hemispheric LTT anomaly is near normal, while NVAP TPW anomaly is large negative. A similar comparison was completed for the reanalyses, and the TPW anomaly is near normal for March 1991 in both reanalyses.

Table 1 lists the latitudinal band area averaged monthly TPW differences between NCEP and NVAP, DAO and NVAP. Hereafter the value of NVAP TPW minus NCEP TWP (DAO TPW) is represented as NVAP/NCEP (NVAP/DAO). NCEP is moister then DAO and NVAP in the $60^\circ S - 30^\circ S$ band, mainly covered by oceans, for all four seasons. For the bands $15^\circ S - 15^\circ N$ and $15^\circ N - 30^\circ N$, NVAP is moister than two reanalyses for all four seasons. The largest discrepancy in NVAP/NCEP and NVAP/DAO TPW differences is over the band $15^\circ N - 30^\circ N$ during the northern hemisphere summer months. The NVAP TPW is 4.50 (4.06) mm greater than DAO (NCEP) reanalysis. The large difference is from the land areas over the Northern Africa, India, and Southwestern China (see Fig. 1 of Jedlovec et al. 1998).

3.2 Regional Analysis

In order to examine the difference in TPW among three data sets, the 60 month climatological means were calculated for each data set. The difference in the climatological mean TPW between NVAP and NCEP (DAO) were calculated and displayed in Fig. 1 top (lower) panel for the region over the Eastern Tropical Pacific and the adjourning Americas. In the Eastern Tropical Pacific just south of the equator, NVAP TPW values are much smaller than NCEP and larger than DAO. The shapes of the difference fields over this region are significantly different between NVAP/NCEP and NVAP/DAO. A couplet of east-west elongated positive and negative differences is seen in the NVAP/NCEP difference field, while a contiguous positive area is present in the NVAP/DAO difference field. The largest discrepancies of NCEP/NVAP area averaged TPW anomalies were identified for March 1989 and 1991 over the region from $2.5^\circ S$ to $12.5^\circ S$ and from $82.5^\circ W$ to $147.5^\circ W$ (Jedlovec et al. 1998). This analysis was extended to include all four TPW data sets over the region from 0° to $10^\circ S$ and from $150^\circ W$ to $90^\circ W$ (hereafter referred as SBOX). Similar analysis were performed for the counter regions over the northern hemisphere and tropics, i.e., over the same longitude width and from 0° to $10^\circ N$ (hereafter referred as NBOX), and from $5^\circ S$ to $5^\circ N$ (hereafter referred as EBOX).

Differences in TPW between NVAP and SSM/I are compared for the SBOX, NBOX and EBOX. In general, SSMI TPW is slightly larger than that of NVAP, the larger differences occur during months with higher precipitation. The possible relationships

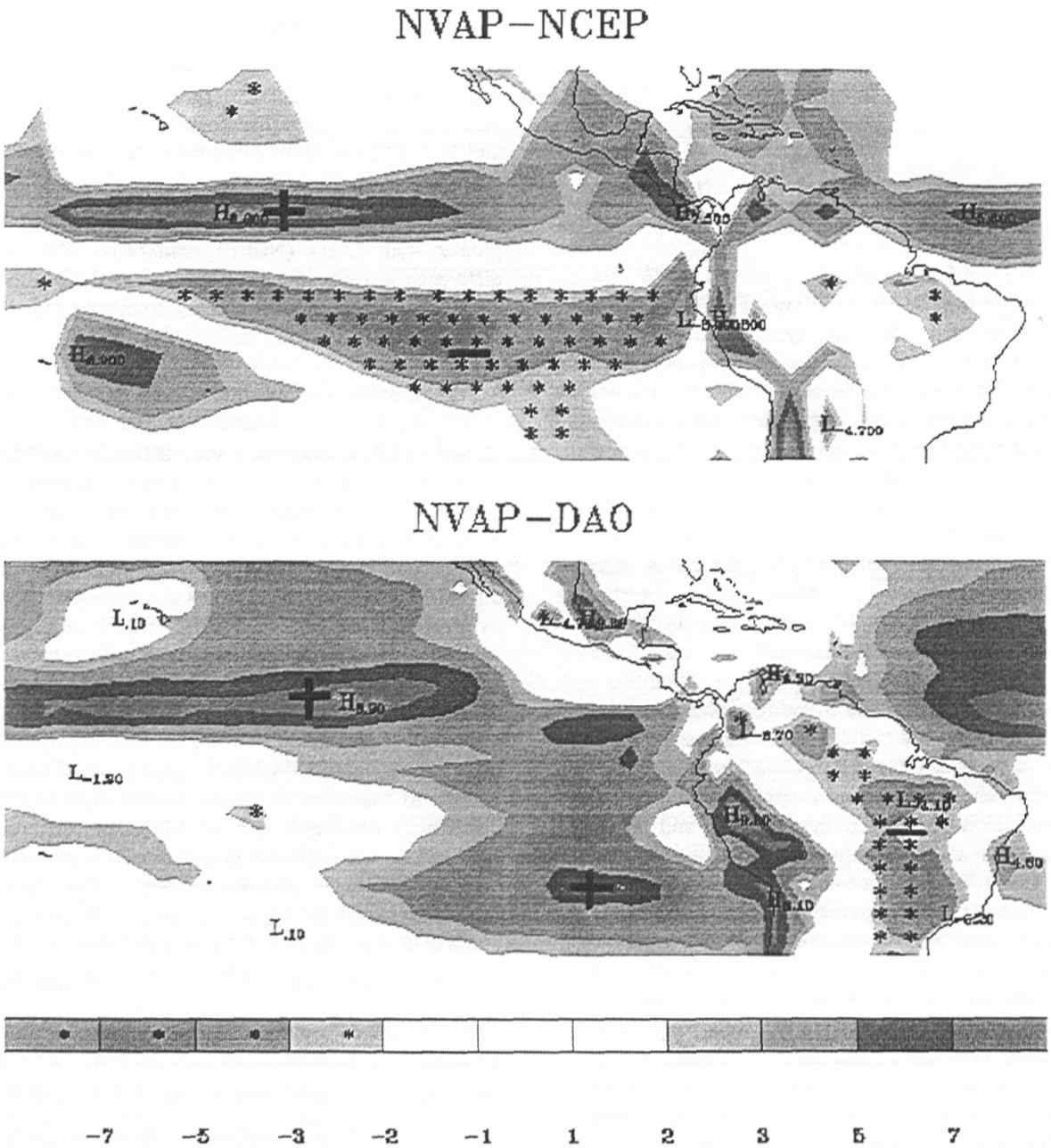

Fig. 1 Climatological difference in total precipitable water (mm) for a period from January through December 1992. NVAP - DAO (left) NVAP - NCEP (right)

TABLE 1

	$60^\circ S - 30^\circ S$		$30^\circ S - 15^\circ S$		$15^\circ S - 15^\circ N$		$15^\circ N - 30^\circ N$		$30^\circ N - 60^\circ N$	
	NCEP	DAO	NCEP	DAO	NCEP	DAO	NCEP	DAO	NCEP	DAO
DJF	-1.85	-0.29	0.86	2.43	2.37	1.93	0.63	2.43	-0.17	0.77
MAM	-1.32	0.04	0.64	2.12	3.35	2.30	1.59	3.02	-0.45	0.73
JJA	-0.73	0.37	-0.26	1.86	1.61	1.81	4.06	4.50	0.66	1.72
SON	-0.96	0.13	0.03	2.43	2.42	2.36	2.45	3.44	0.09	1.22

Differences in Area averaged and seasonal TPW (mm) between NCEP and NVAP; DAO and NVAP
Column NCEP (DAO) is the NVAP/NCEP (NVAP/DAO) difference, unit is in mm

of SST and its anomaly was also examined for all three boxes. In general, SST anomalies is negative for the period from January1988 to mid 1989, and positive from mid 1991 to 1992. This trend seems embedded in the TPW anomalies, however, there is no simple relationship.

Area averaged TPWs over SBOX for three data sets indicate the month-to-month variations of NVAP/NCEP and NVAP/DAO. NCEP TPW has the largest values over much of the period except March 1989. The relative magnitude between NVAP and DAO varies during these 60 months. TPWs reach the largest value in 91/92 winter and precipitation are relatively large at this time. Precipitation ranked the second high for March 1989 during this 60 month period. The two reanalyses have negative anomalies and are about the same magnitude for early 1989, while NVAP anomaly is very small. Large difference in TPW anomaly between the NCEP and NVAP occurs during March 1991 which has the lightest precipitation for this five year period.

Over the NBOX, NVAP TPW is greater than the reanalyses TPWs for all 60 months except March 1989. Some striking features were found during this particular month. TPW values are about the same magnitude for all four TPW data sets. The precipitation is small compared to other March of this five year period. A closer cluster of four TPW and precipitation anomalies appears in the time series compare to that of SBOX.

Over EBOX, the larger and smaller magnitudes of NVAP and NCEP TPW alternate with each other, while DAO is drier over much of the period. Both precipitation and TPW is increasing to maximum in 1991/92 winter.

5. CONCLUSION

Regional analysis of TPW over the Eastern Tropical Pacific shows that TPW are different among the NVAP observations, and NCEP and DAO reanalyses. NCEP is moister than NVAP and DAO south of the equator, while NVAP is moister than two reanalyses north of the equator over the Eastern Tropical Pacific. Overall DAO has the driest TPW over this region. The analysis also indicates that Wentz's SSMI is moister than NVAP during precipitation months. The NVAP data set has relatively large discrepancies with reanalyses over the SBOX during March 1989 and 1991. Over the NBOX, TPW are about the same magnitude for all the four TPW data sets during March 1989. The lightest rainfall of this region occurs at this particular month during this five year period. The results indicate that precipitation bears a relationship to the NVAP/NCEP and NVAP/DAO differences and is being studied in greater detail.

Acknowledgments

This work is partially funded by NASA's Satellite Validation program under the auspices of Dr. James Dodge at NASA Headquarters. The NVAP data were obtained from the NASA Langley research Center EOSDIS Distributed Active Archive Center (DAAC). The SSM/I were archived from Remote Sensing Systems. Sea surface temperature were obtained from NCEP and GPCP precipitation from GSFC DAAC.

References

Bengtsson, L., and J. Shukla, 1988: Integration of space and in situ observations to study global climate change. *Bull. Amer. Meteor. Soc.*, 69, 1130-1143.

Christy, J. R., R. W. Spencer, and R. T. McNider, 1995: Reducing noise in the MSU daily lower-tropospheric global temperature dataset. *J. Climate*, 8, 888-896.

Fleming, H. E., M. D. Goldberg, D. S. Crosby, 1986: Minimum variance simultaneous retrieval of temperature and water vapor from satellite radiance measurements. *2nd Conference on Satellite Meteorology/Remote Sensing and Application*, Williamsburg VA, 20-23.

Greenwald, T. J., et al., 1993: A physical retrieval of cloud liquid water over the global oceans using SSM/I observations. *J. Geophys. Res.*, 98, 18471-18488.

Higgins, R. W., et al., 1996: Intercomparison of the NCEP/NCAR and the NASA/DAO reanalyses (1895-1993), NCEP/Climate Prediction Center Atlas No. 2, NOAA, Washington, D.C., pp169.

Huffman, G. J., et al., 1997: The global precipitation climatologyproject monthly mean precipitation data set. *J. Appl. Meteor.*, 36, 1191-1201.

Jedlovec, G. J., F-C Chang, R. J. Suggs, and A. R. Guillory, 1998: Variations in atmospheric water vapor as seen in satellite data and model reanalysis fields. *Preprint 9th Symposium on Global Change Studies*. 31-35.

Kalnay et al., 1996: The NCEP/NCAR 40 year reanalysis project. *Bull. Amer. Meteor. Soc.*, 77, 437-471.

Randel et. al, 1996: A new global water vapor data set. *Bull. Amer. Meteor. Soc.*, 77, 1233-1246.

Reale, A. L., M. D. Goldberg, and J. M. Daniels, 1989: Operational TOVS sounding using a physical approach. *Proceeding of the IGAPRS 12th Candian Symposium on Remote Sensing*, Vancouver, B.C., 2653-2657.

Reynolds, R. W. and T. M. Smith, 1994: Improved global sea surface temperature analyses. *J. Climate*, 6, 114-119.

Ross, R. J. and W. P. Elliott, 1996: Tropospheric water vapor climatology and trends over North America, *J. climate*, 1973-1993.

Schubert, S. D., R. B. Rood, and J. Pfaendtner, 1993: An assimilated data set for Earth science applications. *Bull. Amer. Meteor. Soc.*, 74, 2331-2342.

Smith, W. L., and H. M. Woolf, 1984: Improved vertical sounding from amalgamation of polar and geoststionary radiance observations. *Proceeding of the Conference on Satellite Meteorology/Remote Sensing and Applications*, Clearwater, Florida, 45-48.

Wentz, F. J., L.A., Mattox, and S. Peteherych, 1986: New algorithms for microwave measurements of ocean winds: Applications to SEASAT and the Special Sensor Microwave Imager. *J. Geophys. Res.*, 91(C2), 2289-2307.

P1.5A

THE USE OF A SATELLITE CLIMATOLOGICAL DATA SET TO INFER LARGE SCALE THREE DIMENSIONAL FLOW CHARACTERISTICS

Jeffrey A. Lerner *
Global Hydrology and Climate Center
University of Alabama in Huntsville
Huntsville, Alabama

Gary J. Jedlovec
Global Hydrology and Climate Center
NASA/Marshall Space Flight Center
Huntsville, Alabama

Robert J. Atkinson
Global Hydrology and Climate Center
Lockheed Martin
Huntsville, Alabama

1. INTRODUCTION

Ever since the first satellite image loops from the 6.3 μm water vapor channel on the METEOSAT-1 in 1978, there have been numerous efforts (many to a great degree of success) to relate the water vapor radiance patterns to familiar atmospheric dynamic quantities. The realization of these efforts is becoming evident with the merging of satellite derived winds into predictive models (Velden et al., 1997; Swadley and Goerss, 1989). Another parameter that has been quantified from satellite water vapor channel measurements is upper tropospheric relative humidity (UTH) (e.g., Soden and Bretherton, 1996; Schmetz and Turpeinen, 1988). These humidity measurements, in turn, can be used to quantify upper tropospheric water vapor and its transport to more accurately diagnose climate changes (Lerner et al., 1998; Schmetz et al. 1995a) and quantify radiative processes in the upper troposphere. Also apparent in water vapor imagery animations are regions of subsiding and ascending air flow. Indeed, a component of the translated motions we observe are due to vertical velocities. The few attempts at exploiting this information have been met with a fair degree of success. Picon and Desbois (1990) statistically related Meteosat monthly mean water vapor radiances to six standard pressure levels of the European Centre for Medium Range Weather Forecast (ECMWF) model vertical velocities and found correlation coefficients of about 0.50 or less. Synoptic scale vertical displacements were quantified by Stout et al. (1984) from GOES Visible Infrared Spin Scan Radiometer (VISSR) Atmospheric Sounder (VAS) brightness temperature (T_B) measurements. They found vertical displacements on the order of 1 μb s^{-1} in a case study over the Atlantic Ocean during summer.

*Corresponding author address: Jeffrey A. Lerner, Global Hydrology and Climate Center, University of Alabama in Huntsville, 977 Explorer Blvd., Huntsville, Alabama 35806; e-mail <lerner@atmos.uah.edu>.

It is hypothesized in the current study that in regions void of diabatic heating, vertical motions may be inferred along an isentropic surface which can be approximated by the pressure height estimated from satellite measurements and a nearby temperature profile.

This paper presents some preliminary results of viewing climatological satellite water vapor data in a different fashion. Specifically, we attempt to infer the three dimensional flow characteristics of the mid- to upper troposphere as portrayed by GOES VAS during a warm ENSO event (1987) and a subsequent cold period in 1988.

2. METHODOLOGY

To demonstrate how GOES winds may be used to infer the three-dimensional flow characteristics of the middle and upper troposphere, we first convey to the reader how water vapor imagery may be viewed as a nearly constant moisture layer that varies in height. Next, horizontal wind streamlines are displayed to locate regions where rising motion or subsidence might be expected. As a first attempt to validate our qualitative inferences, we display NCEP reanalysis (Kalnay et al., 1996) vertical velocity pressure level data. The satellite quantities estimated in this paper are derived from water vapor winds using GOES-7 VAS 6.7 μm channel data during June, July, and August (JJA) of 1987 and 1988. This section briefly summarizes the algorithm used for calculating water vapor wind vectors and our approach to assigning wind vector heights.

2.1 *GOES Winds*

Winds were derived using the Marshall Automated Wind (MAW) algorithm (Atkinson, 1987; Jedlovec and Atkinson, 1998) which uses minimum-difference template matching for feature tracking. Three water vapor images (1100, 1200, and 1300 GMT) were used to determine a pair of wind vectors for each template of the image. The

template is used to mathematically track the movement of a feature from image-to-image. For the current study, the MAW algorithm was applied using a 25 × 49 template of 16 × 8 km pixels. This produces a spatial resolution of about 400 km between adjacent wind vectors. Daily winds were produced for each day of June, July, and August of 1987 and 1988. The current quality control procedures include the elimination of vector pair discrepancies of 15 ms^{-1} in speed and 30 degrees in direction. Using these quality and control procedures, random errors in GOES VAS data are reduced to less than 4 ms^{-1} (Jedlovec and Atkinson 1996). After the vector pair discrepancy quality control step, visual analysis of the individual vectors is carried out to eliminate obvious vectors that are in error (usually occurring in areas of little or no structure in the water vapor field).

2.2 *Wind Vector Heights*

The simple height assignment approach for this study incorporates NCEP model reanalysis temperature profile information at 1200 UTC daily for locating the pressure at which the corresponding satellite T_B is equivalent to the model thermometric temperature. This level approximates the mean level where contribution to the measured T_B is usually greatest. However, the layer contributing to the satellite measured T_B varies in depth and height due to the water vapor profile, to a lesser extent the temperature profile, and also due to the satellite instrument view angle (Fischer et al., 1982). Different cloud types also contribute to the shape of the weighting function profile.

3. RESULTS

Because water vapor emissions of absorbed terrestrial radiation in the 6-7 μm infrared absorption band are almost entirely due to water vapor in the middle and upper troposphere, the satellite signal becomes saturated at a nearly constant amount of absolute humidity in cloudless areas. Stout et al. (1984) determined that the amount of precipitable water (PW) above the water vapor "upper boundary" to vary between 0.5-1.5 mm with GOES-VAS when correlated with a nearby radiosonde profile. Schmetz et al. (1995b), found Meteosat-4 measurements to be sensitive to the upper 3 mm of PW. In our applications, a radiative transfer model was used to simulate the GOES VAS weighting function profile and channel brightness temperature. Using the Air Force Geophysical Laboratory (AFGL) standard tropical profile, we found GOES-VAS sensitive to about the top 2 mm of PW. This was determined by vertically integrating the specific humidity and multiplying each atmospheric layer by the corresponding normalized weight determined from the instrument spectral response or

$$PW = \sum_{i=0}^{sfc}\left[\bar{q}_i \frac{dp_i}{g} \times W_i\right]$$

(Figure 1). This amount of moisture varies with satellite water vapor channel spectral characteristics (e.g., channel spectral bandwidth and center wavelength).

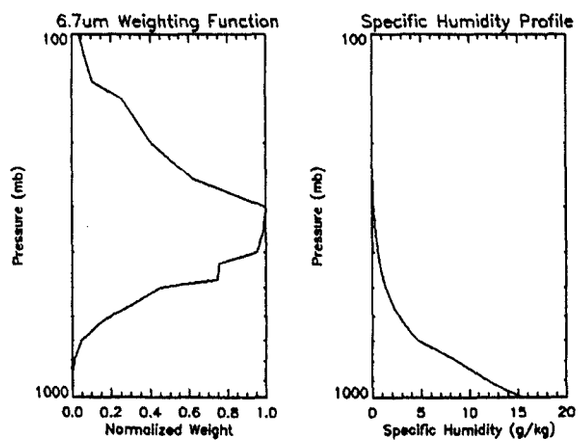

Figure 1: Simulated GOES - VAS 6.7 μm channel weighting function profile and specific humidity (g/kg) profile using the AFGL standard tropical atmosphere.

The hypothesis in the introduction stated that the derived water vapor wind heights from GOES approximate an isentropic surface such that vertical motions may be inferred from cross-isobaric flow. Typically we view isentropes in two dimensional vertical cross sections at synoptic scales to identify air masses, fronts, and regions of rising and sinking motion near mid-latitude baroclinic zones. For this study, we extend our view of an isentropic layer over the GOES viewing area. Indeed, potential temperature will not be constant in the water vapor layer owing to errors that arise in the height assignments (due to assumptions made and model inaccuracies in temperature profile) and also due to the presence of diabatic processes such as radiative heating/cooling and evaporation/condensation. By time averaging the data, we reduce the diabatic effects that occur on small time and space scales. Our results indicate that the potential temperature

(θ) does vary by as much as 20 K from the mid latitudes to the tropics. However, large regions are characterized by nearly constant θ in which our hypothesis is valid. For simplicity, at this time we assume that the flow generally adheres to the layer defined by the water vapor wind heights so that a first order approximation of the vertical motion characteristics may be made.

The flow pattern derived from taking the mean of daily winds during JJA of 1987 and 1988 is displayed in figures 2a and 2b. The streamlines (solid lines) are overlaid on the assigned pressure height (dashed lines). It is readily apparent that in 1988 southwestward flow into the dry subtropics is dominant south of 15° N across the GOES-7 viewing domain. The winds shift southwestward south of a ridge axis near 5-10° S towards the southern hemisphere subtropical jet stream. In 1987, the flow pattern is in stark contrast to the cold La Nina event of 1988. For example, in the tropical Atlantic, more "typical" southeasterlies are observed to form a ridge axis near 10° N.

The contours of pressure height are also shown to highlight the large scale subsidence and rising motion areas that might be expected. Assuming that diabatic processes are small in a mean sense, the flow pattern along the derived water vapor heights should approximate flow on an adiabatic surface. South of 5° N, flow tends to descend which is consistent with zonally averaged estimates of vertical velocities from the NCEP reanalysis model pressure level data (Figure 3). However, even at large time and space scales, the adiabatic assumption is not as strong near the Inter Tropical Convergence Zone (ITCZ) and mid-latitude baroclinic zones. This is why we don't see cross-isobaric flow in regions of tropical convection. Rather, upper-level wind divergence patterns (not shown) are associated with regions of deep convection where rising motion and strong diabatic heating (due to condensation in precipitating convective systems) are present.

In Figure 2a, divergent centers can be observed along the ITCZ over Central America. In 1988, these centers aren't apparent, but the strong cross-isobaric flow in the tropical east Pacific is still present. The pressure gradient along the streamlines in this subsidence region is approximately 5 mb/100 km. With a typical wind speed of 10 m/s, a rough estimate of the subsidence is 0.5 μb/s (~1 cm/s) which is consistent with typical tropical subsidence rates given by Holton (1979).

Another interesting feature from this figure worth noting is the detection of northwesterlies over the eastern half of the United States. The implications of this type of pattern are drier conditions which is consistent with the severe drought endured during the summer of 1988.

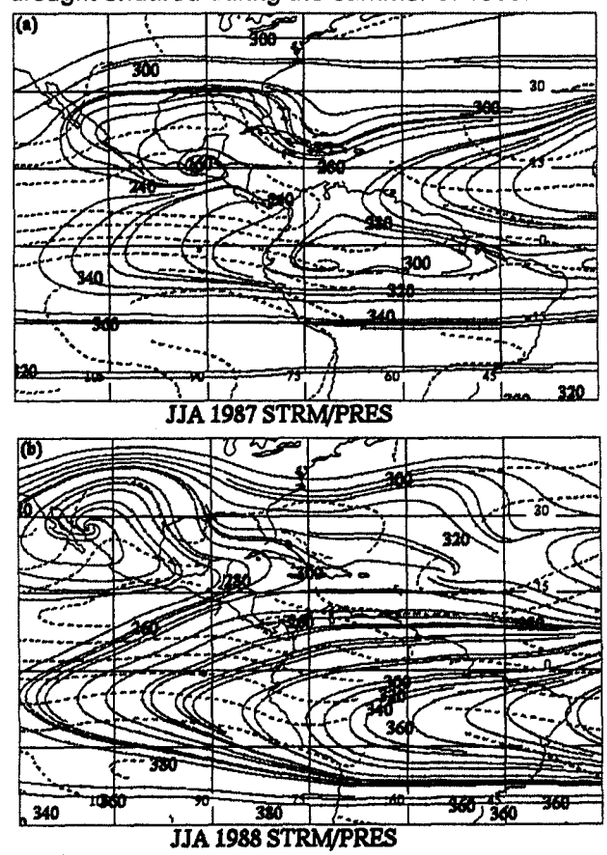

Figure 2: Summer averaged pressure height of the water vapor wind vectors (dashed contours) overlaid on streamlines of the summer mean flow for 1987 (a) and 1988 (b).

Typically, dark bands in the water vapor imagery are associated with dry subsidence zones (e.g. behind cold fronts and in subtropical highs). The height assignments in these dark regions are lower in the atmosphere (higher pressure) owing to the drier upper troposphere (water vapor emissions from lower levels). In Figure 3, the zonal mean NCEP Reanalysis vertical velocities (VVEL) (cm/s) at 400 mb are plotted below the zonal mean pressure height (mb) of the GOES water vapor winds. The zonal mean values are averaged over 30°-120° W. The phases of these two plots show good agreement. The strongest positive vertical velocities near 10° N are associated with the highest height assignment levels corresponding to the coldest brightness temperatures observed in the ITCZ. The strongest subsidence according to

the model data is near 20° S which corresponds to the lowest height assignment level in the GOES wind vectors. At this latitude in the southern hemisphere winter, the subtropical high is well established across the GOES viewing domain. The interannual variations in the zonal means of pressure height are subtle but show that in 1988 the upper troposphere was generally drier (lower height assignments) across all latitudes. The interannual variation in VVEL indicates good agreement at most latitudes with the exception of stronger subsidence extending further south in the southern hemisphere during JJA 1988.

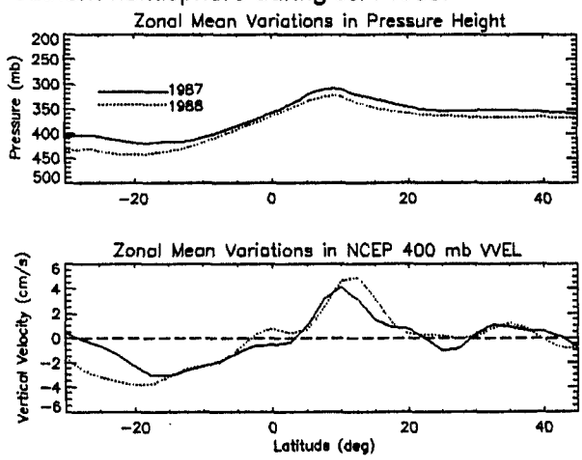

Figure 3: Zonal mean pressure height (mb) of the water vapor winds for 1987 (solid) and 1988 (dotted). Bottom plot displays zonal mean vertical velocities (cm/s) at 400 mb estimated by the NCEP reanalysis model.

4. SUMMARY

The preliminary results presented in this conference paper have shown promise in the final goal of being able to quantify vertical motions from water vapor channel satellite measurements. It was shown that cross-isobaric flow in the GOES measurements is consistent with regions of subsidence portrayed by the NCEP reanalysis model. While our current methodology and results only is a cursory glance at the potential of deriving vertical velocities from long term satellite data, it does not test the original hypothesis that the water vapor layer derived using water vapor wind heights behaves like an isentropic surface. The relative magnitude of diabatic effects needs to be estimated to delineate which regions vertical motions may be quantified with greater confidence. To produce quantitative results from the satellite measurements, a kinematic or adiabatic model needs to be developed that takes advantage of the spatial and temporal changes in the water vapor winds, temperature, and heights. More recent results from these ongoing efforts will be presented on the poster at the conference.

5. REFERENCES

Atkinson, R. J., 1987: Automated mesoscale winds determined from satellite imagery. *Final Report on NAS8-34596*, General Electric Company, Huntsville, AL, 50 pp.

Fischer, N., N. Eigenwillig, and H. Muller, 1982: Information content of METEOSAT and Nimbus/THIR water vapor channel data: Altitude association of observed phenomena. *J. Appl. Meteor.*, **20**, 1344-1352.

Holton, J. R., 1979: *An Introduction to Dynamic Meteorology*. Academic Press, San Diego, 512 pp.

Jedlovec, G. J., and R. J. Atkinson, 1998: The Marshall Automated Wind algorithm for geostationary satellite wind applications. *Proc. of the Ninth Conf. on Sat. Meteor. and Oceanog.*, AMS, Paris, France, P3.6B.

Jedlovec, G. J., and R. J. Atkinson, 1996: Quality and control of water vapor winds. *Proc. of the Eighth Conf. on Sat. Meteor. and Oceanog.*, AMS, Boston, 5-9.

Kalnay, E., M. Kanamitsu, R. Kistler, W. Collins, D. Deaven, L. Gandin, M. Iredell, S. Saha, G. White, J. Woollen, Y. Zhu, M. Chelliah, W. Ebisuzaki, W. Higgins, J. Janowiak, K. C. Mo, C. Ropeleewski, J. Wang, A. Leetmaa, R. Reynolds, R. Jenne, and D. Joseph, 1996: The NCEP/NCAR 40-year reanalysis project. *Bull. Amer. Meteor. Soc.*, **77**, 437-471.

Lemer, J. A., G. J. Jedlovec, and R. J. Atkinson, 1998: Observed changes in upper-tropospheric water vapor transport from satellite measurements during the summers of 1987 and 1988. *Proc. of the Ninth Symp. on Global Change Studies*, AMS, Long Beach, Calif., 23-26.

Picon, L., and M. Desbois, 1990: Relation between METEOSAT water vapor radiance fields and large scale tropical circulation features. *J. Climate*, **3**, 865-876.

Schmetz, J., W. P. Menzel, C. Velden, X. Wu, L. van de Berg, S. Nieman, C. Hayden, K. Holmlund, and C. Geijo, 1995a: Monthly mean large scale analysis of upper troposphere humidity and wind field divergence derived from three geostationary satellites. *Bull. Amer. Meteor. Soc.*, **76**, 1578-1584.

Schmetz, J., C. Geijo, W. P. Menzel, K. Strabala, L. van de Berg, K. Holmlund, and S. Tjemkes, 1995b: Satellite observations of upper troposphere relative humidity, clouds, and wind field divergence. *Beitr. Phys. Atmosph.* **68**, 345-357.

Soden, B. J., and F. P. Bretherton, 1996: Interpretation of TOVS water vapor radiances in terms of layer-average relative humidities: Method and climatology for the upper, middle, and lower troposphere. *J. Geophys. Res.* **101**, 9333–9343.

Stout, J., J. Steranka, and R. A. Petersen, 1984: Vertical displacements of the mid-tropospheric water vapor boundary in the tropics derived from the VISSR Atmospheric sounder (VAS) 6.7 μm channel. *Proc. AMS Conf on Sat. Remote Sensing and Appl.*, Clearwater Beach, FL 86-89.

Swadley, S. D., and J. S. Goerss, 1989: Assimilation of automated winds derived from GOES multispectral imagery. *Preprints Fourth Conf. on Sat. Meteor. and Oceanog.*, AMS, San Diego, Calif., 242-245.

Schmetz, J., and O. M. Trupeinen, 1988: Estimation of the upper tropospheric relative humidity field from METEOSAT water wavor image data. *J. Appl. Meteor.*, 27, 889-899.

P1.6B

1DVAR ANALYSIS OF GPS RADIO OCCULTATION MEASUREMENTS.

P. I. Palmer*, J. J. Barnett*, J. R. Eyre†

1 Abstract

Radio occultation measurements using the Global Positioning System (GPS) represent a new method of obtaining profiles of atmospheric temperature and humidity. The method relies upon refraction: when radio-waves pass through a medium of varying density they are refracted by an angle determined by the variation along the path taken. The cumulative effect of this refraction is a bending angle. A profile of bending angles can be measured by a GPS receiver on a low-Earth-orbiting satellite as it passes behind the limb of the atmosphere relative to the transmitting GPS satellite.

From the measured profile of bending angles a profile of refractivity can be retrieved. Unfortunately there is nothing in the measurement which can be used to separate the effects of temperature and humidity on the refractivity.

The optimal non-linear inversion scheme (1DVAR) that is presented utilises *a priori* information, including the correlation between temperature and humidity errors at different levels, and an estimate of the measurement error. In using this scheme, United Kingdom Meteorological Office (UKMO) numerical weather prediction (NWP) model data are used as *a priori* estimates which can then be combined with actual GPS-MET measurements in such a way that the optimal temperature/humidity profile can be obtained.

2 Introduction

The method of radio occultation has been used extensively to sound extra-terrestrial planetary atmospheres since the mid-sixties: the general method is described in Fjeldbo and Kliore (1971). Because of the accuracy required to measure the terrestrial atmospheric refraction response (about 1°), it was not until the advent of the GPS that radio occultation principles could be applied to the Earth.

Using the well-documented Abelian inversion, or making use of a similar inversion transform when applying Fresnel diffraction theory [8], these bending angle measurements can be inverted to obtain a profile of refractivity.

Refractivity is primarily affected by air density (dependent of pressure and temperature) and water vapour density, and thus the measurement contains information about both. Unfortunately, the measurement contains no information to allow the separation of their effects, and therefore only combined quantities can be retrieved at any one time using conventional methods. If the absolute humidity is judged to be small (e.g. in the polar regions) it may be neglected, and density calculated from refractivity. The hydrostatic relation can be used to calculate values of pressure, and hence temperature. However, if humidity is judged to be significant, then an iterative process may be used to calculate temperature/humidity if an *a priori* profile of humidity/temperature is used. This *a priori* information can be taken from various sources such as collocated NWP output.

3 1DVAR method

The 1DVAR method, utilises *a priori* in the form of a background atmospheric state from an NWP model: information about the error correlations of temperature between levels, specific humidity between levels, and the error correlation between temperature and specific humidity at different levels. Using this information, it is possible to calculate the non-linear optimal solution of temperature and specific humidity .

3.1 Theory

The general idea of this theory is to minimise a penalty function $\xi(x)$, which measures the degree of fit of the measurements to the *a priori* information, and possibly to some other physical or dynamical constraints.

*Atmospheric, Oceanic and Planetary Physics, Oxford University, UK. Corresponding author: p.palmer1@physics.ox.ac.uk

†NWP Division, Meteorological Office, Bracknell, Berkshire, UK

There are a number of methods available to minimise $\xi(\mathbf{x})$: the scheme described here uses the method of Newtonian iteration.

If we assume that the errors involved have Gaussian distributions, then the maximum likelihood penalty functions can be shown to be a sum of quadratic terms.

$$\begin{aligned}\xi(\mathbf{x}) =&(\mathbf{y}-\mathbf{y}')^T\mathbf{S}_y^{-1}(\mathbf{y}-\mathbf{y}') + \\ &(\mathbf{x}-\mathbf{x}_a)^T\mathbf{S}_a^{-1}(\mathbf{x}-\mathbf{x}_a)\end{aligned} \quad (1)$$

where $\mathbf{y}$ is a vector of the measured bending angles; $\mathbf{y}'$ is a vector of simulated measurements corresponding to the atmospheric state (i.e. involving forward model calculations); $\mathbf{S}_y$ is primarily the expected error covariance of the measured bending angles, but should also include the expected error covariance of the forward model; $\mathbf{x}_a$ is the *a priori* atmospheric state (e.g. short-range forecast), and $\mathbf{S}_a$ is its expected error covariance.

The Newtonian iteration in which the nth estimate of $\mathbf{x}$ is updated as follows:

$$\mathbf{x}_{n+1} = \mathbf{x}_n - [\mathbf{H}_x\xi(\mathbf{x})]^{-1}\nabla_x\xi(\mathbf{x}_n) \quad (2)$$

where $\mathbf{H}_x$ is the Hessian operator. $\nabla_x\xi(\mathbf{x})$ is obtained by differentiating equation 1:

$$\nabla_x\xi(\mathbf{x}) = \mathbf{S}_a^{-1}(\mathbf{x}-\mathbf{x}_a) - \mathbf{K}^T\mathbf{S}_y^{-1}(\mathbf{y}-\mathbf{y}') \quad (3)$$

where $\mathbf{K}$ is $\nabla_x\mathbf{y}$. The Hessian matrix is obtained by differentiating again:

$$\mathbf{H}_x\xi(\mathbf{x}) \simeq \mathbf{S}_a^{-1} + \mathbf{K}^T\mathbf{S}_y^{-1}\mathbf{K} \quad (4)$$

Note that relation 4 is approximate since terms involving the gradient of $\mathbf{K}$ have been omitted. If it is assumed that the problem is not *grossly* non-linear, then this assumption is valid.

These equations can be combined and manipulated to derive the form of the Newtonian iteration given by Rodgers (1976):

$$\begin{aligned}\mathbf{x}_{n+1} =&(\mathbf{S}_a^{-1} + \mathbf{K}_n^T\mathbf{S}_y^{-1}\mathbf{K}_n)^{-1}[\mathbf{S}_a^{-1}\mathbf{x}_a + \\ &\mathbf{K}_n^T\mathbf{S}_y^{-1}(\mathbf{y}-\mathbf{y}_n' + \mathbf{K}_n\mathbf{x}_n)]\end{aligned} \quad (5)$$

where n is the order of iteration.

3.2 Implementation

The state vector $\mathbf{x}$ is a vertical atmospheric profile containing the temperature at 40 pressure levels (surface to 0.1 hPa), the specific humidity at 15 pressure levels (surface to 300 hPa), and the surface pressure for the particular occultation event being studied.

The simulated measurements, $\mathbf{y}'$, corresponding to the state vector $\mathbf{x}$ are computed using a forward model which is described in Eyre (1994). The matrix of weighting functions, $\mathbf{K}$, is calculated by perturbing each element of the state vector in turn and looking at the difference in bending angle with the unperturbed simulated measurement.

The *a priori* profile $\mathbf{x}_a$ is obtained from the UKMO NWP model. The model from which the data is derived has 19 levels, and is expressed in hybrid-sigma coordinates (1000 to 30 hPa). The global model has a resolution of 0.833° latitude and 1.25° longitude. The data used are 6-hour forecasts, which have been interpolated to occultation positions.

These levels are linearly interpolated (in log of pressure) onto the state vector levels used for TOVS retrievals (see Eyre (1990) for further details), assuming a 260K temperature at a pressure that corresponds to a height of 50km and 190K at a pressure that corresponds to 90km. The 50km value was chosen to be consistent with the specification of the Jet Propulsion Laboratory (JPL) data files [5], allowing for the optimal solution to be compared with the results from the Abelian inversion (not presented here).

The *a priori* covariance matrix, $\mathbf{S}_a$ was originally obtained from the UKMO (TOVS version), where it was generated from statistics of radiosonde-forecast differences in the lower atmosphere; elements in the upper stratosphere are found by regression from the levels provided (see Eyre (1989)). For the purpose of this preliminary application to radio occultation measurements, the off-diagonal elements corresponding to this process were set to zero.

The measurement vector, $\mathbf{y}$, is obtained from the GPS-MET receiver (in the period 25 April to 1 July, 1995) [6]. The quantity that is assimilated is the bending angle: a typical number of elements ranges from 100—150.

The measurement-error covariance, $\mathbf{S}_y$, is at present a fixed diagonal matrix in bending angle, corresponding to the errors obtained by the experiments described in Luntama (1997). The forward model error is included by adding a 1% error to the diagonal elements of $\mathbf{S}_y$ in the height

range corresponding to the UKMO NWP model; above this level the value for the top model level is used.

4 Error characterisation of method

Once the optimal solution has been calculated, there are many error diagnostic matrices that can be obtained and used to fully characterise the solution.

The error diagnostic presented in this paper, intended to illustrate the nature of the solution, is the solution covariance.

4.1 Solution covariance

The covariance of the solution, $\hat{S}$ is given by (Rodgers (1976)) :

$$\hat{S} = (S_a^{-1} + K^T S_y^{-1} K)^{-1} \qquad (6)$$

An *improvement* vector — the % difference between the square-root of the variances of the principal diagonal elements of S_a and $\hat{S}$, — represents how much the 1DVAR scheme has improved upon the knowledge of the atmospheric state relative to the *a priori* knowledge. It is given by:

$$100 \times \left[1 - \left(\hat{S}_{ii}/S_{a,ii}\right)^{\frac{1}{2}}\right] \qquad (7)$$

where i is the matrix element index.

Figure 1 shows the *improvement* vector. On the left are the elements of the vector corresponding to temperature, and on the right are the elements of the vector corresponding to specific humidity.

The temperature *improvement* vector suggests that the 1DVAR solution has improved upon the *a priori* knowledge of the atmospheric temperature considerably, from the lower-troposphere to the upper stratosphere. For the majority of this region the knowledge of temperature has been improved by more than 65%.

The temperature *improvement* vector declines in the upper stratosphere and mesosphere partly because the bending angles are comparable with the assumed measurement errors, and partly because upper elements of S_a have been set to zero (section 3.2).

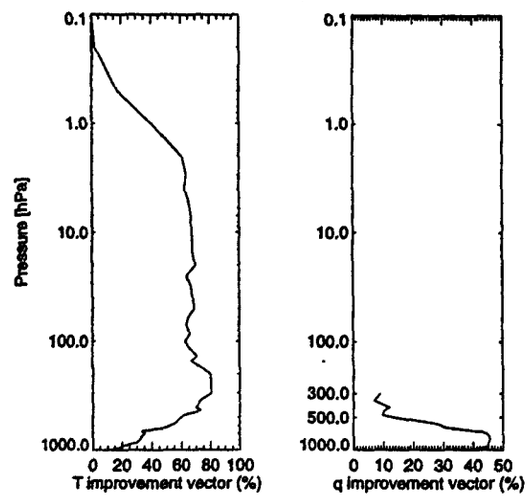

Figure 1: The *improvement* vector. The temperature elements of the vector (left) show that the 1DVAR scheme has improved upon the knowledge of temperature throughout the lower and upper atmosphere. For the majority of this region there is improvement of more than 65%. The vector elements corresponding to specific humidity (right) show that the 1DVAR scheme has improved knowledge of lower tropospheric specific humidity by ~40%. The GPS-MET ID for the occultation event presented is 95-05-05-01:33met_gps25; the collocated NWP information is from 69.06°N, 277.74°E.

The temperature *improvement* vector declines in the lower-troposphere where humidity becomes more significant, and both quantities are retrieved simultaneously.

The humidity *improvement* vector suggests that the 1DVAR solution has improved upon the *a priori* knowledge of lower tropospheric humidity by ~40%. This particular occultation event position contains a relatively small amount of humidity, further improvement in humidity is expected when larger values are present.

Both the temperature and humidity knowledge decline near the surface because the occultation event presented here ends a little way above the surface.

5 Conclusions

The preliminary results presented in this paper suggest that radio occultation measurements from the Global Positioning System, when assimilated with UKMO NWP information improve the knowledge of the atmospheric state significantly. For the majority of the troposphere and stratosphere, knowledge in tempera-

ture is improved by more than 65%; for much of the lower-troposphere, knowledge in humidity is improved significantly.

Acknowledgments

P. Palmer would like to thank Dr. S. Healy for the TOVS format of the UKMO NWP output and many useful discussions; Mr. Juha-Pekka Luntama for a very thorough measurement error analysis; and Dr A. Dudhia and Dr. C. D. Rodgers for their detailed insight on 1DVAR methods. The author would also like to thank JPL for providing the GPS-MET data-set used in the analysis.

References

[1] J. R. Eyre. Inversion of cloudy satellite sounding radiances by nonlinear optimal estimation I: Theory and simulation for TOVS. *Q.J.R. Meteorol. Soc.*, 115(489):1001—1026, 1989.

[2] J. R. Eyre. The information content of data from satellite sounding systems: A simulation study. *Q.J.R. Meteorol. Soc.*, 116:401—434, 1990.

[3] J. R. Eyre. Assimilation of Radio Occultation Measurements into a Numerical Prediction System. Technical Report 199, ECMWF, May 1994.

[4] G. Fjeldbo and A.J Kliore. The Neutral Atmosphere of Venus as Studied with the Mariner V Radio Occultation Experiments. *The Astronomical Journal*, 76:123–139, 1971.

[5] E. R. Kursinski, G. A. Hajj, K. R. Hardy, J. T Schofield, and R. Linfield. Observing the Earth's Atmosphere with Radio Occultation Measurements using GPS. *J. Geophys. Res.*, 1996.

[6] E.R. Kursinski, G.A. Hajj, W.I. Bertiger, S.S.Leroy, T.K. Meehan, L.J. Romans, J.T. Schofield, D.J. McCleese, W.G. Melbourne, C.L. Thornton, T.P. Yunck, J.R. Eyre, and R.N. Nagatani. Initial Results of Radio Occultation Observations of Earth's Atmosphere using GPS. *Science*, 271:1107–1110, February 1996.

[7] Juha-Pekka Luntama. Atmospheric Profiling with Radio Occultation. Master's thesis, Department of Electrical and Communications Engineering, Helsinki University of Technology, Finland, 1997.

[8] M. D. Mortensen and P. Høeg. Fresnel diffraction theory for enhanced vertical resolution in atmospheric profiling using GPS. Solar-Terrestrial Physics Division, Danish Meteorological Institute, Copenhagen, Denmark, 1998.

[9] C. D. Rodgers. Retrieval of Atmospheric Temperature and Composition from Remote Measurements of Thermal Radiation. *Reviews of Geophysics and Space Science*, 14:609–624, 1976.

P1.10B

DAILY EXTENDED 1-KM AVHRR DATA SETS OF THE MEDITERRANEAN

Dirk Koslowsky *
Freie Universität, Berlin, Germany

1. INTRODUCTION

The albedo and the Normalized Difference Vegetation Index (NDVI) are key parameters to monitor changes of land surface parameters.Time series obtained by the Advance Very High Resolution Radiometer (AVHRR) are a powerful source for regional and large scale monitoring and analysis. The successful compromise of temporal, spatial and spectral resolution extended its application towards land surface investigations and environmental changes. Data dissimitation free of charge, low cost receiving stations, new storage media, and high speed computer facilities increased the number of users capable to evaluate the data for research and real time application. Twenty years of data obtained with nearly unchanged instruments are a challenge for investigation of environmental changes.

The lack of onboard calibration facilities for the short wave channels in the red (CH1) and near infrared (CH2) regions is the main disadvantage of the AVHRR instrument. Thus the evidence of trends found in the long term data sets is strongly affected by the quality of the correction methods for changes in sensor sensivity and local observation time due to orbital drifts during the life time of the satellite. The knowlegde of the Bidirectional Reflection Distribution Function (BRDF) is necessary to account for changing illumination conditions and observation geometry. But also the time dependend state of convective cloud development especially in the afternoon observation period, possibly accompanied by precipitation, will affect the data and indicates the difficult transition from correction to information extraction tasks.Thus it is obvious that results of data processing and extraction have a feedback to the correction algorithms itselves.

Not only decission makers of the government instituions but also an increasing number of researchers in environmental, economic and even social sciences ask for reliable primary and derived secondary data for direct application or as input to complex modelling. For instance the thread of desertification in the Mediterranean and its impact to the social-economic problems of this region is one main focus of research funded by the European Union and was stimulus to develop methods for monitoring the earth surface by remote senising techniques on the one hand side and to apply the algorithms to create harmonized and validated long term data sets of the Mediterranean and its adjacent regions, which will be called *Extended 1-km AVHRR Data Sets.*

* *Corresponding author adress:* Dirk Koslowsky, Free Univ., Inst. of Meteorology, D-12165 Berlin;
e-mail kosze@zedat.fu-berlin.de.

2. PREPROCESSING AND CALIBRATION

The satallite receiving station at the Institut for Meteorology at the Free Univeristy of Berlin was founded in 1965, and in 1982 a HRPT station was brought into service. Since late 1988, when digital high density cartridge tapes became available, an archive of full resolution HRPT data of the whole reception circle covering the region from the pole to the Sahara desert and from Greenland to the Aral Sea was started. Simultaneously processing of daily geographic rectified data sets with 1 km resolution of selected windows covering the western Mediterranean and Mid-Europe was started. In 1995 increasing computer capacity allowed to process the full reception area by retaining the full resolution of the AVHRR intrument.

Participating in several international research projects like HIBE, HAPEX-Sahel, LaCrau and EFEDA field messurements, airplane, Landsat, AVHRR and Meteosat data had to be merged together. In the case of the AVHRR shortwave channels the problems of calibration, sensor degradation and surface anisotropy had to be investigated.

The problems with calibration and sensor degradation are settled sufficiently and the effects of surface anisotropy in reflection are identified as one of the major problems for comparisons between data from other sources, normally measured in nadir direction, and AVHRR data due to the large scan angle variations of +/- 55^0. Empirically derived Nadir Correction Functions (NCF) can sufficiently remove the surface anisotropy on a local or even regional scale and give estimates of surface reflectivities in nadir direction, which can be compared directly with nadir measurements. For large scale applications rough first order corrections with simple modelled functions can be performed.This had had consequences for the design of the 1-km data sets: without the knowledge of the radiation geometry AVHRR data have only limited worth (Koslowsky 1998).

During the first years of the mission of the NOAA 11 satellite there was some confusion about the magnitude of the sensor degradation of the AVHRR instrument. If only products like the NDVI, a non-linear combination of the two short-wave channels, is stored a later recalibration is very difficult. At least one of the two channels has to be retained to solve this problem accurately. There is not so much dissense in the calibration of NOAA 14 data. A comparison of calibration coefficients published by NOAA and a method using a RMS fit to the NOAA 11 time series of desert targets is shown in Fig. 1. There are nearly no differences for the red channel. The degradation for the near infrared channel is found to be somewhat to high and causes an increase of NDVI for the desert targets. If this differences are taken as uncertainty in absolute cali-

bration, the errors of landsurface reflectance of sparsely vegetated landsurface are of the order of 1% for CH1 and 2 % for CH2. Final degradation coefficients can be extracted at the end of the mission of the instrument. In the meantime the values are used in a predictive manner untill to the next update (Koslowsky, 1997).

3. DESIGN OF THE DAILY 1-KM DATA SET

Plain raster single channel image format in geographic projection (latitude/longitude with 0.01° resolution) is chosen for the data sets. The knowledge of the geographic coordinates of one pixel is sufficient for the whole data set.The formal digital resolution is 0.01 of units (i.e. % for reflectances, degree for temperatures and angles) multiplied by a factor of 100 and stored as 16 bit signed integers without any offset. The calibrated data of the five AVHRR channels at top of atmosphere (TOA) conditions form the first five files.They are completed by a number of pseudo-channels containing collateral data or derived products coincident pixel by pixel: local satellite and sun zenith distance and azimuth, local scattering angle, broadband albedo, NDVI, and a bitmap. The upper byte of the bitmap channel represents the *origin indicator*, a 6 bit bitmap inserted into the spare bits of every HRPT superpixel at data reception time, which allows to identify the date and the orbit number of every individual pixel, even in the case of multi-day composites like the maximum NDVI. It allows to recover the original digital counts and to apply sophisticated calibration and correction algorithms later on to each individual pixel without a loss in digital resolution.The other byte contains a land/ water bit and a cloud mask and allows to switch between different evaluation algorithms.

A second version of this data set with only 8 bit resolution is also generated. In this case the data are not as self-explaining the 16 bit version and different quantities need different conversion formulas to keep up a resonable accuracy.

In order to cover as many study areas as possible in the Mediterraean and the surroundings and as a result of frequent discussions with the RESMEDES participiants the ***area of interest*** for the 1-km data sets was defined as:

55° N/10° W	55° N/42° E
27° N/10° W	27° N/42° E

Data sets of the total area amount to 2800 lines by 5200 columns with 14,560,000 raster positions. To comply with user requirements and to reduce the size of the datasets, the whole area is divided into four stripes of data. The striping includes some overlapping to represent four main sub-areas. The coordinates of the upper left corners are:

S:	Iberian Peninsula	55° N/10° W
I:	Italy	55° N/ 5° E
B:	Balkan Peninsula	55° N/15° E
E:	East	55° N/27° E

All stripes have the same size of 2800 lines by 1536 columns. Smaller windows can be selected and are completely defined by the geographic coordinates of the upper left corner and the number of lines and columns. These data sets are easily to merge, in case larger areas or the whole Mediterranean have to be considered. Areas for which data are not yet available in supervised form left blank.

This definition is of great importance for the future research in the Mediterranean, especially in respect to the envisaged long term **and** large scale application. Data with considerable higher/lower resolution (i.e. Landsat, Meteosat) should be remapped to latitude/longitude representation with a raster resolution, which are powers of 2 compared to the resolution of these 1-km data sets. Samples that show the extent of the covered area can be found in Fig. 2 and Fig. 3. 10 day NDVI composites of the four stripes are merged together.

REFERENCES

Bolle, H.-J., André, J.-C., Arrue, J.L., et al. (1993), EFEDA: European Field Experiment in a Desertification-threatened Area, *Ann. Geophys.* II:173-189.

Koslowsky, D.: Signal degradation of the AVHRR shortwave channels of NOAA 11 and NOAA 14 by daily monitoring of desert targets. *Adv. Space Res.* **19**(1), 1355-1358.

Koslowsky, D.: Improved long-term AVHRR reflectance and NDVI time series using empirically derived nadir correction factors, this volumn.

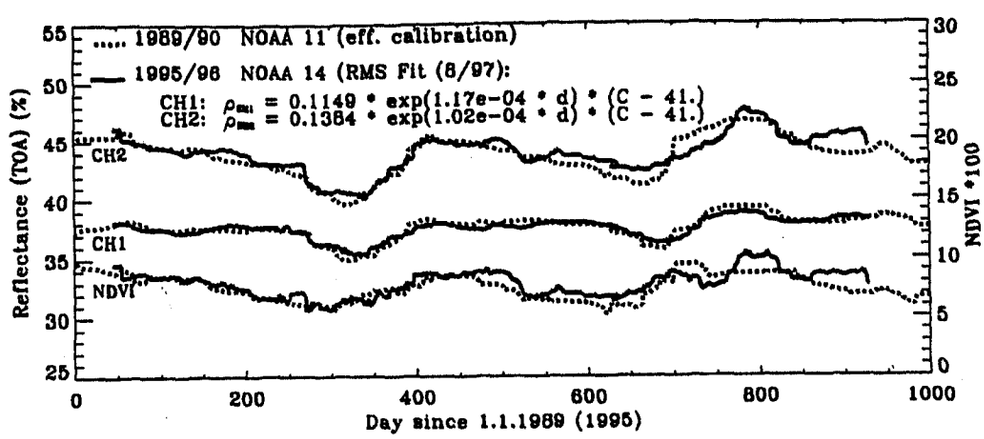

Fig. 1: Intercalibration of NOAA 11 and NOAA 14 AVHRR channel 1 and 2 including sensordegradation.

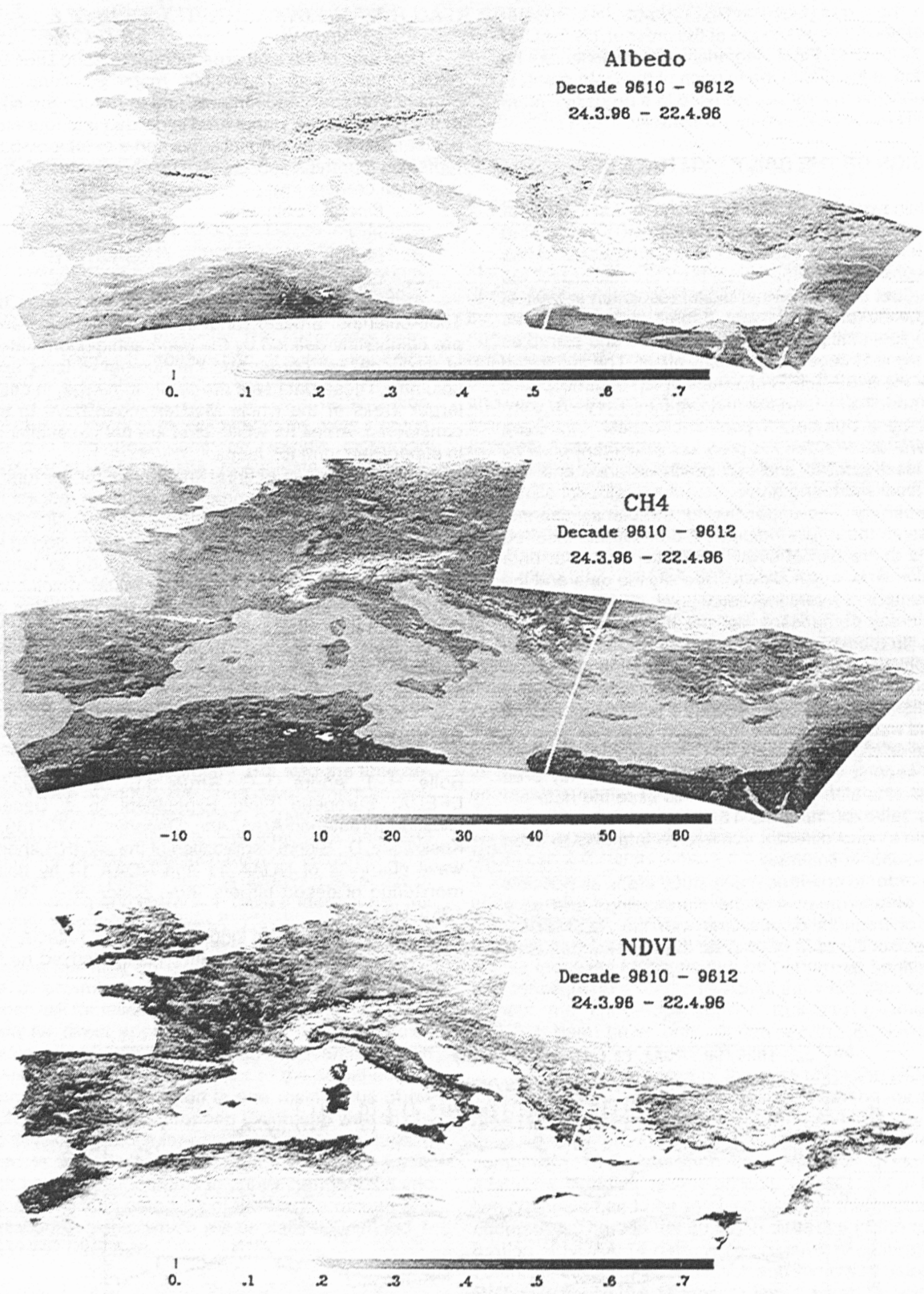

Fig. 2: Sample of running monthly composites of the full area for spring 1996. Broadband albedo and brightness temperature (CH4) according to the maximum NDVI.

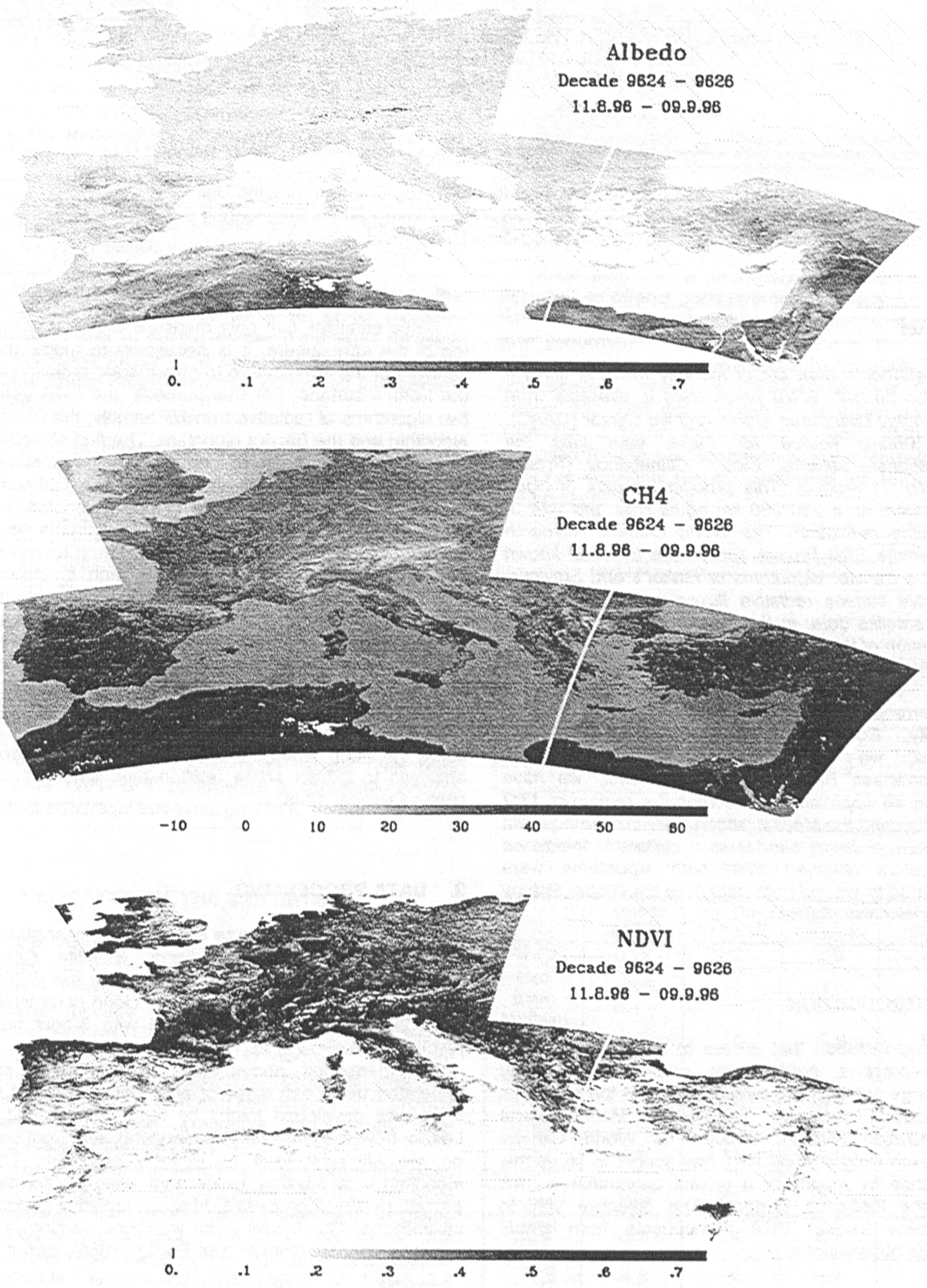

Fig. 3: Sample of running monthly composites of the full area for late summer 1996. Broadband albedo and brightness temperature (CH4) according to the maximum NDVI.

P1.11A

ANALYSIS OF SRB DATA OVER THE MEDITERRANEAN BASIN AS A PRELIMINARY STUDY IN THE RESMEDES (REMOTE SENSING OF MEDITERRANEAN DESERTIFICATION AND ENVIRONMENTAL STABILITY) PROJECT CONTEXT

Gustavo Haba-Ejarque (2), Ernesto Lopez-Baeza* (1) and Jose M. Fuster-Escuder (2)

(1) University of Valencia. Faculty of Physics. Remote Sensing Unit
(2) Polytechnical University of Valencia. Telecommunications Engineering School. Communications Department.

Abstract

*A 46-month data set of monthly average surface radiation budget (SRB) parameters is available from the Langley Distributed Active Archive Center (DAAC). The primary source for these data was the International Satellite Cloud Climatology Project (ISCCP) C1 product. This product consists of cloud parameters on a 280*280 km equal-area grid with 3-hour time resolution. The World Climate Research Programme SRB Project applied the two well known radiative transfer algorithms of Pinker's and Staylor's, to derive surface radiative fluxes on a global scale using satellite data. In this contribution, we study the application of these two algorithms on different scales, namely, global, regional and local. Specifically, and within the RESMEDES (Remote Sensing of Mediterranean Desertification and Environmental Stability, EC Project ENV4-CT95-0094) Project context, we are interested in studying the Mediterranean Basin area, and for that, we have chosen an approximately rectangular region of 17*7 cells covering the Mediterranean Sea and the adjacent countries. The shortwave surface irradiance parameters obtained from both algorithms were compared to ground truth data from the Global Energy Budget Archive (GEBA).*

1. INTRODUCTION

Solar radiation that arrives to the surface of the Earth plays a fundamental part in the energy exchange between the atmosphere and the terrestrial or oceanic surfaces. The World Meteorological Organization (WMO), through its World Climate Research Program (WCRP), has sought to study this exchange by means of a project denominated SRB (Surface Radiation Budget). The objective was to determine several SRB components from global satellite observations.

Since satellites can only measure radiation at the top of the atmosphere, it is necessary to model the behavior of the atmosphere to obtain solar radiation at the Earth's surface. For this purpose, the SRB uses two algorithms of radiative transfer namely, the Pinker algorithm and the Staylor algorithm. The first objective of this work has been to compare their respective performance, always from an eminently practical point of view, to facilitate the choice of one or another by future users of SRB data. Since both algorithms have global vocation, it is reasonable to think that there will be regions where they work better than in others. Thus, the first validation approach has been a zonal one, paying special attention to the Mediterranean Basin. Other conditioning circumstances have also been analysed, like surface type or latitude, for example. The second objective of this work consists of the study of the SRB parameters over the Mediterranean area. To this respect, the properties of some radiation and cloud parameters have been analysed to extract some relationships among them (Haba-Ejarque, 1998).

2. DATA PROCESSING

The primary data source are satellite observations coordinated by the International Satellite Cloud Climatology Project (ISCCP), especifically the ISCCP C1 product. This product consists of cloud parameters on a 280*280 km equal-area grid with 3-hour time resolution (Rossow et al., 1991).

As mentioned above, the SRB products are generated using two different algorithms. The first of them was developed jointly by R. T. Pinker and I. Laszlo, from the University of Maryland, and from now on, we will refer to it as Pinker's algorithm. This algorithm is a physical model that uses an iterative procedure based on delta-Eddington radiative transfer calculations. The model is an improved version of a previous concept (Pinker and Ewing, 1985), and it is

* University of Valencia. Faculty of Physics. Remote Sensing Unit. c/Dr Moliner, 50. Burjassot. 46100 Valencia (Spain). E-mail: Ernesto.Lopez@uv.es

described in detail in Pinker and Laszlo (1992). The second algorithm is due to W. F. Staylor, from the NASA Research Center in Langley, Virginia, and we will refer to it as Staylor's algorithm. This algorithm is a parameterised physical model that uses ISCCP radiances, TIROS Operational Vertical Sounder (TOVS) meteorology and climatological aerosols to determine the clear atmospheric and cloud transmission characteristics. Documentation for the Staylor's model can be found in Darnell et al. (1992). Both models, Pinker's and Styalor's, satisfy the ICRCCM (*Intercomparison of Radiation Codes in Climate Models*) model-validation tests.

After the previously mentioned processing, the SRB data are presented as a set of 52 monthly-averaged and 10 daily-averaged parameters for each of the 6596 ISCCP grid cells that cover the whole world. These parameters may be divided into several types:

a) Cell information, such as latitude or type of surface.
b) Shortwave surface irradiance (Pinker, Staylor and GEBA).
c) Other parameters (temperature, pressure...).
d) Calculated parameters (ratios, differences...).
e) Validation parameters (differences between some Pinker and Staylor parameters and GEBA ground truth values).

These data cover a period of 46 months, from March 1985 through December 1988, and they are available via CD-ROM from the NASA Langley Research Center, Hampton, Virginia 23681-0001 (Whitlock et al., 1993). A 96-month dataset (July 1983 to June 1991) of 7 parameters is accessible on the web at http://agni.larc.nasa.gov/SRB_homepage.html.

3. VALIDATION OF THE SRB DATA

The validation of the SRB parameters has been carried out by comparing the satellite estimations to surface irradiance measurements from the Swiss Federal Institute of Technology's Global Energy Budget Archive (GEBA) (Ohmura and Gilgen, 1991). The GEBA data are monthly averaged downward radiative fluxes from stations located all over the world, mostly in the Northern Hemisphere, that provide shortwave surface irradiance ground-truth data necessary for the comparison.

The scope of our comparison procedure has gone from a global to a more regional one: first, we have considered the whole world, then we focussed ourselves on a group of cells that cover the Mediterranean Basin (Fig. 1), then the Iberian Peninsula, and finally, the region of Castilla-La Mancha in the East of Spain, which is one of the interest areas in the RESMEDES Project.

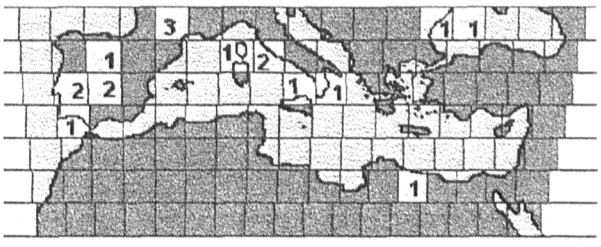

Fig. 1. SRB cells covering the Mediterranean Basin (numbers in some cells indicate the number of GEBA stations included)

Since both Pinker and Staylor algorithms were designed to offer a good average accuracy for every time and location on the globe, it is natural to think that their performance may vary depending on the specific cell we consider. We have studied the variability of the differences of irradiance GEBA-Pinker and GEBA-Staylor and their dependance on time and location. Thus, Fig. 2. shows the evolution of both differences, averaged for the Mediterranean region shown in Fig. 1. Some statistical results, performed for 1987 data, are presented in Table 1.

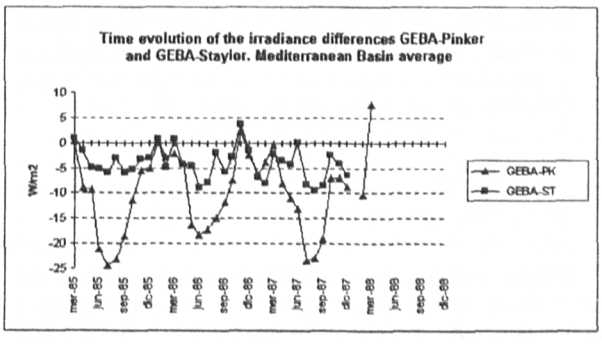

Fig. 2. Time evolution of GEBA-Pinker and GEBA-Staylor irradiance differences (averaged over the Mediterranean Basin)

	Average GEBA-Pk	Std. Dev. GEBA-Pk	Average GEBA-St	Std. Dev. GEBA-St
Spain	0.27	12	4.8	11
Med. Basin	-10.3	19	-4.0	16
Northern Hemisph. (1/87)	-4.8	16	-2.9	14
Northern Hemisph. (7/87)	-10.5	22	-4.1	25
Global (1/87)	-5.6	17	-2.6	15
Global (4/87)	-10.2	21	-4.1	25
Global (7/87)	-3.8	24	-6.4	21
Global (10/87)	-4.5	19	-1.9	14

Table 1. Statistics of the differences of irradiance GEBA-Pinker and GEBA-Staylor

In this zonal approach, accuracies of Pinker's and Staylor's algorithms have been checked according to the following criteria:

a) cell latitude,
b) cell type (water, land or coast),
c) number of GEBA stations per cell.

The conclusions drawn from this analysis are listed below:

1) Both algorithms tend to overestimate ground values, but the estimation error keeps below 10 W/m^2 for most locations.
2) Summer months cause a loss of accuracy of both algorithms. However, the Staylor's algorithm is more insensitive to seasonal changes.
3) The Pinker's algorithm overestimates the Staylor's algorithm at mid-latitudes, and underestimates it at high latitudes.
4) Although the Staylor's algorithm offers a better overall performance, the Pinker's algorithm may be preferred for certain selected regions (for example, the Iberian Peninsula).
5) The cell type has no decisive effect on the behaviour of the algorithms at a global scale, but at a Mediterranean scale, the Pinker's algorithm overestimates irradiance for water cells, while the Staylor's algorithm does it for land cells.

4. STUDY OF SOME STAYLOR PARAMETERS FOR THE MEDITERRANEAN BASIN

Staylor parameters were found more accurate for the Meditearranean Basin, and then, we performed a further analysis on some of them, for example: surface irradiance, surface albedo, net shortwave radiation, cloud fraction and "cloud forcing" irradiance.

The time evolution of Staylor's downward surface irradiance is shown in Fig. 3 for some selected cells, as well as the average for the Mediterranean Basin. In this case, the 96-month dataset was used to test the ability of the SRB data to study long-time trends for specific cells.

The Mediterranean Basin is located in the area of higher slope of the irradiance vs latitude curve (see Fig. 4). This, together with the separating function that the Mediterranean exerts between a desertic climate and a continental one, both accentuate the contrast between North and South in the area of study, so that in hardly 15°, surface irradiance values vary as much as 100 W/m^2. In other parameters, such as albedo, a similar behavior is observed. Net irradiance does not show such an accute variation, because the North-South irradiance differences are compensated by albedo differences in the same direction.

The influence of clouds in the Mediterranean Basin is maximum during spring months and, in a smaller extent, during the autumn ones, although the average cloudiness stays more or less constant, except for the summer months. It is important to stress that cloud fraction is not equivalent to cloud forcing (see Fig. 5). Cloud forcing represents the difference between all-sky and clear-sky surface irradiance, so that it may be considered as a measure of the influence of clouds on irradiance. Cloud fraction, however, only gives account of the percentage of sky covered by clouds. Thus, for the same cloud fraction value, if the clouds are thick, shortwave cloud forcing is smaller (it is a negative value) than if the clouds are thin.

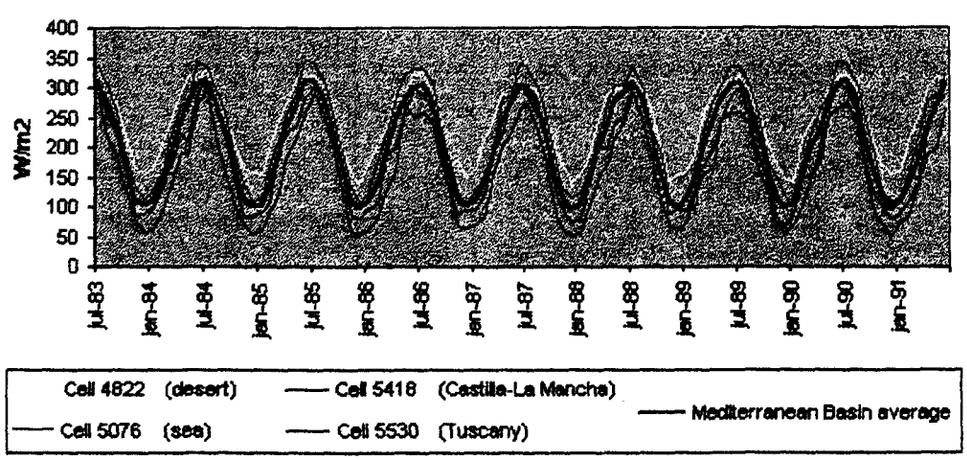

Fig. 3. Time evolution of Staylor surface irradiance for selected cells

5. SUMMARY AND CONCLUSIONS

Thanks to their satellite origin, the main advantage of SRB data consists of the possibility of studying the temporary evolution of certain meteorological parameters for a certain region, with no ground stations. The cell division format facilitates the spatial analysis, allowing for the elaboration of maps with great simplicity. The reliability of the Pinker's and Staylor's algorithms is a warranty for the trustfulness of the results obtained for most of the cells and months of the study.

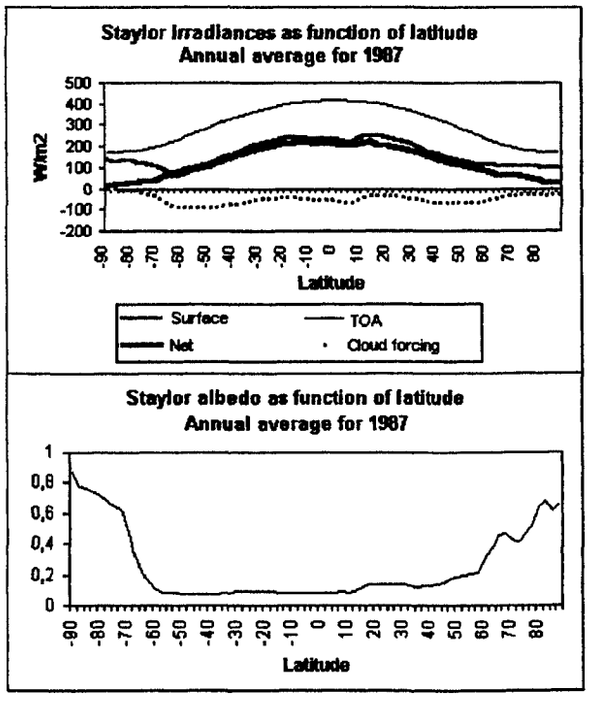

Fig. 4. Staylor irradiance (surface, TOA, net, cloud forcing) and albedo as a function of latitude (averaged for 1987)

Another point to value positively is the organization of the SRB product. The accessibility of these data and their moderate volume allow any user with a "non-very powerful" personal computer to work with them.

An inconvenience is the long time data processing takes before they are available for public use. As an example, data from July 1985 were processed in October 1992, and it was not until 1995 that they were available. Fortunately, these terms are shortening in the last deliveries. The 1995 data were expected to be processed in autumn 1997, and become of public use in 1999.

The resolution is something that would also be susceptible of improvement. Cells of 280*280 km may be too big for certain applications. This is also being revised, since the new data deliveries promise improved resolutions.

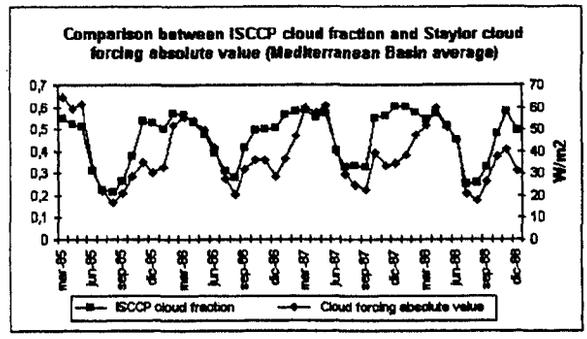

Fig. 5. Time evolution of ISCCP cloud fraction and absolute value of cloud forcing (Staylor values)

6. REFERENCES

Darnell W. L., W. F. Staylor, S. K. Gupta, N. A. Ritchey and A. C. Wilber, 1992: Seasonal variation of surface radiation budget derived from International Satellite Cloud Climatology Project C1 data, *J. Geophys. Res.*, 97, 15741-15760.

Haba-Ejarque G., 1998: Comparación de los algoritmos de Pinker y Staylor para la estimación de flujos de onda corta. Aplicación de los productos del programa SRB (Surface Radiation Budget) a la Cuenca Mediterránea. Proyecto Fin de Carrera. Universidad Politécnica de Valencia,. Marzo 1998.

Ohmura A. and H. Gilgen, 1991: The GEBA database, interactive applications, retrieving data, Global Energy Budget Archive, GEBA, World Climate Program Water Project A7, Report 2, *Zurcher Geographische Schriften.*

Pinker R. T. and J. Ewing, 1985: Modeling surface solar radiation: Model formulation and validation. *J. Climate Appl. Meteor.*, 24, 389-401.

Pinker R.T. and I. Laszlo, 1992: Modeling surface solar irradiation for satellite applications on a global scale. *J. Appl. Meteor.*, 31, 194-211.

Rossow W. B., L. C. Garder, P. J. Lu and A. W. Walker, 1991: International Satellite Cloud Climatology Project (ISCCP) documentation of cloud data, WMO/TD-266, World Clim. Res. Progr., Geneva, March 1991.

Whitlock C. H., T. P. Charlock, W. F. Staylor, R. T. Pinker, I. Laszlo, R. C. DiPasquale and N. A. Ritchey, 1993: WCRP surface radiation budget shortwave data product description, ver. 1.1, NASA Technical Memorandum 107747.

P1.12B

CLOUD CLIMATOLOGY OF THE ALPINE REGION FROM LONG-TERM AVHRR DATA

Martina Kästner and Karl Theodor Kriebel*
Institut für Physik der Atmosphäre, DLR, Oberpfaffenhofen, Germany

1 AIM

Clouds are an element of climate. They modify the radiation budget and, hence, the earth surface temperature, and they are part of the water cycle. Surface observations of clouds are horizontally inhomogeneous. They are local, subjective eye observations because no instrument is used to determine cloud coverage. From satellite data, however, cloud coverage is derived by means of an objective cloud detection algorithm applied to each pixel. Long time series of satellite data build a basis for climate data from which trends can be derived. As a forerunner of an improved cloud climatology which is intended to consist of longer time series in a larger are, this cloud climatology of the Alpine region is based on eight years of full resolution AVHRR data averaged after having been processed over boxes of 0.125 latitude an 0.2 longitude. Fig. 1 shows the test area in which daily cloud charts have been generated from which regional climate charts are derived by means of spatial and temporal averaging. The area of 540 km by 560 km comprises three climate regions: moderate, Alpine, and Mediterranean.

2 METHOD

The cloud detection algorithm package APOLLO (AVHRR Processing scheme Over Land, cLouds and Ocean, [1],[2]) is used to determine cloud coverage from daily multispectral AVHRR data of the NOAA satellites. In this climatology, the status of APOLLO as achieved by 1994 has been applied throughout. Fig. 3 shows the cloud mask in pixel resolutioon of July 10, 1995, generated with APOLLO (cf. Fig. 2). Fully cloudy pixels are vertically distributed in three layers according to their cloud top temperature. Additionally, thin clouds with no other clouds below are identified as cirrus clouds. They can increase the temperature of the

* *Corresponding author address:* Deutsches Zentrum für Luft- und Raumfahrt e.V. (DLR), Institut für Physik der Atmosphäre, D-82234 Wessling; Tel +49 8153 28 2535, e-mail: Martina.Kaestner@dlr.de

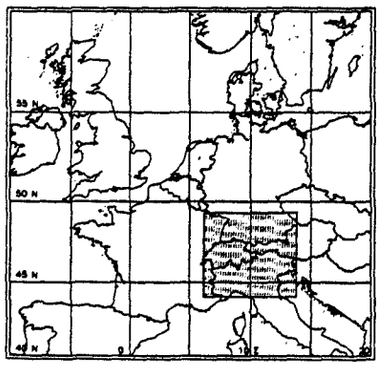

Figure 1: *Position of the test area in Central Europe.*

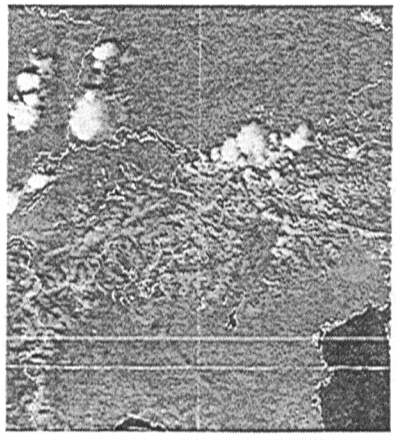

Figure 2: *AVHRR-scene (channels 1, 2, 4) of the test area on July 10, 1995, 12:05 UTC.*

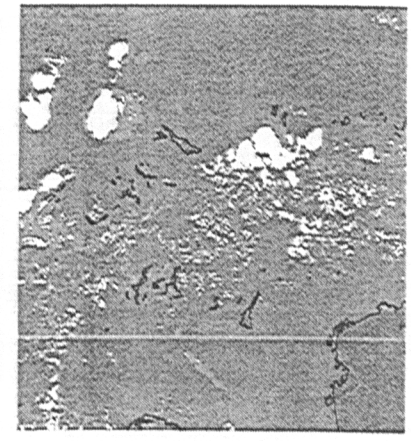

Figure 3: *Cloud mask of Fig. 2: white = totally cloudy, coloured = cloud free, grey = not classified.*

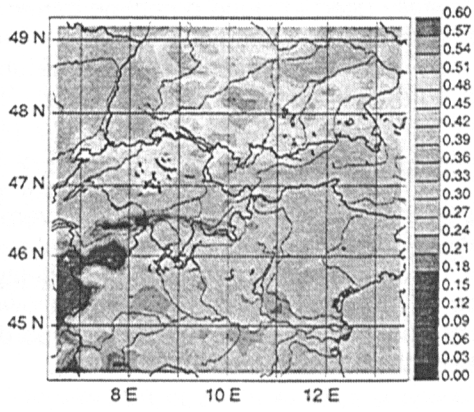

Figure 4: *Monthly mean cloud coverage of thin cirrus in December 1993.*

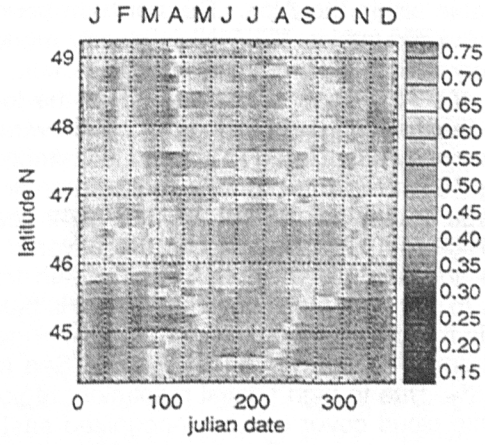

Figure 5: *Mean annual cycle of the total cloud cover (1992-1996) along a north-south cross section from the river Daube to the Appenino.*

3 Results

Fig. 4 shows the monthly mean of the cloud coverage due to thin cirrus in December 1993. Since the beginning of the continuous cloud climatology in the Alpine region in September 1991, the shown month has extreme coverage. Indeed, the monthly mean surface temperature in southern Germany in this month was 2 to 3 K above the 30-year climate normal.

Fig. 5 shows the mean annual cycle of the toal cloud cover of a section from the river Danube across the Alps to the Appennino along the 11.2 E meridian which touches Oberpfaffenhofen. The temporal averaging covers five years and is a gliding mean over 15 contigous days. The most noticeable feature is the low cloud cover in summer. North of the Alps, cloud cover is also low in May,

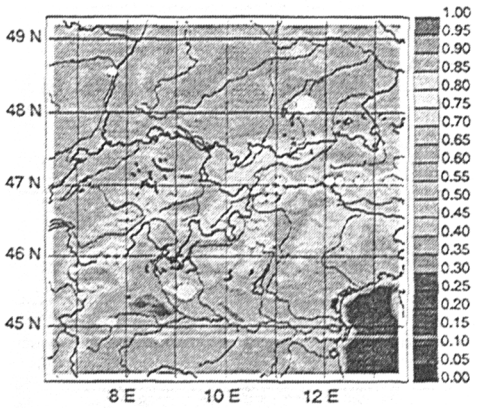

Figure 6: *July mean (1989-1996) of total cloud cover.*

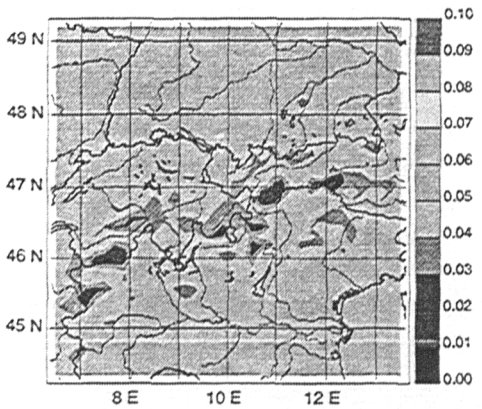

Figure 7: *rms deviation of the July mean (1989-1996).*

south of the Alpine main ridge (47 N), October is favourable within the Alps. The northern boundary of the mountains (47.5 N) is clearly marked by more clouds in summr due to convection. In winter, the Alps show less clouds than the forelands. Regional differences in the cloud coverage are frequently associated to luff and lee effects.

Fig. 6 shows the monthly mean total cloud doverage in July, averaged over the eight years from 1989 to 1996. Bad values are covered by circles according to rms information taken from Fig. 7. In southern Germany cloud cover is below 60%, in the central Alps above 60%, in northern Italy around 40% and over the Adraitic Sea it is only 25%. Due to high spatial resolution, regions with little cloud cover can be recognized east of Munich, around Lake Constance, within the Ticino and north of Lake Garda. Regional climate data are required in agriculture, energy and building industries, as well as in regional planning and leisure industry.

Fig. 7 shows the rms deviations of the means of the July cloud cover in Figure 5. Typical values in southern Germany are ±10% relative. Within a homogeneous climate region, individual low values, as observed over large cities and glaciers, indicate a systematic error in cloud detection over non-vegetated land surface.

4 Conclusions

Continuous and homogeneous satellite data are successfully used in cloud detection schemes to establish a multi-year regional cloud climatology with high spatial resolution. The results derived so far agree well to known climate data. Trends cannot be established yet because the natural variability of the clouds is very high. It is about ±30% in a monthly mean in our climate which yields an accuracy of the total cloud coverage of 1% after 30 years of data. The horizontal averaging of 15 km allows the detection of multi-layered clouds. The high regional resolution allowed to identify weaknesses of the APOLLO cloud detection algorithms and to elemininate them.

References

[1] K. Kriebel, R. W. Saunders, and G. Gesell. Optical properties of clouds derived from fully cloudy pixels. *Beitr. Phys. Atmos.*, 62:165–171, 1989.

[2] R. W. Saunders and K. T. Kriebel. An improved method for detecting clear sky and cloudy radiances from AVHRR data. *Int. J. Remote Sensing*, 9:123–150, 1988.

P1.14B CYCLOGENETIC CLOUDINESS OVER SOUTH AMERICA

N. Fedorova *, G. da C. Pinheiro , D. Fedorov

Meteorological Research Center
Federal University of Pelotas
Rio Grande do Sul, BRAZIL

ABSTRACT

This paper present an observational study of the cyclogenetic cloudiness over South America during 1996 year. The structure of the cyclogenetic cloudiness is analyzed using satellite observations in thermal IR and WV absorption band channels. Were found the characteristics of the cyclogenetic cloudiness. The classification of the cyclogenetic cloudiness was worked out. The characteristics of the temperature fields at surface and 700 hPa level; geopotencial at 700, 500 and 300 hPa levels; streamlines at surface and 250 hPa level; jet stream at 250 hPa; horizontal wind divergence at surface and 250 hPa level; relative vorticity at surface and 250 hPa level in the cyclogenetic cloudiness was found out. The atlas of the cyclogenetic cloudiness over South America including satellite and conventional data was created. The warm air currents from Amazon and Bolivia and the cold air currents from South Argentina formed the cyclogenetic cloudiness. The signs, which are enable to define this current on satellite data are described. It was demonstrated the scheme of the short - term forecast of the cyclogenesis in South America.

1. INTRODDUCTION

The Southern part of South America is one of the regions affected by genesis, intensification and passage of cyclonic vortices. In the spatial distribution of the frequency of cyclogenesis was noted existence of two centers of preference of cyclogenesis, one around Uruguai and other near to Gulf of San Matias in Argentina (Gan, Rao, 1991). The city Pelotas location is near of the cyclogenetic areas and the initial stage identification is very important for the weather forecast. The present investigation is dedicated the problem of the cyclogenetic cloudiness analysis over South America.

* Corresponding author address: Natalia Fedorova
Centro de Pesquisas Meteorologicas / UFPel
Av. Ildefonso Simoes Lopes, 2751
CEP: 96060-290 Pelotas-RS
Brazil
e-mail: natalia@cpmet.ufpel.tche.br

2. DATA AND METODOLOGY

The thermal IR images at intervals of 3 h. and the WV absorption band images twice time por day taken by GOES were used. All data were obtained for one year from January 1996 to December 1996.

The conventional data were obtained from National Meteorological Center, Washington for 00 UTC one time por day.
The following charts have been used in the present study:

- surface temperature;
- temperature at 700 hPa level;
- pressure;
- geopotencial at 700, 500 and 300 hPa levels;
- streamlines at surface and 250 hPa level;
- jet stream at 250 hPa;
- horizontal wind divergence at surface and 250 hPa level;
- relative vorticity at surface and 250 hPa level;
- surface charts for 12 UTC.

The forecast of the horizontal divergence, the relative vorticity, the streamlines and the jet at 24 h. have been used also.
The cloud images were examined visually to identify the cloud vortex. The identification is based on the description given by Anderson et al.(1973). It was selected the cloud vortexs, which were occurred in some stage development in the Southern part of Brazil. These cloud vortexs were analysed since advent until disappearance over area between 10-50°S and 30-80°W, this area covers the South America with the nearest parts of the oceans. The method have identified the surface cyclogenesis, if one closed isobar around a low pressure had observed on surface charts. The initiation of cyclogenesis is the time moment of the first appearance of the closed isobar. The fields of the meteorological elements, namely above, were analysed in the area of the cloud vortex at the IR cloud images. The mean fields were obtained for three stages of the cyclonic vortex development. Two examples of the average fields are shown on the figures 1 and 2. The gradients of the temperature and geopotencial, and also width of the frontal zone were calculated too. The structure of the fields of the relative vorticity, the horizontal wind divergence and the stremlines in the cloud vortex area were investigated. The jet position in this area was analysed too. The atlas of the cyclogenetic

cloudiness over South America including satellite and conventional data was created.

3. RESULTS

17 clouds vortexs were observed during one year. 91% of the process with the cloud vortex development were associated with the surface cyclogenesis. One cloud vortex was associated with a low at 300, 500 and 700 hPa levels. One cloud vortex was observed during 12 h., but the surface charts and charts of the geopotencial at 700, 500 and 300 hPa levels did not indicate any closed isobar or isoheight.

The typical *cloudiness structure(for example figure 1)* in the IR and WV images for the cyclogenetic process have the anticyclone curvature of the cloud's mass in its frontal part and the cyclone curvature in the rear part. In the situations, when cloud's mass have only anticyclonic curvature, it was observed only one time the cyclone formation. In this situation the cyclone was developed due to the thermal advection. The principal sign enable to define the warm air current on satellite IR and WV data is the cloudiness development between the cloudiness in Bolivia - Amazon and Argentina areas. The formation of the cloud's mass with the anticyclone curvature is the good sign of the thermal advection too.

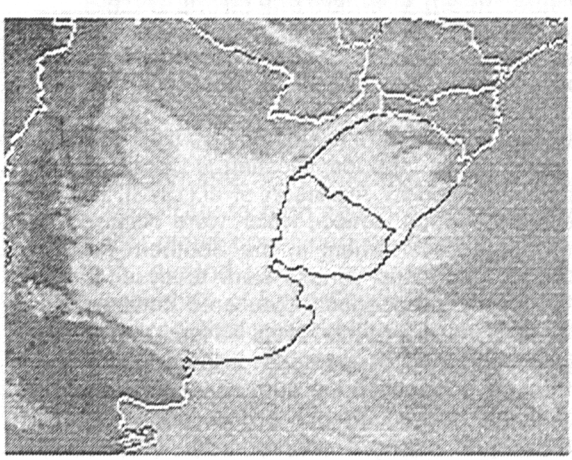

Figure 1. Cyclogenetic cloudiness. GOES, IR, 1500 UTC, January, 11, 1996.

The typical *temperature fields* at surface and 700 hPa level (fig. 2 and 3) show one frontal zone or two, which were united. The warm air displaced in frontal part of the cloudiness, the cold air penetrated in rear part and the asymmetrical temperature fields were formed. The average temperature gradient in the cyclogenetic cloudiness varied from 6 to 10 °/500 km. Average width of the frontal zone varied from 500 to 700 km for the cold part and from 900 to 1000 km. for the warm part.

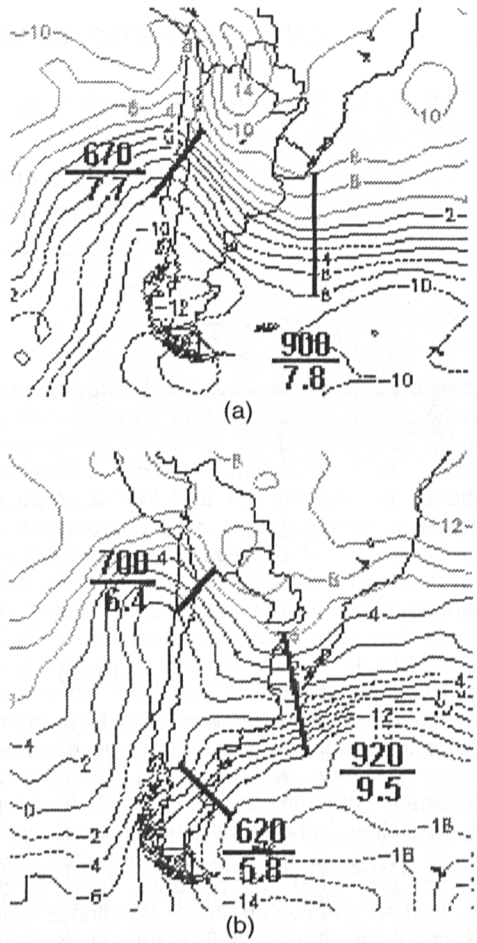

Figure 2. The temperature distribution at 700 hPa, corresponding to the cyclogenetic cloudiness in IR cloud images. The average width of the frontal zone (km., over line) and the average temperature gradient (°/500 km, under line) for some parts of the frontal zone (solid line) for two types (a., b.) of the first stage of the cyclonic vortex development.

The fields of the *geopotencial* at 700, 500 and 300 hPa levels show, that the cyclogenetic cloudiness was formed in the frontal part of the trough on these levels (62%). The cyclones was developed rare in the central part of trough at 500 hPa level (7%) and in the week and non profound trough (6%).

The surface *streamlines* demonstrated the convergence of the currents from Bolivia, Amazon and Southern and central part of Argentina. The streamlines at 250 hPa level show the steering current from the north-west to south-east for all events. The cyclogenetic cloudiness were observed at the rear part of the anticiclone or ridge at 250 hPa level. The steering current was associated with the jet stream in 93% events. The cyclogenetic cloudiness was formed near the jet stream entrance (50%), near the nucleon of jet (22%) and near the jet exit (21%). The cyclogenetic cloudiness were

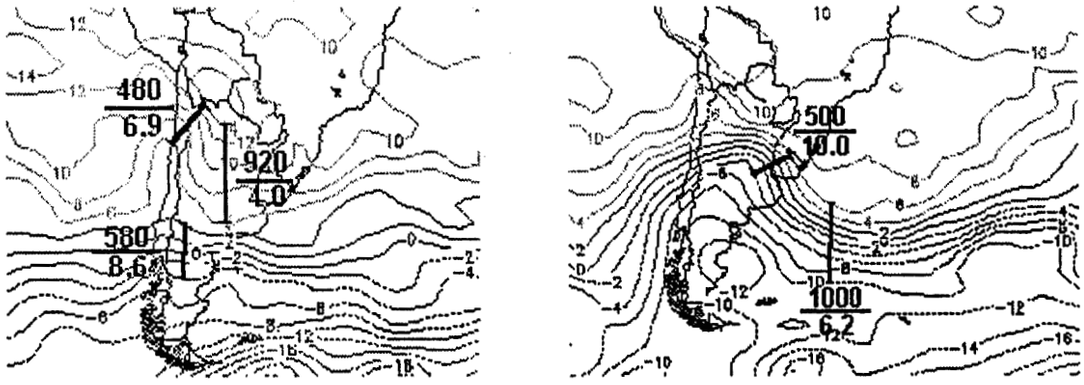

(a) (b)

Figure 3. The same as figure 2, but for the second and third stages of the cyclonic vortex development.

I.

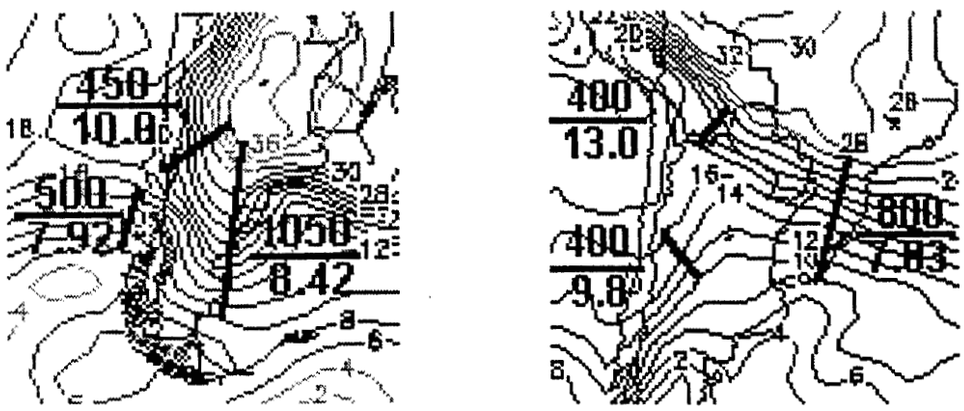

(a) (b)

II. III.

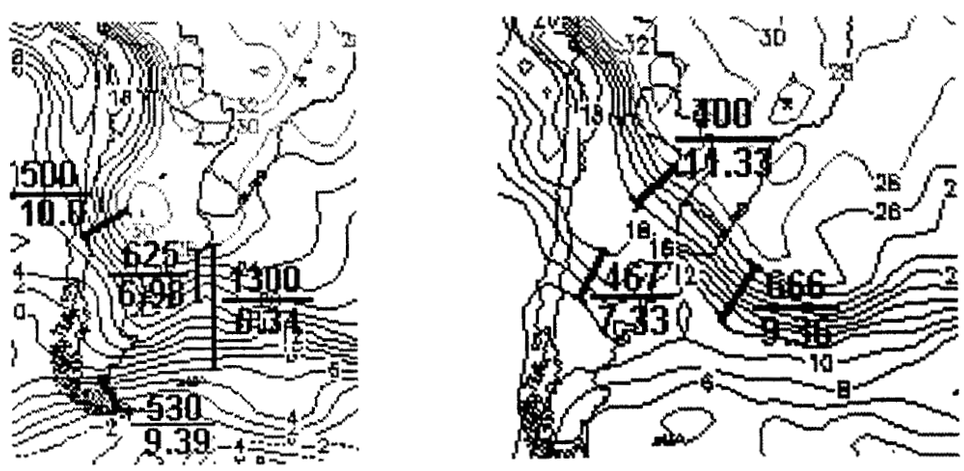

Figure 4. The same as figure 2 and 3, but for the surface temperature.

formed under the jet stream (54%) and on the warm side of the jet (39%).

The fields of the *horizontal divergence* at the surface show the magnitude in excess of -1.5e -05 s^{-1} in the rear part of the cyclogenetic cloudiness and from -1.5e -05 s^{-1} to +05e -06 s^{-1} in frontal part. The same fields at 250 hPa level demonstrated the magnitude in excess from -1.5e -05 s^{-1} to +4.0e -05 s^{-1} in frontal part and from -1.5e -05 s^{-1} to +1.0e -05 s^{-1} in rear part.

The surface fields of the *relative vorticity* (for example Figure 5) were positive (+2.0e -05 s^{-1}) in the frontal part of the cyclogenetic cloudiness and negative (from -4.0e -05 s^{-1} to -1.0e -05 s^{-1}) in the rear part. The highest magnitude in excess of the relative vorticity from -8.0e -05 s^{-1} to -0.0001 s^{-1} in rear part and from +4.0e -05 s^{-1} to +10.0e -05 s^{-1} in frontal part of the cyclogenetic cloudiness were observed at 250 hPa level. This results are in a good agreement with the results obtained by Satyamurty et al.1990, which studied the relative cyclonic vortex at 500 hPa level and found that the magnitude in excess varied from 2.0e -05 s^{-1} to 6.0e -05 s^{-1}.

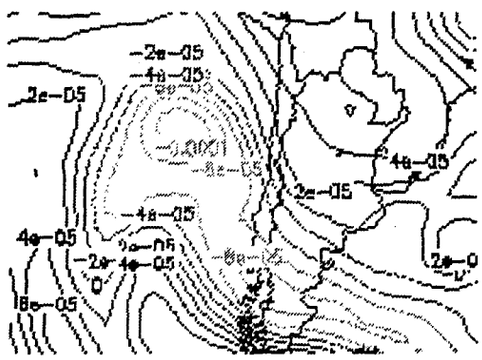

Figure 5. The field of the relative vorticity for the first stage of the cyclonic vortex development.

4. CONCLUSION

The clouds vortex formation accompanied the surface cyclogenesis in 91% events. The cyclogenetic cloudiness was developed in the rear part of the anticiclone or ridge at 250 hPa level, in frontal part of the trough at 300, 500 and 700 hPa levels. The clouds vortexes were formed near subtropical jet stream, under or in the its warm side. The asymmetrical temperature fields were observed in all situation at 700 hPa level. The fields of the horizontal divergence in cyclogenetic cloudiness in the most part of events hadn't high values at surface and 250 hPa level, but in some events reach +4.0e -05 s^{-1} at 250 hPa level. Two areas (positive and negative) of the relative vorticity at 250 hPa level with highest magnitude in excess (-0.0001 s^{-1} and +10.0e -05 s^{-1}) accompanied the cyclogenetic process. This results were base for elaboration of the short - term forecast scheme of the cyclogenesis in South America.

5. REFERENCES

Anderson R.K. et al.,1973. The use of satellite pictures in weather analysis and forecasting. WMO,Technical note No. **124**, Geneva, 275 pp.

Gan, M., A., V. B., Rao, 1991: Surface Cyclogenesis over South America. *Mon. Wea. Rev.*,**119**, 1293-1302.

Satyamurty, P., R., P., C. C. Ferreira and M. A. Gan, 1990: Cyclonic vortices over South America. *Tellus*, **42**, 194-201.

P1.15A COMPARISON OF MONTHLY MEAN SATELLITE ESTIMATES OF PRECIPITATION WITH GAUGES OVER AFRICA

Arnold Gruber *, Jeffrey R. McCollum, and Mamoudou B. Ba
NOAA/NESDIS Office of Research and Applications
Camp Springs, MD, USA

1. INTRODUCTION

The comparison of Global Precipitation Climatology Project (GPCP, Huffman et al. 1997) satellite rainfall estimates with raingage analyses reveals a large discrepancy over an area of central Africa. This is the only tropical region where systematic, large, positive biases are observed between satellite and raingage estimates. The discovery of this bias, for which there is no obvious explanation, has prompted this study. It is important to understand the uncertainties of the GPCP rainfall products so that the users of these products can account for their limitations in accuracy. The possible causes of this overestimation problem should be investigated so that these errors might be better predicted. In addition, important insights into satellite rainfall estimation may be gained, as the physical principles causing the overestimation may be important to consider in all satellite estimation algorithms.

Two of the possible causes for the overestimation of satellite estimates compared to raingage estimates in this region of central Africa are: 1) inefficient rainfall processes due to the properties of the air masses and aerosol contents; and 2) a drier atmosphere under the cloud base resulting in significant depletion of rainfall by evaporation. The first possibility will be discussed based only on the existing literature and on what we know about rainfall microphysical processes, since it is difficult to obtain data for such a study. To investigate the second possibility, the moisture environment of equatorial central Africa will be compared with the moisture environment of a region of equatorial South America where the satellite estimates are of the same magnitude as in Africa but where the raingage estimates are also of the same magnitude.

2. THE OVERESTIMATION PROBLEM

Figure 1 displays results from two GPCP rainfall products, the multi-satellite (GPMS) and raingage (GPCC) estimates. The mean daily GPMS rainfall from 1988-1994 is displayed in the first panel and the second panel shows the difference between the GPMS and GPCC estimates for the grid boxes with estimates from both algorithms. The most significant overestimation (> 5 mm/day) found on the globe occurs in the Himilayan mountain range. It is recognized that neither satellite nor raingage estimates are as useful in areas with mountainous terrain (Arkin et al. 1994), so overestimation over the Himilayas is not as much of a concern as it is in the region of the second largest discrepancy (3-4 mm/day) in equatorial central Africa.

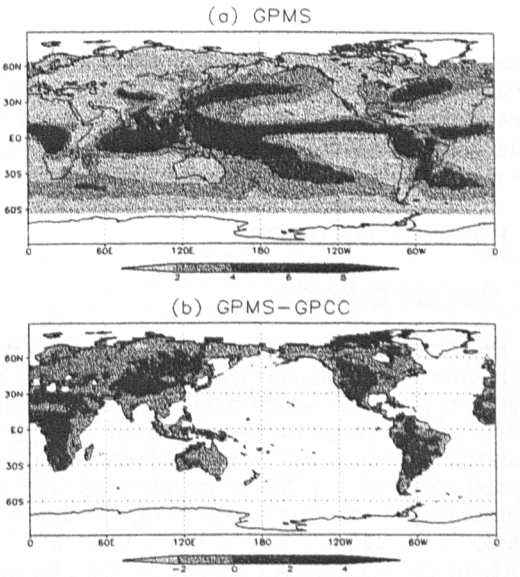

Figure 1: (a) Mean daily estimated rainfall (mm) from 1988-1994 for the merged satellite product (GPMS). (b) the difference between the GPCC and GPMS products (GPCC - GPMS).

Another illustration of the overestimation problem is shown in the time series of GPMS and GPCC rainfall (Figure 2a) for the area average of the region of focus in Africa, from 20° E to 30° E longitude and 10° S to 10° N latitude. For comparison, the time series from a region of South America of similar size and with similar magnitude of satellite-estimated rainfall (from 75° W to 65° W longitude and 10° S to 10° N latitude) is included in the second panel (Figure 2b). There doesn't appear to be an overestimation problem in this region of South America, as the GPCC estimates have similar magnitudes as the GPMS estimates. This region will be used for

* *Corresponding author address:* Arnold Gruber, NOAA/NESDIS/ORA, 5200 Auth Road Rm. 601, Camp Spring, MD, 20746; email: agruber@nesdis.noaa.gov

comparisons to help explain the differences between the two regions.

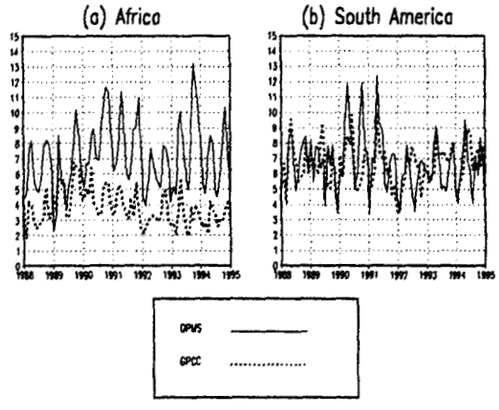

Figure 2: Monthly mean time series for GPMS and GPCC daily precipitation (mm) over (a) equatorial central Africa,; and (b) equatorial South America, 75° W longitude to 65° W longitude and 10° S latitude to 10° N latitude.

3. POSSIBLE SOLUTIONS

3.1 *Drop size distribution*

Precipitation processes are very sensitive to the cloud drop size distribution (DSD). This is due to the physics of accretion, which is the process of raindrop growth falling through the cloud (Kessler 1967), and coalescence processes. If the liquid water droplets in a cloud are small, it is difficult for raindrops to grow to sufficient size to achieve a velocity high enough to overcome the updrafts, fall out of the cloud, and reach the ground without evaporating. DSD depends primarily on the concentration of CCN in the atmosphere. Large numbers of CCN result in the formation of many small droplets, which will compete for the available water vapor. This in turn will limit further the growth of the droplets to larger size. Also, the coalescence is less efficient within clouds of large concentrations of small droplets.

The satellite rainfall overestimation over equatorial central Africa may be influenced by CCN. This region may have large amounts of CCN due to the combination of dust from the northern African desert and biomass burning over dry tropical regions of northern Africa. The aerosol transport into equatorial central Africa described in a case study by Andreae et al. (1992) supports this possibility, but more study is required.

3.2 *Moisture environment*

The moisture availability in a region affects the rainfall processes with relation to the satellite estimation problem. The evaporation of rain after falling from a cloud can be significant (Rosenfeld and Mintz 1988). The condensation level in a drier atmosphere is located at a higher elevation, resulting in a higher convective cloud bases. This means that rain falling from the bases of these clouds will be subject to more evaporation while traveling the distance between the cloud and the ground. Global data sets containing estimates of water vapor amounts and fluxes are used to describe the moisture budget of equatorial central Africa and to compare this region to the region of South America where there are high raingage estimates corresponding to the high satellite estimates.

4. GLOBAL MOISTURE PATTERNS

4.1 *NVAP water vapor data*

Important insights into the global distribution of water vapor can be gained by the NVAP (National Aeronautics and Space Administration Water Vapor Project) data set (Randel et al. 1996). This data set contains global, seven-year (1988-1994), 1° x 1° spatial resolution, atmospheric water vapor products at three layers (1000-700, 700-500, and 500-300 mb). The upper (500-300 mb) and middle (700-500 mb) levels show relatively constant water vapor amounts along any latitude band, with more water vapor as the latitude bands become closer to the equator. However, for the lower level (surface-700 mb) moisture, there is a sharp decline in water vapor over central Africa. While the lower level precipitable water typically has values between 25 and 40 mm along the equator (including the land areas of equatorial South America), the values drop off to between 15 and 25 mm over central Africa. In terms of the total column water vapor, the range over equatorial South America is between 40 and 50 mm, while the values over equatorial Africa range between 30 and 40 mm. This lower level dryness in Africa may result in higher cloud bases and significant evaporation of raindrops, resulting in less rain reaching the ground. Since satellite estimates relate rainfall to cloud level (i.e. cloud top height), this will result in overestimation of rainfall in a drier atmosphere.

4.2 *NCEP reanalysis data*

To study reasons for the low water vapor amounts in equatorial central Africa in comparison to other equatorial regions, NCEP/NCAR reanalysis data (Kalnay et al. 1996) were used. The reanalysis data set was created using a frozen state-of-the-art weather analysis/forecast system and assimilating past data to create a long-term record of global atmospheric fields. This dataset has been used recently (Higgins et al. 1996; Mo and Higgins 1996) for moisture studies similar to the one done here for equatorial Africa and South America.

The NCEP reanalysis data support the results from the NVAP data showing lower moisture contents over the region of Africa than over South America. While the highest resolution NVAP data are monthly averages, the NCEP reanalysis data were obtained at daily resolution. Figure 3 shows the time series of monthly mean precipitable water (total column liquid water equivalent) calculated from NCEP data. The precipitable water values over South America are in general 10 mm higher than those over Africa for the 7-year period of study.

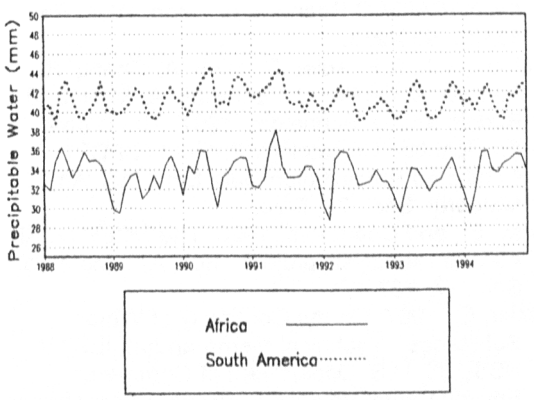

Figure 3: Time series of monthly mean precipitable water from the NCEP reanalysis dataset for the study areas in Africa and South America.

The mean, NCEP, vertically-integrated moisture fluxes from January, 1988-1994, for Africa and South America are displayed in Figure 4. A land-surface elevation map is superimposed.

(a) Africa

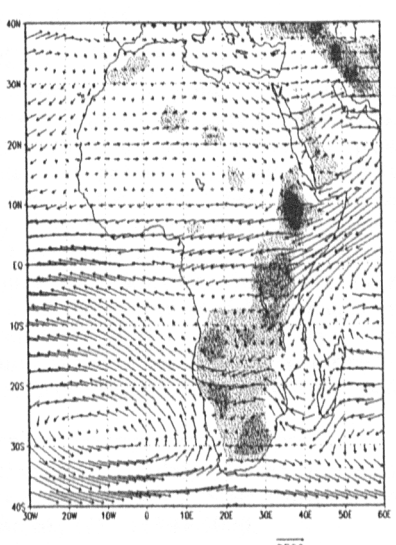

(b) South America

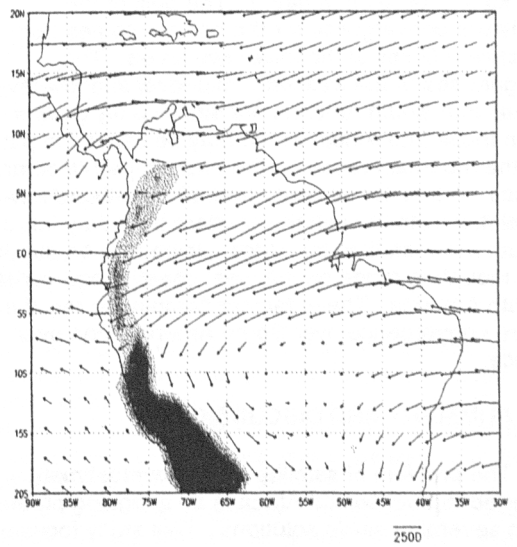

Figure 4: (a) NCEP vertically-integrated moisture flux (units: g (cm s)$^{-1}$) for January, 1988-1994, for the African continent. Topography is indicated by the shading at 400-m intervals (starting at 800 m). (b) Same as Figure 4 for the study region of South America.

Westward moisture flux from the Indian Ocean appears to supply the moisture to central Africa, as indicated by the vectors in Figure 4(b). The vertically integrated flux is influenced most heavily by the lower (1000-865 mb) elevations, so it is possible that the mountain range on the eastern part of central Africa blocks part of the moisture flux. The NCEP moisture flux pattern of equatorial South America shows differences from that of Africa. There again is significant flux from the east, but the topography is on the west coast of South America, which may reduce the flux of moisture out of the region. These moisture flux results provide a possible explanation for the lower levels of water vapor observed in Figure 4.

4.3 *Multi-level moisture convergence*

The daily, multilevel NCEP moisture fluxes were used to calculate vertically and horizontally integrated fluxes into and out of columns of atmosphere above the areas of interest in central Africa and South America. The flux data used in Figure 4 are used in these calculations, which are done to better understand the magnitudes of the NCEP-estimated fluxes. As in previous flux calculations, these were done according to month. The relative magnitudes of the calculated quantities are similar for the different months, so as in the flux results, the results of one particular month, January, are discussed.

The striking difference between the two areas (figures illustrating these calculations are not shown here) is in the magnitude of the flux convergence.

There is approximately six to seven times as much total convergence for the column in South America (66×10^6 kg s^{-1}, or 2.3 mm day^{-1}) than in Africa (10×10^6 kg s^{-1}, or .35 mm day^{-1}). The bulk of the moisture convergence for the column comes from the westward fluxes at the lower two levels. The magnitudes of the westward mid-level and low-level fluxes into South America are significantly greater than those into Africa, which may be caused in part by the mountain range on the eastern part of central Africa. A smaller percentage of the westward low-level flux exits through the western boundary for South America than for Africa, which may be due to the mountain range on the west coast of equatorial South America. These factors combine to result in more convergence over South America than over Africa.

5. SUMMARY AND DISCUSSION

The problem of satellite rainfall overestimation over equatorial central Africa is an intriguing problem with several possible solutions. This study focuses on the moisture environment, an explanation that can be readily studied with data sets that have been produced this decade. The study shows how overestimation may be caused in part by evaporation of raindrops as they fall through the dry lower levels of central Africa. As shown in the results, this lower-level dryness may be due in part to a mountain range on the eastern edge of Africa that blocks the westward flow of moisture from the Indian Ocean. The blockage of maritime moisture means that more of the moisture flux into the region may be from the drier, continental air.

Air over land tends to have more CCN, which result in smaller cloud liquid droplets and less efficient rainfall processes. The lightning data of Christian et al. (1996) provide insight into this concept. The lightning data indicate that there is much more lightning over land than oceans. This is due to stronger updrafts and smaller liquid drops over land, which allow a thicker ice layer to form, resulting in more lightning. The data indicate more lightning over central Africa than over equatorial South America, which suggests a more maritime regime over South America. This is supported by the NCEP fluxes showing strong moisture fluxes from the Atlantic Ocean into equatorial South America. Thus, CCN may be working in concert with the lower moisture environment, resulting in significantly less rainfall than was expected from satellite measurements. This further suggests that current satellite rainfall estimation techniques need to be adjusted for CCN and water vapor in the atmosphere.

REFERENCES

Andreae, M.O., A. Chapius, B. Cros, J. Fontan, G. Helas, C. Justice, Y.J. Kaufman, A. Minga, and D. Nganga, 1992: Ozone and Aitken Nuclei Over Equatorial Africa: Airborne Observations During DECAFE 88. *J. Geophys. Res.*, **97**(D6), 6,137-6,148.

Arkin, P.A., R. Joyce, and J.E. Janowiak, 1994: IR techniques: GOES Precipitation Index. *Remote Sens. Rev.*, **11**, 107-124.

Christian, H.J., Driscoll, K.T., Goodman, S.J., Blakeslee, R.J., Mach, D.A., and D.E. Buechler, 1996: The Optical Transient Detector (OTD). Proceedings of the 10th International Conference on Atmospheric Electricity; Osaka, Japan, pp 368-371.

Higgins, R.W., K.C. Mo, and S.D. Schubert, 1996: The Moisture Budget of the Central United States in Spring as Evaluated in the NCEP/NCAR and the NASA/DAO Reanalyses. *Mon. Wea. Rev.*, **124**(5), 939-963.

Huffman, G.J., R.F. Adler, P. Arkin, A. Chang, R. Ferraro, A. Gruber, J. Janowiak, A. McNab, B. Rudolf, and U. Schneider, 1997: The Global Precipitation Climatology Product (GPCP) Combined Precipitation Data Set. Bull. Am. Meteorol. Soc., 78, 5-20.

Kalnay, E., and Coauthors, 1996: The NCEP/NCAR 40-year reanalysis project. Bull. Am. Meteorol. Soc., 77, 437-471.

Kessler, E., 1967: On the Continuity of Water Substance. Technical Memorandum IERTM-NSSL 33, U.S. Department of Commerce Environmental Science Services Administration.

Mo, K.C., and R.W. Higgins, 1996: Large-scale atmospheric moisture transport as evaluated in the NCEP/NCAR and the NASA/DAO Reanalyses. J. Climate, 9(7), 1531-1545.

Randel, D.L., T.H. Vonder Haar, M.A. Ringerud, G.L. Stephens, T.J. Greenwald, and C. L. Combs, 1996: A New Global Water Vapor Dataset. Bull. Am. Meteorol. Soc., 77(6),.

Rosenfeld, D., and Y. Mintz, 1988: Evaporation of Rain Falling from Convective Clouds as Derived from Radar Measurements. J. Appl. Meteor., 27, 209-215.

P1.16B

EXTENDED-RANGE TROPICAL FORECASTS BASED ON THE SLOW EVOLUTION OF THE MADDEN-JULIAN OSCILLATION USING THE SATELLITE OUTGOING LONGWAVE RADIATION

Duane E. Waliser[1]
Institute for Terrestrial and Planetary Atmospheres
State University of New York, Stony Brook, NY, 11794-5000
Charles Jones
Institute for Computational Earth System Science
University of California, Santa Barbara, CA, 93106-3060
Nicholas E. Graham
International Research Institute, Scripps Institute of Oceanography
University of California, San Diego, CA, 92093

1. INTRODUCTION

This study presents results from experimental extended-range tropical rainfall forecasts based on a statistical model that takes advantage of the slow-evolution of the Madden-Julian Oscillation (MJO; Madden and Julian, 1971). This "oscillation" represents the most significant form of atmospheric variability in the tropics on intra-seasonal time scales, and is generally manifested as an eastward propagating, equatorially-trapped, wavenumber one, baroclinic oscillation in the tropical wind field (e.g., Hendon and Salby, 1994). The propagation speed is on the order of 6 m/s in the eastern hemisphere where it strongly interacts/modulates deep convective activity, and about 12 m/s or greater in the western hemisphere where it continues to propagate without much influence on the cloud field. Interactions between MJO-related anomalies in convection and the large-scale circulation are strongest in the eastern hemisphere, over the Indian and western Pacific Oceans, where the oscillation exhibits its greatest variability and typically reaches its maximum amplitude. Such interactions strongly influence the onset and activity of the Asian-Australian monsoon system (e.g., Yasunari, 1980) and have also been shown to influence extra-tropical regions as well (e.g., Weickman, 1983). Furthermore, coupling with the tropical ocean via westerly wind bursts associated with the passage of an MJO convection event can significantly modify the structure of the thermocline in the equatorial Pacific Ocean (Kessler et al., 1996).

2. MODEL SPECIFICS

The model uses Outgoing Longwave Radiation (OLR) anomalies as a proxy for rainfall anomalies. The model and its predictions are based on five-day (pentad) average, 30-70 day bandpassed, 5x5 degree, OLR data for the global tropics (30N-30S). Predictors for the model are made up of the two most recent bandpassed OLR pentad maps. Predictands for the model are future bandpassed OLR pentad maps, with lead times of 1..10 pentads (i.e., 5, 10, ..., 50 days). For each lead time, a Singular Value Decomposition (SVD) between the predictors and predictands at the given lead, is performed. The output from this procedure provides a set of "modes", one for each lead time, that provide a way of mapping an input predictor (i.e., past and present "rainfall") to the most likely output predictand (i.e., future "rainfall"). The forecast models, one for each lead time, are made up of a subset of these modes, those which are deemed to be 99% statistically significant (3 modes).

The model was originally formulated and tested on pentad OLR data between the period 1979 and 1996. The SVD procedure described above was performed on the first 11 years of data (1979-1989). In addition, the data/models were separated into northern summer (5/16-11/16) and winter (11/17-5/15) due to the differences in the nature of the intraseasonal variability between these two periods (Wang and Rui, 1990). The leading modes of the prediction models illustrate many of the well-known features of the MJO and its evolution. For example, the variability contained within the first few modes is focused over the Indian and western Pacific Oceans, and the first couple modes illustrate the general eastward progression of anomalous rainfall patterns over this same region.

Several variations of the above model were tested to determine the optimal configuration. For example, models based on predictors having only one pentad were not as skillful as the model described above with predictors having two pentads. Predictors made up of three pentads showed a very slight improvement at 5 to 10 day leads but a very slight degradation at longer leads. In addition, the predictor fields were also augmented with dynamic fields from the NCEP/NCAR reanalysis to determine if the addition of this type of information would improve the model's skill. Tests were done with predictor fields made up of OLR plus 200 mb zonal wind, OLR plus 850 mb zonal wind, and OLR plus 200 mb velocity potential. None of these combined predictor fields showed any noticeable improvement in the model skill over those containing OLR alone. In addition, the forecast model was originally developed for just the eastern hemisphere since it was expected to have the most skill there. Extending the model domain to the global tropics did not show any appreciable improvement/degradation in skill for the eastern hemisphere but since the "global" tropical model showed some skill at short lead times in and around Central/South America, it was left in for completeness sake. Finally, canonical correlation analysis was applied instead of SVD with nearly identical results.

3. MODEL VALIDATION AND SKILL

The prediction scheme described above was validated on the OLR data between the 1990 and 1996. In general, the

[1] Corresponding author: Duane E. Waliser, Marine Sciences Research Center, State University of New York, Stony Brook, NY, 11794-5000;
e-mail: waliser@terra.msrc.sunysb.edu..

model shows useful forecast skill over the Indian and western Pacific Oceans, and nearby land masses, out to about 20 days. Figure 1 shows an example 15-day lead forecast in the form of an equatorial time-longitude plot for winter 1994. Apart from the fact that the model is statistical and thus imperfect in nature, part of the differences between the forecasts and the bandpassed observations in these comparisons is due to the fact that only the leading 3 modes are used in the forecast model(s). These leading modes account for about 70% of the covariance between the predictor and predictand fields and about 27% of the variance of the predictand field. Thus, the forecasts have an additional "modal filtering" applied that the observations have not undergone. Figure 2 provides a measure of the model's skill at predicting the bandpassed features of the data for a number of cities in the tropics (left panels). The model's skill remains relatively high out until around 20-25 days at which point it drops off fairly rapidly.

A more conservative and practical measure of the model's skill is via comparisons to actual anomaly data. The right panels of Figure 2 show the skill scores for the same cities as in the left panels, except in this case the comparisons are made to raw anomaly data (annual cycle removed). In addition to the modal filtering/differences described above, the differences between the forecasts and the anomaly data also stems from the fact that the model only predicts variability between 30-70 days and thus is not providing an estimate of time-scales outside this band. It should be noted that the skill scores shown in these anomaly data comparisons are both overrated and underrated due to the following. They are underrated due to the fact that at lead times of 5-20 days, persistence is a reasonable model to use for the low-frequency variability (> 70 days, e.g., ENSO) which would improve their overall skill. The skill scores are overrated due to the difficulty of producing a bandpassed estimate of the most recent two pentads in an operational (or hindcast) framework.

4. OPERATIONAL FORECASTS

At present, our main objective is to use the results from the model as a benchmark for assessing the prediction skill of dynamical extended range forecasts (DERF; e.g., see Liebmann et al., 1997 in this same issue). However, our long-term interests involve employing the model in an operational mode. Some preliminary development and testing has been undertaken with the predictions being produced as follows. The most recent day's global OLR observation is retrieved from NOAA's anonymous ftp site. The tropical portion of this data is subsetted out, the resolution is reduced from 2.5x2.5 to 5x5 degrees, and the climatology from the period 1979-1996 is removed. This data is then appended onto the current record (excluding leap days) of 5x5 degree tropical OLR anomalies. Using the most recent 1825 days (5 years) of this record, the data are averaged into pentads. These data are then bandpassed (30-70) in frequency space using the frequency response of a 29-point Lanczos filter. From this data, the most recent two pentads are used as a predictor in the model(s) described above to predict the 30-70 day bandpassed OLR anomaly. The predictions are then presented in the form of the bandpassed, anomaly, and total values. The latter two forms exclude variability with periods less than 30 days and assume longer-term (> 70 days) anomalous variability remains the same as the current values for the forecast period.

The main hurdle in producing operational predictions from the above scheme is producing an accurate bandpassed estimate of the two most recent pentads (i.e., the predictors). These pentads essentially are end points of time series and conventional/typical bandpass methods can produce spurious end point behavior. In the approach discussed here, the data are padded on either end with zeros and then the filtering is applied. A prediction is performed, and then this data is used concatenated onto the end of the original anomaly record and then the bandpassing is performed again. This iterative procedure ends up improving the results slightly. Performing a number of tests (2 years worth or 146 pentads) on sample data, shows that the predictor patterns resulting from a record extending well beyond the end-point (in a hindcast sense) and those resulting from end-point conditions typically correlate in space at about 0.9 using the 29-point Lanczos filter applied here. A shorter filter would improve this but yet diminish the frequency response of the bandpass filter. Fortunately, it was found that the more energy that the predictor has in the principal model modes the more likely the correlation is above 0.9 and vice versa. Thus when there is a strong MJO component in the weather/climate system, the bandpassed predictor is less likely to contain spurious signals. Efforts are underway to make improvements with respect to this difficulty in order to produce a viable operational system.

Acknowledgments

This work has been supported by the National Science Foundation (DW and CJ), the National Oceanic and Atmospheric Administration (DW and NG), and the Office Of Naval Research (DW). In addition, the project has benefited from comments provided by Stefan Hastenrath (U. Wisc.), Anthony Barnston (NCEP/NOAA), and Robert Wilson (SUNY).

References

Hendon, H. H., and M. L. Salby, 1994: The life cycle of the Madden and Julian Oscillation. J. Atmos. Sci., 51, 2225-2237.

Kessler, W. S., M. J. McPhaden, and K. M. Weickmann, 1996: Forcing of intraseasonal Kelvin waves in the equatorial Pacific. J. Geophys. Res., 100, 10,613-10,631.

Kousky, V. E., and M. T. Kayano, 1993: Real-time monitoring of intraseasonal oscillations. Proceedings of the 189th Annual Climate Diagnostics Workshop, 1-5 Nov. 1993. Boulder, CO. 66-69.

Madden, R. A., and P. R. Julian, 1971: Detection of a 40-50 day oscillation in the zonal wind in the tropical Pacific. J. Atmos. Sci., 28, 702-708.

Wang B., and Rui H., 1990: Synoptic climatology of transient tropical intraseasonal convection anomalies. Meteor. Atmos. Phys., 44, 43-61.

Weickmann, K., M., 1983: Intraseasonal circulation and outgoing longwave radiation modes during Northern Hemisphere winter. Mon. Wea. Rev., 111, 1838-1858.

Yasunari, T., 1980: A quasi-stationary appearance of the 30-40 day period in the cloudiness fluctuations during the summer monsoon over India. J. Met. Soc. Japan., 59, 336-354.

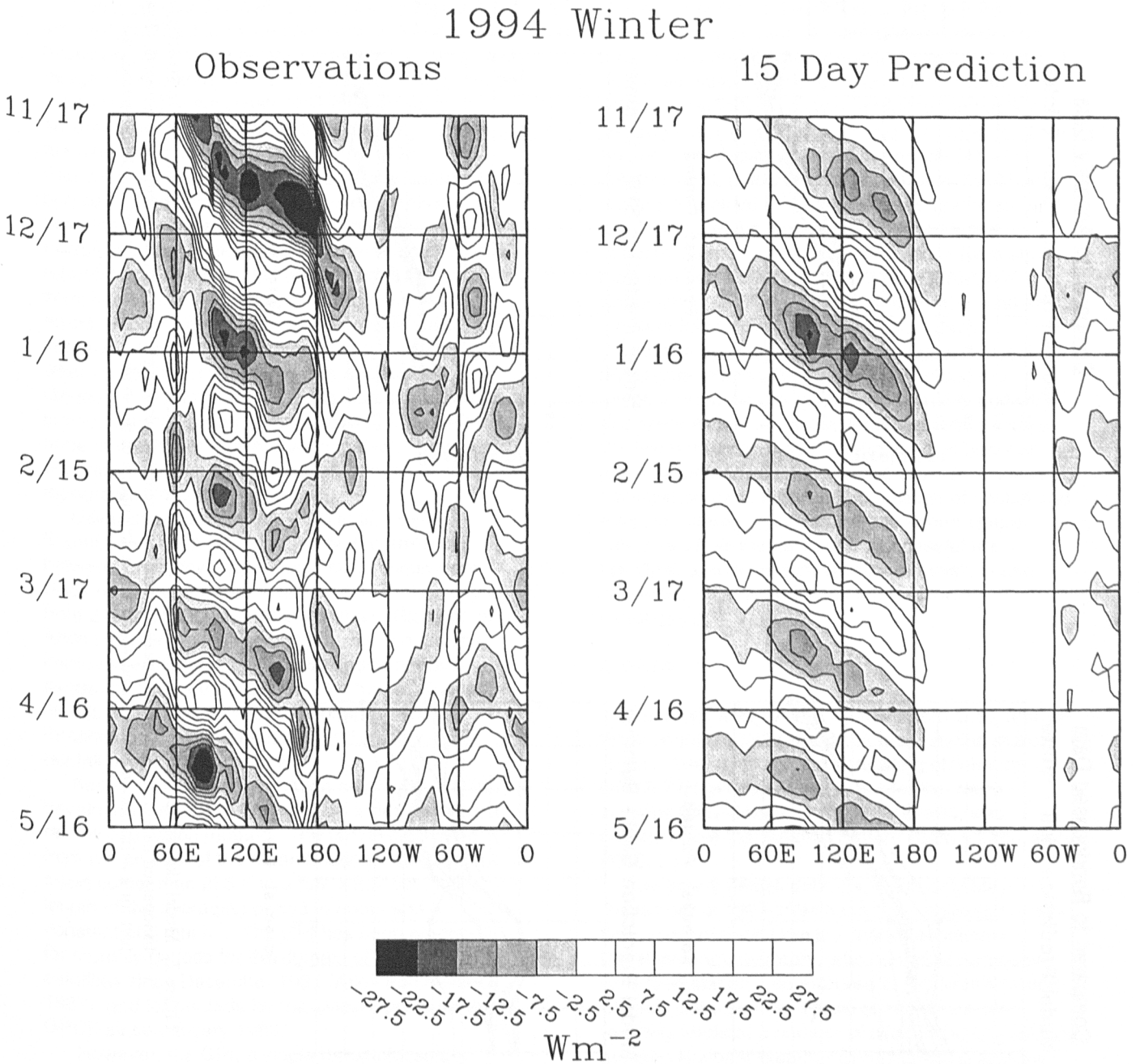

Figure 1. Example 15-day prediction in the form of an equatorial time-longitude plot for 1994-95 northern hemisphere "winter". Negative OLR values indicate positive rainfall anomalies. Note both panels show 30-70 day bandpassed data.

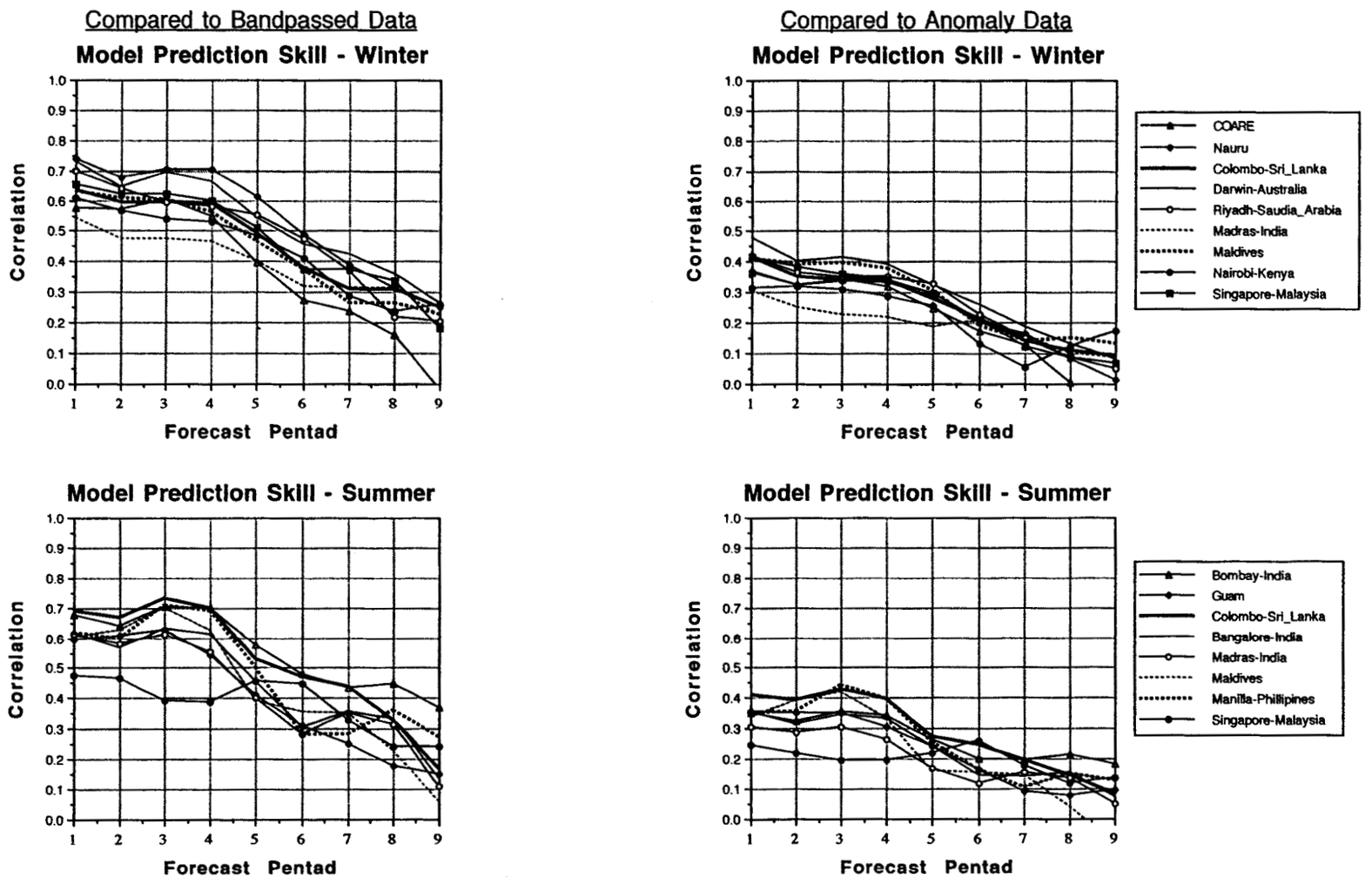

Figure 2. Model skill scores for northern hemisphere winter (top) and summer (bottom) based on comparisons to 30-70 day bandpassed data (left) and raw anomaly (annual cycle removed) data (right) at a number of cities in the tropics. See text for a definition of summer and winter and a description of the model development and validation periods used.

P1.17A ESTIMATION OF OROGRAPHIC PRECIPITATION OVER WESTERN NORTH AMERICA USING GEOSTATIONARY SATELLITE OBSERVATIONS

Robert J. Joyce, Phillip A. Arkin and Wayne Higgins
National Centers for Environmental Prediction

1. INTRODUCTION

Continental and global scale fields of precipitation are being derived from the combination of estimates based on satellite observations, model forecasts, and gauge observations. Large-scale precipitation can be estimated rather successfully from geostationary satellite infrared (IR) observations in many parts of the world, and estimates such as the GOES Precipitation Index (GPI) are widely used for many purposes, both individually and as elements of combined analyses. Estimates derived from passive microwave observations are in general more directly related to precipitation, but are substantially less complete in time and space, leading to sampling errors. Model forecasts, seem to provide useful information in portions of the mid and high latitudes where satellite estimates are less successful. Gauges, while accurate, and dense in some regions, provide poor sampling in many areas. Unfortunately, none of these methods are yet capable of providing accurate definition of precipitation in regions of strong topographic forcing.

Using data from the GARP Atlantic Tropical Experiment, Arkin (1979) found high correlations between areal coverage of cold cloud (equivalent black body temperature less than thresholds ranging from 225 to 255 K) and 6-hour rainfall. Richards and Arkin (1981) demonstrated that these correlations improved with increasing spatial and temporal averaging scales up to 2.5° and 24 hours. These results suggested a linear relationship between thresholded cold cloud amount and climatic-scale rainfall over tropical oceans.

Based on these results, Arkin and Meisner (1987) developed the GOES Precipitation Index (GPI) as a rainfall estimation method. The GPI is calculated from the product of the mean fractional coverage of cloud colder than 235 K in a 2.5° x 2.5° box, the length of the averaging period in hours and a constant of 3 mm h^{-1}. The GPI has been produced for monthly periods for the domain of the GOES satellites since December 1981 (Arkin and Meisner, 1987), and for pentads for the global tropics for the GPCP since January 1986.

However, the GPI, a single threshold, single rainrate technique, was derived from a tropical Atlantic data set (GATE), and cannot be expected to accurately estimate rainfall over varying orographic terrain and climates. It has been suggested that drier environments change the coefficient of the linear relationship between areal coverage of cold cloud and rainfall (Adler and Mack, 1984). Arkin and Miesner (1987) found the slope of the regression between warm season Climate Division rainfall and the GPI to be near 1.0 in several coastal regions and decreased inland. Arkin and Xie (1994) found different coefficients relating rainfall to the fractional coverage (2.2 mm-h for June and 4.4 mm-h for July-August) over Japan for different periods (AIP-1). Johnson et al. (1994) found the optimum threshold relating cold cloud to radar-estimated rainfall to be 31° C higher in the southeast U.S. than in the northern plains. Experiments over Africa have shown that improved estimates are possible through a combination of different IR thresholds with wind and moisture information (Herman et al., 1997).

In this study, we utilize several new data sets to investigate relationships between IR cloud top temperatures, lower tropospheric humidity and winds, and precipitation on various time and space scales. We begin by examining the relationships between precipitation and cloud top temperature for various temperature thresholds and on a range of spatial and temporal averaging scales. Areas where simple indices such as the GPI are unsuccessful are identified, and the potential utility of moisture and circulation data as additional information is investigated.

2. DATA

The study area covers southwestern U.S., and will focus on the summer monsoon precipitation in that region. The satellite data, consisting of 3-hourly GOES-7 IR gridded at 11x12 km for the warm seasons (May-September) of 1990-1994, was obtained from the National Severe Storms Laboratory (NSSL).

The hourly rainfall data, for which only May-September of 1993-1994 have been collected at this time, was obtained from the NWS/Techniques Development Laboratory, who compiled and quality controlled station data archived at the NOAA National Climatic Data Center. These observations are routinely made at a number of sites, including several hundred National Weather Service (NWS) stations and roughly 2000 cooperative stations .

The moisture and circulation data are obtained from the NCEP/NCAR Reanalysis.

3. TEMPERATURE THRESHOLD VALIDATION

The optimum threshold for relating cold cloud and tropical Atlantic rainfall (GATE) from past studies of Arkin (1979) and Richards and Arkin (1981) was 235 K, however that was over the tropical oceans. In an attempt to better understand the connection between cold cloud and rainfall over land, we begin with an investigation of the relationship between cloud thresholded at various temperatures and rainfall over the western U.S.

GOES-7 IR brightness temperatures were thresholded at 5K intervals ranging from 200K to 300K, and averaged daily into (lat, lon) = (1^0, 1^0) regions. Accordingly, Hourly Precipitation Data (HPD) were accumulated at each station for daily totals, and then averaged into identical regions. Serial correlation in each data set was determined by computing correlations at daily lags, from which the time between independent samples (Livezey, 1995) for correlation between the two data sets could be calculated. Correlations were computed for sampling at every other day, and then again to account for the alternate days, the correlations were then averaged.

The highest correlations (exceeding 0.6) are found for thresholds in the 225-245K range in a band extending from Texas to Missouri (Fig. 1). This range of thresholds agree well the with findings of Arkin et al. (1994). However it should be noted that the 245 - 255K range gives the highest correlations from Colorado and Arizona westward, although here the overall values are smaller. The higher thresholds work well for California, where the 275K is as consistent as any other. The colder thresholds (i.e. 215K) provide high values where and when coverage exists, but provide little information for Nevada and California. Analyzed rainfall (Fig. 1, bottom right corresponds well with the correlation results, with heavier rainfall matching higher correlation values of the colder thresholds (i.e. 215K).

Almost the entire country is covered by correlations significant at the 99% level for all thresholds, except those colder than 215K, or warmer than 285K (figure 2). Although not shown, correlation (and its significance) showed similar patterns at each threshold but with lower values for the daily 0.5° x 0.5° lat/lon resolution, and even smaller values for hourly 0.5° x 0.5° lat/lon comparisons. Increasing cold cloud and rainfall correlations with increasing spatial and temporal averaging scales agrees with the findings of Richards and Arkin (1981).

CONCLUSIONS AND FUTURE DIRECTIONS

The relationship between cold cloud and warm season HPD rainfall over the southwestern U.S. is strongest over the southern plains and Mississippi River valley (at least in the 1993-1994 warm seasons), and deteriorates westward towards more mountainous terrain and drier climates, but an area where some promise may exist for the use of warmer thresholds. The relationship between cold cloud thresholded between 215 - 285K and rainfall for 1.0° x 1.0° regions exceeds the 99% confidence level for more than half of the domain. Averaging up from hourly 0.5° x 0.5° to daily 1.0° x 1.0° resolution confirms past findings of increasing correlations.

This is the beginning stage of a study which will include the comparison of wind speed and direction, terrain slope and orientation, and lower tropospheric humidity with rainfall. The use of these parameters in conjunction with IR thresholded at various levels (dependent on geographic location) may improve estimation of precipitation derived by satellite IR.

REFERENCES

Adler, R. F., and R.A. Mack, 1984: thunderstorm cloud height-rainfall rate relations for use with satellite rainfall estimation techniques. *J. Climate Appl. Meteor.*, **23**, 280-296.

Arkin, P.A., 1979: The relationship between fractional coverage of high cloud and rainfall accumulations during GATE over the B-scale array. *Mon. Wea. Rev.*, **107**, 1382-1387.

_____, and B.N. Meisner, 1987: The relationship between large-scale convective rainfall and cold cloud over the western hemisphere during 1982-84. *Mon. Wea. Rev.*, **115**, 51-74.

_____, and P. Xie, 1994: The Global Precipitation Climatology Project: First Algorithm Intercomparison Project. *Bull. Amer. Meteor. Soc.*, **75**, 401-419.

_____, R. Joyce, and J. E. Janowiak, 1994: IR techniques: GOES Precipitation Index. *Remote Sensing Rev.*, **11**, 107-124.

Herman, A., V.B. Kumar, P.A. Arkin, and J.V. Kousky, 1997: Objectively determined 10-day African rainfall estimates created for famine early warning systems. *Int. J. Remote Sensing*, **10**, 2147-2159.

Johnson, L.R., P.L. Smith, T.H. Vonder Haar, and D. Reinke, 1994: The Relationship between Area-Time Integrals Determined from Satellite Infrared Data by Means of a Fixed-Threshold Approach and Convective Rainfall Volumes. *Mon. Wea Rev.*, **122**, 440-448.

Livezey, R. E., 1995: "Field Intercomparison". An Analysis of Climate Variability Applications of Statistical Techniques. Springer-Verlag, Berlin Heidelberg, Germany, H. Von Stroch and A. Navara (eds.)

Richards, F., and P. A. Arkin, 1981: On the relationship between satellite-observed cloud cover and precipitation. *Mon. Wea. Rev.*, **109**, 1081-1093.

Correlation of Daily Fractional Cold Cloud and Station Rainfall for May – September 1993–1994

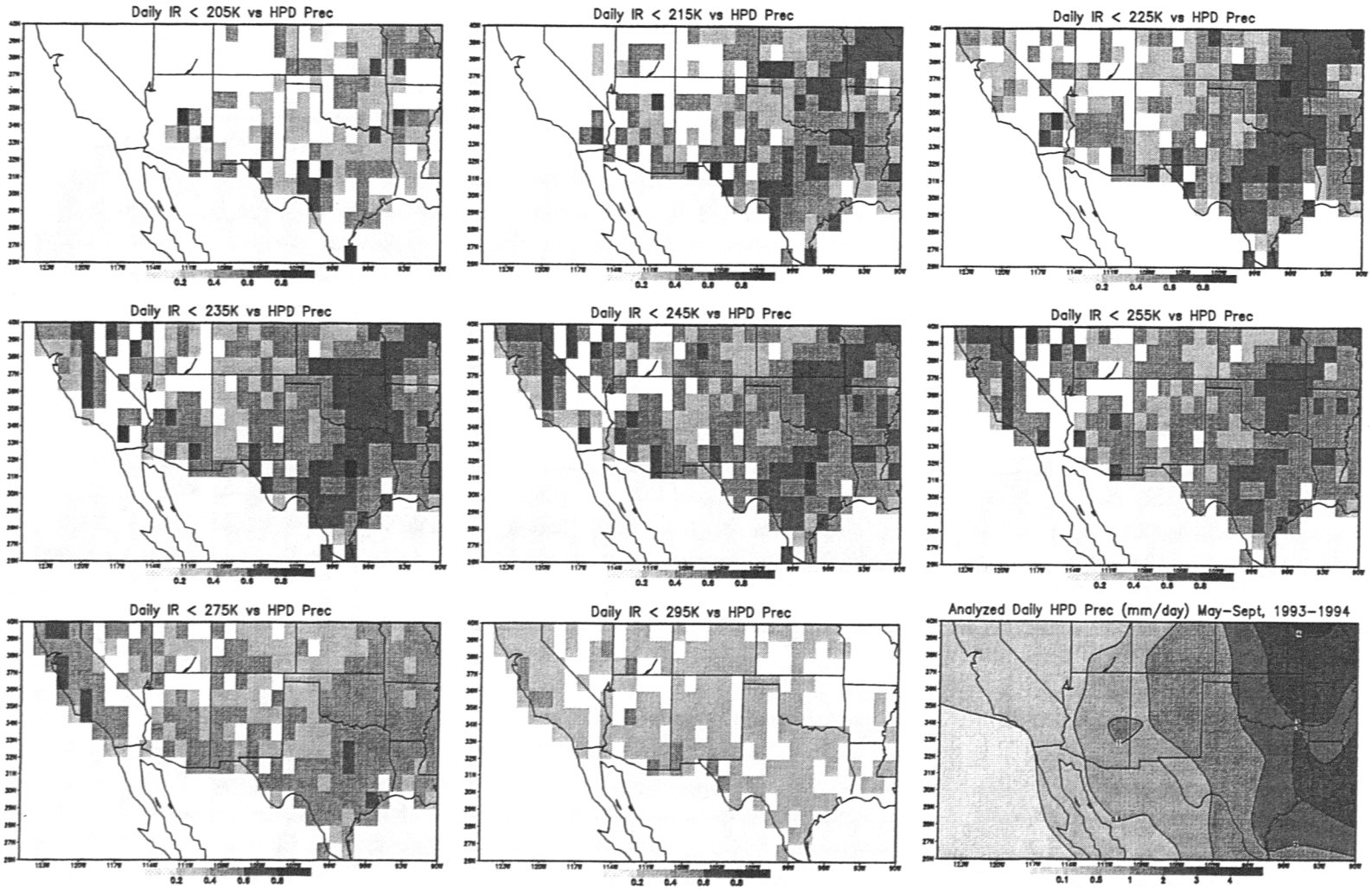

Figure 1. Correlation of 1x1 degree daily averaged thresholded GOES-7 IR and HPD station rainfall.

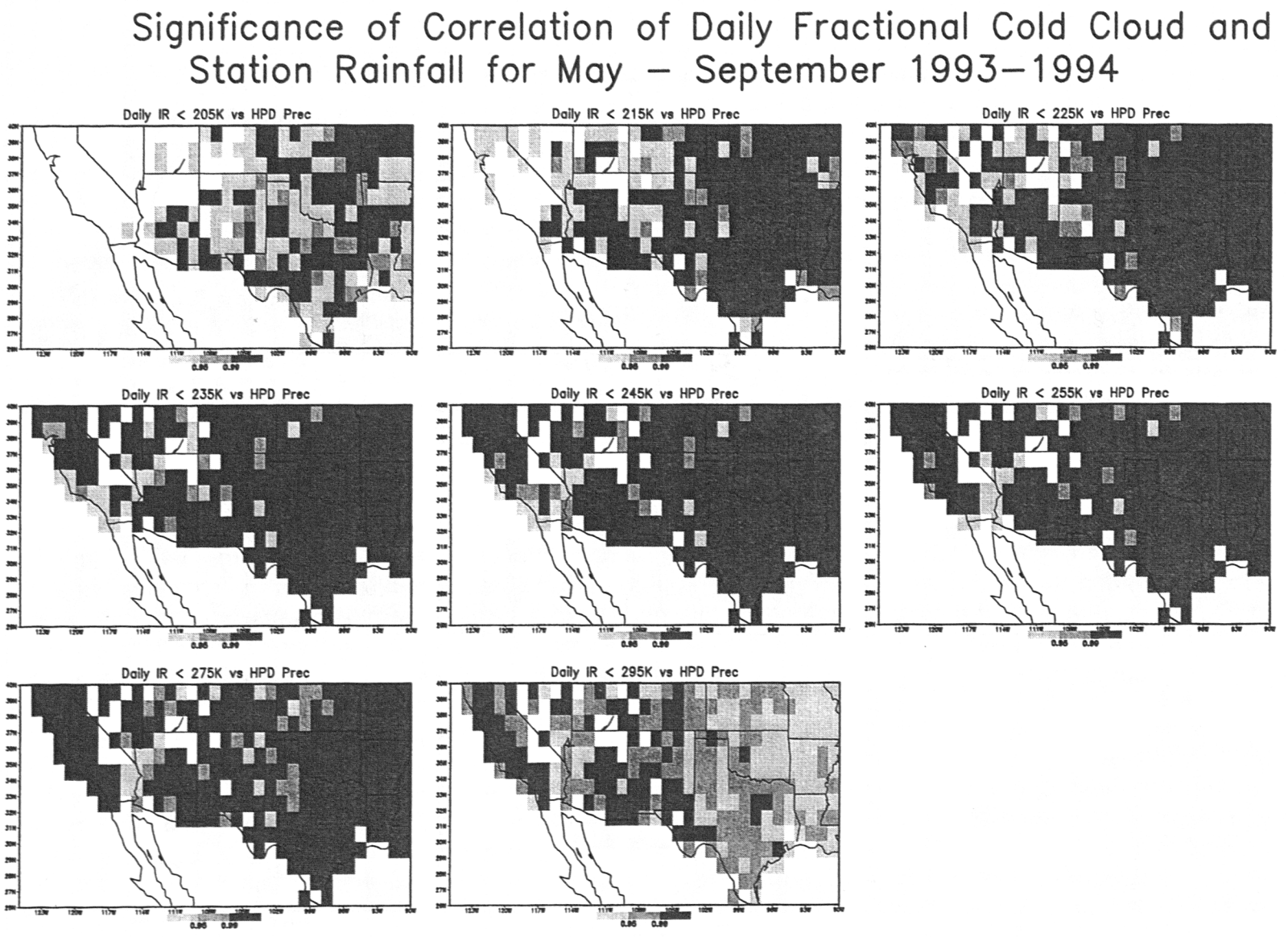

Figure 2. Significance of Correlation of 1x1 degree daily averaged thresholded GOES-7 IR and HPD station rainfall.

P1.18B

ANNUAL AND INTERANNUAL VARIABILITY IN GLOBAL PRECIPITATION FROM 1979 - 1996

Phillip A. Arkin and Pingping Xie*

National Centers for Environmental Prediction
W/NMC, NOAA/NWS Washington DC, 20233

1. INTRODUCTION

Despite the increasing requirements for high quality precipitation data sets, quantitative documentation of global precipitation remains one of the challenging tasks, because of the large spatial and temporal variability of precipitation and because of the lack of a comprehensive observing system. The principal existing sources of climatic-scale precipitation data can be divided into 7 categories, including gauge observations, estimates inferred from satellite observations of IR, OLR, MSU, SSM/I-scattering and SSM/I-emission, and precipitation distributions produced by various numerical models. Xie and Arkin (1995) examined several data sets and found that all of them present similar patterns in large-scale distributions, but with differences in smaller-scale features and in amplitudes, and that at least three major deficiencies exist in these data sets; 1) incomplete global coverage, 2) significant random error, and 3) non-negligible bias. Based on these results, Xie and Arkin (1996) developed an algorithm to construct a gridded field of global monthly precipitation by merging several kinds of individual data sources so as to ensure complete coverage and reasonable quality. Applying this algorithm, we have succeeded in producing global monthly precipitation analysis on 2.5° lat/lon grid for an 18-year period from 1979 to 1996. In this paper, we will report the construction of the data set and describe some of its applications in the analysis of the annual and inter-annual variability in large-scale precipitation. A more complete description of the algorithm, the data set and the analysis results can be found in Xie and Arkin (1997).

2. METHODOLOGY AND DATA SOURCES

One product is selected from each of the 7 categories and used to construct the merged analysis of global monthly precipitation. In this study, a monthly analysis based on gauge observations of the Climate Anomaly Monitoring System (CAMS) of NOAA/CPC and the Global Historical Climatology Network (GHCN) of DOE/CDIAC (Xie et al. 1996), 5 satellite-based estimates - the IR-based GPI (Arkin and Meisner 1987), the OLR-based OPI (Xie and Arkin 1998), the MSU-based Spencer (Spencer 1993), the SSM/I-scattering-based Grody (Grody 1991), and the SSM/I-emission-based Chang (Wilheit et al. 1991), as well as the precipitation data from the NCEP/NCAR reanalysis (Kalney et al. 1996) are selected to represent each category.

A 2-step merging algorithm (Xie and Arkin, 1996) is then applied to reduce the random error and to remove the bias, respectively. First, the 5 kinds of satellite estimates and the reanalysis are combined linearly to minimize the random error. A Maximum Likelihood Estimation method is applied, in which the linear combination coefficients are inversely proportional to the squares of the individual random errors. Over land areas, the random error for each input source is defined for each grid area by comparison with the concurrent gauge-based analysis over surrounding areas. Over oceanic areas, the random error is defined by comparison with the atoll gauge observations of Morrissey and Greene (1991) over the tropics and by extending the tropical results subjectively to the extra-tropics.

Since the output of the first step contains bias passed through from the individual sources, the second step is required to remove the remaining bias. For that purpose, the gauge observations are combined with the first-step-output. Over land areas, the first-step-output and the gauge analysis are blended using the method of Reynolds (1988), in which the first-step-output is used to define the relative distribution, or the 'shape' of the final precipitation field, while the gauge data is used to determine its amplitude. Over oceanic areas, the bias in the first-step-output is estimated by comparison with the atoll gauge observations over the tropics and by

* *Corresponding author address*: Dr. Pingping Xie, National Centers for Environmental Prediction, #800, W/NMC, NOAA/NWS, Washington DC 20233. E-mail: xping@sgi17.wwb.noaa.gov.

applying subjective assumptions concerning the bias structure over the extra-tropics.

3. CLIMATOLOGY

The algorithm is applied to create the global monthly precipitation analysis on a 2.5° lat/lon grid for an 18-year period from 1979 to 1996. For convenience, we call this data set as the CPC Merged Analysis of Precipitation (CMAP). Fig.1 shows the distributions of mean precipitation as obtained from our 18-year CMAP and from the long-term means of Jaeger (1976) and Legates and Willmott (1990). Generally speaking, all of them present similar large-scale distribution patterns, with rain bands associated with the ITCZ, SPCZ and storm tracks. A split in the ITCZ is observed over the central Pacific in the Legates and Willmott climatology and in the CMAP as well although not as distinct, while the Jaeger climatology exhibits wider and smoother distributions for the rain bands. Major differences are observed over the eastern Pacific where the Legates and Willmott climatology presents heavy rainfall while there is no corresponding features in either our merged analysis or in the Jaeger climatology.

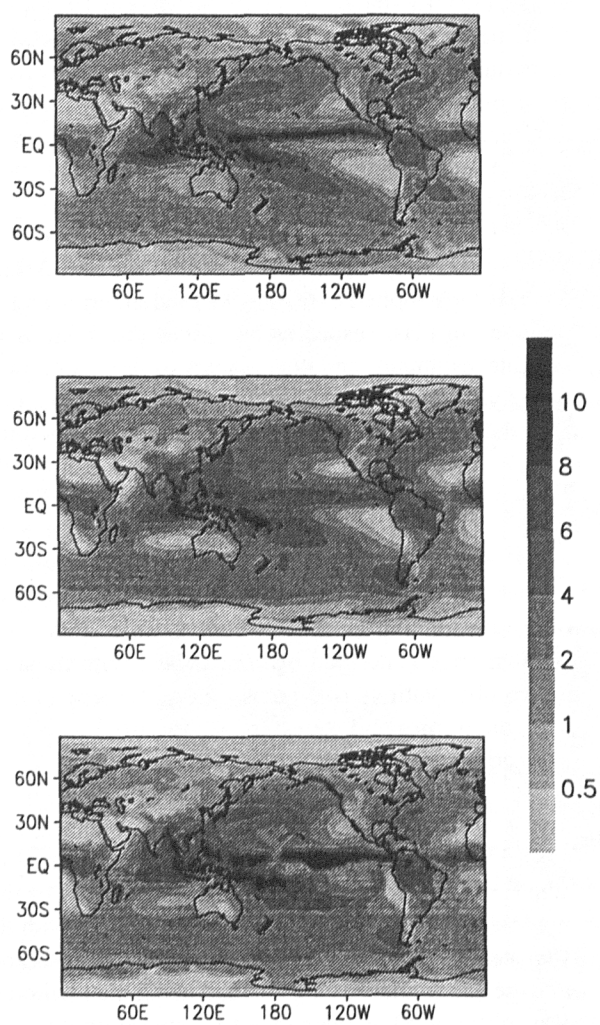

Fig.1 Distributions of the annual mean precipitation (mm/day) as obtained from the 18-year CMAP (top), Jaeger (1976) (middle), and Legates and Willmott (1990) (bottom).

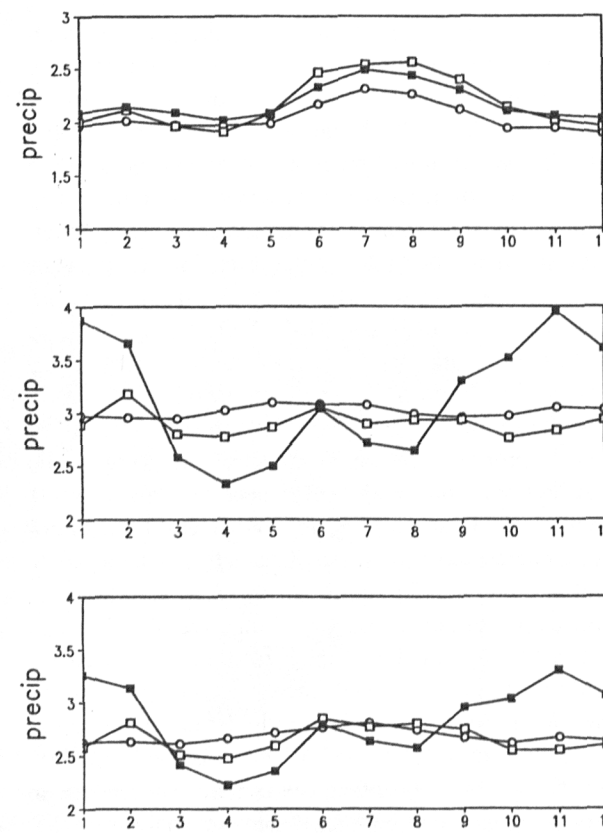

Fig.2 Annual cycles of mean precipitation (mm/day) over land (top), ocean (middle) and the entire globe (bottom) as obtained from the 18-year CMAP (open circle), Jaeger (1976) (open square) and Legates and Willmott (1990) (closed square).

Fig.2 shows the annual cycles of the precipitation averaged over land, ocean and the entire globe as obtained from the 18-year CMAP, Jaeger (1976) and Legates and Willmott (1990). All of the three data sets present similar annual cycles over global land areas, with maxima located at July-August, although the amplitude for the merged analysis is a little smaller. Over the global oceanic areas, the CMAP shows modest annual cycle with similar phase and

close amplitude to that of Jaeger (1976), while Legates and Willmott (1990) presents quite different situation in both the phase and amplitude, mostly because of the significant differences observed over the eastern Pacific. Over the entire global areas, the 18-year CMAP has flat annual cycle, ranging from 2.62 mm/day in March to 2.81 mm/day in June with annual mean of 2.69 mm/day.

4. INTERANNUAL VARIABILITY

The 18-year CMAP is also applied to examine the inter-annual variability associated with the ENSO cycle. Shown in fig. 3 are the time series of the SST anomaly over the NINO3 area (5°S-5°N; 150°W-90°W) and the Hovermöller diagram for the precipitation averaged over the Pacific sector (140°E-60°W). A significant annual cycle is observed over there and it is clearly modified by the SST anomaly. The magnitude of the precipitation becomes larger and the distribution extends farther into south when the SST presents positive anomaly, while the precipitation becomes weaker in general when the SST is colder than normal.

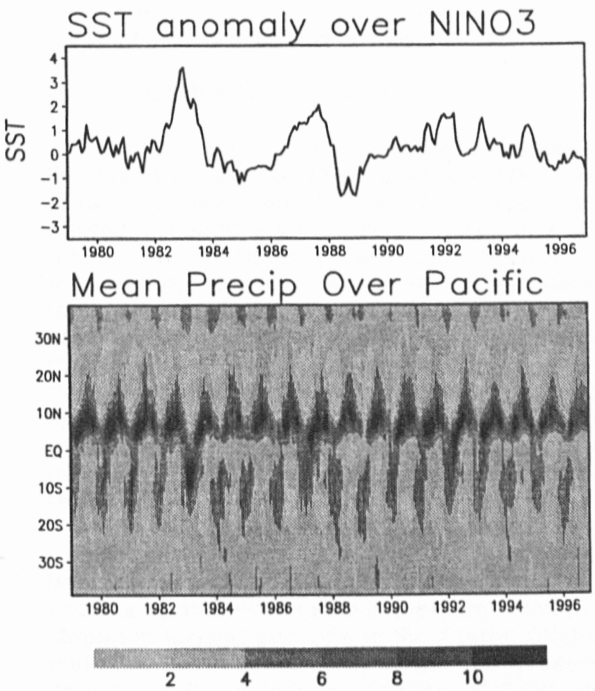

Fig.3 Time series of the SST anomaly over the NINO3 area (top) and the Hovermöller diagram for the precipitation (mm/day) averaged over the Pacific section from 140°E - 60°W (bottom).

Since the Hovermöller diagram is not able to reveal the east-west variation in precipitation, spatial distributions are composited for warm and cold ENSO episodes, and their differences are investigated. Fig.4 shows the distributions of the differences observed during the warm and cold events for the DJF and JJA periods. During the DJF period, the warm episodes are characterized by more precipitation over the central Pacific, the central portion of the South America and over much of the southern North America, and by less precipitation over the western Pacific and over the northern portion of the South America. During the JJA period, the warm episodes bring more precipitation in the Pacific ITCZ, and less precipitation over southeast Asia Monsoon area and over the northwestern Pacific.

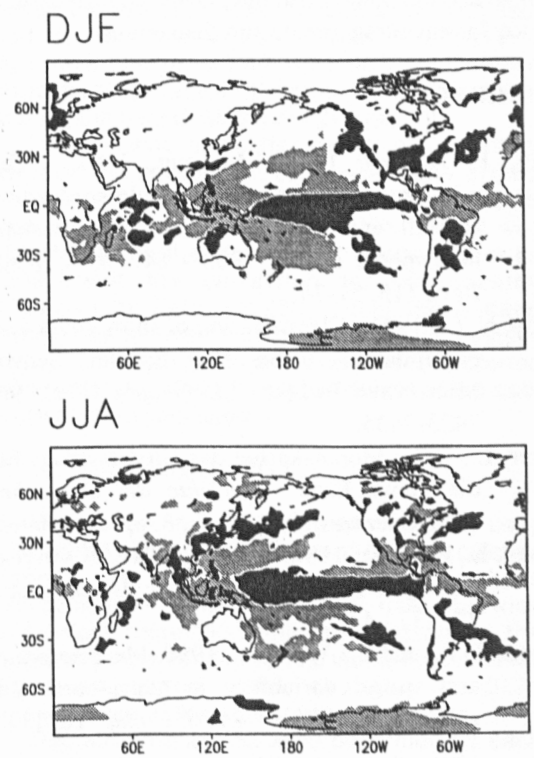

Fig.4 Differences between warm and cold ENSO episodes during the 18-year period from 1979 to 1996 for the DJF (top) and JJA (bottom) precipitation. Areas with wetter/drier warm ENSO episodes, with differences larger than 0.5 mm/day, are plotted in heavy/light hatching.

5. SUMMARY

Global monthly precipitation analysis has been constructed on 2.5° lat/lon grid for an 18-year period from 1979 to 1996 by merging 7 kinds of individual data sources with different characteristics, including the gauge observations, estimates inferred from satellite observations of IR, OLR, MSU and SSM/I, and the NCEP/NCAR reanalysis. The merged analysis is

applied to investigate the annual and inter-annual variability in large-scale precipitation. The mean distribution and the annual cycle of the 18-year merged analysis exhibit reasonable agreements with existing long-term means but with major differences over the eastern Pacific. The inter-annual variability associated with the ENSO is similar to previous findings but with substantial details over ocean.

ACKNOWLEDGMENTS

The authors would like to thank J. Janowiak of the Climate Analysis Center and A. Grube of the National Environmental Satellite, Data and Information Service for encouragements and discussions.

REFERENCES

Arkin, P. A., and B. N. Meisner, 1987: The relationship between large-scale convective rainfall and cold cloud over the eastern hemisphere during 1982 - 84. *Mon. Wea. Rev.*, **115**, 51-74.

Grody, N. C., 1991: Classification of snow cover and precipitation using the Special Sensor Microwave Imager. *J. Geophy. Res.*, **96**, 7423-7435.

Jaeger, L., 1976: Monatskarten des Niederschlags fur die ganze Erde. *Berichte des Deutscher Wetterdienstes*, Offenbach, 33pp, and plates.

Kalney, E., M., at al., 1996: The NCEP/NCAR 40-year reanalysis Project. *Bull. Amer. Meteor. Soc.*, 77, 437 - 472.

Legates, D.R., and C.J.Willmott, 1990: Mean seasonal and spatial variability in gauge-corrected, global precipitation. *Int. J. Clima.*, **10**, 111 - 127.

Morrissey, M.L., and J.S. Greene, 1991: The Pacific atoll raingage data set. *Tech. Rep. Univ. Hawaii*, Manoa, Honolulu, Hawaii.

Reynolds, R.W., 1988: A real-time global sea surface temperature analysis. *J. Climate*, **1**, 75 - 86.

Spencer,R.W., 1993: Global Oceanic precipitation from the MSU during 1979 - 91 and comparisons to other climatologies. *J. Climate*, **6**, 1301 - 1326.

Wilheit, T.J., A.T.C.Chang, and L.S.Chiu, 1991: Retrieval of the monthly rainfall induces from microwave radiometric measurements using probability distribution functions. *J. Atmos. Ocean Tech.*, **8**, 118 - 136.

Xie, P., and P.A.Arkin, 1995: An intercomparison of gauge observations and satellite estimates of monthly precipitation. *J. Appl. Meteor.*, **24**, 1143 - 1160.

--------, and ----------, 1996: Analyses of global monthly precipitation using gauge observations, satellite estimates and model predictions. *J. Climate*, **9**, 840 - 858.

--------, and ----------, 1998: Global monthly precipitation estimates from satellite-observed Outgoing Longwave Radiation. *J. Climate*, 11, 137-164.

--------, B. Rudolf, U. Schneider, and P. A. Arkin, 1996: Gauge-based monthly analysis of global land precipitation from 1971 to 1994. *J. Geophy. Res.*, **101D14**, 19023 - 19034.

--------, and P.A. Arkin, 1997: Global precipitation: A 17-year monthly analysis based on gauge observations, satellite estimates, and numerical model outputs. Bull. Amer. Meteor. Soc., 78, 2539-2558.

P1.19A

RECONSTRUCTION OF 120 YEAR RAINFALL AND WIND SPEED FIELDS FOR THE EASTERN NORTH ATLANTIC

Malcolm Taberner[1] and Dominic R. Kniveton[2]
[1] Centre for Remote Sensing, Department of Geography, University of Bristol, Bristol, UK
[2] Department of Geography, University of Leicester, Leicester, UK

1. INTRODUCTION*

Understanding how the climate varies on monthly to decadal time scales is central to accurately predicting climate change. The North Atlantic Oscillation (NAO) is considered a major source of regional climate variability (Rogers 1997). Associated with changes in surface westerlies across the north Atlantic, NAO has been linked to variations in winter temperatures and precipitation in Europe and Greenland, and to storm track and wave height variability in the north Atlantic (Hurrell 1995, 1996, Barlow et al. 1993, Rogers 1997, Kushnir et al. 1997). In this study we use satellite data, from the Special Sensor Microwave/Imager (SSM/I) and sea level atmospheric pressure data from selected locations to examine how changes in the atmospheric circulation affects the spatial variability of rainfall and wind speed in the eastern north Atlantic. Using regression based relationships derived from this investigation we then attempt to reconstruct historical 120-year parameter fields of rainfall and wind speed.

2. CLIMATE SETTING

Past studies have suggested that changes in the mean circulation, associated with NAO, can produce pronounced shifts in storm tracks and related synoptic eddy activity. These changes affect the transport and convergence of atmospheric moisture, which in turn influences regional precipitation (Hurrell 1995). However, a study by Rogers (1997) has argued that although this might be true for the central Atlantic, storm track variability (and thus precipitation and wind speed variability) in the eastern north Atlantic is associated with low frequency changes in sea level pressure (SLP) in the extreme north east of the region.

The North Atlantic Oscillation has been traditionally defined as a seesaw in pressure between Iceland and the Azores. A simple index of this has been the difference in pressure between a station in Iceland and one in the Azores (Walker and Bliss 1932). In this study we use SLP pressure data from Stykkisholmur (65.0°N, 22.8°W) and Gilbraltar (36.11°N, 5.22°W) to represent variations in NAO, and from Haparanda (65.8°N, 24.2°E) to account for the low frequency changes in sea level pressure (SLP) in the extreme north east. Data from these stations is available dating back to the late nineteenth century.

*Corresponding author address:
Malcolm Taberner, Centre for Remote Sensing, University of Bristol, Bristol, England.
e-mail: Malcolm.Taberner@bristol.ac.uk

3. REMOTE SENSING DATA

The spatial variability of rainfall and wind speed in the Eastern North Atlantic Ocean and the Iceland and North Seas, and their relationships with variation in atmospheric pressure, is described through the use of remotely sensed data. The data used in this study come from the passive microwave sensor, SSM/I, on board the Defense Meteorological Satellite Program(DMSP) satellites covering the period 1988 through 1996.

Rainfall was calculated using an algorithm based on the polarisation difference in the 37GHz channels and was calibrated against a FRONTIERS radar dataset and gauge data. Wind speed was estimated using the algorithm of Goodberlet et al. (1989) with the correction for non-linearity developed by Petty (1993). From these data, monthly rainfall rates and totals and mean monthly wind speeds were produced. The reader is referred to Barrett et al. (1997) for further details of the data set and techniques used.

4. METHODOLOGY

Regression analysis has been previously used by Hurrell (1996) to quantify the effect of circulation changes on temperature for the northern hemisphere. In this study we use stepwise multivariate regression analysis to examine the relationship between the spatial variability of rainfall and wind speed, with changes in SLP, representative of the atmospheric circulation.

Regression analyses were performed for each latitude/longitude grid cell of rain and wind speed data using monthly SLP anomalies of the three stations chosen above, as predictors, for the months of October through to March, for the years 1988 to 1996. SLP anomalies for both the month and the prior month to that of the satellite derived data were used in the analysis. Spatial patterns of 't' values for the wind speed fields for the three co-temporal predictors, and of R^2 values of the wind speed analyses are shown in Figure 1(a-d).

Using the regressional relationships derived above, and historical SLP data, monthly wind speed and rainfall anomalies for the months October to March were calculated for the previous 120 years. In Figure 2 the accumulated monthly anomalies are shown on the top surface for the whole study area, and the monthly anomalies over the last 120 years for the northern and western edges, depicted along the sides. The accumulated and monthly anomalies are shown for the months January to March only. Time series of monthly anomalies for selected

locations in the study area for the last 120 years, derived from this methodology, are shown in Figure 3. The top time series shows an adjusted NAO times series derived using the same normalising period as the technique described above, i.e. 1988-1996. The rationale behind this is to make the different series comparable. Additionally unlike the NAO data of Jones et al. (1997), the pressure data used to derive the adjusted NAO data have not been normalised using standard deviations.

5. RESULTS AND DISCUSSION

The regression analyses show that taken together the SLP predictors explain up to 63% of the variation in the wind speed fields and 53% of the rainfall. R^2 values are highest for the wind speed fields due to accuracy of the wind speed algorithm compared to that of the rainfall algorithm and the lower spatial and temporal variability of wind speed compared to rainfall. The highest explained variance is found off Ireland and Norway in both datasets.

The presentation of 't' values allows an assessment of the extent to which a particular atmospheric location is related to the variance of wind speed and rainfall in different locations. For instance, Figures 1 shows that variations in wind speed in the north east of the study region are related to changes in pressure over Gibraltar, inversely with pressure changes over Haparanda and not with pressure variations over Stykkisholmur. By contrast variations in wind speed off the coast of north west Ireland are nearly exclusively related to pressure variations over Ireland and not the other locations. Similar patterns were also found in the 't' values of rainfall except it was noted that the influence of Haparanda extended further west, of Stykkisholmur further north and south, and of Gibraltar into the North Sea.

The accumulated anomalies depicted in Figures 2a and b show similar spatial patterns between wind speed and rainfall. From these analyses it appears that in the south of the study area, the months from January to March over the last 120 years have been considerably wetter and displaying higher wind speeds than the period from 1988 to 1996. By contrast over the extreme north east it has been drier and with lower wind speeds compared to the recent period. Interestingly the highest variability during the last 120 years, in both rainfall and wind speed anomalies is shown in the western and northern parts of the study area. It can also be seen that in the west of the study region that the patterns of accumulated rainfall and wind speed anomalies differ the most. The selected times series depicted in Figure 3 show that whilst similar trends in rainfall, wind speed and the NAO are apparent in some locations there are noticeable differences between records in others e.g 1960 to 1985 in the rainfall records.

6. CONCLUSIONS

This study has attempted to quantify the spatial variability in rainfall and wind speed over the eastern north Atlantic in the last 120 years, due to changes in the atmospheric circulation. The results show that changes in climate parameters in this region are not solely explained by variations in the NAO index. Additionally it is suggested that the degree to which the NAO signal as defined by the difference in pressure between Stykkisholmur and Gibraltar can be seen identified in past record of rainfall and wind speed varies spatially.

7. ACKNOWLEDGEMENTS

The authors would like to thank Dr. P. Jones of the Climate Research Unit, University of East Anglia for providing pressure data for this study.

8. REFERENCES

Barlow,L.K., J.W.C.White, R.G.Barry, J.C.Rogers, and P.M.Grootes, 1993: The N. Atlantic Oscillation Signature in Deutrium and Deutrium Excess Signals in the Greenland Ice Sheet Project 2 Ice Core, 1840-1970. Geo. Res. Let., **20**, 2901-2904.

Barrett, E.C., Beaumont, M.J., Brown, P.A., Taberner, M.J., Tait, A.B., Todd, M.C., 1997.: A Satellite-Based Atlas of Rainfall and Wind Speed over the Eastern North Atlantic and North Sea. Contract No. EPG 1/9/33, Department of Environment, Transport and the Regions, London.

Goodberlet, M.A., Swift, C.T., Wilkerson, J.C., 1989.: Remnote Sensing of Ocean Surface Winds with the Special Sensor Microwave/Imager. Journal of Geophysical Res., **94**,14547-14555.

Hurrell, J.W., 1995: Decadal Trends in the North Atlantic Oscillation and Its relationships to Regional Temperature and Precipitation. Science, **269**, 676-679.

Hurrell, J.W., 1996: Influence of Variations in Extratropical Wintertime Teleconnections on Northern Hemisphere Temperatures. Geophys. Res. Let., **23**, 665-668.

Jones, P.D., T. Jonsson, and D. Wheeler , 1997: Extension to the North Atlantic Oscillation using Early Instrumental Pressure Observations from Gibraltar and South West Iceland. Int. J. of Clim. **17**,1433-1450.

Kushnir, Y., V.J. Cardone, J.G. Greenwood, and M.A. Cane, 1997: The Recent Increases in North Atlantic Wave Heights. J. of Clim., **10**, 2107-2113.

Petty, 1993: A Comparison of SSM/I Algorithms for the Estimation of Surface Wind. Proc. of the Shared Processing Network DMSP SSM/I Algorithm Symposium, 8-10th June, Monterey, CA.

Rogers, J.C., 1997: North Atlantic Track Variability and Its Association to the North Atlantic Oscillation and Climate Variability of Northern Europe. Journal of Climate, **10**, 1635-1647.

Walker, G.T. and E.W. Bliss, 1932: World Weather V. Mem. R. Meteorol. Soc., **4**,53-84

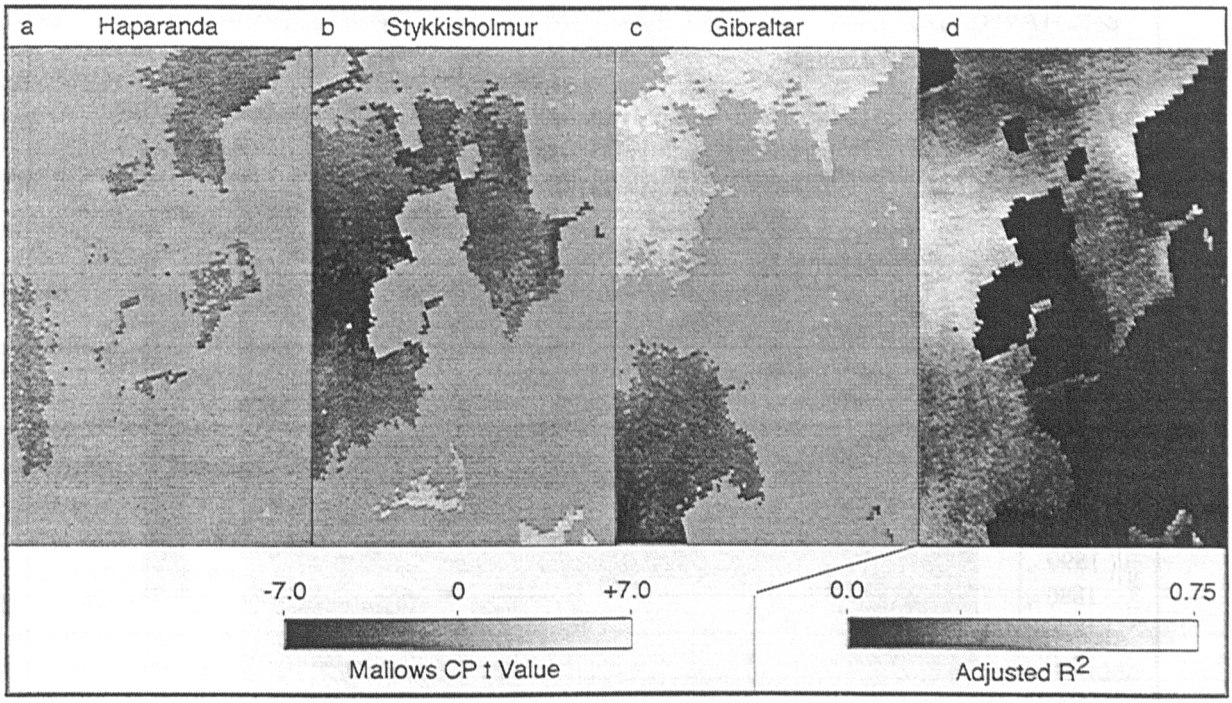

Figure 1. 't' value images for the coefficients from the regression of satellite derived wind speed with station pressure data anomalies and the overall, adjusted R^2 , image.

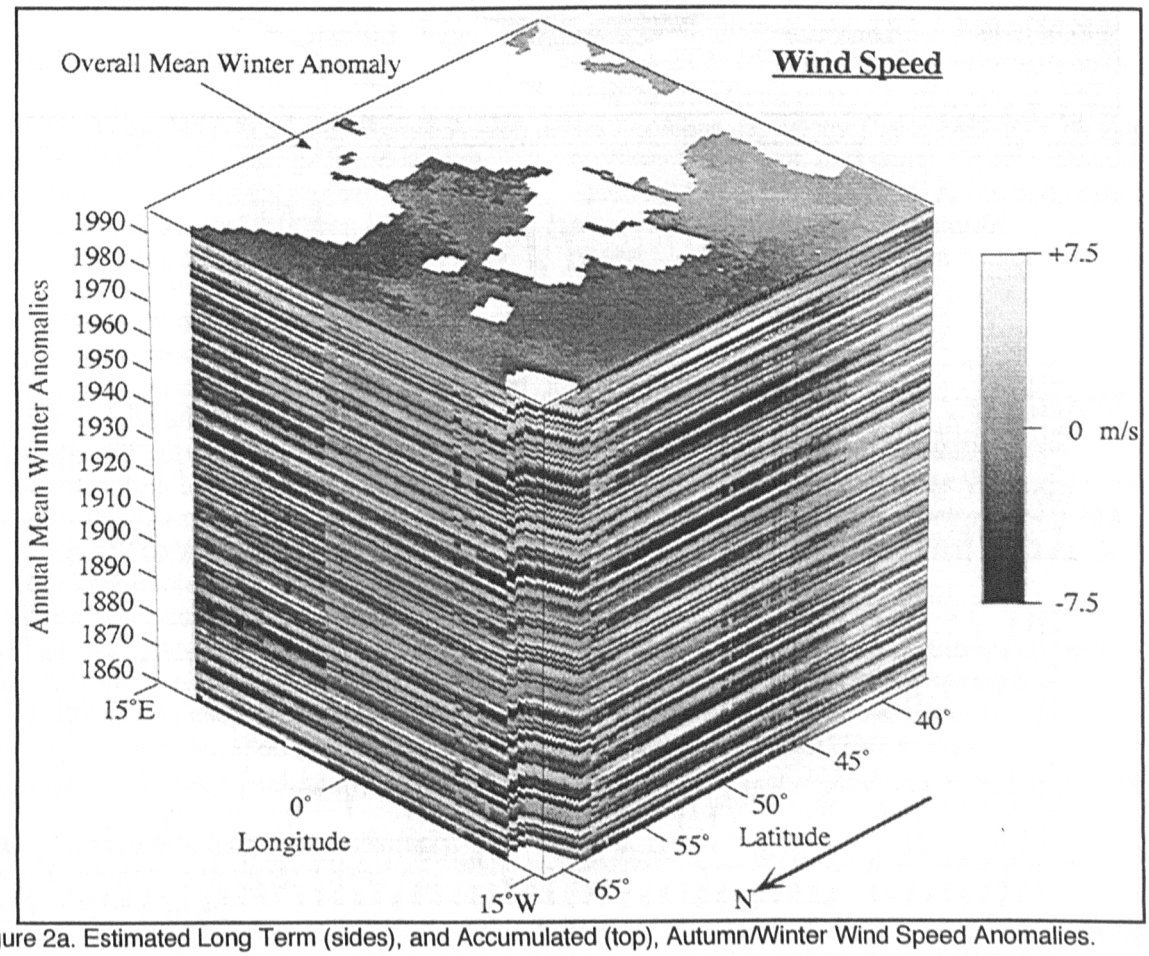

Figure 2a. Estimated Long Term (sides), and Accumulated (top), Autumn/Winter Wind Speed Anomalies.

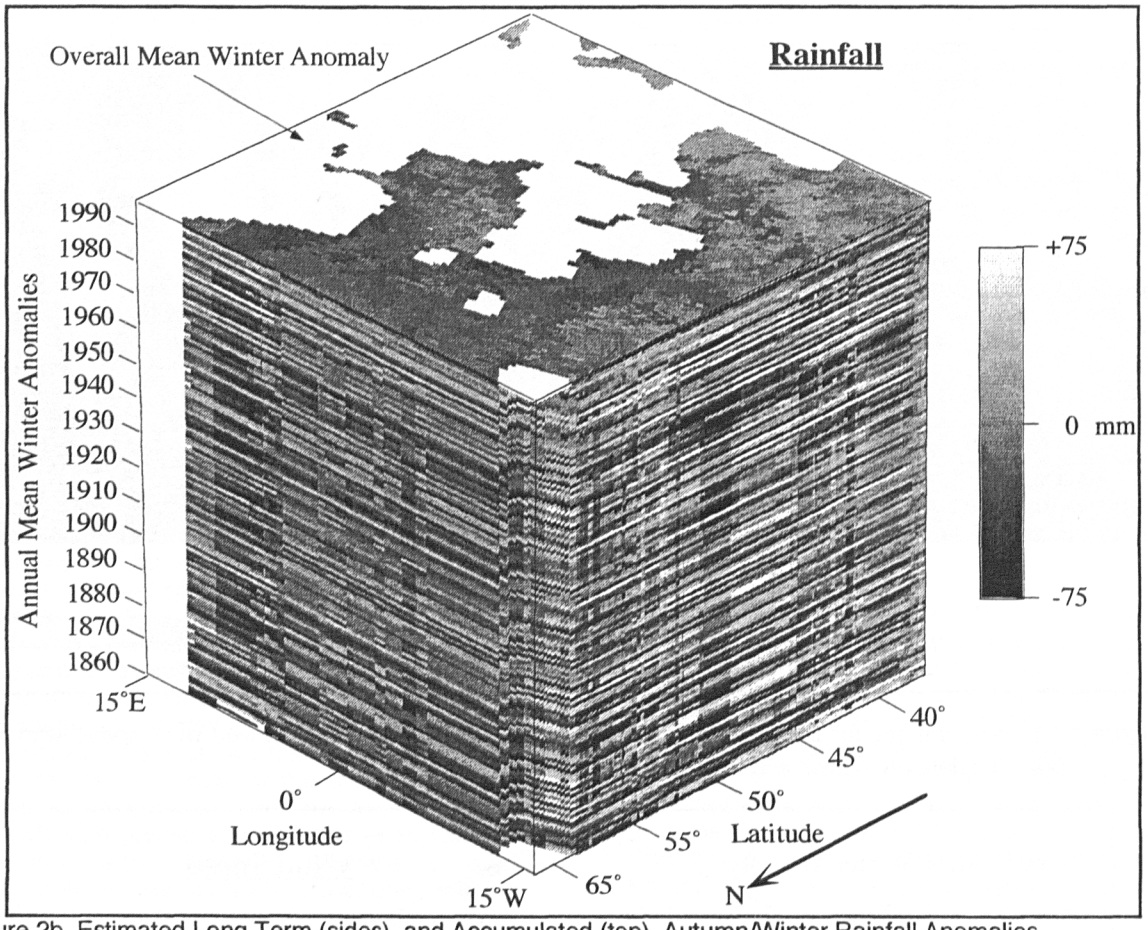

Figure 2b. Estimated Long Term (sides), and Accumulated (top), Autumn/Winter Rainfall Anomalies.

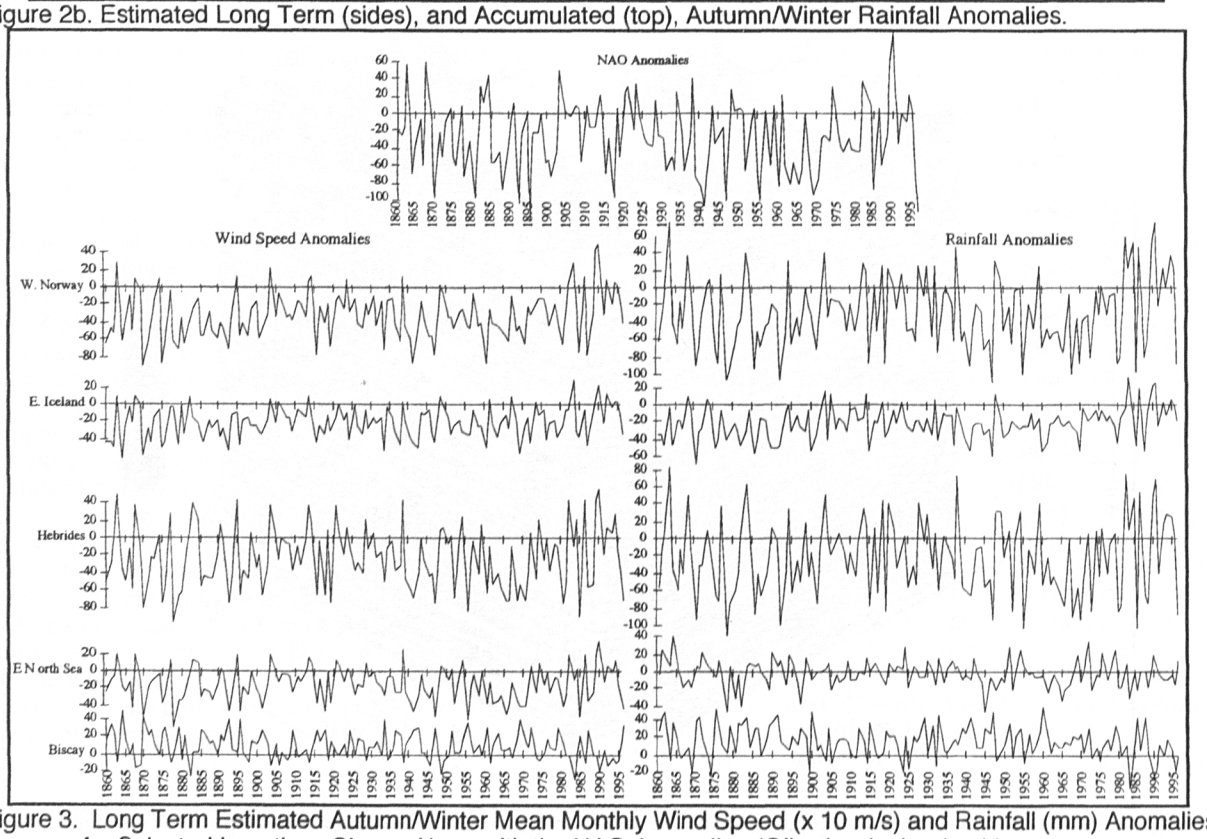

Figure 3. Long Term Estimated Autumn/Winter Mean Monthly Wind Speed (x 10 m/s) and Rainfall (mm) Anomalies for Selected Locations Shown Along with the NAO Anomalies (Gibraltar-Iceland, mb).

P1.20B QUALITY ASSESSMENT OF NEAR SURFACE TROPICAL WIND OBSERVATIONS

Willemien van Hoeve*
KNMI, de Bilt, The Netherlands
Utrecht University, Utrecht, The Netherlands

Ad Stoffelen
KNMI, de Bilt, The Netherlands

1. INTRODUCTION

Tropical wind analysis is very important for both atmosphere and ocean circulation models. A better knowledge of the tropical circulation and air-sea interaction may improve seasonal and climate forecasts. In this study we aim to gain information on the systematic and random errors of respectively *in situ*-, scatterometer- and model observations of the near-surface tropical wind.

2. WIND CALIBRATION

In ocean wind calibration the surface truth is not available as the *in situ* coverage is too sparse, which results in a substantial representativeness error. So all measurement systems contain an error, of which the exact specifications are unknown. Besides, the typical measurement uncertainty is relatively large compared to the dynamic range of the wind speed, i.e. there is a generally small Signal-to-Noise Ratio. As pointed out in Stoffelen (1998), calibration of wind observations without prior knowledge or assumptions on the error characteristics, may be achieved by using triple collocations. In this method the wind component distributions and their error distributions are described by first and second order statistics. When for instance *in situ* winds are assumed to have no systematic error, then a three-way comparison of the data types and their differences allow a simultaneous assessment of the calibration (systematic error) and quality (random error) of the three observation systems.

3. TROPICAL CHALLENGE

Wind calibration in the tropics is even more statistically challenging, since at this latitude (from 10 N to 10 S) the winds are generally light and vertical fluxes larger. The three systems under investigation in this study are respectively the Tropical Atmosphere Ocean (TAO) Array buoy anemometers, the ERS-1 scatterometer and the ECMWF analysis. The inconsistencies between the three systems are partly due to differences in accuracy and spatial representativeness, and partly due to systematic deviations from the true wind. At the conference a more detailed analysis of the error characteristics of the three data sources will be presented.

4. REFERENCES

Stoffelen, Ad, 1996: Error modelling of scatterometer, *in situ*, and ECMWF model winds; A calibration refinement, Technical report 193, published by KNMI, Postbus 201, 3730 AE de Bilt, The Netherlands

Stoffelen, Ad, 1998: Towards the true near surface wind speed; Error modelling and calibration using triple collocation. *J. Geoph. Res.-Oceans* **97JC03180**, in press.

* *Corresponding author address:* Willemien van Hoeve, KNMI, Postbus 201, 3730 AE, de Bilt, The Netherlands;
e-mail: hoevev@knmi.nl

P1.21A

COUPLED ANALYSIS OF ACTIVE AND PASSIVE MICROWAVE MEASUREMENTS. APPLICATION TO THE SEA-SURFACE WIND RETRIEVAL FROM TOPEX-POSEIDON

Sid-Ahmed Boukabara* Laurence Eymard†

1. INTRODUCTION

A simple algorithm is proposed in order to retrieve the sea-surface wind speed from the altimetric backscattering coefficients and the microwave radiometric brightness temperatures. This algorithm is derived by the inversion of a simulated data set. The simulation was performed using a three-scale model over a representative meteorological database. The performances of our algorithm are then compared to other algorithms commonly used in the litterature. Its validation is done by comparison with a large data set of coincident on-ship measurements. The main advantages of this algorithm is that it could be generated for any altimetric configuration, it is developed independently from any buoy nor on-ship measurements, it has an homogeneous behaviour in the low and high wind speeds, consistent with the on-ground data. An other advantage is that it could be improved by the modeling improvement. The relationship between the altimetric measurement (sigma naught) and the wind speed parameter has been the subject of several studies. The theoretical model of the altimeter return shape has been widely described in the litterature ([Barrick, 1972], [Brown, 1977], [Barrick and Lipa, 1985]). The return pulse is related to both (1) the variance of the sea surface elevation, related to the significant wave height H_s, and to (2) the mean square slope of the surface. The wind speed has been first extracted from the mean square slope measure under the assumption that the surface slopes are gaussian and isotropic [Mognard and Lago, 1979]. Indeed, the mean square slope is related to the wind speed via the Cox and Munk (1954) linear relationship or through (Wu 1972)'s logarithmic relationship [Brown, 1979]. Chelton and McCabe (1985), Chelton and Wentz (1986) and Witter and Chelton (1991) used a completely different approach to extract the wind speed, based on a purely empirical relationship between the return power and the sea surface wind speed. This pragmatic approach gives results but does not permit to understand the physics of the process and therefore seems to be a retrograde step as pointed out by Srokosz 1990 [Srokosz, 1990]. We present in this paper a simple method to retrieve the wind speed from the measured sigma naught. The approach adopted here has been successfully applied for the microwave radiometer retrieval of atmospheric parameters (Eymard 1996). It is based on the inversion of a complete scattering model, taking into account the two scales of the sea surface waves (gravity and capillarity) as well as the foam coverage.

*Corresponding author address: Sid-Ahmed Boukabara AER, Inc., 840 Memorial Drive, Cambridge MA 02139, USA. e-mail: sboukaba@aer.com

†Corresponding author address: Laurence Eymard, CETP 10-12 Avenue de l'Europe, 78140, Vélizy-Villacoublay, France. e-mail: eymard@cetp.ipsl.fr

2. METHODOLOGY

The principle of this method of retrieval has already been applied in the field of microwave radiometry [Eymard et al., 1996, Lojou, 1990] for the retrieval of atmospheric parameters (water vapor and liquid water contents). First, a representative meteorological database (global analysis) is extracted from the ECMWF, containing both sea-surface parameters (wind speed, surface temperature) and atmospheric profiles of humidity and temperature. A three-scale sea surface scattering model (taking into account the large and small wave scale as well as the foam coverage) is introduced

in a radiative transfer model [Sobieski et al., 1991, Guissard and Sobieski, 1994] and then applied on the meteorological database. We obtain thus a large data set of altimetric sigma naught and microwave brightness temperatures (more than nine thousands points). The simulation is done with respect to the instrumental configuration (polarisations, frequencies, incidence angles). We find a relationship between the generated sigma naught and brightness temperatures and the wind speed that was used for the simulation. This relationship, obtained by multiple regression, constitutes the retrieval algorithm. One has to note that no buoy nor ship measurements are included for this development, except perhaps through their assimilation into the ECMWF model. The obtained algorithm is completely dependent on the model used for the simulation. So, following the improvement of the modeling, the algorithm could be improved too. The validation of the retrieval model could finally be verified by the comparison between the retrieved data and on-ship or buoys measurements.

3. RESULTS

In case of Topex-Poseidon satellite, and for future missions such as JASON or ENVISAT, the altimeter configuration contains two channels. For Topex for example, the second channel is in the C-band. The use of this C-band data is usually not taken into account for the sea winds retrieval. However this range of frequencies is more sensitive to surface features and less to atmospheric attenuation. Elfouhaily 1996 proposed an algorithm using the two frequencies of Topex Ku and C bands and the results seemed promising [Elfouhaily, 1996]. When adding the C-band sigma naught as a second input for the sea wind retrieval, our algorithm is also significantly improved. Figure 1 represents the relationship between the generated sigma naught (Ku-band) using our model and the wind speed (from ECMWF meteorological data) that served for the simulation. The shape of this curve suggests us to use an hyperbolic function $\frac{1}{(\sigma^\circ)^n}$ for the inversion of the model in order to retrieve the wind velocity. We have tested various power values for n. On the other hand, all the spaceborne altimeters, as they are aimed at the measurement of the satellite range, need to be corrected from the dry and wet atmospheric path delay. The microwave radiometer is dedicated to the measurement of the wet tropospheric path delay. Moreover, this instrument obviously looks to the same scene as the altimeter. The brightness temperatures measured by the microwave passive sensor are thus sensitive to the atmospheric components (especially the 21GHz channel) and also to the sea-surface features (especially the 18GHz channel). In case of ERS-1 and ERS-2 microwave radiometers, there are only two channels at 23.8 and 36.5 GHz. In this case, the retrieval algorithm for the determination of the water vapor-induced path-delay, uses the wind speed retrieved by the altimeter in order to account for the surface effect [Eymard et al., 1996]. In case of TMR (Topex Microwave Radiometer), three channels exist at 18, 21 and 37 GHz. We have made attempts to retrieve the altimeter wind speed by putting also the microwave radiometer measurements as inputs in the retrieval algorithm cited previously. The synergistic use of active and passive microwave measurements is thus proposed to improve the accuracy of the sea-surface wind speed altimeter retrieval. This synergy is natural since the reflectivity Γ and the emissivity e of a natural medium, under thermodynamical equilibrium, are related together by $\Gamma + e = 1$ and since the radiometer is sensitive to the surface emissivity and the radar to its reflectivity. The form used for the radiometric brightness temperatures is suggested by Wilheit [Wilheit and Chang, 1980] for the wind speed retrieval from SSM/I microwave radiometer. The obtained algorithm, taking into ac-

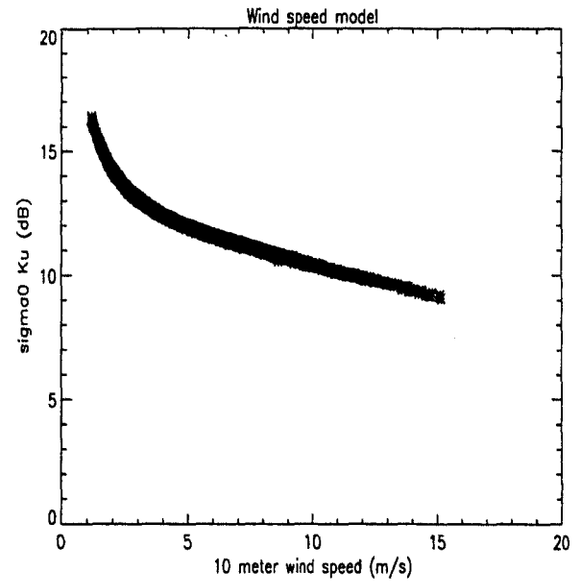

Figure 1: *Altimeter sigma naught versus ECMWF wind speed. Simulation done by a three-scale model taking into account the large and small wave scale as well as the foam coverage*

count the two bands of Topex-Poseidon as well as the TMR brightness temperatures is:

$$u_{10} = 0.520328 + 2.97582e8 \times \frac{1}{(\sigma_C^\circ)^7} - 3.90018e7 \times \frac{1}{(\sigma_K^\circ)^7} + 0.153897 \times \frac{280 - T_{18}}{280 - T_{37}} \quad (1)$$

4. VALIDATION

More than two years of Topex-Poseidon data (between January 1994 and April 1996) have been processed in order to extract the coincident points with on-ship measurements. More than one thousand points have been selected after the filtering of the satellite suspicious data. Only points verifying the condition flag=0 (no anomaly) in the GDR Aviso data were selected. The coincidence criteria adopted were less than 30 minutes in time and less than 0.5° in space (latitude and longitude). The surface was then divided in a 360×720 grid. For each bin containing both a ship point and a satellite track, data have been averaged. Only bins containing more than ten points were kept. The comparison between the retrieved wind and the on-ship measured one is done for the several algorithms (the present one and the Modified Chelton and Wentz MCW one), see figures 2 and 3. In these scatterplots, the wind speed (the one measured by the ship as well as the one retrieved using the altimeter measurements) is plotted versus the TOPEX-POSEIDON measured sigma naught. The large period (more than two years) considered for this comparison ensures the statistical coverage. In the high values, the MCW algorithm seems to underestimate with respect to the ship measurements. Pierson [Pierson, 1990] undertook studies on the validity of the wind speeds measured on ship. His conclusion was that the low winds were overestimated by the ships (against the buoys measurements) and in the high winds, the ship measurements were underestimated when compared to the buoy data. In other words, the underestimation in the low values could be partly due to inaccuracy in the ship measurements. Even if the developed algorithm has been made witout using any buoy nor ship measurements, it gives the weakest mean bias with respect to the on-ship data (ship data minus the retrieved wind). Indeed the mean bias in this case is -0.26 m/s instead of 0.65 for the Modified Chelton and Wentz function. One has to note that the scattering of the plot in case of Lefevre and the coupled algorithm, is due to the fact that the Ku-band data is not the

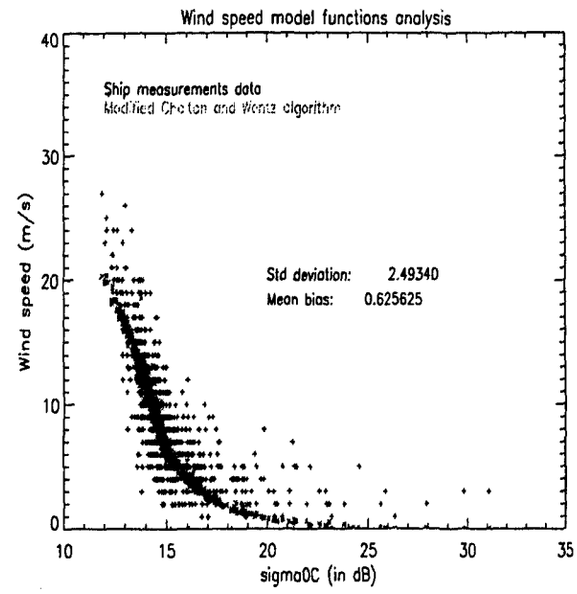

Figure 2: *Wind speed versus the measured Topex sigma naught. The wind speed is from ships and retrieved using the Modified Chelton and wentz function*

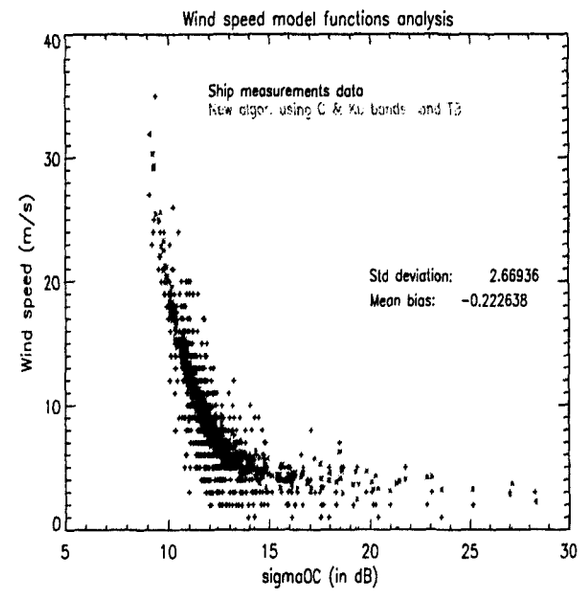

Figure 3: *Wind speed versus the measured Topex sigma naught. The wind speed is from ships and retrieved using the new algorithm function applied on the altimeter measurements.*

unique input in the retrieval model.

5. CONCLUSION

Several algorithms exist for the wind speed retrieval from spaceborne altimeters. Their main limitation is that they are tuned using buoy observations. The number of observations is often weak and the distribution not representative. They are usually given in several branches which causes problems in the general distribution of the wind speed. An other limitation which is often observed is their underestimation of the high wind speeds, the reason for that is simply the weak number of on-ground data in this range of wind speeds, so the tuning is not easy. Our aim was to propose an analytical retrieval algorithm for the wind speed, independent from any on-ground measurement. The developed algorithm is only dependent on the modeling of the backscattering coefficient versus the sea surface state. This was done using a complete three-scale model. The algorithm consists simply in the inversion of the direct model, and could be improved if any improvement in the modeling technique is observed. As it is given in an analytical form so the wind variation is the same everywhere. Tests of robustness have been made on the several algorithms. The developed algorithm seems slightly less sensitive to the noise effects especially in the low values than the other algorithms. When compared to on-ship measurements, its results fit also better than the selected algorithms, especially in the high values (where of course, it is difficult to get on-ground data to tune algorithms) and where underestimation is generally observed.

Acknowledgements

This work was supported under ESA contract $N°$ 11031/94/NL/CN at CETP laboratory. Current work at AER Inc. under NASA/Seawinds project involves the coupling of active scatterometric and passive microwave radiometric data.

References

[Barrick, 1972] Barrick, D. (1972). Remote sensing of sea state by radar. In *Ch.12 in Remote sensing of the troposphere*, ed. V.E. Derr U.S. Govt. Printing Office, Washington DC.

[Barrick and Lipa, 1985] Barrick, D. and Lipa, B. (1985). Analysis and interpretation of altimeter sea echo. *Adv. in Geophys.*, 27:61–100.

[Brown, 1977] Brown, G. (1977). The average impulse response of a rough surface and its applications. *IEEE Tans. Ant. Propag.*, pages 67–74.

[Brown, 1979] Brown, G. (1979). Surface roughness slope density estimates for low sea state conditions. *J. Geophys. Research*, 84:3987–3989.

[Elfouhaily, 1996] Elfouhaily, T. (1996). Modèle couplé vent/vagues et son application à la télédétection par micro-onde de la surface de la mer. Thèse de doctorat, Paris-7 university FRANCE.

[Eymard et al., 1996] Eymard, L., Tabary, L., Gérard, E., Boukabara, S., and LeCornec, A. (1996). The microwave radiometer aboard ERS-1, part II: Validation of the geophysical products. *IEEE Trans. on Geosc. and Remote Sensing*, 34(2):291–303.

[Guissard and Sobieski, 1994] Guissard, A. and Sobieski, P. (1994). A simplified radiative transfer equation for application in ocean microwave remote sensing. *Radio Sci.*, 29(4):881–894.

[Lojou, 1990] Lojou, J. (1990). Algorithmie et méthodes de validation des instruments en radiométrie hyperfréquence. Thèse de doctorat, Paris-7 university FRANCE.

[Mognard and Lago, 1979] Mognard, N. and Lago, B. (1979). The computation of wind speed and wave heights from geos-3 data. *J. Geophys. Research*, 84:3979–3986.

[Pierson, 1990] Pierson, W. J. (1990). Examples of, reasons for, and consequences of the poor quality of wind data from ships for the marine boudary layer: Inapplications for remote sensing. *J. Geophys. Research*, 95:13,313–13,340.

[Sobieski et al., 1991] Sobieski, P., Guissard, A., and Baufays, C. (1991). Synergic inversion technique for active and passive microwave remote sensing of the ocean. *IEEE Trans. on Geosc. and Remote Sensing*, 29(3):391–406.

[Srokosz, 1990] Srokosz, M. (1990). Wave statistics chap.9. In *Surface Waves and Fluxes vol.I*, pages 285–328, Kluwer Academic Publishers G.L. Geernaert and W.J. Plant (Editors).

[Wilheit and Chang, 1980] Wilheit, T. and Chang, A. (1980). An algorithm for retrieval of ocean surface and atmospheric parameters from the observations of the scanning multichannel microwave radiometer. *Radio Sci.*, 15(3):525–544.

P1.23A

A 10-YEAR CLIMATOLOGY OF AMAZONIAN RAINFALL DERIVED FROM PASSIVE MICROWAVE SATELLITE OBSERVATIONS

A. J. Negri*[1], E. N. Anagnostou[1,2], and R. F. Adler[1]
[1]Laboratory for Atmospheres, NASA/Goddard Space Flight Center, Greenbelt, MD 20771
[2]Universities Space Research Association, Seabrook, MD 20706

1. INTRODUCTION

It has been more than a decade since the launch of the first Special Sensor Microwave Imager (SSM/I). This enables us to present a 10 year (+) climatology of rainfall derived from the application of the Goddard Profiling algorithm (GPROF) to the SSM/I observations. Table 1 provides a summary of the available data.

Table 1 Data used in this study

DMSP satellite	Data period	Length (mon)	Eq. crossing (LT)
F08	Jul '87 - Feb '90*	31	0615
F11	Jan '92 - Dec '95	48	0501-0629
F13	Jan '96 - Feb -98	26	0543
F08/11/13 (comb.)	Jul '87 - Feb '90*; Jan '92 - Feb '98	95	0600 (nominal)
F10	Jan '91 - Nov '97	83	0742-1031 (0900 nom)
F08/11/13/10 (comb)	Jul '87 - Feb '90*; Jan '91 - Feb '98	107	0600 /0900 (nominal)
	* except Dec '87		

The GPROF (Kummerow and Giglio, 1994) retrieves instantaneous rainfall at 15 km resolution. The estimates are then aggregated into monthly composites at 0.5° resolution. The monthly estimates are adjusted to account for the diurnal cycle, using the technique of Anagnostou et al. (1998). Morning and evening estimates (left unadjusted) are also aggregated. The estimates cover the northern half of South America from 15°N - 20°S and from 35°W - 80°W. This study extends the work of Negri et al. (1994), which examined only warm-season Amazonian precipitation using a scattering-based technique. In this study, we present climatologies for 1) the mean rainfall; 2) diurnal variability; 3) seasonal rainfall; and 4) interannual variability.

2. RESULTS

Figure 1 presents the mean rainfall in mm/mon during the 107 month period of usable data (see Table 1). Height contours are displayed at 100, 500 and 1000 m elevations. A notable minimum in precipitation is observed over northeast Brazil. The significant maxima that can be discerned are:

- the mean position of ITCZ rainfall along 5N from 50W to 30W, with a distinct northern boundary along 10N;
- the Gulf of Panama, along 80W from 10N to the equator;
- a broad maximum in the Amazon Basin;
- a topographically induced maximum between the Negro and Orinoco Rivers at 2N, 67W;
- a topographically induced maximum in the mountains of Venezuela, near 5N, 63W;
- a coastal maximum near the mouth of the Amazon R., near Belem, at 2S, 48W;
- an elongated maximum along the eastern slope of the Andes from 10S to 20S. Note that the maximum along the Andes itself is spurious, a result of misinterpretation by the GPROF of cold (elevated) surface as rainfall.

Figure 2 presents the rainfall climatology by time of day, for the a period of two-satellite operation (Jan 1992-Nov 1997). Note that the separation time is about 3h. Important diurnal features include:

- the aforementioned Gulf of Panama maximum, exclusively an AM phenomenon;
- a slight preference for AM rainfall offshore in the ITCZ;
- a PM maximum along virtually the entire northern coast (on-shore-side) of South America, particularly from Belem (0,5S) and eastward;
- an AM maximum between the Negro and Orinoco Rivers (2N, 67W);
- a PM maximum between the Negro and Solimoes Rivers, where they come together to form the Amazon R.;
- a PM maximum in eastern Brazil along the rivers of the Mato Grosso plateau
- a morning maximum (both at 6 and 9 AM) along the eastern slopes of the Andes.

Figure 3 presents the seasonal (3-month) climatology for the 95 mon 6 AM/ 6PM series. The migration of the rainfall associated with the ITCZ is evident, both offshore and over the Amazon Basin. The Gulf of Panama maximum shows strong seasonal variation, with a winter/spring maximum. The topographically

* Corresponding author address: Andrew J. Negri, Code 912, NASA/GSFC, Greenbelt, MD 20771; email: negri@irene.gsfc.nasa.gov

induced maximum at 2N, 67W is most prevalent in spring (SON). Rainfall along the northeast coast is predominately a summer/fall phenomenon, with little rainfall during the rest of the year.

Figure 4 presents the interannual variability of precipitation, as exemplified by the months of Dec/Jan/Feb. No data is available from 1990-1992 for this 6 AM/ 6PM series. Substantial year-to-year variability exists in estimates over a 3-month period. Evident however are both the increased precipitation during the La Niña event of 1988-89 and the strong El Niño event of 1997-98. To quantify this, we present Figure 5, time series of area-averaged rainfall for two regions: (10N-10S, 30W-50W) where a decrease in rainfall during El Niño is expected, and over a portion of the Amazon Basin (0-10S, 75W-55W).

3. CONCLUSIONS

The statistical technique of Anagnostou et al. (1998) has allowed us, for the first time, to correct satellite microwave rainfall estimates (from the GPROF) for the biases introduced by uneven sampling of the diurnal cycle. Thus, a 10+ year climatology of gage-adjusted satellite estimates was presented. Climatologies included the mean rainrate, diurnal (4x/day) variation, seasonal variability and interannual variability. the latter included the strong El Niño event of 1997-98. Quantitative results will be presented at the conference.

4. REFERENCES

Anagnostou, E.N., A.J. Negri, and R.F. Adler, 1998: Adjustment of monthly microwave estimates over Amazonia, Preprints, 9th Conf. Satellite Meteorology and Oceanography, AMS, Paris, France, 4 pp.

Kummerow, C. and L. Giglio, 1994: A passive microwave technique for estimating the vertical structure of rainfall from space, Part I: Algorithm description, *J. Appl. Meteor.*, **33**, 3-18.

Negri, A.J., R.F. Adler, E.J. Nelkin and G.J. Huffman, 1994: Regional rainfall climatologies derived from Special Sensor Microwave Imager (SSM/I) data. *Bull. Amer. Meteor. Soc.*, **75**, 1165-1182.

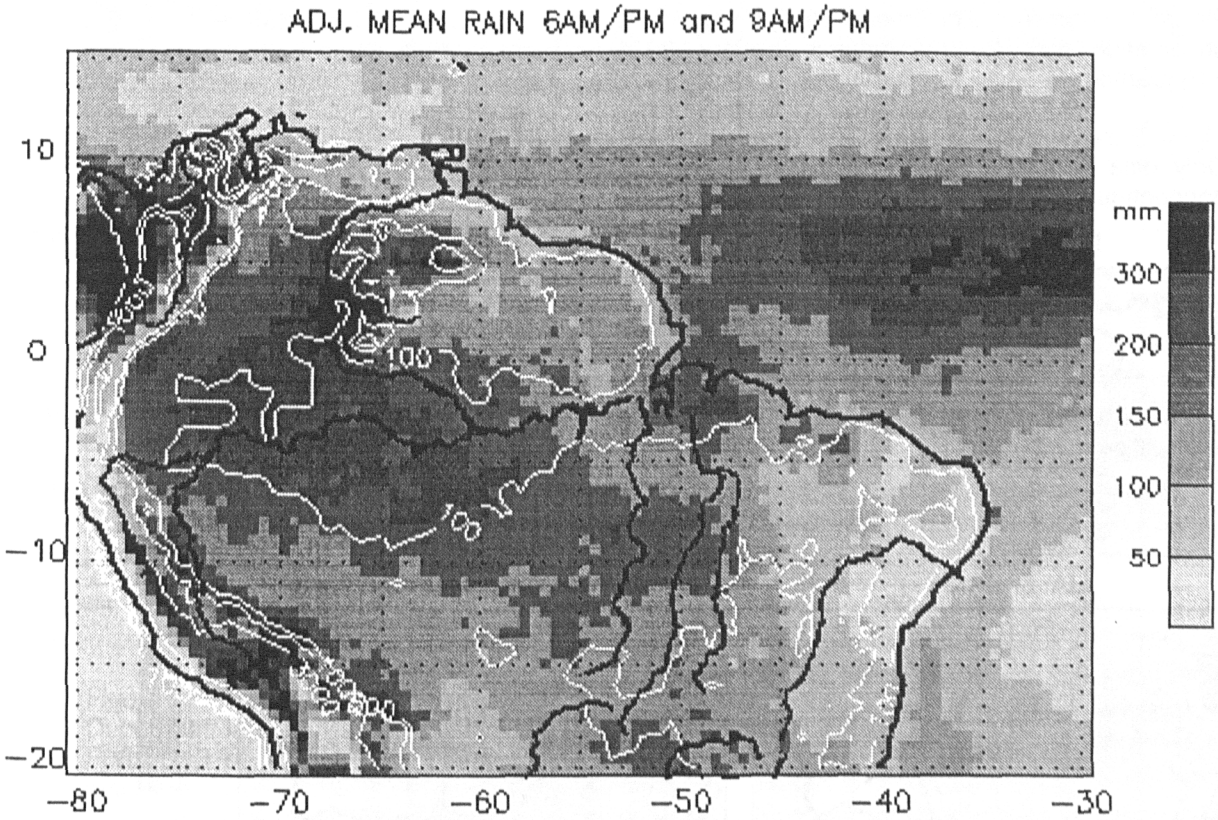

Figure 1. The mean rainfall (mm/mon) during the period July 1987 - February 1998, derived from the GPROF. Data from two series of satellites (F08/11/13, and F10) have been combined, using the technique of Anagnostou et al. (1998) to account for the diurnal cycle. Height contours are displayed at 100, 500 and 1000 m elevations.

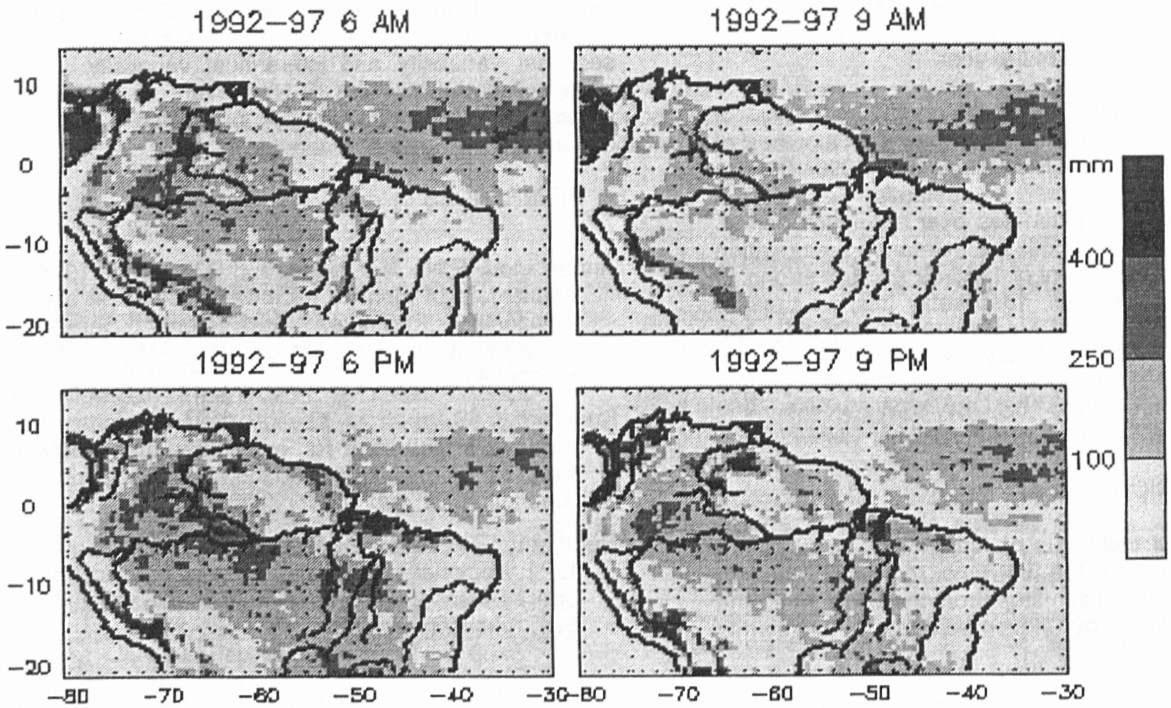

Figure 2 (above). The mean rainfall (mm/mon) from the GPROF, stratified by observation time. The time period is January 1992 - November 1997, when both the F10 (9am/9pm) and F11/13 (6am/6pm) were operating.

Figure 3 (below). The mean rainfall (mm/mon) from the GPROF, stratified by season. Only data from the F08/11/13 series (6am/6pm) are used, which encompass a noncontiguous period of 95 months (see Table 1).

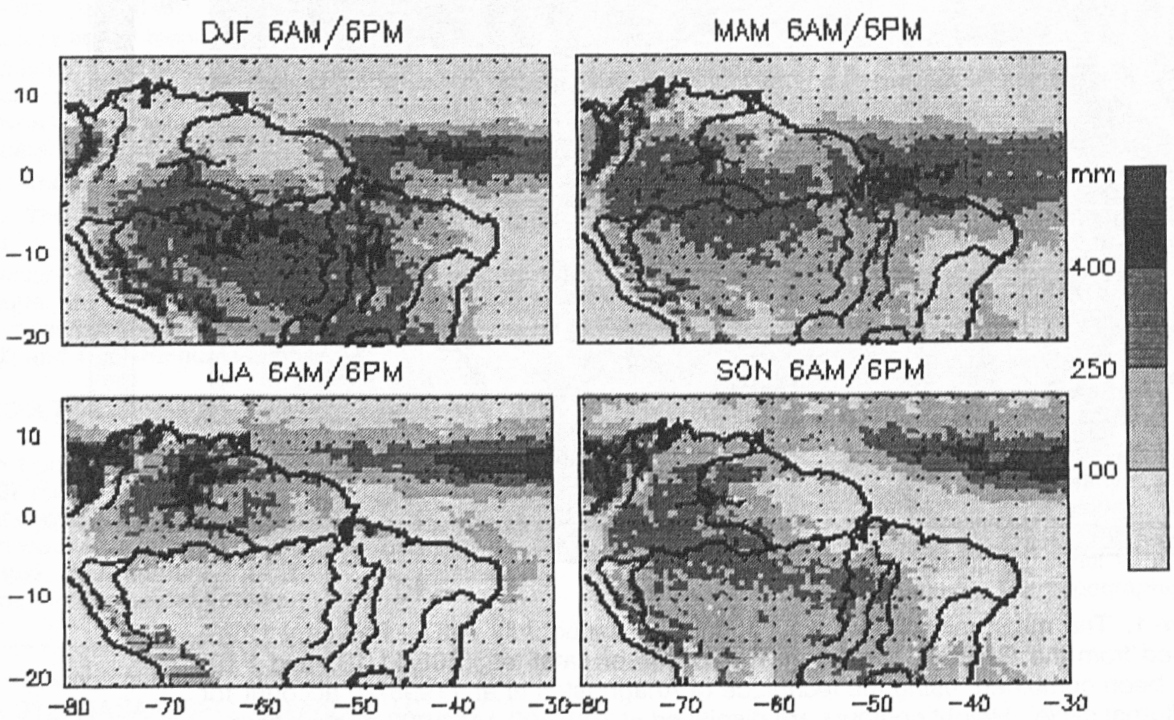

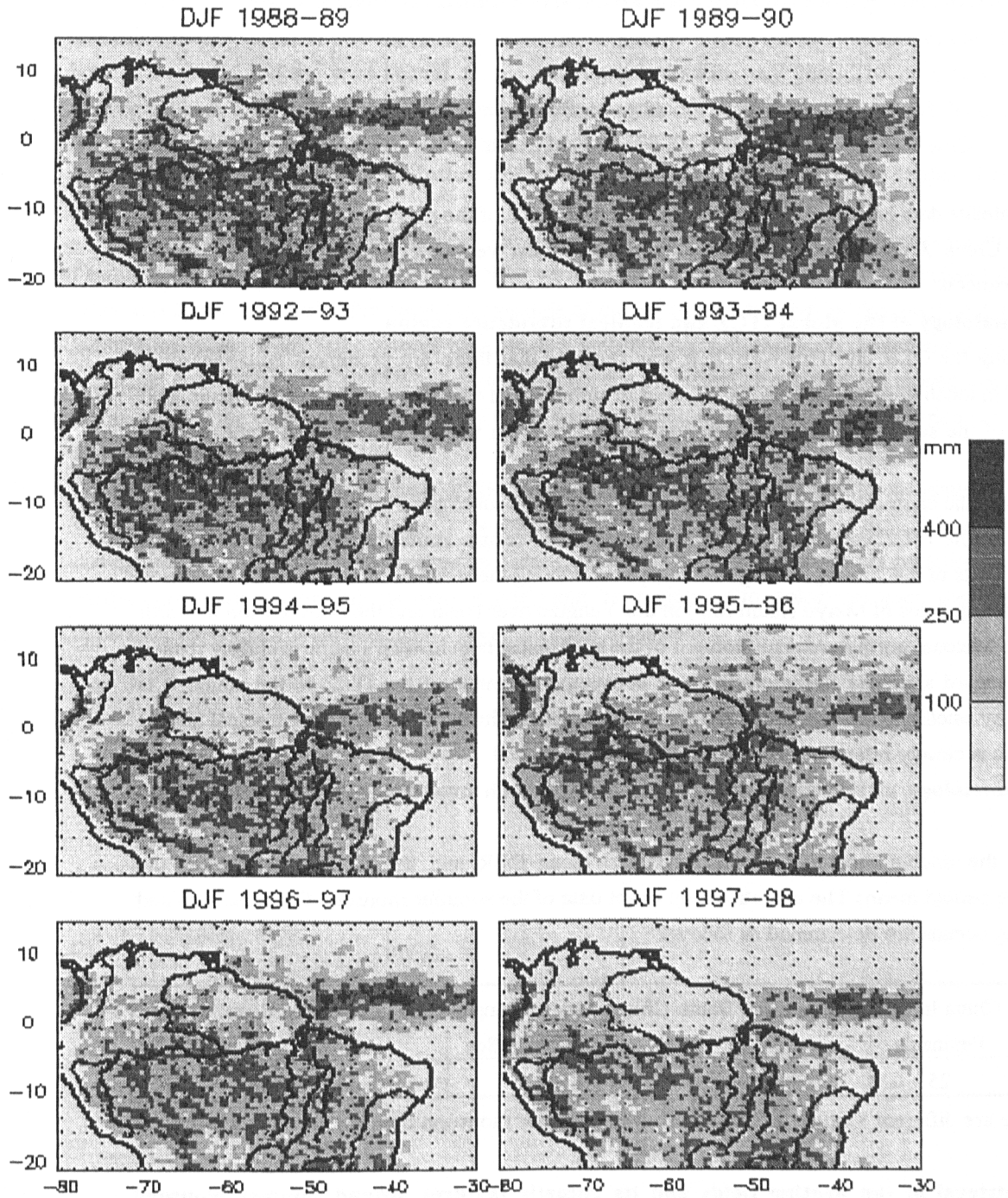

Figure 4. The mean rainfall (mm/mon) from the GPROF for December/January/February of eight different seasons. Only data from the F08/11/13 series (6am/6pm) are used. Data from 1990-91 and 1991-92 are not available.

P1.25A ADVANCES IN APPLIED RESEARCH OF THE SATELLITE OBSERVATIONS ON THE GENERAL CIRCULATION AND CLIMATE VARIATION

Shangcheng Jiang
Department of Geophysics, Peking University
Beijing 100871, P.R.of China

The satellite data has been widely applied on the research of the general circulation and climate variation in China. A review of the advances and the new facts we found of this area are presented in following respects:

1. The climatology of the global ITCZ and tropical subsidence region

By using the OLR and HIRS-Tb12, It was revealed that there are prominent zonal seasonal oscillations in location of the double ITCZ , west in summer and east in winter, over the Pacific. and in position of the subtropical high, east in summer and west in winter, both in the Pacific and the Atlantic.

The climatic characteristics of the longitudinal shift of the subtropical high over west Pacific and its relation to the ITCZ were studied with OLR data. The results show that there are two abrupt northward shifts of the subtropical high in west pacific during the summer half year, which coincide with the starting dates of Meiyu (plum rain) in the Yangtze river basin and the rainy season in North China. The seasonal northward displacement of the subtropical high in west Pacific is closely related to the northward shift and the intensifying of convective activities of the ITCZ to the south. It is confirmed by satellite observation that the seasonal abrupt northward shift of the subtropical high in west Pacific is closely related to the variation of the Hadley cell.

2. The climatology of the summer monsoon onset march over the Asia and neighboring oceans

With the double threshold of OLR (pentad mean OLR and the difference between the consecutive pentad mean) The climatic mean onset date of the summer monsoon Over the Asia and neighboring oceans are determined as follows:

Malaysia	China Indian Peninsula	Philippines	South China Sea	Bay of Bengal Arabian Sea	India, Yangtze River Valley Southern Japan
20	25	27	28	31	33 (Pentad)

There are different features of the onset of the summer monsoon over the equator, tropics and subtropics.

3. The retrieval of the heating fields and its climatic features around summer monsoon onset over the Tibetan plateau

There are good relationship between the anomaly of OLR and Q_1 , Q_2 over the Tibetan plateau. The correlation coefficients are -0.56 and -0.55 respectively.

Analyzing the annual cycle of the climatic pentad mean OLR over the Tibetan plateau It is revealed that they are five consecutive pulse raising resulted from sensitive heating before the onset of monsoon then turn down on 32th pentad during onset of monsoon. It is indicated that the sensitive heating(especially over the western Plateau) are very important for monsoon. The monsoon invade Plateau from southeast first then from southwest and the potential heating is important not only in eastern also in western Plateau.

4. The drought and flood over the Yangtze river basin

The results show that the significant influence of the convective activity in tropic oceans on the anomalies of precipitation over the Yangtze river basin. For the flood year the intensity of the ITCZ both in the India and the west Pacific oceans are stronger than the dry year. The position of the subtropical high and ITCZ is father south in wet year than in dry year. The drought and flood over Yangtze river basin are modulated by the LFO of the convective activity over the west Pacific.

5. The characteristics of the evolution of the equatorial circulation with the typical ENSO event

the evolution of the Walker cell along the equator(10 S-10N) and the local Hadley cell over the Pacific were investigated for 1982-1983 ENSO with the divergence wind in 200hPa calculated from OLR. It is found that during the developing periods of the ENSO, the number of divergent centers in 200hPa increased from 3(the normal case) to 4-5 with the gradual eastward displacement of the latitudinal cell. While the ENSO developing , not only the latitudinal circulation cell moved but also the number of the cells changed and in the mean time the longitudinal circulation cell varied too.

6. The reonal climate in china

It is found that the annual cycle of the radiation budget and OLR have different features in a variety of climatic regions in China. It is interesting that the annual cycle of the OLR also can distinguish the different climatic regions in Tibet plateau. So that the OLR and net radiation of the earth-atmosphere system can be used in analyzing the regional climatology as good parameters except for the meteorological elements observed from the ground..

P1.27A

NEURAL NETWORK APPROACH FOR TOTAL COLUMN OZONE RETRIEVAL FROM NOAA-TOVS DATA

Anton K. Kaifel •
Center for Solar Energy and Hydrogen Research, Stuttgart, GERMANY

Abstract

A new approach using neural networks for total column ozone retrieval from NOAA-TOVS data is presented and will be evaluated by applying it to a long term data set (June 1994 to December 1994) covering whole Europe, North Africa and parts of the Atlantic Ocean. For all atmospheric conditions (clear/cloudy, day/night) the absolute mean error of the neural network approach for the total ozone retrieval on the test data set is less than 10 Dobson Units for the ground measurement stations of the German Weather Service (DWD) in Hohenpeissenberg and Potsdam. The study shows that it is possible to retrieve total column ozone with an accuracy of about 2-3 %. The advantage of the TOVS based ozone data compared to other satellite instruments for ozone retrieval (TOMS, SBUV, GOME) using the solar spectrum is that also during night good accuracy of the TOVS ozone retrieval can be achieved and that long term global TOVS data are available for the last 20 years.

1. Introduction

Currently two different kind of satellite based nadir measurement principles for ozone are available. The first one uses the backscattered ultraviolet radiation of the solar spectrum and is therefore only applicable during daylight. There are mainly the Total Ozone Mapping spectrometer (TOMS) [1] the Solar Backscattered Ultraviolet Spectrometer (SBUV) [2] and Global Ozone Monitoring Experiment (GOME) [3]. The second kind of instruments (TOVS) measures the thermal radiation emission of the earth-atmosphere system around the 9.6 μm absorption band of ozone and for retrieval additional thermal infrared spectral channels of the HIRS and MSU are used. Using these thermal infrared emission enables also measurements during nighttime.

For ozone retrieval from NOAA-TOVS data two different basic approaches can be made. The first one is a physical or semi-empirical retrieval scheme using TOVS ozone absorption channel 9 and some other channels for surface emissivity and other corrections (e.g. water vapor). This scheme of Karcher and Lefevre [4], getting an RMS of 18 - 20 D.U. applying in polar regions and Europe [5]. Some coefficients have to be adjusted before applying it to different climatological regions or for different seasons, which restricts this scheme to regional use only.

A different semi-empirical scheme developed by A. Neuendorffer is used by NOAA/NESDIS operationally for daily global total ozone column retrieval [6,7]. On a global scale the RMS error is about 25 D.U. under "normal circumstances" [6]. For situations with major stratospheric warming in which both temperature and ozone increase rapidly [8] the scheme has problems with the ozone retrieval and therefore a highly nonlinear "ad hoc thermal profile correction" is included to handle such situations [7]. Another disadvantage is that the scheme needs scan angle and water vapor corrected TOVS input data.

The new approach of using neural networks for total ozone column retrieval from TOVS data is presented and validated for all atmospheric conditions. A case study for evaluation and validation is carried out for a period lasting from June 1994 to December 1994.

• *Corresponding author address:* Anton K. Kaifel, Center for Solar Energy and Hydrogen Research, Hessbruehlstr. 21c, 70565 Stuttgart, GERMANY, email: kaifel@zswvs1.e-technik.uni-stuttgart.de

2. Neural Network Approach

For the retrieval of total column ozone amount, multilayer feed forward neural networks are used. This type of neural networks consists of an input layer, at least one or more hidden layers and an output layer. Each layer of the network consists of a number of neurons and each neuron is fully connected with all other neurons in the adjacent layers. The number of input neurons corresponds to the number of input parameters and the output layer has only one neuron representing the total column ozone retrieval value. Fig. 1 shows the used neural network configuration with the pre- and postprocessing (normalization) of the input and output values. Extended studies showed that a neural network with two hidden layers (15 and 10 neurons) give the best retrieval results for the independent test data set [9,10].

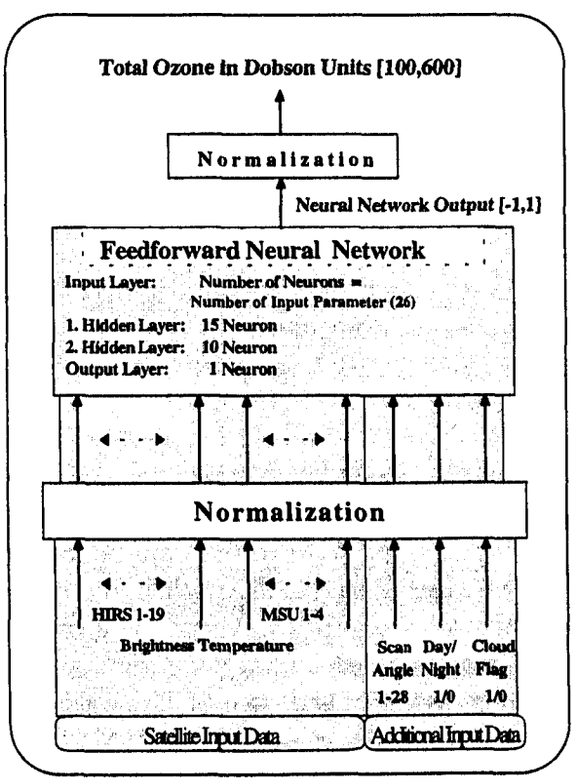

Fig.1: Neural network configuration for total colum ozone retrieval from NOAA TOVS data

For training of the neural networks the Backpercolation Algorithm is used [11]. Extensive tests of various training algorithms stated [12] that Backpercolation is the most stable and fastest algorithm for this kind application.

For input of the neural network calibated TOVS data are used. Fig. 1 shows 3 additional input parameters used by the neural network. The first one, the scan point 1-28 (scan point number from nadir) of the HIRS instrument is intended to be used by the neural network for scan angle correction because no corrections are applied to TOVS input data. The second one is a flag indicating if the TOVS measurement is taken during day or night time in order to take the diurnal cycle of total ozone and temperature profile in the atmosphere into account. The third one is a flag indicating clear/cloudy HIRS pixels because no cloud clearing algorithm is used for the TOVS input data.

3. Case Study

A case study was carried out for evaluation of the proposed neural network ozone retrieval scheme. Therefore 907 satellite overpasses received by the local HRPT station of the DWD in Offenbach (Germany) are processed covering the area of about 70°N - 25°N, 30°W - 60°E. Corresponding ground based measurements (daily mean) of the total ozone amount are collocated with HIRS pixels of the same day.

Table 1: Number of collocation for training and test data set. The training data are used to train a neural network and the independent test data are for evaluation purposes.

Collocation	clear		cloudy		total	
	train	test	train	test	train	test
day	2880	177	9731	539	12611	716
night	1829	114	4965	325	6794	439
total	4709	291	14696	864	19405	1155

For the independent test data set, all available collocations of the two ground measurement stations of the DWD in Germany located in Potsdam (Pots) and Hohen Peissenberg (Peis) are used. The remaining collocations of all other available ground measurements from 43 different stations are used for training of the neural network. Table 1 shows the number of collocations of the training and test data set.

4. Results

One of the most important quality checks for a trained neural network is the comparison of the results on the training and independent test data set. If the results on both data sets are similar then the neural network generalization ability is good or if the results on the test data set are even better it is excellent. Tab. 2 shows the comparison of the mean absolute error (MAE) for the data used in this case study (Tab. 1). The MAE for total ozone retrieval from TOVS data by means of neural network technique is smaller on the test data set as on the training data set. There are two reasons for this behavior which is not quite normal for neural networks. The first already mentioned is the very good generalization ability of the neural network. The second is the different measurement accuracy of the various ground stations because the ground ozone measurements have to be carried out very carefully and measurement equipment should be maintained very well.

Table 2: Mean absolute error (MAE) for total ozone retrieval with neural networks for training and test data set.

MAE D.U.	clear		cloudy		total	
	train	test	train	test	train	test
day	9.34	6.09	9.74	8.02	9.66	7.53
night	10.84	9.21	10.76	7.87	10.78	8.30
total	9.82	7.00	9.98	7.98	9.95	7.72

Table 3: Mean absolute error (MAE) for total ozone retrieval with neural networks for the DWD ground measurement stations of Hohen Peissenberg (Peis.) and Potsdam (Pots) of the test data set.

MAE D.U.	clear		cloudy		total	
	Peis.	Pots.	Peis.	Pots.	Peis.	Pots.
day	5.92	7.71	5.48	9.80	5.54	9.96
night	6.40	9.27	4.50	7.86	5.36	8.35
total	6.00	8.77	5.36	9.39	5.60	9.26

The training data set contains measurements of 43 different ground stations. If we look at the MAE for each station it can be noticed that on good managed stations (so far we know) like Arosa, Switzerland (MAE = 5.23 D.U.), Haute Provence, France (MAE = 6.31 D.U.), Ispra, Italy (MAE = 6.80 D.U.) or Debilt, Netherlands (MAE = 5.93 D.U.) and for several other stations the MAE is smaller as on the total training data set and there are stations where the MAE is larger (Sofia, Bulgaria: MAE = 30.2 D.U.; Lwow, Ukraine: MAE = 17.35 D.U.; Riga, Latvia: MAE = 14.38 D.U.; Thessaloniki, Greece: MAE = 14.04 D.U.).

Nevertheless it proves the robustness of the neural network approach if the results of an independent test data set is better than on the training data set even if there are some less accurate measurements incorporated.

5. Conclusions

This study improves and proves the very good accuracy of the proposed total column ozone retrieval scheme for NOAA-TOVS data by means of neural network technique achieved in a previous study for a smaller time range [9]. It can be shown that for all different types of atmospheric situations (day/night and clear/cloudy) within the study area the mean absolute error (MAE) of the new TOVS ozone retrieval is less than 10 D.U.. This means that the accuracy is better than 3 %. In comparison to other ozone retrieval schemes measuring backscattered UV radiation of the

sunlight (TOMS, SBUV, GOME) the new TOVS data based ozone retrieval schemes using the infrared part of the spectrum are applicable during day and nighttime with the same accuracy of the total column ozone retrieval. This is especially important in polar regions during polar night when no sunlight is present and there are no ozone data available from TOMS, SBUV or GOME. Other major advantages of TOVS data are the good spatial (50km) and temporal resolution and that since 1978 continuous and global TOVS data are available and with the potential to contribute to global ozone climate research.

The neural networks ozone retrieval retrieval is very fast and well suited for real time applicaitons. At the end of last year the retrieval scheme was implemented in the operational satellite data processing facility at the DWD in Offenbach, Germany for real time total column ozone retrieval using the TOVS data from the local HRPT station receiving station.

6. References

[1] Fleig, A.J. ,K.J. Klenk, P.K. Bhartia, and D. Gordon, 1982a: User's guide for the Total Ozone Mapping Spectrometer (TOMS) instrument first-year data set. NASA Ref. Pub. 1096, NASA GSFC, Greenbelt, MD.

[2] Fleig, A.J., K.J. Klenk, P.K. Bhartia, and D. Gordon, 1982b: User's Guide for the Solar Backscattered Ultraviolet (SBUV) instrument first-year data set. NASA Ref. Pub. 1095, NASA GSFC, Greenbelt, MD.

[3] European Space Agency, 1993: Global Ozone Monitoring Experiment: Interim Science Report, ESA, SP1151.

[4] Lefèvre, F., D. Cariolle, S. Muller, F. Kacher, (1991): Total ozone from TIROS Operational Vertical Sounder during formation of the 1987 ozone hole, J. Geophysical Research, Vol.96, 12893-12911.

[5] Karcher, F. , B. Lacroix and P. Caille (1995): Current use of TOVS data at Meteo-France Toulouse, Techn. Proc. 8th Int. TOVS Study Conf., Queenstown, Neuseeland, pp. 227-236.

[6] Neuendorffer, A. C. (1993): The decline n polar stratospheric ozone as observed by NOAA infrared satellites, SPIE Proceedings, Vol. 2047, Atmospheric Ozone, pp. 110-120.

[7] Neuendorffer, A.C. (1996): Ozone monitoring with TIROS-N Operational Vertical Sounders (TOVS), accepted by Journal of Geophysical Review, (personal communication).

[8] Rosen, J.M., N.T. Kjome, V.U. Khattotov, V.V. Fudakov, ÄV.A. Yushov, (1992), Observations of ozone and polar stratospheric clouds at Heiss Island during winter 1988-1989. J. Geo. Res., Vol. 97, 8099-8110.

[9] Kaifel, A, (1995): Evaluation of total ozone retrieval from NOAA-TOVS data by means of neural network technique, Techn. Proc. 8th Int. TOVS Study Conf., Queenstown, Neuseeland, pp. 217-226.

[10] Kaifel, A, (1997): Recent improvements and evaluation of neural network approach for total ozone retrieval from NOAA-TOVS Data, Techn. Proc. 9th Int. TOVS Study Conf., Igls, Austria, in press.

[11] Jurik, M. (1990): Backpercolation: Exploiting the duality between signals and weights. Jurik Res., Aptos,CA.

[12] Kaifel, A. (1994): Backpercolation: Fast learning of neural networks - Extensions and performance evaluation. Proc. IMACS Int. Sym. on Signal Processing, Robotics and Neural Networks, 23 - 26.

P1.28B

A ROTATED PRINCIPAL COMPONENT ANALYSIS OF TOTAL COLUMN OZONE DERIVED FROM TOMS (VERSION 7.0) FOR 1980-1992

Brian K. Eder*
Atmospheric Sciences Modeling Division
Air Resources Laboratory
National Oceanic and Atmospheric Administration
Research Triangle Park, NC 27711 USA

1. INTRODUCTION

The global distribution of total column ozone (Ω) continues to attract great international attention as concerns over reduced ozone abundance intensify. Despite its great importance, the global spatial and temporal distribution of ozone is poorly understood. In order to accurately assess anthropogenic changes to date (a task deemed one of the more difficult in atmospheric physics today by *McPeters and Komhyr*, 1991) and to better understand how Ω may respond to future perturbations, requires a better understanding of its natural intra- and interannual variability as well as the processes that contribute to this variability. Accordingly, the purpose of this analysis is to develop a better understanding of these natural variations across various spatial and temporal scales. This will be achieved through the application of a multivariate statistical technique called rotated principal component analysis (pca) to the Ω data.

2. TOMS DATA

Version 7.0 of the Nimbus-7 Total Ozone Mapping Spectrometer (TOMS) data was obtained from the Ozone Processing Team located at NASA's Goddard Space Flight Center in Greenbelt, MD. The Ω is expressed as the depth that the ozone molecules alone would occupy at standard temperature and pressure. This depth is measured in thousands of centimeters or Dobson Units (DU), where 1 DU = 2.69 x 10^{16} molecules cm^{-2}.

For this analysis, the TOMS data were regridded from their original resolution (1° latitude by 1.25° longitude) to a larger 5° by 5° grid using a simple averaging technique that incorporated all (maximum 20) non-missing grid cells. This yielded a total of 1872 grid cells extending from 65°S to 65°N. A total of thirteen years of data were utilized, from January 1, 1980, through December 31, 1992. Missing data were eliminated through a temporal interpolation scheme resulting in nearly nine million observations.

*On assignment to the National Exposure Research Laboratory, United States Environmental Protection Agency, Research Triangle Park, NC 27711 USA; email: eder@hpcc.epa.gov

3. METHODOLOGY

The main objective of pca is to identify, through a reduction in data, the characteristic, recurring and independent modes of variation across all spatial and temporal scales (*Eder et al.,* 1993). The analysis sorts initially correlated data into a hierarchy of statistically independent modes of variation, which explain successively less and less of the total variation; thereby summarizing the essential in formation of that set so that meaningful and descriptive conclusions can be achieved. This technique is ideal for application to the satellite data sets where the total number of observations can become burdensome.

3.1 Spatial Analysis

Mathematically, the analysis began with the calculation of a square, symmetric correlation matrix ${}_{1872}\mathbf{R}_{1872}$, from the original data matrix ${}_{1872}\mathbf{D}_{4749}$. By using **R** and the identity matrix **I** of the same dimensions, 1872 *eigenvalue - eigenvector* pairs, or *principal components* were derived. By retaining only the first 14 principal components, as deemed statistically significant by the Scree Test, over 70% of the total variance of Ω was accounted for. An orthogonal rotation was then applied to these 14 principal components allowing for the spatial delineation of 14 subregions or regions that exhibit statistically unique and homogeneous Ω characteristics. The elements of each of the 14 eigenvectors were then multiplied by the square root of the associated eigenvalue to obtain the component (subregion) loadings, which represent the correlations between the component and the grid cell. The square of the component loading indicates the proportion of variance in the individual grid cell that can be attributed to that component. Because of space constraints, the analysis will focus on 5 of the more intriguing rotated components or subregions. (Maps of the loadings can be found in Figs. 1a through 1e.)

3.2 Temporal analysis

Another useful parameter that can be derived from pca is the principal component score (pcs) which is simply the weighted, summed values for the 4749 days, for the grid cells, the weights being the component

loadings. When plotted as a time series (Figs. 2a through 2e), the pcs, which are standardized, provide excellent insight into the temporal variance experienced by Ω in each of the subregions.

Spectral density analysis using the finite Fourier transformation was then employed to examine each of the Ω time series associated with the subregions (Figs. 3a through 3e). Such analysis yields a measure of the distribution of variance of the time series across all possible wavelengths. It is used to look for non-random, physically generated cyclical patterns or periodicities in the time series data, which would be represented by a peak in the spectrum at a particular frequency.

4. RESULTS AND DISCUSSION

The ***first rotated principal component (rpc)***, which accounts for 31.9% of the total variance of Ω defines an area encompassing much of the northern extent of the study domain (Fig. 1a). With the exception of the Northern Atlantic, most areas north of 40° N have loadings greater than 0.60, meaning that greater than 36% (0.6^2) of the total variance in Ω is attributable to this component. The time series (Fig. 2a) and spectral density (Fig. 3a) plots indicate a strong annual cycle (f = 0.0172, periodicity ($2\pi/f$) = 365.3 days) that exhibits a sharp late-winter, early-spring peak and a broader late-summer, early autumn minimum. In most years, there is observed a continuous increase in Ω from the end of November through early April. This is followed by a rapid decline from May through August and a short period of relatively constant Ω values during the months of September and October that has been referred to as a "stand-still" period. The driving force of this component is likely dynamical in nature, linked to: 1) the mass transport of ozone from the equatorial upper-stratosphere (source region), to the northern hemisphere middle and lower stratosphere (*Bojkov et al.*, 1994); and 2) the seasonal variance of the tropopause height or "tropopause effect" (*Stanford et al.*, 1995).

The ***second rpc*** (17.7%) covers much of the remainder of the Northern Hemisphere from roughly 5° to 30°N (Fig. 1b). It is strongest in a band from 10° to 25° N, where loadings often exceed 0.80 (again, greater than 64% of the total variance in Ω is explained). The time series (Fig. 2b) and spectral (Fig. 3b) plots likewise indicate a strong annual cycle for this component (f = 0.0172, periodicity = 365.3 days); however, unlike the first component, which was dynamical in nature, the forcing behind the Ω pattern in this region of the northern hemisphere appears to be photochemical in nature. The annual cycle is likely reflecting the production of odd oxygen (either O or O_3) by the photodissociation of molecular oxygen (O_2) which takes place primarily in the lower and middle stratosphere and is controlled by the solar zenith angle. As a result, the timing of the minimum and maximum Ω for this subregion correspond to the winter and summer solstices, respectively. From an annual standpoint, the lowest Ω values in this region are found during the winters of 1982,1983; 1984,1985; 1987,1988 and the end of 1992. These negative anomalies appear to follow strong Quasi-Biennial Oscillation (QBO) events (see discussion below) by 10-12 months, supporting *Herman and Larko* (1994).

The ***third rpc*** (5.8%) defines an area encompassing much of the Southern Hemisphere, stretching from 5° to the 45° S, with greater significance from roughly 10° to 25° S, where loadings exceed 0.60 (Fig. 1c). Examination of the time series (Fig. 2c.) and spectra (Fig. 3c) reveals the presence of three significant cycles including an annual (f = 0.0172, periodicity = 365.3 days), a semi-annual (f =0.0344, periodicity = 182.7 days), and a longer term oscillation (f = 0.0026, periodicity = 2374.5 days). The annual harmonic, which has also been reported by *Shiotani* (1992) can be seen in the times series, reaching a peak during September and October when planetary waves are most active and a minimum in the March through May time frame, when the waves are least active. The semi-annual oscillation (SAO), which peaks around the time of each equinox, was also reported by *Shiotani* (1992), who found the semiannual harmonic to be strongest in an area from southeastern Africa to Indonesia. This SAO in Ω may be linked to the SAO found in the zonal wind in this region. The 6.5 year periodicity also seen in this region is not understood at this time but may be related to the El-Nino Southern Oscillation (ENSO) associated with rpc11 discussed below.

The ***fourth rpc*** (4.2%) defines an area fairly symmetrical about the equator (Fig. 1d) that coincides well with a region associated with the QBO of the tropical winds in the lower stratosphere. This association is confirmed by its time series (Fig. 2d), which peaks in 1980, 1982, 1985, 1987, 1990 and again in 1992 and the spectral density analysis (Fig. 3d), which reaches a maximum power at f= 0.007, corresponding to a periodicity of 897.6 days (roughly two and one-half years). This QBO signal is slightly stronger from 70°E to 80°W (loadings greater than 0.70) and it is slightly asymmetrical, extending a little further north (15°N) than south (10°S), which supports the work of *Herman and Larko* (1994). This latitudinal asymmetry is likely due to stronger horizontal mixing in the lower stratosphere of the northern hemisphere by planetary-scale waves during the westerly phase of the QBO.

The ***eleventh rpc*** (0.9 %) defines a small area in the Southern Hemisphere from New Guinea in the Western Pacific to central South America (Fig. 1e). Its times series (Fig. 2e) and spectral (Fig. 3e) plots are distinctive, indicating a strong oscillation at a f of 0.0040 (periodicity = 1583 days). This rpc clearly identifies the ENSO as the driving force of Ω in this region. It is well known that the ENSO cycle in the equatorial Pacific produces an atmospheric response that extends from the troposphere to about the 50hPa

level in the lower stratosphere (*Zerefos et al.*, 1992; *Bojkov et al.*, 1994). The primary manifestation of the ENSO is a seesaw fluctuation in atmospheric pressure between the subtropical high over the southeast Pacific and a region of lower pressure across the Indian Ocean from Africa to Australia. During ENSO events, the tropical troposphere is warmed over the Pacific, which causes an increase in convection, an increase in the height of the tropopause and an upwelling of air into the stratosphere ensuring a reduction in **Ω** (*Zerefos et al.*,1992; *Shiotani*, 1992). Note that during El-Nino years of 1982-83, 1987, and 1991-2, the **Ω** values are very low, while in non-El Nino years, the **Ω** values are high.

5. REFERENCES

Bojkov, R.D., V.E. Fioletov, and A.M. Shalamjansky, 1994: Total ozone changes over Eurasia since 1973 based on reevaluated ozonometer data, *J. Geophys. Res.*, **99**, 22985-22999.

Eder, B.K., J.M. Davis, and P. Bloomfield, 1993: A characterization of the spatiotemporal variation of non-urban ozone in the United States, Atmos. Environ., **27A** 2645-2668.

Herman, J.R. and D. Larko, 1994: Low ozone amounts during 1992-1993 from Nimbus 7 and Meteor 3 total ozone mapping spectrometers, *J. Geophys. Res.*, **99**, 3483-3496.

McPeters, R.D. and W.D. Komhyr, 1991: Long-term changes in the total ozone mapping spectrometer relative to world primary standard Dobson Spectrometer 83, *J. Geophys. Res.*,**96**, 2987-2993.

Shiotani, M., 1992: Annual, quasi-biennial, and El Nino-Southern Oscillation (ENSO) time-scale variations in equatorial total ozone, *J. Geophys. Res.*, **97**, 7625-7633.

Stanford, J.L., J.R. Ziemke, R.D. McPeters, A.J. Krueger, and P.K. Bhartia, 1995: Spectral Analyses, Climatology, and Interannual Variability of Nimbus-7 TOMS Version 6 Total Column Ozone, *NASA Ref. Pub., 1360.*

Zerefos, C.S., F.B. Alkiviadis, I.C. Ziomas, and R.D. Bojkov, 1992: On the relative importance of Quasi-Biennial Oscillation and El Nino/Southern Oscillation in the revised Dobson total ozone records, *J. Geophys. Res.*, **97**, 10135-10144.

This paper has been reviewed in accordance with the U.S. Environmental Protection Agency's peer and administrative review policies and approved for presentation and publication. Mention of trade names or commercial products does not constitute endorsement nor recommendation for use.

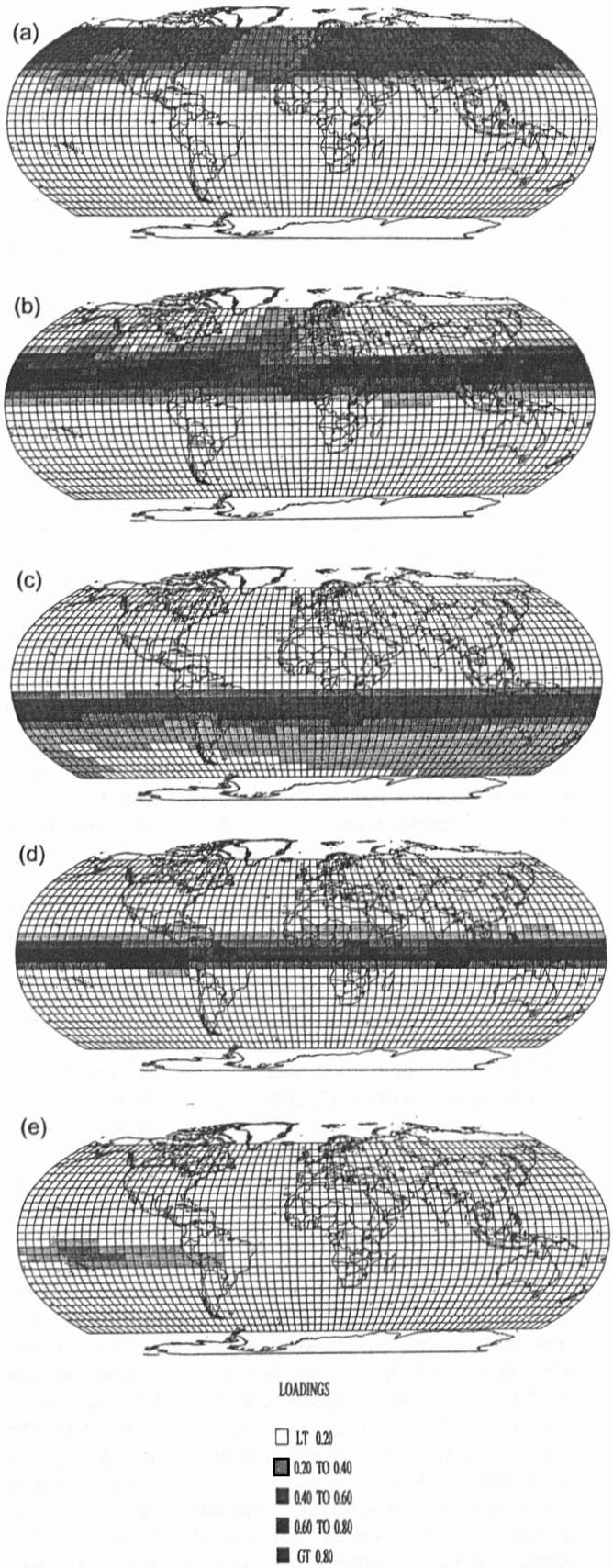

Fig. 1. Principal component loadings associated with subregions 1 (a), 2 (b), 3 (c), 4 (d), and 11 (e).

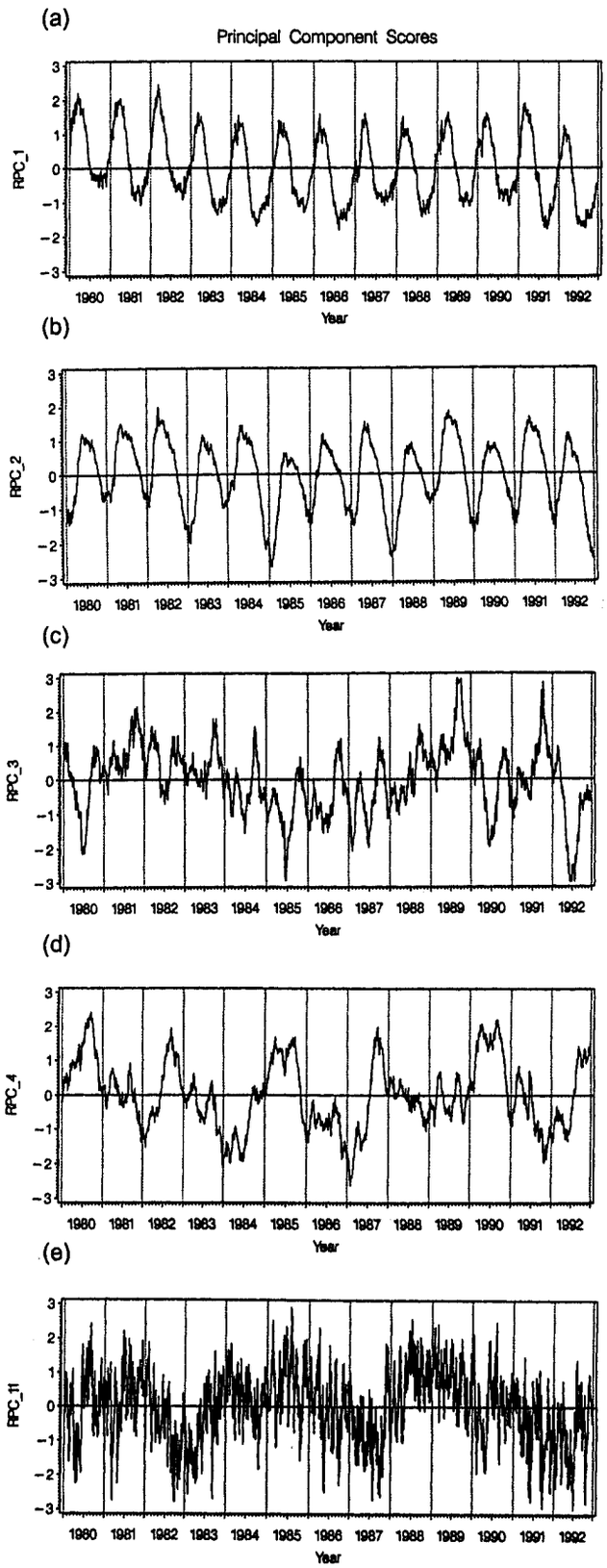

Fig. 2. Standardized principal component scores associated with subregions 1 (a), 2 (b), 3 (c), 4 (d), and 11 (e).

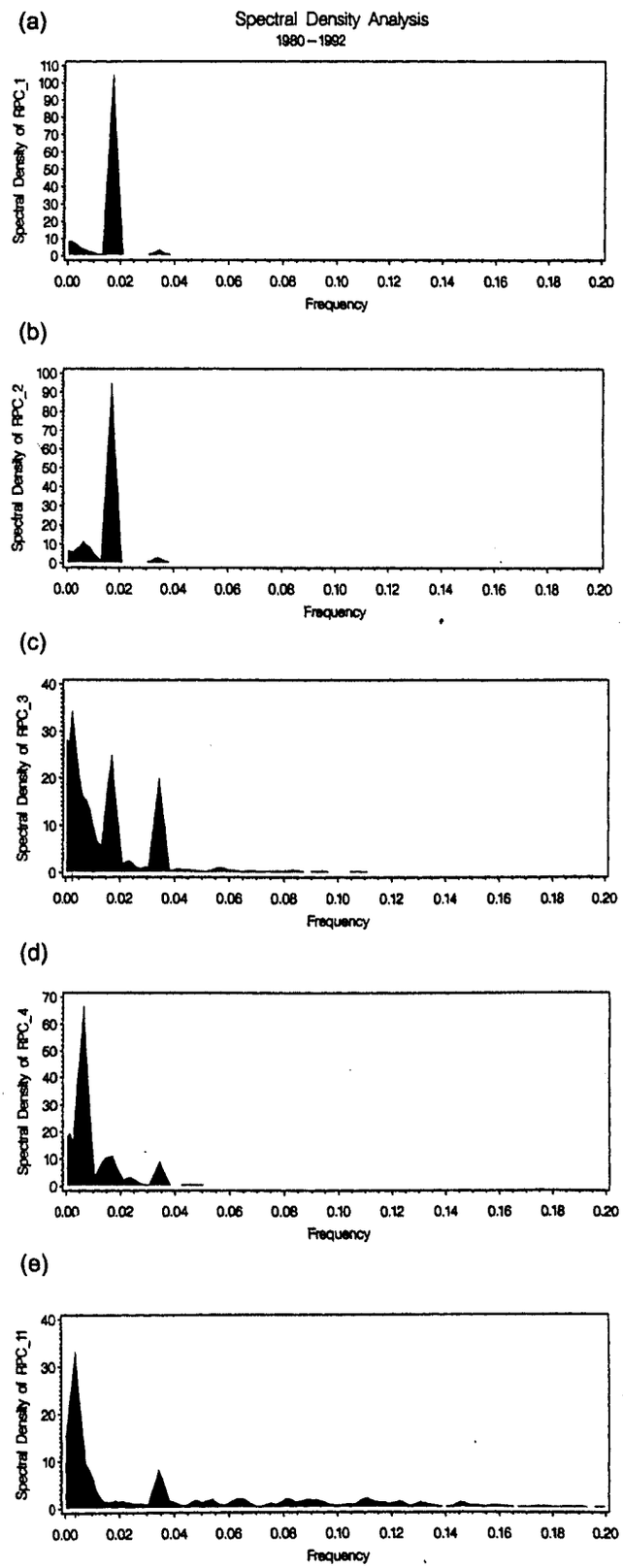

Fig. 3. Spectra of the principal component scores associated with subregions 1 (a), 2 (b), 3 (c), 4 (d), and 11 (e).

ASSIMILATION OF OZONE IN THE ECMWF MODEL

Elías Valur Hólm*, Agathe Untch, Adrian Simmons, Roger W. Saunders, and François Bouttier
European Centre for Medium-Range Weather Forecasts, Reading, UK

1. INTRODUCTION

Ozone is presently being introduced as a model variable in the ECMWF weather forecast model for regular three-dimensional ozone forecasts. As ozone data source radiances from the HIRS-9 channel on TOVS will be used. Here we present the developments necessary for introducing radiances in the ECMWF assimilation. For estimating the relative influence of model and measurements in the assimilation, the ozone model forecast errors need to be known. We will start with an evaluation of the model accuracy, followed by the estimation of the model ozone forecast errors. We will then relate the forecast error to the sensitivity of HIRS-9 radiances to changes in ozone.

2. MODEL COMPARISON WITH SBUV/2

Ozone has been included as a three-dimensional variable in the ECMWF model. The ozone transport is modeled with semi-Lagrangian quasi-monotone advection (Ritchie et al. 1995) supplemented with parameterization of photochemical sources and sinks (Cariolle and Dequé 1986). The ECMWF model has also been extended to the middle mesosphere (0.05 or 0.1 hPa) for all simulations including ozone.

For evaluating the model accuracy, an 80 day simulation of ozone in the ECMWF model was performed for December 1991 to February 1992. The model dynamics were kept close to the real atmosphere by including a term which relaxed the dynamics towards analysed values from UKMO and ECMWF. Ozone was allowed to evolve freely, including the photochemical parametrization.

An initial evaluation of the ozone simulation was made by comparing model values with SBUV/2 satellite ozone data. The data are given as ozone density (in Dobson units) in twelve pressure layers covering the atmosphere. For comparison we use only the SBUV/2 profiles measured within one hour of the model output at 12UTC. This gives about one hundred profiles per day, evenly distributed from 90S to ca. 70N for the present timeperiod. Due to the time limitation, all satellite tracks which are used pass the equator between ca. 30E and 60E.

The standard deviation stays constant throughout the integration at all levels (not shown) and in total ozone (at ca. 10 Dobson units). However, there is a bias in the tropics, where the ozone maximum erodes during the integration. Apart from this bias, the model accurately simulates changes in ozone. Figure 1 shows an example where the model catches the rapid changes in ozone around the 100 hPa level between 27/1 and 29/1 1992 seen in ozone soundings from Payerne (46.8N, 7.0E). For reference we also include the closest SBUV/2 profiles.

We conclude that the model is accurate enough for a first estimate of the ozone model forecast errors needed for the assimilation.

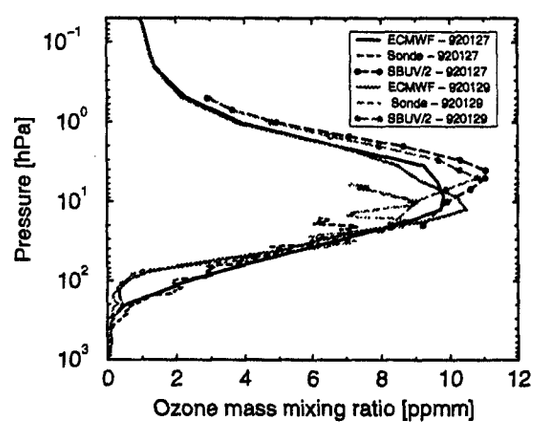

Figure 1: Ozone profiles at Payerne (46.8N, 7.0E) on 27/1 and 29/1, 1992, at 12UTC. Shown are ozone soundings, model profiles from closest gridpoint, and closest SBUV/2 satellite profiles.

3. MODEL FORECAST ERROR FOR OZONE

The forecast error statistics for ozone were derived from the differences of 24 and 48 hour forecasts both starting from the 80-day simulation as initial state and ending at the same time.

The length scale of the horizontal correlations are ca. 600 km in the stratosphere and ca. 300 km in the troposphere (not shown).These horizontal scales are similar to those found for other variables like temperature and humidity in the ECMWF model. The vertical correlations are insignificant except in the lowest stratosphere (80 hPa) and below (not shown). In the absence of vertical error correlations, measurement information can not easily be spread in the vertical in the stratosphere.

In Fig. 2 we show the standard deviation of ozone model forecast error normalized by the model profile from Payerne 29/1 1992. The relative forecast error is

* *Corresponding author address:* Elías Valur Hólm, ECMWF, Shinfield Park, Reading, Berkshire, RG2 9AX, UK; e-mail: dae@ecmwf.int.

largest just above the tropopause, at 100 hPa in the present typical example. Here the standard deviation is ca. 20-25% of the model ozone. This vertical location, just above the tropopause, is where measurements can have largest influence on the model.

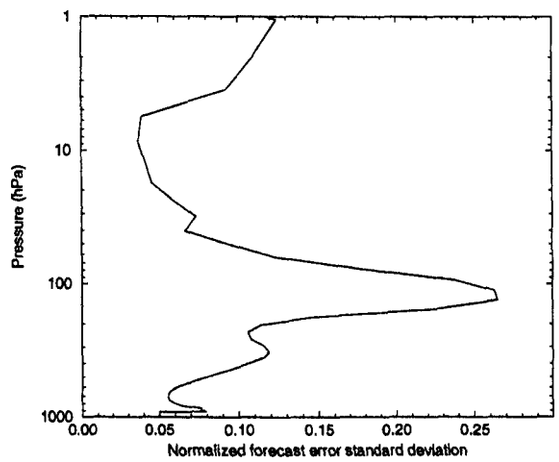

Figure 2: Ozone mass mixing ratio forecast error standard deviation as a fraction of an ozone model profile from Payerne 920129:12h. The relative forecast error is largest at ca. 100 hPa.

We have also developed the tangent linear and adjoint model of the radiative transfer model RTATOV used as interface between the TOVS radiances and the model ozone (see Saunders et al. 1998, in this volume). In Fig. 3 we show the sensitivity of TOVS radiances to small deviations in ozone from a climatological mean profile (in terms of the tangent linear model, i. e. the derivative of brightness temperature with respect to ozone concentration). The influence of ozone is predominantly on the HIRS-9 channel, and peaks at about 200 hPa. This means that the radiances from the HIRS-9 channel can influence the model ozone at ca. 200 hPa through the adjoint model of RTATOV, once RTATOV is combined with prognostic ozone in the variational assimilation system of the ECMWF model. If the errors resulting from processing the radiances with RTATOV are comparable with the forecast-errors in ozone at these levels, there will be a link from the radiances to the dynamics at these levels.

4. CONCLUSION

We have shown that the relative ozone model forecast error is largest just above the tropopause, where the sensitivity of the HIRS-9 radiances to changes in ozone is large as well. At this level, between 100 and 200 hPa, there is some vertical correlation between forecast error. This means that using HIRS-9 radiances as a data source for ozone can be expected to give an impact on model ozone and on the model dynamics (through the

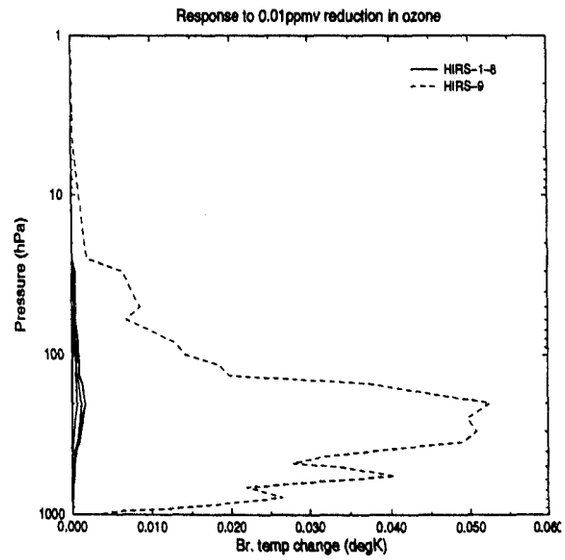

Figure 3: Sensitivity of TOVS channels to changes in ozone concentrations for a typical ozone profile. The maximum sensitivity is for HIRS-9 at ca. 200 hPa.

model adjoint) around the tropopause. This question will be adressed further in assimilation experiments with RTATOV and the ECMWF forecast model.

5. REFERENCES

Cariolle, D., and M. Dequé, 1986: Southern hemisphere medium-scale waves and total ozone disturbances in spectral general circulation model. *J. Geophys. Res.*, **91**, 10825-10846.

Ritchie, H., C. Temperton, A. Simmons, M. Hortal, T. Davies, D. Dent, and M. Hamrud, 1995: Implementation of the semi-Lagrangian method in a high-resolution version of the ECMWF forecast model. *Mon. Wea. Rev.*, **123**, 489-514.

Saunders, R., M. Matricardi, and P. Brunel, 1998: *An improved fast radiative transfer model for assimilation of satellite radiance observations.* In this volume.

ACKNOWLEDGEMENTS

This work was supported by the European Union project Satellite ozone data assimilation (SODA). The SBUV/2 data were obtained from NOAA/NESDIS with support from the NOAA Climate and Global Change Program Atmospheric Chemistry Element.

P1.32B CHARACTERIZING SPATIAL AND TEMPORAL DISTRIBUTIONS OF BIOMASS BURNING USING MULTI-SPECTRAL GEOSTATIONARY SATELLITE DATA

Elaine M. Prins*
W. Paul Menzel
NOAA/NESDIS/ORA/ASPT, University of Wisconsin, Madison, Wisconsin, USA

Joleen Feltz
Cooperative Institute for Meteorological Satellite Studies, University of Wisconsin, Madison, Wisconsin, USA

1. INTRODUCTION

The international scientific community has stressed the need for long-term monitoring of biomass burning for global climate change research. Biomass burning is a distinct biogeochemical process and plays a major role in the global carbon cycle impacting both regional and global climate change. Biomass burning releases significant amounts of reactive trace gases and particulates into the atmosphere. Recent modeling and analysis efforts have suggested that the direct and indirect radiative effects of biomass burning aerosols play a significant role in the radiative balance of the earth and are an important factor in climate change calculations. The majority of biomass burning is concentrated within developing countries in the equatorial and subtropical regions. The extent of burning and the impact of these activities on the global environment are not well understood. Remote sensing offers the most cost effective means for long-term monitoring of fires and associated aerosols.

For the past 10 years the Cooperative Institute for Meteorological Satellite Studies (CIMSS) at the University of Wisconsin - Madison has used Geostationary Operational Environmental Satellites (GOES) to monitor fires and smoke in the Western Hemisphere. CIMSS developed the Automated Biomass Burning Algorithm (ABBA) and the Automated Smoke/Aerosol Detection Algorithm (ASADA) to characterize sub-pixel burning and to catalogue the extent of smoke throughout South America and the South Atlantic Basin. Geostationary fire monitoring capabilities were greatly improved with the launch of GOES-8 in 1994 (Menzel and Prins, 1996). The GOES ABBA and ASADA were revised to take advantage of these improvements. The 1995 burning season in South America represented the first opportunity to monitor diurnal and seasonal burning patterns in this region from GOES-8 and provided detailed information on diurnal fire activity and smoke transport previously not available from any other civilian satellite. This paper will include a brief overview of the GOES-8 ABBA and ASADA and compare results for the 1995 and 1997 fire seasons in South America.

* *Corresponding authors' address:* University of Wisconsin Madison, NOAA/NESDIS/ORA/ASPT, 1225 West Dayton St., Madison, WI 53706

2. THE GOES-8 ABBA AND ASADA

Over the past several years the GOES-8 Automated Biomass Burning Algorithm (ABBA) and Automated Smoke and Aerosol Detection Algorithm (ASADA) have evolved into more robust applications based in part on experienced gained from participation in the Smoke Cloud and Radiation (SCAR) Experiments in California (1994) and Brazil (1995). The latest version of the GOES-8 ABBA (version 5.6) takes advantage of the improved multi-spectral fire monitoring capabilities of the GOES-8 instrument utilizing the visible (VIS, near .65 micron), short-wave infrared window (SIRW, near 4 micron), long-wave infrared window (LIRW, near 11 micron) and ancillary data sets to identify and characterize sub-pixel fire activity. Several components have been added to better characterize background temperatures and screen for sub-pixel and semi-transparent cloud contamination and solar reflectance near local noon. By incorporating dynamic single and multi-band thresholds as well as a SIRW minus LIRW histogram approach to determine background statistics, the occurrence of false positive fires has been significantly reduced (Prins et al., 1998). The GOES-8 ABBA product includes GIF images denoting the locations of detected fire pixels and ASCII files containing fire location (lat./lon.), fire size and temperature estimates, ecosystem type, and a fire flag which indicates fire pixel attributes (processed, non-processed saturated, non-processed cloud-covered, or possible fire pixel).

Validation of the GOES-8 ABBA was attempted with one prescribed burn in the state of Washington (SCAR-C) and two prescribed burns in Brazil. The prescribed burns ranged from 3 to 50 acres in size. Although limited in scope, the results indicated that the GOES-8 can identify fires that are on the order of a few acres in size and that GOES-8 ABBA sub-pixel size and temperature estimates are in line with ground truth observations. These case studies also demonstrated the importance of using high temporal resolution data to capture fires as they occur (Menzel and Prins, 1996; Prins et al., 1998).

The GOES-8 ASADA (version 3.0) incorporates multi-spectral data including the VIS, SIRW, LIRW, and the moisture sensitive long-wave infrared window (often called the dirty window, DIRW, near 12 micron) to map smoke and other aerosols. The ASADA includes single and multi-band difference thresholds, contextual information, solar zenith angle corrected albedo, and

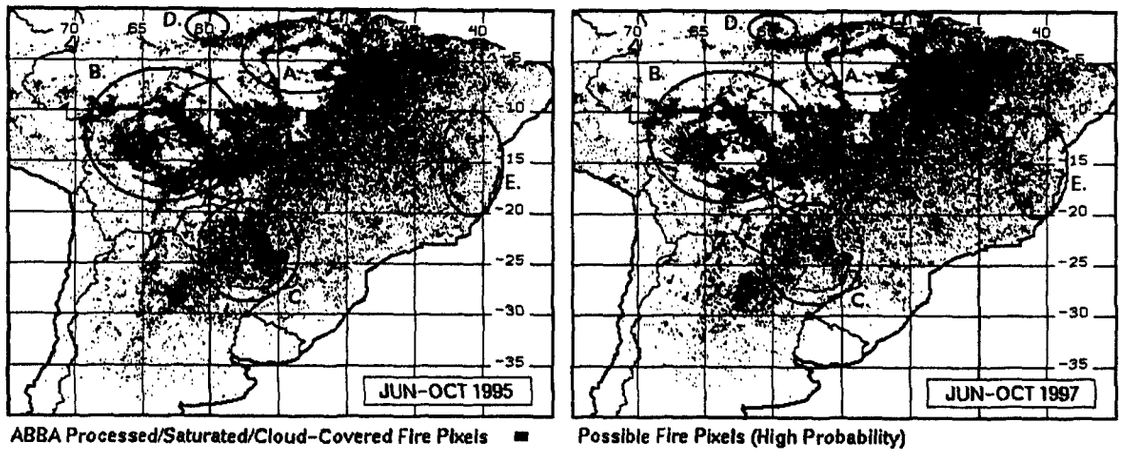

Figure 1. The black markers indicate GOES-8 ABBA detected fire pixels during the 1995 and 1997 fire seasons.

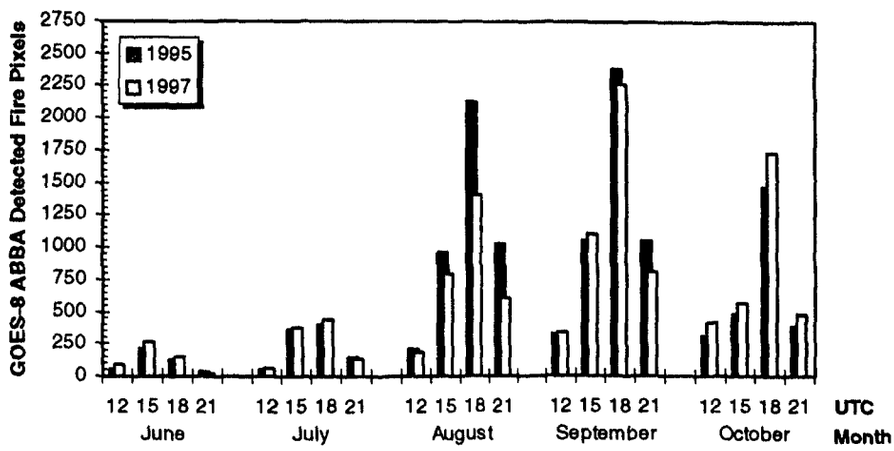

Figure 2. GOES-8 ABBA monthly fire statistics for the 1995 and 1997 fire seasons in South America. The average number of fires detected per day at 1145, 1445, 1745, and 2045 UTC are presented for each month.

solar and satellite viewing geometry to distinguish smoke/haze from multi-level clouds, low-level moisture, and sun glint (Prins et al, 1998). The GOES-8 ASADA product consists of composite imagery and grids that provide a summary of the extent of smoke/aerosol coverage and smoke albedo estimates which give a general indication of the smoke intensity. As with previous instruments, the visible channels of the GOES-8 were calibrated before launch, but there is no on-board calibration capability. More quantitative aerosol analyses require additional post-launch calibration to account for possible sensor gain changes after launch.

3. A COMPARISON OF THE 1995 AND 1997 FIRE SEASONS IN SOUTH AMERICA

Diurnal multi-spectral GOES-8 data collected over South America during the 1995 and 1997 fire seasons (June-October) have been processed with the GOES-8 ABBA (at 1145, 1445, 1745, and 2045 UTC) and ASADA (at 1145 UTC). The GOES-8 ABBA study region extends from 0 to 40° S and from 35 to 75°W including portions of Brazil, Peru, Bolivia, Paraguay, Uruguay, Northern Argentina, and Chile. Composites of GOES-8 ABBA processed, saturated, cloudy, and high-probability possible fire pixels detected at 1745 UTC during the 1995 and 1997 fire seasons show similar burning patterns (Figure 1). Much of the burning occurred along the perimeter of the Amazon in the Brazilian states of Maranhao, Tocantins, Para, Mato Grosso, Amazonas, Rondonia, and Acre and in Bolivia, Paraguay, and Northern Argentina. The spatial distribution of fires shows patterns and details similar to those identified by Skole and Tucker (1993) in their analysis of deforestation observed in Landsat imagery. Both composites in Figure 1 show distinct burning patterns along rivers and in areas with recent road construction (location A). More fires were detected at Locations B (Rondonia, Brazil; Bolivia) and C (Paraguay) in 1995 than 1997. In 1997 increased burning was observed near the city of Manaus in

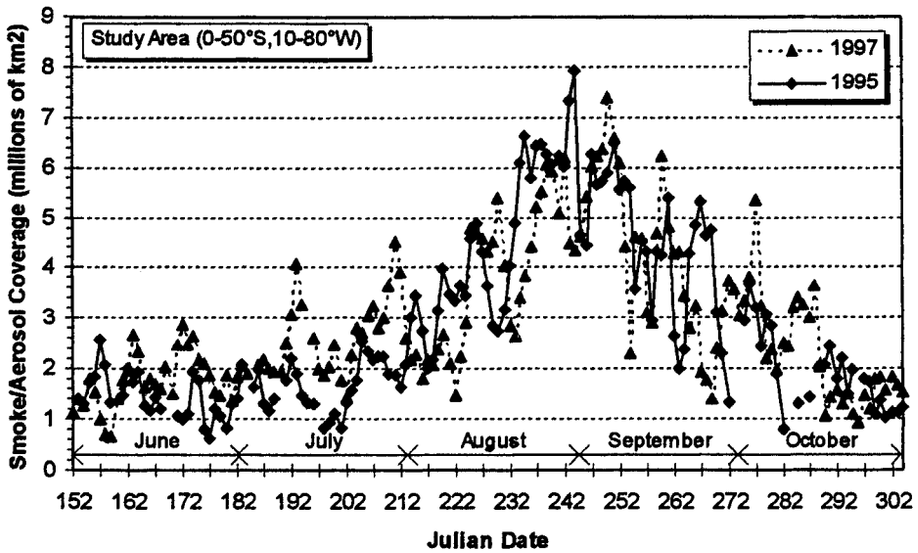

Figure 3. Daily GOES-8 ASADA smoke/aerosol coverage estimates for the 1995 and 1997 fire seasons.

Amazonas, Brazil (location D) and in Bahia and Minas (location E).

Figure 2 provides an overview of GOES-8 ABBA monthly and diurnal fire statistics for the 1995 and 1997 fire seasons in South America. The average number of fires detected per day at 1145, 1445, 1745, and 2045 UTC are presented for each month. The diurnal cycle is clearly evident in both years with peak burning in the early to middle of the afternoon local time at 1745 UTC for the months of July through October. In June of 1995 and 1997 peak burning was observed at 1445 UTC. The fire statistics for June and July are similar in both years. In August, the number of fires detected in 1995 was greater than in 1997 at all time periods. Over 2100 fires were detected per day at 1745 UTC in August 1995; roughly 1400 fires were detected per day at the same time period in 1997. The month of September represented the peak of the fire season in both years with nearly 2400 fires detected per day in 1995 and approximately 2300 fires detected per day in 1997 at 1745 UTC. In both years fire activity decreased in October, although the October 1997 statistics were slightly higher than observed in 1995. Overall, there was an 8% decrease in GOES-8 ABBA observed fires from 1995 to 1997. It is important to note that in both years 70-80% of the fires observed at a given time period were not observed at the other times. This indicates the importance of monitoring fires throughout the day, not only at peak burning times.

The distribution of burning by ecosystem type was nearly identical in both years. During both years over 90% of the burning occurred in 6 ecosystems types. The majority of the fires were located in seasonal tropical broadleaf forests (34%-1995, 33%-1997); savanna/ grassland/seasonal woods (27%-1995, 25%-1997); mild/warm/hot grass/shrub (19%-1995, 22%-1997); and succulent and thorn woods or scrub (7%-1995,1997).

GOES-8 multi-spectral data collected daily at 1145 UTC during the 1995 and 1997 fire seasons were processed with the GOES-8 ASADA in an effort to catalogue the extent and relative intensity of smoke/aerosol coverage. The aerosol monitoring study area extends from 0 to 50°S and 10 to 80°W including most of the continent of South America and the South Atlantic Ocean. In order to compare smoke/aerosol coverage for the 1995 and 1997 fire seasons it is necessary to account for degradation in the GOES-8 visible channels since 1995. An offset representing a 10% degradation in the GOES-8 visible was included in the GOES-8 ASADA for 1997. This offset was based on information provided by the NOAA National Environmental Data Information Service (NESDIS) (M. Weinreb, personal communication, 1997).

Figure 3 shows a comparison of ASADA estimates of smoke/aerosol coverage for each day during the 1995 and 1997 fire seasons. The results for both years show a gradual increase in smoke coverage during the last half of July with maximum values in August and September (7.9 million km^2-1 September 1995; 7.3 million km^2-7 September 1997) corresponding to the peak in the burning season (see Figure 2). Several peaks in smoke/aerosol coverage observed in July include regions that were clear and may be attributed to the degradation offset used in 1997 (10%).

Figure 4 summarizes the distribution and relative intensity of smoke/aerosol (on a .5° grid) throughout the Amazon Basin and the South Atlantic Ocean for 1995 and 1997. Figure 4a, b shows the percentage of time the GOES-8 ASADA reported smoke/aerosol for a given location. In both years the regions most often effected by smoke were collocated with or downwind of the most intensive burning regions (see Figure 1). These composites show the highest smoke/aerosol occurrences and albedo estimates along the front range of the Andes Mountains in Brazil, Bolivia, and

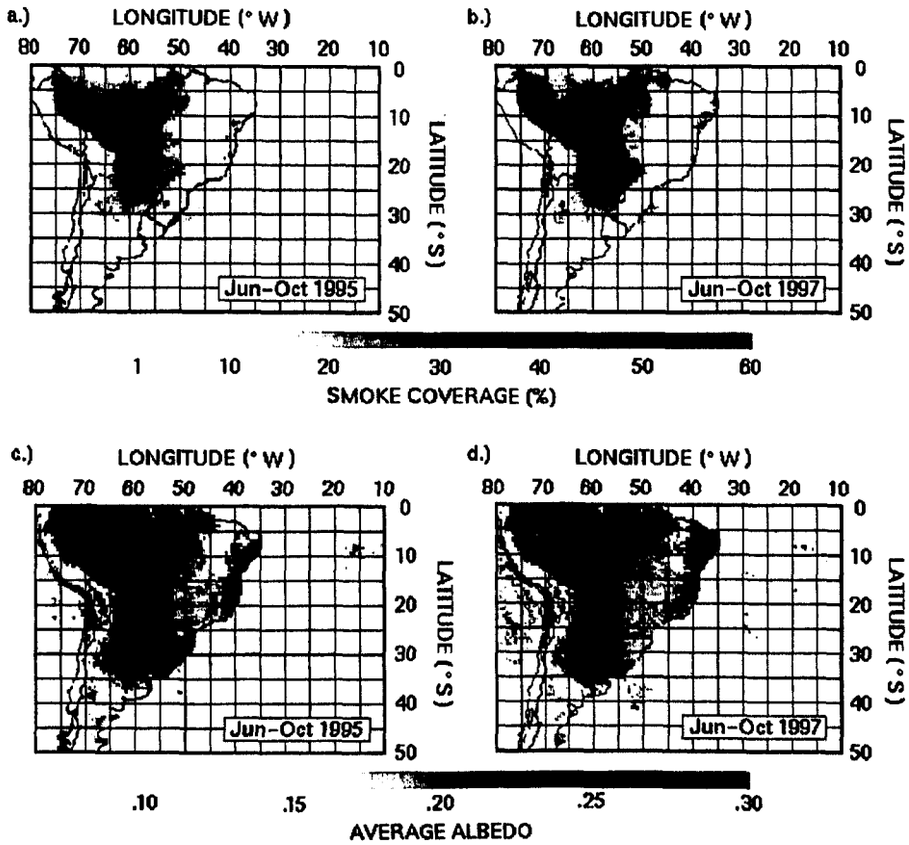

Figure 4. Composites (a) and (b) show the percentage of time a given area (on a .5° grid) was smoke covered from June through October in 1995 and 1997, respectively. Composites (c) and (d) show the average GOES-8 ASADA derived smoke albedo estimates for the same time periods.

Paraguay and along the boundary between forest and grassland in central Brazil. Transport over the Atlantic Ocean was observed in both years, although it was more pronounced in 1995. The seasonal average GOES-8 ASADA derived albedo estimates for 1995 and 1997 are depicted in Figure 4c, d, respectively. In both years the highest values are found in the states of Para, Mato Grosso, and Rondonia, Brazil; Bolivia; Paraguay (1995 only); Northern Argentina; and Uruguay where derived smoke albedo estimates are 2 to 3 times higher than clear background values. The GOES-8 ASADA derived albedo composite for 1995 shows slightly higher albedo estimates throughout the region, most notably in Rondonia, Brazil; Paraguay; Uruguay; and Northern Argentina. These composites closely reflect the similarities and differences in burning as observed in the GOES-8 ABBA for 1995 and 1997.

4. CONCLUSIONS

The GOES-8 ABBA and ASADA fire and smoke products for 1995 and 1997 show the utility of using geostationary satellites to characterize spatial, diurnal, and interannual trends in biomass burning throughout South America. The success of GOES-8 fire monitoring in South America suggests the need for a global geostationary fire monitoring effort. This will be possible with the launch of the Japanese Multi-functional Transport Satellite (MTSAT) in 1999 and the European METEOSAT Second Generation (MSG) satellite scheduled for launch in the year 2000. Together with the NOAA GOES and POES platforms and other NASA Earth Observing System (EOS) satellites, this suite of sensors will be able to effectively characterize biomass burning around the globe, separating diurnal changes in burning from seasonal and interannual trends.

5. REFERENCES

Menzel, W.P., and E.M. Prins, 1996: Monitoring biomass burning with the new generation of geostationary satellites. In Biomass Burning and Global Change, edited by J.S. Levine, pp. 56-64, The MIT Press, Cambridge, MA.

Prins, E.M., J.M. Feltz, W.P. Menzel, and D.E. Ward, 1998: An Overview of GOES-8 Diurnal Fire and Smoke Results for SCAR-B and the 1995 Fire Season in South America, submitted to SCAR-B special issue of JGR-Atmospheres.

Skole, D., and C. Tucker, 1993: Tropical deforestation and habitat fragmentation in the Amazon: satellite data from 1978 to 1988, Science, 260,1905-1910.

P.1.33A

CONFIRMATION OF HELMHOLTZ RECIPROCITY USING SCARAB SATELLITE DATA

Michel CAPDEROU *
LMD, Palaiseau, France

1. INTRODUCTION

The Helmholtz reciprocity principle is often invoked to derive the bidirectional reflectance distribution functions, then the anisotropic function, used for converting satellite radiance measurements into fluxes in Earth radiation budget satellite observation. This is only possible using satellites in low but non-sun-synchronous Earth orbit, and even in this case situations allowing reciprocity verification are rare.

2. BI-DIRECTIONAL REFLECTANCE AND THE RECIPROCITY PRINCIPLE

1.1 Bi-directional reflectance

To interpret the measured SW radiation (reflected solar radiation), we must consider the three angles of the Sun-Target-Satellite geometry: solar zenith angle θ_O, satellite viewing zenith angle θ, relative Sun-Earth scene-Satellite azimuth ϕ.
For each pixel, the ScaRaB SW-channel provides the radiance L (θ_O, θ, ϕ) and we define the bi-directional reflectance as (where E is the corrected normal solar irradiance):

$$\rho(\theta_O, \theta, \phi) = \frac{\pi L(\theta_O, \theta, \phi)}{E \cos \theta_O} \qquad (1)$$

1.2 Reciprocity principle applied to reflectance

In the field of remote sensing, the Helmholtz reciprocity principle (hereinafter abbreviated as HRP) is often applied to bidirectional reflectances (Suttles et al., 1988; Capderou and Kandel, 1995).
This theorem, first formulated by Helmholtz in 1883, was more recently analized by S. Chandrasekhar (1960). For the remote sensing studies, if we denote solar zenith angle, viewing zenith angle, and relative azimuth, in this order, in the reflectance expression, the above described principle of reciprocity may be written as:

$$\rho(\theta_O, \theta, \phi) = \rho(\theta, \theta_O, \phi) \qquad (2)$$

so, for a given relative azimuth, we can exchange the values of solar and viewing zenith angles without change of the reflectance value.

3. THE SCARAB DATA

3.1 ScaRaB instrument aboard Meteor-3-07

ScaRaB (Scanner for Earth Radiation Budget)
is a joint project of France, Russia and Germany (Kandel et al., 1994). This instrument is a four-channel scanner (Monge et al., 1991). Here we use solar channel (SW) data. The scanning is across track (orthogonal to direction of motion) with a swath of 97.82°. The pixel (instantaneous field of view) is 48 mrd x 48 mrd, corresponding to 58 km x 58 km at the nadir. Data were received from 24 February 1994 until the scanner failed on 05 March 1995. Thus we have one year of data. The Meteor-3-07 orbit (altitude: 1200 km, inclination: 82.56°) is polar non-Sun-synchronous. The orbital preces-sion leads to a shift of local time: 24 hours in 213 days (Capderou, 1995).
The ScaRaB/Meteor mission ensures follow-on of the Earth Radiation Budget Experiment (ERBE) (Barkstrom et al., 1989).

3.2 ScaRaB data

We restrict our study to clear sky over desert zones: *clear sky*, to be certain that clouds do not change the observed scenes, *desert*, because they have virtually no vegetation, relatively slow surface changes, and the atmosphere over hyper-arid regions is relatively stable.
For our studies on bi-directional reflectance, we use 1.25° x 1.25° areas, named DES for desert, so that four DES areas make up one ERBE area. We consider the four great warm

* *Corresponding author address*: Michel Capderou, Laboratoire de Météorologie Dynamique du CNRS, Ecole Polytechnique, 91128 Palaiseau, France; e-mail: capderou@lmd.polytechnique.fr

deserts of the planet: Sahara (SHR), Arabian Desert (ARA), Namib-Kalahari (NKL) and Australian Desert (AUS).
For each pixel we have a value for the three angles and radiance, and we compute the reflectance. Then, with a threshold for N_{pix} ($N_{pix} \geq 5$), we obtain the mean reflectance ρ , for each DES area, each overpass.

4. NORMALIZED ANISOTROPY PARAMETERS

4.1 Angular bins

In order to choose angular intervals to study HRP, we must define normalized quantities applying to the general anisotropic situation. Altough very fine angular intervals can characterize anisotropy in great detail, available cases will be too few. Conversely, excessively broad intervals yield large samples but no significant information. After computation of several cases, we choose for the different angular bins, 6° for θ_0 and θ, 18° for ϕ. These bins are respectively noted I, J, and K.

4.2 Definition of normalized anisotropy parameters

The Helmholtz reciprocity principle asserts that for certain pairs of viewing and illumination angles (reciprocity in solar and viewing zenith angles) reflectances should be identical. For perfectly isotropic reflectance (Lambertian reflectance, *i. e.* reflectance independent of any of the viewing or illumination angles) HRP is trivial. However, for non-isotropic reflectance, we can define a normalized anisotropy, comparing reflectances for any pair of viewing and illumination angles:

$$h(I', J', K'; I'', J'', K'') = \frac{\rho' - \rho''}{\frac{1}{2}(\rho' + \rho'')} \qquad (3)$$

with $\rho' = \rho'(I', J', K')$ and $\rho'' = \rho''(I'', J'', K'')$. In the general case, $h \neq 0$.

For a Helmholtz reciprocity pair ($I'=J''$; $J'=I''$; $K'=K''$) we shall write the same function as:

$$f(I', J', K') = h(I', J', K'; J', I', K') \qquad (4)$$

and this will be zero if HRP is verified. Thus in this special case the normalized anisotropy parameter can be characterized as a normalized departure from reciprocity: this function, f, is called reciprocity factor.

4.3 Study of the Helmholtz Reciprocity Principle

This study is based on data obtained for the four great deserts over the Earth, during one year, with the bin sizes seen above. For each DES area, we "fill" these (I, J, K) boxes, then we search, inside a month, the cases where the reciprocity conditions are verified.

If we plot f values versus angular bin, there is no correlation between reciprocity factor f and the angular bins I, J or K.

For each situation of reciprocity verification, we have one f value related to two reflectance values, ρ' and ρ''. If we plot f versus ρ', we obtain a cluster of points centered on f=0; the same holds for f versus ρ''. There is no correlation between reciprocity factor and reflectance.

5. COMPARISON BETWEEN SITUATIONS OF RECIPROCITY AND ARBITRARY SITUATIONS. STUDY OF THE "SHARPNESS"

5.1 Aim of this comparison

It is interesting to compare situations of HRP verification with arbitrary situations. If the reflection processes were lambertian, there should appear no difference between situation of reciprocity verification and any other situation, and standard deviations of these two distributions should be determined solely by measurement uncertainties.

5.2 Reciprocity factor f (case of HRP verification)

We distribute the f values in 1% intervals to obtain a normalized histogram, representing the normalized frequency of f. The derived graph shows a marked peak, centered on 0 value. The standard deviation $\sigma(f)$ is, in %, 4.37 for SHR, 3.21 for ARA.

5.3 Anisotropy factor h (general case)

We consider, for a given area and a given month, any two boxes (I, J, K) with the following reflectance values ρ' and ρ''. In this way, we obtain a very great number of h values, and the distribution of h is represented by a smoothed frequency graph.

5.4 Sharpness coefficient

The distribution of anisotropy factor h represents the most general case of correlation

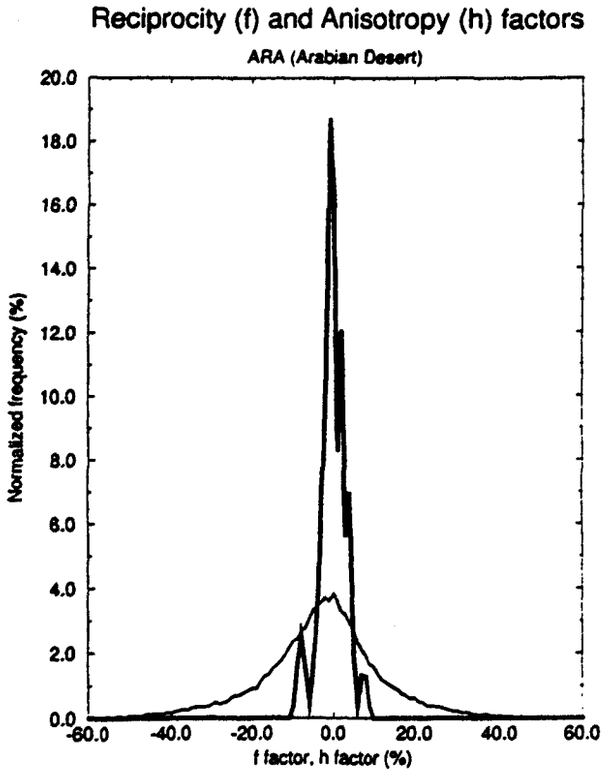

FIG. 1. Comparison of the reciprocity and anisotropy factors for ARA (Arabian desert). Normalized frequency (percent) of the distribution of the factors. Using all the ScaRaB data (March 1994 to February 1995), with bin sizes : 6° for I and J, 18° for K. Reciprocity factor f in bold solid line, anisotropy factor h in solid line.
Value of α, see eq. (5): $\alpha = 15.15 / 3.21 = 4.72$

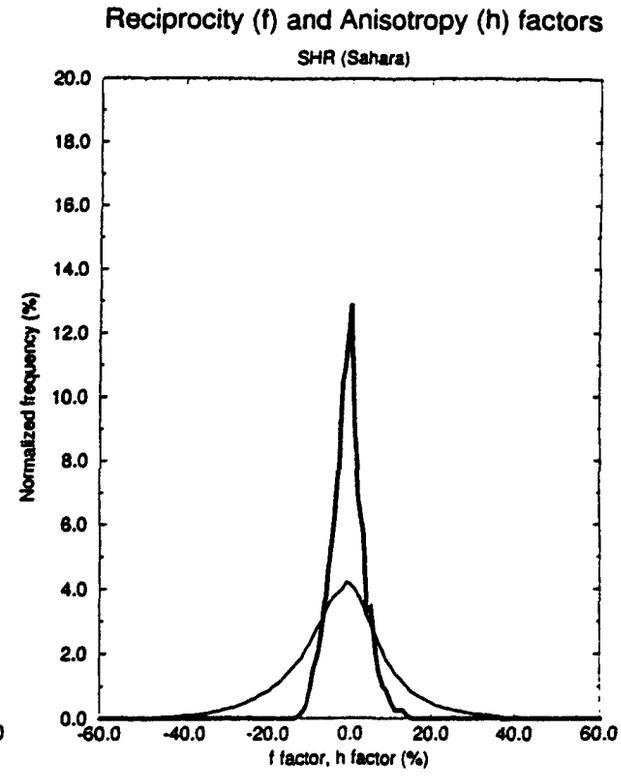

FIG. 2. The same as Fig. 1, but for SHR (Sahara).
Value of α, see eq. (5): $\alpha = 12.94 / 4.37 = 2.96$

between any two situations, as opposed to the distribution of reciprocity factor f, representing the correlation between two particular situations of HRP verification. Then we define the coefficient of "sharpness", α, as the ratio of the standard deviations of these two distributions:

$$\alpha = \frac{\sigma(h)}{\sigma(f)} \qquad (5)$$

The greater is α, the sharper is the f distribution against the flat h distribution.

We note a very high α value for ARA (Fig. 1), with α near to 5, high value for SHR (Fig. 2), with α equal to 3, and weaker values for NKL and AUS.

CONCLUSION

After choosing the size for the study areas (1.25° in latitude, 1.25° in longitude), the geotype (desert, clear-sky), the optimal size for the three angular bins (bin width: 6° for solar and viewing zenith angles, 18° for relative azimuth angle), we have obtained enough angular situation pairs allowing verification of the Helmholtz reciprocity principle.

The reciprocity factor, defined as relative difference between two reflectances obtained in reciprocity situation, proves quantitatively that reciprocity is very well verified with our observation conditions. The standard deviation of the reciprocity factor distribution is around 4% (for 33% of cases, HRP is verified at ± 1%, for 75% of cases, verified at ±5%). This verification is very clear for Sahara and Arabian Desert (SHR and ARA), less for the other deserts.

If we compare with the distribution of the anisotropy factor, relative difference between two reflectances obtained for an arbitrary angular situation pair, we see that this general distribution is very flat (the standard deviation is 3 to 5 times greater for reciprocity factor distribution). Therefore reciprocity pairs are distinctly different from arbitrary viewing/illumination geometry pairs. The conditions of reciprocity are therefore relevant.

The reciprocity principle being very well verified with satellite observations over desert, with clear sky, the use of this principle is justified to construct the anisotropic function from observations with a limited set of angles in the study of reflectance, at least for clear sky desert.

Acknowledgments.

For this paper (as for the precedent publications issued from the ScaRaB data) I thank very warmly Robert Kandel for helpful discussions and for reviewing the manuscript.

REFERENCES.

Barkstrom, B.R., E.F. Harrison, G.L. Smith, R.N. Green, J. Kibler, R. Cess, and the E.R.B.E. Science Team, 1989. Earth Radiation Budget Experiment (E.R.B.E.) archival and April 1985 results. *Bull. Amer. Meteorlog. Soc.*, **70**, 1254-1262.

Capderou, M. and R.S. Kandel, 1995. Determination of the shortwave anisotropic function for clear-sky desert scenes from Meteosat data. *J. Appl. Meteorol.*, **34**, 1349-1374.

Capderou, M., 1995. *Une année de ScaRaB (A year of ScaRaB) - Orbitographie et échantillonnage temporel pour le satellite Meteor-3-07/ScaRaB (Février 1994 - Mars 1995). Le logiciel IXION.* Note technique LMD n° 199 (Septembre 1995), 250 pp, 174 fig. & tables. Ecole Polytechnique, Palaiseau.

Chandrasekhar, S., 1960. Radiative Transfer, Dover Publications, New-York.

Kandel, R.S., J.L. Monge, M. Viollier, L.A. Pakhomov, V.I. Adasko, R.G. Reitenbach, E. Raschke, and R. Stuhlmann, 1994. The ScaRaB project: Earth radiation budget observations from the Meteor satellites. *Adv. Space Res.*, **14**, 1, 47-54.

Monge, J.L., R.S Kandel, I.A. Pakhomov, and B. Bauche, 1991. ScaRaB Earth radiation budget scanning radiometer, *Metrologia*, **28**, 261-284.

Suttles, J.T., R.N. Green, R., P. Minnis, G.L. Smith., W.F. Staylor, B.A. Wielicki, I.J. Walker, D.F. Young, V.R. Taylor, and L.L. Stowe, 1988. Angular Radiation Models For Earth-Atmosphere system. Vol. I : Shortwave radiation. NASA Ref. Publ. 1184. [NTIS 89N20587]

P1.34B

SATELLITE DATA ANALYSIS FOR EARTH RADIATION BUDGET (ERB) : 1. SIMULATION OF TIME SAMPLING ERRORS IN THE SHORTWAVE DOMAIN FOR VARIOUS SATELITTE ERB EXPERIMENTS.

P1 34B Michel Viollier, Arnaud Rodelet and Carsten Standfuss
Laboratoire de Météorologie Dynamique du Centre National de la Recherche Scientifique, Ecole Polytechnique, F-91128 Palaiseau, France.

1. INTRODUCTION

One of the inherent problem of the Earth Radiation Budget (ERB) satellite determination is the limited temporal sampling (only one or two observations a day and per satellite). Attempts to correct sampling errors were sought by physical models and by using two or three satellites (ERBE, Barkstrom *et al.*, 1989, CERES, Wielicki et al., 1996). The ScaRaB experiment (Kandel *et al.*, 1998) were on board only one satellite. The basic Monthly Time Space Averaging used in the ERB experiments has been described by Brooks *et al.*, 1986. In the shortwave (SW) domain the algorithm takes into account the insolation cycle (computed from the solar geometry) and the modeled angular albedo variations but not the meteorological (clouds) variations between the observations.

For many regions the random characteristics of the errors decrease the risk of biased results as far as the monthly average computations are concerned. But other regions show a pronounced coherent diurnal variation of clouds. In a broad sense low-level marine clouds (statocumulus) occur in the morning west of the continents (off Perou, California, Angola, ...), whereas high-level clouds occur in the afternoon and evening over moist convective regions over the continents. Consequences are large in the computation of the monthly mean of SW reflected flux : Haeffelin (1997) and Standfuss (1997) estimated to 40 Wm^{-2} the maximum errors for these specific regions by comparing ERBE with 1 to 2 and 3 satellites.

Hereafter we estimate these errors, in the SW domain, for sun-synchronous satellite mission as a function of the equatorial crossing local time. In a second paper (Standfuss and Viollier, this issue, P1 35A), we search how to correct these errors using auxiliary data (geostationary data, ISCCP, climatic data base).

2. MODELING TOOL

A specific software, called TIMSO (Time Integration of Multiple Satellite Observations) has been developed. The software package enables

- the calculation of satellite observation times as a function of the chosen circular orbit parameters and of the instrument characteristics (total field of view)
- the modelling of the diurnal cycle as a function of the simulated satellite observations (taken from a reference) per day, and a subsequent calculation of daily and monthly means,
- the comparison between daily/monthly means of the simulated satellite mission and those of a reference, representing truth.

As reference data serve the ERBE observations of December 1986 when three satellites (NOAA-9, NOAA-10, ERBS) obtained the highest temporal resolution of ERB satellite observations.

Apart from estimating the time sampling errors caused by the ERBE satellites NOAA-9, NOAA-10 and ERBS relative to the triple-satellite configuration (reference), several sun-synchronous single- and double-satellite missions are simulated to determine regional and global time sampling errors as function of the equatorial crossing time.

For the simulation of the orbit tracks, orbits are assumed as circular, which considerably reduces the computation costs without introducing important errors to the simulation results. Pixel centers are located and time-recorded assuming the mission instrument is a crosstrack fixed-azimuth scanner. The useful total field of view and altitude of the fictitious missions are chosen to yield orbit coverage and view angles comparable to ERBE. The local time of the observations and the solar zenith angle is then computed and used in the SW diurnal model.

The purpose of the SW diurnal model is to extrapolate flux from observation time t_{obs} to the 24 local hour boxes centered on the local half hour

t_h : 0030, 0130, .., 2330. The extrapolation equation (see Brooks *et al*, 1986) takes into account the predictable variation of the solar zenith angle and its influence on the albedo. These directional albedo variations depend upon the fraction of identified scenes within the considered region (four cloud cover ranges for a given surface type). If at least 2 SW observations are available two series of extrapolated flux estimations are computed, and the flux is linearly interpolated between the two observation hours.

3. VALIDATION

The algorithms and software are validated by comparing the ERBE 3 satellite results to our simulations, starting either from the true ERBE regional instantaneous means, or from the orbit calculations (full simulation). Both tests are successful : the standard deviation of the differences between reference and model is very low (0.4 $W.m^{-2}$). We didn't succeed to fully eliminate the remaining small deviations. This is probably due to unknown details in the ERBE algorithm, for example the way to interpolate the angular albedo variation. Nevertheless the remaining differences are small compared to the expected magnitude of time sampling errors

4. RESULTS

4-1 One satellite Mission

The differences between simulations of a sun synchronous mission with local time of ascending node (LTAN) between 0 and 24 and reference have been computed. The reference monthly means are shown on figure 1. From zero in the highest northern latitudes the reflected flux increases up to 300 $W.m^{-2}$, and more , in the southern polar region. In the tropical zone the highest values reveal clouds (ITCZ) and desert.

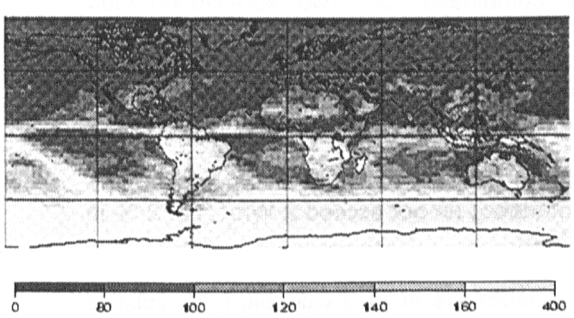

Figure 1 : Monthly mean of the regional shortwave reflected flux, determined from the 3 ERBE satellites for December 1986 (the last range of the gray scale has been expanded).

Figures 2,3, and 4 show the difference for LTAN=3, 9 and 12 local time. Clearly the afternoon orbit (LTAN 3 , figure 2) causes negative errors (< -20 Wm^{-2}) over marine stratus areas (off Peru, off Angola) : they don't sample the highest albedos of the morning cloudiness. On the contrary, the morning orbit (LTAN 9, figure 3) overestimates (>+20 $W.m^{-2}$) the flux in these areas. Errors of opposite sign are observed in continental areas (South America, South Africa) where convective cloudiness frequently occurs during the afternoon. All these errors are not observed for the noon orbits (figure 4) : it is suggested that for a local noon observation the asymmetrical diurnal deviations are balanced.

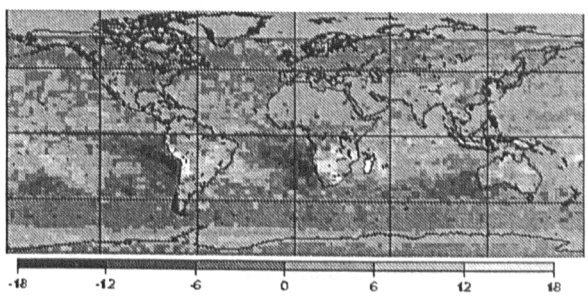

Figure 2 : Difference between simulations of a sun synchronous mission with local time of ascending node (LTAN) at 03. The largest errors of diurnal modeling are shown in black (< -20 Wm^{-2}) over marine stratus areas and white (> 20 Wm^{-2}) over continental convective cloudiness.

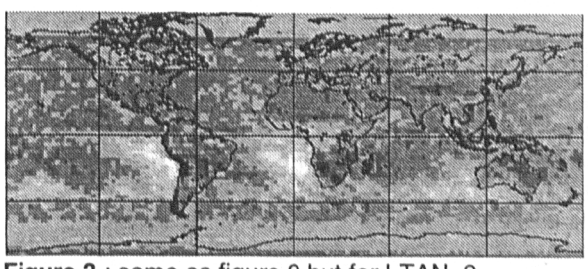

Figure 3 : same as figure 2 but for LTAN=9.

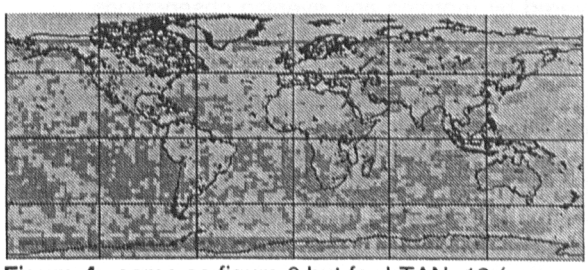

Figure 4 : same as figure 2 but for LTAN=12 (same gray scale as in figure 1).

The sun rise and sun set (LTAN 6 and 18) should not be recommended since they don't

provide valuable day-time measurement at latitudes higher than 40° in the winter hemisphere even though errors on the summer hemisphere and in low latitudes remain small.

Figure 5 summarizes the one-satellite conclusions showing the errors (global means and standard deviation) as a function of the local time of the ascending node. The global bias is balanced for near-noon orbits, and never exceed 2 Wm^{-2}. The standard deviation of regional errors varies between 1.7 Wm^{-2} for high-noon orbits and up to 6 Wm^{-2} for near-twilight orbits.

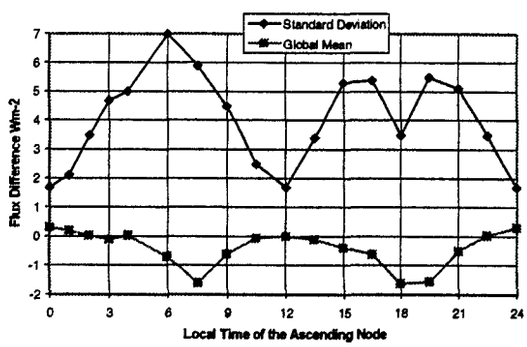

Figure 5 : Global bias of simulated sun-synchronous missions and standard deviation of regional means from the reference as a function of the local time of the ascending node (Wm^{-2})

The conclusions from figure 5 are :

- High-noon orbits (LTAN 0, 12) cause the smallest diurnal errors in the shortwave.
- Near-terminator orbits (LTAN → 6, 18) cause the most important errors.
- The terminator orbits (LTAN 6, 18) are specific since monthly means are based on an equivalent number of morning and evening observations. For December, the error for LTAN 18 is small because most regions are covered by morning and evening observations. LTAN 6 obtains no daylight observations at all in northern high latitudes, and the elevated standard deviation is explained by extraordinary errors in northern mid latitudes which are caused by insignificant half-light observations.
- LTAN 3 and LTAN 9 yield smaller standard deviations than the corresponding LTAN 15 and LTAN 21, respectively. This is due to the opposite diurnal observation characteristics in southern (summer) high latitudes (no observations at noon for LTAN 15 and LTAN 21).
- Thus, the above mentioned asymmetries can be understood as seasonally dependent, and an inverted asymmetry is expected for summer months of the northern hemisphere.

4-2 Two-satellite mission

In the same way the remaining errors corresponding to the combination of two satellites have been simulated : morning and noon orbits, morning and afternoon orbits, noon and afternoon orbits. The standard deviations of the regional errors are listed below.

sun- synchronous LTAN	Standard Deviation Wm^{-2}
09 + 12	1.7
09 + 15	1.1
12 + 15	2.3

It is shown that a 2-satellite mission combining either morning or afternoon observation with noon observations does not provide as valuable results as the coupled morning-afternoon orbits.

5. CONCLUSIONS

Our TIMSO software (time integration of multiple satellite observations) has been used to simulate the regional and global errors in the estimation of the SW reflected flux (monthly means). The following conclusions are drawn :

1 for a mission with only one sun-synchronous satellite, the observations close to noon (local time of ascending node : 0 or 12) yield the minimum errors : the standard deviation of the regional errors is equal to 1.7 Wm^{-2}).

2 for a combination of two sun-synchronous satellite missions, the symmetrical morning-afternoon observations reduce the errors to 1.1 $W.m^{-2}$. Other combinations of two satellites are not superior to the one-satellite case at noon.

3 the errors in the SW global mean due to the diurnal modeling do not exceed 2 Wm^{-2}, i.e. 2 % in relative term.

These results are at least valuable for a solstice month, such as December, since our tests are based upon experimental data from ERBE 1986 December.

ACKNOWLEDGEMENT : This investigation is supported by the European Space Agency under ESTEC Contract # 12173/97/NL/CN.

REFERENCES

Barkstrom, B.R., E.F. Harrison, G.L. Smith, R. Green, J. Kibler, R. Cess, and the ERBE Science Team, "Earth Radiation Budget Experiment (ERBE) archival and April 1985 results", 1989 : *Bull. Amer. Meteorol. Soc.*, **70**, 1254-1262.

Brooks, D.R., E. H. Harrison, P. Minnis, J. T. Suttles, and R. Kandel, 1986: Development of Algorithms for Understanding the Temporal and Spatial Variability of the Earth's Radiation Balance, *Rev. Geophys.*, **24**, 2, 422-438.

Haeffelin, M., R. Kandel, and C. Stubenrauch, 1997 : Improved diurnal interpolation of reflected broad-band shortwave observations using ISCCP data, *J. Atmos. Oceanic Technol.*, submitted, being revised.

R. Kandel, M. Viollier, P. Raberanto, J.Ph. Duvel, L.A. Pakhomov, V.A. Golovko, A.P. Trishchenko, J. Mueller, E. Raschke, R. Stuhlmann, and the International ScaRaB Scientific Working Group (ISSWG) The ScaRaB Earth Radiation Budget Dataset, *Bulletin of the American Meterological Society*, in press.

Standfuss, C., 1997 : Synergie von Satellitendaten am Beispiel der Modellierung des Tagesganges der planetaren Strahlungsbilanz. GKSS Report 97/E/24, 103 pp. [available from GKSS Forschungszentrum Geesthacht, Bibliothek, Postfach 1160, D-21494 Geesthacht, Germany].

Wielicki, B.A., *et al.*, 1996 : Clouds and the Earth's radiant energy system (CERES): an Earth Observing System experiment, *Bull. Amer. Meteor. Soc.*, **77**, 853-868.

P1.35A SATELLITE DATA ANALYSIS FOR EARTH RADIATION BUDGET (ERB): 2. SUPPORT OF THE SHORT-WAVE DIURNAL INTERPOLATION AND EXTRAPOLATION PROCEDURE (DIEP) USING MEASUREMENTS FROM GEOSTATIONARY SATELLITES.

Carsten Standfuss and Michel Viollier *
Laboratoire de Météorologie Dynamique du C.N.R.S., Palaiseau, France.

1. INTRODUCTION

The poor time sampling from low polar orbits constitutes a main error source for regional monthly means of the short-wave (SW) component of the Earth Radiation Budget. Time sampling errors reach, dependent upon the orbit characteristics, up to $40Wm^{-2}$ in regions characterised by a coherent diurnal cycle of cloud cover fraction. The Earth Radiation Budget Experiment ERBE (Barkstrom et al., 1989), the Scanner for Radiation Budget ScaRaB (Kandel et al., 1998) and the Clouds and the Earth's Radiant Energy System CERES (Wielicki et al., 1996) are contributing (with interruptions) to the time series of ERB measurements beginning in 1985. Long-term time series of space-borne ERB measurements are essential with respect to the analysis of the inter-annual climate variability, the understanding of cloud-radiative interactions and climate modelling purposes. However, the time sampling error compromises its value, in particular by masking inter-seasonal and inter-annual climate variability.

The magnitude of time sampling errors for both ERB components and a variety of orbit characteristics have been estimated in numerous studies, e.g. Minnis and Harrison (1984), Rieland and Raschke (1991), analysing observations from geostationary satellites in at least 3-hourly time resolution. However, operational algorithms for correcting these errors have not been established.

We present two methods to support the conventional diurnal interpolation and extrapolation procedure (DIEP) by incorporation of diurnal information on visible radiances or cloud cover fraction provided by measurements of geo-stationary satellites. In different approaches, the B2, D1 and D2 data sets of the International Satellite Cloud Climatology Project (ISCCP) are used. These methods are inter-compared and validated on the base of January 1987 ERBE results which are hardly affected by time sampling errors due to a 3-satellite configuration during the first two decades of the month.

* *Corresponding author address:* Carsten Standfuss, Laboratoire de Météorologie Dynamique / C.N.R.S., Ecole Polytechnique, F-91128 Palaiseau, France; e-mail: standfuss@lmd.polytechnique.fr

2. THE ERBE-DIEP (SW)

Described by Brooks et al. (1986), the ERBE-DIEP in the short-wave spectral domain converts the available instantaneous regional flux estimates per day and region (2.5°×2.5°) into the daily mean flux. To extrapolate an instantaneous flux, it is taken into account: (1) the diurnal cycle of the incoming solar flux, (2) the directional albedo variation with the solar zenith angle for 12 possible scene types (composed out of 4 cloud cover ranges and 5 surface types). In case of several measurements per day, the independently extrapolated fluxes are linearly interpolated between successive observations. Hence, in case of one measurement per day, very common for single-satellite missions, meteorological variations of neither the cloud cover fraction nor the cloud reflectivity are taken into account.

In spite of this obvious shortcoming, the ERBE-DIEP has been used for the calculation of daily and monthly regional means for the entire operational period of ERBE (1985-1990) with varying orbit characteristics as well as for the first ScaRaB mission on Meteor 3-7 (1994-1995).

Unless future projects are designed as multi-satellite missions, any attempts to improve the ERBE-DIEP must replace the assumption of diurnally constant meteorology. This must be done by adding diurnal information either directly of the planetary albedo, or indirectly of cloud parameters, e.g. the cloud cover fraction or the clouds' optical thickness.

3. DIEP-B2

Diurnal information on parameters relevant to the ERB can be obtained from measurements of geostationary origin. A first attempt following up Standfuss et al. (1996) is using diurnal albedo information retrieved from measurements in the visible spectral range (VIS) of the Meteosat-B2 data set, i.e. a sampled version of original images in 3-hourly temporal resolution and in a spatial resolution of approximately 30km×30km at nadir. The retrieval of the planetary albedo from Meteosat B2 data consists of the following steps.

- Calibration of the Meteosat VIS-signal with respect to solar (broadband) radiances according to Vesperini and Fouquart (1994). This step combines the calibration to VIS-radiances and the spectral correction from the visible to the short-wave range.
- Scene identification corresponding to the ERBE cloud cover range classification by determining the effective cloud cover on the base of monthly, 3-hourly minimum VIS images (representing the clear-sky state) and modelled VIS radiances representing average overcast conditions.
- Anisotropy correction (i.e. radiance to flux conversion) by means of the ERBE bi-directional reflectance functions (Suttles et al., 1988). The distinct anisotropy factors have been interpolated within pre-defined angular bins to account for the fixed viewing geometry from geostationary platforms.
- Application of the ERBE-DIEP. Since Meteosat observations are available once per 3 hours, the assumption of constant meteorology is almost eliminated.

A comparison between monthly means of the reflected short-wave flux for January 1997, independently calculated from Meteosat-B2 and ERBE (3 satellites) yields a rather close correspondence. Differences are slightly scene dependent, which is probably due to scene independent spectral correction of Meteosat VIS-radiances. Nevertheless, the standard deviation between regional monthly means amounts to 9.8 Wm^{-2} which only slightly exceeds the expected magnitude for time sampling errors of single satellite ERB missions.

Despite obvious disadvantages of the Meteosat albedo retrieval due to the incomplete coverage of the solar spectrum and due to the fixed viewing geometry, valuable information on the diurnal variability can be extracted.

DIEP-B2 considers the diurnal cycle of the planetary albedo retrieved from Meteosat-B2 in synergy with instantaneous ERB observations. The basic idea is to correct the ERBE reflected short-wave flux extrapolated from observation time t_{obs} to any other time t of the day $F_{SWE}(t)$ by the ratio between the Meteosat estimate $F_{SWM}(t)$ and the extrapolated flux $F'_{SWM}(t)$ resulting from a virtual Meteosat observation at t_{obs}. So the ERBE time sampling error is superimposed to the Meteosat estimate in $F'_{SWM}(t)$.

$$F_{SW}(t) = F_{SWE}(t) \cdot \frac{F_{SWM}(t)}{F'_{SWM}(t)} \qquad (1)$$

In general, Meteosat and the direct ERB observation yield different scene identifications at t_{obs}. However, extrapolated values at t depend upon the scenes identified at t_{obs}. By consequence, the ratio $F_{SWE}(t)/F'_{SWM}(t)$ introduces an error due to inconsistent scene identifications of the two systems. Thus, an extended approach of DIEP-B2 applies a 4-dimensional formulation of equation (1) separately for each scene type.

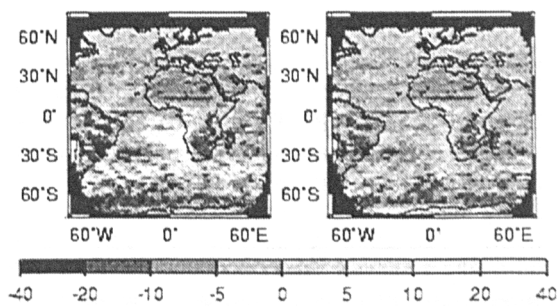

Figure 1 : Monthly mean difference of the regional short-wave reflected flux for January 1987 in [Wm^{-2}]. Left : ERBE NOAA10 - ERBE 3Sat, right: DIEP-B2 NOAA10 - ERBE 3Sat.

Results obtained by this advanced approach are illustrated for January 1987 in figure 1. On the left, the monthly mean difference of the reflected short-wave flux calculated from ERBE-NOAA-10 observations (approximately at 7 :30 local time) and all available observations from NOAA-9, NOAA-10 and ERBS is shown. It represents the time sampling error caused by morning observations because the time sampling error for the 3-satellite configuration can be regarded as small. Main patterns are overestimated fluxes for marine stratocumulus off Angola/Namibia due to a coherent diurnal decrease of cloud cover during daylight hours and inverse errors for parts of Africa and South America where a diurnal maximum of cloud cover is expected in the second half of the day due to moist convection.

On the right, DIEP-B2 has been applied to ERBE-NOAA-10 observations. Considerable corrections can be noticed for marine stratocumulus, where errors up to +40Wm^{-2} are reduced to less than +10Wm^{-2}. Errors of the opposite sign indicating convective cloudiness in the afternoon are corrected with a slightly smaller efficiency. Apart from a few regions in high southern latitudes, no error amplification can be observed.

The standard deviation of regional monthly errors decreases from 8.7 to 5.6 Wm^{-2}, whereas the bias averaged over the entire Meteosat disk intensifies from -2.0 to -3.4 Wm^{-2} due to the higher efficiency

of DIEP-B2 in stratocumulus regions. Nevertheless, DIEP-B2 reduces the mean square error by 46%.

The assessment of DIEP-B2 in application to NOOA-9 , i.e. afternoon observations, confirms the results for NOAA-10 with respect to the characteristic of the correction pattern and the magnitude of error reduction.

4. DIEP-ISCCP D1/D2

In search of a globally applicable but little costly method to correct for time sampling errors of the ERB short-wave component, a DIEP using cloud cover data of the ISCCP D1/D2 data set in synergy with ERB observations has been established, following up the method of Haeffelin et al. (1998) using ERBE and ISCCP C2 cloudiness data. ISCCP-D data (Rossow et al., 1996) provide vertically resolved cloud parameters in a spatial resolution of approximately 280km×280km, principally retrieved from the global net of operational geostationary satellites. D1 data provide 3-hourly observations, D2 data the corresponding monthly mean diurnal cycle.

Though attractive in view of the relatively small data amount, the physical approach for DIEP-ISCCP remains necessarily approximate, because ISCCP data does not enable a direct retrieval of the planetary albedo. However, cloud cover variations prescribed by ISCCP data can be used to replace the assumption of constant meteorology within the ERBE-DIEP. Opposite to the similar approach from Haeffelin et al. (1998), we attempt to match the ERBE scene type fractions with the corresponding ISCCP cloud cover fraction at t_{obs}. The fundamental steps of DIEP-ISCCP are:

- Explicit determination of the cloud cover for each ERBE scene type as a function of ERBE scene type fraction and ISCCP cloudiness.
- Variation of the ERBE scene type fraction according to the ISCCP cloud cover variation.

Thus, cloud cover variations are taken into account by a diurnally variable weighting of the scene albedo appointed to each ERBE scene type at t_{obs}.

DIEP-ISCCP is applicable to both, D1 and D2 data. The validation results for January 1987 ERBE-NOAA-10 observations are shown in figure 2 accordingly to figure 1 for DIEP-B2 (initial error at the top, errors left by DIEP-ISCCP D1 and D2 at the centre and bottom, respectively).

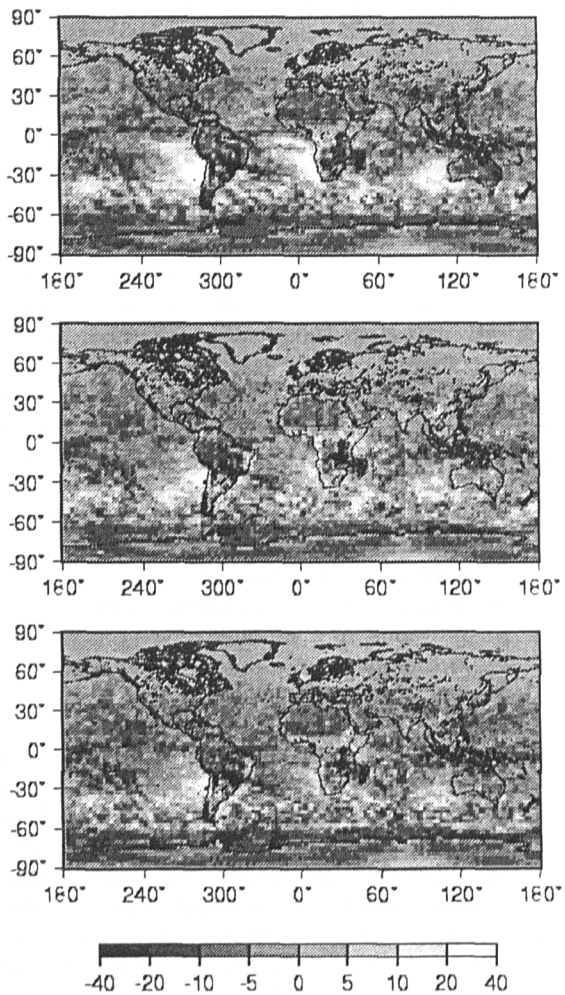

Figure 2: Monthly mean difference of the regional short-wave reflected flux for January 1987 in [Wm^{-2}]. Top: ERBE NOAA-10 - ERBE 3Sat, centre: DIEP-ISCCP D1 NOAA-10 - ERBE 3Sat, bottom: DIEP-ISCCP D2 NOAA 10 - ERBE 3Sat.

Errors in stratocumulus areas off the continental west coasts are corrected for to a smaller extent than by DIEP-B2. More unsatisfactory, the algorithm appears nearly insensitive to errors due to convective cloud development in the afternoon in most parts of South America and Africa.

An inter-comparison between D1 and D2 (including results for ERBE-NOAA-9, not shown) reveals that DIEP-ISCCP D2 corrects better for errors in stratocumulus regions, but worse in regions characterised by a more incoherent and inverted diurnal cycle of cloud cover. This is comprehensible since the averaged diurnal cycle does not represent incoherent variations with regard to their non-linear influence on the planetary albedo.

On global scale, the mean square error is reduced by 27% and 11% by DIEP-ISCCP D1 and D2, respectively. Bias and standard deviation amount to -2.4±7.9Wm^{-2} (D1), -4.3±8.0Wm^{-2} (D2) and -3.2±9.1Wm^{-2} (ERBE-DIEP).

5. CONCLUSION

Two different approaches to improve well-known shortcomings of the conventional ERBE-DIEP in the short-wave spectral domain are presented.

DIEP-B2 uses short-wave broadband fluxes retrieved from Meteosat VIS observations on pixel scale to prescribe the diurnal shape of albedo variation relative to the available ERB observation. It obtains important error reductions on global and regional scale. Global applicability can be achieved by using the ISCCP-B3 data set. However, the data processing appears relatively costly for an operational application to any ERB satellite experiment.

Less costly, DIEP-ISCCP approximates the diurnal variation of the planetary albedo from regionally averaged diurnal cycles of cloud cover relative to the ERBE scene identification. Its global efficiency is significantly smaller than that of DIEP-B2. More complex approaches, especially considering the ISCCP cloud types in place of the total cloud cover have been investigated by Haeffelin et al. (1998). Even though valuable improvements are stated, in particular for marine stratocumulus regions, the global performance appears limited for all considered methods.

ACKNOWLEDGEMENT: This investigation is supported in parts by the European Space Agency under ESTEC Contract # 12173/97/NL/CN.

REFERENCES

Barkstrom, B.R., E.F. Harrison, G.L. Smith, R. Green, J. Kibler, R. Cess and the ERBE Science Team, 1989: Earth Radiation Budget Experiment (ERBE) archival and April 1985 results.
Bull. Am. Met. Soc., **70**, 1254-1262.

Brooks, D.R., E.H. Harrison, P. Minnis, J.T. Suttles and R. Kandel, 1986: Development of algorithms for understanding the temporal and spatial variability of the Earth's radiation balance.
Rev. Geophys., **24**, 2, 422-438.

Haeffelin, M., R. Kandel and C. Stubenrauch, 1998: Improved diurnal interpolation of reflected broad-band shortwave observations using ISCCP data.
J. Atmo. Oce. Tech., submitted, revised.

Kandel, R., M. Viollier, P. Raberanto, J.P. Duvel, L.A. Pakhomov, V.A. Golovko, A.P. Trishchenko, J. Müller, E. Raschke, R. Stuhlmann and the International ScaRaB Scientific Working Group (ISSWG), 1998: The ScaRaB Earth radiation budget dataset.
Bull. Am. Met. Soc., in press.

Minnis, P. and E.F. Harrison, 1984: Diurnal variability of regional cloud and clear-sky radiative parameters derived from GOES data, III, November 1978 parameters.
J. Clim. Appl. Meteorol., **23**, 1032-1051.

Rossow, W.B., A.W. Walker, D. Beuschel and M. Roiter, 1996: International Satellite Cloud Climatology Project (ISCCP); Description of new cloud datasets.
WMO/TD-No. 737, World Climate Research Program (icsu and WMO), Geneva, February 1996, 115pp.

Rieland M. and E. Raschke, 1991: Diurnal variability of the Earth radiation budget : Sampling requirements, time integration aspects and error estimates for the Earth Radiation Budget Experiment (ERBE).
Theor. Appl. Met., **32**, 826-843.

Suttles, J.T., R.N. Green, P. Minnis, G.L. Smith, W.F. Staylor, B.A. Wielicki, I.J. Walker, D.F. Young, V.R. Taylor and L.L. Stowe, 1988: Angular radiation models for Earth-atmosphere system, Volume I - Shortwave radiation.
NASA reference publication 1184, 144pp.

Standfuss, C., E. Raschke, R. Stuhlmann and V. Jost, 1996: Earth Radiation Budget - General purpose data base.
ZMK Report No.A27, University of Hamburg, ESTEC contract No. 11336/95/NL/CN, 82pp.

Vesperini, M. and Y.Fouquart, 1994: Determination of broad-band shortwave fluxes from the Meteosat visible channel by comparison to ERBE.
Beitr. Phys. Atm., **67**, 121-132.

Wielicki, B.A. , B.R. Barkstrom, E.F. Harrison, R.B. Lee III, G.L. Smith and J.E. Cooper, 1996 : Clouds and the Earth's radiant energy system (CERES): an Earth Observing System experiment.
Bull. Am. Met. Soc., **77**, 853-868.

P1.36B

REMOVING SATELLITE EQUATORIAL CROSSING TIME BIASES FROM THE DAILY GLOBAL OUTGOING LONGWAVE RADIATION DATASET

Lisanne E. Lucas and Duane E. Waliser*
Institute for Terrestrial and Planetary Atmospheres
State University of New York, Stony Brook, NY

John E. Janowiak
National Centers for Environmental Prediction /National Oceanic and Atmospheric Administration
Silver Spring, MD

Brant Liebmann
Cooperative Institute for Research in Environmental Sciences
University of Colorado, Boulder, CO

1. INTRODUCTION

For the last 24 years, NOAA's fleet of polar-orbiting satellites have been sending back daily information on the outgoing longwave radiation (OLR) of the Earth. There have been 12 satellites over this 24 year period, each with its own unique orbital characteristics, such as equatorial crossing time (ECT) and orbital drift rate. (Figure 1) This dataset has been used in a multitude of climatological studies including studies on tropical circulation (convection), the El Niño / Southern Oscillation (ENSO) phenomenon, and the Earth's radiation budget. As far back as 1983, Gruber and Krueger (1984) pointed out that changes in a satellite's ECT will introduce significant biases in diurnally varying quantities, such as OLR. In a recent study of a tropical subset of monthly OLR Waliser and Zhou (1997) show that transitions between satellites with different ECTs introduce abrupt changes as high as 16 W m^{-2}. Although many of the climatological studies using OLR have proven invaluable, proper interpretation of the low-frequency components of the data could be limited by the presence of biases of the order 16 W m^{-2}. Therefore, it is imperative to ensure that the OLR dataset is kept as accurate as possible.

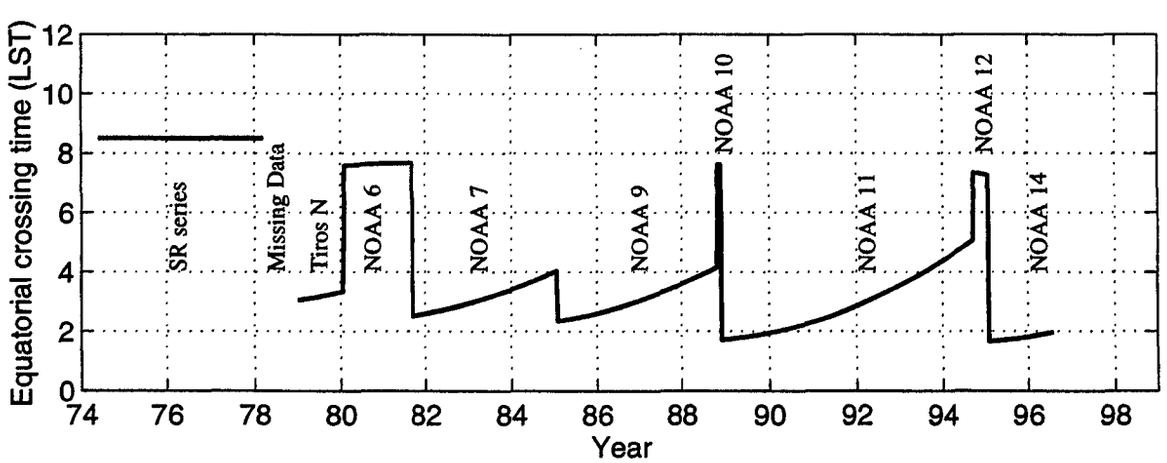

Figure 1. Satellite Equatorial Crossing Times (Local Standard Time)

Eigen analysis, like the empirical orthogonal function (EOF) analyses done by Chelliah and

* *Corresponding author address*:

Duane E. Waliser, Institute for Terrestrial and Planetary Atmospheres, SUNY, Stony Brook, NY 11794-5000; waliser@terra.msrc.sunysb.edu

Arkin (1992) and Waliser and Zhou (1997), has been used previously to isolate spatial loading patterns that are described as "satellite modes." These modes exhibit a strong loading over land and a weaker loading of the opposite sign over the ocean. The time-dependent amplitudes associated with these modes fluctuate with the changes in the satellite ECTs. Waliser and Zhou (1997) successfully used their analysis technique to remove the ECT bias from a tropical subset (30° N - 30° S) of the monthly OLR data. This study presents the preliminary results of utilizing these techniques to remove ECT biases from the daily, global OLR dataset, and the plans for the incorporation of this correction method into a continuos, operationally produced, corrected OLR dataset.

2. METHOD

The input data for this procedure is the "raw" 2.5° X 2.5° gridded twice-daily (denoted as A.M. and P.M.) satellite dataset produced by NCEP/NOAA. The dataset is 8111 days long, from 01 June 1974 to 20 August 1996. Within this period there is a nine month data gap from 17 March 1978 to 31 December 1978 due to satellite failure.

The correction process begins with a check of the data for missing and/or bad values. This quality assurance test isolates data of suspect quality and marks them as "missing" so that they can be replaced by interpolated values. Using the technique developed by Liebmann and Smith (1996), a series of interpolations are conducted to fill in the missing data. The first interpolation is made temporally, but only if there is sufficient "good" data before and after the missing point. The second interpolation is made spatially, with a similar constraint in the spatial domain for "good" data. This is repeated, decreasing the tolerance for "good" data points with every pass until all values are filled. This method is superior to the traditional spatial-only interpolation used by NCEP because for instances where an entire satellite swath (~ 1500km in width) is missing, the error resulting from interpolating over time at a given point is typically much smaller than the error resulting from interpolating across space at a given time.

Once all of the missing data are filled (except for the nine month gap), the A.M. and P.M. values are averaged to create daily values. The annual cycle is then computed based on the entire length of the dataset. Anomalies are computed with respect to the annual cycle, and ten-day area-weighted averages are created from the anomalies. Ten-day averages are used in order to reduce the influence of synoptic variability that could hinder the identification of the low-frequency satellite bias.

The isolation of the actual pattern and the magnitude of the satellite bias is achieved by rotated empirical orthogonal function (REOF) analysis of the area-weighted 10-day anomaly OLR dataset. The unrotated EOF analysis, by definition, acts to maximize for each mode, the variance explained over the entire analysis domain. The first mode returned, therefore, contains the maximum variance that a single mode can account for, and the second mode, contains the highest variance that a single mode can account for and still be orthogonal to the first mode, and so on. This makes the resulting EOF modes very sensitive to domain size and spatial resolution. Rotation of the EOF modes stabilizes the spatial loading, and provides a more physical interpretation. For more information on EOF and rotated EOF analysis refer to Richman (1986) or Waliser and Zhou (1997). This procedure also extracts a series of time-dependent amplitudes for each mode. A polynomial regression of the amplitudes of the satellite mode and the periods of precisely known ECTs is made to determine a functional relationship between the two. This relationship is used together with the spatial loading of the satellite bias mode to model the ECT bias and extract it from the satellite dataset.

3. PRELIMINARY RESULTS

The first four modes of the REOF analysis account for 14.3% of the anomaly variance. The spatial loadings for the first two modes have strong east-west dipoles located in the Tropics. These modes strongly resemble ENSO and ENSO-related phenomena. The third mode is also a dipole, and is localized in the tropical western Pacific and Indian Oceans, somewhat reminiscent of the Madden-Julian oscillation. The fourth mode shows some land-sea contrast, but also contains signatures of the intertropical convergence zone (ITCZ) and South Pacific convergence zone (SPCZ).

The fifth mode (Figure 2) isolates the artificial variability associated with the changing ECTs. It has the characteristic spatial loading pattern that is described by Chelliah and Arkin (1992) and Waliser and Zhou (1997). It accounts for 2.5% of the anomaly variance in the entire dataset. Note the strong positive loading over the equatorial land masses and the negative loading over the ocean.

The time series for mode five is shown in Figure 3. It is evident that there is a good correlation with the low-frequency variations that are associated with changes in the ECT of the

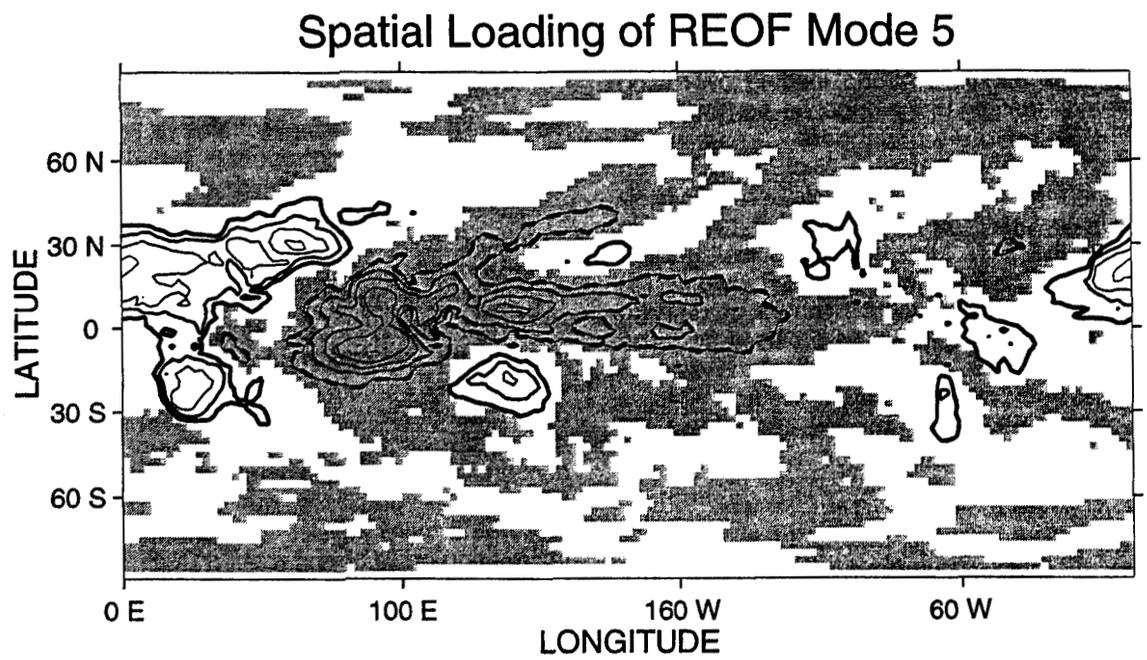

Figure 2. Spatial loading pattern of satellite bias mode. Gray areas denote negative values. Contour lines are placed at 2 W m^{-2} intervals. The zero line and the coastline have been omitted.

satellite. The thick line in Figure 3 is based on a third order polynomial regression between the precisely known A.M. ECT of each satellite and the amplitude of the mode five time series. This relationship has a correlation of 0.57 for 781 points. (Figure 4) The amplitude, evaluated for each satellite's exact crossing time, will be referred to as the "synthetic amplitude". The synthetic amplitude multiplied by the spatial loading gives the time series of the bias at each grid point.

The maximum spatial loading values are centered in the Sahara Desert region (near 20° N 0° E) and range from +5.8 to +7.5 W m^{-2}. The minimum spatial loading values are centered in the eastern Indian Ocean (4° S 90° E) ranging from -7.5 to -9.3 W m^{-2}. Using these values and the synthetic amplitude, the maximum ECT bias for land is 7.8 W m^{-2}, and the maximum bias in the ocean is 9.6 W m^{-2}.

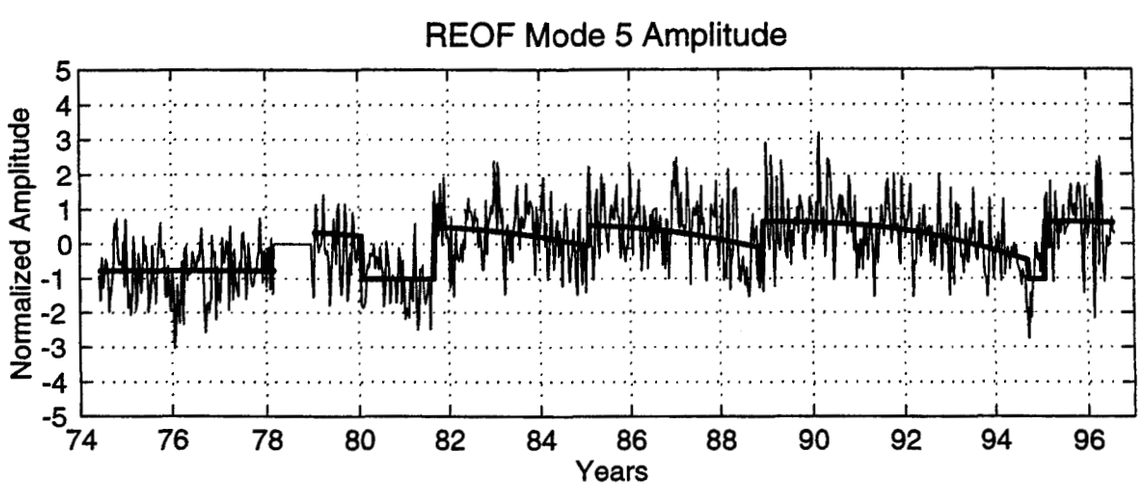

Figure 3. Time series of Mode 5 of the REOF analysis. The thick line is the third order best-fit polynomial created from Figure 4.

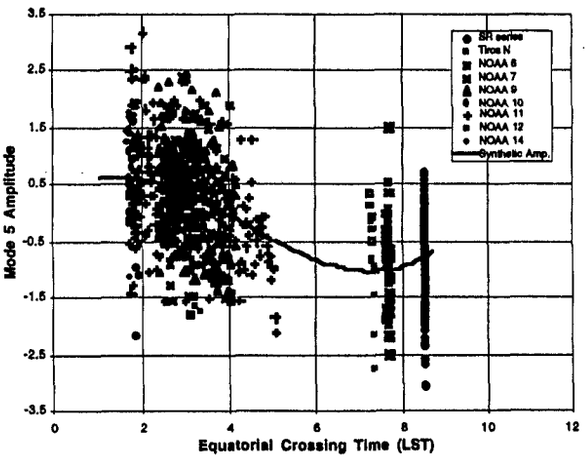

Figure 4. Scatterplot of A.M. ECT vs. the REOF Mode 5 amplitude. The solid line is the third order polynomial best-fit regression. (N=781; Correlation = 0.57)

4. FUTURE WORK

The maximum calculated bias of 9.6 W m^{-2} seems low when compared to previous studies. This suggests that further investigation of the other modes is needed before the actual removal of the bias can be done. Further study is also needed to determine the most effective time averaging that will isolate the satellite bias while still suppressing synoptic variability. In addition, the input dataset used for this study spans the period from 01 June 1974 to 20 August 1996. We plan to extend this dataset to the present and perform a reanalysis with the additional data. This should help to better establish the regression relationship for deriving the synthetic amplitude.

From the bias-corrected daily dataset, pentad and monthly bias-corrected datasets will be derived. Additionally, the final correction procedures will be incorporated into an operational method to correct new daily OLR data as it becomes available and to append it to the final bias-corrected datasets. These datasets will be available in the future on NCEP's world wide web page for public access.

Acknowledgments

Support for this project is provided jointly by National Oceanic and Atmospheric Administration (NOAA) and National Aeronautical and Space Administration (NASA).

References

Chelliah, M., and Arkin, P., 1992: Large-Scale Interannual Variability of Monthly Outgoing Longwave Radiation Anomalies over the Global Tropics. *Journ of Climate*, **5**, 371-389

Gruber, A., and Kruger, A., 1984: The Status of the NOAA Outgoing Longwave Radiation Data Set. *Bull. Amer. Meteor. Soc.*, **65**, 958-962.

Liebmann, B., and Smith, C. A., 1996: Description of a Complete (Interpolated) Outgoing Longwave Radiation Dataset. *Bull. Amer. Meteor. Soc.*, **77**, 1275-1277.

Richman, M. B. 1986: Rotation of Principal Components. *Journal of Climate*, **6**, 293-335.

Waliser, D. E., and Zhou, W., 1997: Removing Satellite Equatorial Crossing Time Biases from the OLR and HRC Datasets. *Journal of Climate*, **10**, 2125-2146.

P1.37A

APPLICATION OF BROADBAND FLUXES FROM SCARAB AND AVHRR NARROWBAND RADIANCES FOR BALTEX AND MAGS

R. Hollmann[1], J. Feng[2], J. Mueller[1], H.G. Leighton[2], R. Stuhlmann[1]
[1] GKSS Research Centre, Geesthacht, Germany
[2] McGill University, Montreal, Canada

1. ABSTRACT

A strong emphasis of MAGS and BALTEX is to study the energy and water cycle with its responsible cloud-radiation interactions. Within these regional scale experiments, regional models are in use, which have to be validated. The disadvantage in case of earth radiation budget at the top of the atmosphere, measured from well calibrated instruments on low earth orbiting satellites is the coarse time sampling of roughly two overpasses per day over a given site. To overcome this disadvantage auxiliary data of the operational satellites have to be used to improve the time sampling. Their narrowband radiances have to be converted to broadband fluxes for synergy with the ERB data. In this paper we discuss two different approaches for a narrow to broadband conversion, based on measurements from the ScaRaB instrument. We demonstrate their capability and usefulness and we present first results of their application.

2. INTRODUCTION

The objective of the Global Energy and Water cycle Experiment (GEWEX) is to make available reliable tools for analysing and predicting the complete energy and water cycle of our climate system on both, global and regional scales (WMO, 1990). For regional scales, this work is done within five GEWEX continental scale experiments of which two are the Baltic Sea Experiment (BALTEX) (Raschke et al., 1998) and the Mackenzie GEWEX Study (MAGS). For these experiments, special regional models are being applied, which have to be validated against available surface and satellite measurements. As part of this validation, we use data from the well-calibrated Scanner for Radiation Budget (ScaRaB) experiment to compare regional satellite estimates of the top of the atmosphere (TOA) earth radiation budget (ERB) over the BALTEX and MAGS areas against that calculated by the Regional Scale Model (REMO). Since the variability in the regional TOA ERB is mostly determined by the interaction of clouds with radiation, such a comparison gives inside into reliability of the model representation of clouds. The ScaRaB experiment (Kandel et al., 1998), a French-Russian-German co-operation, is a successor of the American Earth Radiation Budget Experiment (ERBE) (Barkstrom et al, 1989) and is designed to measure the short-wave and long-wave components of the ERB within a very high accuracy on scales of about 250x250 km^2. For our purpose, these data are used to derive regional ERB products on a scale of about 18x18km^2. The data of the ScaRaB instrument are limited to the lifetime of the mission, March 1994 to February 1995, and during its lifetime to the roughly two overpasses per day. In order to derive a complete diurnal cycle and also to extend the investigations to times at which no ScaRaB data are available, a synergy with data from the operational satellites as NOAA-AVHRR and METEOSAT has to be done.
At first, we describe the ScaRaB instrument, after that we discuss our two developed narrow to broad-band conversion functions. Finally we conclude and give an outlook of future work.

2. THE SCANNER FOR RADIATION BUDGET

The Scanner for Radiation Budget (ScaRaB) has been a recent successor of the scanning broadband instruments used by ERBE. ScaRaB has four channels, a visible (0.5 to 0.7 μm), a shortwave (0.2 to 4.0 μm), an atmospheric window (10.5 to 12.5 μm) and a total channel (0.2 to 50. μm). More detailed information about the instrument are given in Table 1. The French space agency made available a preliminary ScaRaB data set which was used for this study

[1] Corresponding author address: Rainer Hollmann, GKSS Research Center, Institute of Atmospheric Physics, 21502 Geesthacht, Germany, e-mail: hollmann@gkss.de

(Kandel et al., 1998). From March 1994 to March 1995 ScaRaB was flown on a non-sunsynchronous orbit. The height was about 1200 km, so that the field of view of the instrument for the nadir pixel is approximately 60 by 60 km (Viollier et al., 1995), being to some extend larger than the ERBS field of view of 50x50 km².

Dynamic range		
(solar channel)	:	up to 425 Wm^2sr^{-1}
(total channel)	:	up to 500 Wm^2sr^{-1}
Sampling Interval	:	34 mRad
Sampling Period	:	62.5 ms
Scan Period	:	6 s
Useful Scan Time	:	3.18 s
Scan Angle	:	100°
Pixels per Scan	:	51
Mass	:	40 kg

Table 1: Instrument specifications of ScaRaB FM-1.

One main emphasis during the development of ScaRaB was on calibration. The calibration error before launch was obtained to be less than 1.5% in the solar domain (Mueller et al., 1997). Bess et al. (1997) compared measurements of March 1994 ScaRaB observations with collocated ERBS nonscanner observations. Both data sets agree to 0.76 W/m² for shortwave fluxes, to 0.55 W/m² and 3.8 W/m² for longwave fluxes at night and day, respectively.

3. TWO MODELS FOR THE NARROW-TO BROADBAND CONVERSION OF SCARAB

For regional studies the most critical point for an investigation of the ERB is the poor time sampling with roughly two overpasses a day, depending on the latitude. To extent these two observations per day to other times of the day in order to derive daily means, we are going to use additional data from other instruments, i.e., AVHRR. AVHRR has only spectral narrowband channels, so that a narrow-to-broadband conversion is necessary. Because ScaRaB has a narrowband channel as well, this is used together with the broadband channel to develop two narrow-to-broadband conversion algorithms (NTB) from the ScaRaB data. The ratio *F* of the filtered radiance L^{fil}_{cha1} of channel 1 in W/(m²sr), and the unfiltered radiance L^{unf}_{cha2} in W/(m²sr) of the broadband channel 2, can be written as:

$$F = \frac{L^{fil}_{cha1}}{L^{unf}_{cha2}} = f(sfc, cc, \vartheta_0, \vartheta, \varphi, t) \quad (3.1)$$

Here denotes *sfc* the observed surface type, *cc* the observed cloud cover, ϑ_0 the solar zenith angle, ϑ the satellite zenith angle, φ the relative azimuth angle, and *t* the time.

The surface is classified within five geotypes: land, ocean, snow, desert, and land-ocean mix. The cloud cover is defined as : clear (less than 5% cloud cover), partly cloudy (between 5% and 50% cloudy), mostly cloudy (between 50% and 95% cloudy), and overcast (more than 95% cloudy). The cosine solar zenith angle and cosine satellite zenith angle are divided into 10 bins and 8 bins, respectively. The relative azimuth angle is grouped into 7 classes.

In the first narrow to broadband conversion method, hereafter referred to M1, for each scene type, cloud cover, cosine solar zenith angle bin, and cosine satellite zenith angle bin, a linear expression, $L^{unf}_{cha2} = aL^{fil}_{cha1} + b$ is derived from correlations of L^{fil}_{cha1} and L^{unf}_{cha2} as measured by ScaRaB. A lookup table was devised to put the coefficients a and b. This has been done for the month August 1994, for the limited area MAGS. In August 1994 the MAGS area was not snow covered. To derive the relation for snow , too, data from March 1994 were used in addition.

A second narrow to broadband conversion (M2) has been developed with a different approach. A sensitivity study shows that the major contribution to the ratio *F* is by the cosine solar zenith angle, cloud cover , and surface type. This means that the general dependency of the NTB (Eq. 3.1) can be simplified to $F = f(sfc, cc, \vartheta_0)$. To derive this function we sorted all measurements from August 1994 into classes of the above discussed bins. Then we built the average for each binned angle class and computed a regression for *F*.

The result is shown for the clear sky geotypes in Figure 1: Scene 01 correspond to clear sky over ocean, 02 to clear sky over land, scene 03 to clear sky over ice, and scene 05 to clear sky for ocean-land mix. The NTB conversion for desert, was not calculated since MAGS and BALTEX are regions with no desert geotype. The values of land found to be the smallest, on contrary to the ice and snow cases (scene 05). The number of observations within the sun zenith angle bins 1 to 3 for scene 03 and 05 are small compared to the other bins. We derived therefore the

regression only from the well observed other bins. For all cases a regression with a quadratic equation yield to sufficient correlation coefficients.

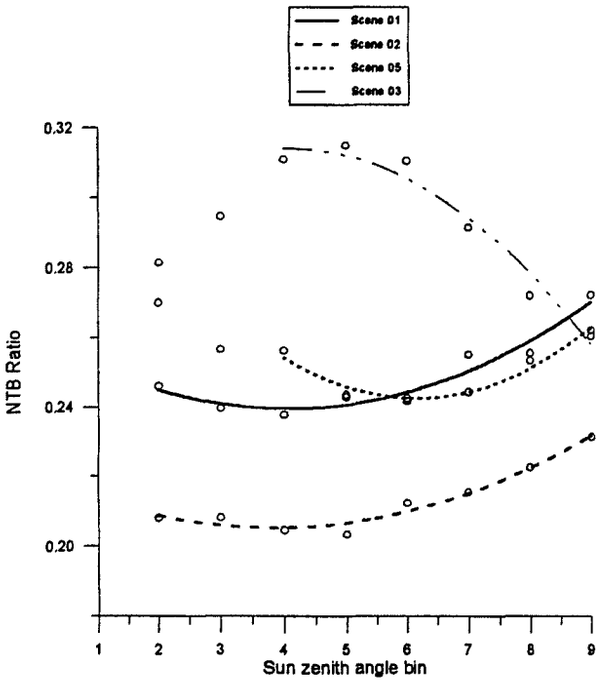

Figure 1: Ratio F for clear sky cases

For both approaches, we applied our conversion functions to an independent month of ScaRaB data to test the reliability.
The main differences between both approaches are: M1 considered two angles, i.e. the solar zenith and satellite zenith angle, whereas M2 uses only the solar zenith angle dependence.

4. SPATIAL AND SEASONAL APPLICATIONS

The derived two algorithms were applied to the August data, where they were derived from. This gives an estimate for the methodical error. The difference between the new algorithm on the MAGS area, derived from the broadband data and M1 gives +1.5 W/m² with a variability of ±15.51 W/m² (rms). M2 yields +3.21 (± 22.51 W/m²). The observed mean flux and variability over the MAGS area are 222.42 ± 129.14 W/m². Both methods yield not to an offset for the data. It can be noted, that both methods reproduce the A2 ScaRaB data very well, although M2 has larger differences and a greater variability.
In a next step we applied these models to other independent months. The regional distributions of the mean differences for July 1994 are shown in Fig 2 for M1 and in Fig. 3 for M2. The regional distribution for both methods over most of the MAGS area is smaller than 7.5 W/m². In both cases, there are three localisations with larger differences. First in an area near the Canadian pacific coast, second in the northern part of the MAGS area, and third in an area between 245° E to 260° E and 50° N to 55° N. Results for these regions are also conspicuous in other months.

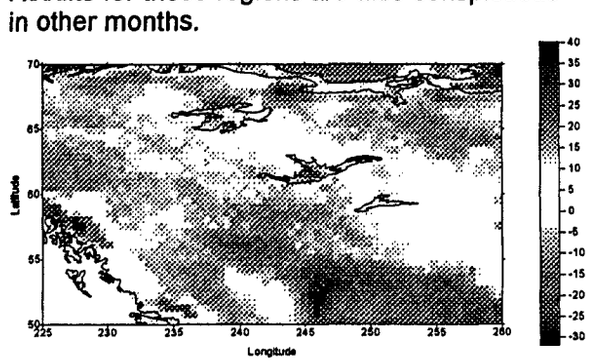

Figure 2: Regional distribution of mean differences in W/m² of July 1994, M2.

The errors at the Canadian pacific coast is because the large field of view of ScaRaB contains on one side ocean and on the other side land parts. This yield to systematic overestimation of that zone. The error in the northern is similar to them. An investigation of the region in the Southeast of MAGS in comparison with a more detailed landuse

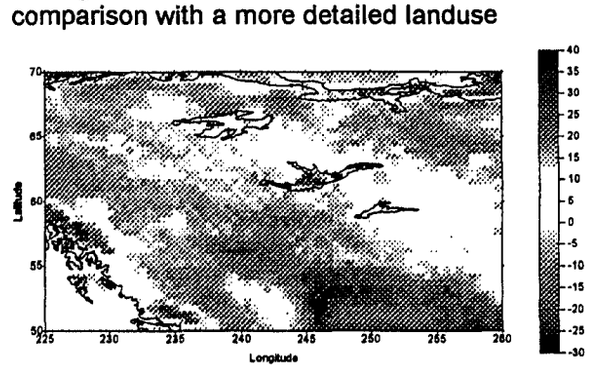

Figure 3: Regional distribution of mean differences in W/m² of July 1994, M1.

classification gives the reason: Here we have a large zone with a unique landuse. We conclude, that this region has a systematically different narrow to broadband ratio as the general used ratio for surface type land. This indicates the used distinction of surface type especially for land is not sufficient. The MAGS area is most of the year covered by snow. This leads to an

increase of errors for the months March and May 1994. In both cases these errors are greater than the errors in the discussed three zones.

5. CONCLUSIONS

We presented two methods for a narrow to broadband conversion. The first derived from a regional data set, the second from a global one. The methodical error of both methods is comparable small. We found that the used land classification in five surface types, as ERBE did, is not enough for regional studies. But one can not avoid the errors at the border of two neighbouring surface types as we showed for the land-ocean mix surface type. In that cases the mean differences are increased to 30-40 W/m². Generally, both methods represent the A2 data from ScaRaB very well and provide therefore the means to use these expression for our goal to derive with them broadband fluxes from NOAA AVHRR or METEOSAT.

7. OUTLOOK

The next step will be to apply the expressions to received NOAA AVHRR data for the BALTEX region. First results of derived broadband flux from narrowband AVHRR radiances will be presented.

6. REFERENCES

BALTEX, 1995: BALTEX Initial implementation plan. *International BALTEX secretariat publication series*, **2**, 84 pages. Available at International BALTEX Secretariat, GKSS Forschungszentrum Geesthacht, Germany.

Barkstrom, B. R., E. F. Harrison, G. L. Smith, R. Green, J. Kibler, R. Cess, and the ERBE Science Team, 1989: Earth radiation budget experiment (ERBE) archival and April 1985 results. *Bull Amer. Meteorol. Soc.*, **70**, 1254-1262.

Bess, T. D., G. L. Smith, R. N. Green, D. A. Rutan, R. S. Kandel, P. Raberanto, and M. Viollier,1997: Intercomparison of scanning radiometer for radiation budget (ScaRaB) and earth radiation budget experiment (ERBE) results. *Preprints of 9th conference on atmospheric radiation, Long Beach (CAL),* Amer. Meteorol. Soc., Boston, 203-207.

Kandel, R., M. Viollier, P. Raberanto, J. Ph. Duvel, L. A. Pakhomov, V. A. Golovko, A. P. Trishchenko, J. Mueller, R. Stuhlmann, and E. Raschke, 1998: The ScaRaB Earth Radiation Budget Datasets. *Bull. Amer. Meteorol. Soc*, in press.

Mueller, J., R. Stuhlmann, R. Becker, E. Raschke, H. Rinck, P. Burkert, J.-L. Monge, F. Sirou, R. Kandel, T. Tremas, and L. A. Pakhomov, 1997: Ground characterisation of the Scanner for Radiation Budget (ScaRaB) flight model 1. *J. Atmos. Oceanic. Technol.*, **14**, 802-813.

Raschke, E., U. Karstens, R. Nolte-Holube, R. Brandt, H.-J. Isemer, D. Lohmann, M. Lobmeyr, B. Rockel, R. Stuhlmann, 1998:The Baltic Sea Experiment, BALTEX: A brief overview and some selected results. *Surveys of Geophysics*, **19**, 1-22.

Viollier, M., R. Kandel, and P. Raberanto, 1995: Inversion and space-time-averaging algorithms for ScaRaB (Scanner for Radiation Budget). Comparison with ERBE. *Ann. Geophysicae*, **13**, 959-968.

WMO, 1990: Scientific plan for the global energy and water cycle experiment (GEWEX). *WMO/TD*, Nr. 376.

P1.38B

A NEW SATELLITE METHOD TO COMPUTE MONTHLY OCEAN AIR TEMPERATURE, SPECIFIC HUMIDITY AND LATENT HEAT FLUX

Catherine Gautier[1], Charles Jones and Pete Peterson
University of California, Santa Barbara, California

1. INTRODUCTION

The estimation of latent (LH) and sensible (SE) heat fluxes over the global oceans has been a continuing challenge to resolve the large-scale variability of the surface energy balance (Glecker and Weare, 1995, Jourdan and Gautier, 1995). In general, LH and SE are estimated from surface observations of basic meteorological parameters (pressure, wind speed, air temperature and specific humidity, and sea surface temperature) and the bulk aerodynamic approach. Several previous studies have used in-situ observations from ship reports to estimate LH and SE on a global scale, although confidence in those estimates is restricted to the highly sampled shipping lanes. This paper presents our new method to estimate surface air temperature (Ta) and specific humidity (Qa) from space measurements of total precipitable water (W) and sea surface temperature (SST) based on an artificial neural networks (ANN) approach. Then, we present computations of LH made using these two parameters, Ta and Qa , surface winds from SSM/I (WS) and SST.

2. DATA

Monthly averages of Ta and Qa are obtained using two parameters that are routinely available from satellite observations and numerical weather prediction analysis. Monthly averages of total precipitable water (W) are obtained from the Special Sensor Microwave Imager (SSM/I) data (Wentz, 1992). The sea surface temperature (SST) field is derived from the National Centers for Environmental Prediction (NCEP) operational analysis, which is based on the method of Reynolds and Smith (1994). The data record spans from January 1988 through August 1997 (1° latitude x 1° longitude resolution). The development and testing of the new method are accomplished by using observations from the Surface Marine Data (hereafter SMD, da Silva et al., 1994). The SMD is obtained from ship reports and extends from January 1988 through November 1993.

LH is obtained by applying a similarity-based model to monthly mean fields. The input parameters to this model are: Ta, Qa, WS and SST. We compared monthly averages (1988-1993) of Qa and Ta from SMD and ANN. In addition, two estimates of LH derived from NCEP/NCAR reanalysis (Kalney et al. 1996) and SMD data are compared with the satellite estimation of LH (classical method). The first one (classical method) is computed from monthly averages of WS, SST, Qa and Ta. The second one computes monthly averages from individual estimates of LH and is denominated sampling method.

3. A NEW SATELLITE METHOD FOR ESTIMATING TA AND QA

The methodology used in this paper to estimate Ta and Qa is fully described in Jones et al. (1998, hereafter JPG). It involves two phases: data classification and artificial neural net.

3.1. Data Classification

The data classification requires some preliminary sorting and classification to ensure adequate observations for both development and testing analyses. First, the initial data sets of W (SSM/I), SST (NCEP), Ta (SMD) were divided into two sub-samples. The 47-month period including January 1988-July 1988, August 1989-July 1992 and August 1993-November 1993 was used to train the neural networks (Sample-I). The 24 - month period of August 1988-July 1989 and August 1992-July 1993 was reserved for evaluation of the methodology (Sample-II).

The main goal of this study is the derivation of empirical relationships relating W and SST to Ta. We developed an algorithm that takes

Catherine Gautier, ICESS University of California Santa Barbara, Santa Barbara, CA 93106
email: *gautier@icess.ucsb.edu*

triplets of observations [W (SSM/I), SST (NCEP), Ta (SMD) Qa(SMD)] from Sample-I and from all grid cells in the analysis. The next step consists of computation of a sampling parameter , defined as $\alpha = (\sigma / (N)1/2$, based on surface marine observations of Ta and Qa. In this expression (σ is the standard deviation of the climatological monthly averages, and N is the number of ship observations used to compute the monthly average. This sampling parameter is defined to optimize the selection of (W, SST, and Ta) and (W, SST, and Qa) observations that will be used in the ANN training.

3.2. Artificial Neural Network (ANN) Approach

An artificial neural network (ANN) algorithm is applied to derive transfer functions relating the pairs of (W, SST) observations (inputs) to the surface marine observations of Ta or Qa (outputs). This was performed in two phases. In the first phase, the ANN used a supervised fully connected feed-forward network employing a 2-6-2-1x architecture (Riedmiller, 1994). It consists of two inputs (W and SST), six nodes in the first hidden layer, two nodes in the second hidden layer and one output (Ta or Qa). The "x" indicates that there are additional connections between the input and output layers. In order to "train" the ANN, a sub-set of triplets of (W, SST, and Ta) or (W, SST, and Qa) is randomly taken from the available data meeting the selection criterion described in the previous section. This sub-set is designated as "training set", whereas another randomly taken set of triplets constitutes a "testing set". The training set is run through the network with the weights at each node of the ANN updated using a back-propagation algorithm. Conversely, the testing set is used to independently monitor the mean error between the observed and estimated Ta and Qa values (see Riedmiller, 1994 and Jones et al., 1998 for details).

The first phase of the ANN training provides monthly mean maps of Ta and Qa for the Sample-I data period. These maps are compared with observed Ta and Qa from the surface marine data to produce a set of mean biases (SMD - ANN) for each month. In the second phase, the mean biases are included as a third parameter to train a second ANN. The second ANN consists of a 3-6-2-1x architecture with inputs W (SSM/I), SST (NCEP) and bias and Ta and Qa as outputs.

4. RESULTS

4.1 Ta and Qa

The performance of the new approach using the Sample-II data, which were not used in the ANN training, is presented on Fig. 1 (Ta) and 2 (Qa). They show root-mean square (rms) differences between Ta and Qa from the JPG method and SMD observations for most of the global oceans. As expected, the global mean bias for both Ta and Qa are very small (0.050°C ± 0.26°C), since the ANN final training includes mean bias as an input parameter.

For Ta, the spatial distribution of the bias is relatively homogeneous, suggesting well behaved results and with only a few regions of enhanced magnitude (not shown). The rms differences have a global mean of 0.73°C and standard deviation of 0.37°C. The spatial distribution shows small magnitudes except over: 1) the Southern hemisphere, South of 30°S, where the differences reach large values, and 2) the equatorial Pacific and the Western boundary currents, where values of about 1°C are found.

For Qa, the spatial distribution of the mean bias is also very homogeneous (not shown). The global mean bias is small 0.010 (± 0.23 g kg^{-1}). This is even the case in regions of very low sampling of surface marine observations such as in the tropical and southern oceans. The small bias is not a total surprise, since the ANN final training includes mean bias as an input parameter. Over most oceanic areas, the rms between ANN and SMD are on the order of 0.6 to 1.2 g kg^{-1}. The global rms is 0.77 (± 0.39 g kg^{-1}). In particular, very low rms values between the JPG method and SMD observations are found over the northern Pacific and Atlantic Oceans and Arabian Sea. Note, for example, that in the North Atlantic and North Pacific, the rms is on the order of 0.6 g kg^{-1} and further substantiates the usefulness of the new method. Root-mean-square differences on the order of 1.2 g kg^{-1} or higher, however, are observed over the southern Indian, Pacific and Atlantic Oceans, which probably indicates the effect of very low number of observations in the monthly averages of surface marine data.

4.2 Fluxes

The comparison study indicates that monthly averages of surface wind speeds from SSM/I are in much better agreement with SMD than the NCEP/NCAR reanalysis (not shown). Relative to SMD data, NCEP/NCAR fields underestimate surface wind speeds by about 3.5-

4.5 m s-1, whereas SSM/I data underestimate by about 1.0 m s-1. In addition, root-mean square (rms) differences for the NCEP/NCAR and SSM/I fields are on the order of 4.0 m s-1 and 1.3 m s-1, respectively.

Latent heat fluxes derived from the satellite method (classical method), however, show larger differences with LH from SMD (sampling method) than the NCEP/NCAR fields (sampling method), as can be seen in Figs. 3a and 3b. On average, rms differences in the satellite LH are about 25-30 W m-2, whereas in the NCEP/NCAR fields they are on the order of 15-25 W m-2. In contrast, a more direct comparison using only the classical method, Figs. 3c and 3d, shows that the satellite method compares better with the SMD data than the NCEP/NCAR reanalysis. Root-mean square differences for LH from the satellite method in regions of high ship observations are typically on the order of 20 W m-2 (Fig. 3c), while in the NCEP/NCAR fields they are about 40-50 W m-2 (Fig. 3d). This indicates the important difference between the two approaches (classical and sampling methods) to compute latent heat fluxes.

5. CONCLUSIONS

The new satellite method shows that artificial neural networks are useful mathematical tools for extracting complex nonlinear relationships among geophysical parameters. The new approach uses total precipitable water (W) and SST to derive global fields of Qa and Ta. The ANN methodology produces better estimates of Ta and Qa than previous satellite methods with significantly less systematic and random errors (Jones et al., 1998). This is specially important in oceanic regions with low sampling observations. In addition, monthly averages of surface wind speeds from SSM/I, Ta and Qa from ANN are in better agreement with in-situ observations (SMD) than NCEP reanalyses.

6. REFERENCES

Glecker, P.J., and B.C. Weare, 1995: Uncertainties in global ocean surface heat flux climatologies derived from ship observations. Program for Climate Model Diagnosis and Intercomparison, PCMDI Report No. 26, Lawrence Livermore National Laboratory, Livermore, CA.

da Silva, A. M., C. C. Young, S. Levitus, 1994: Atlas of surface marine data 1994. Volume: algorithms and procedures. NOAA Atlas, U. S. Government Printing Office, Washington D. C., 83 pp.

Kalnay, E., Kanamitsu, M., Kistler, R., Collins, W., Deaven, D., Gandin, L., Iredell, M., Saha, S., White, G., Woollen, J., Zhu, Y., Chelliah, M., Ebisuzaki, W., Higgins, W., Janowiak, J., Mo, K., Ropelewske, C., Wang, J., Leetmaa, A., Reynolds, R., Jenne, R., Joseph, D., 1996: NCEP/NCAR 40-Year Reanalysis Project. Bull. Amer. Meteor. Soc., 77, 437-471.

Jones, C., P. Peterson, and C. Gautier, 1998: Artificial neural networks: a new approach for deriving ocean surface specific humidity and air temperature. J. Applied Meteorology (in revision)

Jourdan, D., and C. Gautier, 1995: Comparison between global latent heat flux computed from multisensor (SSM/I and AVHRR) and from in situ data. J. Atmos. Oceanic Technol., 12, 46-72.

Reynolds, R. W., and T. M. Smith, 1994: Improved global sea surface temperature analyses using optimum interpolation. J. Climate, 7, 929-948.

Riedmiller, M. 1994: Advanced supervised learning in multi-layer perceptrons from back propagation to adaptive learning algorithms. Int. J. Computer Standards and Interfaces, 16, 265-278.

Wentz, F. J., 1992: User's manual SSM/I monthly ocean tape. Remote Sensing Tech. Rep., 20 pp.

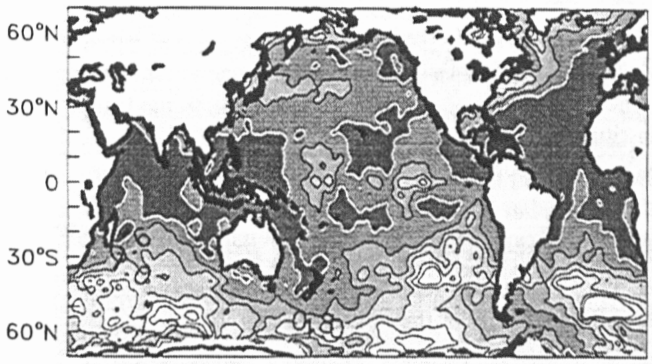

Figure 1. Surface air temperature (T_a) root–mean square (rms) difference (°C) between SMD and JPG method.

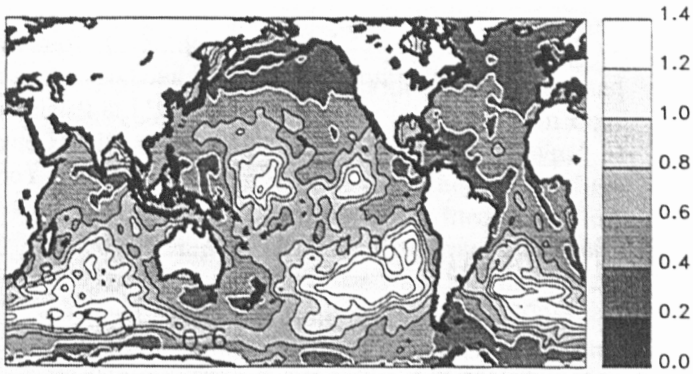

Figure 2. Surface specific humidity (Q_a) rms difference (g kg^{-1}) between SMD and JPG method.

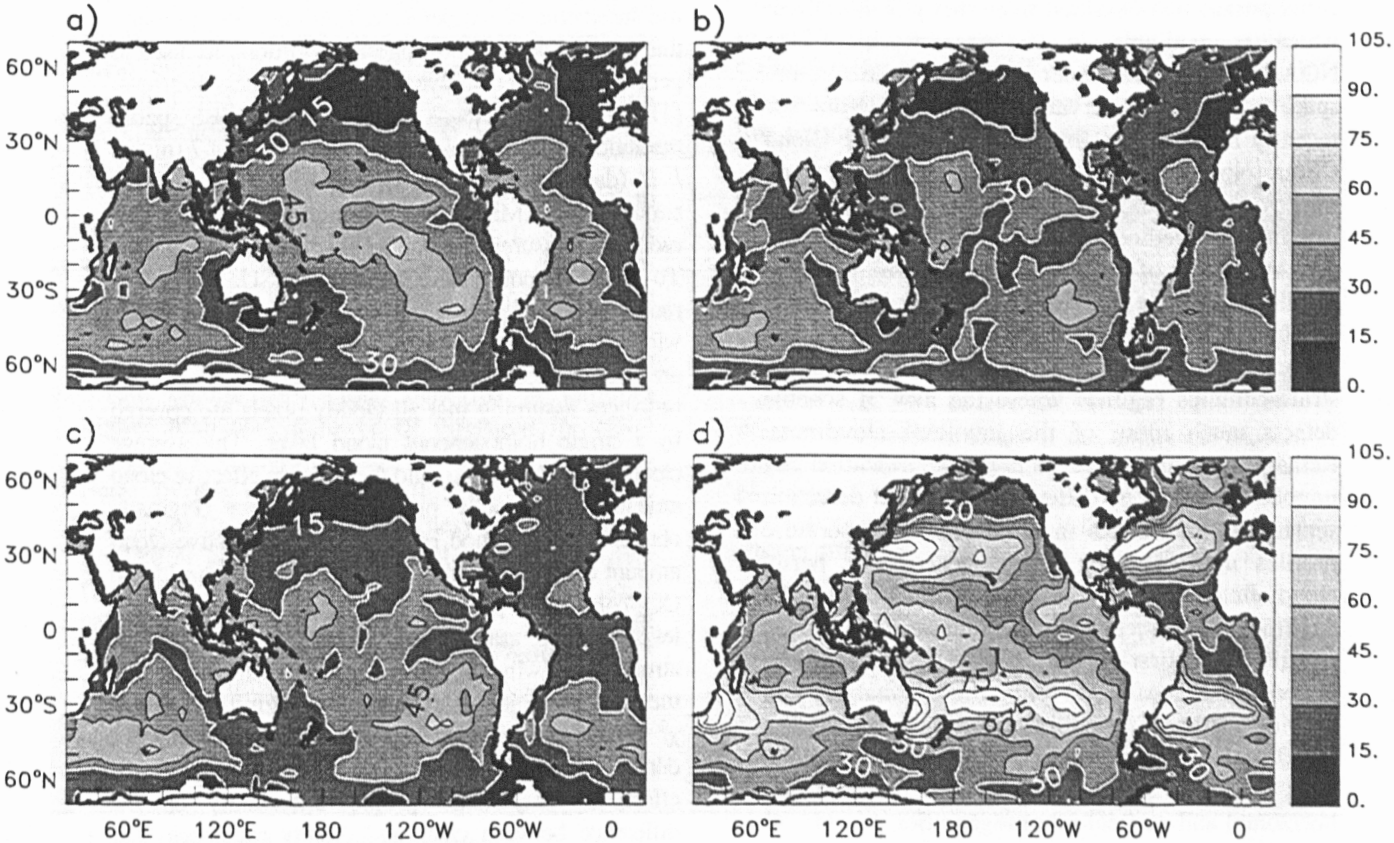

Figure 3. (a) Latent heat flux rms difference (W m^{-2}) between JPG (classical method [CM]) and SMD (sampling method [SM]). (b) As in (a), but between NCEP/NCAR reanalyses (SM) and SMD (SM). (c) Latent heat flux rms difference between JPG (CM) and SMD (CM). (d) As in (c), but between NCEP/NCAR reanalyses (CM) and SMD (CM).

P1.41A

CLOUDS AS SEEN BY SATELLITE SOUNDERS (3I) AND IMAGERS (ISCCP)

C. J. Stubenrauch[+], W. B. Rossow*, N. A. Scott[+], A. Chédin[+]
[+]Laboratoire de Météorologie Dynamique du C. N. R. S., Ecole Polytechnique, 91128 Palaiseau, France
*NASA Goddard Space Flight Center, Institute for Space Studies, 2880 Broadway, New York, N.Y. 10025, USA

1. INTRODUCTION

The Improved Initialization Inversion (3I) algorithm converts TIROS-N Operational Vertical Sounder (TOVS) observations from the NOAA Polar Orbiting Environmental Satellites into atmospheric temperature and water vapor profiles, together with cloud and surface properties. The iterative process of detailed comparisons between cloud parameters obtained from this global dataset, which is available in the framework of the NOAA/NASA Pathfinder Program, with time-space collocated observations of clouds from the recently re-processed International Satellite Cloud Clima-tology Project (ISCCP) dataset has led to an improved 3I cloud analysis scheme based on a weighted χ^2 method. This process also provides a first evaluation of the ISCCP re-analysis. The new 3I cloud scheme obtains cloud properties very similar to those from ISCCP for homogeneous scenes. Improvement is especially notable in the strato-cumulus regimes where the new 3I scheme detects much more of the low-level cloudiness. Remaining discrepancies in cloud classification can now be explained by differences in cloud detection sensitivity, differences in atmospheric temperature profiles used, and by inhomogeneous or partly cloudy fields. Cirrus cloud identification during the daytime in the recent ISCCP dataset is improved relative to the first version of ISCCP, but is still an underestimate. At night only the 3I analysis can provide cirrus information. Correlations between cloud optical thickness (ISCCP) and IR cloud emissivity (3I) are highly sensitive to mesoscale horizontal and vertical inhomogeneities.

2. METHODS AND DATASETS

The High resolution InfraRed Sounder (HIRS) instrument, which is part of the TOVS system (Smith *et al.* 1979), measures radiation emitted and scattered from different levels of the atmosphere at 19 infrared (IR) wavelengths as well as one visible (VIS) wavelength. The 3I algorithm (Chédin *et al.* 1997) transforms these radiances into atmospheric, cloud and surface properties. The LMD fast line-by-line radiative transfer model, Automatized Atmospheric Absorption Atlas (4A), and a huge collection of radiosonde measurements of temperature, humidity and pressure that are grouped by atmospheric conditions are used to generate the Thermo-dynamic Initial Guess Retrieval (TIGR) data set. Clouds are detected at HIRS spatial resolution (18 km at nadir) by a succession of 7 (night) / 8 (day) threshold tests, which depend on the simultaneous Microwave Sounding Unit (MSU) radiance measurements that probe through the clouds. To insure more coherence with MSU, the HIRS radiances are averaged over clear and cloudy pixels within 100 km x 100 km regions. Cloud para-meters are determined from the averaged cloudy pixel radiances assuming that all cloudy pixels are covered by a single homogeneous cloud layer. The average cloud-top pressure, p_{cld}, and the average effective cloud amount over cloudy pixels, $N\varepsilon_{cld}$, were originally obtained by a method relying on the effective cloud amount coherence within four radiances in the 15 µm CO_2-band (with peak responses from 400 to 900 hPa levels in the atmosphere) and in the 11 µm IR atmospheric window. In the new 3I cloud scheme, these variables are obtained by minimizing a weighted χ^2 (Stubenrauch *et al.* 1998b). Empirical weights, depending on cloud level and frequency, reflect the effect of temperature profile uncertainty on the difference between clear and cloudy radiances. The global 3I Pathfinder data are organized on a 1° latitude x 1° longitude grid. The effective cloud amount over a 1° grid, εN, is then the product of the extracted $N\varepsilon_{cld}$ over cloudy pixels and the fraction of cloudy HIRS pixels inside the grid.

For a global cloud climatology, ISCCP (Rossow *et al.* 1996) has put emphasis on temporal and spatial

Corresponding author address: Claudia J. Stubenrauch, LMD, Ecole Polytechnique, 91128 Palaiseau cédex, France, e-mail: stubenrauch@lmd.polytechnique.fr.

resolution, rather than on spectral resolution, by using one visible (day only) and one IR atmospheric window radiance measurement from imagers on the suite of geostationary and polar orbiting weather satellites. The initial spatial resolution of about 5 km is sampled to intervals of about 30 km, which means that about one pixel out of 36 is kept for cloud information. Clear sky conditions are associated with low IR and VIS spatial and temporal variability. ISCCP cloud properties are determined by comparing the observed radiances with a detailed radiative transfer model. The model includes the effects of the atmosphere, with properties specified from the operational analysis of the TOVS data (only one profile per day is available), and surface determined from clear radiances. Cloud top temperature, T_{cld}, is first retrieved assuming that all clouds are black bodies. During daytime, when VIS radiances can be used to retrieve cloud optical thicknesses, τ, the cloud-top temperature of «transmissive» clouds ($\tau_{IR} < 5.5$) is corrected to account for the radiation transmitted from below, T_{cld} is decreased as a function of τ. Based on these cloud properties, each cloudy pixel can be classified into one of nine cloud types (only during day), according to three cloud-top pressure intervals and three τ intervals.

The current ISCCP dataset has been subject to comparisons with various datasets (e. g. Rossow et al. 1993, Liao et al. 1995, Jin et. al. 1996). Recently, the ISCCP data have been re-processed. The most important changes have been the use of the Advanced High Resolution Radiometer (AVHRR) 3.7μm channel for cloud detection at latitudes higher than 50°, a lower IR threshold for cloud detection over land and the use of fractal ice particles in the cloud optical thickness calculation, leading to smaller optical thickness for ice clouds.

The 3I cloud parameters and ISCCP pixel data (current: CX, re-processed: DX) from the polar satellite NOAA-10 (observations at ~ 7h30 local time) have been combined into 1° latitude x 1° longitude gridboxes for July 1987 and January 1988.

3. ANALYSIS HIGHLIGHTS

3.1 Evaluation of 3I cloud parameters

Figs. 1 and 2 show geographical maps of the difference between time-space collocated 3I and reprocessed ISCCP cloud parameters: a) cloud-top temperature and b) effective cloud amount. In the ISCCP dataset, the effective cloud amount has to be calculated from the optical thickness of cloudy pixels inside a 1° grid (Stubenrauch *et al.* 1998c). Since ISCCP can determine cloud optical thickness, and therefore effective cloud amount, only during day and NOAA-10 morning observations in July and in January are made under daylight conditions only in the summer hemisphere, results in Figs. 1 and 2 are from July in the Northern hemisphere and from January in the Southern hemisphere. In Figs. 1, the results are obtained from the nominal 3I algorithm, whereas Figs. 2 show the results of the new 3I cloud scheme using a weighted χ^2 method. By considering the cloud-top temperature difference in Fig. 1a, one observes for less than half of the globe an agreement within 5K between ISCCP and 3I. Over land, 3I identifies warmer clouds than ISCCP, a mismatch due to the difficult distinction between partly cloudy low clouds and Cirrus. Another feature are lower cloud-top temperatures in the Intertropical Convergence Zone (ITCZ), mostly due to larger Cirrus regions determined by 3I. Considering the effective cloud amount difference in Fig. 1b, one observes a systematic underestimation by the original 3I cloud scheme in all Stratocumulus regions; in other regions with mostly low clouds the difference is less significant.

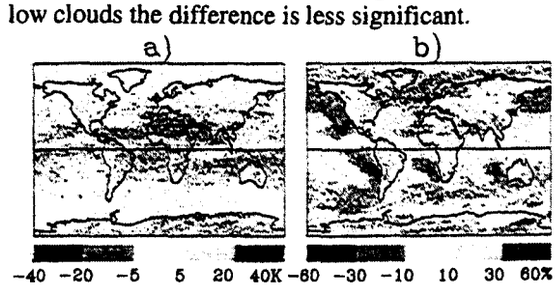

Figs. 1: Geographical maps of the difference between time-space collocated original 3I and ISCCP cloud parameters during day. a) 3I-ISCCP cloud-top temperature difference and b) 3I-ISCCP effective cloud amount difference.

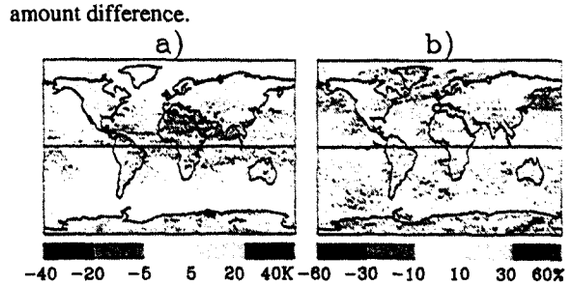

Figs. 2: Geographical maps of the difference between time-space collocated new 3I and ISCCP cloud parameters during day. a) 3I-ISCCP cloud-top temperature difference and b) 3I-ISCCP effective cloud amount difference.

This global comparison has led to a review of cloud parameter determination methods from IR sounder measurements and to a further development

of these methods, by taking into account the effect of temperature profile uncertainties on the difference between clear sky and cloudy radiances dependent on cloud levels and spectral channels. Using the new 3I weighted χ^2 scheme, the Nε structures in all Strato-cumulus regions disappear, leading globally to a much better agreement between ISCCP and 3I. Also the cloud-top temperatures in Fig. 2a agree much better, leaving only some regions like the Sahara, Antarctica and some parts of the Northern hemisphere land with disagreement due to misidentification between Cirrus and partly cloudy low clouds.

More details of the 3I and ISCCP cloud parameter evaluation are given in (Stubenrauch *et al.* 1998a).

3.2 Heterogeneity effects on the determination of the effective cloud amount

The different spatial resolutions of the radiance measurements (20 km and 5 km) and the different data volume reductions (averaging and sampling) make the collocated 3I - ISCCP cloud dataset an interesting tool for studying the effects of cloud spatial heterogeneity on the satellite retrieval of cloud properties. Variability within each area can arise because of partial coverage (broken cloudiness), because of horizontal inhomogeneities of the optical and thermal properties of a cloud layer, and because of multi-layer cloud structure.

To test these effects, we consider high, midlevel and low-level clouds, and for each cloud category, we distinguish three cases of cloud inhomogeneity over each 1° grid: (1) a homogeneous cloud cover defined by ISCCP showing the same cloud type (out of the nine cloud types defined in section 2) for all cloudy pixels (called a homogeneous layer cloud), (2) ISCCP clouds all in the same height category but with varying optical thicknesses (called a heterogeneous layer cloud), and (3) ISCCP clouds with different heights and different optical thicknesses (called a multi-layer cloud).

The ratio of the ISCCP effective cloud amount and the 3I effective cloud amount, separately for high-, mid- and low-level clouds as identified by 3I, is shown in Figs. 3 under the three inhomogeneity conditions explained above (for the three geographical regions: Northern hemisphere land, NL, North Atlantic, NA and Southern hemisphere ocean, SH). εN determined by 3I is about the same (within 10%) as the one determined by ISCCP for all cloud heights in the case of a homogeneous layer cloud. Variability in optical thickness leads to an about 30% smaller εN determined by 3I (averaged) than εN determined by ISCCP (sampled) for all cloud height categories. Note that this effect would be increased by using one of the other two methods for averaging the ISCCP cloud emissivity. In the case of multi-layer clouds, the effective cloud amount calculated by 3I is about 50% smaller for high clouds than the one obtained by ISCCP, whereas εN is the same for low-level clouds. This last result indicates that, in the case of thin cirrus clouds mixed with low- or midlevel clouds, which occur for about 25% of all clouds (Jin and Rossow 1997, Warren et al. 1985), the 3I result is dominated by the properties of the overlying cirrus clouds whereas the ISCCP result from the visible reflectivity includes the (usually larger) effective cloud amount of the thicker cloud underneath.

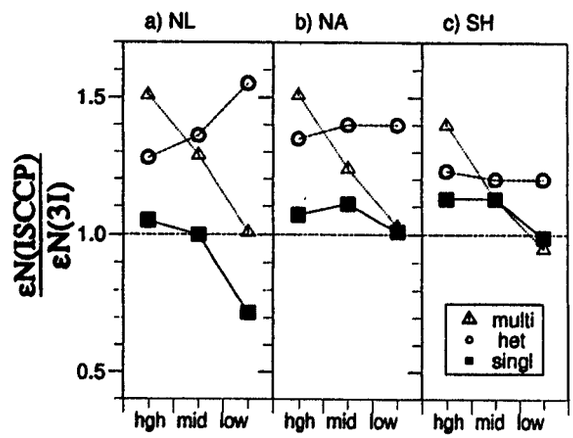

Figs.3: Ratio of effective cloud amounts εN determined by ISCCP and by 3I at 1° spatial resolution for 3I high, midlevel and low-level clouds over three geographical regions: a) Northern hemisphere land (NL), b) North Atlantic (NA) and c) Southern hemisphere midlatitude ocean (SH). Three spatial heterogeneity situations are shown: P homogeneous one-layer cloud, O heterogeneous one-layer cloud and D multi-layer clouds.

3.3 Cloud type radiative effects

Cloud radiative effects have been studied in combination with Earth Radiation Budget Experiment (ERBE) fluxes. The global mean cloud warming effect is about 20 Wm^{-2} at 7h30 am local time, the zonal mean cloud warming varies between < 5 Wm^{-2} for partly cloudy, low-level cloud fields and 150 Wm^{-2} for overcast, high opaque clouds in the tropics, as shown in Figs. 4. The warming effect of cirrus reaches 80 Wm^{-2}, followed by overcast midlevel clouds and thin cirrus with a maximum warming effect of 40 Wm^{-2}. Compared to the earlier ISCCP results, which show cloud warmings by high opaque and cirrus clouds that are much closer to each other,

there is a considerable improvement in the re-processed ISCCP cirrus cloud identification leading to a better radiative distinction that is in better agreement with the 3I results. Still, the 3I high opaque clouds have a cloud warming that is about 10 Wm^{-2} larger than the ISCCP results, especially in the tropics: this effect could result from the different interaction of the different wavelengths used in the two analyses with the very «diffuse» tops of most tropical clouds (Liao *et al.* 1995). Note in addition that only the 3I results provide this distinction during the night (southern hemisphere in July and northern hemisphere in January); the ISCCP results at night treat all clouds as opaque. These cloud type dependent radiative effects can be compared to global circulation models (Stubenrauch *et al.* 1997) to gain a better under-standing of parametrizations of different clouds.

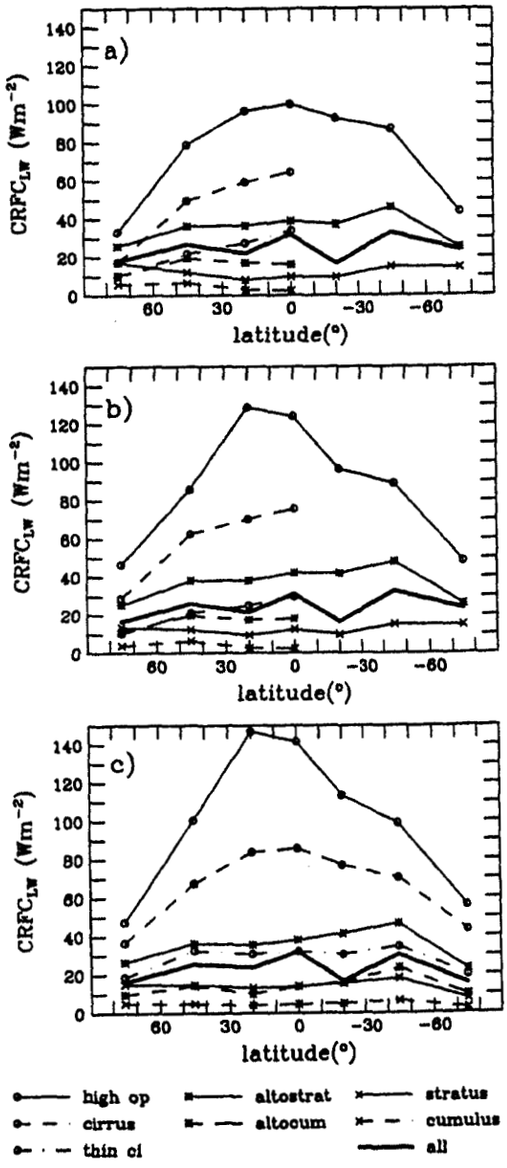

Figs. 4: Zonal cloud warming at 7h30 am local time in July 1987 (daylight on Northern hemisphere) over ocean with cloud fields identified by a) current ISCCP, b) re-processed ISCCP and c) new 3I.

REFERENCES

Chédin A., N. A. Scott, J. P. Chaboureau, F. Chéruy, C. J. Stubenrauch, R. Armante, D. Kasysavanh, 1997: Reanalysis of a multi-year Archive of TOVS NOAA Satellite Data for Climate Studies, *1rst International Conference on the Reanalyses*, Washington D.C., USA, 27-31 Oct. 1997, 6pp.

Jin Y., W. B. Rossow and D. P. Wylie, 1996: Comparison of the Climatologies of High-Level Clouds from HIRS and ISCCP, *J. Climate*, **9**, 2850-2879.

Jin Y., and W. B. Rossow, 1997: Detection of cirrus overlapping low-level clouds, *J. Geophys. Res.*, **102**, 1727-1737.

Liao X., W.B. Rossow and D. Rind, 1995: Comparison between SAGE II and ISCCP High-Level Coulds, Part II: Locating Cloud Tops, *J. Geophys. Res.*, **100**, 1137-1147.

Rossow W. B., A. W. Walker, and L. C. Garder, 1993: Comparison of ISCCP and other cloud amounts, *J. Climate*, **6**, 2394-2418.

Rossow W. B., A. W. Walker, D. Beuschel and M. Roiter, 1996: International Satellite Cloud Climatology Project (ISCCP): Description of New Cloud Datasets. WMO/TD-No.737, *World Climate Research Programme* (icsu and WMO), Geneva, 115pp.

Smith, W. L., H. M. Woolf, M. C. Hayden, D. Q. Wark, and L. M. McMillin, 1979: The TIROS-N Operational Vertical Sounder. *Bull. Amer. Meteor. Soc.*, **60**, 1177-1187.

Stubenrauch, C. J., W. B. Rossow, F. Chéruy, A. Chédin, and N. A. Scott, 1997a: Clouds as seen by Infrared Sounders (3I) and Imagers (ISCCP): Part I) Evaluation of Cloud Parameters. *J. Climate*, in revision.

Stubenrauch, C. J., A. Chédin, R. Armante, and N. A. Scott, 1997b: Clouds as seen by Infrared Sounders (3I) and Imagers (ISCCP): Part II) A New Approach for Cloud Parameter Determination in the 3I Algorithms. *J. Climate*, in revision.

Stubenrauch, C. J., W. B. Rossow, N. A. Scott, and A. Chédin, 1997c: Clouds as seen by Infrared Sounders (3I) and Imagers (ISCCP): Part III) Combining 3I Cloud Parameters and ISCCP for better understanding of Cloud Radiative Effects. subm. to *J. Climate*.

Stubenrauch C. J., A. D. Del Genio and W. B. Rossow, 1997: Implementation of Sub-Grid Cloud Vertical Structure inside a GCM and its Effect on the Radiation Budget, *J. Climate*, **10**, 273-287.

Warren S. G., C. J. Hahn, and J. London, 1985: Simultaneous Occurrence of Different Cloud Types, *J. Clim. Appl. Meteor.*, **24**, 658-667.

P1.42B ANALYSIS OF A GLOBAL, SATELLITE-DERIVED CLIMATOLOGICAL DATA SET

Roberta DiPasquale *
Analytical Services and Materials, Inc., Hampton, VA

Paul Stackhouse
NASA Langley Research Center, Atmospheric Sciences Division, Hampton, VA

1. INTRODUCTION

Historically, surface radiation data sets have relied on a network of in-situ measurements. However, space provides an ideal vantage point for global observations. Over the past two decades, methods to estimate surface properties from satellite observations have evolved. Using historical satellite data, a climatological, Surface Solar Energy (SSE) data set has been created by the NASA Langley Research Center and the National Renewable Energy Laboratory for the solar energy industry. This SSE data set is a synthesis of the World Climate Research Program/Surface Radiation Budget (WCRP/SRB) Version 1.1 satellite-derived shortwave (SW) data set and International Satellite Cloud Climatology Project (ISCCP) data products for the March 1985 through December 1988 time frame.

Due to the global coverage of this data set, it has proven to be a valuable resource to the solar energy industry in remote regions of the world. Several organizations have used the data successfully for their applications where no ground measurement data exist. Solar Cookers International (SCI) and Consultants on Household Uses of Solar Energy (CHUSE) are two non-profit organizations promoting the use of solar cooking. Both have used the data for determining the viability of solar cooking in various locations around the world. Sun Frost, a small business producing energy efficient refrigeration, utilized the SSE data set to re-design a solar-powered vaccine storage refrigeration system for use in equatorial regions. This new system will provide a car battery for backup power, in place of a deep cycle battery. The SSE data set is available on the web at http://eosweb.larc.nasa.gov/DATDOCS/Surface_Solar_Energy.html

* *Corresponding Author Address*: R. DiPasquale, Analytical Services and Materials, Inc., One Enterprise Pkwy, Suite 300, Hampton, VA 23666; e-mail: r.c.dipasquale@larc.nasa.gov

The purpose of this paper is to validate the SSE data set estimates of downward SW surface irradiance by comparing these data to ground site measurements collected over the same time frame. Validation of the SSE surface data set will provide a basis for estimating the uncertainty in the results and provide a foundation for its use in global and regional solar energy applications.

2. DATA

The SSE data set contains 52 monthly averaged parameters which are useful in the application of solar energy technologies. The SSE data set is a synthesis of three global, satellite-derived data products.

The WCRP/SRB Version 1.1 data set, archived in the Earth Observing System Data and Information System (EOSDIS) at the Langley Distributed Active Archive Center (DAAC), is one component of the SSE data set. It consists of 46 months (March 1985 through December 1988) of daily and monthly averaged radiation, cloud, and meteorological data useful for analyzing the surface radiation budget (Whitlock et al. 1995a). SRB monthly averaged data products included in the SSE data set are: top-of-atmosphere downward SW irradiance; average, minimum, and maximum downward SW surface irradiance; and aerosol optical depth. The irradiance values are calculated from the Pinker Satellite Algorithm for Shortwave Radiation Budget (SASRAB) using ISCCP C1 data as input. SASRAB is a physical model based on radiative transfer calculations using the delta-Eddington approximation (Pinker and Laszlo 1992).

The ISCCP data products, both C1 and C2, are also included in the SSE data set. ISCCP C1 contains 3-hourly satellite data on an equal area grid (6596 cells). Each grid cell represents an area equal to that of a 2.5 degree latitude/longitude cell at the equator (approximately 280 X 280 km). The ISCCP C2 product contains monthly

means of the ISCCP C1 data. ISCCP monthly averaged products included in the SSE data set are: cloud fraction; cloud optical depth; total column and near surface precipitable water; and near surface air temperature.

In this analysis, monthly averaged estimates of downward SW surface irradiance over 46 months derived on the ISCCP 2.5 degree equal area grid are compared to ground measurements archived at the World Radiation Data Center (WRDC). The WRDC, in St. Petersburg, Russia, contains data from over 1000 measurement sites throughout the world. Only sites that passed the quality control procedures implemented by the WRDC were used in this analysis.

3. DISCUSSION

Figure 1 shows the ground sites available from March 1985 through December 1988. For this time period, there are 271 sites which correspond to 119 ISCCP cells. Most cells only contain one or two ground site stations. However, in Region C, where ground sites densely populate Europe, cells may contain as many as 10 ground site stations.

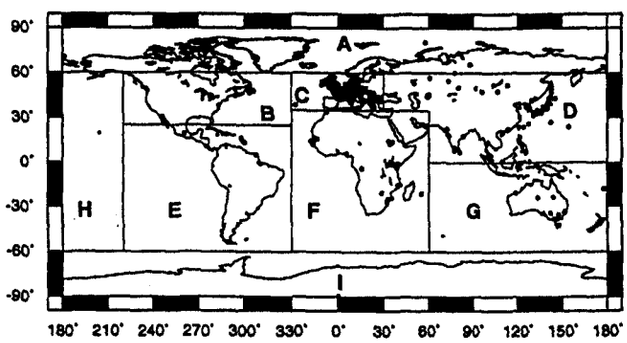

Figure 1. WRDC Surface Sites for March 1985 through December 1988.

Figures 2 though 5 are seasonal scatter plots of monthly averaged ground site measurements and satellite-derived results from SASRAB over the 4 years. Each region is plotted with a different symbol, however, no persistent regional bias appears to be present. The site averages over the globe for each season are as follows: January, 117 W/m^2; April, 190 W/m^2; July, 207 W/m^2; October, 141 W/m^2. Based on these seasonal averages, the SASRAB estimates are generally within 10% of the ground site measurements; and, we can conclude that the SASRAB results provide a reasonable estimate of downward SW irradiance at the surface.

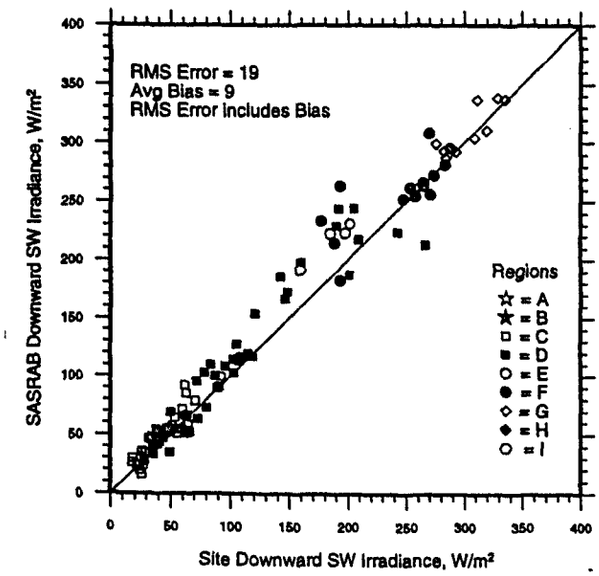

Figure 2. Comparison of site measurements to SASRAB satellite-derived results for January.

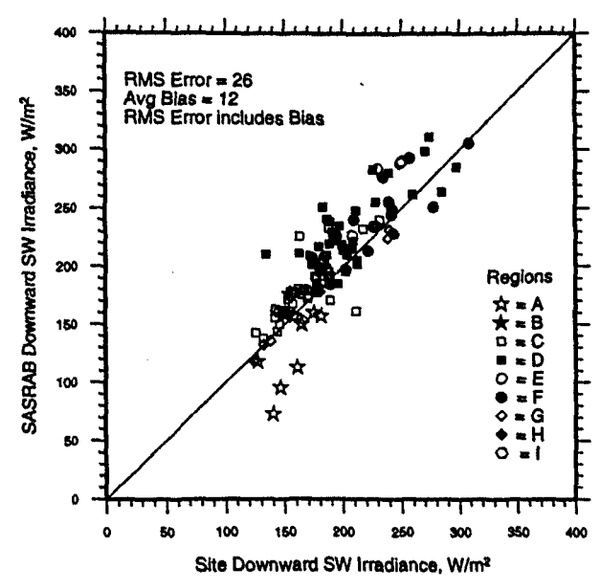

Figure 3. Comparison of site measurements to SASRAB satellite-derived results for April.

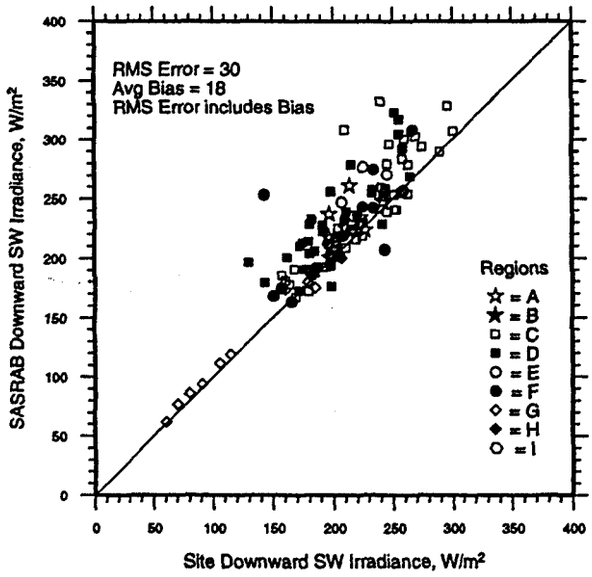

Figure 4. Comparison of site measurements to SASRAB satellite-derived results for July.

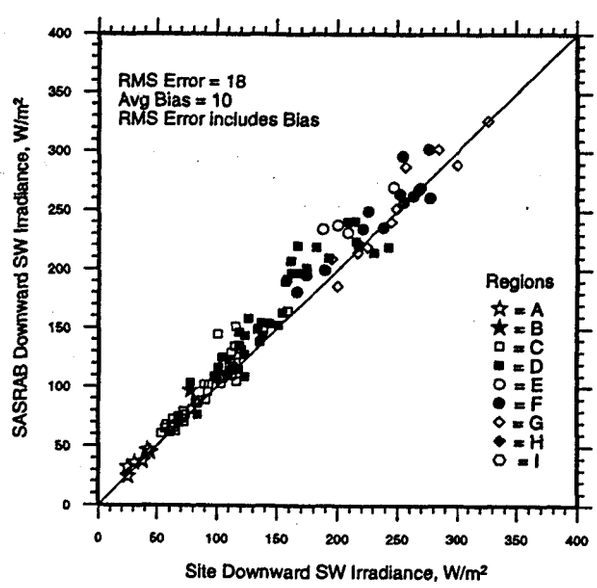

Figure 5. Comparison of site measurements to SASRAB satellite-derived results for October.

In addition to determining the agreement between the SSE data set and ground measurements, we also performed regional comparisons. Figures 6 through 8 show monthly time series comparing ground site averages and satellite estimates of maximum and minimum downward SW surface irradiance obtained from the 4-year climatology for three different climate regimes. Figure 6 displays a monthly time series for a northern mid-latitude region in France (ISCCP cell 5631). This region is typical of forest/cropland vegetation. In this example, four sites (Tours, Bourges, Limoges, and Clermont-Ferrand) are located within the boundaries of the cell. Each month, the average of the ground site measurements falls within the maximum and minimum of the satellite-derived SASRAB estimates.

Figure 7 shows results from an equatorial region in Africa (ISCCP cell 3313). Two Kenya sites, Kitale and Eldoret, are located within the cell and have tropical/grassland vegetation. For most of the year, the site-average measurements fall within the range of the satellite-derived estimates. However, for the month of August, the site average falls almost 10W/m^2 below the minimum satellite-derived estimate. Based on a study by Whitlock et al. (1995b), the SRB data set may be up to 40% in error during months of biomass burning since smoke is not accounted for in the analysis algorithms. The burning season for this area in Africa is April through October, and is one possible explanation for the higher SASRAB estimates of SW irradiance at the surface.

Figure 8 depicts a monthly time series for a scrubland/desert vegetated region in Central Australia. Only one ground station, Alice Springs Airport, falls within the boundaries of the ISCCP cell (1954). For most of the year, the climatological ground measurements fall between the maximum and minimum estimates from the SSE data set. However, in the summer months, the satellite-derived minimum results are slightly higher (about 10 to 15W/m^2) than the site measurements. One possible explanation could be a high summertime aerosol content in the atmosphere due to airborne dust. This would cause a ground measurement value to be lower than the SASRAB estimate, since the algorithm can not account for this type of atmospheric phenomenon.

Based on the three climate regimes shown, monthly averaged ground measurements generally fall within the minimum and maximum satellite-derived estimates of downward SW irradiance at the surface. In cases where site

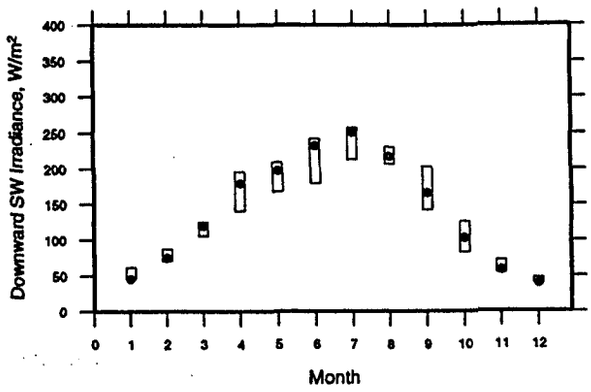

Figure 6. Monthly time series of a forest/cropland region.

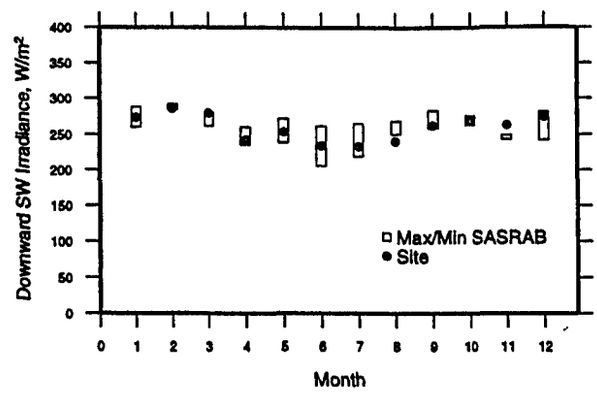

Figure 7. Monthly time series of a tropical/ grassland region.

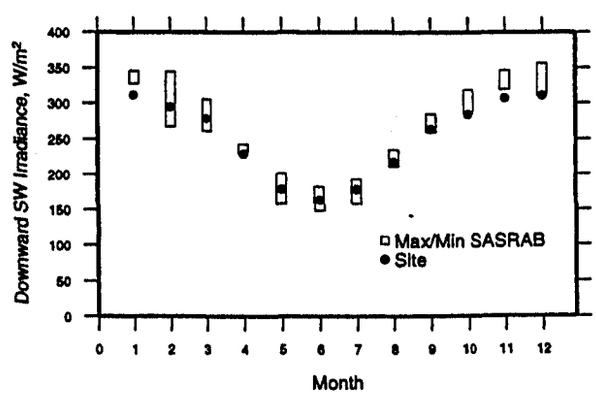

Figure 8. Monthly time series of a scrubland/desert region.

measurements lie outside of the range of SASRAB results, possible site specific meteorological conditions may play a role.

4. CONCLUDING REMARKS

The SSE data set, created for the solar energy industry, is a global, climatological data set derived from satellite observations. Several organizations, such as Solar Cookers International and Sun Frost, have used the SSE data set successfully for applications in remote regions of the world where ground measurement data are not available. The SSE data set has been validated using quality surface observations available from the WRDC. Globally, satellite-derived estimates of monthly averaged downward SW surface irradiance are generally within 10% of surface measurements. With cell specific data, averaged ground site measurements usually fall between the maximum and minimum values of downward SW surface irradiance obtained from the 4-year climatology. Due to the low spatial resolution of the satellite-derived data, anomalies may occur for site specific meteorology which is not modeled into the Pinker SW algorithm.

5. REFERENCES

Whitlock, C.H., T.P. Charlock, W.F. Staylor, R.T. Pinker, I. Laszlo, A. Ohmura, H. Gilgen, T. Konzelmann, R.C. DiPasquale, C.D. Moats, S.R. LeCroy, N.A. Ritchey, 1995a: First Global WCRP Surface Radiation Budget Data Set. *Bulletin American Meteorological Society*, 71, 905-922.

Pinker, R.T., I. Laszlo, 1992: Modeling Surface Solar Irradiance for Satellite Applications on a Global Scale. *Journal of Applied Meteorology*, 31, 194-211.

Whitlock, C.H., D.R. Cahoon, T. Konzelmann, 1995b: Effects of Biomass Burning on Satellite Estimates of Surface Radiation On Central Africa. AGU Chapman Conference on Biomass Burning and Global Change. Williamsburg, VA, March 13-17.

P 1.44B THE 16-YEAR AVHRR PATHFINDER GLOBAL DATASET: EVALUATING THE EFFECTS OF AEROSOL PARTICLES ON CLOUD RADIATIVE FORCING

Melanie A. Wetzel
Desert Research Institute, Reno, Nevada

Larry L. Stowe
National Oceanographic and Atmospheric Administration, Camp Springs, Maryland

1. INTRODUCTION

Monitoring and interpretation of global trends in climatological parameters is essential in determining the relative roles of anthropogenic and natural climate forcing mechanisms. This information is needed for progress in the amelioration of climate impacts through strategies as wide-ranging as international negotiation and local pollution source control. Particulates (aerosol) are thought to alter atmospheric conditions and climate processes via their effects on radiative transfer, cloud structure, and precipitation efficiency.

Aerosol radiative forcing is broadly defined as the quantitative effect on the net radiation budget which can be attributed to changes in aerosol through their impacts on cloud physical characteristics (an indirect effect) and/or their role in atmospheric extinction (a direct effect). Cloud formation in an air mass which contains a relatively high concentration of cloud condensation nuclei (CCN) often leads to a high droplet density, compared with formation in low-CCN environment. Various field studies and cloud model results suggest that if other physical parameters such as liquid water path are comparable, these clouds have typically smaller droplet size and greater shortwave albedo (Twomey, 1984; Albrecht, 1989).

A modeling study conducted by Bott (1997) demonstrated that stratus cloud droplet distribution formed from continental aerosol characterized by high CCN concentration experiences much slower diffusional growth and leads to smaller droplet size than the distribution in clouds formed from a typical marine aerosol population. Differences in net shortwave radiative flux between the marine and continental cloud were more than 100 W m^{-2}, such that the daily radiative energy deposited in the boundary layer was 25% less for the case of a continental cloud. Therefore, aerosol-influenced cloud microphysical structure can cause changes in the radiative flux divergence profile which further influences cloud evolution (a feedback process). Secondary effects on the vertical profile of the droplet distribution, precipitation efficiency, and entrainment provide additional feedbacks to the processes of aerosol production and transformation.

Corresponding author address: Dr. Melanie Wetzel, Atmos. Sciences Center, Desert Research Institute P.O.Box 60220 Reno NV 89506;e-mail: wetzel@dri.edu

The impact of biomass burning aerosol on satellite-estimated cloud albedo and microphysics has been documented by Kaufman and Nakajima (1993), where satellite data were used to relate local changes in aerosol column amount to clouds that form in the vicinity of these aerosol. The presence of smoke particles is associated with a 15 to 9 μm decrease in the typical cloud droplet modal radius. At the same time, heavy aerosol loading can cause the visible albedo of clouds to appear darker, since these carbonaceous aerosol from biomass burning absorb shortwave radiation.

Climate-scale numerical simulations that include the role of anthropogenic aerosol have produced estimates of globally-averaged direct forcing in the range of -0.3 to -1.1 W m^{-2} (Kiehl and Briegleb, 1993; Chuang *et al.*, 1997), while reported results for modeling of global average indirect sulfate forcing are -0.5 to -1.6 W m^{-2} (Jones *et al.*, 1994; Boucher and Lohmann, 1995). Combined indirect and direct anthropogenic aerosol forcing of the radiation budget on a global scale has thus been estimated to be comparable to greenhouse gas forcing but of opposite sign.

2. THE *PATHFINDER ATMOSPHERE* DATASET

Satellite multi-channel data provide a means of assessing certain aspects of the aerosol direct and indirect radiative forcing characteristics. Long-term operational data collection of global satellite observations is conducted within the scope of the NOAA-NASA Pathfinder Program, using both polar-orbiting and geostationary meteorological satellites. The Advanced Very High Resolution Radiometer (AVHRR) Pathfinder Atmosphere (PATMOS) Project is a NOAA/NESDIS component of the NOAA-NASA Pathfinder Program and has produced an extensive archive of daily cloud cover, clear and cloud radiance, aerosol (over ocean), and radiation budget parameters for July 1981 to the present.

The NOAA polar-orbiting satellite series provides twice-daily AVHRR overpass imagery with a nominal pixel field-of-view of 1.1 km and Global Area Coverage (GAC) data at 4 km sampled resolution. The AVHRR calibrated radiance data from NOAA/7,9,11,14 afternoon satellites have been used to produce a long-term global daily, pentad (5-day) and monthly mean dataset that is available for application to a wide variety

of climatological and meteorological studies (Stowe and Jacobowitz, 1997).

The presence of clouds and clear pixels for 4-pixel arrays of the 4-km GAC data is diagnosed with a combination of AVHRR channel threshold and uniformity discriminators (Stowe *et al.*, 1991). PATMOS produces clear and overcast pixel area statistics for a global grid with 110-km equal-area cells corresponding to one degree latitude-longitude increments at the Equator. The resulting data parameters are applicable to further compositing and cloud classification.

The PATMOS dataset includes AOT retrieved in the same manner as the NESDIS AVHRR daily AOT mapping (Stowe *et al.*, 1997). This quantity is defined as the vertically integrated aerosol extinction coefficient at 0.63 μm, evaluated from the ocean surface to the observing satellite sensor. Hence, AOT includes all aerosol in a column of the troposphere and stratosphere. In most years and regions, the AOT value is strongly dominated by aerosol in the lower troposphere.

The PATMOS aerosol optical thickness was used as a measure of the relative concentration of aerosol available in the atmospheric boundary layer. The AOT retrievals are currently possible only over the ocean surface and within restricted conditions of viewing geometry to avoid sunglint and other sources of retrieval error. Note that periods following volcanic eruptions were not used in the primary analysis of the relationship of AOT to stratus cloud droplet size and optical thickness. These periods are not useful in directly associating tropospheric cloud with the apparent aerosol amount due to the significant proportion of aerosol burden which is located above cloud level.

3. COMPARISON OF AOT AND EFFECTIVE RADIUS

The relationship between tropospheric aerosol and cloud microphysical and radiative parameters was evaluated by selecting horizontally homogeneous stratiform water cloud (in order to reduce ambiguity due to non-uniform bidirectional reflectance from cumuliform cloud tops, small cumulus clouds, and highly broken cloud fields). A stratus cloud classification method was developed to select grid cells containing simultaneous AOT and uniform stratus area from all daily datasets.

Grid cells containing predominantly low- and mid-level stratiform cloud were selected from the PATMOS dataset using cloud screen techniques. We employed multiparameter cluster analysis on global scatterplots of pixel characteristics, implementing threshold and uniformity tests for data from the AVHRR Channel 1 (0.58-0.68 μm), Channel 2 (0.72-1.10 μm), and Channel 4 (10.3-11.3 μm). The stratus classification steps utilized: (1) grid-cell average cloud-top equivalent blackbody temperature in Channel 4, TC > 253 K; (2) difference between Channel 4 clear-sky ocean surface temperature and cloud-top temperature, TDIF < 16 K; (3) standard deviation of Channel 4 cloud-top temperature, SDT < 4 K, (4) standard deviation of Channel 2 cloud-top albedo, SDA < 14 %. This classification is designed to select horizontally homogeneous stratiform cloud with little cloud top convective structure. The AVHRR cloud albedo may be slightly biased by aerosol coexisting with for optically thin cloud. We therefore applied a minimum Channel 1 cloud albedo threshold of 20% in order to limit the cloud layers chosen to those in which the cloud shortwave radiance should only be impacted by aerosol through an indirect effect on cloud microphysical characteristics (although there may also be included cases of heavy aerosol loading above cloud).

The cloud parameters were then used with a radiative transfer model to retrieve satellite estimates of cloud optical depth as well as cloud droplet effective radius (r_e), defined by numerical integration over the droplet size distribution N(r), as

$$r_e = \frac{\int N(r) r^3 dr}{\int N(r) r^2 dr} .$$

Cloud microphysical parameters were estimated by interpolating the grid-average stratus cloud reflectances for AVHRR Channel 3 (3.55-3.95 μm) and Channel 1 to model-calculated channel reflectances for a wide range of cloud droplet size distributions, cloud depths, and sun-target-satellite geometry. Narrowband reflectances were calculated using the Streamer model (Meier *et al.*, 1997) based on the Discrete Ordinates method (Stamnes *et al.*, 1988). Cloud optical properties were parameterized as a function of droplet effective radius and liquid water concentration (Hu and Stamnes, 1993), and gas absorption parameters were obtained using the Exponential Sum Fitting Technique (Tsay *et al.*, 1989).

Global grid cells which met the tests for stratus cloud and AOT were sub-selected to develop a new dataset containing grid cell parameters such as average cloud visible (Channel 1) reflectance, average cloud Channel 3 radiance, and average cloud Channel 4 radiance. The Channel 4 radiance was used to calculate an effective emittance for Channel 3 (assuming a Channel 3 emissivity calculated from the radiative transfer model for the marine stratus and a cloud emissivity of 100% in Channel 4). Interpolation of the PATMOS visible and near-infrared reflectances to model results was used to estimate and map cloud droplet size as well as cloud optical depth. These results were then composited into monthly average distributions.

Analysis of the monthly average geographic distributions of PATMOS-derived droplet effective radius by comparison with the monthly mean patterns of AOT indicates that stratus droplet size is well correlated with AOT in the oceanic regions adjacent to

western South America, northeastern North America, northwestern Africa, southwestern Africa, and northeastern Asia. In areas such as these, AOT of 0.10 or lower is associated with droplet size r_e = 10 - 16 µm, while AOT > 0.10 is generally coincident with areas of r_e = 6 - 10 µm.

We have also evaluated seasonal and long-term trends for the hemispheric, latitudinal, and regional relationship between aerosol optical thickness and droplet size in collocated stratiform cloud. Figure 1 presents PATMOS-derived monthly, zonal averages of these parameters for each latitude zone (at 10° intervals) between 50° S and 50° N. An association between smaller droplet size and higher average aerosol optical thickness is clearly shown.

Evaluation of the latitudinal dependance for these months indicates that stratus droplet size typically decreases from the Southern to the Northern Hemisphere, from values ~ 13-14 µm in the zonal band -50° to -40° S, to ~ 9-10 µm in the 40° - 50° N zone. The exception is the month of January, when droplet size is ~9 µm in the southern latitudes and increases by 1-2 µm in the northern latitudes. The correspondence between aerosol amount and droplet size is also seen in regional comparisons. Figure 2 demonstrates the distinct differences between r_e values as well as AOT values for the predominantly clean mid-ocean region of the central Pacific and the typically polluted region downwind of the northeastern coast of Asia.

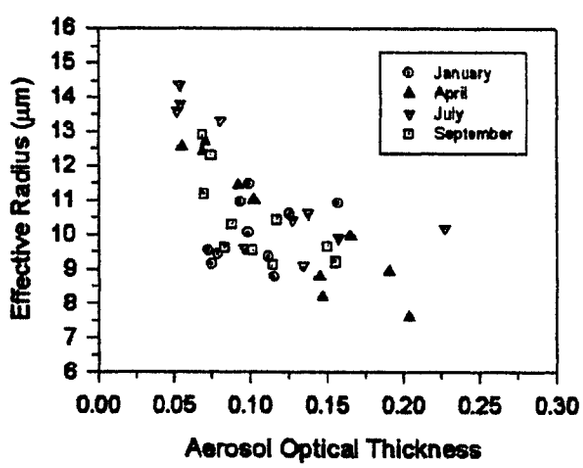

Figure 1. Relationship between the monthly zonal averages of AOT and r_e during 1989.

4. CLOUD RADIATIVE FORCING

The PATMOS data includes archived values of the absorbed solar flux (ASF) for the clear (cloud-free) cell area and for the total cell area (clear plus

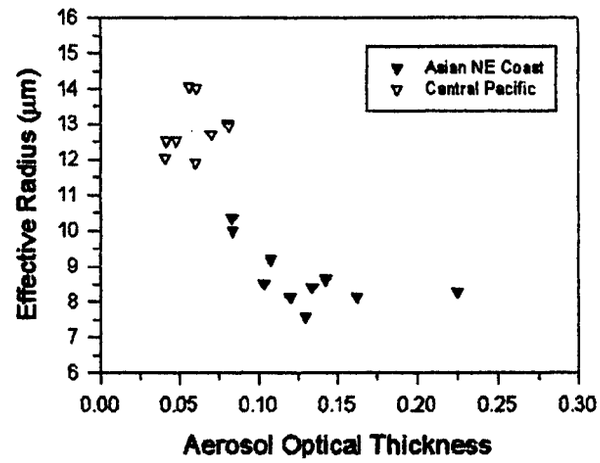

Figure 2. Regional July averages of AOT and r_e for several years during the period 1981-1997.

cloud). These are calculated from the available solar energy (ASE) determined at the top of the atmosphere, as a function of grid cell solar zenith angle and Julian date, and the reflected solar flux (parameterized from the combined Channel 1 and Channel 2 albedo values). The PATMOS archive also contains the outgoing longwave radiation (OLR) for both clear and total grid pixel populations, calculated from the AVHRR thermal channel radiance data.

The magnitude of indirect radiative forcing associated with aerosol is evaluated by relating variations in AOT to changes in the cloud radiative forcing as well as variations in the retrieved microphysical characteristics. Cloud shortwave radiative forcing can be defined from the differences of the outgoing solar radiation for clear and total-sky (clear+cloud pixels) conditions expressed in terms of absorbed solar flux as $SWF_{cloud} = (ASF_{total} - ASF_{clear})$. Figure 3 shows results for shortwave cloud forcing and aerosol optical thickness derived for 10-degree latitude

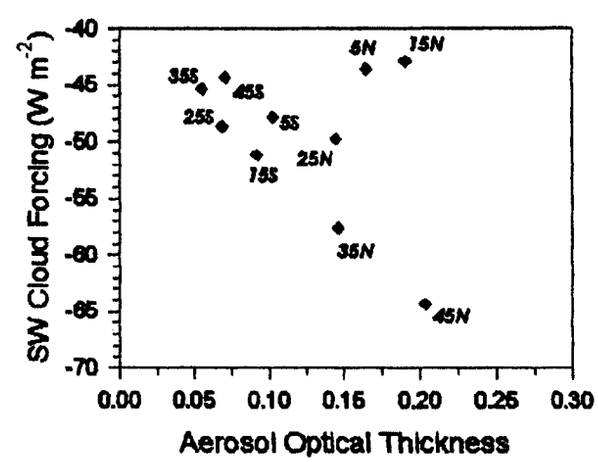

Figure 3. April 1989 zonal average AOT and SWF.

zones from the April 1989 PATMOS data. There is an overall increase in the absolute magnitude of SWF as aerosol loading increases, indicating an enhancement of the impact of the stratus cloud on regional radiative cooling of the atmosphere. The points are labelled according to their latitude band. The high values AOT with smaller magnitudes of SWF for the 5N and 15N zones can be attributed to Saharan dust effects in this latitude region, and suggest a direct aerosol effect on the computed forcing rather an indirect effect of aerosol on cloud albedo.

5. DISCUSSION

The PATMOS dataset permits the analysis of long-term variability in radiative and cloud physical parameters that are associated with aerosol burden. Results of the present study indicate seasonal and geographic patterns of stratus droplet size reduction as AOT increases, with a coincident and relatively linear increase in SWF. The evaluations described here are part of an ongoing effort to determine the global effects of aerosol on the Earth's radiation budget.

6. ACKNOWLEDGMENTS

This research was initiated while Dr. Wetzel was on a 4-month appointment as a Senior Visiting Scientist at NOAA/NESDIS. Continuing work is partially supported the Office of Naval Research (Dr. Wetzel), and by NOAA and NASA (Dr. Stowe).

7. REFERENCES

Albrecht, B.A., 1989: Aerosols, cloud microphysics and fractional cloudiness. *Science*, **245**, 1227-1230.

Bott, A., 1997: A numerical model of the cloud-topped planetary boundary layer: Impact of aerosol particles on the radiative forcing of stratiform clouds. *Q. J. R. Meteorol. Soc.*, **123**, 631-656.

Boucher, O., and U. Lohmann, 1995: The sulfate-CCN-cloud albedo effect: A sensitivity study with two general circulation models. *Tellus*, **47B**, 281-300.

Chuang, C.C., J.E. Penner, K.E. Taylor, A.S. Grossman, and J.J. Walton, 1997: An assessment of the radiative effects of anthropogenic sulfate. *J. Geophys. Res.*, **102**, 3761-3778.

Hu, Y.X., and K. Stamnes, 1993: An accurate parameterization of the radiative properties of water clouds suitable for use in climate models. *J. Climate*, **6**, 728-742.

Jones, A., D.L. Roberts, and A. Slingo, 1994: A climate model study of indirect radiative forcing by anthropogenic sulphate aerosols. *Nature*, **370**, 450-453.

Kaufman, Y.J., and T. Nakajima, 1993: Effect of Amazon smoke on cloud microphysics and albedo — Analysis from satellite imagery. *J. Appl. Meteor.*, **32**, 729-744.

Kiehl, J.T., and B.P. Briegleb, 1993: The relative roles of sulfate aerosols and greenhouse gases in climate forcing. *Science*, **260**, 311-314.

Meier, W.N., J.A. Maslanik, J.R. Key, and C.W. Fowler, 1997: Multiparameter AVHRR-derived products for Arctic climate studies. *Earth Interactions*, **EI009**, 43 pp.

Stamnes, K., S.C. Tsay, W. Wiscombe and K. Jayaweera, 1988: Numerically stable algorithm for discrete-ordinate-method radiative transfer in scattering and emitting layered media. *Appl. Opt.*, **27**, 2502-2509.

Stowe, L.L., 1991: Cloud and aerosol products at NOAA/NESDIS. Palaeogeography, Palaeoclimatology. *Palaeoecology (Global Planetary Change Section)*. 90, 25-32.

Stowe, L.L., and H. Jacobowitz, 1997: The AVHRR Pathfinder Atmosphere Project, *Proc., AMS 9th Conf. Atmos. Radiation*, 2-7 February, Long Beach, CA, 196-197.

Stowe, L.L., A.M. Ignatov, and R.R. Singh, 1997: Development, validation and potential enhancements to the second-generation operational aerosol product at the National Environmental Satellite, Data, and Information Service of the National Oceanic and Atmospheric Administration. *J. Geophys. Res.*, **102 (D14)**, 16923-16934.

Tsay, S.-C., K. Stamnes, and K. Jayaweera, 1989: Radiative energy budget in the cloudy and hazy Arctic. *J. Atmos. Sci.*, **46**, 1002-1018.

Twomey, S.A., M. Piepgrass, and T.L. Wolfe, 1984: An assessment of the impact of pollution on global cloud albedo. *Tellus*, **36B**, 256-266.

P1.45A

THE NASA TOVS POLAR PATHFINDER: 18 YEARS OF ARCTIC DATA

Jennifer Francis
Institute of Marine and Coastal Sciences, Rutgers University, New Jersey
Axel Schweiger and David Groves
Polar Science Center, University of Washington, Seattle, Washington

1. INTRODUCTION

The potential benefit of satellite remote sensing is greatest in regions of the world that have poor conventional data coverage and that are of great importance. The polar regions qualify in both these categories. Recent simulations with global climate models suggest that climate change will be largest in high latitudes, and that feedbacks involving snow, sea ice, and clouds may be among the strongest in the Earth's climate system (e.g., Houghton et al, 1990). The model's forecasts seem to be gaining credibility as recent observational studies corroborate that the poles are indeed warming abnormally rapidly during the past few decades since greenhouse gas concentrations began rising significantly (e.g., Johannessen et al, 1995; Carmack et al, 1997). Many questions have arisen, however, regarding the veracity of model parameterizations of polar processes and the quality of their simulations of even present-day climate (e.g., Boer et al, 1992). High-latitude data sets for forcing and validating models are lacking. Our knowledge of feedback processes in high latitudes is sketchy. Our understanding of spatial and temporal variability is incomplete.

In recognition of these open questions and the potential contribution that satellite data could make to addressing them, NASA initiated the Pathfinder program (see http://xtreme.gsfc.nasa.gov/pathfinder/). The data set we describe, produced with funding from this program, is designed to shed light on processes governing the Arctic climate. The TIROS Operational Vertical Sounder (TOVS) has flown on NOAA polar-orbiting satellites since 1978 and has generated one of the longest and most complete satellite data records in existence. We have subsetted radiances from the global TOVS data set, processed them for the Arctic Basin, and presented the retrieved products on a regular grid in a user-friendly format. This paper briefly describes the data set, some of the applications for which it is being used, and how you can access it.

2. ANATOMY OF PATH-P

The TOVS Polar Pathfinder (Path-P) data set, when it is completed in late 1998, will extend from 1978 through 1996. The TOVS radiances are processed with a version of the Improved Initialization Inversion ("3I") algorithm (Chedin et al, 1985) that has been modified to enhance accuracy over snow- and ice-covered surfaces (Francis, 1995). We process scan lines north of 60°N then average the retrievals to produce one Arctic-wide field per 24-hour period centered on 12 UTC. The products are gridded on the Equal-Area SSM/I Earth (EASE) grid (Armstrong and Brodzik, 1995), which is that used for polar passive microwave products and other Arctic data sets. This facilitates combining our data set with others, and opens the door to many studies with data from a variety of sources. The spatial resolution is approximately 100 km. The data files are presented in Hierarchical Data Format (HDF), which is easily accessed with a number of commercially available packages. We also provide sample read programs in Fortran and C. The products contained in the Path-P data set are listed in Table 1.

Table 1: Path-P Products

Parameter	Description	Units	~rms
TEMP	mean-layer temps (39)	K	2-3
WVAPOR	precipitable water (5)	mm	30%
TOTPRECIP	total precipitable water	mm	30%
SKTEMP	surface skin temp	K	3
FCLD	effective cloud fraction	%	30
CLDTEMP	cloud-top temp	K	TBD
CLDPRESS	cloud-top pressure	mbar	TBD
EMISS	surface emissivity @50GHz		5%
PBLSTRAT	bulk PBL stratification	K	5
Cg	geostrophic drag coeff.		10%
ALPHA	wind turning angle	deg	20
ZANGLE	average view angle	deg	
TB	brightness temp HIRS (14)	K	
THICK	layer thicknesses (11)	m	TBD
DAYNIGHT	day/night flag		
ISEICE	surface type		
PRESS	surface pressure (NCEP)	mbar	
std dev.	all products		

3. VALIDATION

Validation of satellite retrievals in the polar regions is always a challenge owing to the lack of suitable con-

**Corresponding author address*: Jennifer Francis, Institute of Marine and Coastal Sciences, 71 Dudley Rd., Rutgers University, New Brunswick, NJ 08903-0231; email: francis@imcs.rutgers.edu.

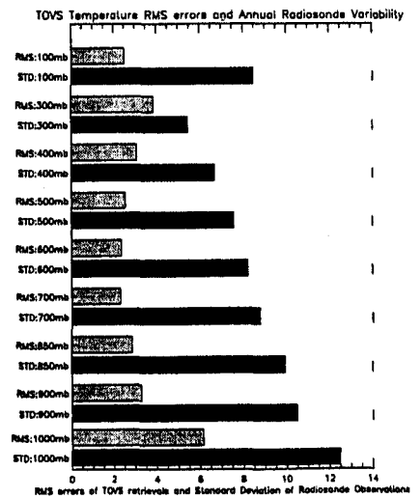

Figure 1: Comparison of TOVS-retrieved upper-level temperatures to rawinsonde data from Russian NP stations. Dark bars are the standard deviation or raw-insonde temperatures; lighter bars are r.m.s. err in TOVS retrievals.

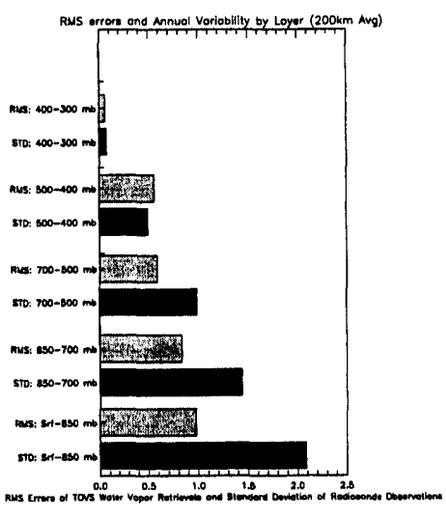

Figure 2: As in Figure 1, but for water vapor (mm).

ventional data. This is particularly true with cloud properties. We have, however, compared our temperature and water vapor retrievals with rawinsonde data from the Russian North Pole ice stations, which drifted on the Arctic sea ice from the 1950s until 1990 (Figures 1 and 2).The rms errors are much lower than the natural variability at all levels except the lowest layer (which is excluded from the Path-P data set) and near the tropopause. The comparison of water vapor amounts to rawinsonde values (which are themselves suspect in very cold conditions) is also encouraging. As seen in Figure 2, the retrieval accuracy and water vapor amounts increase with pressure, thus we believe these data should be useful for a variety of applications.

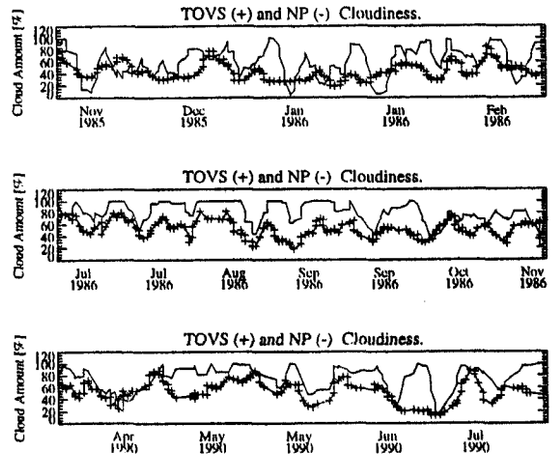

Figure 3: Comparison of surface-based observations on cloud fraction from Russian NP stations (solid line) to TOVS-derived effective cloud fraction (+).

Clouds, on the other hand, are extremely difficult to validate well. Not only are there few observations, but comparisons between the fraction reported by a surface observer, whose field of view depends on cloud base height, and that in a 100-km satellite estimate are inherently mismatched. At the surface lower clouds may block the view of high clouds, while from space low clouds may be obscured by high clouds. In addition, surface observers report the fraction of the sky covered by cloud with no regard to its optical thickness, while the TOVS retrieval is an effective cloud amount, the product of the cloud fraction and emissivity. If the sky were completely covered in cirrus, for example, the surface observer would report 100% coverage while TOVS may retrieve 50% owing to the non-black nature of the cloud. Arctic clouds are often non-black, thus the result of these issues should be that TOVS cloud fraction is lower than the surface-based observations, except in near-clear sky conditions. Figure 3 is a comparison of TOVS and NP cloud fractions, which bears out this theory. A great deal more validation is needed, especially retrievals of cloud top. We are optimistic, however, that data from the Surface Heat Balance in the Arctic (SHEBA) field program, presently underway in the Arctic Ocean north of Alaska, will provide cloud information that is more suitable for satellite validation.

4. APPLICATIONS

A number of applications using the Path-P data set are already underway, and many more are envisioned or possible. For example, the surface energy budget during half the year is dominated by longwave radiation fluxes. Francis (1997) computes surface radiation fluxes from Path-P temperatures, moisture, cloud conditions, and HIRS brightness temperatures. An example of the longwave flux for 8 November 1988 is shown in Figure 4.

The primary source of energy for the Arctic energy budget as a whole is advection of sensible heat and moisture from low latitudes. A preliminary calculation of

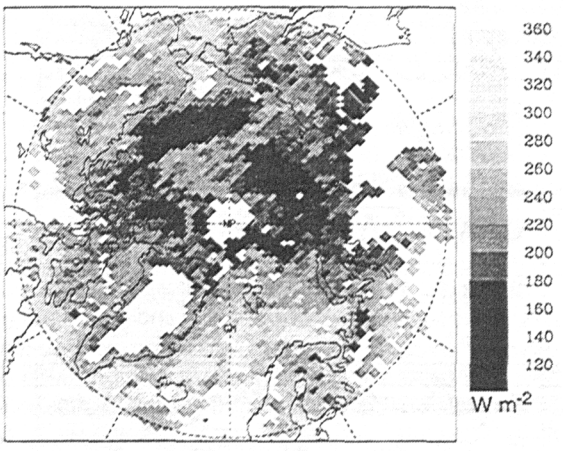

Figure 4: Surface downwelling longwave flux on 8 Nov. 1988 computed from Path-P data.

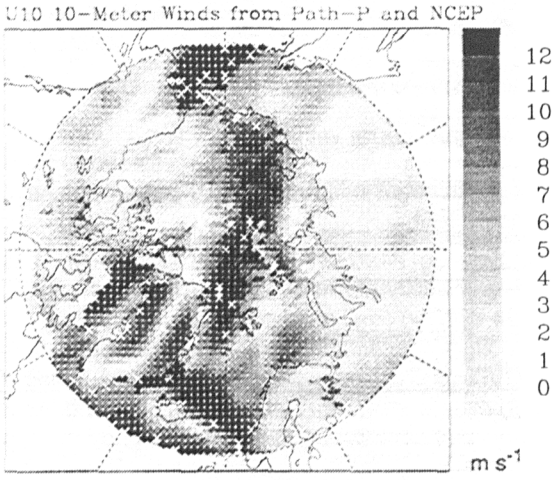

Figure 5: 10-meter wind speed on 4 January 1987 derived from Path-P data over sea ice and obtained from NCEP reanalyses elsewhere.

column warming due to sensible heat convergence is described in Francis (1995). D. Groves is extending this method to calculate the freshwater balance of the Arctic Basin. He computes advected moisture from Path-P data using winds from numerical analyses (NCEP) and from TOVS-derived thermal winds. Examples of his results will be presented in our poster.

Turbulent fluxes are also important components of the surface energy budget in certain regions and seasons. A critical variable in their calculation is the 10-m wind speed. An example for 4 January 1987 is shown in Figure 5. We compute ten-meter winds over sea ice from Path-P boundary layer stratification and NCEP surface pressure analyses (Francis, 1995). Over open water and in areas where TOVS retrievals are not available, we fill in with NCEP winds. These wind fields are being used in two research projects at Rutgers University: to force an Arctic coupled ice/ocean model (P.I.: D. Haidvogel) and to estimate the wind-forced component of the freshwater flux through the Canadian Archipelago (P.I.: A. Munchow).

Path-P is also being combined with AVHRR and passive microwave Pathfinder data sets into a 100-km resolution "P-Cube," which presents products from each of these projects in one easy-to-use format and grid. The P-Cube will be available to the community by 1999.

5. SUMMARY

The NASA TOVS Polar Pathfinder data set will span 18 years (1978 to 1996) when it is completed in late 1998. Basin-wide fields are produced daily at a 100 km resolution on the EASE grid in HDF format. It is the first resource of its kind to diagnose atmospheric and surface characteristics almost entirely from satellite data, thereby filling a conspicious void in the conventional data network. Several process and climate-oriented studies applying the data are already underway, and numerous others are possible. Its easy combination with other data sets, particularly those from polar Pathfinders, add to its potential value.

Two years of the data set are presently available on the www from http://psc.apl.washington.edu/pathp/pathp.html, as well as sample Fortran and C programsto read the HDF files, the User's Guide, and some example plots.

6. REFERENCES

Armstrong, R.L. and M.J. Brodzik, 1995: An earth-gridded SSM/I data set for cryospheric studies and global change monitoring, *Adv. Space Res., 16,* 155-163.

Boer, G.J., K. Arpe, M. Blackburn, M. Deque, W.L.Gates, T.L. Hart, H. LeTreut, E. Roeckner, D.A. Sheinin, I. Simmonds, R.N.B. Smith, T. Tokioka, R.T. Wetherald, and D. Williamson, 1992: Some results from an intercomparison of the climates simulated by 14 atmospheric general circulation models, *J. Geophys. Res., 97,* 12,771-12,786.

Carmack, E.C., K. Aagaard, J.H. Swift, R.G. Perkin, F.A. McLaughlin, R.W. MacDonald, E.P. Jones, J. Smith, K. Ellis, and L. Kilius, 1997: Large changes in the Arctic Ocean, in press, *Deep-Sea Research.*

Chedin, A., N.A. Scott, C. Wahiche, and P. Moulineir, 1985: The Improved Initialization Inversion method: A high resolution physical method for temperature retrievals from satellites of the TIROS-N series, *J. Clim. Appl Meteorol., 24,* 128-143.

Francis, J.A., 1995: Improvements to TOVS retrievals over sea ice and applications to estimating Arctic energy fluxes, *J. Geophys. Res., 99,* 10.395 - 10,408.

Francis, J.A., 1997: A method to derive downwelling longwave fluxes at the Arctic surface from TIRS operational vertical sounder data, *J. Geophys. Res., 102,* 1795-1806.

Houghton, J.T., G.J. Jenkins, and J.J. Ephraums (Eds.), 1990: *Climate Change. The IPCC Scientific Assessment.* Cambridge University Press, 365 pp.

Johannessen, O.M., M. Miles, and E. Bjorgo, 1995: The Arctic's shrinking sea ice, *Nature, 376,* 126-127.

P1.46B MODEL SIMULATED INTERANNUAL SST VARIABILITY IN NORTH INDIAN OCEAN

S. K. Behera & P. S. Salvekar
Institute for Global Change Research, Tokyo 105, Japan

1. Introduction

The annual cycle in the surface forcing of the Indian Ocean due to monsoons, induces dramatic changes in the thermodynamic characteristics of the upper ocean. The seasonal variability in the thermodynamic characteristics in the upper ocean of the region is understood to some extent but their interannual variabilities are being addressed only recently. Data scarcity has been a major factor for the restriction of such studies. Ocean models provide a reasonable scope for understanding and predicting these fields and their variabilities in both space and time. Evolution of ocean circulation and heat content in the upper layers generally depend more on the surface forcing fields than on the internal dynamics. Hence, reliable knowledge of the forcing in both space and time is essential for the modelling studies. However, uncertainties still remain in estimating the surface fluxes, may be due to the sampling problems both in space and time and due to uncertainties in prescribing the drag coefficients. In order to avoid sampling problems, composite of all the available historical observations for each calendar month is generally used for the computation of surface fluxes in modelling studies.

Since, wind observations have more sampling coverage and better estimations, many modelling studies have used interannual wind stress forcing in the ocean models. Luther and O'Brien (1989) simulated the interannual variability in the upper layer circulation of the Indian Ocean by forcing a simple reduced gravity model with interannual wind fields. In this study, a model of intermediate complexity (McCreary et al 1993, hereafter MKM) is used to simulate the interannual SST variability of the Indian Ocean. MKM has shown the model's ability to produce realistic climatology of SST and circulation in the upper Indian Ocean using climatological wind stress(Hellerman and Rosenstein 1983) and heat fluxes (COADS). In this work, the surface fluxes of momentum and heat are derived from the NCEP reanalysis data (Kalnay et al 1996).

2. The Model and Surface Forcings

The model used in this study has two active layers overlying a deep motionless layer of infinite depth. The upper two active layers interact with each other through entrainment and detrainment while conserving mass and heat of the total system. In simpler form the surface uppermost layer is a single layer with a thickness of h_1 and temperature T_1. However, once entrainment and detrainment start taking place the surface layer assumes a more complex form in which it separates into two sub-layers i.e. a well-mixed upper turbulent sub-layer of thickness h_m and temperature T_m and a non-turbulent fossil sub-layer of thickness h_f and temperature T_f. In both of its simple one layer form and the most complex two sub-layer forms, the surface layer has velocity $\mathbf{v}_1$. Thus there is no vertical shear in velocity field in the sub-layers of the surface layer.

The uppermost sub-layer of the surface layer that can be termed as upper mixed layer entrains or detrains water in a process in which the mixing is maintained by turbulence generated by both wind stirring and cooling at surface. The non-turbulent fossil layer i.e. the second sub-layer of the surface layer being formed by the detrainment of water from the upper mixed layer is kept isolated from the surface turbulence. However, it can be engulfed into the mixed layer either during the strong entrainment periods or upwelling regions where h_1 becomes shallow significantly. There is also provision for detrainment of water from the upper surface layer to the model second layer to conserve mass of the layers as entrainment through the base of the surface layer takes mass from the second layer. The model second layer has velocity $\mathbf{v}_2$, thickness h_2 and temperature T_2. The temperature (T_m) of the uppermost turbulent sub-layer is considered as representative of Sea Surface Temperature (SST).

The model equations are solved numerically on a staggered grid (Arakawa C grid) with T points located at h points and having a horizontal resolution of 55 km for north Indian Ocean (north of 30S). Time integration is done using leapfrog scheme with a time step of 1 hour. The fields are averaged between successive time levels at every 41 time step to inhibit time splitting instability.

The surface fluxes used in the model are derived from the monthly fields of the NCEP (National Center for Environment Prediction) reanalysis data (from the period 1982-1991) of net solar radiation (incoming fluxes - outgoing fluxes), air temperature (at 2m), specific humidity (at 2m) and wind components (at 10m). The model simulated SST fields are used for the heat flux computations instead of observed SSTs. The data sets are linearly interpolated to model grid points from the available 2° X 2° grid. The wind stress fields are then computed from the wind fields with drag coefficient $C_D = 1.25 \times 10^{-3}$ and air density $\rho = 1.2$

Corresponding author address: S.K. Behera, Inst. For Global Change Research, SEAVANS N 7F, 1-2-1 Shibaura, Minato-Ku, Tokyo 105, Japan

Kg m^{-3}. For simplicity model calendar is considered of 360 days having 30 days in each month.

3. Results and Discussion

The model is first spun up for 10 years with the mean forcing that is obtained by 10 year averaging (1982-1991) of the surface flux fields that have been derived from the NCEP reanalysis data sets. The numerical solution reached a quasi-equilibrium state by 10th year and these solutions are considered as model initial conditions for the interannual run in which the model equations are integrated for further 10 years with the interannually varying monthly surface forcing. The values of the model variables at day 15 of each month are considered to represent the monthly values. Monthly anomalies are departures from the monthly mean of the variables.

3.1 *Mean SST and Current*

Figure 1 shows the 10-year average model SST and upper layer current fields for the month January and July. In general, the model current and temperature fields are found to be in agreement with observation. However, the model SST is found to be colder in most of the places by 0.5C, and upto 1.0C near Somali Coast during summer monsoon. This might be because the model SST is the average temperature of the upper mixed sub-layer that has a much higher depth compared to the depth considered for SST observation. In January, the eastward North Equatorial Current (NEC), the South Equatorial Current (SEC), the westward Equatorial Counter Current (ECC), the southward Somali Current (SC) and the northward East India Coastal Current (EICC) are well simulated by the model. The warm equatorial band of >28C SST is also simulated well by the model. In April, the warm equatorial band of SST has moved northward in response to the annual northward march of the Sun. The development of eastward equatorial Wyrtki Jet (WJ), disappearance of NEC, southward displacement of the SEC and northward turning of SC that are found in the current field, are in agreement with observation. In July, the intense monsoon winds have produced coastal upwelling and cooling of SST along Somali Coast and Indian Coasts. The cooler surface water has then spread to the interior ocean. The well known cold tongue of cold SST can be seen between 5N and 10N, off the Somali Coast. The strong northward SC and the two associated gyres, i.e. one around equator and the other around 5N, are the dominant features of the July current field. The SC still persists in October and the WJ has already developed, in agreement with observation. The coastal upwelling has reduced and the warming of SST in Arabian Sea and Bay of Bengal has started.

In the lower layer a westward counter current is found north of equator, below the NEC. The lower layer SEC is present throughout the year. South of 10S, the temperature fields are mostly found to be greater than 18C, which gradually reduces to 13C in the northern Arabian Sea. In April, the currents are southward between 5N and equator and a warm core clockwise gyre is found between equator and 5S, off the Somali Coast. The westward equatorial counter currents found in January are replaced by eastward currents that are in opposite direction to the surface WJ. The temperature field suggests a warming in the northern Bay of Bengal and Arabian Sea. The northward SC is found in the lower layer, in June and July. The coastal upwelling is found even in the lower

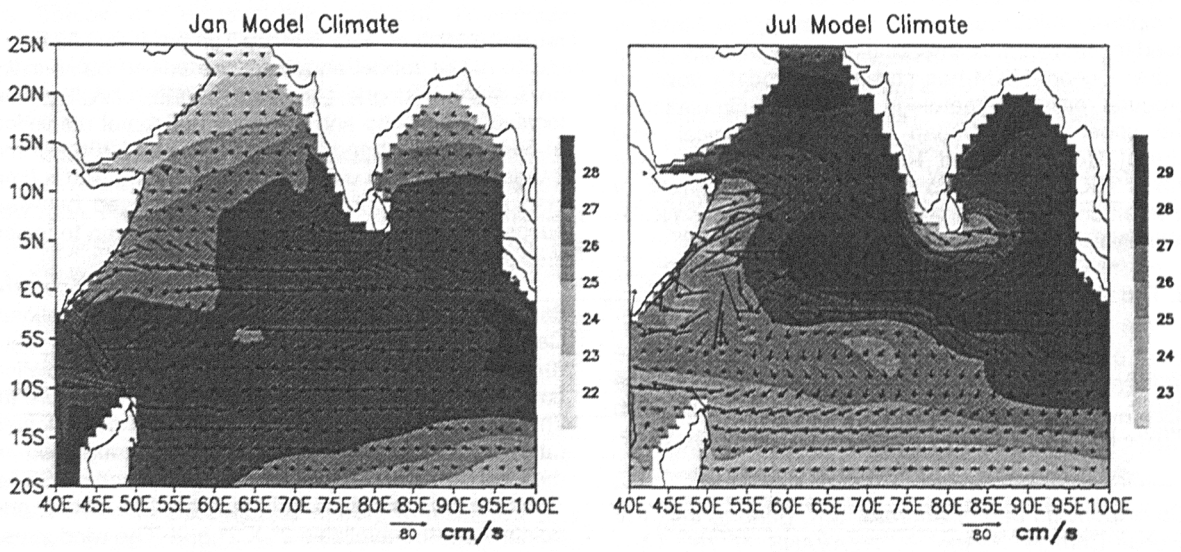

Fig.1 Model upper layer current and SST climatology for the months of January and July

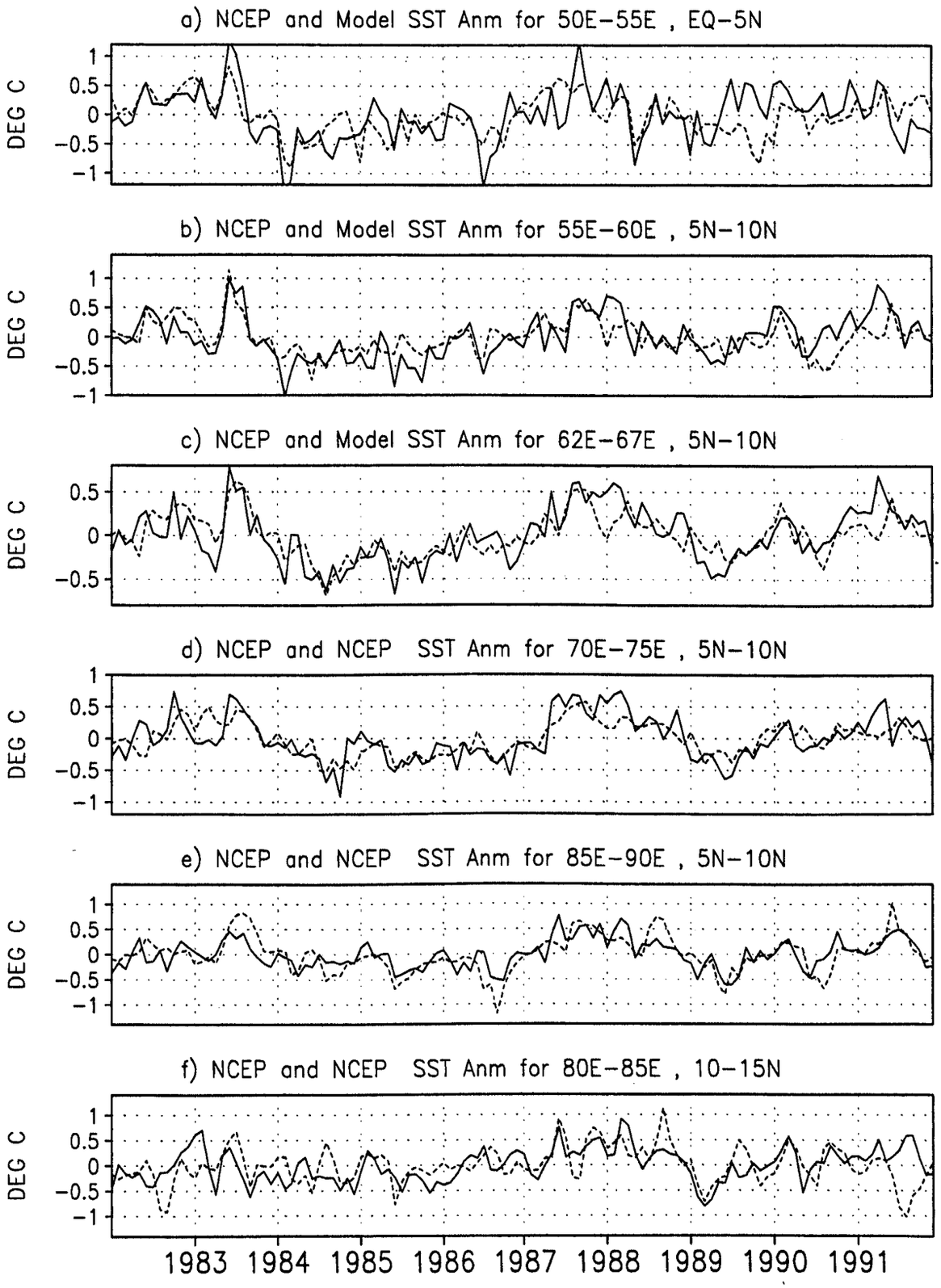

Fig. 2 Time series of observed (solid lines) and model SST anomalies (dashed lines) for the six small regions as indicated in the figure titles.

layers all along the northern coasts in July. The northward SC and the coastal upwelling persist till October. These results are in agreement with the model results of MKM and the limited observational evidences as referred in MKM.

3.2 *Interannual variability*

Standard deviation (SD) of model SSTs is computed at each grid point to understand the ability of the model in producing SST variability in response to interannual wind. High values of SD are found in equatorial region, along African Coast, along west coast of India and southern Indian Ocean.

In order to have a closer look at the model performance in simulating the realistic interannual SST fields, four small (5x5) regions are considered in the Arabian Sea and two in the Bay of Bengal. Figure 2 shows the time series of Reynolds reanalysis SST (Reynolds and Marisco 1993) anomalies and the model SST anomalies. In general, the phase and the amplitude of model anomalies are found to be in good agreement with the observed anomalies. The trends of warming and cooling in both model and the observed anomalies have not occurred monotonously but have occurred through events. And these seasonal variabilities or the events are well comparable between the model and the data. The warm event of 1983 summer, seen most prominently in the Arabian Sea is simulated well by the model. In region (a) (off the Somali Coast), peak amplitude of the model anomaly is found to be 0.5C colder than the observed anomaly. Similarly, the peaks in the cold anomaly in 1986, and the warm anomaly in 1987, are not well reproduced by the model. However, the trend of warming from the cold event of 1986 to warm event in the 1987 and the subsequent cooling has been well simulated by the model in all the regions. There is a phase difference found in the model anomaly and the observed anomaly during most part of 1989, in region (a). The observed anomaly shows a warming of 0.5C with a large seasonal variability as compared to a cooling of the same order found in the model anomaly with less seasonal variability. The region is dynamically active and the model SST anomalies are mostly found to be influenced by the wind steering parameter. In region (b), (c), (i.e. south central Arabian Sea) and the region (d), (i.e. off the west coast of India) the model results are well comparable with the observation. The SST of the region (b) and (c) are dominantly influenced by the advection from the Somali Coast and it seems the model has produced it realistically. The SST of the region (d) is influenced by local upwelling, and the advection from the interior Arabian Sea. The close agreement in the model and observed anomalies in the region suggest that the mechanisms are well reproduced by the model.

In Bay of Bengal, in the region (e), i.e. off Sri Lanka, the model anomalies are in agreement with that of the observed. However, the peak of the model cold anomaly in 1986, is colder by 0.5C than that of the observed. More differences are found between the model and the observed anomalies, in the region (f) i.e. off the east coast of India. This region is influenced by various mechanisms e.g., local wind stress curl, advection, Ekman pumping and Rossby waves radiated from the eastern rim of the Bay. Combination of these mechanisms might be responsible in the variability in the SST of the region. So, it is difficult to say which mechanism might be responsible for the model deficiency. The model results are being compared with the satellite derived SST fields.

Acknowledgment : The authors are grateful to Dr. J.P. McCreary for kindly providing the ocean model and helpful suggestions. The first author is thankful to Prof. Toshio Yamagata for his encouragement to carry out the work. Thanks are due to Dr. Bryan Doty of COLA for kindly providing the GrADS software.

References

Hellerman S and Rosenstein M 1983 Normal monthly wind stress over the world ocean with error estimates; *J. Phy. Oceanogr.* **13** 1093-1104

Kalnay E., Kanamitsu M., Kistler R., Collins W., Deaven D., Gandin L., Iredell M., Saha S., White G., Woollen J., Zhu Y., Chelliah M., Ebisuzaki W., Higgins W., Janowiak J., Mo K.C., Ropelewski C., Wang J., Leetmaa A., Reynolds R., Roy Jenne, and Dennis Joseph, 1996, " The NCEP/NCAR 40 year reanalysis project", *Bull. Amer. Meteor. Soc.*, ***77***, 437-471.

Luther M E and O'Brien J.J 1989 Modelling the variability in the Somali current; Mesoscale/Synoptic coherent structures in Geophysical Turbulence, Eds Nihoul J C J and Jamart B M *Elsevier Science Publ. Amsterdam* 373-386

McCreary J P, Kundu P K and Molinari R L 1993 A numerical investigation of dynamics, thermodynamics, and mixed layer processes in the Indian Ocean; *Prog. Ocean.* **31** 181-244

Reynolds R W and Marisco D C 1993 An improved real-time global sea surface temperature analysis; *J. Climate* **6** 114-119

P1.47.A

RELATIONSHIP BETWEEN SEA SURFACE TEMPERATURE, VERTICAL DYNAMICS, AND THE VERTICAL DISTRIBUTION OF ATMOSPHERIC WATER VAPOR, INFERRED FROM TOVS OBSERVATIONS

Jean-Pierre Chaboureau*, Alain Chédin, and Noëlle A. Scott
Laboratoire de Météorologie Dynamique du CNRS, École Polytechnique, France

1. INTRODUCTION

Water vapor is the most important greenhouse gas. Its interaction within the atmosphere plays a fundamental role in regulating the Earth's climate at all time scales. Therefore the water vapor feedback is considered as a major scheme of warming in the general circulation models. Despite its importance, the influences on the atmospheric humidity are poorly understood. Indeed, it is well know that the Sea Surface Temperature (SST) controls in large part the atmospheric humidity over oceans through the Clausius-Clapeyron relationship (e.g. Raval and Ramanathan 1989). But in order to explain the processes limiting the rise in SST, recent studies have pointed out the role of the large-scale vertical motions (e.g. Bony et al. 1997).

To infer the large-scale vertical dynamics from only observations, an original method is developed based on the power law which depicts approximately the distribution of water vapor on the vertical. A specific indicator of the large-scale vertical dynamics is then defined and validated using, in particular, the retrieved cloud distribution. The method permits us to express the relationship between the water vapor vertical structure, the SST and the large-scale vertical motions.

2. THE TOVS-3I DATA

Data are derived from the TIROS-N Operational Vertical Sounder (TOVS), aboard the NOAA series of polar satellites, operational since 1979. They are obtained by the Improved Initialization Inversion (3I) algorithm (Chédin and Scott 1984). The inversion algorithm 3I is a physico-statistical method relying on pattern recognition. It determines airmass type, temperature profiles (from the surface to 10 hPa), cloud heights, amounts and types, surface parameters (temperature, emissivity), water vapor contents (surf-.850, 850-700, 700-500, and 500-300 hPa). The water vapor retrieval scheme is based upon a neural network approach, directly coupling satellite observations to water vapor contents. Cross-comparisons with a wide variety of independent observations (in situ measurements, other satellite retrievals and analyses) have been conducted to fully evaluate the method (Chaboureau et al. 1997). Done in the framework of the NOAA/NASA Pathfinder project, this study is limited to the tropical band (±30° latitude) for a two year period, April 1987 to March 1989, from NOAA-10 observations. It uses monthly averages onto a 1° longitude by 1° latitude grid.

3. DISTRIBUTION OF HUMIDITY AND LARGE-SCALE VERTICAL DYNAMICS

The mean decrease of humidity with increasing altitude may be approximately described by a power law: $q = q_0 (p/p_0)^{\lambda}$, where q is the specific humidity at pressure p, q_0 and p_0 are the respective surface values and λ the power factor. By integrating this relation from the surface to the top of the atmosphere, and by using an approximate Clausius-Clapeyron relation, the total water vapor content (in cm), w_{tot}, can be written as:

$$w_{tot} = 10,82 \left(\frac{r_0}{1+\lambda}\right) \exp[a(SST - 288)] \quad (1)$$

$a = 0.064\mathrm{K}^{-1}$ and r_0 the relative humidity at the surface (Stephens 1990). This equation expresses the linear relationship between $\log w_{tot}$ and the SST, relation established using satellite observations by Raval and Ramanathan (1989). Using expression (1), we can compute λ knowing the SST and w_{tot}. Earlier results (Prabhakara et al. 1979; Stephens 1990) show that values of λ smaller than 3.5 suggest moisture convergence and/or moist air advection, and values of λ greater than 3.5, indicate the influence of subsidence or dry air advection.

This approach may be refined by observing the vertical structure of water vapor rather than using w_{tot}. It follows from the integration of the power law, that the ratio of w_{par}, water vapor content

* *Corresponding author address:* J.-P. Chaboureau, Dept of Meteorology, Univ. of Reading, PO Box 243, Reading RG6 6BB, UK; e-mail: J-P.Chaboureau@reading.ac.uk

between the pressure levels p_{sup} and p_{inf}, to w_{tot}:

$$\frac{w_{par}}{w_{tot}} = \left(\frac{p_{sup}}{p_0}\right)^{\lambda_i+1} - \left(\frac{p_{inf}}{p_0}\right)^{\lambda_i+1} \quad (2)$$

where λ_i applies to the layer $(p_{inf}; p_{sup})$. The values of λ_i for three layers of the troposphere have been computed. Among the latter, λ_2 associated to the 700-500 hPa layer is the most variable. The more contrasted behavior results from a more important influence of the large-scale vertical dynamics as shown now. To assess this affirmation, we use one of the signatures of such an influence: the high level clouds (for which top pressure is less than 440 hPa), which include deep convective clouds associated with an upward motion. More precisely, we compute the frequency of occurrence of high clouds per month (FOHCM).

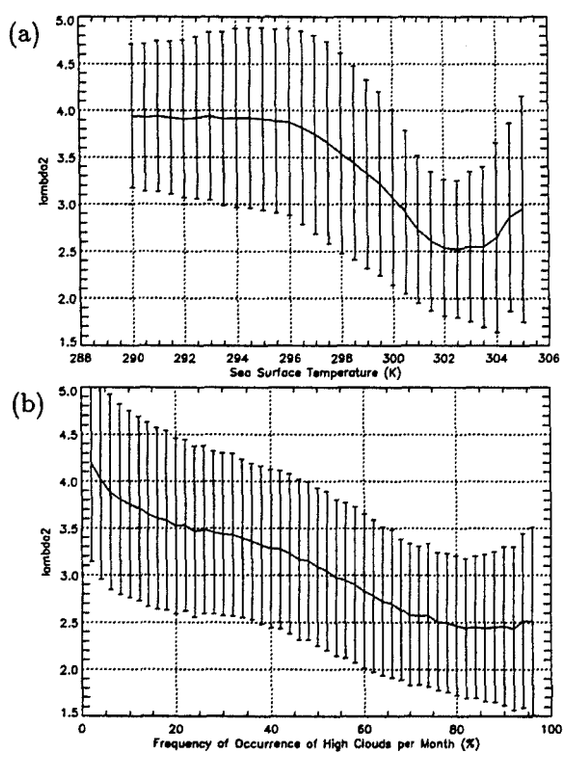

Figure 1: Monthly averaged values of λ_2 (a) for each SST interval of 0.5 K and (b) for each FOCHM interval of 2 % over oceans for which SST is greater than 290 K, from April 1987 to March 1989. Vertical bars represent ± one standard deviation around the two-year mean.

Fig. 1 presents the variation of λ_2 versus SST and FOHCM, over oceans. The most important feature is the anticorrelation between FOCHM and λ_2 up to 80 % of FOHCM. As λ_2 decreases, FOCHM increases, showing enhanced deep convection (upward motions): the link between λ_2 and large-scale vertical dynamics associated to deep convection is straightforward. Consistently, within 299-303 K, the required SST range for deep convection (Waliser et al. 1993), λ_2 also rapidly decreases from 3.5 to 2.5. Outside these ranges, when FOCHM increases from 0 to 20 %, λ_2 decreases from 4.2 to 3.5: both small values of FOCHM and large values of λ_2 highlight the subsidence and/or dry air advection. Values of λ_2 greater than 3.5 for SST less than 299 K also indicate the occurrence of the subsidence. Beyond 303 K for SST or 80 % for FOHCM, the increase of λ_2 is clearly associated with convection decrease.

4. WATER VAPOR, SST AND VERTICAL DYNAMICS

4.1 Seasonal variations

At each gridpoint, seasonal variations of each of the three variables (water vapor content, SST, and λ_2) are computed by subtracting the annual average from April 1987 to March 1988 (respectively from April 1988 to March 1989) to monthly means, from April 1987 to March 1988 (from April 1988 to March 1989). Relative changes of vertical dynamics with respect to SST may be described by the ratio of $\Delta\lambda_2$ to ΔSST. So I_c, the index of change of λ_2 with respect to SST, is defined as: $I_c = \Delta\lambda_2/\Delta SST$, and is computed only if $\Delta SST > 0.01°C$, to avoid unstable values for I_c. Three modes may then be defined: the mode 1 where $I_c < -0.2K^{-1}$ corresponds to SST increase which goes with a λ_2 decrease, e.g. ascending movement increase, notably the deep convection cases. The mode 2 where $I_c > 0.2K^{-1}$ refers to cases for which the SST increase goes with a λ_2 increase, e.g. ascending movement decrease. The change of λ_2 cannot be explained by a local SST change and thus should imply a remote forcing of the atmosphere (e.g. the large-scale subsidence). The mode 3 for which $-0.2K^{-1} < I_c < 0.2K^{-1}$ relates to no (or weak) correlation between SST and vertical dynamics. Note the choice of $0.2K^{-1}$ as the threshold is not critical for the following.

Fig. 2 shows the geographical distribution of the occurrence (in %) of 2 modes. The mode 1 is mainly located between 10-20° latitude. It corresponds to the seasonal migration of the vertical branches of the Hadley circulation. These regions which show large occurrence of mode 1 are located in the vicinity of the 298-300 K isotherm, required SST threshold for deep convection. Thus

it highlights the cooperative action of a simultaneous increase of SST and of upward motions, in such a mechanism. The mode 2, corresponding to a simultaneous increase of SST and large-scale subsidence, mainly occurs over Pacific and Indian oceans where SST is the warmest. This decoupling between the vertical motion and the SST can be explained by the seasonal monsoon circulation and/or the influence of Madden and Julian oscillation (Bony et al. 1997). The mode 3 is located over subtropical oceans and off the west coast of lands. In these regions, the vertical dynamics changes are weak with regard to SST changes. This method to characterize the relative change of vertical motion with respect to SST is derived from a study by Bony et al. (1997). The two studies show similar results. However, the present approach uses the indicator λ_2, directly obtained from observations, whereas Bony et al. use the vertical velocity at 500 hPa computed by a general circulation model. The good agreement shows the coherence between the vertical velocity from a model and the vertical dynamics indicator as inferred from TOVS-3I.

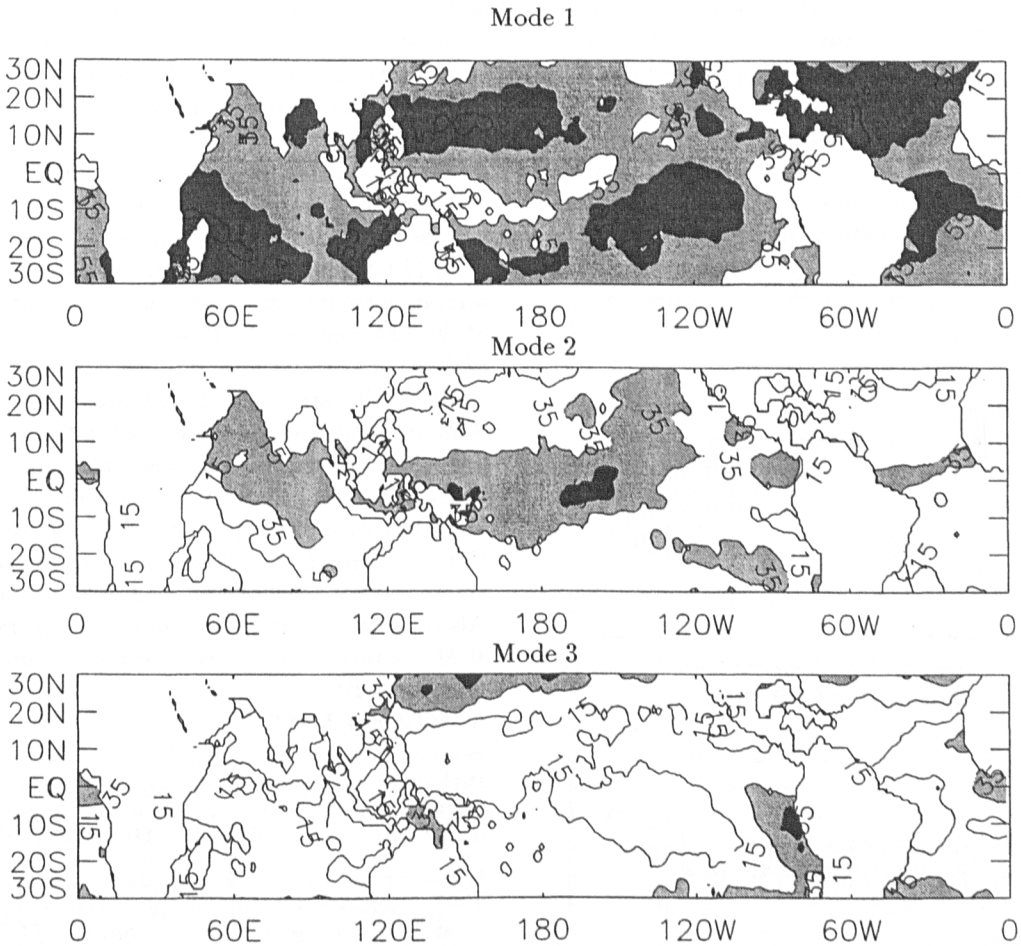

Figure 2: Geographical distribution of occurrence (in %) for the 2 of the 3 different modes of I_c (see text) for the seasonal variation. Contour interval is 20 % and values between 15 and 35 % (respectively over 35 %) are shaded in light (dark) gray.

4.2 Global Relationship

Using equations (1) and (2), it follows: $dw_{par}/w_{par} = adSST - b_{par}(\lambda)d\lambda/(\lambda + 1)$, where $b(\lambda)$ is a positive function increasing with λ, in the interval of λ considered here, and depending on p_{sup} and p_{inf}. In particular, for the 700-500 hPa layer, the latter equation becomes:

$$\frac{1}{w_{700-500}} \frac{\Delta w_{700-500}}{\Delta SST} = a - b_{700-500}(\lambda_2) I_d, \quad (3)$$

where $I_d = I_c/(\lambda_2 + 1)$ and thus it is the index of relative change of λ_2 with respect to SST. It expresses the relationship between the variations of the water vapor content in the 700-500 hPa layer, on the one hand, and the large-scale vertical dynamics, on the other, with the SST. Since $b_{700-500}$ slightly increases from 2 to 2.5 when λ increases from 3 to 4, $1/w_{700-500} \times \Delta w_{700-500}/\Delta SST$ is

positive (respectively negative) when I_d is smaller than a/b, notably for the mode 1 (greater than a/b, especially for the mode 2).

Fig. 3 shows the observed relative change of w_{par} with SST for the two layers according to I_d. In addition, the function $a+b_{par}I_d$ have been plotted with b_{par} values of 0.2 for the surface-700 hPa layer and of 1.5 for 700-500 hPa layer. The values of each b_{par} have been chosen to best fit the observations. Note that a value of $b_{700-500}$ equal to 1.5 corresponds to a realistic value of λ_2 around 2.5.

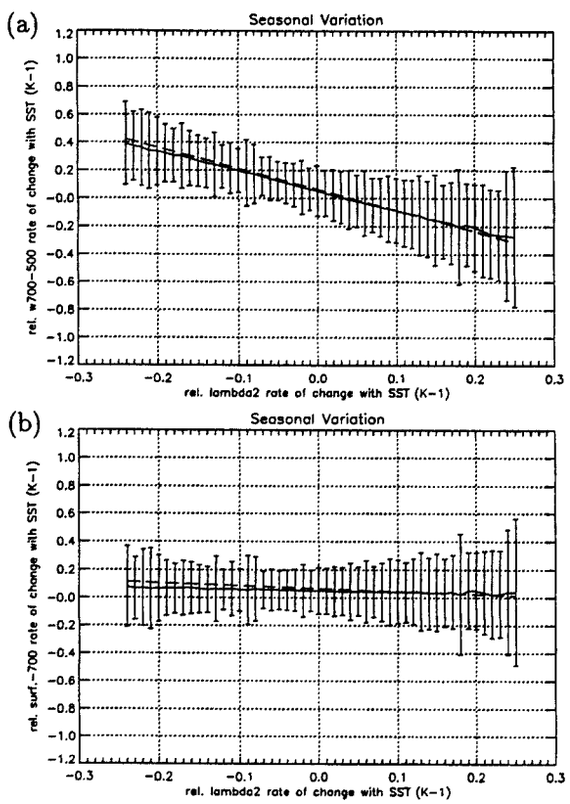

Figure 3: Seasonal variation of $1/w_{par} \times \Delta w_{par}/\Delta SST$ according to I_d, (a) in the 700-500 hPa layer, and (b) in the surface-700 hPa layer.

It shows that relation (3) is approximately verified in the 700-500 hPa layer as well in the 500-300 hPa layer (not shown) with the same gradient. In the surface-700 hPa layer, the rate of change of the water vapor content with respect to SST does not vary too much with I_d. It follows that the role of the vertical dynamics on the water vapor content in the lower troposphere is negligible with respect to that of the SST.

On the contrary, in the upper layers, the vertical dynamics has an important contribution to the distribution of the water vapor. For instance, with a positive SST perturbation of 1 K, a 10 % enhancement of upward motion leads to a 20 % increase of the water vapor content in the 700-500 and in the 500-300 hPa layers. In contrast, for the same SST perturbation, a 10 % diminution of upward motions lead to a 10 % decrease of the water vapor content in the same layers.

5. FUTURE WORKS

Presently limited in time, this global analysis of the vertical distribution of water vapor content will be extended to the almost 20 year observations (1979 to now) of NOAA satellites. Moreover, a more complete and unambiguous understanding of the link between SST, water vapor distribution, and vertical dynamics implies a strong coupling between climate modeling and observation.

Acknowledgments. The satellite data were provided to us within the framework of the NOAA/NASA Pathfinder Programme. This work has been supported by CNRS, CNES and by the Commission of the European Community, contracts EV5V-CT92-0131 and EV5V-CT94-0441. Also this work has been supported by grants from IBM. Computations have been performed on IDRIS of CNRS.

6. REFERENCES

Bony, S., K.-M. Lau, and Y.C. Sud, 1997: Sea surface temperature and large-scale circulation influences on tropical greenhouse effect and cloud radiative forcing. *J. Climate*, **10**, 2055-2077.

Chaboureau, J.-P., A. Chédin, and N.A. Scott, 1997: Remote sensing of the vertical distribution of atmospheric water vapor from the TOVS observations. Method and validation. *J. Geophys. Res.*, in press.

Chédin, A. and N.A. Scott, 1984: Improved Initialization Inversion procedure ("3I"), In *Proc. First TOVS Study Conf., Igls, Austria*, Cooperative Inst. for Meteor. Satellite Studies, 14-79.

Prabhakara, C., G. Dalu, R.C. Lo, and N.R. Nath, 1979: Remote sensing of seasonal distribution of precipitable water over the oceans and the inference of boundary-layer structure. *Mon. Wea. Rev.*, **107**, 1388-1401.

Raval, A. and V. Ramanathan, 1989: Observational determination of the greenhouse effect. *Nature*, **342**, 758-761.

Stephens, G.L., 1990: On the relationship between water vapor over the oceans and sea surface temperature. *J. Climate*, **3**, 634-645.

Waliser, D.E., N.E. Graham, and C. Gautier, 1993: Comparison of the highly reflective cloud and outgoing longwave radiation datasets for use in estimating tropical deep convection. *J. Climate*, **6**, 331-353.

P1.48.B

CLEAR SKY ATMOSPHERIC LONGWAVE COOLING WITH THE TOVS/PATH-B DATASET

F. Chéruy, F. Chevallier , N. A. Scott
Laboratoire de Météorologie Dynamique (CNRS), École Polytechnique, France.

1. INTRODUCTION

The ability of the atmosphere to lose its excess of energy depends on both the OLR and the LW radiation emitted by the atmosphere towards the surface: the DLR. While the OLR is essentially emitted in the 10-12 μm atmospheric window, the DLR is mostly emitted in the carbon dioxide (around 15 μm) and water vapor (around 6.3μm and 25μm) absorbing regions. Consequently the sensitivity of the OLR and the DLR to the vertical structure of the atmosphere might be different. Owing to ERBE data numerous studies have been conducted on the TOA OLR and on the so called greenhouse effect,G (difference between the LW flux emitted at the surface and the OLR). In this paper, we focus on the total IR cooling, C^T, which corresponds to the difference between the net LW flux at the surface and the OLR. It can be expressed as the difference between G and the DLR. Since direct and global estimations of the DLR are not yet available, we derive them from estimations of the thermodynamic vertical structure of the atmosphere with the help of a radiative transfer model.

2. THE DATA

We extracted temperature, and water vapor information from the daily files of the TOVS/PathB (NOAA-10) dataset for the months of January and July 1988, see Chédin et al., 1985, Chaboureau et al. and Stubenrauch et al,(this issue) for a description of the inversion algorithm. Comparison of instantaneous estimation of the retrieved profiles with a large set of co-located radiosonde reports (Armante, personal communication) allowed to infer a rough estimation of the uncertainties in C^T: they are less than 5% of the mean C^T value. However, it should be stressed that the performances of the TOVS retrievals are not uniformly distributed over the globe. In particular, intrinsic limitation of the infrared sounding leads to a dramatic overestimation of the total water vapor content over regions associated with large scale subsidence (Stephens et al., 1994). In order to overcome this difficulty, we fitted the TOVS total content with the SSM/I content which does not suffer such a limitation. The vertical repartition of water vapor as deduced by TOVS is assumed to be correct. Though its weaknesses, TOVS is the only instrument which can provide global estimations of the temperature profile as well as of the vertical distribution of water vapor content. Then we used the ECMWF code (Morcrette, 1991, Zhong et al., 1995) to compute the components of the LW fluxes from the TOA to the surface for clear as well as partly cloudy situations.

3. GEOGRAPHICAL AND SEASONAL VARIATIONS OF C^T

Global maps of the absolute value of C^T, C_a^T, are displayed in figure 1 for January 1988 and July 1988. For the mid-latitude regions C^T exhibits strong seasonal variations. It is maximum in the summer. For the tropics, the seasonal variations are small, but there are significant geographical variations. The geographical distribution of C_a^T, exhibits similarities with principal features of the atmospheric tropical general circulation. Maxima are mainly situated in the subsidence zones over the tropical oceans. However, the land subsidence zones correspond to local minima. Over the tropical ascending zones one observes local minima except in the warming pool around the ocean continent where maxima can arise. The extrema follow the seasonal migration of the tropical dynamics: the intensification of the Hadley and Walker cells in the winter hemisphere and the meridional migration of the ITCZ. The behavior of C_a^T can be linked to the geographic and vertical temperature and water vapor large scale structure of the atmosphere. Over the middle and polar latitudes, C_a^T decreases with the latitude and is minimum in the winter hemisphere. This has to be related to the fact that water vapor content

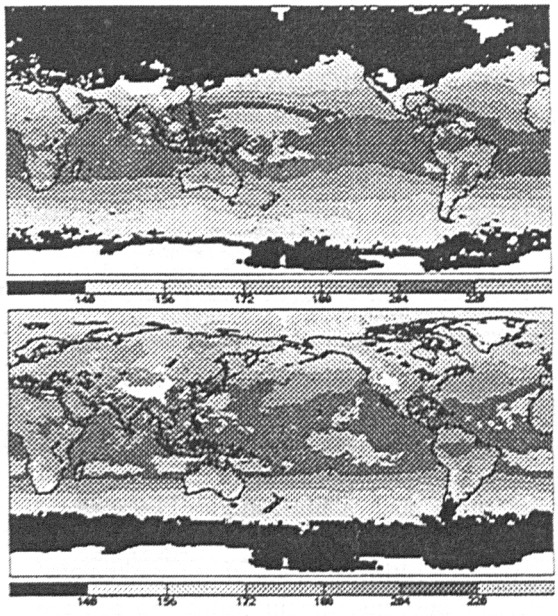

Figure 1: C_a^T for January (upper panel) and July 1988 (lower panel)

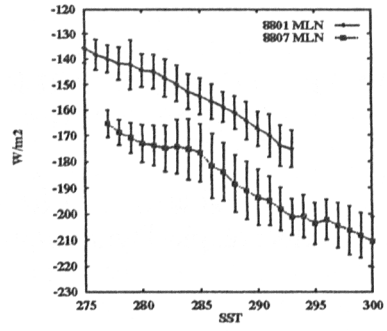

Figure 2: Variations of C^T for January, July 1988 in the mid-latitude north band as a function of the SST

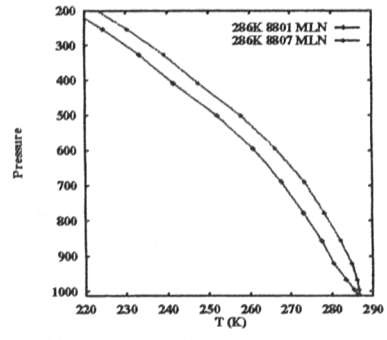

Figure 3: mean temperature profile in January and July 1988, for a mean SST value of 286K

is mimimum and the atmospheric temperature colder. In the subtropical regions of subsidence, the water vapor is compressed in the lowest part of the troposphere. The evaporation which occurs over the oceans tends to humidify the lowest troposphere. The dry middle and upper troposphere is transparent to the radiation which can escape to space increasing the cooling to space. The high values of the water vapor content in the lower troposphere act to increase the cooling to surface. In the ascending branch of the Hadley circulation the low troposphere water vapor content is still high, but the upper troposphere is also very moist, reducing the cooling to space and consequently explaining the differences with the descending branch of the tropical circulation. Over the land, the water vapor burden is very low, making atmosphere more transparent than over the ocean, leading to a weak radiative activity.

4. RELATIONSHIP BETWEEN C^T AND THE SST

The discussion is restricted to ice free oceans. The reasons which govern this decision are threefold: SSM/I cannot be used to derive water vapor content over land, and the TOVS content may not be reliable over large-scale land subsidence regions as it is over ocean, surface temperature retrieval over land is very difficult due to the failure to estimate the surface emissivities, the diurnal cycle is expected to play a significant role in the modulation of C^T and the temporal sampling of the NOAA-10 satellite does not allow to account for it.

We examine the variations of C^T in conjunction with the variations in the mean temperature and water vapor profiles for the months of January and July 1988.

4.1 mid-latitudes north regions(60N-30N)

The variations of C^T binned into SST intervals of 1K are reported in figure 2. The errorbars correspond to the standard deviation of C^T within each SST interval. C^T decreases as the SST increases. For the same SST values C_a^T is larger in July. This is not surprising since, given the higher atmospheric temperature, higher water vapor content is expected in July from the thermodynamics. Inspection of the associated binned temperature profiles reveals that winter and summer profiles differ essentially in the lower troposphere where the summer profile is rather isothermal, while the winter one is steeper (see figure 3). Webb et al., 1993,

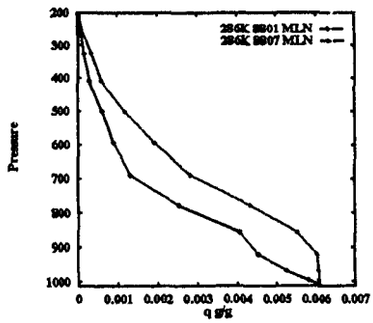

Figure 4: mean water vapor profile in January and July 1988, for a mean SST value of 286K

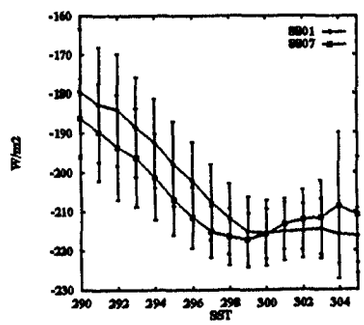

Figure 5: C^T binned into SST intervals of 1K for July 1988 and January 1988 in the tropics.

related a similar behavior in temperature profiles extracted from ECMWF analysis, eventhough they observe inversions rather than isothermal profiles. Both the steepest vertical temperature gradient and lower water vapor content act to reduce C_a^T. While temperature and water vapor effect on G are of opposite sign, making its seasonal variations controlled by seasonal changes in atmospheric temperature (Webb et al., 1993), the atmospheric temperature and water vapor seasonal variations act in the same way to control variations of C^T.

4.2 tropical regions (30N-30S)

For SST less than 298K, C^T decreases as the SST increases (see figure5). The cooling is more pronounced in July. When looking at the water vapor profiles, it appears that the upper troposphere is slightly more humid in January compared to July (see figure 6), while the temperature profiles are nearly identical. This feature acts to increase C_a^T. The differences in the mean water vapor profiles might be due to variations in the tropical vertical motions, and particularly to a predominance of the subsiding motions in July in relation with the seasonal migration of the Hadley cells as well as to the land/ocean asymmetry between the 2 hemispheres. For SST around 300K, C^T reaches a threshold after which it becomes either constant in January or increases slightly in July. This feature is a manifestation the super-greenhouse effect firstly observed by (Raval et al.,1989) owing to ERBE data. The mean temperature and water vapor profiles for SST values of 297 and 302 are plotted in figure 5. Consistently with previous studies (for instance Inamdar et al., 1994), one observes more unstable and moister conditions for supergreenhouse situations. We conducted sensitivity experiments based on the differences between the super-greenhouse and normal temperature and water vapor profiles. For SST greater than 300K, we modified the binned profiles as follows: the temperature profile was modified such as to get the same vertical gradient as the binned temperature profile whose SST is 5K colder (case A). The water vapor profile was modified such as to get the water vapor profile corresponding to a 5K colder SST but conserving the total content, (case B). This results in a drying of the upper troposphere and a moistening of the lowest troposphere (see figure 5). Then, radiative computations with the perturbated profiles, including both temperature and water vapor perturbations (case C) were done. The water vapor perturbation (case B) is the most efficient to suppress the breakdown in the slope of the C^T/SST curve. Temperature perturbation acts only on the absolute value of C^T. As for the super-greenhouse effect, the water vapor, especially its vertical distribution, controls

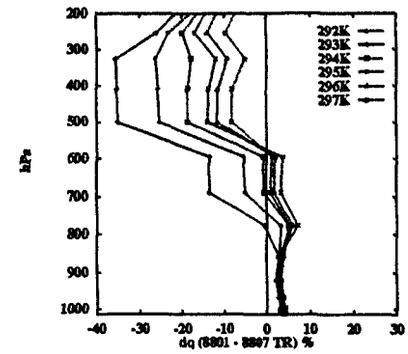

Figure 6: differences in the water vapor profiles between January and July expressed in % of the mean specific humidity for increased SST values

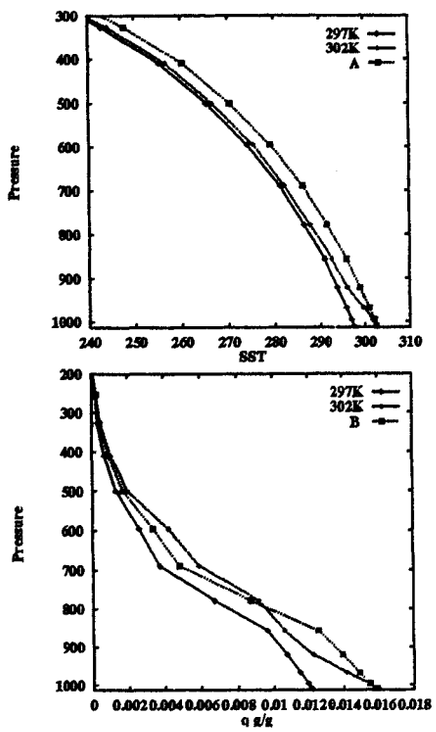

Figure 7: mean temperature and specific humidity profiles for SST values of 297K, 302K in January 1988 and cases A and B -see text-

the variations of C^T. Looking at the components of C^T, reported in table 1, one observes that the rate of increase of DLR with the SST is faster than the rate of increase of G with the SST (29.1 W/m^2 versus 15. W/m^2). These results confirm those of Inamdar et al.(1994) obtained with radiosonde reports. Furthermore, the rate of increase of G increases from normal (SST$\geq$300K) to super-greenhouse (SST$\leq$300K) conditions (15. versus 22.2W/m2), the rate of increase of DLR decreases (29.1 versus 21.1). As a consequence, the increase in cooling due to the increase in G is compensated by the decrease in cooling due to the slower rate of increase of DLR. This means that, while in normal conditions the atmosphere is more cooled as the SST increases, in super-greenhouse conditions, the troposphere tends to be less cooled. This behavior results from the fact that for the highest SST, the atmosphere does not re-radiates the LW radiation toward the surface as efficiently as it traps it.

Acknowledgments: Authors wish to thank J.-J. Morcrette for having made the ECMWF radiative code available to them and G.L. Liberti for valuable comments.

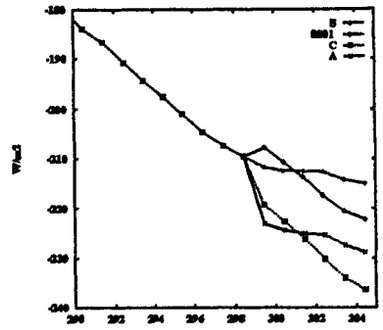

Figure 8: sensitivity experiment for C^T binned into SST intervals of 1K in the tropics -see text-

δSST	δC^T W/m^2	δG W/m^2	δDLR W/m^2	δnets W/m^2
295-298	14.1	15.	29.1	11.4
300-303	1.	22.2	21.1	3.6

Table 1: increase rate of G, of the total downward emitted flux, DLR, and of the net LW flux at the surface, nets, for "normal" (SST values of 295 and 298 K) and "super-greenhouse" (SST values of 300 and 303K) conditions

REFERENCES

Chédin, A., Scott, N. A., Wahiche, C. and Moulinier , P., 1985: The Improved Initialization Inversion Method : a high resolution physical method for temperature retrievals from the TIROS-N series, J. Climate Appl. Meteor., 24, 124-143.

Inamdar, A. K. and V. Ramanathan, 1994: Physiks of Greenhouse Effect and Convection in warm ocean, J. Climate., 7, 715-731.

Morcrette, J.-J., 1991, Radiation and Cloud Radiative Properties in the European Center for Medium Range Weather Forecasts forcasting system, J. Geophys. Res., 96, D5, 9121-9132.

Raval, A. and V. Ramanathan, 1989, Observationnal determination of the greenhouse effect. Nature, 351, 27-32.

Stephens, G.-L., D.L. Jackson, and J.J. Bates, 1994, A comparison of SSMI/I and TOVS column water vapor data over the global oceans, Meteorol., Atmos. Phys, 54, 183-201.

Webb, M.J., A. Slingo and G.L. Stephens, 1993, Seasonnal variations of the clear-sky greenhouse effect: The role of changes in atmospheric temperature and humidities, Clim. Dyn., 9, 117-129.

Zhong, W. and Haigh, J. D., 1995, Improved broadband emisivity parametrization for water vapor cooling rate calculations, J. Atmos. Sci., 52, 1, 124-138.

P1.51A

Use of the GLA TOVS Pathfinder Data Set for Climate Studies

J. Susskind (NASA Goddard Space Flight Center, Laboratory for Atmospheres, Mail Code 910.4, Greenbelt, MD 20771; 301-286-7210; e-mail: f41js@rcarson.gsfc.nasa.gov);
E. Anyamba, L. Iredell, A. Mehta, and P. Piraino (All at GSC, NASA Goddard Space Flight Center, Laboratory for Atmospheres, Mail Code 910.4, Greenbelt, MD 20771)

1. Overview

The GLA TOVS (Path A) Pathfinder Data Set is comprised of surface and atmospheric geophysical parameters obtained from analysis of NOAA 9, 10, 11, 12, and 14 HIRS2/MSU data and currently covers the period January 1985-June 1996. All time periods were analyzed using a frozen physically based retrieval system. Real time NOAA 11, 14 data, starting August 1997, is also being analyzed using this processing system. The data set includes surface skin and air temperature, atmospheric temperature profile to 10 mb, atmospheric water vapor profile to 300 mb, cloud top height and longwave radiatively effective fractional cloud cover. In addition, Outgoing Longwave Radiation (OLR), Longwave Cloud Radiative Forcing, and precipitation estimate are computed based on the individual soundings. Individual soundings are done over roughly a 60 x 60 km area, and the products are averaged on a 1° x 1° latitude-longitude grid on a daily, pentad, and monthly mean basis, with results stored separately for ascending and descending orbits for each satellite. More details of the data set and examples of validation studies of a number of products are given in Susskind et al. (1997). Anyamba and Susskind (1998) have done a detailed assessment of the GLA TOVS Pathfinder ocean skin and surface air temperatures and demonstrated that they compare well with in-situ data. Lakshmi et al. (1998) found good agreement of monthly mean TOVS surface air temperature and specific humidity with land based in-situ observations over contrasting climate regions. The entire data set, covering the period 1979-1997, is expected to be completed in 1999. This paper will show some results regarding OLR and atmospheric temperature profiles and their use for studying interannual variability and possibly trends. The sounding products are available from the GSFC DAAC at daacuso@daac.gsfc.nasa.gov or the GSFC SRT at srt@srt.gsfc.nasa.gov. For more information about the data set, see our home page at http://faster.gsfc.nasa.gov/srt.html.

2. OLR

OLR has been used as an important diagnostic to measure climate variability. The two most commonly used OLR data sets come from the ERBE scanner (Barkstrom, 1989) and AVHRR (Gruber and Kruger, 1984). The ERBE data measures broad band flux at a discrete angle and uses model calculations to angle integrated the flux to give OLR. ERBE has flown on NOAA 9, NOAA 10, and ERBS, in roughly 1:30 AM/PM local time and 7:30 AM/PM local time orbits, and in an asynchronous low inclination orbit respectively. Data from NOAA 9, ERBS covers the period February 1985 - December 1986, and data from NOAA 10, ERBS covers December 1986 - May 1989. The final OLR product for any time period uses model calculations to infer a daily average value based on the observed data at given times. AVHRR OLR is derived from window measurements of AVHRR based on regression relationships between theoretical calculations of AVHRR measurements and OLR. AVHRR has flown on the same satellites as HIRS2/MSU and AVHRR OLR is available from 1979 to the present. It is considered less accurate than ERBS scanner data however.

The TOVS OLR is derived from the individual TOVS Pathfinder soundings of surface skin temperature, temperature moisture profile, and cloud height and radiatively effective cloud fraction, using radiative transfer calculations. As with the AVHRR data set, the TOVS OLR data

represent values at the time of observation with no attempt made to estimate what would be observed if measured over the course of the whole day.

In this study, we compare monthly mean values of TOVS OLR for the period February 1985 - May 1989 with those of ERBE and AVHRR, all done on a 2° x 2° grid. If accurate, TOVS OLR not only serves to validate the individual TOVS sounding products, but also allows one to interpret temporal and spatial variability of OLR in terms of the variability of the temperature, moisture, and cloud geophysical parameters. Figure 1 shows a scatter diagram of global monthly mean grid point OLR values comparing TOVS, ERBE, and AVHRR OLR for the whole time period. The regression based AVHRR measurements show an apparent limitation, compared to both ERBE and TOVS, of damping at the high and low extremes. The scatter of AVHRR OLR with either TOVS or ERBE OLR is also considerably larger than that of TOVS with ERBE. Table 1 shows mean differences, standard deviations, and correlations of all three data sets, indicating TOVS is closer to ERBE in both the mean and standard deviation sense, and has a considerably higher correlation coefficient than any other pair of data sets. Table 1 also shows statistics for OLR monthly mean anomalies. In all cases, the standard deviations are smaller than in the monthly mean data sense, indicating spatially and/or temporally systematic components to the differences. TOVS anomalies and ERBE anomalies correlate the best.

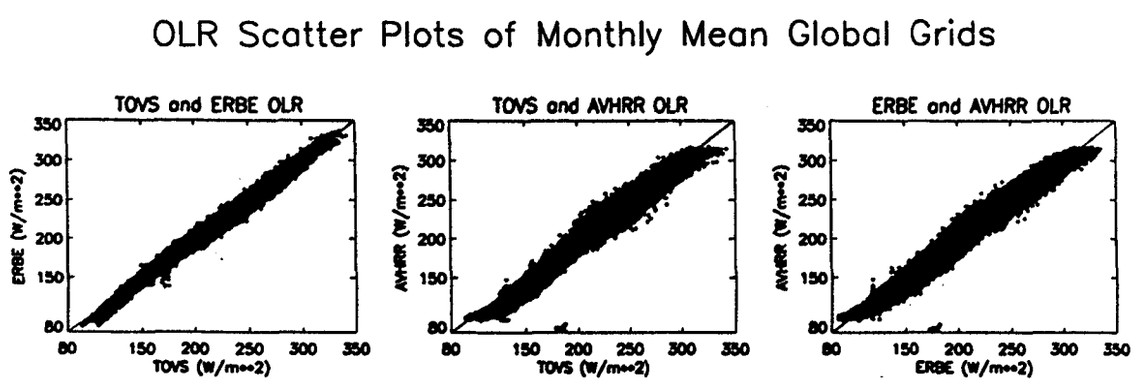

Figure 1

Table 1

	OLR			OLR Anomalies	
	Mean Difference $W.m^{-2}$	St. Dev. of Difference $W.m^{-2}$	Correlation Coefficient	St. Dev. of Difference $W.m^{-2}$	Correlation Coefficient
TOVS-ERBE	3.73	3.86	0.996	2.87	0.921
TOVS-AVHRR	7.76	6.28	0.987	3.27	0.887
ERBE-AVHRR	4.03	6.67	0.986	3.32	0.892

Figure 2 shows global mean monthly mean values of the data sets as a function of time, and also includes global mean monthly mean anomalies. All data sets show similar annual cycles of OLR, but displaced from each other. The AVHRR curves are the smoothest, and ERBE has the most fine structure. The difference curves indicate that AVHRR may have a spurious value in September 1985. They also imply that some of the fine scale structure in ERBE may be noise, especially during the NOAA 9 period. It is most interesting to look at the anomalies of all the

data sets. ERBE data shows a generally low anomaly for the period up to December 1986, followed by high anomaly for the subsequent time period. This appears to be an artifact, corresponding to the switch from NOAA 9 to NOAA 10. TOVS data, also obtained from NOAA 9 and NOAA 10 during the same periods, does not show this feature.

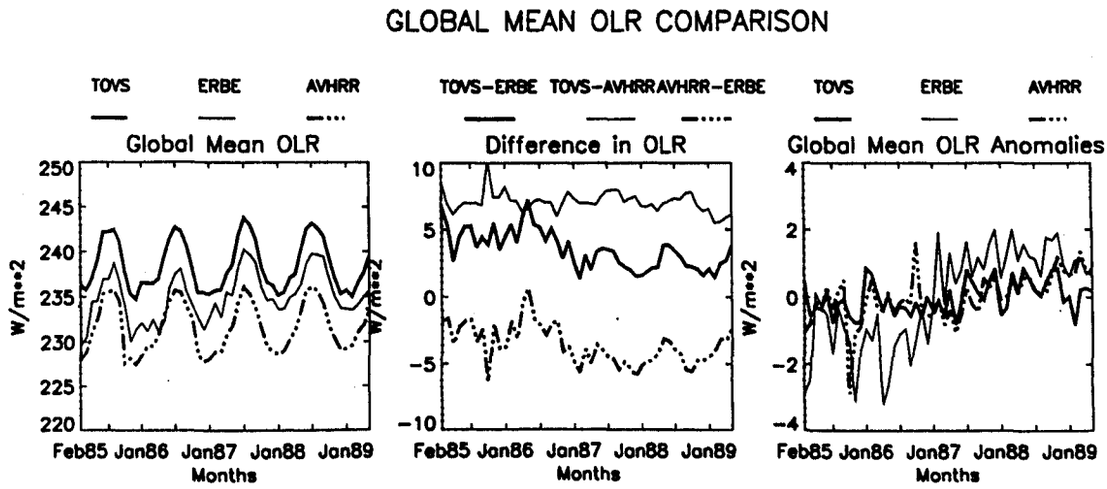

Figure 2

3. Temperature Profiles

There has been considerable interest of late in regard to the extent, if any, of global warming over the last 20 years. Spencer and Christy have introduced measures of temperature variability and trends in the mid to lower troposphere (1992 a,b) and lower stratosphere (1993) based on observations of MSU channels 2 and 4 respectively. These two measures, MSU2R and MSU4, represent integrals of atmospheric temperature over deep atmospheric layers, primarily coming from the surface to 300 mb, and 200 mb to 10 mb respectively. We generate the same measures by performing the appropriate integrals using our retrieved atmospheric temperature profiles, including surface contribution based on our retrieved surface skin temperature and microwave surface emissivity.

Before one can study interannual variability and trends from observations made by different satellites, with different orbits which also vary as a function of time, it is necessary to be able to account for any systematic differences arising from these factors. We apply systematic error correction procedures in the analysis of data from each satellite and make no subsequent attempt to adjust observations from one satellite to what they would be if they were on another satellite other than to account for differences in observing time. In general, the 7:30 orbit is stable in time, while the 1:30 orbit drifts to later in the day. We have used the 6 year period January 1989 - December 1994, measured at 7:30 AM/PM by NOAA 10 and NOAA 12, and orbits varying from 1:30 to 5:30 by NOAA 11, to study the differences of observations averaged at Z AM/PM from those at 7:30 AM/PM. The differences depend on location, but tend to repeat year after year in the form of an annual and semiannual cycle. The differences were also found to be proportional to a simple function of (Z-7:30), and be independent of which satellites are involved. Using this form, we can adjust observations at date t from an afternoon satellite with orbit time Z_t to what it would have been if observed at 7:30. If data from two satellites are present in a given month, we average the 7:30 observations with the adjusted Z_t observations to give the final product. Otherwise, we use only the value from the single satellite.

We have generated monthly mean anomalies for the period January 1985-May 1996 for a number of temperature quantities, based on their 11 year mean 1985-1995. Figure 3 shows the global mean values of anomalies for MSU2R and MSU4, both as observed by Spencer and Christy and computed from our own soundings, as well as their differences. The vertical bars on the figures indicate times when changes in satellite configuration took place. There is good agreement between both MSU2R time series, with a correlation of 0.83 and a standard deviation of 0.11°C. The temporal variability in MSU4 is considerably larger than in MSU2R. The very significant warming in July 1991 corresponded to the Mt. Pinatubo eruption. Our analysis of the variability of the temperature profile as a function of height showed a maximum warming at 30 mb. This was followed by a cooling period occurring primarily from 300 mb to the surface, which manifests itself in the negative MSU2R anomaly in 1992-1993. The two MSU4 time series are highly correlated (0.91) because of the large signals involved, but have a standard deviation of 0.19K. The difference between the two anomalies indicates a discontinuity at about January 1991 that remains to be explained.

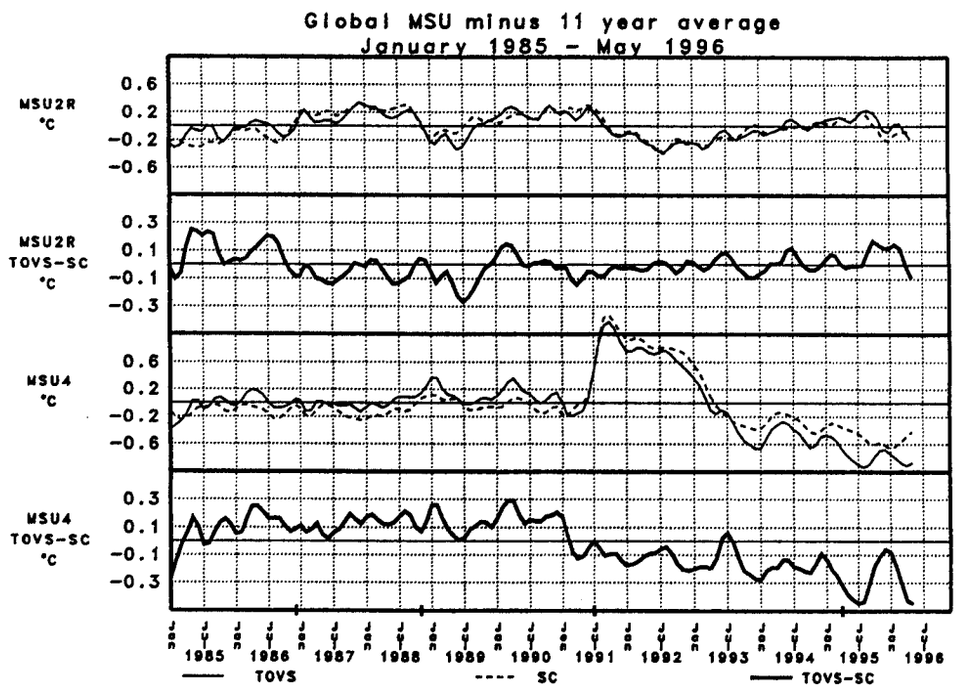

Figure 3

The trends of the 11 1/2 year global mean values of MSU2R and MSU4 are plotted in Figure 4a at the pressures contributing mostly to the signals. The global trends of MSU2R from both TOVS and Spencer and Christy are both close to 0 for this time period. Significant differences exist for MSU4 however, for which TOVS has a cooling of .03K/yr. while Spencer and Christy has a warming of .006K/yr. This difference is a direct result of the discontinuity discussed above. Figure 4a also includes the trends of global surface air temperature and temperatures at mandatory levels from 850 mb to 30 mb from both TOVS Pathfinder products and the NCEP reanalysis. The NCEP reanalysis is based heavily on radiosondes where available and a combination of NOAA operational TOVS retrievals and model generated fields elsewhere. In the case of NCEP, we are using the 1000 mb temperature analysis in place of surface air, which was not reported after 1995.

There is a rough agreement of the trends of the two detailed global mean temperature profile time series, with differences in vertical structure. By definition, TOVS MSU2R and MSU4 trends represent the appropriate integrals of the trends of the temperatures shown (with additional

contributions from surface skin temperature and temperature above 30 mb). The Spencer and Christy MSU4 trend does not appear to be consistent with either set of temperature trends however. Figure 4b shows a similar plot, this time for northern hemisphere extra-tropical land areas which are densely covered by radiosondes. Agreement between TOVS and NCEP temperature trends is considerably better than globally. The radiosondes are used only weakly in our analysis and we expect the global TOVS trends to be of comparable accuracy. It is interesting to note that in this region, both TOVS and Spencer and Christy show a warming trend with regard to MSU2R, of 0.03K/yr. and 0.015K/yr. respectively. In both data sets, this is compensated for globally by a cooling trend in the southern hemisphere with essentially zero trends in the tropics.

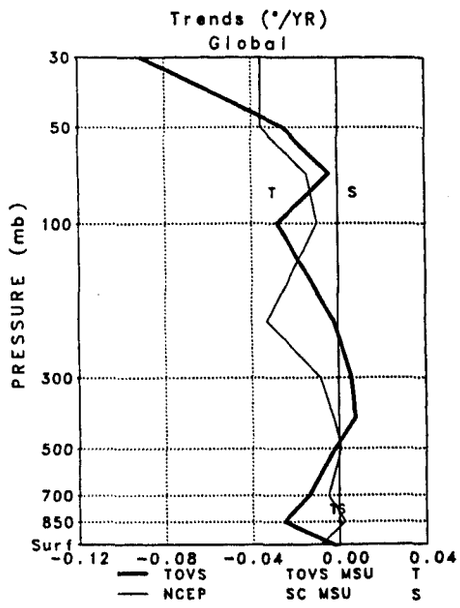

Figure 4a

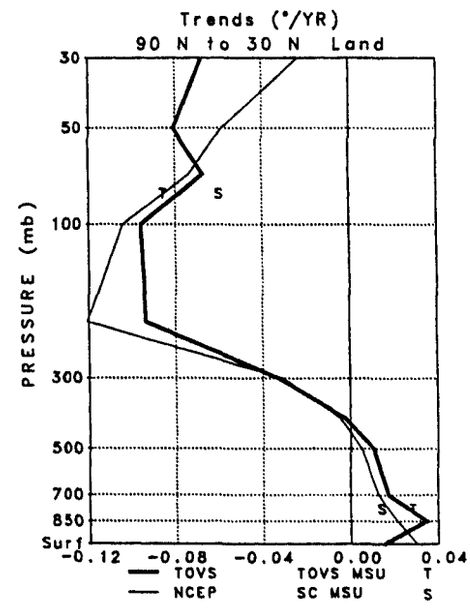

Figure 4b

References

Anayamba, E. and J. Susskind (1998). A Comparison of TOVS Ocean Skin and Surface Air Temperatures with Other Data Sets. JGR (in press).

Barkstrom, B. (1989). Earth Radiation Budget Experiment (ERBE) Archival and April 1985 Results. Bull. Am. Met. Soc., 70, 1254-1262.

Gruber, A. and A. F. Krueger (1984). The Status of the NOAA Outgoing Longwave Radiation Data Set. Bull. Am. Met. Soc., 65, 958-962.

Lakshmi, V., J. Susskind, and B. Choudhury (1998). Determination of Land Surface Skin Temperatures and Surface Air Temperatures and Humidity from TOVS HIRS2/MSU Data. Advances in Space Research (in press).

Spencer, R. W. and J. R. Christy (1992a). Precision and Radiosonde Validation of Satellite Gridpoint Temperature Anomalies. Part I: MSU Channel 2. J. Climate, 5, 847-857.

Spencer, R. W. and J. R. Christy (1992b). Precision and Radiosonde Validation of Satellite Gridpoint Anomalies. Part II: A Tropospheric Retrieval and Trends During 1979-1990. J. Climate, 5, 858-866.

Spencer, R. W. and J. R. Christy (1993). Precision Lower Stratospheric Temperature Monitoring with the MSU: Validation and Results 1979-1991. J. Climate, 6, 1994-1204.

Susskind, J., P. Piraino, L. Rokke, L. Iredell, and A. Mehta, 1997. Characteristics of the TOVS Pathfinder Path A Dataset. Bull. Am. Met. Soc., 78, 1449-1472.

P 1.53A DIRECT RADIATIVE FORCING BY AEROSOLS AS OBSERVED FROM THE NOAA/AVHRR PATHFINDER ATMOSPHERE (PATMOS) MULTI-YEAR DATASET

Larry Stowe, Herbert Jacobowitz, Chandracekhara. Kondragunta[1], and Gang Luo[2]
Office of Research and Applications, NOAA/NESDIS, Washington, DC
[1]UCAR Visiting Scientist, NOAA/NESDIS, Washington, DC
[2]Scientific Management and Applied Research Technologies, Inc., Silver Spring, MD

1. INTRODUCTION

Several recent studies have shown that climate model predictions of the regional pattern of global warming due to greenhouse gas increases are more closely in agreement with patterns of observed surface warming when regional distributions of sulfate aerosols produced by fossil fuel burning, and their direct effect on the radiation balance, are included in the models (Kiehl and Briegleb, 1994, Santer, 1996).

Climate-scale numerical simulations that include only the role of anthropogenic aerosol have produced estimates of globally-averaged direct forcing in the range of -0.3 to -1.1 W m^{-2} (Kiehl and Briegleb, 1993). Therefore, direct aerosol forcing, particularly once all sources of aerosol are included, may affect the radiation budget on a global scale in magnitudes comparable to greenhouse gas forcing, but of opposite sign.

As an initial attempt to observe the direct aerosol forcing from satellites, we have processed the first thirteen years of September monthly mean parameters of the NOAA/NASA Advanced Very High Resolution Radiometer (AVHRR) Pathfinder Atmosphere (PATMOS) datasets (1981-1993) (Stowe and Jacobowitz, 1997). This analysis provides maps of maximum change in aerosol optical thickness and the extremes in direct shortwave radiative forcing caused by that change. These observations are not constrained to sulfate aerosols, so results will indicate where the Earth's radiative balance depends on other aerosol species, e.g. smoke and dust, as well.

2. THE PATMOS DATASET

Satellite multi-channel data provide a means of assessing certain aspects of the aerosol direct radiative forcing characteristics. The (PATMOS) Project at NOAA/NESDIS has produced an extensive archive of daily cloud cover, clear and cloud radiances, aerosol (over ocean), and radiation budget parameters (total and clear-sky) for July 1981 to the present. Data from NOAA/7,9,11,14 afternoon satellites have been used to produce these long-term global daily, pentad (5-day) and monthly mean radiation parameters with 110-km equal-area grid cells constructed from one degree latitude-variable longitude increments. The NOAA polar-orbiting satellite series provides twice-daily AVHRR overpass imagery with a nominal pixel field-of-view of 1.1 km and Global Area Coverage (GAC) data at 4 km resolution.

Corresponding author address:
Dr. Larry L. Stowe, Office of Research and Applications, E/RA1, NOAA/NESDIS, 4700 Silver Hill Road, Stop 9910, Washington, DC20233
e-mail:lstowe@nesdis.noaa.gov

The presence of clouds and clear pixels for 4-pixel arrays of the 4-km GAC data is diagnosed with a combination of AVHRR channel threshold and uniformity discriminators (Stowe et al., 1991).

The PATMOS dataset includes aerosol optical thickness (AOT) at 0.63 microns, retrieved using the same algorithm as the NESDIS AVHRR daily AOT mapping (Stowe *et al.*, 1997). However, it is applied to grid cell average clear-sky radiances, instead of 2x2 pixel array averages. Because of the linearity between radiance and aerosol optical thickness, this difference does not contribute to any significant bias. AOT is defined as the vertically integrated aerosol extinction coefficient, evaluated from the ocean surface to the observing satellite sensor. Hence, AOT includes all aerosol in a column of the troposphere and stratosphere.

The daily average reflected flux, Fsw, has to be computed as the difference in two quantities on the PATMOS dataset, available solar energy (ASE) minus absorbed solar flux (ASF). These two shortwave radiation budget components are estimated using grid cell mean values of channel 1 and 2 radiances, incorporating ERBE Bidirectional Reflectance Directional Models (BRDF) and solar zenith angle dependent albedo models, Hucek and Jacobowitz, 1995.

3. COMPUTATIONAL APPROACH

The initial time period processed with the PATMOS system were the months of September, from 1981 to 1993. This was done so that assessments could be made as to the stability of the products for interannual studies. One of our first scientific objectives for this dataset was to estimate the possible range in magnitude of the effect of aerosols over oceans on the shortwave flux of solar energy leaving the top of a cloud-free atmosphere, Fsw(clear-sky). This was done in two ways, using the monthly mean statistics from PATMOS daily values.

In the first approach, the year in each 110 km grid cell with the minimum and maximum aerosol optical thickness was determined, and a map was constructed of the maximum change in AOT, delAOT over the thirteen years. Next, a map of the direct effect of this maximum change on the observed Fsw (clear-sky) was constructed as the difference between Fsw (clear-sky) in the year of minimum AOT and the Fsw (clear-sky) in the year of maximum AOT, delFsw. This yields an aerosol forcing result consistent with cloud forcing terminology. If the aerosol causes a net loss (gain) of solar radiation to the system, i.e.,cooling (warming), the forcing will be negative (positive). This map represents the extremes in aerosol direct shortwave radiative forcing observed in these 13 September years.

In the second approach, as a consistency check

of the first, a linear regression was performed in each grid cell over the thirteen years to predict Fsw (clear-sky) as a function of AOT. The slope of the regression line gives an estimate of the sensitivity of Fsw (clear-sky) to changes in AOT. The product of this slope with (-)delAOT (minus sign needed for consistency in definition of forcing) gives an independent estimate of the extreme effect of the aerosol on Fsw (clear-sky). The explained variance of the regression line indicates regions over the oceans where the estimates of radiative forcing by the aerosols are reliable, i.e., the errors in retrieval of AOT and Fsw are not significantly affecting their relationship.

4. RESULTS

Space does not permit inclusion of any figures from the above analysis, but a brief verbal description of them follows. The map of maximum change in oceanic AOT over the 13 years of Septembers shows that changes as large as 0.8 occurred in the tropics, between about 30N and 20S. This is due to tropospheric aerosol resulting from wind blown dust off the west coast of Africa and smoke from agricultural burning in Africa, South America and Indonesia (Husar et al., 1997), the latter being the most prominent feature. It is also due to the occurrence of two major volcanic eruptions, El Chichon, 1982/83 and Mt. Pinatubo, 1991/92, whose stratospheric aerosol layers may have contributed up to half of the total change observed (Long and Stowe, 1994). Outside the tropics, delAOT was generally less than 0.2, with the exception of the North Atlantic Ocean, where many grid cells exhibited values as large as 0.5, coming from the sulfate/carbonaceous aerosol plume generated in North America primarily by fossil fuel burning.

The map of the effect of this maximum observed aerosol change on Fsw shows consistency with the map of delAOT. The aerosols are generally cooling in the tropics, with maximum loss of shortwave energy being about - 40Wm^{-2}, over Indonesia, with values around - 20Wm^{-2} being more typical. There are a few isolated grid cells in the tropics which exhibit warming (delFsw < +10Wm^{-2}). In the extra-tropics, many more grid cells appear to exhibit warming, sometimes as large as +20Wm^{-2}. Many of these grid cells have delAOT values in excess of 0.3, especially in the north Atlantic. When delAOT is lower, it would appear this technique cannot reliably estimate aerosol forcing. The occurrence of positive forcing in the North Atlantic, where delAOT > 0.3, suggests that carbonaceous (absorbing) aerosols may dominate over sulfate (purely scattering) in September.

The above findings are confirmed by the results of the regression analysis, where it appears that the explained variance has to be greater than 0.5 for the analysis to be reliable. The analyses are more suspect in the southern extratropics because fewer years contribute to the statistics (less than 6 southward of about 45S) due to the drift of the afternoon NOAA satellites to later equator crossing times (reduced solar illumination).

5. PRELIMINARY CONCLUSIONS

Preliminary conclusions from this initial study into the observed effect of aerosol on the solar component of the Earth's radiation balance are: volcanic eruptions and biomass burning are the major causes of interannual variability in direct aerosol forcing over these thirteen September months. Extremes in aerosol forcing ranged from -40 to +20Wm^{-2}, with negative forcing occurring primarily in the tropics and positive forcing occurring sporadically in the extratropics, with the exception of the North Atlantic ocean, where the North American aerosol plume showed persistent positive forcing. This suggests that carbonaceous aerosol may dominate sulfate aerosol effects in September in this area. These analyses are unreliable when aerosol optical thickness is less than about 0.3. Below this value, the monthly mean estimates of clear-sky reflected flux are not well correlated with aerosol optical thickness for reasons that are yet to be determined. In the future, after understanding and possibly adjusting for the cause of limitations in these approaches, other seasons will be studied and years with volcanic aerosol will be excluded to assess only the effect of tropospheric aerosols, which are influenced by anthropogenic activity. We will also evaluate the performance of these approaches at times and locations where intensive field measurement programs have been conducted, i.e., TARFOX, and ACE-2. Eventually trends will be examined for implications to global climate change and for comparison with climate model computations.

6. REFERENCES

Hucek, R. and H. Jacobowitz, 1995: Impact of scene-dependence on AVHRR albedo models, *J. Atmos. & Oceanic Tech.*, **12**, 697-711.

Husar, R., J. Prospero, L.L. Stowe, 1997: Characterization of Tropospheric Aerosols over the Oceans with the NOAA/AVHRR Optical Thickness Operational Product. *Jml. Geophys. Res.*, 102, D14, 16,889 - 16, 910.

Kiehl, J.T., and B.P. Briegleb, 1993: The relative roles of sulfate aerosols and greenhouse gases in climate forcing. *Science*, **260**, 311-314.

Long, C.S., and L.L. Stowe, 1994: Using the NOAA/AVHRR to study stratospheric aerosol optical thicknesses following the Mt. Pinatubo eruption. *Geophysical Research Letters.*, 21, 20, 2215-2218.

Santer, B., et al., 1996: A search for human influence on the thermal structure of the atmosphere. *Nature*, **382**, 39-46.

Stowe, L.L., 1991: Cloud and aerosol products at NOAA/NESDIS. Palaeogeography, Palaeoclimatology. *Palaeoecology (Global Planetary Change Section)*. 90, 25-32.]

Stowe, L.L., and H. Jacobowitz, 1997: The AVHRR Pathfinder Atmosphere Project, *Proc., AMS 9th Conf. Atmos. Radiation*, 2-7 February, Long Beach, CA, 196-197.

Stowe, L.L., A.M. Ignatov, and R.R. Singh, 1997: Development, validation and potential enhancements to the second-generation operational aerosol product at the NOAA/NESDIS. *J. Geophys. Res.*, **102 (D14)**, 16923-16934.

P1.55A

A 3-DIEMNSIONAL DAILY OZONE ANALYSIS USING SBUV/2 AND TOVS MEASUREMENTS: SMOBA

Shi-Keng Yang and Shuntai Zhou
Research and Data Systems Corp, Greenbelt, MD

Alvin J. Miller
Climate Prediction Center/NCEP/NOAA, Camp Spring, MD

1. Introduction :

The Stratosphere Monitoring Group at Climate Prediction Center (CPC) / National Centers for Environmental Prediction (NCEP)/NWS/NOAA has recently developed an algorithm for 3-D daily ozone analysis. The algorithm uses the measurements from the Solar Backscatter Ultraviolet instrument (SBUV/2) (Bhartia, et al, 1996) which doesn't observe in the polar-night, blended with TOVS infrared ozone estimates (Neuendorffer, 1996) in the regions of polar night to achieve global coverage. It is thus called the Stratosphere Monitoring Ozone Blended Analysis (SMOBA). For its operational stability and global coverage, SMOBA is adopted as the ancillary input data to the Cloud and Earth Radiant Energy System (CERES) of EOS interdisciplinary study (Wielicki et al, 1996) which is to estimate atmospheric radiative divergence/ heating rates by utilizing the meteorological, aerosol and ozone data from independent sources. CPC is also using SMOBA as the initial conditions for experimental numerical forecast of ozone.

The selection of operational measurement of SBUV/2 and TOVS ozone as the basis for developing the SMOBA algorithm is prompted by the long term stable global data stream required for supporting the CERES/EOS mission in studying climate variation and climate changes. TOVS total ozone is derived from the HIRS 9.7 mm channel, which can provide information for the regions which is not sun-lit. In fact, the effective coverage of SBUV/2 is limited by the solar zenith angle of less than.80°, which is a function of the satellites' equatorial crossing time. Moreover, this blacked-out region tends to expands as the operational satellite precesses to later equatorial crossing times. Hence we have formulated an algorithm, blending SBUV/2 and TOVS to add additional information for the polar-nights. Continuous daily SMOBA covers the most comprehensive domain from surface to stratopause, from the pole to the pole.

2. Data Analysis Algorithm:

The process of SMOBA starts from the orbital information of the daily measurements of ozone mixing ratio and total column ozone that are obtained from the NOAA polar orbiting satellite, currently NOAA-14. The retrieved SBUV/2 ozone data include 19 levels of mixing ratio from 0.3 hPa to 100 hPa and total column ozone. Layer ozone amounts are also included for 12 discrete layers from the surface to ~60 km, but the vertical resolution is very coarse in the troposphere (only 2 layers).The input data are arranged along satellite orbit tracks, over the sun-lit portion of the earth. We have performed objective analysis from the orbital data to a global, 2.5 x 2.5 degree latitude-longitude grid by a commonly used successive correction method (SCM) (Daley, 1991). The output includes ozone mixing ratio at 24 pressure levels (0.2, 0.3, 0.4, 0.5, 0.7, 1, 1.5, 2, 3, 4, 5, 7, 10, 15, 20, 30, 40, 50, 70, 100, 150, 200, 250, 300 hPa) where we have added the 5 levels (300, 250, 200, 150, and 0.2 hPa) to the 19 level input mixing ratio, which are derived from ozone amount data in layers 2 (256 - 128 hPa), 3 (128 - 64 hPa) and 12 (0.25 - 0.12 hPa) respectively. We also assume a uniform ozone mixing ratio from 300 hPa to 1000 hPa, derived from the ozone amount in the lowest layer (1000 - 256 hPa). The total ozone is directly from the retrieved data, which is the sum of 12 layer ozone amounts.The lower stratospheric ozone retrievals are guided by climatology used in the ozone retrieval algorithm, and corrected by the measured layer ozone amounts. The uniform tropospheric mixing ratio also captures the main feature shown in ozone sonde measurements.

Because the SBUV/2 algorithm is based on the sunlight absorbed and reflected by the atmosphere (iincluding ozone), there are no data in polar night. To fill in the polar night gap, we use NOAA TOVS total ozone derived from infrared measurements as the auxiliary information. However, TOVS does not measure vertical ozone profiles. From other satellite data such as UARS MLS,and CLAES, we have determined that the shapes of ozone vertical profiles are similar in polar latitudes to those at high mid-latitudes. Therefore, we assume polar night ozone mixing ratio to be such that its shape is the same as that of SBUV/2 ozone at the boundary of the polar night, and the integrated polar total column ozone is equal to TOVS measurement. As will be shown, this assumption is a reasonable approximation when the polar night gap is not too large. Since TOVS total ozone is slightly different from SBUV/2 total ozone (~5% at the boundary of polar night), a linear adjustment is applied to the polar ozone so that the filled data joint smoothly at the boundary. This procedure is the so-called blended data analysis.

3. Temporal and Spatial Variations from SMOBA

Stratospheric ozone constitutes an important greenhouse gas with substantial temporal and spatial variation that is not revealed in the seasonal variation. Significant temporal variations of ozone usually occur in the day-to-day scale, which could be significant departures from the monthly climatologies or monthly means. Fig. 1 depicts the standard deviations of the ozone mixing ratio sampled from the daily analysis and normalized to the monthly means for March 1997. This result is in contrast to the interannual variance shown in Nagatani et al. (1988) which samples the monthly means from 8 years data. The normalization enhances the significance of the variability in the lower stratosphere, between 150 hPa and 75 hPa, where the ozone concentration is the highest.

The maximum of the normalized standard deviation generally occurs around 125 hPa for most of the latitudes, and ranges from 9% to more than 24%. At this altitude, the maximum of the normalized standard deviation occurs at 33 ^{0} N with the intensity of 27%. Not mirroring the northern hemisphere, southern hemisphere has a maximum of more than 15% at 45° S. Although the features in the northern hemisphere is not symmetric to the southern hemisphere from 30 hPa upward, there is a gradual poleward increase of normalized standard deviation from 3% at 30° N and S to 9% at poles, while the tropics is quite homogeneous.

The boreal spring equinox is selected for illustrating the deviation from the zonal means around the globe. Fig. 2 is constructed by calculating the standard deviations about the zonal means normalized by the zonal means. Region-wise the general global pattern of this figure somewhat resembles the temporal variations of Fig. 1, with very homogeneous field in the tropics from 30 hPa upward, i.e. the ozone distribution in this region is very zonal. At the lower stratosphere, around 175 hPa, the normalized standard deviation has much larger magnitudes ranges from 10% to 20% for the spring equinox. A maximum of 20% locates at 175 hPa, 27° N, is the largest in the lower stratosphere, while there are less clearly defined maximums in the southern hemisphere at 15° S and around 55° S with a magnitudes of 10%. Very distinctive from Fig. 2 is from 30 hPa upward at southern polar region, where a well defined maximum of 20% is located at 20 hPa 70°S with substantial gradients from the center.

The implication from the results of temporal and spatial variations is that there could be errors of heating rates were the zonal averaged climatology used in the radiative transfer calculations in global NWP models or general circulation models.

4. Profile Comparison with MLS

Limited ozone profiles from Microwave Limb Sounder (MLS) are available for comparison from UARS, which is in a 58° inclined orbit. For this particular period under study, the UARS is operating under a power deficiency, so that all instruments can not be on all the time. SAGEII, also, is limited in coverage of the polar regions. Therefore, we have focused attention on the MLS (Version 4) , which provides 2 days of comparision from April 1 (South facing) to April 10 (North facinging). The facing of UARS enable MLS to measure further poleward then the terminator of orbital inclination. the MLS provides profiles from 100 hPa up with coarser vertical resolution than SMOBA.

On April 10, 1997, the SMOBA profiles at

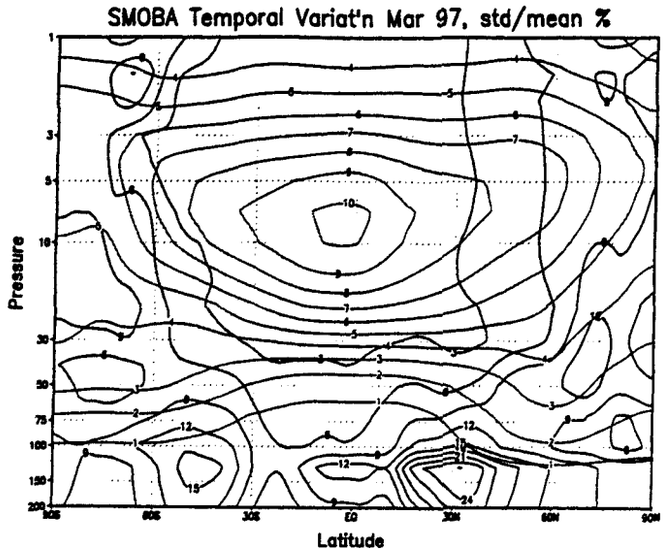

Fig. 1 : SMOBA temporal variation for March, 1997. The thick lines are the standard deviations from daily ozone mixing ratio divided by the monthly mean, in %. contour interval is 3%. The thin lines are the contours of monthly mean mixing ratio in ppmv. Contour interval is 1 ppmb.

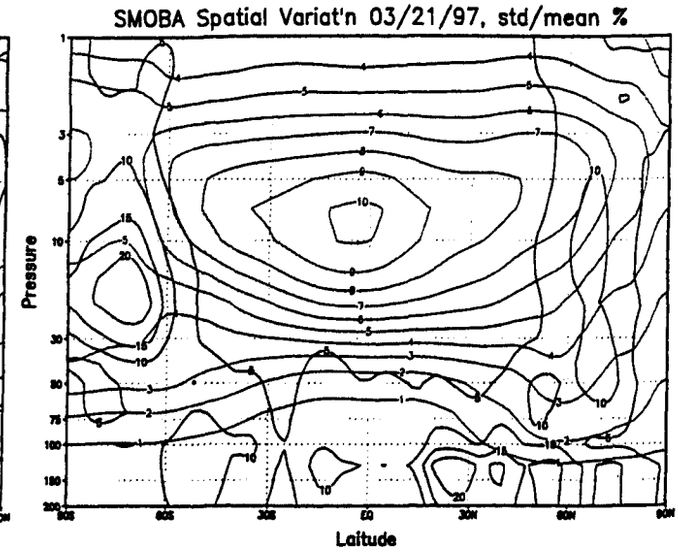

Fig. 2: SMOBA spatial variation for March 21, 1997. The thick lines are the standard deviations of ozone mixing ratio divided by the zonal mean, in %. contour interval is 3%. The thin lines are the contours of zonal mean mixing ratio, in ppmv. Contour interval is 1 ppmb.

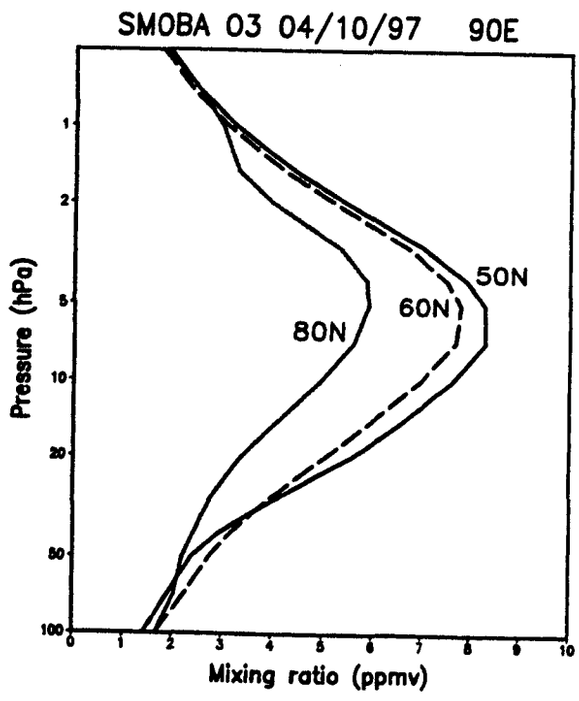

Fig. 3a: SMOBA Ozone profiles at (50° N, 90°E), (60° N, 90°E) and (80° N, 90°E) for April 10, 1997, in ppmv

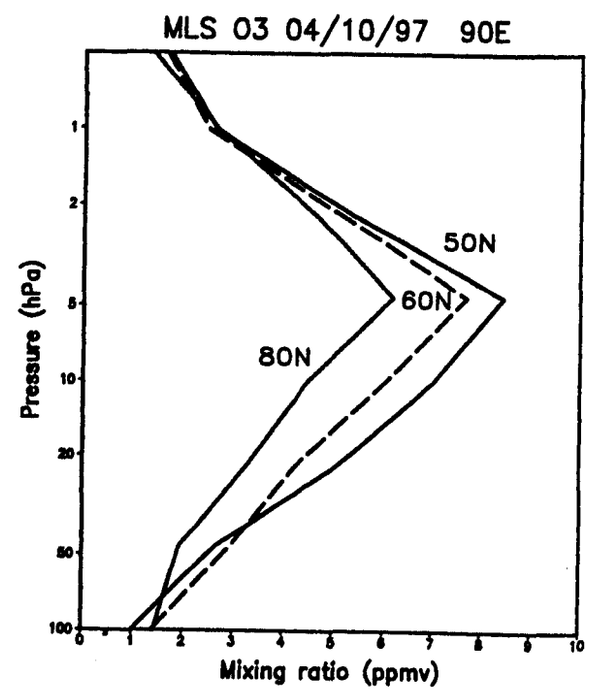

Fig. 3b: Same as Fig. 3a, but from MLS.

three locations, 90°E and 50° N, 60° N, and 80° N, respectively, are on Fig. 3a. The corresponding MLS profiles are on Fig. 3b. This is a case that SBUV/2 has coverage up to 80° N, thus most of the profiles are from measurements instead of blending with TOVS ozone. It is clear that the higher resolution of SMOBA makes the profiles smoother. Nevertheless, there is very good agreement as both MLS and SMOBA have profiles peaks around 5 hPa for all the three locations. The magnitudes of the peaks at 50°N (60°N) for SMOBA agree with that of MLS, within 0.2 (0.1) ppmv out of 8.4 (7.7) ppmv, while the one at 80°N differ slightly larger, 0.5 ppmv out of 6.2 ppmv. Although there is precise agreement for the peak at 60°N, profile-wise, SMOBA overestimates MLS from 20 hPa to 5 hPa with largest difference of 0.7 ppmv at 10 hPa. The profiles at the other two locations are in good agreement within 0.4 ppmv for all the altitudes. Although not shown, we have also compared similar profiles for the same latitudes at 0° E, 180°, and 90° W. All of them have the similar characteristics and good agreement.

5. Summary:

For computing global heating rate, CERES/EOS has adopted a 3-D daily global ozone analysis, SMOBA, as an ancillary input. The analysis developed at CPC/NCEP employes a successive correction method and uses operational SBUV/2 measurements in the sun-lit regions, blended with the total ozone measurements from the 9.7 mm channel of HIRS/TOVS in the polar- night regions. Currently, both measurements are from the polar-orbiting satellite, NOAA-14. This near real-time analysis can also be used for other applications, such as the initial conditions for numerical ozone forecasts that CPC/NCEP is experimenting.

Since began daily operation on March 1, 1997, SMOBA has proven itself to be a very stable and reliable algorithm required by the coming CERES operations. Monthly mean cross sections of ozone mixing ratio for the period of March, 1997 is presented. As compared to the SBUV-only climatology of Nagatani et al. (1988), which uses Cressman objective analysis, SMOBA shows that ozone profiles in the polar regions are a smooth extension from the sun-lit latitudes. An analysis of temporal variations of mixing ratio is conducted for March, 1997. The results show that the largest temporal variation are located in the lower stratosphere around 175 hPa for most of the latitudes where the ozone concentration is the highest. In the upper stratosphere from 30 hPa up, polar regions exhibit large seasonality, while the tropics remain fairly calm. Spatial variations for Boreal equinox is also analyzed. Region-wise, the results are very similar to the temporal variations.

The SMOBA vertical profiles are compared with the measurements from MLS (Version 4) onboard UARS. The results show that there is very good agreement in shapes and magnitudes for the sun-lit northern hemisphere case (South facing for UARS) of April 10, 1997. The higher bias is very possible caused from TOVS overestimation. Since there are limited ozone profiles available for polar night, the result calls for more research before adjustment to the shape of profile can be made.

SMOBA started the routine operation on March 1, 1997. A ten-day rotating file has been set up for anonymous FTP at the node: nic.fb4.noaa.gov, under the directory /pub/nws/nmc/cac/SMOBA.

References:

Bhartia, P. K., R. D. McPeters, C. L. Mateer, L. E. Flynn, and C. Wellemeyer, 1966: Algorithm for the estimation of vertical ozone profiles from the backscattered ultraviolet technique, J. Geophy. Res., 101, No. D13, 18793-18806.

Daley, R., 1991: Atmospheric Data Analysis, Cambridge University Press, 457pp

Nagatani, R.M., A. J. Miller, K. W. Johnson, and M.E. Gelman, 1988: An eight-year climatology of meteorological and SBUV ozone data, NOAA Tech. Report, NWS40. U.S. Dept of Commerce, 125pp.

Neuendorffer, A.C., Ozone monitoring with TIROS-N operation vertical sounders, 1996: J. Geophy. Res., 101, No. D13, 18807-18828.

Wielicki, B. A., B. R. Barkstrom, E. F. Harrison, R. B. Lee, G. L. Smith and J. E. Copper, 1996: Clouds and the Earth's Radiant Energy System (CERES): An Earth Observing System Experiment, Bull. Amer. Meteo. Soc., 77, 853-868.

O2.2A

WEATHER PRODUCTS VIA THE INTERNET

Thomas F. Lee*, Jeffrey Hawkins, Kim Richardson, Joe Turk
Naval Research Laboratory
Marine Meteorology Division
Monterey CA 93943-5502

1. Introduction

NRL-Monterey has developed a variety of satellite meteorological applications for both geostationary and polar orbiter sensor data that are now available via the Internet. This web page:
http://www.nrlmry.navy.mil/sat_products.html

permits; a) the U.S. Navy, the academic community, and other users to provide valuable feedback on our research projects, b) near real-time testing on literally thousands of cases using identical data to that in field operations, c) robust algorithms that can readily be transitioned for operational use throughout the world, and d) satellite meteorology education at all levels within the Navy.

NRL-Monterey specializes in multi-satellite and multi-sensor data fusion. This is accomplished by accessing four geostationary satellites (GOES-8,9, GMS-5 and Meteosat-6) either directly via satellite downlink or via cooperative agreements with other research and development users. In addition, Special Sensor Microwave Imager (SSM/I) data are acquired from the Fleet Numerical Meteorology and Oceanography Center (FNMOC) for all three operational SSM/I sensors. Our efforts are geared to near real-time processing, such that coincident data sets for specific purposes can be processed, extracted, viewed and saved for further study. This capability dramatically reduces the data sets to manageable sizes.

The NRL web page currently contains applications ranging from cloud and water vapor-tracked winds, aircraft icing aides, low cloud enhancements, cloud classification, cloud advection forecasts and the ability to overlay model output on satellite imagery. Multi-sensor capabilities are highlighted in our tropical cyclone link, where coincident SSM/I and visible/infrared views are created automatically for storms worldwide. The reader is encouraged to connect to the homepage address listed above and view the applications. This preprint focuses on the presentation of global tropical cyclones and estimation of precipitation rate from a combination of polar-orbiting and geostationary sources.

2. Tropical Cyclones: This section organizes information by storm in six basins: western north Pacific, central north Pacific, eastern north Pacific, north Atlantic, north Indian Ocean, and southern hemisphere. The creation of images follows the movement of a storm, centering each view on the latest (four a day) center fix from the appropriate operational centers. This allows preparation of continuous close-up views of each storm without human intervention. In addition to sectors from the appropriate geostationary satellites, this section gives the corresponding views from the SSM/I. This juxtaposition of visible/infrared information with passive microwave close-ups creates a powerful tool for users to observe and track these storms.

The SSM/I applications include windspeed, integrated water vapor, and three 85 GHZ displays. These three are: a polarization-corrected temperature image (Spencer et al. 1989), a horizontal polarization display, and an enhanced horizontal polarization display for weak storms. The 85 GHZ displays, at a resolution of 12 km, reveal valuable detail about precipitation occurrence and storm structure (Hawkins et al. 1998). The polarization-corrected image removes the effects of cloud-free sea surfaces which can resemble the signatures of convection on uncorrected images. Thus, it shows convection unambiguously. The 85 GHZ display for weak storms enhances the signal of low-level water clouds and rain clouds, giving information about storm position and intensity where deep convection is absent.

For storms in the Atlantic and eastern Pacific, the tropical cyclone application also contains a bispectral GOES innovation that gives users more information about weak tropical cyclones at night. At night, most infrared images lack the necessary contrast to expose low cloud bands

* Corresponding Author: Thomas F. Lee, Marine Meteorology Division, Naval Research Laboratory, 7 Grace Hopper Avenue, Monterey CA 93943-5502, lee@nrlmry.navy.mil.

which characterize many weak storms in the absence of convection. This lack of contrast occurs because the low clouds and the sea surface have roughly the same infrared temperature. Using infrared images, users may fail to identify important low-level structure or the central position of the storm. Thus, in place of the visible image at night, the application places a bispectral enhancement (Ellrod 1995; Lee et al. 1997) which shows low clouds in white, thin cirrus as black, and thick cirrus/cumulonimbus in speckled gray shades. The enhancement of the low cloud is based on the differential emissivities of low clouds in the shortwave infrared vs. the longwave infrared channels of GOES. The enhancement of cirrus derives from the semi-transparent nature of thin clouds. The speckling is an artifact from the noise in the shortwave channel that occurs at low brightness temperatures. Over cold clouds, the enhancement can distinguish between deep convection which may contain precipitation (speckled) vs. thin cirrus (black).

3. Precipitation: This NRL web application also shows examples produced by combining the capabilities of existing geostationary and polar platforms to estimate instantaneous and accumulated rainfall over the tracks of storms. While geostationary infrared sensors provide the required rapid update cycle, they are not sensitive to the underlying cloud rainfall. Conversely, the operational SSM/I is sensitive to the vertical microphysical composition and capable of instantaneous rainrate estimation, but limited temporally to a polar-orbiting perspective. Data from the four geostationary sensors (GOES-8/9, GMS-5, Meteosat-6) are processed in near-realtime at NRL Monterey, and coincident rainrates from the SSM/I are tied to these geostationary data through a dynamic, probabilistic histogram-matching approach, providing a continuous update of rainfall over an area.

4. Conclusions: The NRL webpage illustrates that this capability is truly global, covering a variety of tropical cyclone basins and both southern and northern hemispheres. The realtime combination of visible, infrared and SSM/I images offer a number of applications. In particular, inferences of storm intensity are much improved compared to traditional methods which rely solely on visible and infrared images. From viewing this webpage, field users in distant parts of the world give valuable feedback which fuel further improvements. Please email us at the address at the bottom of the first page with comments.

5. Acknowledgments: The support of the research sponsors: the Office of Naval Research, Program Element (PE-060243N); and the Oceanographer of the Navy through the program office at the Space and Naval Warfare Systems Command (PMW-185; PE 0603207N) is gratefully acknowledged.

6. References:

Ellrod, G.P., 1995: Advances in the detection and analysis of fog at night using GOES multispectral infrared imagery. *Wea. Forecasting*, 10, 606-619.

Hawkins, J.D., D.A. May, J. Sandidge, R. Holyer, and M.J. Helveston, 1998: Satellite Tools for monitoring tropical cyclone intensity change. Preprints *AMS Symposium on Tropical Cyclone Intensity Change*, 51-55.

Lee, Thomas F., F. Joseph Turk, and K. Richardson, 1997: Stratus and Fog Products using GOES 8/9 data. *Wea. Forecasting.*, 12, 664-677.

Spencer, R.W., H.M. Goodman, R.E. Hood, 1989: Precipitation retrieval over land and ocean with SSM/I: Identification and characteristics of the scattering signal. *J. Atmos. Ocean. Technol.*, 6, 254-273.

O2.5B

SATELLITE RETRIEVALS OF SEA SURFACE TEMPERATURE FOR LONG-TERM CLIMATE MONITORING

Andrew R. Harris[1]*, C. J. Merchant[2], B. Candy[1], C. A. Clayson[3], M. J. Murray[4], A. M. Závody[4] and M. R. Allen[4,5]
[1]The Meteorological Office, Bracknell, U.K.
[2]University College London, U.K.
[3]Purdue University, West Lafayette, Indiana
[4]Rutherford Appleton Laboratory, Didcot, U.K.
[5]Oxford University, Oxford, U.K.

1. INTRODUCTION

Sea surface temperature (SST) has long been recognized as one of the most important parameters in the climate system. It is a key diagnostic for climate change detection, and exerts a controlling influence on the exchange of heat between the ocean and atmosphere. For the past decade and a half, satellite-based retrieval methods have been used to map SST on a routine basis, with all the advantages (and disadvantages) that remote sensing entails. In 1991, the first of a new generation of spaceborne radiometers was launched on the ERS-1 platform. This instrument, the along-track scanning radiometer (ATSR) promised to provide, for the first time, SST measurements to the accuracy required for climate research from a single sensor. The three main improvements over other sensors were much improved calibration sources (3-σ drift error of <0.1 K over the mission, Mason *et al.*, 1996), the use of a two-angle view of the surface to assist in accounting for the contribution of the atmosphere to the measured radiances, and a Stirling cycle active cooling system for the detectors. Early validation results (Mutlow *et al.*, 1994, Harris *et al.*, 1995, Barton *et al.*, 1995, Harris & Saunders, 1996) indicate that the instrument performs well, but some significant problems remain. In order to ascertain the priorities for improvement, we need to review the primary goals of such research. The desire is to construct a long-term record of SST using data from ATSR, ATSR-2 (launched in April 1995) and eventually the advanced-ATSR (AATSR, due for launch at the end of 1999). In order to produce such a record of SST for climate change detection purposes, the stability of the observing system must be better than 0.1 K decade^{-1} (Allen *et al.*, 1994). It is for this reason that such care has been taken to provide accurate and stable calibration sources. However, there are other effects, both geophysical and instrumental, that can potentially compromise the goal. Firstly, the ATSR SST retrieval process is designed to retrieve the skin temperature, which may be some tenths of a degree different (usually cooler) than the bulk temperature measured by buoys and ships. Secondly, different retrieval algorithms display different sensitivities to changes in stratospheric aerosol loading, and also to water vapour loading. The key point is this: for climate change purposes, changes in retrieved SST resulting from changes in any other parameter affecting the retrieval process cannot be tolerated. Stratospheric aerosols generated by volcanic eruptions are a particular problem since they can cause secular trends in retrieved SST over a period of years.

2. SKIN OR BULK?

It is important to recognize that, irrespective of algorithm development method, either regression against *in situ* bulk measurements or theoretical brightness temperatures produced by a radiative transfer model, that a spaceborne infrared radiometer detects radiance emitted from no lower than the skin of the ocean. Regressing measured brightness temperatures directly against *in situ* measurements of bulk temperature will remove the mean bias (along with errors in calibration and the radiative transfer model), but it will be unable to deal effectively with the rapid temporal and spatial variability of the skin effect. It might be argued that the skin SST is a better parameter to use

* *Corresponding author address:* Andrew R. Harris, Meteorological Office, London Road, Bracknell, Berkshire, RG12 2SZ, England, U.K. e-mail: arharris@meto.gov.uk.

than the bulk temperature, since it is that temperature that directly affects the exchange of heat, but there are several problems with this. Firstly, the skin effect is a function of the net heat loss from the ocean surface, combined with the surface renewal of the boundary layer which is almost entirely a function of wind speed. These parameters change with time of day and cloud cover, but sun synchronous polar orbiting satellites view a given part of the ocean at the same time each day, and only provide measurements under cloud-free conditions. Secondly, the temperature of the mixed layer is the best indicator of the store of heat, which is a function of the long-term integral of the heat flux - a far more important diagnostic quantity for climate models than the instantaneous value.

3. A STAGED APPROACH

In consideration of the above, we have decided to adopt a staged approach to the construction of a bulk SST record of the accuracy required for climate monitoring.

3.1 *Accurate Retrieval of Skin SST*

The first step is to retrieve an accurate skin SST from the satellite radiometer measurements. This precludes the use of regression against *in situ* bulk measurements, and a line-by-line radiative transfer model developed from that of Závody *et al.* (1995) and geographically and seasonally diverse set (~1300) of profiles is used to generate top-of-atmosphere brightness temperatures at 3.7, 11 and 12 μm for both the nadir and forward views (~55° zenith angle) of the ATSR. The radiative transfer model includes updated absorption database information. Stratospheric and tropospheric aerosols are also modeled using a hybrid scheme. Robustness against stratospheric aerosol is achieved by using a Lagrange multiplier constraint within the regression procedure, and is shown, in simulations, to produce zero bias under all realistic aerosol loadings. Absence of a comprehensive set of in situ skin temperatures prevents absolute validation, but when applied to real data, inter-algorithm biases are reduced from ~0.7 K to 0.02 K. The new continuum model is shown to remove the cold bias present in previous algorithms in regions of high water vapour loading such as the W. Pacific Warm Pool. The main reason why it is necessary to achieve zero bias between the 2-channel and 3-channel dual-view retrievals is that ATSR's 3.7 μm channel failed in May 1992, while the aerosol loading from Mt. Pinatubo was still fairly high, and SST records produced using the pre-launch retrieval coefficients showed a pronounced drop after this time which slowly recovered thereafter. The details of this work is described in more detail in a companion paper (Merchant, 1998).

3.2 *Skin to Bulk Conversion*

The second step is to use surface fluxes of heat and momentum in models from a numerical weather prediction (NWP) analysis to parametrize the skin effect. A variety of models are examined for their applicability and tolerance to errors in the analysis fluxes. The results of the various models are tested against match-ups of *in situ* temperatures from drifting buoys with ATSR-2 skin SSTs to evaluate their relative success. The criteria for a good validation matchup are also explored at this point in terms of cloud cover, time and space location, etc. and also avoidance of possible diurnal effects. Matchups with high-quality validation data yield a reduction in rms from ±0.31 K to ±0.25 K, which approaches the minimum deviation expected from error analysis. This work is described in a companion paper (Candy, 1998).

3.3 *The Diurnal Thermocline*

The third step is to correct for the diurnal cycle of temperature in the top part of the mixed layer. The approach is to use a time history of fluxes from a NWP analysis to force a high resolution vertical mixing model of the near-surface. A variety of bulk and turbulence diffusion models are being evaluated, initially by comparison with SSTs from shallow (~10 cm) sensors such as WOCE SVP drifters (see Figure 1) which measure the temperature within the stratified layer. High resolution (~10 cm) temperature profile data have just been obtained from Univ. Iwate, Japan, and estimates of the fluxes of heat and momentum using *in situ* meteorological measurements should be more accurate than those from NWP analyses. Although the diurnal thermocline only becomes significant about 15% of the time, it displays strong geographical preferences and must therefore be accounted for if one hopes to provide a comprehensive dataset of bulk SST estimated from space. This work also poses

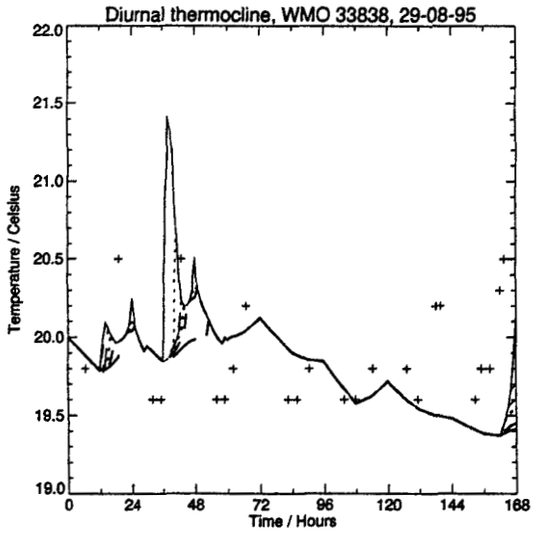

Figure 1: The diurnal thermocline as modelled using 6-hourly archived analysis fluxes for the position of WOCE-SVP drifting buoy 33838 for one week during August–September 1995. The solid trace is the 10 cm temperature as predicted by an adapted Kraus-Turner model, and the buoy temperature reports are marked as crosses. The various dashed and dotted lines indicate temperatures at depths of 0.5, 1.0, 1.5, 2, 3 and 5 metres, and only separate from the 10 cm trace when stratification is present.

some interesting questions regarding the definition of bulk temperature.

i

4. OTHER ISSUES

Although one conclusion of the above work is that the limit of validation accuracy is already being approached, the exercise has only been conducted for a restricted set of conditions. There are other aspects of the retrieval process and instrument that need to be addressed.

4.1 *Validation of skin temperatures*

Since our initial satellite retrieval is of the skin SST, it will be beneficial to validate the retrievals against high quality *in situ* measurements of skin SST made by specialized ship-borne (and platform-based) thermal IR radiometers. Such measurements are the preserve of specialist oceanographic cruises and are consequently sparsely distributed in both space and time – there have simply been too few to date. However, recent efforts to co-ordinate such measurement activities for the purposes of validating a number of upcoming spaceborne radiometers are to be strongly encouraged, as are the attempts to install stand-alone systems on ships of opportunity. If provided with associated meteorological measurements, then these data will be also be invaluable for use in the development and testing of improved parameterizations of the skin effect, the fruits of which can then be fed back into the skin-to-bulk conversion process described in §3.2.

4.2 *Long-term Validation*

Although validation against skin temperatures is desirable, such measurements are never likely to be sufficiently widespread to give full confidence. Indeed, their main purpose will be to form a basis for evaluating and improving the radiative transfer modelling and other aspects of the skin SST retrieval process. In addition, it is the bulk product that is the desired end quantity, and measurements of this are much more widespread. Another consideration is that bulk measurements are the only feasibly sufficient source of validation data for the ATSR mission (and much of the ATSR-2 mission), and they function as the common reference that will be needed to overcome potential effects due to differences in the instruments. Any long-term record of bulk SST produced from satellite data should be continuously checked against high quality *in situ* measurements. We are not advocating empirical tuning of the end-product, however. Instead, the results of this analysis would be used to improve our understanding of the various physical processes and instrumental effects contributing to the retrieval.

4.3 *Other Effects*

There are a number of areas which require investigation in order to assess their impact on the retrieval scheme. Chief among these is the nature of cloud masking schemes. Primary issues for consideration are: 1) what is the impact of the loss of the 3.7 μm channel on ATSR cloud masking? 2) what is the impact of increased detector noise (due to the gradual degradation of cooler performance) on ATSR cloud masking? 3) what is the impact of the extra channels on ATSR-2 cloud masking relative to that of ATSR? Finally, 4) what is the impact of using different approaches to cloud screening, and might these lead to differences in the retrieved bulk SST record? In particular, is there likely to be a change in retrieved bulk SST

due purely to changes in cloud characteristics over time, and if so, might other cloud masking schemes make the retrieval process more robust to such changes?

Other effects which may compromise the retrieval process include changing concentration of trace gases. In addition, the gradually degrading cooler performance of ATSR results in a small spectral shift in the 12 μm filter function, which could certainly cause a secular trend in retrieved SST of 0.1 – 0.2 K over the lifetime of the mission if not accounted for.

5. SUMMARY

For the case of SST retrieval, the observing system comprises far more than just the spaceborne radiometer. The requirement of <0.1 K decade^{-1} encompasses the entire retrieval process, from measurement of top-of-atmosphere radiances to final retrieval of bulk SST. It is a stringent target, but one which must be met in order to contribute to the timely detection of climate change.

REFERENCES

Allen, M. R., C. T. Mutlow, G. M. C. Blumberg, J. R. Christy, R. T. McNider and D. T. Llewellyn-Jones, 1994: Global change detection. *Nature*, **370**, 24–25.

Barton, I. J., A. J. Prata and R. P. Cechet, 1995: Validation of the ATSR in Australian waters. *J. Atmos. Oceanic Technol.*, **12**, 290–300.

Candy, B., 1998: Investigating the thermal skin of the ocean by satellite. *This volume.*

Harris, A. R., M. A. Saunders, J. S. Foot, K. F. Smith and C. T. Mutlow, 1995: Improved sea surface temperature retrievals from space. *Geophys. Res. Lett.*, **22**, 2159–2162.

—, and M. A. Saunders, 1996: Validation of the along-track scanning radiometer against drifting buoys. *J. Geophys. Res.*, **101**, 12,127–12,140.

Mason, I. M., P. H. Sheather, J. A. Bowles and G. Davies, 1996: Blackbody calibration sources of high accuracy for a spaceborne infrared instrument: the Along-Track Scanning Radiometer. *App. Optics*, **35**, 629–639.

Merchant, C. J., 1998: Highly accurate retrieval of skin sea surface temperature. *This volume.*

Mutlow, C. T., A. M. Závody and D. T. Llewellyn-Jones, 1995: Sea surface temperature measurements by the along-track scanning radiometer on the ERS 1 satellite: Early results. *J. Geophys. Res.*, **99**, 22,575–22,588.

Závody, A. M., C. T. Mutlow and D. T. Llewellyn-Jones, 1995: A radiative transfer model for sea surface temperature retrieval for the along-track scanning radiometer. *J. Geophys. Res.*, **100**, 937–952.

O2.6B

SEA ICE REMOTE SENSING FROM SPACE

Alain Cavanié *
IFREMER, Centre de Brest, France

1. INTRODUCTION

Sea ice observations are important in different scientific and economic fields of human activity: transportation, fishing, ecology, oceanography, meteorology, climatology, ... They are impossible to obtain in sufficient quantity and quality, in situ, because of the vast areas to be monitored, hash weather conditions, darkness in winter, and the presence of the ice itself, which hampers ship navigation. Moreover, sea ice is a dynamic medium, submitted to the short-term influence of oceanic currents, winds and waves, as well as to seasonal and interannual modifications. Monitoring sea ice is therefore a long term endeavor.

It is natural that satellite remote sensing play an eminent role in this task. Satellites in polar orbit have been used systematically to observe radiometric properties of sea ice since the time of the ESMR on Nimbus 5, launched in December1972. It was relayed by the SMMR, followed by the series of SSM/I which are programmed in operation by the DMSP until the year 2005. With SEASAT, launched in 1978, the possiblities offered by active sensors, the Synthetic Aperture Radar (SAR) and wind scatterometer, were tested. Since the launch of ERS-1 in 1991, large amounts of SAR and scatterometer data over sea ice have been processed and analyzed. Along with these passive and active microwave instuments, infrared and visible radiometers (LANDSAT, SPOT, AVHRR) continue to furnish valuable informations for sea ice monitoring, although they are considerably limited by the presence of clouds, too often present in polar and sub-polar regions.

Clearly, a sea ice monitoring program must consider a large number of different, interlinked, and often contradictory criteria concerning the satellite data to be employed: cost, long term availability, revisit interval, ground resolution, physical interpretability. These criteria will be given a different weight as a function of the program's specific objectives.

Excellent and exhaustive presentations of individual sea ice remote sensing sensors have been published and no attempt is made here to reproduce them. Rather, we will insist on the latest developments in this field and on the possibilities offered by multi-sensor approaches. To clarify the presentation, low (10 to 50 km), medium (1 to 10 km) and high (10 to 200 m) resolution sensors will be considered separately. Higher resolution sensors, say below 1 m, would be required for certain applications (detection of small, sparcely distributed multi-ice floes or growlers calved from icebergs), but must presently be flown on airplanes or helicopters, in order to reduce the observation distance.

2. LOW RESOLUTION SENSORS

The current series of SSM/I (Special Sensor Microwave Imager) flown on DMSP satellites (Defence Meteorology Satellite Program) offers brightness temperature measurements at 19, 37 and 85 GHz, to which different algorithms are applied to obtain ice type and ice concentration estimations, as well as ice limits. For a detailed description of these algorithms and their limitations, see Steffen et al (1992). If the total ice concentration is stably determined in winter, caution must be applied when evaluating separately the first year and multi-year ice concentrations with the present algorithms. Surface melting and ponding, which may represent up to 30% of the ice surface in summer, modify the surface emissivities at all frequencies, and make interpretation in this period much less accurate than in winter.

For a meteorologist, the large swath of the instrument which allows it to totally cover both polar oceans daily, its guaranteed operation over a long time period, and near real time access to the data make it an essential tool for sea ice monitoring at polar ocean scales. For climatologists, the data, as archived and distributed by the NSIDC (National Snow and Ice Data Service), is convenient to use.

Since 1991, the C-band scatterometers on ESA's ERS satellites, the AMI in Wind mode, have

**Corresponding author address*: Alain Cavanié, DRO/OS, Centre IFREMER de Brest, B.P 70, 29280, Plouzané, France; e-mail: cavanie@ifremer.fr

furnished a continuous flow of backscatter measurements over both polar oceans. Since backscatter for large footprint sizes is isotropic in azimuth over sea ice, this data has been used to produce backscatter maps from which different ice types can be distinguished by their backscatter level, and followed in their slow drift and seasonal evolution. The long series of such weekly maps is available on a CD-ROM produced by the CERSAT (Centre ERS d'Archivage et de Traitement) for the ERS-1 period, and by Internet from 1991 to the present (http://www.nrsc.no:8001/IMSI), with a two to three week delay. With the launch of METOP in 2003, the ASCAT, a two-swaths instrument, unhampered for this purpose as is the AMI by a SAR mode, will permit production of backscatter maps every three days.

NSCAT, NOAA's Ku-band scatterometer on ADEOS, furnished nine month of backscatter data which was used to produce three-day backscatter maps over both polar oceans with about 60 km resolution (These maps are available at the same Internet address as the C-band maps). The comparison of AMI and NSCAT maps, carried out by Ezraty et al (1997), shows that backscatter is significantly more sensitive to ice type evolution at Ku-band than C-band, and that data at both frequencies, used jointly, can better separate different ice types in the Arctic ocean. However, during the summer melt period, both Ku- and C-band scatterometers give low backscatter values over the whole Arctic ocean, and can no longer be used to distinguish beteen different ice regions.

The launch of Quikscat (Ku-band) at the end of 1998, and later on of SeaWinds, will provide easily processed sea ice data, since the constant incidence angles of the rotating antennas on these instruments make interpolation to a nominal incidence angle unnecessary.

3. MEDIUM RESOLUTION SENSORS

At resolutions of one to a few kilometers, fairly long leads and coastal polynyas can be detected, while some information about the large-scale structure of the ice can already be gained.

Presently, the thermal infrared bands of the AVHRR (Advanced Very High Resolution Radiometer) on NOAA satellites, and of the ATSR (Along Track Scanning Radiometer) on ESA satellites, are the major sources of information generally available concerning sea ice at this resolution. While such images give very valuable informations under clear sky conditions, their major drawback is that even light clouds rapidly obscure the ocean surface and, when undetected, lead to erroneous sea ice concentrations. The AVHRR, whose data can be acquired by local receiving stations in real time, somewhat compensates for this drawback by offering several observations per day.

In the former Soviet Union, side looking radars on OKEAN satellites, with a ground resolution around 1.5 km, were used for sea ice observations in a systematic fashion by the Arctic and Antarctic Institute in St. Petersburg. This program has been continued through a cooperative effort between Russia and Ukraine, and data of the SICH sensor can be ordered and acquired through NITS IPR (State Scientific Research Center for Natural Resources Studies, Moscow).

4. HIGH RESOLUTION SENSORS

Passive sensors in the visible or near infrared bands, such as LANDSAT or SPOT offer spectacular images of sea ice at 10 to 20 m resolution. However, they are severely limited by cloudiness and can be used only during daylight. Therefore, they are of limited use for sea ice monitoring but can serve to evaluate equivalent or lower resolution sensors.

Following the SEASAT SAR in 1978, a number of similar instruments have flourished world-wide (Russian ALMAZ, Japanese JERS-1, European ERS-1 and ERS-2, Canadian RADARSAT). The data from these instruments can be used to determine ice type, concentration, limit, as well as motion from successive images. The most efficient product for ice monitoring is presently the RADARSAT ScanSAR wide mode with its 100m resolution, because of its 500 km swath which gives a daily coverage north of 75° North and every second day from 65° to 70° North. For a full description, see Ramsay et al (1993).

A major problem linked to the high resolution images is the amount of analysis and accompanying data reduction to be done before transmission to the final users (A 500 x 500 km image with 50 m pixel represents one hundred Megabytes, coded one byte per pixel). It is probable that no unique policy will be acceptable in this matter and that, in years to come, an effort will be made to send the image, or a compressed version of it, to selected ships such as ice-breakers, while ice charts, improved by SAR

data, will continue to be produced and broadcast for the general commercial traffic.

5. FUTURE ORIENTATIONS

Active sensors launched in the 1990's, and the rapid distribution of both active and passive sensor data, have considerably increased the potential for sea ice monitoring from space. However, we still have to improve the significance and practical use of these informations, using multi-sensor approaches conceived in terms of international cooperations.

The cost of SAR images is presently, and most probably will remain in the near future, too high to employ this instrument alone, outside of shipping lanes of strategic importance. The long series of low resolution, passive and active microwave data covering both polar oceans, readily and freely available, will continue to meet the needs of many meteorological services. However, they would certainly benefit from a reinterpretation in the light of specific SAR informations, and could be used to extend the sparse coverage of this instrument.

Because of the small penetration depth in sea ice of electromagnetic waves of reasonable wavelengths, there will probably never be a direct measurement of sea ice thickness from satellite sensors. However, the contribution of remote sensing to the estimation of local ice thickness distributions could be to classify ice 'regions' and their limits which evolve in time, thus increasing the significance of available in situ data. The regular evolution of mean sea ice thicknesses, measured along a submarine track extending northward to the pole from 72° North through the Fram Strait, as analyzed by Wadhams (1997), give some credibility to this proposition.

REFERENCES

Ezraty R., Cavanié A., and F. Gohin, 1997. Monitoring Arctic sea ice using C- and Ku-band scatterometers. Proceedings of the Conference on Polar Processes and Global Climate Orcas Island, Washington, USA. Int. ACSYS Project Office, Oslo, Norway. 48-50

Gloersen P., W. J. Campbell, D. J. Cavalieri, J. C. Comiso, C. L. Parkinson, and H. J. Swally, 1992. Arctic and Antarctic sea ice, 1978-1987: Satellite passive microwave observations and analysis, NASA SP-511 [Available from NASA Scientific and Technical Information Program, Washington D.C.]

Massom R., 1991. Satellite remote sensing of polar regions, applications, limitations and data availability. Belhaven Press, London, in association with the Scott Polar Research Institute.

Parkinson C. L., J. C. Comiso, H. J. Swally, D. J. Cavalieri, Gloersen P., and W. J. Campbell, 1987: Arctic sea ice, 1973-1976: Satellite passive microwave observations, NASA SP-489 [Available from NASA Scientific and Technical Branch, Washington D.C.]

Ramsay B., T. Hirose, J. Falkingham, R. Gale, D. Barbier, M. Shokr, B. Danielowitz, B. Gorman, and C. Livingstone, 1993. Potential of RADARSAT for sea ice applications, *Canadian J. of Rem. Sens.*, **19**, 352-362.

Steffen K., J. Key, D. J. Cavalieri, J. Comiso, P. Gloersen, K. St. Germain, and I. Rubinstein, 1992. The estimation of geophysical parameters using passive microwave algorithms. Chapter 10 in Microwave remote sensing of sea ice, F. Carsey, Ed. AGU Geophysical Monograph 68. 201-231

Wadhams P., 1997. Downstream variability of Arctic ocean sea ice thickness and its relationship to heat flux. Proceedings of the Conference on Polar Processes and Global Climate Orcas Island, Washington, USA. Int. ACSYS Project Office, Oslo, Norway. 277-279.

P2.1A

THE EUMETSAT ATOVS AND AVHRR PROCESSING PACKAGE (AAPP), AN EXAMPLE FOR INTERNATIONAL CO-OPERATION

K. Dieter Klaes* and Michel Langevin
EUMETSAT, Darmstadt, Germany

1. INTRODUCTION

The NOAA-K,L,M polar orbiting weather satellites will replace the current NOAA/TIROS-N polar orbiting weather satellite system. The new system will comprise two sun-synchronous polar orbiting spacecraft, one in the morning (AM) orbit, the other one in the afternoon (PM) orbit.

The Microwave Sounding Unit (MSU) will be replaced by Advanced Microwave Sounding Units (AMSU), thus providing improved microwave sounding capability for temperature (AMSU-A) and humidity (AMSU-B) profiles. An improved version of the High Resolution Infrared Radiation Sounder (HIRS/3) will provide the continuity of the infrared sounding capability. The Stratospheric Sounding Unit (SSU) will no longer be embarked.

The ATOVS (Advanced TIROS Operational Vertical Sounder) sounding package will be complemented by a new version of the Advanced High Resolution Radiometer (AVHRR/3) multi-spectral imager.

The software development initiative co-ordinated by EUMETSAT is focused towards a standard processing package for local received HRPT (High Resolution Picture Transmission) ATOVS and AVHRR data. The first development step resulted in two sub-packages, the INGEST and the PRE-PROCESSING which allow the reception of the data (direct read-out), the decommutation/demultiplexing of the sensor data, the calculation of calibration coefficients, and also the calculation of radiances and brightness temperatures, the identification and the treatment/adjustment of contamination effects to the ATOVS data and the mapping of the different sensor data to a common sensor grid. The processing includes the use of AVHRR data, the deduction of a cloud mask and their mapping to a the HIRS FOVs. The resulting processing package, the ATOVS and AVHRR Processing Package (AAPP) allows the processing of current TOVS data and also the future ATOVS data. The AAPP is now ready in a first integrated form for TOVS and is being tested at various sites. After the launch and commissioning of NOAA-K further tests are foreseen with ATOVS data. The first version of AAPP for ATOVS is planned to be finalised about three months after the end of the commissioning of NOAA-K.

*Corresponding author address: Dr. K. Dieter Klaes, EUMETSAT, Am Kavalleriesand 31, D-64295 Darmstadt, Germany; e-mail: klaes@eumetsat.de

A third processing step is the RETRIEVAL/INVERSION and is subject to a further development slice. Since different centres will have their own priorities and approaches, it is anticipated to develop the interfaces to AAPP on one hand and to a, already defined retrieval file, on the other hand. The necessary interfaces exist and first steps are already undertaken to integrate retrieval packages.

2. AAPP DESIGN

A development group of European Organisations has designed and developed AAPP (see Fig. 1). It has been decided to keep the design of AAPP close to the ITPP (International TOVS Processing Package) structure. The AVHRR processing has been kept in a separate processing chain. This design allows to keep the processing as flexible as possible. The software includes modules for orbit predict, clock correction and navigation.

FIGURE 1 : The EUMETSAT ATOVS Development Group

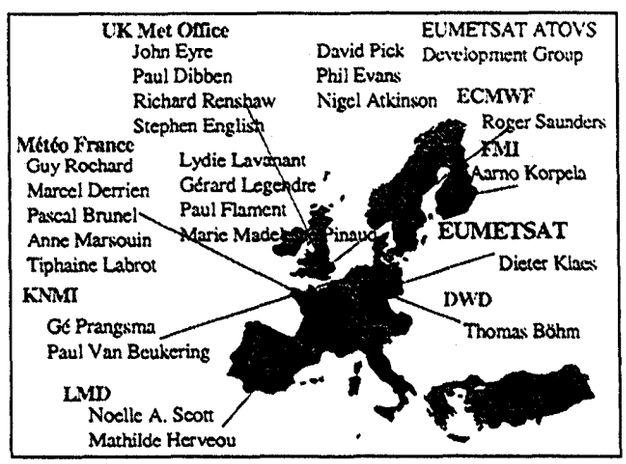

The following Figures 2 and 3 depict the major sub-packages of AAPP and also the organisations who performed the development of the respective modules. The first module HRPTDC receives the HRPT data from the receiving equipment. The data processing chains for TOVS/ATOVS data and AVHRR are then activated.

2.1 *ATOVS Processing*

ATOVDC (see Fig. 2) performs the decommutation of the AIP (AMSU Information Processor) and/or TIP (TIROS Information Processor) data, depending whether NOAA-K,L,M or one of the current NOAA/TIROS-N satellites has provided the data. Level 1a data, i.e. counts from HIRS/3, AMSU-A and AMSU-B (or HIRS/2 and MSU) are the

FIGURE 2 : AAPP Design: ATOVS Ingest and Pre-Processing

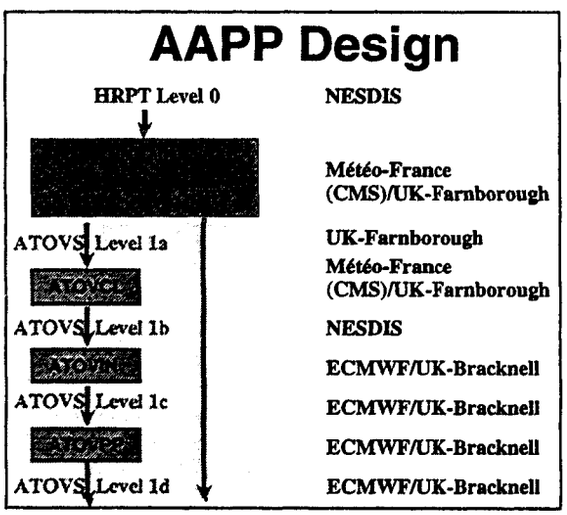

result. They are input to the module ATOVCL. It performs the calibration, i.e. the extraction and calculation of calibration coefficients, and the navigation (earth location) of the data. The resulting calibration coefficients and location parameters are appended to the counts, forming the level 1b data set. The module ATOVIN then transforms the counts into radiances and further the radiances into brightness temperatures. The processing includes quality control, e.g. checking of consistency in time, the viewing angles, brightness temperature boundaries, etc. The results are the level 1c data.

The Pre-Processing of ATOVS data is performed by the module ATOVPP. Pre-Processing means: examining the data for effects which deem them unsuitable for further processing (e.g. precipitation contamination, contamination by large cloud ice particles etc.) A further task within the pre-processor is the mapping of one set of instrument data to the grid of another. The mapping from any grid to any other grid is planned to be implemented. At present ATOVS Pre-Processing includes HIRS and AMSU-A. The output of the present AAPP version is instrument brightness temperatures, mapped onto HIRS FOVs, with optional other instrument combinations on the AMSU-A or AMSU-B grid. Pre-Processing flags and Pre-Processing information is added to the data, and also mapped to the target grid. The resulting data format is called level 1d and is the interface of AAPP towards further subsequent processing.

2.2 *AVHRR Processing*

Fig. 3 depicts in a similar way the AVHRR processing. AVHRR data are decommutated and demultiplexed within the module AVHRDC, the latter forming the entry point into the AVHRR

FIGURE 3 : AAPP Design: AVHRR Processing Chain

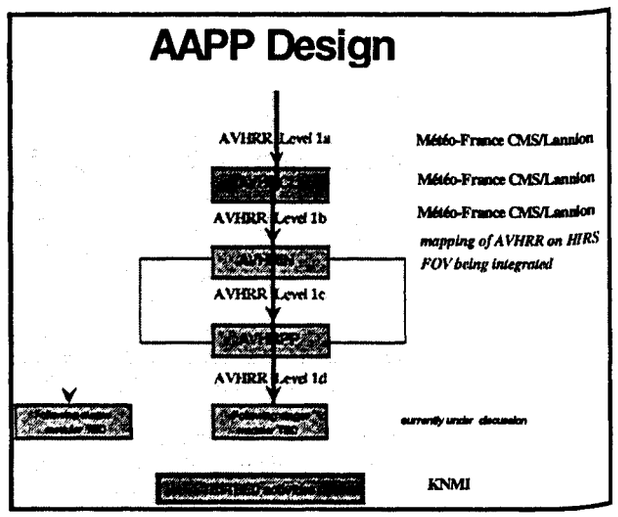

processing. Navigation and the extraction of calibration parameters is performed by the module AVHRCL, producing an AVHRR level 1b data set, i.e. AVHRR counts with appended calibration coefficients and earth location information.

In AVHRIN the calibration coefficients are applied to the AVHRR counts. The resulting level 1c data form the input to the AVHRPP module which could perform a Pre-Processing of the AVHRR data, e.g. a cloud analysis. AVHRIN and AVHRPP may be considered as one processing bloc. At present the integration of both a cloud mask algorithm and the mapping of AVHRR data onto the HIRS Field of View is under way. The final AVHRR information will be included into the level 1 d data set.

3. DEVELOPMENT AND INTEGRATION

The development of the above mentioned modules has been done by the involved institutions from 1995 through 1997. The modules were coded in FORTRAN77, with some agreed extensions. At the beginning of the development it was decided to develop the package for a UNIX environment. UNIX is available for nearly every possible platform, and should thus not form an obstacle for a wide spread use. (A possibility to run the package on a PC under LINUX is presently under investigation and is expected be available in 1998.)

Testing is being finalised at the developers sites with a first integrated version for TOVS data. The testing is done with current TOVS data, both with a common test data set and also with HRPT data of an agreed time period, received at different sites. The results have

demonstrated that successful installations can be made on the following platforms:

- SUN
- DEC alpha
- HP
- SGI

Tests on further platforms are currently ongoing (e.g. IBM RISC and PC under LINUX) and are also envisaged through an extended test phase.

4. STATUS

The above mentioned modules are all coded and tested (Figure 4 shows examples for results with the TOVS test data set). The ATOVS related modules, in particular the calibration, had been tested at module level with data from thermal vacuum chamber testing of NOAA-K, which

FIGURE 4: AAPP Results, NOAA-12, 18 December 1996, 06:55 - 07:00 UTC.

top: level 1c data, MSU channel 2 and HIRS channel 8 BT; bottom: level 1d data, MSU channel 1 BT, on original grid and mapped onto HIRS FOV.

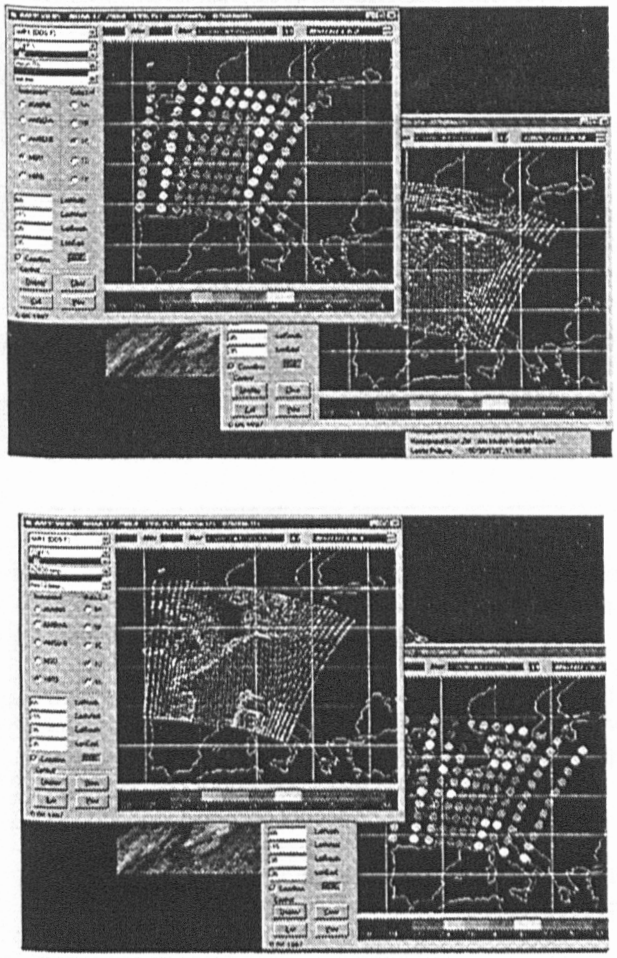

NESDIS has made available to the development group. The ATOVS related modules will be tested in a second test campaign after the launch and the commissioning of NOAA-K. After this phase, with the probably required adjustments another integration phase will be done. The documentation and installation guide, and also the design document, composed from contributions of all developers, will be updated. The whole AAPP package is anticipated to be available in its first final ATOVS/TOVS integrated form at the end of 1998.

5. OUTLOOK

Further discussion is currently devoted to the integration of retrieval/inversion code into AAPP, thus completing the full end-to-end processing chain. Within the development group, the structure of a retrieval file has been defined. Together with the file definitions in the AAPP the interfaces are identified. To keep the approach as modular as possible, for each retrieval package, planned to be integrated into the AAPP environment, interface routines have to be developed separately.

Potentially additional modules need to be developed, e.g. AVHRR processing and/or HIRS cloud processing. Some of them might have to be integrated into the respective retrieval packages. It is anticipated that a high-level switch will be integrated into AAPP to allow for the use of several retrieval packages. With retrieval modules integrated a full processing chain for the processing of the HRPT direct readout data from the NOAA-K,L,M spacecraft will be available.

6. REFERENCES

Bloom, H.J. and A. Reale, 1997: Current status of the RTOVS software system and enhancements to the ATOVS software system in preparation for launch of NOAA-K.
Proceedings of the Ninth International TOVS Study Conference, Igls, Austria, 20-26 February 1997, in press.

Derrien, M., and G. Legendre, 1997: A pilot AAPP-based operational processing scheme.
Proceedings of the Ninth International TOVS Study Conference, Igls, Austria, 20-26 February 1997, in press.

Dibben, P. C., S.J. English, J.R. Eyre and R.J. Renshaw, 1997: Plans for the processing of ATOVS data at the UK Met Office.
Proceedings of the Ninth International TOVS Study Conference, Igls, Austria, 20-26 February 1997, in press.

English, S.J., R.J. Renshaw, P.C. Dibben and J.R. Eyre, 1997: The AAPP module for identifying precipitation / ice cloud, liquid water and surface type on the AMSU-A grid.
Proceedings of the Ninth International TOVS Study Conference, Igls, Austria, 20-26 February 1997, in press.

Klaes, K. D., 1997: ATOVS data processing in Europe.
Proceedings of the Ninth International TOVS Study Conference, Igls, Austria, 20-26 February 1997, in press.

Nieman, S., T. Achtor, W. P. Menzel, W. L. Smith, H.M. Woolf, B. Burns, F. Nagle, H.-L. Huang, 1997: Utilization of AAPP within ATPP-1.
Proceedings of the Ninth International TOVS Study Conference, Igls, Austria, 20-26 February 1997, in press.

Saunders, R.W. and M. Matricardi, 1997: A fast forward model for ATOVS (RTATOV).
Proceedings of the Ninth International TOVS Study Conference, Igls, Austria, 20-26 February 1997, in press.

Hervéou, M. and N.A. Scott, 1997: The retrieval of temperature and water vapour profiles from ATOVS data: an adaptation of the 3I scheme.
Proceedings of the Ninth International TOVS Study Conference, Igls, Austria, 20-26 February 1997, in press.

P2.2B

AN OPERATIONAL SOUNDING SCHEME FOR HRPT STATIONS

L. Lavanant*, G. Rochard, P. Brunel, S. Levasseur
Météo-France / Centre de Météorologie Spatiale
Lannion, France

1. INTRODUCTION.

A retrieval scheme, ICI for "Inversion Coupled with the Imager", retrieves atmospheric profiles in temperature and humidity from TOVS/ATOVS observations. It has been developed at the Centre de Météorologie Spatiale, with the following rules :

- it is independent of the NWP model. Only two surface forecasts are used, when available
- it takes benefits of the AVHRR cloud cover and skin surface temperature in the HIRS ellipse
- it is a regional model as it needs the AVHRR full resolution
- the retrievals are made at the HIRS resolution
- it daily uses radiosondes or analyses to create a initial profile library, to tune all the statistical coefficients of ICI and to validate the retrievals.

The ICI model has been operational since mid 1996 and provides the french NWP model with retrievals for its monitoring, over Europe and North-East Atlantic. We will present in a first part the main characteristics of the ICI software and its accuracy compared to radiosondes and analyses.

Several demands from Météo-France and others institutions have lead to the development of an exportable version of ICI from the HRPT acquisitions to the retrievals. The specific updates are described in the second section wheras the first results obtained from 7 consecutive days of observations dealing with the La Réunion island are displayed at the end.

2. ICI MODEL

2.1. General description

This section summarizes the main characteristics of the ICI inverse radiative transfer model. More details are given in Lavanant (1997).

forward model: ICI uses the fast forward radiative transfer model RTTOV developed by J. Eyre (1991) and implemented at ECMWF and in the french NWP model. RTTOV is used in delayed time to create the library of initial profiles, while in real time it is used in each situation by the inversion module.

Corresponding author adress: Lydie Lavanant, Centre de Météorologie Spatiale, BP 147, F22302 Lannion , France; e-mail: lydie.lavanant@meteo.fr

initial profile: It is selected in a compilation of ancillary profiles supposed to be "representative" of the current meteorological situation. The procedure is the following. A meteorological base is fed 4 times per day with radiosondes reports and with analyses from the french NWP model. The extraction zone is North Hemisphere from 100W to 65E. All the analyses of the 00h cycle of the ten preceeding days, on a 10 degree square grid, are used to create the dataset. The library is daily updated. It corresponds to about 1800 profiles. For each profile, clear brightness temperatures, covariance matrix and total transmittances are computed with RTTOV, for different incident and surface conditions.The initial profile selection is based on the minimization of the least square distance between the observations (corrected from the forward model biases) and the synthetic brightness temperatures. The selection is improved by the use of a surface pressure forecast, when available (otherwise, the sea level pressure is taken as 1013 hPa) and by the adjustment of the synthetic brightness temperatures to the current AVHRR skin surface temperature.

inversion: It consists of the minimization of the cost function J(x), after selection of the first guess:

$$J(x)=(x-x_b)^t.B.(x-x_b)+(y_{mes}-y(x))^t.(O+F).(y_{mes}-y(x))$$

x, x_b the searched profile and the first guess

y_{mes}, y(x) the observations and the synthetic brightness temperatures computed for x with RTTOV

B, O+F the first-guess error covariance matrix and those of observations and forward model together

The routine has been written to be able to iterate for non-linear situations (ex: water vapor channels, cloudy observations). For the moment, only one iteration is done (computer time consuming) for TOVS channels. For AMSU-B observations, sensitive to water vapor, the iteration will be tested.

channels definition: the cloud cover from the AVHRR mask allows the discrimination of the observations in 3 main classes: clear, partly cloudy and cloudy. The channels involved in the scheme depend on the cloud class. When available, the forecast air temperature at 1000 hPa, is added as an observation (additional channel) in the first guess selection to improve the profile near the surface.

tuning: the tuning of ICI internal statistical coefficients is crucial to obtain accurate retrievals: the scheme includes a tuning routine which daily updates all these coefficients. For all the acquired orbits, the

satellite observations, the in-situ atmospheric profiles (radiosonde, analyses), the first guess and retrievals are colocated and archived. The departure is less than 3 hours in time and 100km in space. The matched files of the ten past days are used to update the forward biases, the diagonal O+F error covariance matrix, the first-guess biases and B error covariance matrix.

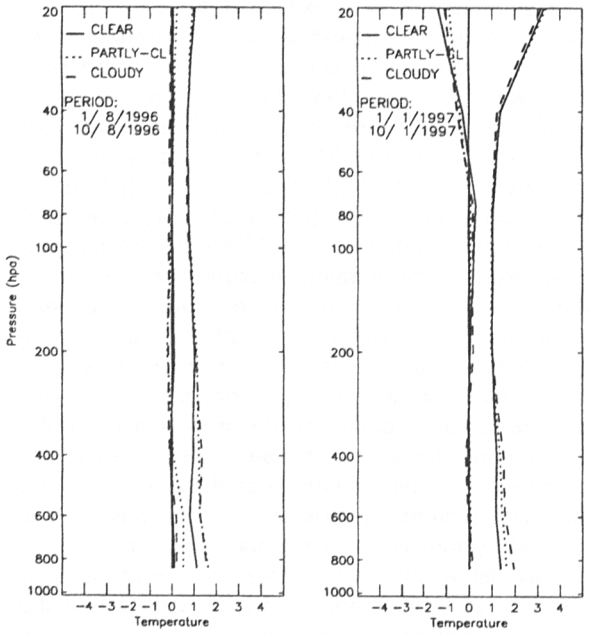

Figure 1: ICI accuracy for two ten-day periods. Noaa14. over sea.

The ICI scheme has been written in order to answer to the necessary constraints of an operational software and to be easily modified for future evolutions. The software has been developed under UNIX in Fortran 90. The real-time processing, at a 1 pixel/3, line/3 resolution, takes about 3 minutes on a SUN SPARC 10 machine.

Some specific parameters help a new ICI user to create his own application. A first one allows to modify the characteristics of the first guess library (sampling, number of rolling days, update frequency) or to replace it by a climatological library. This can be important for stations without "real-time" radiosondes and NWP products archiving. A second one suppress the tuning procedure, when the in-situ profiles are not available. However, periodically updating the coefficients is crucial to obtain accurate retrievals. In the standard version, the tuning is daily done. For users who do not regularly receive analyses or radiosondes, it is also possible to manually inject new coefficients obtained from an other way.

2.2. retrieval accuracy

The operational ICI version have been implemented in mid 1996. Its accuracy is daily evaluated by using the matched files described in the previous section. The following figures are in virtual temperature, according to 7 layers from 1000 to 10 hPa.

Figure 1 shows for Noaa14 over sea, the statistics of error in bias and standard deviation, for two ten-day periods in summer and winter. These examples are representative of the other months and Noaa12. The statistics are given for the three cloud classes on the same graph. They are based on several thousands of colocations. The results, of about 1K in standard deviation everywhere, are very satisfactory except the upper layer 30-10 hpa of the winter case for which the standard deviation reaches values of about 3 degrees (the worse case) due to the climatological extrapolation of the profiles.

Figure 2 express the good global accuracy stability, since the beginning of the operational production. The results correspond to monthly standard deviations for Noaa14, over sea and for the 3 cloud classes. We can see, the improvement of the model during these two years due to successive updates of the version. We also can notice seasonal evolution of the error for the upper layer.

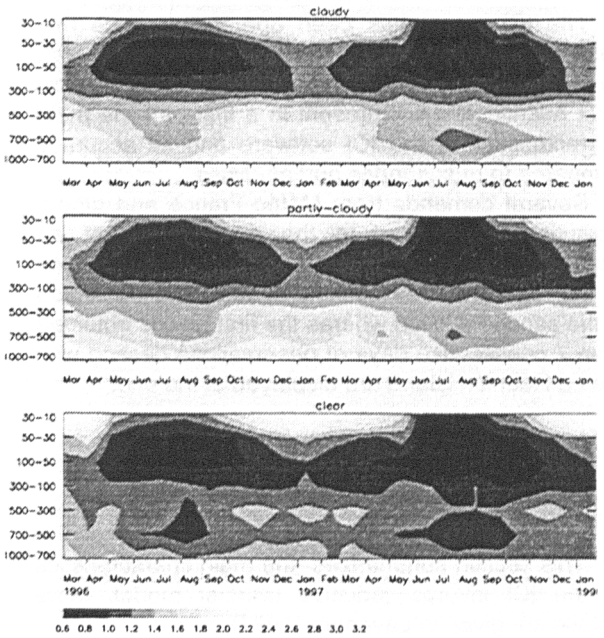

Figure 2: ICI accuracy over 2 years. Noaa14. Marine conditions.

3. EXPORTABLE VERSION

An exportable processing scheme from HRPT acquisitions up to retrieved profiles is currently running at CMS in parallel to the operational scheme.

It includes the preprocessing softwares (ingest, calibration, navigation, instrument mapping..) of the AAPP package developed under the EUMETSAT coordination for NoaaK. A complete description is

given in Klaes, 1997. This package is also usable for the current Noaa14 satellite. The ICI software is interfaced with the level 1d format, output of the AAPP modules.

A cloud mask has been integrated in the preprocessing as a routine of the mapping procedure. It computes, in the ellipse, the cloud cover and the skin surface temperature which are needed in the retrieval scheme.

3.1. cloud mask

The cloud detection is based on a threshold technique, applied to every AVHRR pixel in HIRS ellipse and to various combinations of channels. The combination used depends on the geographical location of the pixel (land, sea, coast), on the solar illumination and the viewing geometry. The tests are part of those applied in the CMS AVHRR operational scheme which produces a more global imagery analysis. The thresholds are either constant values defined previously over Europe (Le Gléau, 1989), either computed with empirical functions (viewing angles, total water vapor content) or depending on external data (climatologies of SST and albedo, topography, air surface temperature forecast). The tests are partly adapted to other acquisition zones by the use of the external data.

The mask has been used for situations acquired by ORSTOM stations at Dakar and La Réunion. A precise study of its output outside Europe will be done by specialists in next months. However, a fast analysis indicates that:

- for Dakar orbits, the results seem satisfactory. A test on the T4-T5 combination has been added for the detection of sand in the atmosphere. This threshold remains crude and should be tuned in the next months.
- for La Réunion, the mask seems a little too strict, particularly for night situations. It classifies as completely cloudy, ellipses which are, probably, partly contaminated. This is due to the fact that the value of the T4-T5 threshold was computed for total water vapor content representative of mid-latitude profiles and should be updated for wetter tropical conditions. However, the results are good enough to allow a feasibility study of the overall scheme up the retrievals.

An additional study is now undertaken to dynamically adapt the tests and thresholds to other HRPT areas.

3.2. La Réunion feasibility study

This study was undertaken as part of a contract with the french army. It is also useful to evaluate the sounding product accuracy before the software implementation at the Météo-France station of La Réunion or for ORSTOM research studies. We have used the 20-26 January 1997 acquisitions - 32 Noaa14, Noaa12 orbits - supplied few months later by the ORSTOM team.

As we used ancient data , it was not possible to run ICI in optimal conditions: the two forecasts parameters were not available and have been replaced by the suitable analyses - of course incestuous. However, from a past study in mid latitude regions, these forecasts seem very accurate and the impact on this study should not be too important.

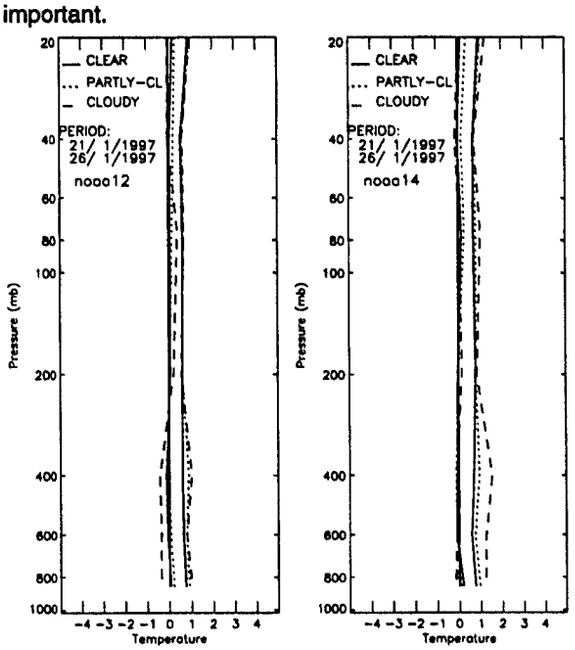

Figure 3: Retrieval accuracy for La Réunion study

In the ICI standard version, 10 days are necessary to start the application for setting up all the statistical coefficients. In this study, that was not possible. The approach was to run the first day with the coefficients of the CMS acquisition zone and to build the colocation files for adjusting the forward model biases to the new area. The same day was runned again with the "correct" biases to obtain a relying initial profile and error covariance. The statistical coefficients was now correctly defined for this first day and it was possible to run the software in a standard way for the following days.

3.3. Results

Figure 3 shows the statistics of error (retrieval - analysis) in virtual temperature, for Noaa12 and Noaa14 individually. Except the small bias for Noaa12 in the lower troposphere and in cloudy condition, the accuracy is very good and stable (not shown) for all the period.

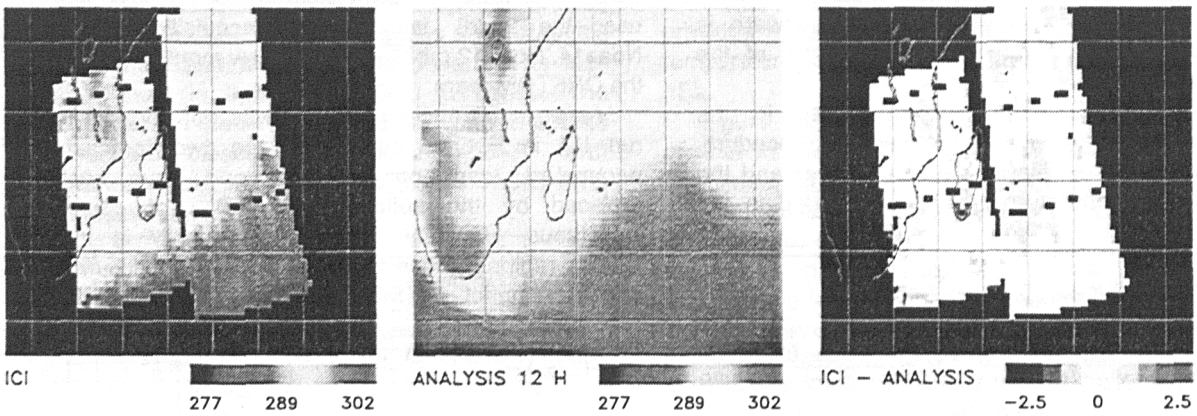

Figure 4: ICI, time nearest analysis and departure temperature fields, NOAA14. Layer 1000-700 hPa. 25/01/1997. 9h57, 11h39. Orbits: 10679, 10680

These results are clearly better than those obtained within the CMS acquisition zone. This can be explained by the fact that the tropical areas are more stable and by the way easier to process. However, this study deals with a tropical cyclone event which destroyed part of South-Madagascar. Therefore, we desarchived the few radiosonde reports available in the area to verify the results. The main colocations are Seychelles and Tromelin stations. Table 1 gives the rms of error, Noaa12 and Noaa14 together, over sea, between 21 and 26/01, for the 3 cloud types. These results agree with the preceding comparisons.

	clear	partly-cloudy	cloudy
nb coloc	7	3	9
30-10	1.86	2.53	1.39
50-30	0.90	0.64	1.69
100-50	1.16	1.92	1.70
300-100	0.71	0.76	0.47
500-300	0.73	0.27	1.63
700-500	0.56	0.61	1.16
1000-700	0.82	1.44	0.94

table1: RMS of error compared to colocated RS

Figure 4 is an example, for the 1000-700 hPa surface layer, of the retrieved ICI field for two consecutive Noaa14 orbits and of the nearest field of the french NWP model. The right figure shows the difference between the retrieved and analyzed fields. The color gradation is 0.5K. The difference is everywhere less than 1K except in south of Madagascar where the retrieved field is colder than the analysis of about 2K. This departure is also observed for other layers and days. The radiosonde report of 25/01-12h of Tolanaro (south of Madagascar) confirms the departure which may be due to heavy precipitations linked to the cyclone.

4. SUMMARY

We have presented the characteristics and the accuracy of the ICI procedure which retrieves atmospheric fields of temperature and humidity. It has been shown that temperature retrievals produce satisfactory results. The humidity profiles are not sufficiently accurate yet for operationnal use: a very clear improvement is expected with AMSU-B.

The software, which has been operational for two years at the CMS, is being implemented in other HRPT stations (La Réunion , Tchek Republic and Hungary). This exportable version has given accurate retrievals for the test with La Réunion observations and should be improved by the dynamic adaption of the cloud mask thresholds to other climates.

5. REFERENCES

Eyre, J.R., 1991: A fast radiative transfer model for satellite sounding systems. ECMWF technical Memorandum no 176.

Klaes, D., 1997: ATOVS data processing in Europe. ITSC IX.

Lavanant, L., P. Brunel, G. Rochard, T. Labrot, D. Pochic, 1997: Current status for the ICI retrieval scheme. ITSC IX.

Lavanant, L., G. Rochard, P. Brunel, T. Labrot,, D. Pochic, S. Levasseur, 1997: Atmospheric sounding: the ICI retrieval scheme. Veille climatique satellitaire, n° 58, 59. 78 - 89.

Le Gléau,H., M. Derrien, L. Lavanant,1989: Operational cloud mask using the AVHRR of NOAA11. Fourth AVHRR data users' meeting, 85 - 89.

P2.3A

USE OF TOVS OBSERVATIONS FOR THE IDENTIFICATION OF TROPOPAUSE-LEVEL THERMAL ANOMALIES

N. Fourrié[1 2*], C. Claud[1], R. Armante[1], B. Pouponneau[2], J.-P. Cammas[3]
[1]Laboratoire de Météorologie Dynamique, Palaiseau, France.
[2] METEO-FRANCE, Toulouse, France
[3]Laboratoire d'Aérologie, Toulouse, France

1. INTRODUCTION

The forecasting of oceanic mid-latitude storms and associated weather patterns is still a challenging problem for operational meteorologists mainly due to the sparsity of conventional measurements. To address this issue, one has to rely largely on observations provided by satellites which are the only ones acquired on a routine and global basis. More specifically, for looking at features and processes occuring in the upper troposphere and the lower stratosphere, which play a critical role in the dynamics of the tropospheric weather systems (Hoskins et al., 1985), three types of observations have been currently used in the past: water vapor fields from geostationnary satellites, ozone fields, especially from the TOMS (Total Ozone Mapper Spectrometer), and the Microwave Sounding Unit (MSU) channel 3 brightness temperature fields aboard NOAA satellites.

In this study we propose a finer characterization of the temperature around the tropopause which relies not only on MSU observations, but on HIRS information too (also aboard NOAA satellites) and on a pre-computed data bank, the TOVS Initial Guess Retrieval (TIGR) one.

The aim of this paper is to show that TLS (Temperature of the Lower Stratosphere is a valuable diagnostic tool for the identification of upper-level anomalies. It is illustrated on a specific case study, an Intensive Observing Period of the FASTEX (Front and Atlantic Storm-Track Experiment) experiment (Joly et al., 1997), conducted in January and February 97 over the Atlantic Ocean. In Section 2, we describe the 3I inversion algorithm with a special emphasis on the determination of TLS. Section 3 follows with the application of the method to the FASTEX IOP 18. TLS fields are described and compared to other diagnostic products. In Section 4, results are summarized and discussed.

* *Corresponding author address*

LMD, Ecole Polytechnique, 91128 Palaiseau Cedex, France. E-mail: fourrie@jungle.polytechnique.fr.

2. OVERVIEW OF TOVS/3I. DETERMINATION OF THE TEMPERATURE OF THE LOWER STRATOSPHERE

2.1 TOVS/3I

The TIROS-N Operational Vertical Sounder (TOVS), which flies aboard NOAA satellites, consists mainly in two passive vertical sounding instruments: the High resolution Infrared Radiation Sounder (HIRS-2), a radiometer with 19 channels in the infrared band and one in the visible band; the Microwave Sounding Unit (MSU), a microwave sounder with 4 channels in the vicinity of 55 GHz. The spatial resolution of the HIRS-2 sounder is about 17 km at nadir, whereas the spatial resolution of the MSU sounder is 100 km at nadir ; the swath width is about 2400 km. There are two operational TOVS satellites operating simultaneously.

The retrieval algorithm used to convert the TOVS (HIRS-2 + MSU) observations into atmospheric parameters is the Improved Initialization Inversion (3I). The 3I method developed at Laboratoire de Meteorologie Dynamique (LMD) has been extensively discussed in the literature, and for a complete description of the method, the reader is referred to Chedin and Scott [1985], and Chedin et al. [1985]. 3I is a physical and statistical algorithm which determines temperature profiles from the surface up to 10 hPa as well as other atmospheric parameters (cloud occurence, cloud amount and height, total water vapor content and relative humidities in 3 tropospheric layers...). All these variables are retrieved in so-called "boxes" of 100 by 100 km^2, resulting from a compromise between HIRS-2 and MSU spatial resolutions. The inversion of the radiative transfer equation is split into two steps: the first step consists in the initial guess from among a vast selection of atmospheric situations archived in advance trough a distance calculation. This library of atmospheric situations, TIGR (TOVS Initial Guess Retrieval), consists of

1761 situations carefully sampled out of 80000 by statistical methods and physical thresholds (Escobar, 1993). Atmospheric transmissions, radiant energies and weighting functions for all HIRS-2 and MSU channels have been precalculated for every TIGR atmospheric situation (temperature and humidity profile) using the 4A (Automatized Atmospheric Absorption Atlas, [Scott and Chedin, 1981]) forward model. Moreover, these 1761 situations are classified into 5 classes (called hereafter tropical, mid-latitude 1 and 2, polar 1 and 2)(Achard, 1991), depending on their virtual temperature profile. In the second step, the deviations between the observation and the initial solution are minimized (retrieval temperatures) using a Bayesian type direct estimation method.

2.2 TLS

In the distance calculation (see above), not only are HIRS-2 and MSU channels used for the proximity recognition, but also the so-called TLS (Temperature of the Lower Stratosphere), which is supposed to represent the temperature around the tropopause. TLS is obtained through a combination of 5 TOVS channels:

$$TLS = a_1 + a_2 TBHIRS2 + a_3 TBHIRS3 + a_4 TBMSU2 + a_5 TBMSU3 + a_6 TBMSU4$$

where the a_i coefficients are obtained from TIGR for all observing conditions (viewing angle, air mass type, surface pressure, ...) and TBHIRS(TBMSU)i is the brightness temperature of HIRS (MSU) channel i. For the determination of the a_i coefficients from the TIGR data set, a different level of the tropopause is assumed for each air mass type. Figure 1 shows the variation of a_i, used in the determination of TLS as a function of the surface pressure level. The most important contribution is from channel 3 of MSU; when the surface pressure decreases, the effect of HIRS3 increases. The channels used in the regression have the advantage of being relatively insensitive to clouds, except extended precipitating clouds in the case of MSU2. But, as seen on Figure 1, MSU2 plays a minor role in the determination of TLS.

The determination of TLS is also essential in itself since it can be used for detecting Potential Vorticity (PV) anomalies and therefore for better understanding mechanisms which can lead to the development of atmospheric disturbances. As a matter of fact, a warm anomaly in the TLS field may be the indication of a lower tropopause corresponding to an extrusion of relatively warmer stratospheric air into the troposphere. Such a warm anomaly represents an upper-level PV maximum, since warmer stratospheric air contains relatively higher values of PV (Hoskins et al., 1985).

Figure 1: Variations of a_i coefficients used for TLS calculation as a function of surface pressure (level 1 corresponds to a surface pressure of 1013 hPa,level 19 to 472 hPa). Air mass type is mid-latitude 2 and this figure corresponds to nadir observations.

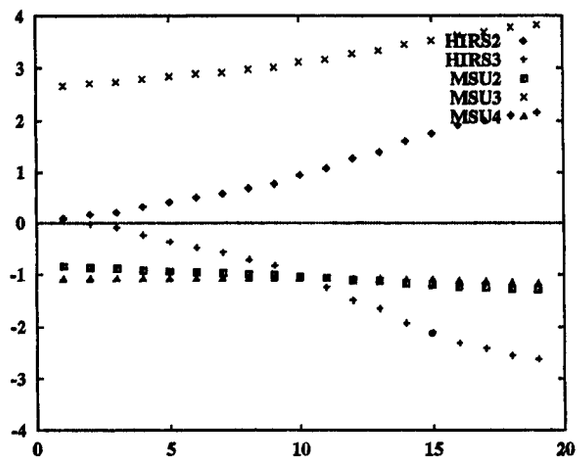

3. APPLICATION TO THE FASTEX INTENSIVE OBSERVING PERIOD (IOP) 18: 22-23 FEBRUARY 1997

The Fronts and Atlantic Storm-Track Experiment (FASTEX) has been conducted in January-February 1997 to study the life cycle of cyclones evolving over the North Atlantic Ocean and to improve the forecasting of North Atlantic storms. Among the numerous scientific objectives of the campaign, an important issue concerned the genesis mechanism and more specifically the existence of preexisting upper-level anomalies. The involvement of 4 ships, 5 aircrafts and extensive dropsonde activity have permitted the realization of 19 IOPs which provide a large synoptic situations set. IOP 18 corresponds to an explosive cyclogenesis characterized by a very well identified upper-level precursor : a potential vorticity core located on the 2 PVU surface. The upper level precursor moved closer to the entrance area of the intensifying polar jet stream, then the surface cyclogenesis appeared. The vortex showed up as a small closed circulation over the Labrador Sea with strong winds in the incipient stage. The low appeared in cold environment north of the baroclinic zone. On the 22 February at 22 UTC, a low located at 58°N 55°W with a central pressure of 985 hPa formed over the Labrador Sea and moved deepening over the At-

Figure 2: TOVS-retrieved Temperature in the Lower Stratosphere (TLS) in K.

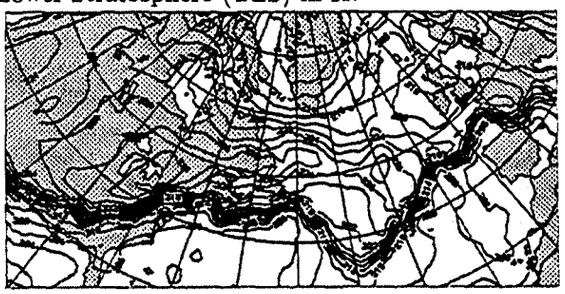

(a) NOAA12 22 February 1997 a.m.

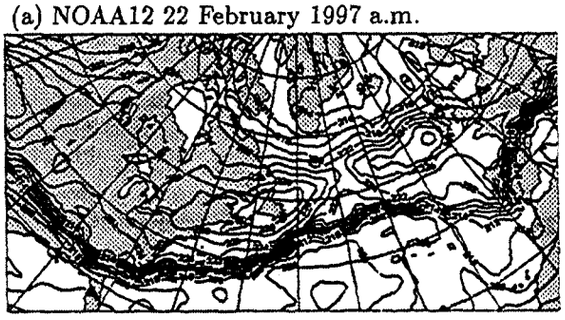

(b) NOAA12 23 February 1997 p.m.

lantic Ocean. On the next day at 00 UTC, it was situated southeast of Greenland (55°N 30°W) and the central pressure was 975 hPa. 12 hours later, the surface low had deepened of 15hPa and was situated at 58°N 25°W. A minimum pressure of less than 950 hPa was reached on 24 February at 18 UTC.

3.1 Description of TLS fields

TOVS data sounded by NOAA12 and NOAA14 covering the period 22 February 00UTC to 24 February 00UTC have been processed. TLS warm anomalies are generally observed in air classified as mid-latitude 2.

On 22 February at 06 UTC (not shown), a relatively weak, small-scale warm TLS anomaly (228 K) is located at 50°N 60°W, a wide zone of high TLS values (229 K) is present over the Great Lakes. South of this zone, we observed strong TLS gradient corresponding to a tropopause break on the cyclonic-shear side of the upper level jet. This zone is present during all the period and moves eastwards (about 10°). At about 12UTC, the amplitude of the TLS anomaly increases (Figure 2 (a)). In the evening (not shown), the anomaly is observed at 40°W 53°N. On 23 February in the morning, it has moved eastwards south of Iceland. The amplitude of the anomaly has increased with a maximum value of 233 K aloft the surface cyclo-

Figure 3: Temporal evolution of surface pressure and TLS

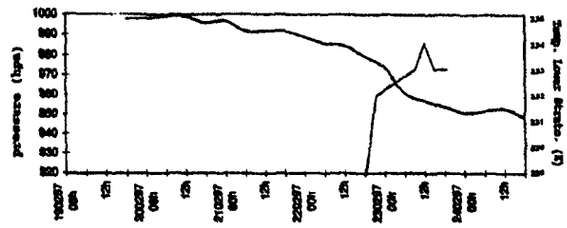

genesis. In the evening of 23 February, its extent and amplitude have decreased (Figure 2 (b)).

Comparison between temporal evolution of TLS maximum value and the surface pressure shows clearly a reinforcement of anomaly amplitude when the surface low deepens (Figure 3): when the surface pressure decreases from 20hPa (between 22 February at 18UTC and 23 February at 09UTC), a significant TLS increase of about 5 K is observed. On 23 February between 09UTC and 18UTC, pressure decreases only by 6 hPa and TLS warm anomaly weakens. The strengthening of the surface low and the upper-level warm anomaly are coincident in time, indicating a coupling and joint development of surface and upper-level signatures.

3.2 Comparison with other diagnostic tools.

3.2.1 MSU3 Brightness Temperatures

During the IOP, MSU3 fields present a quasi-zonal distribution with strong gradients in the region between about 47°N and 55°N. It is only on 23 February at 12UTC that a warm anomaly in MSU3 appears at about 50°N 19°W and it disappears a few hours later. Quantatively, MSU3 brightness temperature maps present less variability than TLS fields (TLS values are between 200 and 235 K, MSU3 brightness temperatures between 210 and 230K). For this period, MSU 3 brightness temperatures do not permit to detect the presence of an upper-level anomaly over western Atlantic Ocean.

3.2.2 2PVU potential temperature fields

Potential temperature fields at 2PVU (which represents the dynamical tropopause) are deduced from the ARPEGE model analysis (Météo-France). An upper-level precursor corresponds to a cold potential temperature core. The potential temperature minimum (not shown) appears on 19 February at 00UTC, at 68°N 77°W, at this time, none anomaly still appeared in TLS fields. Figure (4) displays TLS anomalies centers(*) and 2PVU potential temperature core (T) trajectories

Figure 4: Comparison of TLS anomaly center (*) and potential temperature core (T) trajectories between 22 February at 00UTC and 24 February at 00UTC. Local potential temperature minima on the 2PVU surface were derived from Arpege analyses.

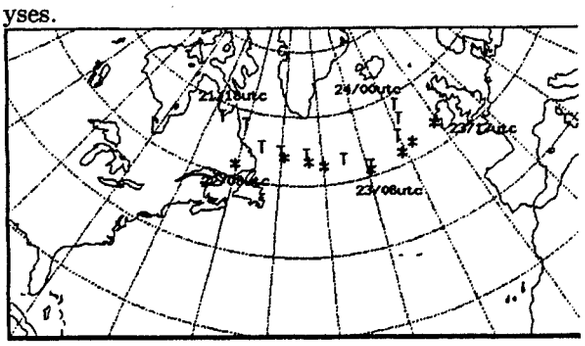

between 22 February at 00UTC and 24 February at 00UTC. Both trajectories present similarities between 22 February at 15 UTC and 23 February at 12 UTC. However, between 22 February at 06 UTC and 15 UTC and 23 February from 12 UTC to 18 UTC, the potential temperature core positions are northern than TLS anomaly centers trajectory.

4. DISCUSSION AND SUMMARY

We have shown, on a specific case, that the Temperature of the Lower Stratosphere could constitute a valuable diagnostic tool for the identification of upper-level anomalies. This case was selected from the FASTEX set of situations. We have observed that when the surface pressure of the associed low decreased, TLS increased. In comparison to the use of MSU3 for such a detection, the TLS shows more variability due to better a spatial and vertical resolution. Comparisons between independently obtained anomalies from TLS fields and from the ARPEGE model show that trajectories are globally comparable,with the exception that potential temperature anomaly appeared earlier than the TLS anomaly. TOVS data covering the period (20-21 February) are presently processed to indentify exactly when the TLS anomaly was first observed.

Other IOP studies are in progress in order to assess the reliability of this variable for a wide range of meteorological situations.

ACKNOWLEDGMENT

The authors would like to acknowledge NOAA/NESDIS for providing the basic measurements employed in this study as well as the Centre de Météorologie Spatiale and the FASTEX Data Base Group at Météo-France for refinement in this basic set and gathering together other sources of weather informations.FASTEX is supported by many institutions including NOAA and NSF in the USA, the UKMO in the UK, CNRS and Météo-France in france as well as the European Commission (Environment and Climate Programme) and WMO. FASTEX data is available for scientific research at www.meteo.fr/cnrm/fastex/. This research benefited from discussions with Dr A. Joly (CNRM).

REFERENCES

Achard, V., 1991 : Trois problèmes clés de l'analyse 3D de la structure thermodynamique de l'atmosphère par satellite : mesure du contenu en ozone ; classification des masses d'air ; modélisation hyper rapide du transfert radiatif. PhD thesis, Univ. Paris VI.

Chedin, A., and N.A. Scott, 1985 : Initialization of the radiative transfer equation inversion problem from a pattern recognition type approach. Applications to the satellites of the TIROS-N series, Advances in Remote Sensing Retrievals, Academic press, A. Deepak Ed., 495-515.

Chedin, A., N.A. Scott, C. Wahiche, and P. Moulinier, 1985 : The Improved Initialization Inversion method : a high resolution physical method for temperature retrievals from satellites of the TIROS-N series, J. Clim. Appl. Meteorol., **24, 124-143.**

Escobar-Munoz, J., 1993 : Base de données pour la restitution de variables atmosphériques à l'échelle globale. Étude sur l'inversion par réseaux de neurones des données des sondeurs verticaux atmosphériques satellitaires présents et à venir. PhD thesis, Univ. Paris VII.

Hoskins, B.J., M.E. McIntyre, and A.W. Robertson, 1985 : On the use and significance of isentropic potential vorticity maps, Quat. J. Roy. Metor. Soc., **111, 877-886.**

Joly, A. et al., 1997 : The Fronts and Atlantic Storm-Track experiment (FASTEX): Scientific Objectives and Experimental Design. Bull. Amer. Meteor. Soc., **78(9), pp. 1917-1940.**

Scott, N.A. and A. Chédin, 1981 : A fast line-by-line method for atmospheric absorption computations : the Automatized Atmospheric Absorption Atlas. J. Clim. Appl. Meteor., 20, pp. 802-812.

SURFACE AND ATMOSPHERIC TEMPERATURE RETRIEVAL WITH THE HIGH RESOLUTION INTERFEROMETER IASI

Filipe Aires*, Raymond Armante, Alain Chédin, and Noëlle A. Scott
Laboratoire de Météorologie Dynamique du CNRS, École Polytechnique, France

1. INTRODUCTION

This work concerns the regression of a noisy inverse function in high dimensional space problem related with vertical remote sounding. The utilization of neural network methods in this context is possible; such an approach has been used in the past for the retrieval of the temperature profile with the AIRS (Advanced Infrared Radiation Sounder) instrument [Escobar 93] [Cheruy 1993]. We demonstrate in this paper that neural network methods can be successfully improved in real and complex problems if we introduce *a priori* information. Advantages of such methods are rapidity, small amount of memory and quality of restitutions.

Here we use this technique in a high-resolution interferometry application with the IASI (Improved Atmospheric Sounding in the Infrared) instrument, planned on board the METOP/ESA platform in 2002. We are confronted, in this work, with problems related to the ill-posed character of the inverse problem, the sensitivity to noise and specific to IASI, the dimension of the data. We resolve these difficulties using a Multi-Layer Perceptron (MLP) neural networks technique, by introducing a maximum of *a priori* information upon the physical model. Therefore, we have combined three ways: the structural stabilization of the network function, the regularization of the learning algorithm and an optimized selection of the data. We present applications in the case of the surface temperature and atmospheric temperature profile retrievals.

2. THE IASI HIGH RESOLUTION INTERFEROMETER

2.1 The Radiative Transfer in the Atmosphere

The radiance measured by an instrument at the top of the atmosphere depends on the atmospheric geophysical and surface parameters. This dependence is described by the Radiative Transfer Equation (RTE):

$$I(\nu) = \varepsilon_s B(T_s,\nu)\tau_{s\nu} + \int_{P_s}^{P_{top}} B(T(P),\nu) \frac{\partial \tau_\nu}{\partial \ln P}(P) d\ln P \qquad (1)$$

where ν is the wavenumber (cm^{-1}), ε_s the Earth's surface emissivity, $B(T(P),\nu)$ the Planck function which indicates the radiance emission by a black-body at temperature T and atmospheric pressure P, τ_ν the transmission factor between the satellite and the level pressure P. $\frac{\partial \tau_\nu}{\partial \ln P}(\cdot)$ is often referred to as the weighting function. This RTE expresses the two radiative contributions at the top of the atmosphere: one proceeding from the grey body of surface (first term in right hand side) and one from the atmosphere (second term in right hand side). The equation complexity lays in the transmission factors which depends on pressure, temperature, concentration of gases, spectroscopic characteristics of the absorbing gases (CO_2, H_2O, O_3, ...).

To retrieve atmospheric parameters from radiative measurements at the top of the atmosphere, the inverse of equation (1) has to be computed. The analytical inversion of this function is not possible, only an inference approach can be used.

2.2 The IASI instrument

With current instruments, like TOVS (TIROS-N Observational Vertical Sounding) radiometer, retrievals are carried out in coarse atmospheric layers. It is expected that with the next generation instrument, like IASI or AIRS instruments, the high resolution power ($\lambda/d\lambda \simeq 1200$) will help reaching the $1K \times 1Km$ accuracy goal. IASI spectral range is 645-2860 cm^{-1}. So, the under-constrained problem with TOVS (24 channels) becomes with IASI an over-constrained problem (more than 8000 channels). The noise for this spectral coverage is presently simulated by a white gaussian noise with a $NE\Delta T$ characterization

* *Corresponding author address:* Filipe Aires, CNRS/LMD, École Polytechnique, 91128 Palaiseau Cedex, France; e-mail: aires@ara01.polytechnique.fr

at 280 K [Cayla 95] (Table 1). For brigthness

ν in cm^{-1}	$NE\Delta T$ in K	ν in cm^{-1}	$NE\Delta T$ in K
650	0.28	1660	0.34
770	0.28	2090	0.5
790	0.34	2100	0.5
980	0.34	2420	0.5
1000	0.28	2430	0.6
1070	0.28	2500	0.77
1080	0.34	2600	1.1
1200	0.34	2700	1.58
1210	0.28	2760	1.97
1650	0.28		

Table 1: Noise characteristics of IASI at 280 K

temperature values T' lower than 280 K, standard deviation of noise $st_{T'}(\nu)$ increases by relation:

$$st_{T'}(\nu) = \frac{\frac{\partial B(Tb=280,\nu)}{\partial Tb}}{\frac{\partial B(Tb=T')}{\partial Tb}} \cdot st_{280}(\nu) \qquad (2)$$

The future IASI interferometer will be used for studies related to climatology, meteorology and atmospheric chemistry.

3. THE NEURAL NET APPROACH

To perform retrievals (temperature, ozone and moisture concentration,...) we have to invert, in the RTE, a determinist and well-defined operator. This inverse problem is ill-posed in the Hadamard sense because existence, unicity or stability of solution are not always satisfied. So, different atmospheric situations may yield to the same value of the brightness tempetrature.

a same value of the brightness temperature can yield to different atmospheric situations. This ambiguity problem is referred to as "compensation phenomenon".

We have chosen to use the "direct inversion" (a MLP neural network optimized with back-propagation error algorithm). We overcome the "black-box" modeling conception (no assumptions about the physical problem) via the utilization of all *a priori* available knowledge. The *a priori* knowledge is the information about the solution of the problem which is additional to the information induced by the data set.

There are three ways of resolving an ill-posed problem introducing *a priori* knowledge: the structural stabilization, the regularization and the feature selection. Our numerical experiments have shown that the introduction of this kind of *a priori* information is very useful and makes training possible with relatively few data.

3.1 Structural stabilization

The MLP network is a mapping model composed of parallel processors called "neurons". These processors are organized in distinct layers: the first layer (number 0) represents the input $X = (x_i; 0 \leq i \leq m_0)$ of the mapping with m_0 is the number of neurons in layer 0. The last layer (number L) represents the outputs mapping $Y = (y_k; 0 \leq k \leq m_L)$. The intermediate layers $(0 < m < L)$ are called the "hidden layers". These layers are connected via neuronal links (Figure 1): two neurons i and j between two consecutive layers have synaptic connections associated with a synaptic weight w_{ij}. A neuron executes two

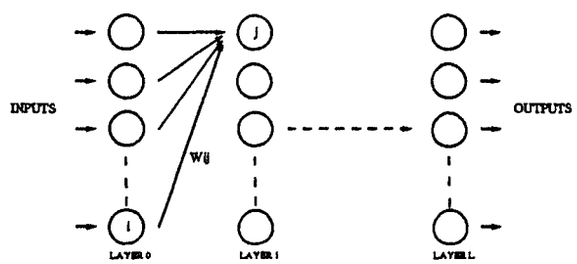

Figure 1: Architecture of a MLP neural network

simple operations: first, it makes a weighted sum of the inputs, and then transfers this signal to its output through a so called "transfer function" like $g(a) = tanh(a)$. The ouput z_j of neuron j is given by: $z_j = g\left(\sum_{l \in \text{Inputs}(j)} \omega_{lj} \cdot z_l\right)$. Generally, for regression problems, the output units has no transfer function.

Sontag [Sontag 1991] has demonstrated that any inverse problem can be resolved by a two-hidden layers MLP network since two hidden layers neural networks can take into account discontinuities and high variations, contrarily to one-hidden layers MLP that approximates continuous functions. In practice, with noise-data corrupted, a one-hidden layer can be sufficient. Our experiments show that in a regularization strategy, a smooth solution shall be obtained by a one hidden layer.

3.2 Input Perturbation regularization

The learning algorithm is the optimization technique that estimates the optimal network pa-

rameters $W = \{\omega_{ij}\}$ by minimizing a loss function $C(W)$ to approach as much as possible the desired function by the neural mapping. The most used criterion to adapt W is the mean square error in network outputs:

$$C(W) = \frac{1}{2}\sum_{k=1}^{m_L}\int\int (y_k(x;W) - t_k)^2 \cdot P(t_k/x) \cdot P(x) \cdot dt_k \cdot dx \quad (3)$$

with t_k the kth desired output component, y_k the kth neural output component, $P(\cdot)$ the probability density in input data x. The Error Back-Propagation (BP) Algorithm [Rumelhart 1986] is used to minimize $C(W)$. It is a stochastic steepest descent very well adapted to this neural architecture because the computational cost is linearly related to the number of parameters.

To reduce the estimation sensitivity to input noise in data, we use the Input Perturbation technique. It is an heuristic method to control the effective complexity of the neural network mapping. This regularization technique limits the number of free-parameters in the neural network to bring nearer its complexity to those of the function to estimate. This limitation reduces the class of possible solutions and then makes the solution of the problem unique. The technique consists, during the learning step, in adding to each input a random vector related to instrumental noise. It has been demonstrated [Bishop 1996] that, under certain conditions (low noise assumption), training with noise is closely related to regularization technique. In Input Perturbation method, the usual error function $C(W)$ (equation (3)) takes the form:

$$\tilde{C}(W) = \frac{1}{2}\sum_{k=1}^{m_L}\int\int\int (y_k(x+\eta;W) - t_k)^2 \cdot P(t_k/x) \cdot P(x) \cdot P(\eta) \cdot dt_k \cdot dx \cdot d\eta$$

If the noise η is sufficiently small, we can expand the network function $y_k(x+\eta;w)$ to the first order. Then, we obtain the relation:

$$\tilde{C}(W) \simeq C(W) + \nu \cdot \Omega(W)$$

where ν is the noise variance and

$$\Omega(W) = \frac{1}{2}\sum_{i=1}^{m_0}\sum_{k=1}^{m_L}\int \left(\frac{\partial y_k}{\partial x_i}\right)^2 \cdot P(x) \cdot dx$$

is a Tikhonov stabilizator penalizing solutions with high gradients (high variations of the neural function). So the minimization of this new criterion $\tilde{C}(W)$ constrains solutions to be smooth.

3.3 Feature selection

A MLP neural network could, in principle, be used to map any input vector space to any output vector space. But, in practice, this simplistic strategy would give poor results. High dimensional data space have to be reduced to limitate the curse of dimensionality. The curse of dimensionality stipulates that as the dimension d of the input space increases, the difficulty of the learning procedure increases significantly, and the number N of examples required to the regression increases exponentially with the dimension d. The curse of dimensionality is not so dramatic because the intrinsic complexity of the function to estimate does not increase exponentially with the dimension. The MLP network, like linear regression, is very well adapted to high dimensions because the processors (the neurons), making a scalar product (the weighted sum), acts in the entire data space and not in a pavement of this space like some other methods (radial basis function, splines interpolators,...). Anyway, practical problems occur in high dimensional data: for example, the number of parameters W increases with d. This excess of degrees of fredoms in the neural interpolator combined with the introduction of non-informative data, may perturb the learning process: the quality criterion is more complexe to minimize and computations are longer.

Thus, the goal of dimension reduction is to present to the neural network the most relevant information from initial rough data. One way to reduce the dimension of input data is the feature selection (a selection of coordinates in rough data). By studying the RTE Jacobians (derivatives of the transmittance with respect to one geo-physical parameter), it is possible to analyze mutual information between measured brightness temperatures and geo-physical variables. But we need to make a compromise between reducing data dimension and preserving the redundant information in rough data to alleviate wrong effects of noise.

4. LEARNING AND TEST DATA BASES

4.1 The TIGR data base

We will use in our application the two TIGR (Thermodynamical Initial Guess Retrieval) data bases of the ARA group: TIGR1 (861 atmospheres) [Chedin 1985] and its 1990 revisited version TIGR2

(1761 atmospheres) [Escobar 91] [Achard 91]. Both of them are constituted with real atmospheres (described by their temperature and gas concentration profiles) sampled in more than 26000 radiosonde measurements. The 4A (Automatized Atmospheric Absorption Atlas) algorithm [Scott 1981] [Tournier 1995] has been used to compute the IASI brightness temperatures associated to these 2622 atmospheres. The 4A algorithm also allows for an analytical computation of the Jacobians [Cheruy 1995].

4.2 Improved representation of Ts in TIGR

In the current TIGR data base, the surface temperature Ts has been set equal to the temperature of the 40th (lowest) atmospheric level T40. We then statistically generate, for each atmosphere, 10 different Ts using the T40 information. To do that, we have studied the statistical distribution of T40-Ts in a data base of 26000 radiosonde measurements and then obtain the mean and the variance of a gaussian modelization of the (T40-Ts) stochastic variable (Figure 3). For every atmosphere, knowing T40, we choose randomly 10 Ts with this estimated density probability. We obtain a tropical Ts data base of 3220 atmospheres (322 × 10).

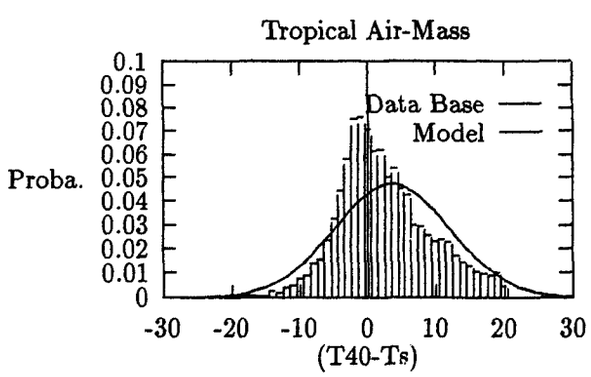

Figure 2: Statistical estimation of the (Ts-T40) probability distribution from 2600 situations

5. SURFACE TEMPERATURE RETRIEVAL

This study is here limited to clear sky and ocean situations and we limit ourself to tropical air mass case.

5.1 Channel Selection

There are essentially two windows (spectral regions sensitive to the surface characteristics) in IASI spectra: 800-980 and 2500-2750 cm^{-1}. However, in these regions, some channels may be contaminated by other atmospheric constituents. To eliminate the corrupted channels and in order to reduce effects of curse of dimensionality, we use a channel selection process based upon an analysis of the sensitivity to Ts variation. We define sensitivity as the mean repercussion of the variation of 1 K of Ts in $I(\nu)$ (see equation (1)). In the first window, channels with a sensitivity higher than a fixed threshold (Figure 4) are selected, we keep 357 channels in the first window, with a threshold of 70

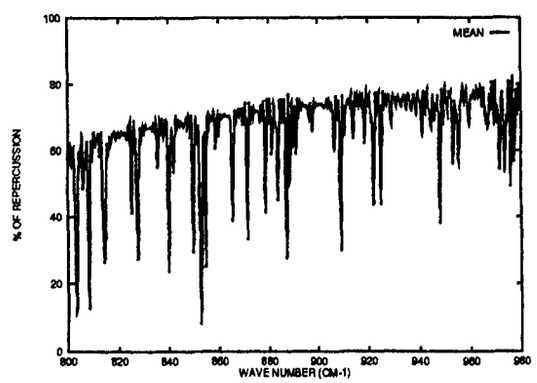

Figure 3: Sensitivity in % to 1 K perturbation of surface temperature vs wavenumber in the first IASI window (800-980 cm^{-1})

5.2 Network Learning and Testing

The TIGR data base (section) is divided into a learning base of 3000 atmospheres to make the regression and a generalization base of 220 atmospheres to test the generalization ability of the considered neural mapping.

To restitute the Ts variable, we have used a one-hidden layer MLP neural network. For the first window the neural structure is 357-20-1: 357 neurons in the input layer (357 selected brightness temperature), 20 neurons in the hidden layer and 1 neuron in the output layer (representing Ts).

This neural mapping is then trained by Error BP-algorithm in the learning base. The Input Perturbation regularization technique is used: simulated noise (according to the NEΔT specifications) is added to input data during the learning step. The generalization ability of our model has been tested on noisy data computed on the 220 test atmospheres. The retrieval of Ts from noisy data gives a generalization RMS of approximately 0.4 K. Similar results are obtained using only the second spectral window.

6. ATMOSPHERIC TEMPERATURE RETRIEVAL

The present study is also limited to clear sky and ocean situations.

6.1 Channel Selection

There are essentially two "CO_2 regions" used to atmospheric temperature retrieval in IASI spectra: $645-800\ cm^{-1}$ and $2200-2500\ cm^{-1}$. We choose, in a fisrt stage, the first spectral range since the noise is lower in this region.

To reduce effects of curse of dimensionality, we have to select channels within the 621 channels of this spectral range ($645-800\ cm^{-1}$ with $0.25\ cm^{-1}$ resolution). The feature selection method is based upon the study of the Jacobians in order to define the sensitivity of a channel to atmospheric temperature. The mean Jacobian in TIGR2 indicates the sensitivity relation between atmospheric layers and channels. The standard deviation of the Jacobian (around the mean) is negligible except near the surface; this means that the mean Jacobian is robust to the atmospheric situation except in the lower atmospheric layers.

The feature selection process is divided into two steps. First, channels are selected which are satisfying some quality criterions, ie specifying an information as unambiguous as possible: the Jacobian extent of a channel (characterized by the area below the Jacobian) has to be smaller than a fixed threshold; the Jacobian width at mid-height has to be lower than a fixed threshold; the Jacobian center of a channel has not to be near surface; the Jacobian has to have single peak. We obtain 442 channels among the nominal 621.

The second step in the channel selection process consists in uniformly selecting channels upon the vertical. In the $645-800\ cm^{-1}$ spectral region, the IASI instrument hardly gives information beyond 10 hpa (32 lower layers of 4A). We have chosen 9 channels for each 32 layer between 1013 and 10 hPa so we select 270 channels. However, it is important to note that the layers 23-28 have a deficit in channels and that the sensitivity is higher in low atmosphere (Figure 4).

6.2 Network Learning and testing

We have merged the TIGR1 and TIGR2 data bases and the resulting 2622 atmospheres have been randomly subdivided into a learning base of 1761 atmospheres and a test base of 861 atmospheres. All atmospheres are described by 32 atmospheric temperatures (up to 10 hpa) and the corresponding 270 selected brightness temperatures computed by 4A. The neural structure adopted to this regression problem is 270-50-32: 270 units in the input layer (the 270 selected channels), 50 units in the hidden layer and 32 units in the output layer (the 32 lower atmospheric temperatures).

Figure 5 represents the RMS error for the 32 atmospheric layers at the end of the learning stage in the learning and the test set. We see that we have the major problems in layers of the top of the atmosphere, since IASI has poor information up to 10 hpa.

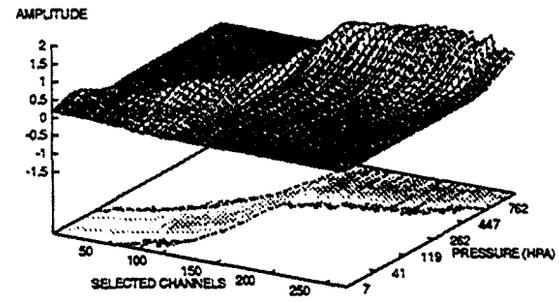

Figure 4: Mean Jacobian over TIGR 2 for the 270 selected channels

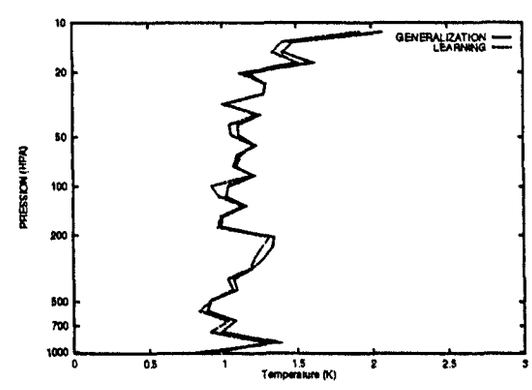

Figure 5: RMS error profile in the atmospheric temperature retrieval in the learning set (solid line) and the testing set (dotted line)

7. PERSPECTIVES

This neural network approach, using a maximum of *a priori* information limits the number of free parameters in our modelization to constrain the retrieval of surface and atmospheric temperature towards a well-posed problem. We plan to use independently a neural network for each 3 considered air masses (tropical, temperate and polar) and to include the 4.3 μm information systematically using some denoising technique. An another perspective is the use of this methodology to retrieve, with the same IASI instrument, the water vapor and the ozone profiles.

Acknowledgments. All computations are made on a CRAY C90 of the IDRIS (Institut du Developpement et des Ressources en Informatique Scientifique) computational center of the CNRS (Centre National de la Recherche Scientifique).

8. REFERENCES

V. Achard, 1991: Trois problèmes clés de l'analyse tridimensionelle de la structure thermodynamique de l'atmosphère par satellite : mesure du contenu en ozone, classification des masses d'air, modélisation hyper-rapide du transfert radiatif. *PhD thesis*, Université Pierre et Marie Curie (Paris VI).

C.M. Bishop, 1996: Neural networks for pattern recognition. *Clarendon Press - Oxford.*

F. Cayla, B. Tournier, and P. Hebert, 1995: Performance budgets of iasi options. *Technical Report*, IA-TN-0B-5476-CNE, CNES.

A. Chedin, N.A. Scott, C. Wahiche, and P. Moulinier, 1985: The improved initialization inversion method: a high resolution physical method for temperature retrievals from TIROS-N series. *J. Clim. Appl. Meteor.*, **24**:128-143.

F. Chéruy, J. Susskind, N.A. Scott, A. Chedin and J. Joiner, 1993: GLA and LMD Approaches to the precessing of AIRS and IASI observations. *NATO ASI Series: High Spectral Resolution Infrared Remote Sensing for Earth's Weather and Climate Studies*, Springer-Verlag **Vol.I 9**:101-112.

F. Chéruy, N.A. Scott, R. Armante, B. Tournier, and A. Chedin, 1995: Contribution to the development of radiative transfer models for high spectral resolution observations in the infrared. *J. Quant. Spectrosc. Radiat. Transfer*, **53**(6):597-611.

J. Escobar, 1993: Base de données pour la restitution de paramètres atmosphériques à l'échelle globale ; étude sur l'inversion par réseaux de neurones des données des sondeurs verticaux atmosphériques satellitaires présents et à venir. *PhD thesis*, Université Denis Diderot (Paris VII).

J. Escobar, A. Chedin, F. Chéruy, and N.A. Scott, 1993: Réseaux de neurones multicouches pour la restitution de variables thermodynamiques atmosphériques à l'aide de sondeurs verticaux satellitaires. *CRAS*, 911-918.

D.E. Rumelhart, G.E. Hinton, and R.J. Williams, 1986: Learning representations by back-propagating error *MIT Press*, volume I, chapter 8, pages 318-362.

N.A. Scott and A. Chedin, 1981: A fast line-by-line method for atmospheric absorption computations : the automatized atmospheric absorption atlas. *J. Appl. Meteor.*, **20**:802-812.

E.D. Sontag, 1991: Feedback stabilisation using two-hidden-layer nets. *Technical Report*, **11**, Rutgers Center for Systems and Control.

B. Tournier, R. Armante, and N.A. Scott, 1994: Stransac-93, 4A-93. développement et validation des nouvelles versions des codes de transfert radiatif pour application au projet IASI. *Technical Report*, **201**, LMD/ARA Group.

P2.5A

ANALYSIS OF RADIANCE FLUCTUATIONS IN THE CO_2 ν_3 BAND AROUND 4.3 µm : EFFECTS OF NONLOCAL THERMODYNAMIC EQUILIBRIUM FOR NADIR OBSERVATIONS

Gabriel Castelain+, Pierre Simoneau+, Véronique Achard+, Bernard Rozier+, J.C. Buriez*
+ONERA, Palaiseau, France
*LOA/University of Villeneuve d'Asq, Lille, France

Abstract: Research was conducted on how sun zenith angle variations affected the radiances observed in the CO_2 ν_3 band at 4.3 µm when a satellite aiming near the nadir. The SHARC and FASCODE radiation transfer codes were used to model atmospheric radiation under different illumination conditions, taking the effects of Nonlocal Thermodynamic Equilibrium (NLTE) into account. The research showed that NLTE effect caused large variations in the center of the band, up to 40 percent when the sun is at the zenith. The impact of NLTE on the radiances measured by the HIRS/2 instrument carried on NOAA 12 and 14 satellites was studied.

1. INTRODUCTION

This work is the first stage of research on atmospheric background radiation fluctuations around the 4.3 µm band of CO_2. We investigated the radiance variations induced by a modification of the sunlight conditions during a satellite sighting.

As has been shown by many authors, this region of the spectrum is strongly affected by nonlocal thermodynamic equilibrium (NLTE) effects above 80 km. This is because the molecular densities at such altitudes are no longer sufficient to satisfy Boltzmann's equilibrium [*Lopez Puertas et al., 1986 and 1989; Kumer, 1983; Rodgers, 1992*]. Most of these publications discuss limb measurements. They show a large temporal and spatial variability in the CO_2 ν_3 band around 4.3 µm.

Calculations were made for observation angles from the nadir up to 60 degrees and especially at the wavelengths corresponding to the channels of the HIRS/2 radiometer. This instrument has two channels in the center of the CO_2 4.3 µm band (channel 16 at 4.40 µm and channel 17 at 4.23 µm on NOAA 12; channel 16 at 4.40 µm on NOAA 14). The Phillips Laboratory SHARC-3 [*Sharma et al., 1996*] and FASCODE-3 [*Wang et al., 1996*] radiative transfer codes were used to simulate the radiances measured by this instrument under various observation conditions. The resulting radiances were then integrated over the bandwidth of filters 16 and 17. The tests were conducted for an observer located at an altitude of 180 km aiming at the ground, for observation angles from 0 to 60 degrees and for sun zenith angles from 0 to 80 degrees.

Corresponding authors address : Gabriel CASTELAIN
Office National d'Etudes et de Recherches Aérospatiales
Chemin de la Hunière - 91120 Palaiseau - France
E-mail : castelain@onera.fr

The variations observed when the NLTE effects were taken into account were then compared with the radiance variations caused by small changes in the temperature profile.

2. RADIATIVE TRANSFER MODELS USED

Radiance in the 4.3 µm band is due to the radiative and vibrational energy transfers between the molecules of the atmosphere. In the lower layers, the molecular densities are high enough to satisfy Boltzmann's equilibrium, but this is no longer true in the upper atmosphere (h > 80 km) where the molecular densities decrease rapidly and radiative processes are in competition with collisional processes. Sunlight is absorbed at 4.3, 2.7 and 1.6 µm and is generally followed by emission of a photon at 4.3 µm (Einstein's coefficient for spontaneous photon emission is much higher in the 4.3 µm band than in the other two) [*Nebel et al., 1994*]. Since the sun's radiation at 2.7 µm is strong at such altitudes, NLTE effects are particularly strong in daylight [*Lopez Puertas et al., 1989*].

NLTE effects are modeled by the SHARC radiance code, which can be used to calculate vibrational temperatures and radiances along an atmospheric path between 50 and 300 km. The molecules taken into account are the main isotopes of NO, CO, H_2O, O_3, OH, CH_4, and CO_2. To satisfy NLTE conditions, it takes radiative energy transfers (sunlight absorption, absorption of the Earth's radiations, absorption of radiation from other molecules and de-energizing by spontaneous emission) into account as well as vibrational energy transfers. In its most recent version, it has a spectral resolution of 0.1 cm^{-1} [*Sharma et al., 1996*].

Since SHARC cannot make calculations below 50 km, vibrational temperatures computed by SHARC we introduced the in the FASCODE line-by-line code, which can then calculate the radiance in NLTE. In order to preserve a thin vertical layering of the atmosphere and because the number of layers is limited, we restricted ourselves to a path between the ground and 180 km, with the observer located at 180 km. The atmospheric profile of US Standard 76 and HITRAN96 spectroscopic database [*Rothman et al., 1997*] have been used.

Figure 1 shows the radiance computed by FASCODE for an observer looking at the nadir, with the sun located vertically above the observer. Radiances increase at the center of the band is due to the radiation in the upper atmosphere as well as NLTE effects.

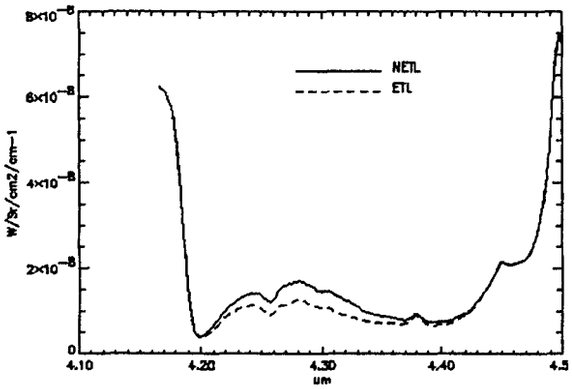

Figure 1 : Radiance around 4.3 mm in LTE and NLTE for an observer looking at the nadir and a sun at zenith.

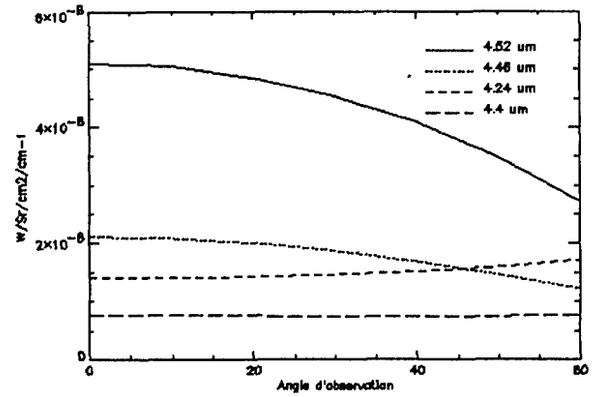

Figure 2. Radiance variability versus observation angle (sun at the zenith + NLTE).

3. RADIANCE VARIABILITY AT 4.3 µm ACCORDING TO OBSERVATION ANGLE

Figure 2 shows the radiance variations computed in NLTE by FASCODE on certain characteristic wavelengths according to the observation angle, with the sun at the zenith. The order and type of these variations differ according to the wavelength analyzed.

The radiances in the center of the band, at around 4.26 µm, are due only to the radiance of the upper atmosphere. As the observation angle increases then the optical path through the radiating layers is longer, and the radiance increases. Conversely, when investigating the wavelengths at the edges of the band, the radiance decreases as the angle of observation increases. The radiance associated with these frequencies is due essentially to the lower layers of the atmosphere or to the Earth's surface. It has to travel a longer optical distance, during which it is absorbed more.

4. RADIANCE VARIABILITY AT 4.3 µm ACCORDING TO SUN ZENITH ANGLE

NLTE calculations were made for several sun zenith angles to study the influence of sunlight on the radiances near 4.3 µm.

Figure 3 shows that the radiances calculated in NLTE could be up to 40 percent higher than those calculated assuming LTE for observations made at the nadir. These effects have a maximum near the center of the band. At the edges of the band, where the atmosphere is less absorbent, NLTE effects are negligible.

The sun's radiation is rapidly absorbed by the upper layers of the atmosphere, then re-emitted as fluorescence. This radiation is low at 4.3 µm, but quite high at 2.7 µm. As already mentioned, the radiation absorbed at 2.7 µm is very likely to be re-emitted at 4.3 µm. NLTE effects are therefore larger during the day than at night. There is however some fluorescence at night due to vibrational energy transfers from OH to CO_2 via N_2 [*Kumer, 1981*]. This energy transfer is not taken into account by SHARC-3 when calculating vibrational temperatures.

Figure 4 shows the increases in radiance due to the NLTE effect on NOAA-12/HIRS/2 channels 16 and 17 as computed by FASCODE. To achieve this, we weighted the spectral radiances obtained with the functions of HIRS/2 filters 16 and 17. The graph also shows the radiance variations at 4.3 µm. There is an increase in radiance of 25 percent (HIRS17) and 10 percent (HIRS16) between an observation with the sun on the horizon and one with the sun at the zenith. Since the shape of this curve is simple, it may provide an initial basis for modeling a bias between the LTE and NLTE, to be taken into account in radiance codes that do not account for the NLTE.

5. RADIANCE SENSITIVITY TO VERTICAL TEMPERATURE PROFILE AT 4.3 µm

The temperatures in the upper atmosphere can be retrieved from radiances at wavelengths near the center of the band, the contribution of the underlying layers being absorbed. Our research showed that the radiances are strongly affected by the NLTE in daylight.

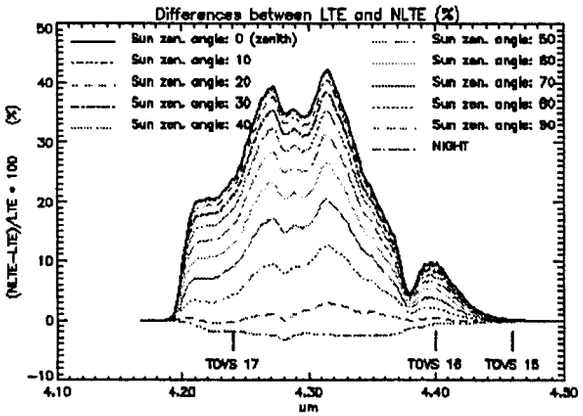

Figure 3. Illustration of NLTE effects in the 4.3 µm band. Relative difference (%) between radiances computed in LTE and NLTE for an observer at the nadir and sun zenith angles from 0 to 90 degrees.

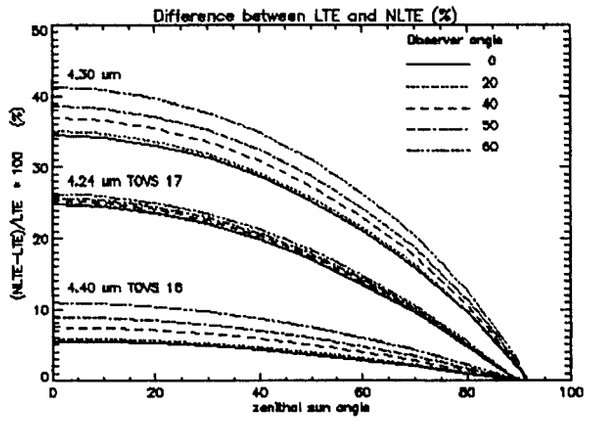

Figure 4. Variations caused by NLTE effects around 4.3 µm for several observation angles. For this curve, we multiplied the radiances simulated by the functions of filters TOVS 16 and 17. Sun is at the zenith.

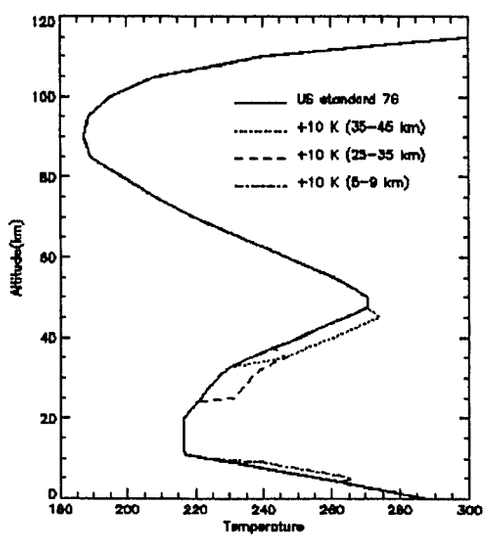

Figure 5. Modified atmospheric profiles.

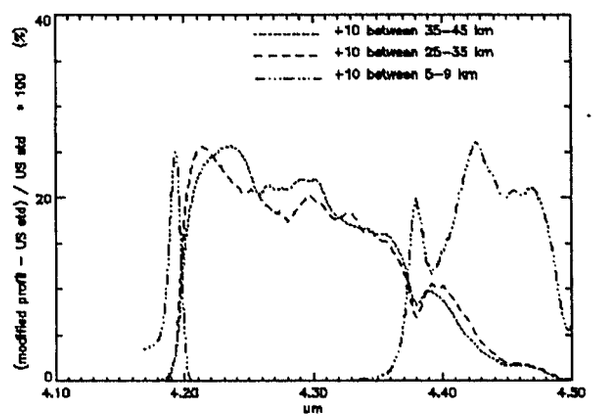

Figure 6. Radiance variations caused by modification of atmospheric profiles. Difference between an NLTE calculation with the US standard and an NLTE computed with a modified temperature profile. Sun is at the zenith; Observation angle: nadir.

We analyzed the sensitivity of the radiance to the temperature profile. To do so, we altered the US Standard 76 profile by a few degrees and compared the resulting radiance variations with those obtained with the non altered profile. The profile modifications are shown in Figure 5. They are located at the altitudes pointed by the weighting functions of filters 16 (NOAA 12 and 14) and 17 (NOAA 12). The differences between the radiances computed for each temperature profile are shown in Figure 6.

A 10 K increase in temperature between 5 and 9 kilometers causes an increase in radiance of approximately 20 percent at around 4.40 µm (central wavelength of HIRS/2 channel 16 filter). The results of Figure 4 show that neglecting the NLTE can cause an error of around 10 percent (when the sun is at the zenith) in the radiance calculation.

Similarly, a 10 K increase in temperature between 25 and 35 kilometers or between 35 and 45 kilometers causes a radiance variation of approximately 20 to 25 percent at around 4.24 µm (central wavelength of NOAA_12 HIRS/2 channel 17 filter). This variation is of the same order of magnitude as the error caused by neglecting the NLTE in the radiance calculation (when the sun is at the zenith).

Taking radiances into account at these wavelengths in inversion procedures which do not model the NLTE for retrieving temperature can therefore cause an error. This error cannot be quantified directly from these results since other CO_2

infrared bands (15 µm) or microwave bands (MSU) are generally used at the same time.

6 - DISCUSSION AND CONCLUSION

Much research has shown that nonlocal thermodynamic equilibrium effects cause strong variations in limb measurements in the 4.3 µm band. The results of our calculations, made using the SHARC-3 and FASCODE-3 codes, show that the same is true for measurements at the nadir.

These calculations show the high radiance variability according to sunlight conditions when NLTE effects are taken into account. These variations can be up to 40 percent in certain cases.

The NOAA_12-HIRS/2 radiometer has two channels near the center of the 4.3 µm band, i.e. channels 16 and 17. Channel 16 also exists on NOAA_14. We simulated the radiances received by this instrument by integrating the radiances computed by FASCODE with the functions of these filters. The variations observed for channels 16 and 17 can be up to 10 and 25 percent respectively (with the sun at the zenith) between a calculation made with LTE and another taking NLTE effects into account.

The codes allowing the temperature to be estimated from the TOVS sounder (RTOVS[1] [*A.L. Reale et al., 1994*], 3I[2] [*Chedin et al., 1985*], ICI[3] [*Lavanant, 1996*], ITPP[4], etc.) use channels 16 and 17 very little or not at all because of the width of their weight functions and also because of NLTE effects. Temperature inversion for high altitudes is thereby limited. It would perhaps be possible to use channels near 4.3 µm by introducing a bias on the radiances in this band according to the sun zenith angle.

HIRS/3 on NOAA-K.L.M has no channels in the center of the 4.3 µm band. However, the use of radiances in this band could be considered with next generation of sounders such as IASI or AIRS which should allow a better vertical resolution.

Acknowledgments. Thanks are due to the Phillips Laboratory for providing us the SHARC-3 and FASCODE-3 radiative transfer codes.

REFERENCES

Chedin A., N.A. Scott et al. : THE IMPROVED INITIALIZED INVERSION METHOD: A HIGH RESOLUTION PHYSICAL METHOD FOR TEMPERATURE RETRIEVALS FROM THE TIROS-N SERIES
J. Clim. Appl. Met., **24**, No. 2, 128-143, 1985

Kumer J. B.: SUMMARY ANALYSIS OF 4.3 µm DATA
Atmos. Earth and the Planet, 1975

Kumer J. B. : REVIEW OF SOME NONLOCAL-THERMODYNAMIC-EQUILIBRIUM HIGH-ALTITUDE 4.3 µm BACKGROUND EFFECTS
SPIE **304**, Modern Utilization of Infrared Technology VII, 1981

Kumer J. B., R. M. Nadile, W. Grieder: DETAILED ANALYSIS OF 4.3 µm EARTHLIMB DATA
SPIE, Modern Utilization of Infrared Technology IX, 1983

Lavanant L., P. Brunel, G. Rochard: TOVS SOUNDING PRODUCTS AT CMS - THE ICI MODEL
Proceedings of the International TOVS Study Conference IX, 1997

Lopez Puertas M., F.W. Taylor: CARBON DIOXIDE 4.3 µm EMISSION IN THE EARTH'S ATMOSPHERE : A COMPARISON BETWEEN NIMBUS 7 SAMS MEASUREMENTS AND NLTE RADIATIVE TRANSFER CALCULATIONS
J. Geophys. Res., **94**, No. D10, 13045-13068, September 20, 1989

Lopez Puertas M., R. Rodrigo, J. J. Lope Moreno : A NON-LTE RADIATIVE TRANSFER MODEL FOR INFRARED BANDS IN THE MIDDLE ATMOSPHERE. II. CO_2 (2.7 AND 4.3 µm) AND WATER VAPOUR(6.3 µm) BANDS AND $N_2(1)$ AND $O_2(1)$ VIBRATIONAL LEVELS
J. Atmos. Terr. Phys., **48**, No. 8, 749-764, 1986

Nebel H. et al. : CO_2 NON-LOCAL THERMODYNAMIC EQUILIBRIUM RADIATIVE EXCITATION AND INFRARED DAYGLOW AT 4.3 µm - APPLICATION TO SPECTRAL INFRARED ROCKET EXPERIMENTAL DATA
J. Geophys. Res., **99**, 10409, 1994

Rodgers C. D., M. Lopez Puertas et al. : LOCAL THERMODYNAMIC EQUILIBRIUM OF CARBON DIOXIDE IN THE UPPER ATMOSPHERE
Geophys. Res. Letters, **19**, No. 6, 589-592, 1992

Rothman L. S. et al. : The 1996 HITRAN Molecular Spectroscopic Database and HAWKS - HITRAN Atmospheric Workstation, JQSRT, Vol. in Preparation

Sharma R. D. et al. : USERS' MANUAL FOR SHARC3
Phillips Laboratory, HANSCOM AFB, MA, 01731-3010, 1996

Wang, J., G.P. Anderson, H.E. Revercomb, R.O. Knuteson VALIDATION OF FASCOD-3 AND MODTRAN-3: COMPARISON OF MODEL CALCULATIONS WITH GROUND-BASED AND AIRBORNE INTER-FEROMETER OBSERVATIONS UNDER CLEAR-SKY CONDITIONS, Appl. Optics, 35, 1996.

---

[1] Revised TOVS, NOAA, NEDIS
[2] 3I: Improved Initialized Inversion method
[3] Inversion Coupled with the Imager
[4] International TOVS Processing System

P2.6B ADVCLD: AIR FORCE WEATHER AGENCY'S IMPROVED CLOUD FORECAST MODEL

Thomas J. Kopp *, Margaret M. Wonsick, Louis E. Cantrell and Francis D. Bieker
Headquarters Air Force Weather Agency, Offutt AFB, NE, USA

1. INTRODUCTION

The United States Air Force Weather Agency (AFWA), formerly known as Air Force Global Weather Center, has provided global cloud forecasts to customers for over 20 years. The original models producing these cloud forecasts were the 5-Layer and TRONEW models (Crum, 1987). The 5-Layer model operated on a 190.4 km polar stereographic grid valid only for mid-latitude and polar regions, while TRONEW was a simple persistence forecast for tropical locations. These models were state-of-the-art when first introduced in the 1970's, but better capabilities in wind forecasting and model processing made them obsolete.

In December 1996, AFWA implemented a new cloud forecast model called Advect Cloud (ADVCLD). ADVCLD retains 5-Layer's unique capability to directly incorporate cloud fields into the initial analysis, but provides increased resolution, improved trajectories, longer forecast range, and the extension of trajectories into the tropics. This paper will summarize how ADVCLD produces a cloud forecast and will present forecast verification information.

2. CHARACTERISTICS

ADVCLD executes every three hours, producing cloud forecasts at 47.6 km resolution from 0 to 12 hours and at 95.2 km resolution from 0 to 48 hours. The forecasts are hemispheric in scale, with clouds forecast at 5 different levels (gradient, 85, 70, 50, and 30 kPa) plus a total cloud amount.

3. METHOD

ADVCLD requires three inputs: winds, moisture, and clouds. Winds are used to produce trajectories and moisture values are required at grid points where clouds do not exist. The manner in which these fields are used to forecast clouds is discussed below.

Global wind fields are obtained from the Navy Operational Global Atmospheric Prediction System (NOGAPS) model (Baylor and Lewit, 1992). The winds are stored at AFWA on a 2.5 by 2.5 degree grid, and must be interpolated to the 95.2 km polar stereographic grid used by ADVCLD. Next, the trajectories are calculated. The trajectories are three-dimensional, with the trajectory components for each forecast hour based on the winds for the preceding time period:

$$dx = \bar{u}dt \quad (1)$$
$$dy = \bar{v}dt \quad (2)$$
$$dp = \bar{w}dt \quad (3)$$

Note that dx, dy, and dp represent upstream displacement from the trajectory endpoint to the trajectory origin. They are subtracted from the grid point to determine the trajectory origin, i.e. a 'backward" trajectory. This technique saves regridding the field each time step, and adds stability to the model. Since dt is specified by the forecast interval, the only variables required to solve (1) - (3) are the mean winds. ADVCLD calculates the mean winds through an iterative method described in Staniforth and Cote (1991).

ADVCLD converts the cloud and moisture inputs into condensation pressure spread (CPS) units (Edson, 1965). CPS represents the upward displacement, in pressure coordinates, required to saturate a parcel. High values of CPS imply drier conditions, while low values of CPS indicate a parcel near saturation. CPS values are first obtained by converting cloud amounts from AFWA's Real-Time Nephanalysis (RTNEPH) model (Hamill et al, 1992) into CPS units using look-up tables. Once all clouds have been considered, NOGAPS dew-point depressions in cloud-free areas are converted to CPS.

Armed with trajectories and CPS, the cloud forecast is produced. For all but the gradient level, horizontal motion is determined by subtracting the trajectory from the grid point of interest to locate the trajectory origin. The CPS value at the trajectory origin becomes the starting CPS value at the grid point of interest. The vertical wind component then modifies the CPS; upward vertical motion decreases CPS while downward vertical motion increases CPS. Entrainment may also modify the final CPS value. Gradient level advection takes into account friction and terrain-induced vertical motion.

After forecast CPS values at all levels are completed, ADVCLD passes a horizontal smoother over all levels for each grid point. This smoother prevents holes in the cloud cover due to shearing. After the smoothing, CPS values are converted back to cloud amounts. Total cloud is determined by stacking the layer clouds at each point and applying a random overlap assumption. This procedure prevents unrealistic cloud amounts (i.e., greater than 100%).

4. RESULTS

AFWA verifies ADVCLD both quantitatively and qualitatively. Table 1 shows, for various geographical regions, the Root-Mean Square Error (RMSE) between the 24-hour ADVCLD forecast and the RTNEPH cloud analysis valid at the same time. More statistics will be

*Corresponding author address: Thomas J. Kopp
HQ AFWA/DNXM, 106 Peacekeeper Dr STE 2N3,
Offutt AFB NE 68113-4039; email: koppt@afwa.af.mil

Table 1. RMSE for the 24-hour forecast for various regions around the globe.

NH	SH	US	EUROPE	SE ASIA	SW ASIA	MID-LATS	TROPICS
39.6	39.9	39.0	41.2	33.1	42.9	39.4	42.1

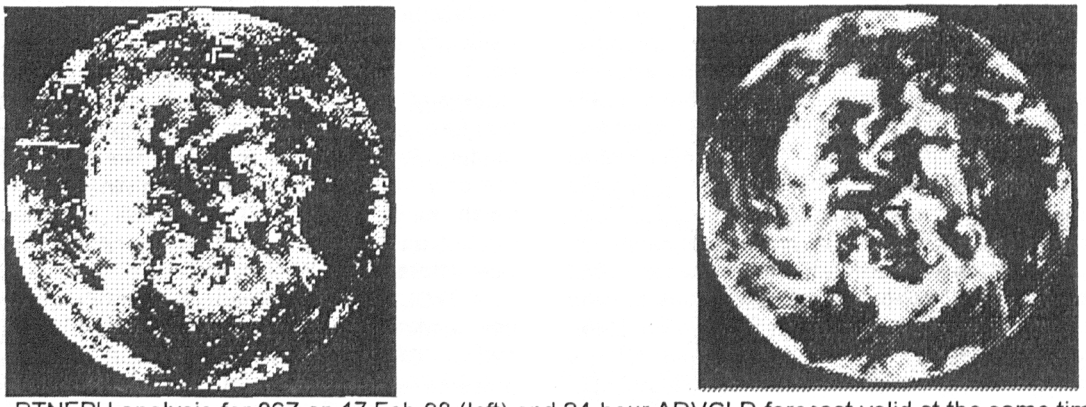

Figure 1. RTNEPH analysis for 06Z on 17 Feb 98 (left) and 24-hour ADVCLD forecast valid at the same time (right), in polar stereographic hemispheric view centered on the North Pole.

presented at the conference. As expected, the RMSEs increase with time, from about 35.0 at the 6-hour forecast to approximately 43.7 at 48 hours. The model performs best over mid-latitude locations, especially the United States and Southeast Asia. In regions where convection dominates, such as the tropics, the model's forecast does not verify as well. However, it is important to note that although ADVCLD does not capture mesoscale cloud development, it is capable of developing and dissipating synoptic-scale clouds using the vertical component of the trajectories.

Perhaps more meaningful than the RMSEs are the visualizations of ADVCLD output. Figure 1 shows ADVCLD's 24-hour forecast compared to the verifying RTNEPH analysis for 06Z on 17 Feb 98. Although it misses some of the finer details of the cloud field, ADVCLD's ability to accurately forecast synoptic cloud patterns is readily apparent. Rather than the hemispheric view shown in Figure 1, AFWA supplies the Department of Defense (DoD) with visualizations of ADVCLD covering four different windows of interest (US, Europe, Southwest Asia, and Southeast Asia). Several examples of ADVCLD forecasts for these windows, with verifying satellite imagery, will be displayed at the conference.

5. CONCLUSION

ADVCLD is AFWA's newest and most accurate cloud forecast model. It forecasts clouds out to 48 hours quite successfully. Planned short-term improvements to the model include running it at higher horizontal resolution and applying finer scale input for winds, clouds, and moisture. In the long-term (2000 - 2001), ADVCLD will initialize with geostationary satellite data in addition to the polar orbiter data currently used. The addition of this more timely data source should significantly improve the model's accuracy. These enhancements will continue to make ADVCLD the cloud forecast of choice for the DoD into the twenty-first century.

6. REFERENCES

Baylor, G., and H. Lewit, 1992: The Navy Operational Global and Regional Atmospheric Prediction Systems at the Fleet Numerical Oceanography Center. *Wea. Forecasting*, **7**, 273-279.

Crum, T.D., 1987: AFGWC Cloud Forecast Models. AFGWC Tech. Note AFGWC/TN-87/001, Air Force Global Weather Central, Offutt AFB, Nebraska, 66 pp. (Source: Air Force Weather Technical Library (AFWTL), Scott AFB IL)

Edson, H., 1965: Numerical Cloud and Icing Forecasts. 3WW Tech. Note 3WW/TN-13, 3rd Weather Wing (Air Weather Service), Offutt AFB, Nebraska, 97 pp. (Source: AFWTL, Scott AFB IL)

Hamill, T.M., R.P. d'Entremont, and J.T. Bunting, 1992: A Description of the Air Force Real-Time Nephanalysis Model. *Wea. Forecasting*, **7**, 288-306.

Staniforth, A., and J. Cote, 1991: Semi-Lagrangian Integration Schemes for Atmospheric Models--A Review. *Mon. Wea. Rev.*, **119**, 2206-2223.

P2.7A

COMPARISON BETWEEN GLOBALLY MAPPED, LAYERED CLOUD AMOUNT FROM CLAVR, ISCCP, AND RTNEPH

Gang Luo, Larry L. Stowe[1] and Kenneth A. Campana[2]
Scientific Management & Applied Research Technologies, Inc., Silver Spring, MD
[1]NOAA/NESDIS, Office of Research and Applications, Washington, DC
[2] NOAA/NCEP, Environmental Modeling Center, Washington, DC

1. INTRODUCTION

Global Area Coverage (GAC) data from the NOAA AVHRR (Advanced Very High Resolution Radiometer) onboard the afternoon NOAA/7,9,11,14 satellites are used in the global CLAVR (CLoud from AVHRR) project at NOAA/NESDIS (Stowe et al. 1991,1998). Three phases of the project have been developed: CLAVR-1, which produces cloud/clear/mixed classifications for 2x2 GAC pixel arrays and mapped total cloud cover, CLAVR-2, for clear and multiple layer cloud type classifications at the GAC pixel resolution and mapped cloud amount by layered type (Davis et al. 1998a, b), and CLAVR-3, which uses dynamic multi-channel thresholds, derived from time/view angle-dependent analysis of CLAVR-1 clear pixel arrays, to separate clear from cloud contaminated pixels over seven different Earth scene types (Vemury et al., 1997).

Luo et al. (1997, 1998) compared the results from CLAVR-1 and CLAVR-2 with those from the DX-level data of ISCCP (International Satellite Cloud Climatology Project, Rossow and Schiffer 1993) over the FIRE (First ISCCP Regional Experiment) Cirrus-II site near Coffeyville, Kansas on November 28, 1991. Independent sources used in the comparison included the co-located results of Baum et al. (1995) and Ou et al. (1996) and the radar/lidar and meteorological observations during FIRE-II. In addition, a Reference Cloud Analysis Algorithm (RCAA) was developed to provide an independent estimate of "cloud truth". The RCAA included image interpretation, spatial coherence and histogram analysis (Coakley and Bretherton 1982, Coakley and Baldwin 1984), and pixel neighbor-checking (Luo et al. 1995).

The study of Luo et al. (1997, 1998) suggested that cloud amounts were over-estimated in ISCCP DX data; that mid-level cloud reported in ISCCP DX data were not reliable, i.e. they could actually be high-level semi-transparent cloud or broken thick high cloud; and that the cloud layers reported from CLAVR-2 data were consistent with meteorological observations, showing that the spectral signatures of clouds employed in CLAVR were capable of identifying and separating thin cirrus clouds from their optically thick counterparts. As Luo et al. (1998) pointed out, however, these conclusions were based on limited case studies and, therefore, their representativeness needed to be substantiated with a globally extensive set of similar studies.

In this study, the comparison is extended to the globally mapped results from CLAVR and ISCCP for the month of September, 1989. Independent resources include the results of RTNEPH (the U.S. Air Force's Real-Time Nephanalysis -Hamill et al. 1992). Regions of significant differences shown on the global maps are investigated. Each such region is examined on the GAC pixel level with the algorithms developed in Luo et al. (1997, 1998).

2. DATA SETS

Both globally mapped data sets and GAC pixel data sets are used in this study. Cloud amounts and layers from CLAVR and ISCCP are compared first between the mapped global images. The comparison goes to the pixel-scale level for regions where the cloud amounts or cloud layers from CLAVR and ISCCP show significant disparity.

The orbital product of CLAVR-1 is similar in structure to AVHRR 1B data, except that solar zenith, satellite zenith and relative azimuthal angles, brightness temperatures, albedos, and CLAVR-1 cloud classifications are included. The cloud classification labels each pixel array (2 adjacent scan lines and 2 adjacent pixels) with a cloud test by which the pixel array was found to be cloud contaminated in a sequence of such cloud screening tests, and then flags each pixel array into one of the three general categories: cloud filled, mixed, and clear. When mapping into 110 km equal-area grid cells, the cloud filled pixels are given cloud amount 100%, and the clear pixels 0%. The cloud amount of the mixed pixels in a grid is determined using the method suggested by Molnar and Coakley (1985). The mapped results are included in the NOAA/NASA AVHRR Pathfinder Atmosphere (PATMOS) data sets (UCAR, 1994; Stowe and Jacobowitz, 1997).

The CLAVR-2 Multiple-Layer Cloud Analysis (MLCA) orbital product is similar in structure to CLAVR-1, except that SSMI snow/ice flags, desert flags, clear-sky brightness temperatures from a climatological data base, and CLAVR-2 cloud type and sublayer information are included, all of which is available at the individual pixel resolution, not at the 2x2 array level. Four generic cloud types, low-level (water phase), mid-level (mixed phase), thin cirrus and glaciated deep convective (ice phase) clouds, are classified from a multi-spectral sequence of both cloud screening and cloud typing tests. A cloud contaminated pixel can be filled with a single

Corresponding author address: Gang Luo, Scientific Management & Applied Research Technologies, Inc., 8401 Corporate Drive, Suite 430, Landover, MD 20785-2230; e-mail <lgang@orbit.nesdis.noaa.gov>

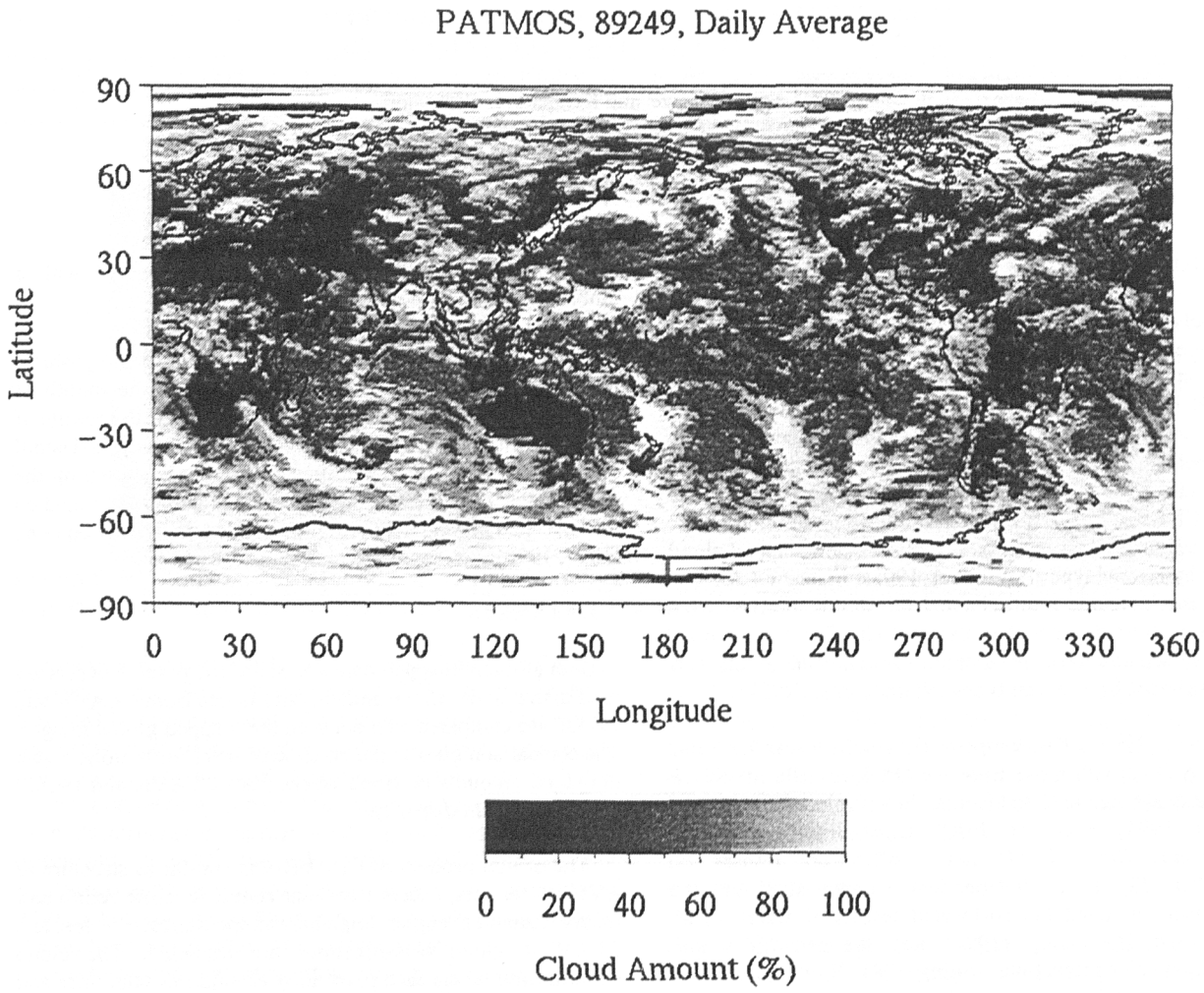

Figure 1. Daily-averaged cloud amounts from PATMOS/CLAVR-1 for September 6, 1989.

cloud type (overcast), or a mixture of cloud layers/types (mixed), or partly filled with clear and one or more cloud layers (partly cloudy). A pixel filled by a cloud type is further processed into as many as three sublayers of that type. When mapping into 110 km equal-area grid cells, the cloud filled pixels of a certain cloud type are given cloud amount 100% of that type, and the clear pixels are given cloud amount 0%. The cloud amount of the mixed pixels and partly cloudy pixels in a grid are determined using a generic gross radiometric balance method used in producing global CLAVR-2 CLDS (Cloud Layered Data Set) products (Davis et al. 1998b). The mapping is done for the cloud amount of each of the generic cloud types, as well as for the total cloud amount.

The mapped ISCCP D1 data contain, for each 275 km equal-area grid cell and for each 3-hour interval, 202 parameters including cloud amount and a variety of cloud property descriptions. The pixel-level ISCCP DX data for AVHRR is composed of 2x2 GAC pixel averages (8 km resolution) of albedo and brightness tempeature, sampled every 32 km. It contains, among other parameters, cloudy/clear classification, cloud top pressure (CTP) and optical thickness (COT). According to ISCCP cloud layer classification (Rossow and Schiffer 1993, Rossow 1996), each pixel can be mapped in association with one of the following cloud types: low cloud (CTP > 680 mb), mid-level cloud (680 mb > CTP > 440 mb), high cloud (CTP <440 mb and COT > 3.6), and thin cirrus cloud (CTP <440 mb and COT < 3.6).

RTNEPH data also contain cloud type/layer information.

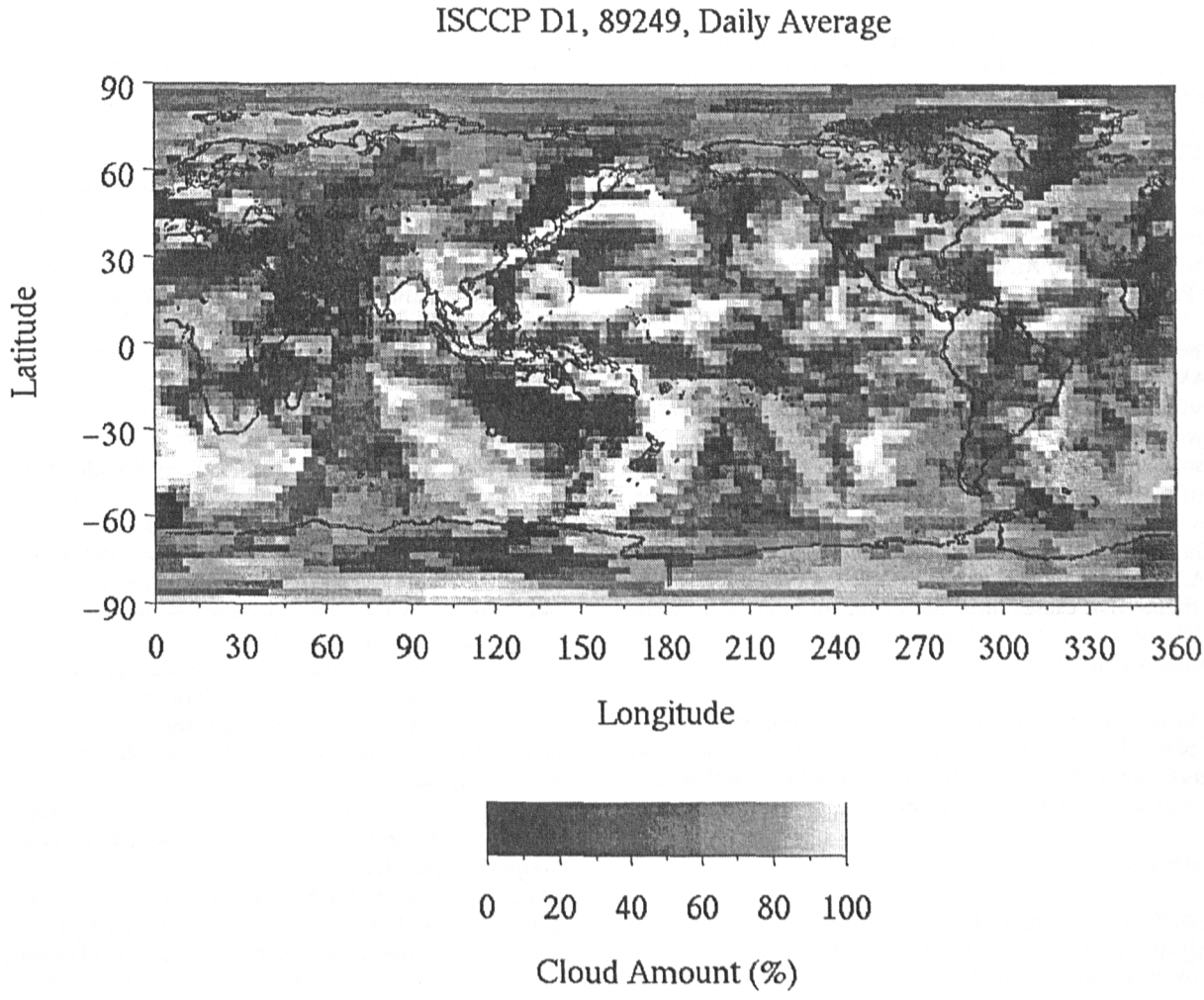

Figure 2. Daily-averaged cloud amounts from ISCCP D1 data for September 6, 1989.

Such information provides an independent source for the comparison. The US Air Force routinely produces (every 3 hours) a global cloud analysis. Data sources are primarily infrared and visible sensors on two DMSP satellites, but the algorithm is not a multi-spectral technique. Other data sources are surface observations and a manual bogus. Data are placed on polar stereographic grids of the northern and southern hemispheres, where horizontal resolution is 47.625 km at 60 degrees latitude. The RTNEPH dataset consists of total cloud and up to 4 distinct layered clouds (containing cloud cover, geopotential height of cloud bases/tops, observation time, and diagnostic information). Hamill et.al. (1992) note that the intent of the RTNEPH is to maximize the probability of cloud detection, so there is a tendency to over-estimate both clear and overcast conditions, while under-estimating partly cloudy situations.

Once a region is selected for investigation on the pixel-scale level, the Reference Cloud Analysis Algorithm (RCAA) developed in Luo et al. (1997, 1998) is used to provide an independent estimate of "cloud truth". Manual image interpretation is used to separate clear pixels from cloud contaminated ones. Cloud overcast pixels are separated from the rest of the cloud contaminated ones by a spatial coherence analysis (Coakley and Bretherton 1982, Coakley and Baldwin 1984), and the cloud fraction of each of the rest of the cloud contaminated pixels is determined using a neighbor-check method (Luo et al. 1995).

3. DISCUSSION

Figure 1 shows the globally mapped total cloud amounts for the day of September 6, 1989 from PATMOS/CLAVR-1. Daytime (ascending) and nighttime (descending) parts are merged into a daily average. The cloud amounts for the same day from ISCCP D1 data are averaged from the eight 3-hour intervals and shown in Figure 2. Aside from the different spatial resolution, these two maps display similar cloud patterns. However, noticeable differences in cloud amounts appear, for example at the southern end of Africa, in the polar regions, and over the mid Pacific Ocean.

The initial results from CLAVR-2 indicate a possible bias of CLAVR-1 in reporting extensive cloudiness in polar regions (Davis et al. 1998a ,b), suggesting an inadequate treatment of snow/ice in CLAVR-1's cloud retrieval. AVHRR images over the southern end of Africa have been visually examined and no significant cloudiness has been found, indicating that the CLAVR analysis is more correct. Quantitative analysis will be performed for these and other regions in disagreement with the RCAA, the CLAVR-1 & 2, and ISCCP-DX orbital datasets to determine what causes these algorithms to produce different cloud results. Also, RTNEPH mapped data will be compared as an independent check.

In addition to cloud amounts, cloud layers will also be compared. Regions showing significant differences in cloud layers between CLAVR and ISCCP will also be investigated at the pixel-scale, orbital database level.

References

Baum, B. A., T. Uttal, M. Poellot, T. P. Ackerman. J. M. Alvarez, J. Intrieri, D. O'C. Starr, J. Titlow, V. Tovinkere, and E. Clothiaux, 1995: Satellite remote sensing of multiple cloud layers. *J. Atmos. Sci.*, **52** (23), 4210-4230.

Coakley, J. A., Jr. and D. G. Baldwin, 1984: Towards the objective analysis of clouds from satellite imagery data. *J. Climate Appl. Met.*, **23**, 1065-1099.

Coakley, J. A., Jr. and F. P. Bretherton, 1982: Cloud cover from High-Resolution Scanner data: Detecting and allowing for partially filled fields of view. *J. Geophys. Res.*, **87**, 4917-4932.

Davis, P. A., L. L. Stowe, G. Luo, and E. P. McClain, 1998a: Automated generation of global cloud datasets from polar orbiting satellites. Part I: CLAVR-2 orbital pixel-scale Multiple Layer Cloud Analysis (MLCA). *J. Atmos. Ocean. Tech.* (submitted).

Davis, P. A., L. L. Stowe, G. Luo, and E. P. McClain, 1998b: Automated generation of global cloud datasets from polar orbiting satellites. Part II: CLAVR-2 gridded clear and cloud layered data sets. *J. Atmos. Ocean. Tech.* (in preparation).

Hamill, T. M., R. P. d'Entremont, and J. T. Bunting, 1992: A description of the Air Force Real-Time Nephanalysis model. *Wea. Forecasting*, **7**, 288-306.

Luo, G., P. A. Davis, L. L. Stowe, and E. P. McClain, 1995: A pixel-scale algorithm of cloud type, layer, and amount for AVHRR data. Part I: Nighttime. *J. Atmos. Ocean. Tech.*, **12** (5), 1013-1037.

Luo, G., L. L. Stowe, and P. A. Davis, 1997: Comparison of total and layered cloud amount from CLAVR, ISCCP, and MSMR over the FIRE-II site. *Proceedings Ninth Conference on Atmospheric Radiation*, AMS, Long Beach, CA. 431-435.

Luo, G., L. L. Stowe, and P. A. Davis, 1998: An intercomparison of total and layered cloud amount between CLAVR and ISCCP for the November 28, 1991 FIRE-II region. *J. Atmos.Ocean. Tech.* (submitted).

Molnar, G., and J. A. Coakley, Jr., 1985: Retrieval of cloud cover from satellite imagery data: A statistic approach. *J. Geophys. Res.*, **90**, 12,960-12,970.

Ou, S. C., K. N. Liou, and B. A. Baum, 1996: Detection of multilayer cirrus cloud system using AVHRR data: verification based on FIRE II IFO composite measurements. *J. Appl. Meteor.*, **35**, 178- 191.

Rossow, W. B. and R. A. Schiffer, 1991: ISCCP cloud data product. *Bull. Amer. Meteor. Soc.*, **72**, 2-20.

Rossow, W. B., 1996, private communication.

Stowe, L. L., P. A. Davis, and E. P. McClain, 1998: Global cloud cover from NOAA/AVHRR data: Scientific basis and evaluation of the CLAVR-I classification algorithm. *J. Atmos. Ocean. Tech.* (Submitted).

Stowe, L. L., E. P. McClain, R. Carey, P. Pellegrino, G. Gutman, P. Davis, C. Long and S. Hart, 1991: Global distribution of cloud cover derived from NOAA/AVHRR operational satellite data. *Adv. Space Res.*, **11**, 51-54.

Stowe, L, and H. Jacobowitz, 1997: The AVHRR Pathfinder Atmosphere Project. *Proceedings 9th Atmospheric Radiation Symposium*, AMS, Boston, MA, 196-197.

UCAR, 1994: The NOAA-NASA Pathfinder Program. The *Univ. Corp for Atmos. Res.*, Boulder CO, 22 pages.

Vemury, S., L. Stowe and R. Anne, 1997: Effect of dynamical prediction models from Clear-sky Radiation Data sets (CRDS) on CLAVR Classifications. *Proceedings 9th Atmospheric Radiation Symposium*, AMS, Boston, MA. 355-357.

P2.9B

A COMPARISON OF 15 GLOBAL, NON-PARAMETRIC, AUTOMATED THRESHOLD SELECTION PROCEDURES FOR CLOUD DETECTION

Larry Di Girolamo*
Institute of Atmospheric Physics, University of Arizona, Tucson, AZ, USA

1. INTRODUCTION

The Multi-angle Imaging SpectroRadiometer (MISR) will be launched in the summer of 1998 as part of the EOS-AM1 platform (Diner *et al.* 1997a). Part of MISR's cloud detection strategy (Diner *et al.* 1997b) uses a global, histogram-based, non-parametric automated technique for selecting threshold values needed to discriminate clear pixels from cloudy pixels. Such techniques have also been employed by other cloud detection algorithms (*e.g.*, Simpson and Gobat 1995). The literature presents many similar techniques that have been used for a variety of applications, including robotic target recognition, text recognition, medical imaging analysis, machine parts inspection and foreign object recognition in packaged foods. Several papers exists that intercompare many of these techniques (*e.g.*, Weszka 1978; Sahoo *et al.* 1988; Lee *et al.* 1990; Glasbey 1993; Pal and Pal 1993). The general conclusion from such comparisons is that the performance of the automated threshold selection technique (ATST) depends on the data being analyzed. This paper addresses which technique performs best for cloud detection as applied to data taken from the AVHRR instrument. The best technique will be included in the MISR cloud detection algorithm.

Only a small sample of ATSTs were chosen for this comparison relative to the large number that exist in the literature. The selection criteria was based on the following points: (1) the technique should be a global, histogram-based, non-parametric technique suitable for the MISR cloud detection approach and processing load, and (2) the technique should exist in the refereed literature within a full article. [It is likely that some techniques that should have been included in this study were overlooked; for this, I apologize]. Based on these criteria 15 techniques were chosen for the comparison, and are listed in Table 1. This represents the largest comparison of automated threshold selection techniques to date.

Given that the performance of the ATST depends on the data being analyzed, this paper also explores how the performance of the ATST varies for several commonly used spectral and textural observables that can be used for MISR cloud detection. In doing so, the sensitivity of cloud detection to the selected threshold is examined as a function of the various observables. The results are then ranked in order to conclude which are the best ATSTs and observables for MISR cloud detection.

Table 1. The 15 ATSTs examined in this study

Tech #	Reference	Type
1	Ridler and Calvard (1978)	Information Theoretic
2	Otsu (1979)	Information Theoretic
3	Rosenfeld and De La Torre (1983)	Graph Theoretic
4	Tsai (1985)	Information Theoretic
5	Kapur *et al.* (1985)	Information Theoretic
6	Kittler and Illingworth (1986)	Information Theoretic
7	Whatmough (1991)	Graph Theoretic
8	Pal and Dasgupta (1992)	Fuzzy Logic
9	Li and Lee (1993)	Information Theoretic
10	Pal and Bhandari (1993)	Information Theoretic
11	Yen *et al.* (1995)	Information Theoretic
12	Huang and Wang (1995)	Fuzzy Logic
13	Pal (1996)	Information Theoretic
14	Brink and Pendock (1996)	Information Theoretic
15	Sahoo *et al.* (1997)	Fuzzy Logic

2. ATST

ATSTs can coarsely be divided into two types of techniques: local and global. Local thresholding techniques divide the image into smaller sub-images and a threshold for each sub-image is chosen based on local properties. Global thresholding techniques use a single threshold value to segment the entire image. For our purpose, the global threshold is derived from the histogram of observations that make up the image. The advantages of global thresholding techniques over local thresholding techniques are that they are simple to understand, implement, and compute.

The key idea behind histogram-based global threshold selection is to try and select an optimum

**Corresponding author address:* Larry Di Girolamo, Institute of Atmospheric Physics, P.O. Box 210081, University of Arizona, Tucson, AZ 85721-0081; email <larry@papagayo.atmo.arizona.edu>

threshold that best segments the image into clear and cloudy regions by minimizing the misclassification of the image pixels. Theoretically, this can be achieved by choosing the optimal threshold value according to Bayes' rule (*e.g.,* Gonzalez and Woods 1992). This requires the gray-level distribution of clear and cloudy pixels to be known. In practice, however, these distributions are not known, and what we have instead is a mixture of the two distributions that form the histogram. Moreover, it isn't even clear if these distributions truly exist given the quantitatively ill-defined nature of what constitutes a cloud (Di Girolamo and Davies 1997).

Another approach would be to find the valley that lies between the clear and cloudy distributions. Ideally, the histogram will have a deep, sharp valley between two peaks that represents the clear and cloud populations. Unfortunately, the effects of noise, pixel resolution, unequal distributions of clear and cloud, and multiple cloud and surface types within real satellite images make a simple valley-finding method difficult to derive and implement. As a result, more sophisticated techniques are required.

Such techniques exist and can be divided into graph theoretic, information theoretic, and fuzzy logic techniques. Graph theoretic techniques use only the shape of the histogram to select the threshold. Information theoretic techniques select the threshold by optimizing some criterion function that is based on information theory and derived from the histogram. Fuzzy logic techniques are similar to information theoretic techniques except that the criterion function is based on fuzzy set theory. The types of ATST used in this study are summarized in Table 1 and are all non-parametric; that is, the techniques do not require the histogram to be modeled by some *a priori* determined parametric form before the techniques are applied (*e.g.*, Gonzalez and Woods 1992).

3. EVALUATION METHOD

The data used in this experiment comes from the Advanced Very High Resolution Radiometer (AVHRR) flown aboard the NOAA-11 spacecraft. AVHRR data taken in the local area coverage mode, which has a sub-satellite ground track resolution of 1.1 km, was used. 21 scenes were extracted, 256 x 256 pixel in size, centered about (43° N, 73° W), and spanning the period of August 1 to October 30, 1993. This region is characterized as a mix of conifer and deciduous trees and open pasture. The criteria for selection were that the scenes must be 5 - 95% cloud covered and must be of good data quality. The ATST fails to produce good results for completely clear and overcast scenes. [For MISR, this situation is avoided since the histograms are constructed by ecosystem type, which are typically large in spatial extent and are constructed over a one month period before the ATST is applied (Diner *et al.* 1997b), as opposed to being applied to a single image snapshot as done in this study]. The method used to calibrate the AVHRR radiometric data is described in Di Girolamo and Davies (1997).

From the AVHRR data for each scene, 4 observables that are applicable for MISR cloud detection are constructed: R_{670}, *NDVI*, *D*, and *DSVI*. R_{670} is the AVHRR 670 nm channel reflectance. *NDVI* is the normalized differenced vegetation index equal to $(R_{860} - R_{670})/(R_{860} + R_{670})$, where R_{860} is the AVHRR 860 nm channel reflectance. *D* is a parameter introduced by Di Girolamo and Davies (1995) and is equal to $NDVI^{b}/R_{670}^{2}$, where the exponent *b* is chosen to maximize the separation between clear and cloudy pixels. For vegetated surfaces, $b = 0.6$. *DSVI* is the spatial variability index of *D* and is equal to $|D_m - D_c|$, where D_m is the mean *D*-value of the 3 x 3 matrix centered on the value D_c. The ATSTs are applied to all 84 images.

Zhang (1996) demonstrated that the best objective method for evaluating any ATST is the empirical-discrepancy (ED) method. The ED-measure is the difference between an ATST-segmented image and the correct or ideal segmented image (called the reference image). The reference image is derived from visual analysis of the gray scale image of the observable using an image software package. This is a time consuming task. For each scene, there are 4 reference images, one for each observable. Each of the 4 reference images per scene may have a different cloud fraction, because the reference image associated with an observable represents the best representation of the cloud field that can be segmented using only that observable. There are cases when the reference image is significantly different than the "true" cloud field. Keep in mind that for global thresholding, we cannot expect the ATST to do better than the analysts. Given that different analysts would produce different reference images (*e.g.*, Stowe 1984), an ED-measure of less than 10% cloud fraction is deemed to be produced by a good ATST-derived threshold.

4. RESULTS

A summary of the overall bias and RMS error for the ED-measure of the 21 scenes is presented in Table 2. A positive bias indicates that the ATST tends to underestimate the amount of clouds. The shaded areas represent the best technique(s) for each observable. It is clear from Table 2 that the ATSTs perform best on average for *D* and *DSVI*. On average, the ATST that works best for all observables is Technique #9 (Li and Lee 1993), followed by Technique #12 (Huang and Wang 1995) and Technique #8 (Pal and Dasgupta 1993).

Although the ATST works best for *D* and *DSVI*, it is also desirable to have the results of thresholding to be as insensitive to threshold variability as possible. Such insensitivity ensures that small errors in threshold value do not lead to large errors in cloud fraction. To test the sensitivity of the 4 observables, the average reference-image-threshold for the 21 scenes is applied to each scene. The resulting segmented image is subtracted from its corresponding reference image. The variability in this quantity is a measure of the sensitivity. Table 3 summarizes the results. From Table 3, *D* is the best and the *NDVI* is the poorest observable to use for cloud detection based on the sensitivity of cloud fraction to the threshold.

Table 2. Biases and RMS errors of the ED-measure for the 15 ATSTs applied to the 4 observables. A positive bias indicates that the ATST tends to underestimate the amount of clouds. The shaded areas represent the best technique(s) for each observable.

	R_{670}		*NDVI*		*D*		*DSVI*	
Tech. #	Bias	RMS	Bias	RMS	Bias	RMS	Bias	RMS
1	0.29	0.14	0.03	0.13	-0.13	0.09	-0.08	0.09
2	0.28	0.14	0.10	0.12	-0.13	0.09	-0.07	0.09
3	0.22	0.22	0.30	0.54	0.15	0.07	0.13	0.09
4	0.30	0.14	0.10	0.11	-0.15	0.08	-0.10	0.09
5	0.35	0.15	0.15	0.17	-0.23	0.18	-0.21	0.19
6	0.14	0.13	0.14	0.15	0.07	0.19	0.11	0.23
7	0.10	0.12	0.17	0.25	0.11	0.09	0.20	0.11
8	0.21	0.12	0.08	0.13	-0.09	0.12	0.05	0.10
9	0.22	0.12	0.11	0.12	0.15	0.10	0.02	0.09
10	0.24	0.13	0.23	0.35	0.05	0.10	0.02	0.10
11	0.32	0.15	0.13	0.15	-0.20	0.20	-0.17	0.20
12	0.23	0.12	0.10	0.12	-0.08	0.11	0.01	0.09
13	0.26	0.15	0.16	0.21	-0.01	0.25	0.04	0.24
14	0.14	0.19	0.09	0.21	-0.06	0.14	0.01	0.12
15	0.20	0.18	0.52	0.26	-0.08	0.12	-0.04	0.17

Table 3. RMS errors of the difference in cloud fraction when using the reference image threshold and average reference-image-threshold of the 21 scenes for the 4 observables.

Observable	R_{670}	*NDVI*	*D*	*DSVI*
RMS	0.11	0.20	0.08	0.10

In order to better understand the results from Table 2 and 3, a look at some histograms is in order. Figure 1 shows histograms for the 4 observables for one particular scene that is representative of all scenes; however, a wide variety of histogram shapes are possible. The histogram for R_{670} shows a single peak with plenty of bins filled to the right of the peak. The peak represents clear pixels. In this case, a second peak representing clouds does not exist to the right of the clear sky peak. The reference image threshold was placed at a value of 0.09 for this scene. The ATST thresholds ranged from 0.11 to 0.44 with an average of 0.28; hence, the cloud amount is underestimated. The histogram for *NDVI* shows a bi-modal distribution. The peak near 0 represents cloud, and the smaller peak to the right represents clear. The reference image threshold for this scene was 0.32. The ATST threshold ranged from -0.04 to 0.33 with an average of 0.18; hence, the cloud amount is underestimated. Note that for the R_{670} and *NDVI* histograms, a small error in threshold can lead to a large error in cloud amount. For the *D* and *DSVI*, the histograms are strongly peaked at a value near 0, which represents cloudy pixels. The scale is truncated but, in truth, extends out to about a value of 1000. The reference image thresholds for *D* and *DSVI* were 27 and 16, respectively. The ATST threshold ranged from 2 to 130 with an average of 56 for *D*, and 1 to 65 with an average value of 27 for *DSVI*; hence, the cloud amount tends to be overestimated. Note, however, that a small error (relative to its large dynamic range) in *D* and *DSVI* thresholds lead to a small error in cloud amount.

5. CONCLUSION

This study has determined that *D* and *DSVI* perform better than R_{670} and *NDVI* as observables for cloud detection over vegetated surfaces. This conclusion is based on a sensitivity analysis of cloud fraction to threshold value and on the ability of the ATSTs to choose the appropriate threshold. The MISR cloud detection algorithm has already adopted the *D* and *DSVI* as observables for cloud detection. However, based on preliminary findings of only 5 ATSTs, the method of Otsu (1979) was tentatively chosen as the ATST for MISR until further research was performed. The findings in this study would suggest that the method of Li and Lee (1993) would produce better results than the Otsu method, at least for vegetated surfaces. This study will be extended to a variety of other ecosystem types before any final decision is made regarding a change to the MISR algorithm.

Finally, it should be noted that the choice of the best ATST determined in this study is only relative to cloud detection for the observables tested. The ATSTs that performed poorly for cloud images may well prove to be the best techniques for other types of images.

6. ACKNOWLEDGMENTS

Support from the Jet Propulsion Laboratory of the California Institute of Technology under Contract 959085 and from the Natural Sciences and Engineering Research Council of Canada is gratefully acknowledged.

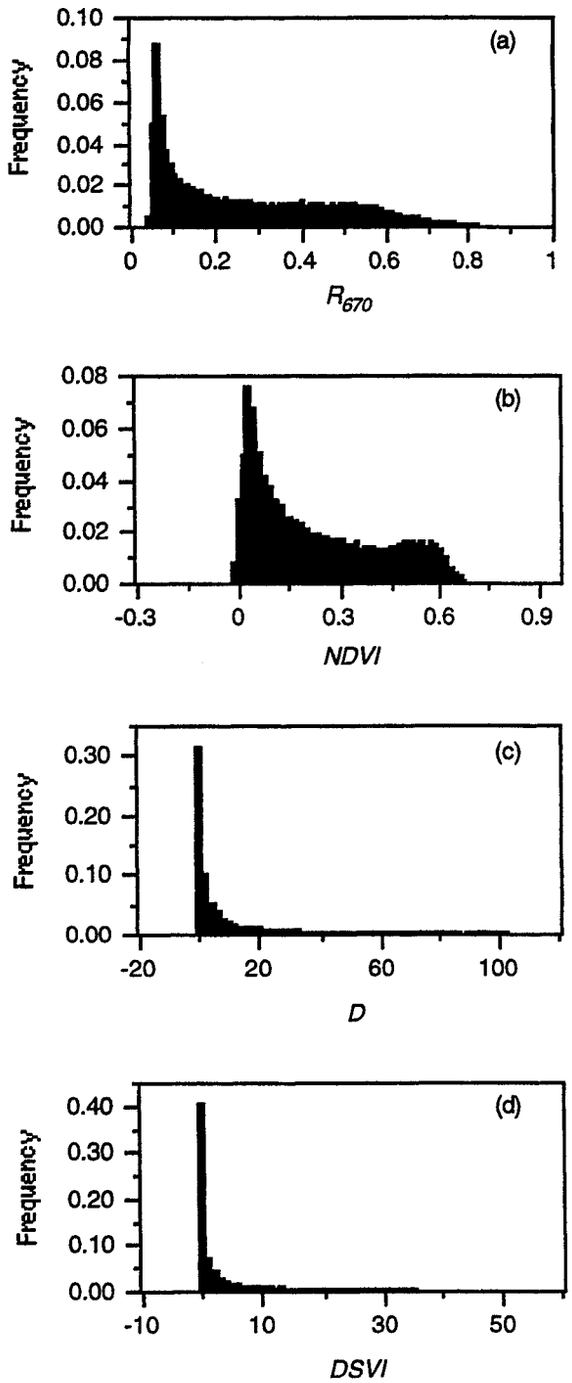

Figure 1. Histograms of the 4 observables for one scene that is representative of all scenes. The horizontal axis for the *D* and *DSVI* histograms has been truncated.

7. REFERENCES

Brink, A.D. and N.E. Pendock, 1996: Minimum cross-entropy threshold selection. *Pattern Recogn.* **29**, 179-188.

Di Girolamo, L. and R. Davies, 1997: Cloud fraction errors caused by finite resolution measurements. *J. Geophys. Res.* **102**, 1739-1756.

Di Girolamo and R. Davies, 1995: The image navigation cloud mask for the Multi-angle Imaging SpectroRadiometer (MISR). *J. Atmos. Oceanic Tech.* **12**, 1215-1228.

Diner, D.J. and co-authors, 1997a: Multi-angle Imaging SpectroRadiometer (MISR) instrument description and experiment overview. *IEEE Trans. Geoscl. Remote Sens.* (submitted).

Diner, D.J., L. Di Girolamo and E.E. Clothiaux, 1997b: MISR Level 1 cloud detection algorithm theoretical basis. *JPL D-13397, Rev. A*, Jet Propulsion Laboratory, Pasadena, CA, pp. 37.

Glasbey, C.A., 1993: An analysis of histogram-based thresholding algorithms. *CVGIP: Graph. Models Image Process.* **53**, 532-537.

Gonzalez, R.C. and R.E. Woods, 1992: *Digital image processing*, Addison-Wesley Publishing Co., NY.

Huang, L.-K. and M.-J.J. Wang, 1995: Image thresholding by minimizing the measures of fuzziness. *Pattern Recogn.* **28**, 41-51.

Kapur, J.N., P.K. Sahoo, and A.K.C. Wong, 1995: A new method for gray-level picture thresholding using the entropy of the histogram. *Comput. Vision Graph. Image Process.* **29**, 273-285.

Kittler, J. and J. Illingworth, 1986: Minimum error thresholding. *Pattern Recogn.* **19**, 41-47.

Lee, S.U., S.Y. Chung and R.H. Park, 1990: A comparative performance study of several global thresholding techniques for segmentation. *Comput. Vision Graph. Image Process.* **52**, 171-190.

Li, C.H. and C.K. Lee, 1993: Minimum cross entropy thresholding. *Pattern Recogn.* **26**, 617-625.

Otsu, N., 1979: A threshold selection method from gray-level histograms. *IEEE Trans. Syst. Man Cybern.* **SMC-9**, 62-66.

Pal, N.R., 1996: On minimum cross entropy thresholding. Pattern Recogn. 29, 575-580.

Pal, N.R. and D. Bhandari, 1993: Image thresholding: some new techniques. *Signal Process.* **33**, 139-158.

Pal, N.R. and S.K. Pal, 1993: A review on image segmentation techniques. *Pattern Recogn.* **26**, 1277-1294.

Pal, S.K. and A. Dasgupta, 1992: Spectral fuzzy sets and soft thresholding. *Inform. Sci.* **65**, 65-97.

Ridler, T.W. and S. Calvard, 1978: Picture thresholding using iterating selection method. *IEEE Trans. Syst. Man Cybern.* **SMC-8**, 630-632.

Rosenfeld, A. and P. De La Torre, 1983: Histogram concavity analysis as an aid in threshold selection. *IEEE Trans. Syst. Man Cybern.* **SMC-13**, 231-235.

Sahoo, P., S. Soltani and A.K.C. Wong, 1988: A survey of thresholding techniques. *Comput. Vision Graph. Image Process.* **41**, 233-260.

Sahoo, P., C.Wilkins and J. Yeager, 1997: Threshold selection using Renyi's entropy. *Pattern Recogn.* **30**, 71-84.

Simpson, J.J. and J.I. Gobat, 1995: Improved cloud detection in GOES scenes over the oceans. *Remote Sens. Environ.* **52**, 79-94.

Stowe, L.L., 1984: Evaluation of Nimbus-7 THIR/CLE and Air Force 3D-nephanalysis estimates of cloud amount. *J. Geophys. Res.* **89**, 5370-5380.

Tsai, W.-H., 1985: Moment-preserving thresholding: a new approach. *Comput. Vision Graph. Image Process.* **29**, 377-393.

Weszka, J.S., 1978: A survey of threshold selection techniques. *Comput. Vision Graphics Image Process.* **7**, 259-265.

Whatmough, R.J., 1991: Automatic threshold selection from histogram using the "exponential hull". *CVGIP: Graph. Models Image Process.* **53**, 592-600.

Zhang, Y.J., 1996: A survey on evaluation methods for image segmentation. *Patt. Recogn.* **29**, 1335-1346.

P2.11A

Multi-channel IR observations of clouds and collocated microwave radiometer observations

Toshiro Inoue
Meteorological Research Institute, Tsukuba, Ibaraki, Japan

1.INTRODUCTION

In the climate system, clouds play an important role through radiative processes and latent heat release. Different cloud types play different roles in the climate. Convective clouds provide the dominant contribution to precipitation while stratiform clouds, with their larger horizontal extent, have a greater influence on the radiation budget. Therefore, the classification of cloud and precipitation regime is very important to the understanding of cloud effects on the Earth's environment, particularly in the tropical ocean.

Because of the lack of conventional cloud and precipitation observations over oceans, use of satellite data is obviously necessary. Satellite data have been extensively used in studies of cloud properties and cloud classification in the last few decades. Infrared and visible data were first used by Shenk et al.(1976) and recently by Rossow and Schiffer(1991) to classify cloud types.

Methods for satellite determination of cirrus properties were developed by Szejwach(1982), Wu(1987), Wielicki et al.(1990), Parol et al. (1991), Minnis et al.(1994) and Ou et al.(1993). Inoue(1985) used the two infrared channels in the atmospheric "window" region to estimate cirrus cloud temperature and effective emissivity. He also developed a method to classify cirrus cloud and optically thick cloud by use of the split window (11μm and 12μm) (Inoue,1987a). The CO2-slicing method is used to determine cloud top temperature and effective cloud amount (Smith et al. 1974; Smith and Platt 1978; Menzel et al. 1983). Han et al.(1994) studied the global distribution of effective particle size in liquid water clouds using ISCCP data.

Cloud liquid water path was studied by Alishouse et al.(1990), Liu and Curry (1993) and Greenwald et al.(1993) using microwave satellite data. Many rainfall estimation techniques using microwave data have been developed and are inter-compared in the AIP-3 (Ebert,1996). Liu et al.(1995) developed a new cloud classification scheme that combines microwave and single infrared satellite observations.

Inoue(1985) found that cirrus clouds can be identified by the BTD of the split window (BTD=TBB11μm - TBB12μm). The absorption by ice at 12μm is stronger than that at 11μm. Using this characteristic, an objective cloud type classification method was developed by Inoue(1987a). The feasibility of delineation of rainfall areas was studied by comparing split window cloud types and radar observations over Japan during the summer season (Inoue,1987b).

The objective of this study is to understand the relative amounts of rainfall and the liquid water and ice water paths associated with different cloud types as determined by the multi-infrared data.

2. CLOUD TYPES BY SPLIT WINDOW AND SSM/I

In this study, we compared cloud type information determined by the split window method and rain signals from SSM/I data using collocated GOES-9 and SSM/I imagery. We mapped GOES-9 data onto a 0.1 degree latitude/longitude grid, and SSM/I data onto a similar 0.2 degree grid. We selected corresponding image data based on a time difference of no more than 15 minutes. GOES-9 data were processed by the McIDAS system developed by the University of Wisconsin. The original temperature resolution was 0.1K, but a 0.5K temperature resolution was used in this study. Cloud type classifications are done based on Inoue(1987). BTD thresholds for optically thick clouds and cirrus clouds are set to 1K and 3K, respectively. The threshold for discriminating between high clouds and low clouds was set to 253K.

Liu et al.(1995) used a microwave index, f, defined as follows to represent the strength of the microwave signal from a cloudy pixel:

$$f=(1-D/D0) + 2(1-PCT/PCT0),$$

where D represents the polarization at 19GHz given by D=TBB19V-TBB19H and TBB19V and TBB19H are vertically and horizontally

Corresponding author address: Dr. Toshiro Inoue, Meteorological Research Institute 1-1 Nagamine, Tsukuba, Ibaraki, 305 Japan. e-mail: tinoue@mri-jma.go.jp

polarized brightness temperatures at 19 GHz, respectively; D0 is D at the threshold for precipitation; PCT is the 85GHz polarization-corrected temperature defined by Spencer et al. (1989) as PCT=1.818TBB85V-0.818TBB85H and TBB85V and TBB85H are, respectively, vertically and horizontally polarized brightness temperatures at 85GHz; and PCT0 is PCT at the threshold for the onset of precipitation. The first term on the right hand side of the equation represents the microwave emission signal and the second term represents the scattering signal. A factor of 2 is given to the scattering term to balance the emission term for rainfall estimation. Liu et al.(1995) modeled the values of (1-D/D0), (1-PCT/PCT0) and f versus rainfall rate for mixed-phase deep cloud using the radiative transfer model described by Liu and Curry(1992,1993). Positive values for emission and scattering index correspond to rainfall. It was shown that the emission term increases rapidly with rainfall rate up to 12 mm/h and saturates for higher rainfall rates. The scattering term increases for the wide range of rainfall rates up to 50 mm/h, indicating the scattering effect by large ice particles and raindrops.

Figure 1 shows an example of infrared and microwave observations over the area of 4-10N and 113W-95W: (a) GOES-9 infrared image taken at 1315 UTC on December 2, 1995; (b) cloud type classification map by split window; (c) emission index computed from SSM/I 19 GHz taken at 1330 UTC on December 2,1995; (d) scattering index computed by SSM/I 85 GHz. The infrared image is colored depending on TBB in Kelvin colder than 270K. The cloud type map is colored (1-7) depending on cloud type. Cumulonimbus cloud is colored red, cirrus clouds are colored yellow depending on optical thickness and TBB, low level cumulus/stratocumulus is colored green and cloud free area are colored blue. The emission and scattering index are shown in (1-D/D0)*100 and (1-PCT/PCT0)*100.

The convective system is easily identified along 7N in the cloud type map and IR image which correspond to higher scattering and emission indices from the SSM/I. The generally higher indices of emission and scattering are correlated in this case. This suggests that convective rain is occurring in the cloud system. The area of rainfall shown by the microwave signal is smaller than that of TBBs 253K or colder which is associated with rainfall in infrared-only rainfall estimation schemes. The higher emission area corresponds to cumulonimbus and dense cirrus clouds in the cloud type map, and colder than 210K in the infrared image. The northern edge of the clouds in this convective system shows a relatively sharp boundary in the infrared image. The emission index is slightly enlarged to the north in comparison with the infrared image and scattering index. The emission index is derived from the low spatial resolution 19GHz data. This might be the cause of the area coverage difference on the northern edge of the clouds due to the beam filling effect.

On the contrary, the southern boundary of the scattering index is slightly enlarged relative to the emission index. This area corresponds to anvil where there is a signal of scattering index but none in the emission index. Generally, the 85GHz is transparent to cirrus clouds but it might be affected by ice when ice particles become large and dense. Therefore, these anvil areas are covered by large and dense ice particles and are not associated with rainfall.

Inoue(1997) showed the BTD is saturated over the clouds of optical thickness is greater than 10. On the contrary, the BTD between 3.7μm and 11μm shows larger difference for the optically thicker clouds. At the meeting some results using the 3.7μm and 11μm will be shown. Further, some results from TRMM data will also be shown at the meeting.

3. Summary

Cloud type information from GOES-9 split window and microwave rainfall information from SSM/I are compared using the same map projection. Emission index and scattering indices developed by Liu et al.(1995) generally correspond to optically thick clouds as classified by the split window. There are some regions where there is a signal in the scattering index but none in the emission index . This condition implies that large and dense ice particles exist near the cloud tops but no rainfall is falling. These areas correspond to thick cirrus or cumulonimbus clouds as determined by the split window.

Acknowledgment

This study was partly supported by TRMM program of NASDA(National Space Development Agency of Japan).

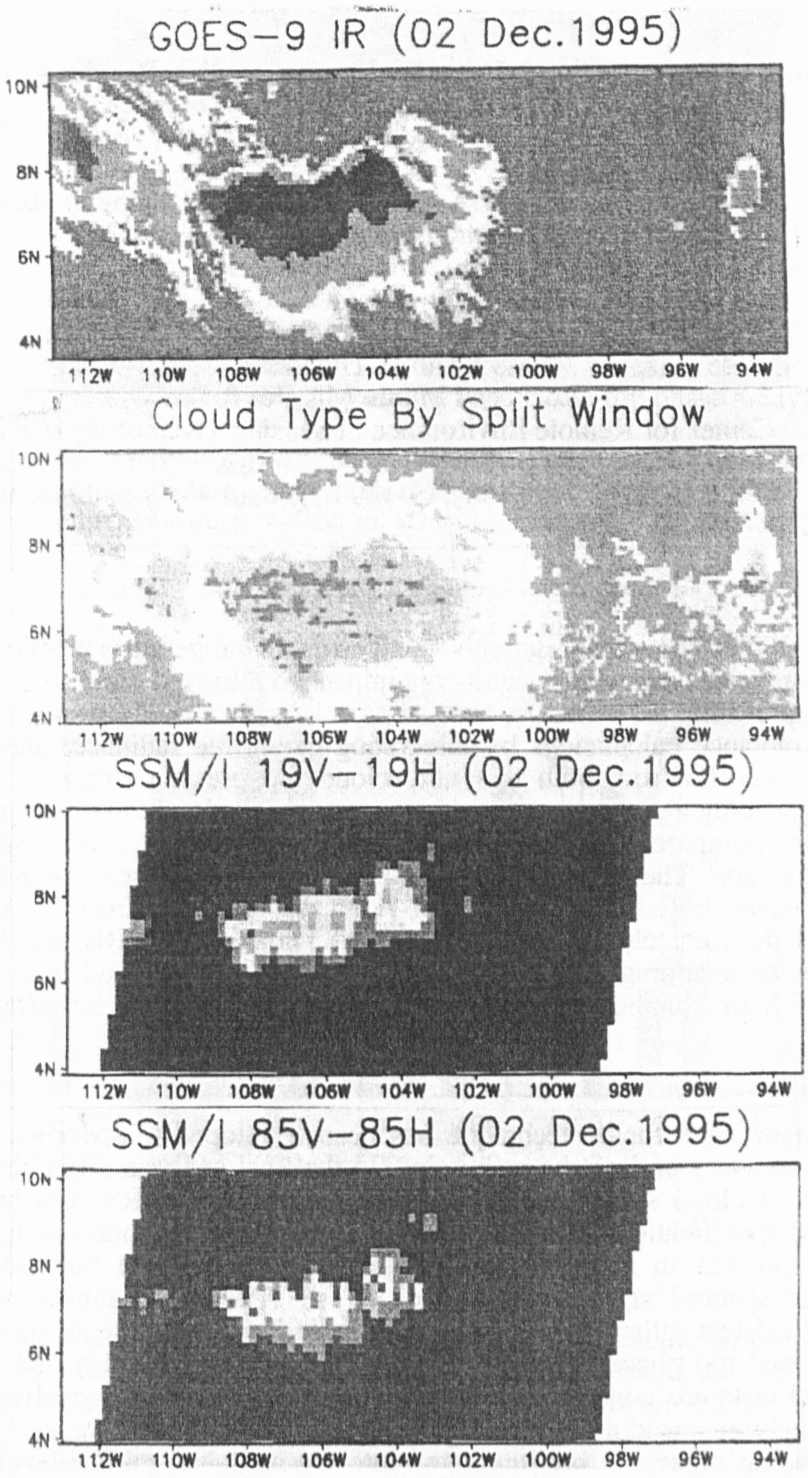

Figure 1. Infrared and microwave observations over the area of 4-10N and 115W-95W: (a) GOES-9 infrared image taken at 1315 UTC on December 2, 1995; (b) cloud type classification map by split window; (c) emission index computed from SSM/I 19 GHz taken at 1330 UTC on December 2,1995; (d) scattering index computed by SSM/I 85 GHz.The cloud type map is colored depending on cloud type. Cumulonimbus cloud is colored red, cirrus clouds are colored yellow depending on optical thickness and TBB, low level cumulus/stratocumulus is colored green and cloud free areas are colored blue. The emission and scattering index are shown in (1-D/D0)*100 and (1-PCT/PCT0)*100.

P2.12B

The Application of Cloud-Free Radiances to the Retrieval of Cloud Top Pressures from HIRS Data

H. L. Huang
Cooperative Institute for Meteorological Satellite Studies
University of Wisconsin, Madison

and

Keith D. Hutchison
Lockheed Martin Missiles & Space
Center for Remote Environmental Sensing Technology (CREST)
Sunnyvale, California
Tele: 408-756-2328; Fax: 408-743-1795; E-mail: keith.hutchison@lmco.com

ABSTRACT

Sensitivity studies show that relatively small errors in temperature profiles used to calculate upwelling radiances can have a significant impact on retrieved cloud top pressures with the CO_2 slicing technique. Thus a new approach is evaluated to reduce inaccuracies in upwelling radiance calculations by integrating cloud-free radiances into the CO_2 slicing algorithm. Results from both this new cloud top pressure retrieval approach and the regular CO_2 slicing algorithm are used in the automated cloud top phase algorithm and final analyses are compared against a manual interpretation of ice and water clouds in the AVHRR imagery. The modified CO_2 slicing algorithm that uses cloud-free radiances was found to improve both the distribution of cloud top pressures from the HIRS data and the accuracy of the final cloud top phase analysis with the AVHRR imagery. These initial results provide encouragement to further explore the use of cloud-free radiances from the AVHRR 10.8 μm channel in the analysis of cloud top pressure with infrared sounder data.

INTRODUCTION

A multisensor, data fusion technique has been developed to specify cloud top phase in AVHRR/2 imagery and assess uncertainty in the final analysis (Hutchison et al., 1997a). The fusion of cloud signatures in AVHRR imagery and HIRS data has been shown to improve the specification of cloud top phase in the higher resolution imagery and reduce the ambiguity inherent in analyses based solely upon bi-spectral methods. The approach exploits the spectral signature of clouds in all AVHRR channels using tests created primarily to detect either ice or water clouds. Since no single bi-spectral test uniquely specifies cloud top phase in existing AVHRR imagery, pixels detected with both ice and water cloud tests are considered ambiguous and their phase is resolved using cloud top pressure analyses based upon the CO_2 slicing of HIRS data. However, before results from the CO_2 slicing algorithm are integrated into the analysis, middle-level water clouds are identified using a third bi-spectral test, based upon the 3.7- minus 10.8-μm brightness temperature difference feature, since these clouds are both relative cold and highly reflective in daytime AVHRR imagery. Thus, results from the CO_2 slicing of HIRS/2 data are only applied to pixels classified as ambiguous in an intermediate cloud top phase analysis and, in effect, are used primarily to differentiate between low-level water clouds and thin cirrus in the AVHRR imagery. However, cloud top pressures derived from the CO_2 slicing of HIRS/2 data may erroneously change cloud top phase classifications of some ambiguous pixels that were correctly typed as ice clouds in the intermediate cloud top phase analysis to water clouds in the final analysis (Hutchison et al., 1997a). Thus, an improved cloud top pressure analysis of HIRS data is desirable.

Sensitivity studies were conducted to quantify the impact of inaccuracies in the specification of atmospheric parameters on results obtained with the CO_2 slicing algorithm. In Figure 1, results reveal that the frequency of middle-level clouds (700-400 mb) decreases and higher clouds (< 400 mb) increases significantly, compared to the regular algorithm (solid), when a two degree bias is introduced into the temperature profile (dots). To a lesser degree, the use of adjusted surface radiances (hashed) forces the retrieved cloud top pressures toward a more bi-modal distribution, which is desirable for this data fusion technique, since pixels with cloud top pressures in the 700-400 mb range remain ambiguous in the final cloud top phase analysis of AVHRR data. However, it is necessary to examine whether these changes in cloud top pressure improve or degrade the final cloud top phase analysis.

Figure 1. Distribution of retrieved cloud top pressures from CO_2 slicing of HIRS/2 data for 4144 FOVs using the regular algorithm, regular algorithm with 2K bias, and a modified algorithm based upon adjusted surface radiances. Data correspond to the scene in Figure 2.

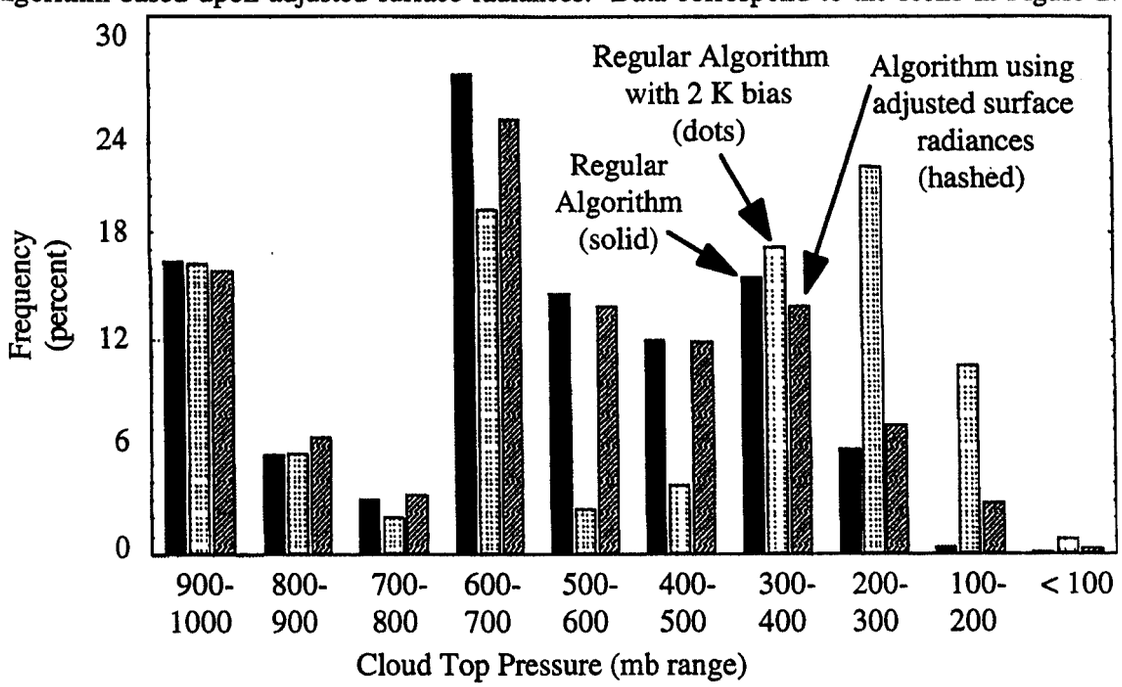

RESULTS

The value of using adjusted cloud-free radiances in the retrieval of cloud top pressures with HIRS data is demonstrated in the case study shown in Figure 2, a scene that has been used extensively to study the ability to detect and classify optically-thin cirrus clouds over diverse land backgrounds (Hutchison et al., 1997a; Hutchison et al., 1997b). The analysis area is approximately a 1000 km square and extends in the north-south direction from near Portland, Oregon to Los Angeles, California and from the border of Utah and Nevada to the 130 degree west meridian in the east-west direction. Panels A(1) and A(2) contain AVHRR channel 2 (0.9 μm) and channel 5 (12.0 μm) respectively. Thin cirrus clouds are present from the middle left-center through the upper-right of the scene while other cirrus clouds are seen across the lower part of the image. Lower-level water clouds are evident in the left half of the channel 2 image while cloud-free, snow-covered surfaces are seen along the right, especially in the mountainous terrain contained in most of the lower right quadrant. Manual ice and water cloud top phase analyses are shown in B(1) and B(2), respectively. Panels C(1) and C(2) show final cloud top phase analyses of the AVHRR imagery using cloud top pressures shown in Figure 1 for the regular CO_2 slicing algorithm

Figure 2. NOAA-12 AVHRR imagery collected at 1505 GMT on March 19, 1996.

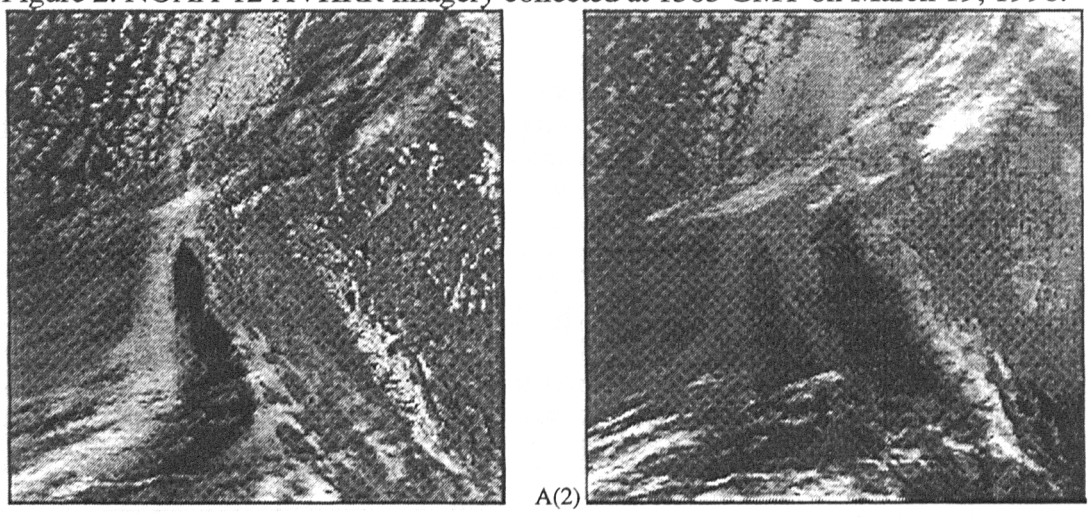

A(1) A(2)

Panel A. Highly reflective clouds are seen in AVHRR channel 2, A(1), while thin cirrus appear most evident in channel 5, A(2).

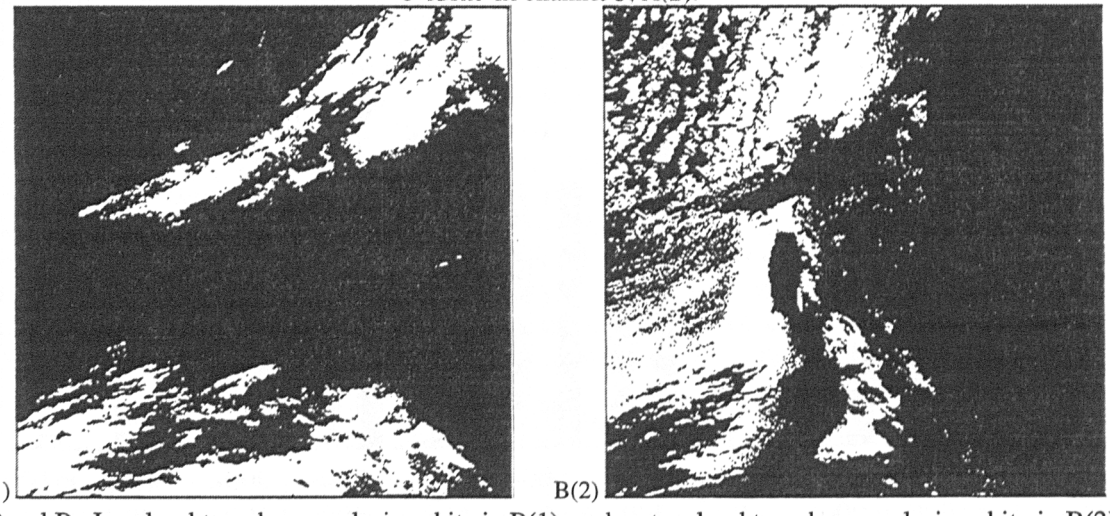

B(1) B(2)

Panel B. Ice cloud top phase analysis, white in B(1), and water cloud top phase analysis, white in B(2), created from the manual interpretation of all AVHRR multispectral images (Hutchison et al., 1997b).

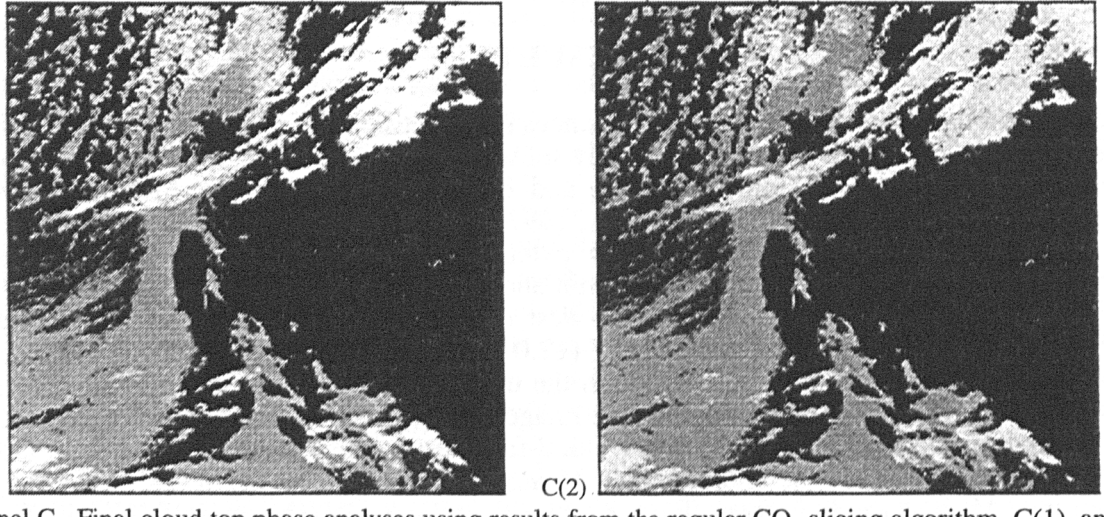

C(1) C(2)

Panel C. Final cloud top phase analyses using results from the regular CO_2 slicing algorithm, C(1), and adjusted surface radiances, C(2). Fewer misclassified water clouds are seen in top center of C(2).

and the adjusted surface radiances, respectively. In these analyses, ice clouds are lightest, water clouds are the middle gray shade, and cloud-free areas are black.

A comparison of results contained in Panel C(1) and Panels B(1) and B(2) of Figure 2 show the misclassification of numerous water clouds in the upper-center of the image. These misclassifications occur for two reasons. First, these pixels are detected by both the ice and water cloud bi-spectral tests which causes them to be classified as ambiguous in the AVHRR imagery. In addition, cloud top pressures from the CO_2 slicing of HIRS/2 data are between 700 and 400 mb, which causes them to remain classified as ambiguous and be interpreted as ice clouds in the final cloud top phase analysis (Hutchison et al., 1997a).

Similar results are shown in Panel C(2) of Figure 2 except that the cloud top pressures in this case were retrieved using the adjusted cloud-free radiances in the CO_2 slicing algorithm. In this case study, a relatively small, but significant, number of water clouds, that were misclassified by the regular CO_2 slicing algorithm, have been classified correctly in Panel C(2) because the retrieved cloud top pressures are now larger than 700 mb. This improvement is considered significant because the surface radiances were only adjusted over the ocean area, which is the location where the more accurate cloud top phase analyses occurred using results from the modified CO_2 slicing algorithm. Thus, the use of adjusted surface radiances, which forced the retrieved cloud top pressures toward a slightly more bi-modal distribution in Figure 1, improved the final cloud top phase analysis is an area where the largest number of misclassifications occurred with the regular CO_2 slicing algorithm.

CONCLUSIONS

Sensitivity studies have been completed and reveal that relatively small biases in temperature profiles used to calculate upwelling radiances can have a significant impact on retrieved cloud top pressures obtained with the CO_2 slicing of HIRS data. Erroneous cloud top pressures may result in misclassifications of cloud top phase when used in a new data fusion approach that merges the spectral signatures of clouds in AVHRR imagery with those from HIRS/2 sounder data. Thus, a modified approach is sought for retrieving cloud top pressures to reduce inaccuracies in upwelling radiance calculations by the application of cloud-free radiances into the CO_2 slicing technique. A comparison of results obtained with this modified cloud top pressure retrieval algorithm and the regular CO_2 slicing algorithm, against a manual interpretation of ice and water clouds in the AVHRR imagery, reveals that the new approach decreases the number of misclassifications in the final cloud top phase analysis of the AVHRR data. These initial results provide encouragement to further examine the use of 10.8-μm cloud-free radiances, obtained with the aid of an automated cloud, no cloud analysis of AVHRR imagery, in the analysis of infrared sounder data.

ACKNOWLEDGMENT

The authors gratefully acknowledge funding from the Advanced Technology Center of Lockheed Martin Missiles & Space that supported this project.

REFERENCES

Hutchison, K. D., Etherton, B. J., Topping, P. C., and A. H. L. Huang, 1997: "Cloud Top Phase Determination from the Fusion of Signatures in Daytime AVHRR Imagery and HIRS Data ," Int. J. Rem. Sens., **18**, pp. 3245-3262.

Hutchison, K. D., B. J. Etherton, and P. C. Topping, 1997: "Validation of automated cloud top phase algorithms: distinguishing between cirrus clouds and snow in a-priori analyses of AVHRR imagery," Opt. Eng., **36**, pp. 1727-1737.

P 2.13A COMBINING IMAGER AND SOUNDER DATA TO DERIVE CLOUD PRODUCTS

Dongsoo Kim
Cooperative Institute for Research in Environmental Sciences (CIRES)
University of Colorado/NOAA Forecast Systems Laboratory, Boulder, Colorado, USA

1. INTRODUCTION

The current series of operational environmental satellites carry instruments that are designed for the needs of specific users. For instance, the satellite imager is an instrument that scans rapidly with high horizontal resolution of interest to the weather forecaster. However, the satellite sounder instrument is used primarily by the numerical weather prediction (NWP) community. It has lower horizontal resolution than the imager but includes numerous spectral bands that allow retrieval of the vertical structure of the atmosphere (for general information, see Rao et al., 1990).

The Geostationary Operational Environmental Satellites (GOES) now carry both a 19-channel sounder, which is similar to polar orbiter's High-resolution Infrared Radiation Sounder (HIRS), and the 5-channel imager. The GOES satellites are situated at 75° E longitude (GOES-8) and 135° E longitude (GOES-9). The resolution of the imager for the infrared channel is 4 km and the resolution of the sounder is 8 km. The imager scans every 15 min and the sounder scans every hour. The addition of the sounder on the GOES platform is a significant improvement over the previous series (up to GOES-7). A more comprehensive discussion of upgrade in GOES-8/9 can be found in Menzel and Purdom (1994).

NOAA's Forecast Systems Laboratory (FSL) accesses GOES data in real-time and in a raw data format. Our primary purpose of combining both GOES imager and sounder data is to obtain a national-scale cloud analysis, and direct cloudy radiance assimilation to the Mesoscale Analysis and Prediction System (MAPS, Benjamin et al., 1998). Cloud variables include cloud fraction, cloud-top height, and cloud phase. With real-time data, processed satellite data can be ready when the assimilation cycle begins. This paper discusses some problems and challenges in combining spatially, temporally, and spectrally different imager and sounder data to extract cloud information, notably cloud fractional coverage and cloud-top height.

Author address: Dongsoo Kim, NOAA/ERL/FSL, 325 Broadway, R/E/FS1, Boulder, CO, 80303-3328, e-mail: dkim@fsl.noaa.gov

2. SAMPLE DATA

The data are sampled in the neighborhood of reference location (36.61° N latitude and 97.49° E longitude), where the cloud profiling radar is operating. The size of samples is about 22 for sounder, and 199 for imager, which covers ± 0.3° latitude and longitude coordinate. These data have been collected hourly at FSL since October of 1997. The observation time of the sounder and imager is 1-min before and 4-min after the hour respectively. If the satellite is in global scan mode, the imager data get collected 11-min before the hour. Therefore, the measurement time difference turns out to be between 5 and 10 minutes. This difference appears to be an insignificant error source between the two samples.

Figures 1a and 1b are hourly plots of the mean and standard deviation (vertical bar stands for ±1 standard deviation) of brightness temperature sounder 'band 8' and imager 'band 4' in the window channels near 11 μ. The larger vertical bar indicates cloudy samples.

3. HYPOTHESIS TESTING

One of the primary goals of this research is to investigate the feasibility using the higher resolution imager data to complement the lower resolution sounder data. First, we employ the statistical testing procedure. The first task is to determine statistically how similar or different the data are. The null hypothesis is that there is no difference in the sample mean between sets of sounder and imager data, while the alternative hypothesis is that there is difference;

$$H_o : \bar{X} - \bar{Y} = 0$$

$$H_1 : \bar{X} - \bar{Y} \neq 0.$$

To test the hypothesis we compute the test statistic, which is a modified T statistic defined by

$$T = \frac{\bar{X} - \bar{Y}}{\sqrt{s_x^2/n_x + s_y^2/n_y}} \qquad (1)$$

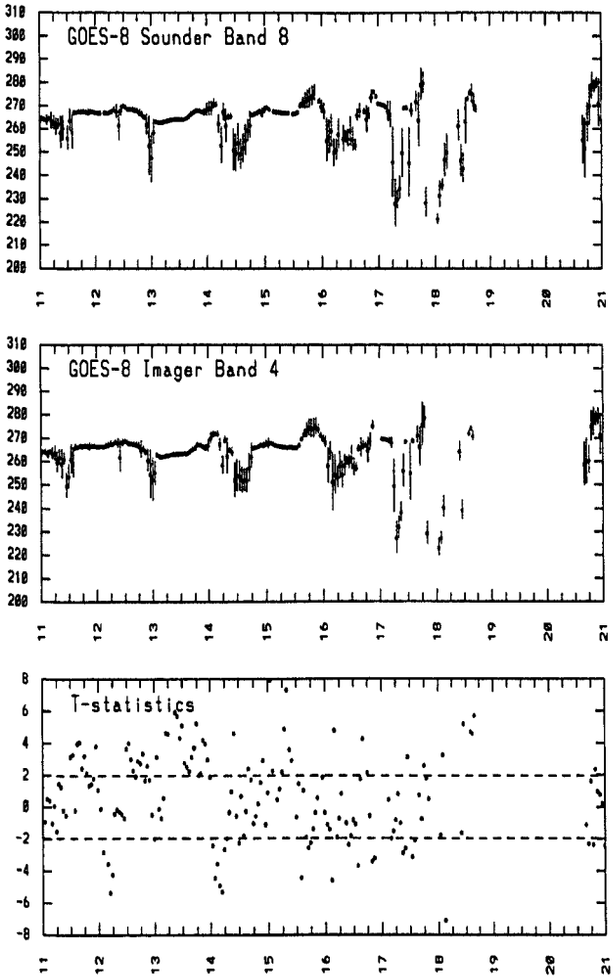

Fig. 1.a, top. The mean (circle) and standard deviation (vertical bar) of GOES-8 sounder 'band 8' brightness temperature for 11 - 20 January 1998. Fig. 1.b, middle. The same as Fig. 1.a except for GOES-8 imager 'band 4'. Fig. 1.c, bottom. The modified T-statistic, of which two horizontal dashed lines indicate ± 1.96.

where $\bar{X}$, $\bar{Y}$ are the sample means of the sounder and imager data respectively; s_x^2, s_y^2 are the sample variances of the sounder and imager; n_x, n_y are the number of degrees of freedom for the respective samples. If the computed T value is beyond a predetermined critical value, the null hypothesis is rejected. We approximate the critical value as the standardized normal score of ±1.96 for large samples.

The cases of rejected null hypothesis (i.e., imager samples and sounder samples were not from the same population) occurred most often when the observed data had the smallest variations. The small standard deviation cases may be thought to occur when the atmosphere is either clear or uniform cloud. The larger variation cases occur under partially cloudy conditions. In order not to be rejected in the hypothesis testing, the sample means have to be very close in the clear cases. Even though differences in the sample means are smaller than 0.5 $degK$ we can not assert that two samples are from the same population because standard deviations are also small. Yet, in the cloudy case, fractional cloud information from imager data can complement sounder data because the null hypothesis is not rejected.

4. CIMSS CLOUD PRODUCTS

Hourly GOES-derived cloud products are available from the Cooperative Institute of Meteorological Satellite Studies (CIMSS; anonymous ftp: rets.ssec.wisc.edu /pub/cldtxt8). The CIMSS cloud product is based on the CO_2 absorption technique using 3 x 3 sounder data (Menzel et al., 1997). The data included in the CIMSS products are observation time, latitude, longitude, cloud coverage, cloud-top pressure, cloud-top temperature, number of cloudy data out of maximum 9, minimum cloud-top pressure, maximum cloud-top pressure, and the standard deviation of cloud-top pressure.

5. FSL CLOUD PRODUCTS

FSL is developing a cloud product based on imager band 4 radiance data only. The algorithm employs the following steps: (1) Collect GOES-8 imager band 4 data for a specified domain (nominal number of data is 199), and arrange them for a relative frequency histogram. (2) Smooth the histogram to partition areas under peaks. The partitioned areas correspond to fractional coverage. Each fraction also has representative radiance value (see example in Kim and Nychka, 1998). (3) The forward model based on the Strow-Wolfe transmittance model (Personal communications with van Delst) computes imager band 4 radiance by using the NWP model first guess temperature and humidity profile and skin temperature. The first guess used here is the 1-h forecast of MAPS, and computed the radiance assumes clear sky. (4) All representative radiance values within samples are compared with computed radiances to calculate pressure levels of radiating levels. If the computed radiance of band 4 is not larger than that of the lowest radiating level by 3.5^oK, then the value of assigned cloud fraction is set to 1.

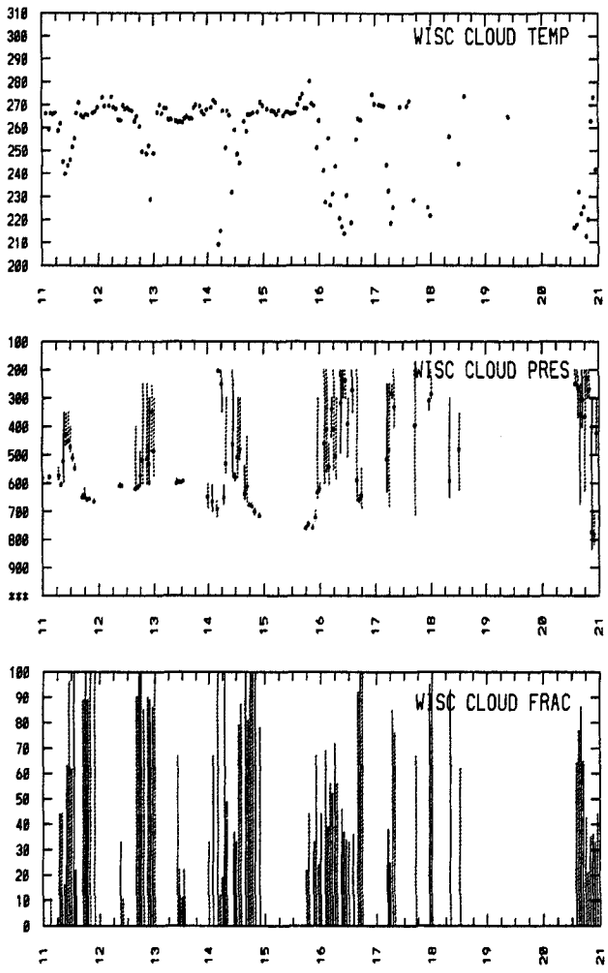

Fig. 2. The CIMSS cloud products during 11 - 20 January 1998. Fig. 2.a, top. Cloud-top brightness temperature. Fig. 2.b, middle. Cloud-top pressure. The bars indicate the spread between maximum and minimum pressures. Fig. 2.c, bottom. Fractional coverage of clouds.

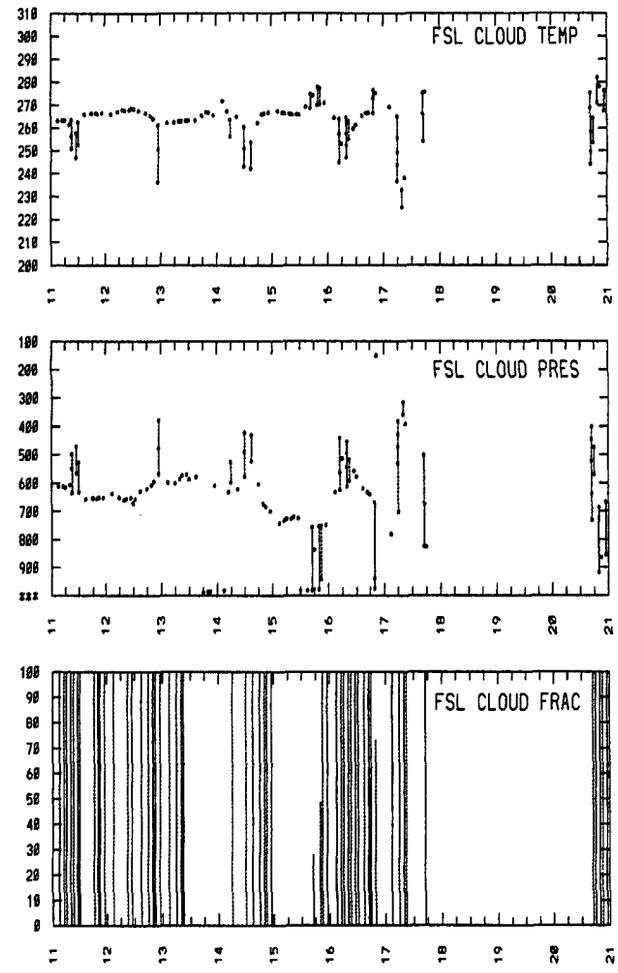

Fig. 3.a The FSL's experimental cloud products of cloud-top brightness temperatures during 11 - 20 January 1998. The small dots indicate multilevel clouds and the vertical bars connect minimum and maximum values. Fig. 3.b. The same as Fig. 3.a except cloud-top pressure. Fig. 3.c. The same as Fig. 3.a except cloud coverage.

Comparisons of CIMSS and FSL cloud products are interesting. In general, FSL cloud products depict smaller cloud-top variations because the imager data have been smoothed. The CIMSS cloud products, in particular the cloud fractional coverage, tend to be under-estimates. A close examination of CIMSS products during the period 11 - 20 January 1998 showed that CIMSS products reported 37 cases of overcast, of which 9 sounder data were declared as cloudy, but 25 cases were reported having less than 100 % of cloud coverage. It is prominent during 1900 - 2300 UTC 12 January, and 1400 - 2000 UTC 20 January (see Fig. 2.c). This lack of consistency needs to be understood. On the other hand, cloud-top pressures of both CIMSS and MAPS around 1500 - 2300 UTC 11 January were very close.

6. SUMMARY AND PLAN

The combining of GOES sounder and imager data is a logical extension of earlier works by Kim et al., 1997, where sounder and imager data from polar orbiter were combined to derive cloud parameters. The GOES combination will require additional study because there is considerable difficulty in matching the sounder and imager data due to the scanning schedule. However, the preliminary re-

sults for the comparisons between cloud products produced from the sounder only (CIMSS product) and the imager only (FSL experimental product) showed remarkable similarity for the low-level cloud top pressures (about 600 hPa). Even though the limited number of channels in the imager data does not allow the vertical cloud distribution to be used to its full potential, the better horizontal resolution of the imager data can improve the quality of the sounder data if the two sources are combined correctly. The success of the combination depends on how similar the data are from two sources. It was shown earlier that the combination is more beneficial during cloudy situations.

FSL is currently developing a method to assimilate GOES radiance data directly into the model. The method will use GOES sounder data complemented by information from the imager. While this study used only one grid box ($\pm$ 0.3^o latitude and longitude grid), the same procedure of deriving cloud product from imager data will be used in the current 40-km MAPS model domain. The first experiment will be to ingest area mean sounder data.

7. ACKNOWLEDGMENTS

The author benefitted from discussions with Anthony Schreiner, Robert Aune and Timothy Schmit. Thanks are extended to Paul van Delst who provided latest GOES forward model based on Strow-Wolfe, and to Barry Schwartz for the scientific review of this paper and to Nita Fullerton for her editorial review.

8. REFERENCES

Benjamin, S. G., J. M. Brown, K. J. Brundage, , B. E. Schwartz, T. G. Smirnova, T. L. Smith, L. L. Morone, and G. J. Dimego, 1998: The operational RUC-2. *16th Conference on Weather Analysis and Forecasting*, Phoenix, Arizona, AMS.

Kim D., B. Stankov and K. P. Moran, 1997: Evaluation of multilevel cloud parameters with cloud profiling radar. To be published in the preprint of the *Ninth International TOVS Study Conference*, Igls, Austria.

Kim, D. and D. Nychka, 1998: Comparisons of density smoothers to combine satellite imager and sounder data. *14th Conf. on Probability and Statistics in Atmospheric Sciences.* 12-16 January 1998, Phoenix, Arizona.

Menzel, P. and J. Purdom, 1994: Introducing GOES-I: The first of a new generation of geostationary operational environmental satellites. *Bull. Amer. Meteor. Soc.*,**75**, 757-781.

Menzel, P., F. C. Holt, T. J. Schmit, R. M. Aune, A. J. Schreiner, G. S. Wade, G. P. Ellrod and D. G. Gray, 1997: Application of GOES-8/9 soundings to weather forecasting and nowcasting. Submitted to *Bull. Amer. Meteor. Soc.*.

Rao, P., S. Holmes, R. Anderson, J. Winston, and P. Lehr, 1990: *Weather Satellites: Systems, Data, and Environmental Applications.* American Meteorological Society, 503 pp.

P2.14b COMBINED SATELLITE- AND SURFACE-BASED OBSERVATIONS OF CLOUDS

Bryan C. Weare*
Atmospheric Science Program
University of California, Davis

1. INTRODUCTION

A new method for combining satellite and surface-based cloud observations into a self-consistent three-dimensional field is presented. This method derives the probabilities of the possible cloud states which are most consistent with all of the observations and assumptions concerning the nature and relative uncertainties of the observations. It is applied to a three layer atmosphere using monthly satellite- and surface-based cloud observations.

2. BASIC METHODOLOGY

This paper will depart from the usual convention of looking at cloud vertical structure in terms of an "overlap assumption," but will instead define a three-dimensional cloud system in terms of the probabilities of all possible cloudiness configurations. For instance, one can define all of the possible cloud configurations in a **three-layer atmosphere** by eight classes illustrated below

TABLE 1 Structure of each cloud probability class in a three-layer atmosphere

high	x	x	x	x				
middle		x	x		x	x		
low			x	x		x	x	
class	p_1	p_2	p_3	p_4	p_5	p_6	p_7	p_8

Using the above definition a set of probabilities $\mathbf{p}=(p_1, p_2, \ldots)$ can be used to describe any "observation" such that

$$A \cdot \mathbf{p} = \mathbf{n} \qquad (1)$$

where $\mathbf{n}$ is any combination of surface and satellite observations, and A is a known matrix, which need not be square. In general this equation is underconstrained. However, it can be "solved" for $\mathbf{p}$ given a first guess $\mathbf{p_o}$ if:

1) the requirement that the desired solution fit as well as possible the data, and
2) one can assume that the desired x_i's ($x_i = p_i - p_{oi}$) are the smallest possible corrections.

Under these conditions the best choices for the x_i's are given by

$$\mathbf{x} = W_e^{-1} \cdot A^T \cdot [(A \cdot W_e^{-1} \cdot A^T) + W_\sigma]^{-1} \cdot (\mathbf{n}-\mathbf{n_o}) \qquad (2)$$

where W_e and W_σ are diagonal matrices of the squared uncertainties of the cloud state probabilities and observations, respectively, and $\mathbf{n_o}$ is based upon (1) with the first guess of $\mathbf{p_o}$ (Menke, 1984; Isemer et al., 1989).

3. SENSITIVITY ANALYSIS

One set of available approximately coincident observations to which to apply this method are the monthly surface-based estimates of total cloud and low cloud cover summarized by Hahn et al.(H; 1996) and the satellite-based estimates of low, middle and high cloud amounts as seen from above developed by the International Satellite Cloud Climatology Project (ISCCP; Rossow and Schiffer, 1991). Various combinations of the first guess and uncertainties were tested. Results for a representative point are shown in Fig. 1, which illustrates reconstructed values of observations using Eqn. 1 and the results from Eqn. 2.

FIGURE 1 Differences between the reconstructed and original cloud observations

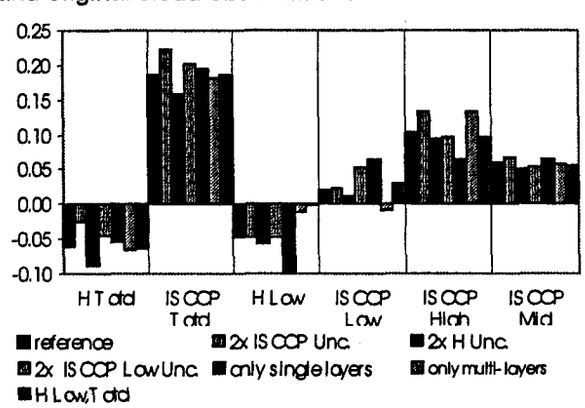

Based upon the full array of sensitivity results and the general conviction that adequately sampled surface-based observations represent the most unbiased initial estimates of the true cloud state of the atmosphere, then the most appropriate choices for $\mathbf{p_o}$ and W_s correspond to the choices labeled *H Total,Low.*, which represents a first guess based upon surface-derived low cloud data and approximately equal uncertainties for the satellite and surface data.

*Corresponding author address: Bryan C. Weare, Dept. of L.A.W.R., Univ. of California, Davis, CA 95616; e-mail: bcweare @ucdavis.edu

4. MEAN HIGH CLOUD

Fig. 2 shows the percent differences between the reconstructed and the directly observed ISCCP C2 annual mean high cloud for the years 1984-1988. Areas with no data do have no surface observations with which to make a reconstruction. The method leads to increases in high cover of between 0.04 and 0.12 over most of the globe. The largest changes are in the relatively clear subtropical high zones, where the satellite observations appear to be 'missing' higher cloud. Overall, the high cloud adjustments agree with Jin et al. (1996) and Liao et al. (1995), who suggest that ISCCP high cloud observations underestimate the 'true' values by about a third. However, the earlier works do not readily explain the present result suggesting large numbers of missing high cloud in the subtropical high zones.

FIGURE 2 Difference between annual mean reconstructed and original ISCCP high cloud cover

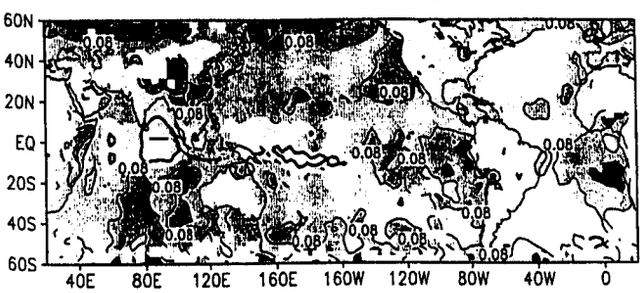

Fig. 3 shows the intra-annual (only long term annual means are removed) empirical orthogonal functions of high cloud directly from the ISCCP analysis and from the current reconstruction for the period 1984-1988. The associated time coefficients (not shown) both have strong annual cycles with nearly equal amplitudes. The patterns of variation shown in Fig. 3 a and b are quite similar except that the amplitude of the changes in the original ISCCP data are nearly everywhere larger than those of the reconstructions. Thus, although the reconstructed mean high cloud amounts are larger than the original values, the seasonal variability is smaller. This could have important consequences in global climate modeling.

Other variables such as low cloud amount seen either by satellites or surface observers have been investigated. Also, using this methodology it is possible to estimate from the observations important parameters which are not directly observed, such as the fraction of clouds which occupy only one layer or measures of cloud overlap.

FIGURE 3 Empirical functions of a) ISCCP high cloud and b) reconstructed high cloud amounts

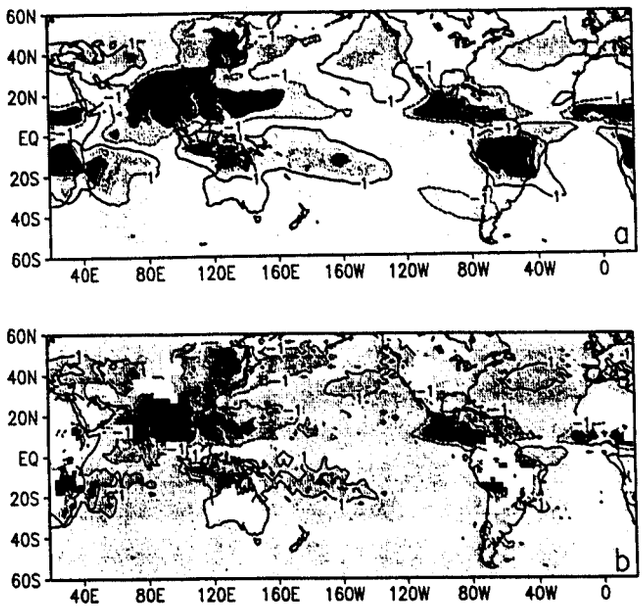

5. REFERENCES

Hahn, C. J. , S.G. Warren and J. London, 1996: *Edited Synoptic Cloud Reports from Ships and Land Stations over the Globe, 1982-1991*. Tech. Report, NDP026B, Carbon Dioxide Information Analysis Center, Oak Ridge National Laboratory, Oak Ridge, TN

Isemer, H.-J., J. Willebrand and L. Hasse, 1989: Fine adjustment of large scale air-sea energy flux parameterizations by direct estimates of ocean heat transport. *J. Climate*, **2**, 1173-1184.

Jin, Y., W.B. Rossow and D.P. Wylie, 1996: Comparison of the climatologies of high-level clouds from HIRS and ISCCP. *J. Climate* , **9**, 2850-2879.

Liao, X., W.B. Rossow and D. Rind, 1995: Comparisons between SAGE II and ISCCP high-level clouds. 1. Global and zonal mean cloud amounts. *J. Geophys. Res.*, **100**, 1121-1135

Menke, W., 1984: *Geophysical Data Analysis: Discrete Inverse Theory*. Academic Press, Orlando FL, 260pp.

Rossow, W.L. and R.A. Schiffer, 1991: ISCCP cloud data products. *Bull. Amer. Meteor. Soc.*, **72**, 2-21.

P2.15A

SIMULTANEOUS OBSERVATION OF SNOWING CLOUDS BY MULTICHANNEL AIRBORNE MICROWAVE RADIOMETER AND X-BAND DOPPLER RADAR

Masaki Katsumata*, Hiroshi Uyeda*, Koyuru Iwanami** and Guoshung Liu***

* Division of Earth and Planetary Sciences, Graduate School of Science, Hokkaido University, Japan.
** Nagaoka Institute of Snow and Ice Studies, National Research Institute for Earth Science and Disaster Prevention (NIED), Japan.
*** Department of Aerospace Engineering Sciences, University of Colorado, Colorado, U.S.

1. INTRODUCTION

To retrieve the cloudphysical parameters from upwelling microwave radiation, it is important to evaluate the effects of the snowing layer aloft. Scattering, especially, is a key factor in the use of higher frequencies, which are suited to retrieving higher resolution data. However, few studies have been done to evaluate the effects of the snowing layer alone on microwave radiation. Additionally, the estimation of the suitable vertical profile of the hydrometeors is needed to evaluate the amounts of the hydrometeors from the data of microwave radiometer.

To contribute to these areas, we investigate the characteristics of microwave radiation through a snow cloud, in which the whole layer is colder than 0C, by the simultaneous observation of the airborne microwave radiometer and Doppler radar. Radiative transfer simulation is also used to validate the observational results.

2. DATA

The Airborne Microwave Radiometer (AMR) of NASDA, Japan, was developed for the validation and the pre-launch observation of the Advanced Microwave Scanning Radiometer (AMSR), aboard the Advanced Earth Observation Satellite - II (ADEOS-II), which will be launched in 1999. The channels are designed the same as AMSR/ADEOS-II: horizontally and vertically polarized channels for six frequencies from 6.925 to 89.0 GHz. The antenna horns of all channels are fixed at the nadir angle of 53.1 degrees to the back of the aircraft. The data are obtained on the line trailing the flight track of the aircraft. The EFOV depends on the altitude of the aircraft. The TB's on two higher frequencies (36.5 and 89.0 GHz) are used, because the data on these channels are sensitive to emission from little amount of cloud water in snow clouds, or scattering caused by cloud ice and snow.

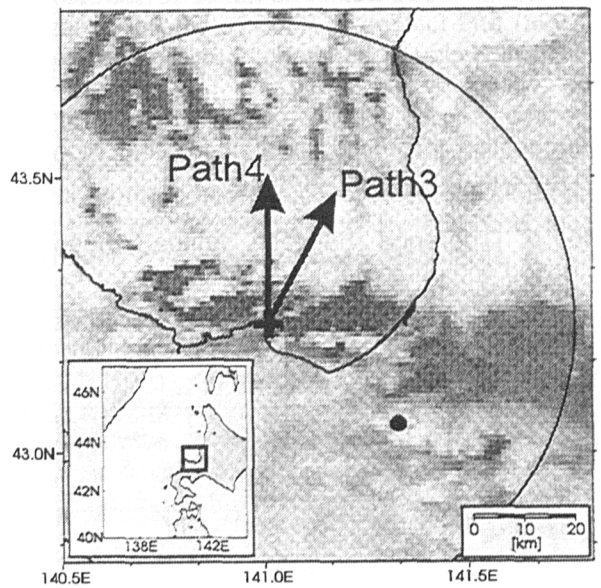

Fig. 1: AVHRR/NOAA infrared image at 0354GMT on February 16, 1996. The circle and cross show the observation range and location of NIED radar. The dot shows the location of the aerological observation site of Sapporo. The arrows show the direction of Path3 and Path4 of AMR observation.

For these frequencies, we introduce the polarization ratio P, $P_\lambda = T_{B\lambda H} / T_{B\lambda V}$, as determined by Katsumata et al. (1998). This value increases in response to scattering and emissions, thus the value indicates the existence of cloud and precipitation particles.

In addition, X-band Doppler radar of National Institute of Earth Science and Disaster Prevention (NIED), Japan, obtained the reflectivity and Doppler Velocity for the 60 km range. The observation area is shown in Fig. 1.

* *Corresponding author address*: Masaki Katsumata, Graduate School of Science, Hokkaido Univ., Sapporo 060-0810 JAPAN;
e-mail: katsu@geophys.hokudai.ac.jp

3. OBSERVATIONAL RESULTS

The observation was carried out in the winter of 1995/1996 and 1996/1997 for three events. Among them, the case on February 16, 1996, shows characteristic results. In this case, the typical streak clouds appeared on the Sea of Japan with the outbreak of the winter monsoon from the Eurasian Continent. The observed system was one of the streaks, which extended across the observation area from west to east. As shown in Fig. 1, the width of the cloud is about 10 km, and the maximum height of the cloud top and radar echo top were 3.5 km and 2.5 km, respectively. The aircraft flew over the system with the altitude of 3.8 km. The altitude of the aircraft force the size of the EFOV about 1.5 km at sea surface.

In the streak cloud, convective cells were aligned along the streak clouds, and moved west with the speed of about 15 m/s. Among them, two convective cells were observed in Path 3 and Path 4 for the direction shown in Fig. 1, among five flight paths.

The vertical cross sections of radar data and corresponding AMR data are shown in Fig. 2 for Path 4. On the radar data, the reflectivity core is located in the upper part of the echo at a distance of 11 km from radar. Around the echo core, the Doppler velocity field shows a horizontal convergence below the height of 1 km, and a horizontal divergence above the height, as shown by arrows in Fig. 2d. This result corresponds to the characteristics of a convective cell in the developing stage.

In this cell, the maximum drop of T_{B89V} was observed in the radiation through the echo core. (The broken line indicates the point of maximum drop in Figs. 2ab, or the ray path of this point in Fig. 2c.) At this point, T_{B89V} dropped about 8 K from the value over the cloud-free area. This T_{B89V} drop is recognized as the result of a large extinction by scattering, which was caused by a large amount of precipitation particles, shown as the echo core of 25 dBZ in the reflectivity field. In contrast, both T_{B89V} and P_{89} show the highest values at the distance of 11 km (indicated by dotted line), just beside the maximum drop of T_{B89V}.

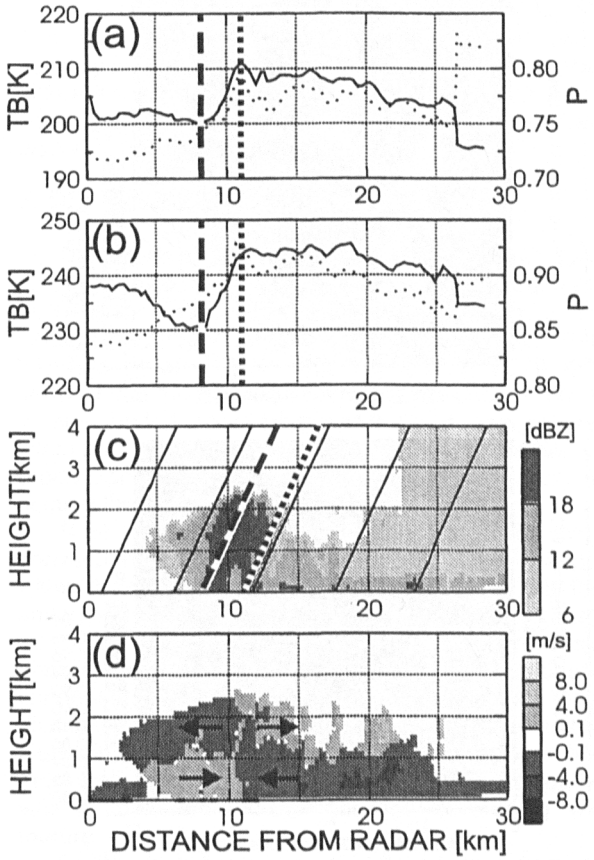

Fig. 2: The data on Path 4. (a) T_{B36V} (thin solid line) and P_{36} (thin dotted line), (b) T_{B89V} (thin solid line) and P_{89} (thin dotted line), (c) radar reflectivity, and (d) Doppler velocity. AMR data, (a) and (b), are plotted on the point where the antenna horn pointed at surface level, and ray paths every 1 minute are shown as solid lines in (c). See article for thick broken and thick dotted lines.

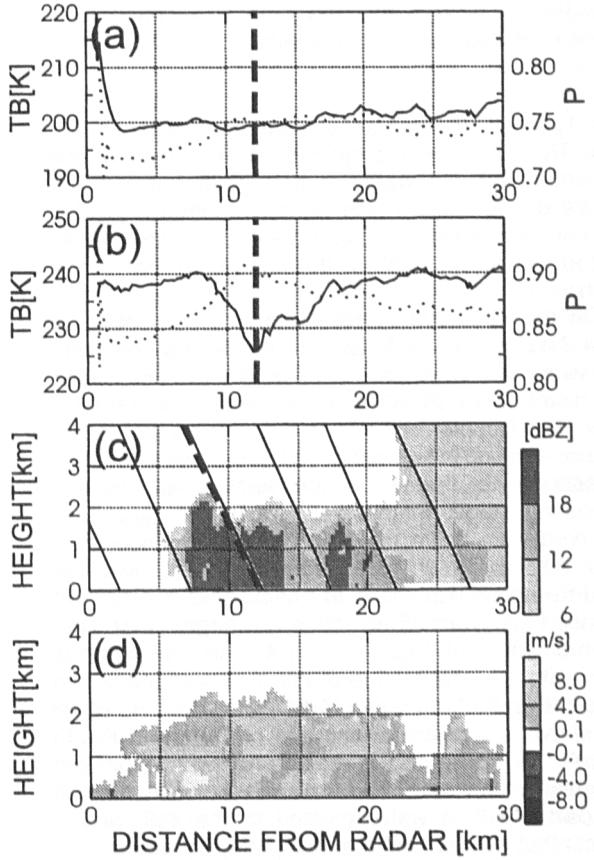

Fig. 3: Same as Fig. 2, but for Path3.

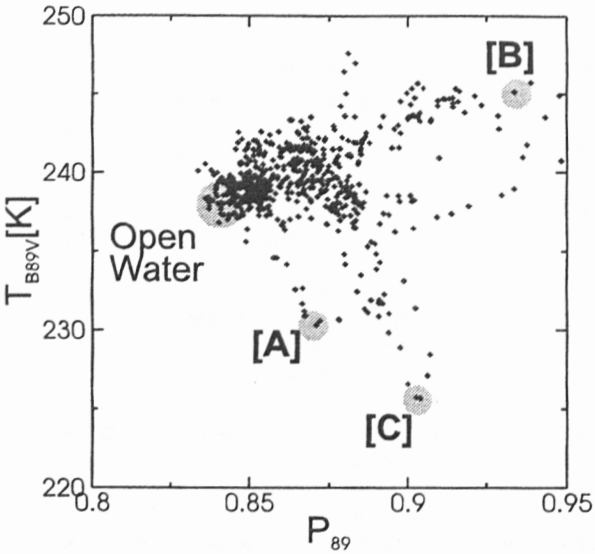

Fig. 4: Scatter diagram of observed T_{B89V} and P_{89} in the all paths for the observation on February 16, 1996. The data on land, and the data with large variance in incident angles (larger than 1.5 degree from standard value) are excluded. The marked points are observed value at the points of (A) minimum T_{B89V} on Path 4, (B) maximum P_{89} on Path 4, and (C) minimum T_{B89V} on Path 3, respectively.

Here T_{B36V} and P_{36} also show the highest values in the path. This could be recognized as the signal of the existence of liquid water in a large amount. Such signals do not exist in the nearer (southern) part of this convective cell. It also means that liquid water existed just in the north of the echo core, not in the south.

On the other hand, the vertical cross section of radar data on Path 3 (Figs. 3ab) shows that the echo core was in the lower part of the convective cell, which was distributed from 8 km to 13 km in distance from radar. The Doppler velocity field shows no significant pattern around the echo. These characteristics correspond to that of a convective cell in the dissipating stage. In this cell, a drop of T_{B89V} was observed from 8 km to 18 km in the distance from radar. The maximum drop from the value over the cloud-free area was 12 K at the point of the broken line in Figs. 3ab. The value is larger than the maximum drop of T_{B89V} in Path 4. This corresponds better with the larger value of the observed maximum reflectivity in Path 3 than in Path 4. However, no other part shows a significant increase of T_{B89V} and P_{89} in Path 4. The T_{B36V} and P_{36} also show no significant increases in this path. This means that no significant rich part of cloud water existed in the cell, and it reflects that the cell is in the dissipating stage.

These data were the most significant part among the effective data in the case. In Fig. 4, the data of (A) minimum T_{B89V} part in the echo core in the developing stage (Path 4) and (C) minimum T_{B89V} in the echo core in the dissipating stage (Path 3) are significant in low T_{B89V}. At the same time, the amount of depressions of T_{B89V} in these parts correspond to the radar reflectivity; stronger reflectivity and larger depression of T_{B89V} at (A) than (B). This suggests that the T_{B89V} well reflect the amount of precipitation particles.

In contrast, (B) maximum P_{89} in the developing stage (Path 4) is significant in high T_{B89V} and high P_{89}. This result well reflects the existence of a significantly high amount of cloud water. This result, however, could not be directly validated by other observational data. Thus the radiative transfer simulation was performed to validate these cloud water signals.

4. RADIATIVE TRANSFER SIMULATION

In the radiative transfer simulation (RTS), the improved scheme based on Liu et al. (1993) was used. The vertical profile of temperature, pressure and relative humidity was adopted from the aerological observation at Sapporo (The location is shown in Fig. 1.) at 0000GMT. The geometrical thickness of each layer was set to 0.25 km below the cloud top, and to 1.00 km above the cloud top.

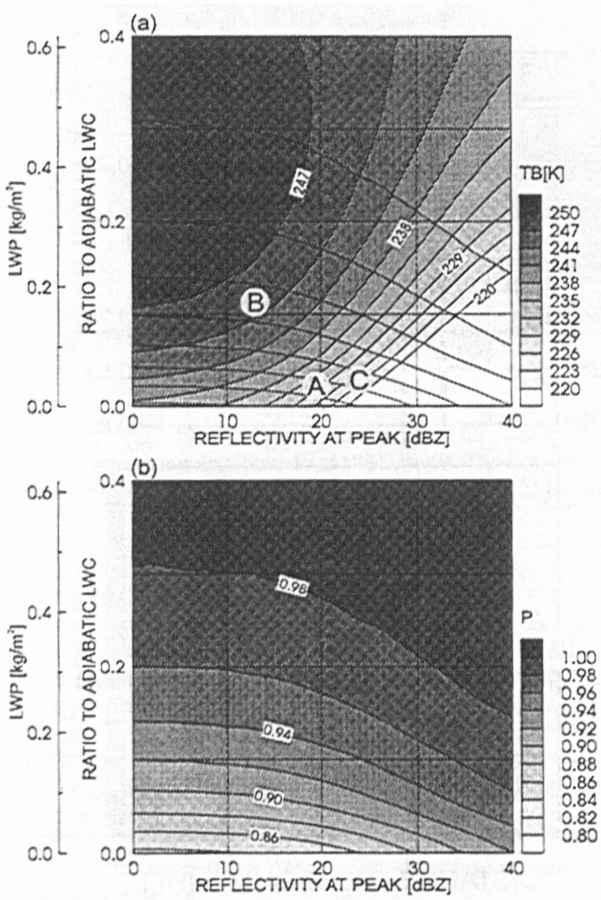

Fig. 5: Results of radiative transfer simulation on 89-GHz channels using the aerological profile above Sapporo at 00GMT on February 16, 1996. The variation of (a) T_{B89V} and (b) P_{89} with the variation in the amount of liquid water and amount of precipitation are shown. The contour of P_{89} is superimposed in (a). The observed T_{B89V} and P_{89} at the three points, (A), (B) and (C) in Fig. 4, are plotted in (a).

Under the conditions described above, the two hydrometeors, the liquid water content (LWC) and the amount of snow, were varied to simulate the variation of TB's. The LWC of each layer was determined by varying the ratio to the adiabatic LWC, by lifting air parcel with 70 % of relative humidity. The amount of snow was converted from the idealized profile of equivalent radar reflectivity; the maximum reflectivity was at 2.50 km, while the reflectivity was 0 dBZ at the surface and 3.00 km. Equivalent radar reflectivity was converted to snow amount by the method of Sekhon and Srivastava (1970).

The results of 89-GHz channels are shown in Fig. 5. In the figure, T_{B89V} varies with the change of both liquid water path (LWP) and precipitation amount. On the other hand, P_{89} principally increases with the increase of LWP, and the effect of precipitation is relatively smaller than in T_{B89V}. These results allow us to recognize that the part of high P_{89} with high T_{B89V} contains a relatively large amount of cloud water, and low T_{B89V} with high P_{89} part contains a large amount of precipitation.

The three significant values on AMR data are projected in Fig. 5. The corresponding LWP values are (A) 0.03 kg/m^2, (B) 0.18 kg/m^2 and (C) 0.05 kg/m^2. These values show a significant difference in LWP, not only in the raw observed data: T_{B89V} and P_{89}. This difference supports that the part with a lot of liquid water and the part with a lot of snow could be distinguished by using T_{B89V} and P_{89}.

5. DISCUSSION

The retrieved LWP at the highest P_{89} and T_{B89V} part in developing cloud, (B), corresponds to only 12% of adiabatic LWP. This ratio does not seem to be caused by subgrid structure within the EFOV. Both Yamada et al. (1994) and Yamada et al. (1997) showed that the horizontal extent of the updraft region in an isolated convective snow cloud was several kilometers. This implies that the horizontal scale of production area of cloud water is large enough to occupy the EFOV.

Thus, the low ratio seems to reflect the high conversion rate from cloud water to snow and graupel within the cell. Murakami et al. (1994) showed that the snow clouds in the mature stage included less than 10 % of LWC with adiabatic condensation, while almost the same amount of LWC with adiabatic condensation existed in the developing stage. They discussed that this small amount of LWC reflected the high conversion rate from liquid water to ice particles. This also suggests that the convective cell at path4 was in the middle stage between developing and mature.

On the other hand, the equivalent radar reflectivity in the RTS from AMR data are lower than the observed reflectivity by NIED radar. This implies that the assumed vertical profile, or the variation on the form of precipitation particles, needs improvement to evaluate the amount of hydrometeors more precisely.

6. CONCLUSIONS

The AMR observation shows that it is possible to use the 89-GHz channel data to evaluate the amounts of the cloud water and the precipitation in snow clouds in high resolution. In addition, the distribution could determine the stage of the development and the structure of the convection. This could be applicable in determining the vertical distribution of the hydrometeors, which is applicable to the precise evaluation of the amount of the hydrometeors.

< ACKNOWLEDGMENT >

The authors would thank to Dr. K. Imaoka, NASDA/EORC, for the provision of the AMR data.

This study is partly supported by JSPS Research Fellowships for Young Scientists.

< REFERENCES >

Katsumata, M., H. Uyeda and K. Kikuchi, 1998: Characteristics of a cloud band off the west coast of Hokkaido Island, Japan, as determined from AVHRR/NOAA and SSM/I data. *J. Meteor. Soc. Japan*, **76**, in press.

Liu, G. and J. A. Curry, 1993: Determination of characteristic features of cloud liquid water from satellite microwave measurements. *J. Geophys. Res.*, **98**, 5069-5092.

Murakami, M., T. Matsuo, H. Mizuno and Y. Yamada, 1994: Mesoscale and microscale structures of snow clouds over the Sea of Japan. Part I: Evolution of microphysical structures in short-lived convective snow clouds. *J. Meteor. Soc. Japan*, **72**, 671-694.

Sekhon, R. S., and R. C. Srivastava, 1970: Snow size spectra and radar reflectivity. *J. Atmos. Sci.*, **27**, 299-307.

Yamada, H., H. Uyeda, K. Kikuchi, M. Maki and K. Iwanami, 1997: Generation of downdraft outflow from convective snow clouds. *Proc. 28th Conf. Radar Meteor.*, 481-482.

Yamada, Y., T. Matsuo, M. Murakami, H. Mizuno and K. Iwanami, 1994: Mesoscale and microscale structures of snow clouds over the Sea of Japan. Part II: Time change in airflow structures in isolated snow clouds derived from dual-Doppler radar observations — A case study —. *J. Meteor. Soc. Japan*, **72**, 695-707.

P2.16B RETRIEVAL OF CIRRUS MICROPHYSICAL AND BULK PROPERTIES USING RADIANCE DATA FROM THE ALONG TRACK SCANNING RADIOMETER (ATSR-2)

Anthony J. Baran*
U.K. Meteorological Office

Philip D. Watts
Rutherford Appleton Laboratory

Peter N. Francis
Meteorological Research Flight

1. INTRODUCTION

The importance of cirrus to the earth-radiation balance is now well established. However, there is still a lack of information regarding tropical cirrus microphysical (i.e., most common habits, crystal size) and bulk (i.e., optical depth and ice water path) properties. The current cirrus parameterisations that are used in climate models can only be improved through global observations of these basic properties. In this paper we show how such important information can be derived through the use of radiance data obtained from a dual-viewing radiometer (ATSR-2).

The ATSR-2 instrument onboard the European Remote Sensing Satellite (ERS-2) was launched during April 1995. It has channels located at 0.55, 0.66. 0.865, 1.6, 3.7, 10.8 and 11.9 μm each having a near-nadir and 55° forward view. The application of ATSR-2 radiance data to retrieval of most common shape, crystal size, optical depth and estimation of ice water path is described in Baran et al. (1996), Baran (1998a) and Baran et al. (1998b). A description of the retrieval scheme itself can be found in Watts (1995) and Watts (1996).

In this paper we concentrate on the importance of crystal geometry to retrieval of microphysical and bulk properties at solar wavelengths. We also compare retrievals of extinction optical depth at 10.8 μm using ATSR-2 data with retrievals of optical depth made at 0.87 μm. The solar measurements were made with the Met Office airborne SAFIRE (Scanning Airborne Filter Radiometer Instrument) onboard the C-130 aircraft. The SAFIRE instrument is very similar to ATSR-2 with regard to dual-views and channel locations though SAFIRE has extra channels located at 2.2 μm and 8.55 μm.

*Corresponding author address: Anthony J. Baran, Meteorological Office, Satellite Soundings, Room 339, Bracknell, Berkshire, RG12 2SZ, UK; email: ajbaran@meto.gov.uk

2. CRYSTAL SIZE AND SHAPE

The problem encountered by single view instruments in determining crystal size is compounded by not knowing which crystal habit to assume for the forward model. Such retrievals often require a-priori knowledge of crystal habit and/or size. However, ATSR-2 has an extra degree of freedom, i.e. a dual-view capability, as well as channels situated at 0.87 and 1.6 μm. It should be noted that ATSR-1/2 are the only space based instruments with a 1.6 μm channel currently in use. The extra degree of freedom given by ATSR-2 could be used to determine crystal shape and then size as shown by Baran et al. (1998a). Having retrieved the crystal habit using the dual-view at 0.87 μm the appropriate phase function can be used at 1.6 μm to retrieve the crystal size. Although this size retrieval was initially used by Foot (1988), the problem of an appropriate phase function still remains. Watts and Baran (1996) showed that at least for backscattering the Macke (1993) polycrystal phase function seems to dominate in the tropics, other more simple shapes such as "pristine" hexagonal columns and hexagonal plates were unable to fit the reflectance data at 0.87 μm.

Fig. 1 shows a typical case of tropical anvil cirrus using the 0.87 μm ATSR-2 data. The case is enclosed by a boxed area, this indicates from where the data presented in the next few sections originate. This case is a good example of a tropical convective system, and it is a

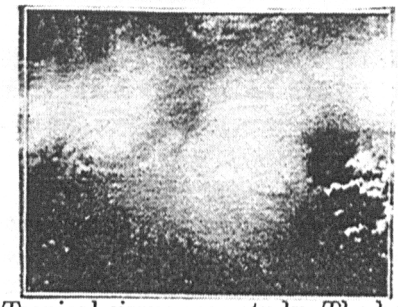

Figure 1: Tropical cirrus case study. The box indicates from where the data used in the following figures originate.

typical representation of the tropics. Note on either side of the box two large convective systems which are connected by semi-transparent cirrus. There is little evidence of underlying water cloud. Such a system provides a good test of the retrieval scheme. Reflectance data (0.87 μm) from the boxed region shown in Fig. 1 is shown in Fig. 2. The figure shows that for each of the major habits now represented in the retrieval scheme (hexagonal columns, hexagonal plates, 6-branched bullet-rosettes, and polycrystals) how well they fit to the dual-sampled reflectance data. It is common practice to assume hexagonal columns or plates in retrieval schemes but as can be seen from the figure these shapes do not fit the data. However, more complex shapes such as polycrystals and bullet -rosettes better fit the reflectance data, though bullet-rosettes do not fit the region representing lower optical depths. In general from Fig. 2 the best fit is the polycrystal. This fitting to the dual-sampled data by the polycrystal is typical throughout the tropics (Watts and Baran (1996)).

Having obtained what we believe to be the dominating crystal habit we can now apply this phase function to obtain crystal size (in terms of maximum crystal dimension) and these retrievals are shown in Fig. 3 using (a) polycrystal and (b) hexagonal column for comparison. The size is plotted as a function of optical depth. From Fig. 3 it is apparent that if hexagonal columns were assumed for the boxed region shown in Fig. 1 then the retrieved size would at most be about half that retrieved using the polycrystal phase function. The reason for this is due to the large asymmetry parameter (typically 0.80-0.85 at visible wavelengths) for hexagonal columns requiring smaller crystals to fit the 1.6 μm reflectance data. However, polycrystals

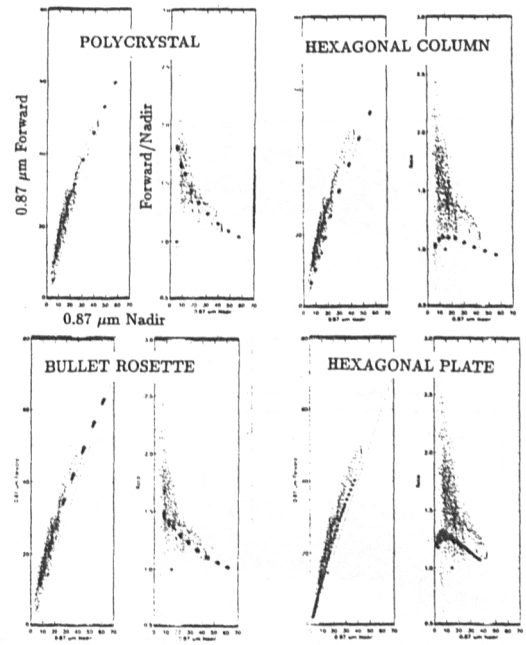

Figure 2: Identification of most common habit. Polycrystal, hexagonal column, bullet-rosette and hexagonal plate. The figure indicates the polycrystal as being the most common habit. The points on the figure indicate simulations using the different phase functions.

have lower asymmetery parameters (0.74 for visible wavelengths) thus requiring larger crystals to fit the same data. As to whether real ice crystals have such low asymmetry parameters is yet to be determined. Though it is clear from the figure that assumed shape is very important and will determine retrieval of crystal size and optical depth. Work done using airborne data at solar wavelengths (Francis et al. (1997)) and at infrared wavelengths (Baran et al. (1998c)) also suggest that particle geometry is the first order effect. It is also clear from Fig. 3 that the distribution of size as a function of optical depth represents the range in penetration depth at 1.6 μm. The penetration optical depth at 1.6 μm is shown in Fig. 4 assuming the polycrystal with the symbols representing different size gradients (size vs height). From the figure at most the penetration optical depth is around 1 this translates into a penetration distance of about 400 m–2.5 km depending on assumed crystal size distribution function. Since ATSR-2 is dual viewing this penetration depth maybe suitable to retrieve a coarse vertical size profile.

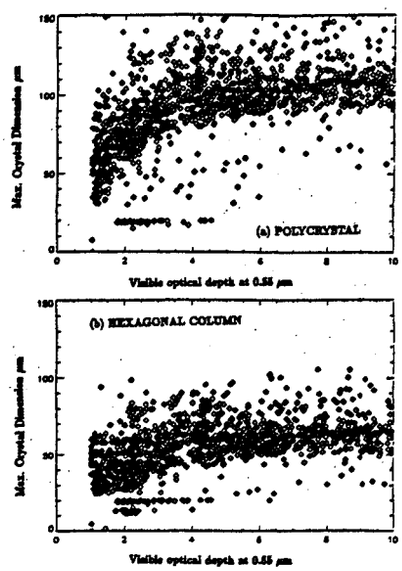

Figure 3: Retrieval of crystal size using the ATSR-2 1.6 μm channel. (a) Retrieved size using polycrystal and (b) hexagonal column.

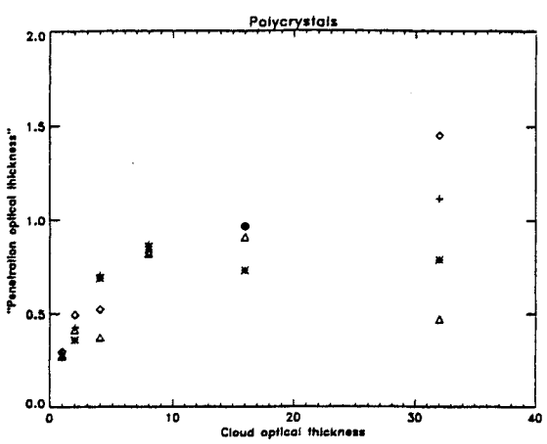

Figure 4: Penetration optical depth at 1.6 μm.

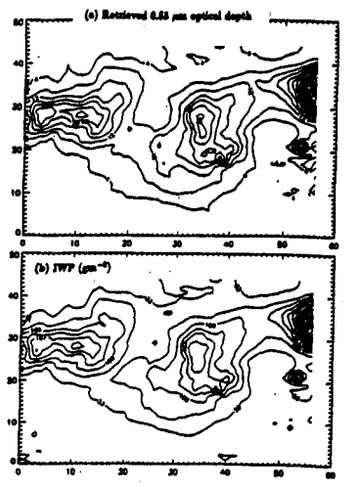

Figure 5: Contour plots of retrieved (a) visible optical depths at 0.55 μm and (b) estimated IWP.

3. OPTICAL DEPTH AND IWP

A contour plot of optical depth (based on the polycrystal) retrieved at 0.55 μm and estimated IWP (Baran et al. (1996)) is shown in Fig. 5. Comparing the optical depth with Fig. 1 shows reasonable behaviour for the retrieved optical depth with small optical depths in the thinner regions of about 4 increasing to over 100 in the thickest regions. The largest optical depths are indeterminate based on reflection measurements since at these optical depths reflectance asymptotes. Since particle geometry, optical depth and crystal size have been retrieved an estimate of IWP is possible and a contour map of IWP is shown in Fig. 5 (b). The IWP estimates show quite typical values for convective cloud though presently we have no other satellite based information with which we can compare against. However, at least with ATSR-2 we have the fundamental microphysical and bulk properties that climate models require information on. It is interesting to note that if the hexagonal column or plate had been assumed then the retrieved optical depth, due to large asymmetry parameters, would have increased by 2 or more times the optical depth shown in Fig. 5 (a) and the IWP would have been similarly increased. In retrieving cirrus properties the assumed shape is clearly important and shape information can only be gained through multiple-view instruments.

4. CONSISTENCY BETWEEN VISIBLE AND THERMAL OPTICAL DEPTH RETRIEVALS

On the 9th November 1996 the Met Office C-130 aircraft underflew and nearly overflew a piece of semi-transparent cirrus off the North East coast of England. One and a half hours before this the ATSR-2 passed over the same piece of cirrus. This piece of cirrus was reported to be homegeneous and stable so little development probably took place in the time between ATSR-2 and the aircraft. The SAFIRE instrument measured both downwelling and upwelling radiance at both visible and thermal wavelengths at the channels previously indicated. The 2-DC probes measured in-situ particle size and this r_e was measured to be about 50 μm. The average extinction optical depth retrieved at 0.87 μm from the SAFIRE instrument (downwelling radiance) was found to be 1.35±0.68. Given the measured r_e and according to extinction calculations using ADT assuming nonspherical particles the ratio between visible extinction and thermal extinction should be 1. Since ATSR-2 has a 10.8 μm channel the retrieved extinction optical depth at 10.8 μm should be close to the SAFIRE retrieved extinction optical depth.

The retrieved thermal extinction optical depth was accomplished using an analytic retrieval equation inclusive of scattering based on Toon et al. (1989) and can be found in Baran (1998b). The inputs to this equation require the single scattering properties of nonspherical particles, single scattering albedo and asymmetry parameter, which were taken to be 0.5 and 0.97 respectively. These parameters being based on ray-tracing calculations. Other inputs are cloud-free nadir and forward view and measured cloud radiance at 10.8 μm. For this particular day the cloud-free measurements were 284 K and 282.5 K respectively. Given this information the ATSR-2 retrieved extinction optical depth at 10.8 μm was found to be 1.53±0.73, this being in good agreement with the SAFIRE derived visible extinction optical depth. Thus we have shown consistency of retrieval between a thermal and visible channel. This is important to demonstrate as a check on internal consistency (since ATSR-2 also has visible channels) and a means of applying visible retrievals directly to thermal wavelengths. For this kind of application information on phase function and optical properties of ice at visible and infrared wavelengths becomes important. Another important aspect is cloud vertical inhomogeneity which has not been discussed but is in the process of being researched.

5. CONCLUSION

In this paper we have demonstrated the significance of a multi-view, multi-wavelength instrument in retrieving cirrus microphysical and bulk properties. We have further shown the usefulness of a 1.6 μm channel aboard a space based instrument which bodes well for the next AVHRR. We have shown the significance of being able to retrieve information on particle geometry and the effect this has on other retrievals particularly on crystal size, optical depth and IWP. We stress that shape information can only come about through the application of dual-view or multiple view instruments. The application of ATSR-2 and the future AATSR (Advanced) to retrieval of global ice cloud products is now a distinct possibility and will be undertaken in due course. Such products will play an important role in climate model validation. Further validation of the retrieval schemes are required and hopefully future co-incident measurements will become available.

Acknowledgements. We thank Rutherford Appleton Laboratory for making the data available and DETR (UK) for funding A. J. Baran under contract PECD/97.

References

Baran, A. J., P. D. Watts, J. S. Foot and D. L. Mitchell, Crystal size, shape and IWP retrieval using along track scanning radiometer observations of tropical anvil cirrus at 0.87 and 1.6 μm, In Proc. International Radiation Symposium (IRS), Alaska, pgs 476-479, 1996.

Baran, A. J., P. D. Watts and J. S. Foot,Potential retrieval of dominating habit and size using radiance data from a dual view and multi-wavelength instrument: A tropical cirrus anvil case, In Press, J. Geophy. Res., 1998a.

Baran, A. J., S. J. Brown, J. S. Foot and D. L. Mitchell, Retrieval of tropical cirrus thermal optical depth, crystal size and shape using a dual-view instrument at 3.7 and 10.8 μm, In Press, J. Atmos. Sci., 1998b.

Baran, A. J., J. S. Foot, and D. L. Mitchell, he question of ice crystal absorption: A comparison between theory and implications for remote sensing, In Press, Applied Optics. 1998c.

Francis, P. N., P. Hignett, and A. Macke, The retrieval of cirrus cloud properties from aircraft multi-spectral reflectance measurements during EUCREX'93, In Press., Q. J. Roy. Meteorol. Soc., 1998.

Foot, J. S. Some observations of the optical properties of clouds. II: Cirrus. Q. J. Roy. Meteorol. Soc, 114, 145-164.

Macke, A. Scattering of light by polyhedral ice crystals. Appl. Opt., 32, 2780-2788.

Watts P. D. and A. J. Baran, A survey of mid-latitude and tropical cirrus, In Proc. ERS-2 Data Users Conference, March 1997, Florence.

Watts P. D., Potential uses of along-track scanning radiometer data for cloud parameter retrieval, In Proc. Passive Infrared Remote Sensing of Clouds and the Atmosphere III, SPIE 2578, pgs 30-45., 1995.

Watts P. D., Estimation of cloud droplet size, optical depth and phase from the along track scanning radiometer,IRS, Alaska, pgs 578-581.

P2.19A

DETERMINATION OF THE CLOUD DROPLET EFFECTIVE RADIUS BY USING SSM/I DATA

by Constantin A. Pontikis and Elizabeth M. Hicks
Météo-France/Université des Antilles et de la Guyane

1. INTRODUCTION

The droplet effective radius R_e (ratio of the third to the second moment of the cloud droplet spectral distribution) and the optical thickness τ of warm clouds are two important parameters that are used in General Circulation Models (GCMs) in order to evaluate the cloud radiative properties. In such models, both empirical parameterizations, deduced from the experimental behavior of limited data sets (e.g. Stephens, 1978b; Fouquart et al., 1989; Bower and Choularton, 1992) as well as pertinent (theoretically founded) parameterizations (Pontikis and Hicks, 1992; Pontikis, 1993; Kiehl, 1994; Pontikis, 1995, Pontikis, 1996) have been used to estimate the values of R_e and τ. The accuracy degree of these parameterizations may be determined by comparing the calculated R_e and τ values to experimental values obtained during field experiments (Stephens and Platt, 1987; Pontikis and Hicks, 1993; Martin et al., 1994) and/or to data sets concerning large oceanic and/or continental areas extracted from satellite imagery (Nakajima et al., 1991; Han et al., 1994). Although the comparisons reveal that the accuracy degree of some of the above mentioned parameterizations is high at small scales, this does not warrant their accuracy at model grid scales. Thus, the use of satellite imagery that leads to algorithms that allow the direct estimation of R_e and/or τ from the pixel brightness temperatures seems to be more useful for GCMs, since it allows the validation of the R_e and τ parameterizations by using global data sets that can be adequatedly processed in order to coincide with the corresponding GCM grid.

The Special Sensor Microwave/Imager (SSM/I) onboard the satellites of the Defence Meteorological Space Program (DMSP) series constitutes another mean in estimating τ by using Stephens' (1978b) parameterization and the SSM/I determined liquid water path L. Further, R_e may be deduced from τ by using the approximate relation $\tau=3L/2\rho_l R_e$, where ρ_l is the liquid water density (Drusch et al., 1994). However, the L values determined by different SMM/I liquid water path algorithms (e.g. Alishouse et al., 1990; Petty, 1990; Liu and Curry, 1993) are very different, thus limiting the precision in the estimation of R_e and τ. In order to bypass the uncertainties attached to the SSM/I liquid water path estimation algorithms, two linear algorithms are presented in this paper that relate directly the effective radii and corresponding cloud optical thicknesses of oceanic cloud fields to the seven SSM/I channel brightness temperatures. In order to determine these algorithms, the following methodology has been used. First, the cloud thickness H values of oceanic layer cloud fields (stratus, stratocumulus) have been determined by using infrared Meteosat 3 high resolution images. Secondly, since such clouds usually reveal adiabatic microphysical characteristics (Bower and Choularton, 1992; Martin et al., 1994), the adiabatic cloud droplet effective radius and optical thickness expressions derived by Pontikis (1993), Pontikis et al. (1995) and Pontikis (1996) have been used in relation to the H values in order to obtain the corresponding R_e and τ values. The latter have then been related to the seven SSM/I channel brightness temperature values extracted from the collocated SSM/I images by means of linear multi-regression techniques. Finally, the algorithm that allows the determination of R_e has been used in relation to SSM/I images in order to determine the effective radius values of Atlantic cloud fields.

2. THEORETICAL BACKGROUND

For layer clouds (stratus, stratocumulus) for which the adiabaticity hypothesis is valid, the cloud droplet effective radius and the corresponding cloud optical thickness may be written as follows (Pontikis, 1993; Pontikis et al., 1995; Pontikis, 1996) :

Corresponding author address : Constantin Pontikis, Météo-France/Université des Antilles et de la Guyane, 97159, Pointe à Pitre Cedex, Guadeloupe, France (F.W.I.)

$$\overline{R_{ea}} = K(d)\left(\frac{3}{4}\right)\left(\frac{9A}{8\pi^2\rho_l^2\overline{\rho_A}N_a^2}\right)^{1/6} L_a^{1/6} \qquad (1)$$

$$\tau_a = \frac{9}{10\rho_l K(d)}\left(\frac{512\pi^2\overline{\rho_A}\rho_l^2 N_a^2}{9A}\right)^{1/6} L_a^{5/6} \qquad (2)$$

with $K(d)=(1+3d^2)^{2/3}/(1+d^2)$, where $\overline{\rho_A}$, N_a, L_a, d, A are respectively the mean air density between the cloud base and the cloud top, the cloud droplet concentration, the liquid water path, the droplet spectral dispersion and the proportionality constant relating the liquid water content Q_l (expressed in terms of mixing ratio) to the corresponding height h above cloud base, Q_l=Ah. The index « a » denotes adiabatic cloud conditions. By introducing into (1) and (2) the L expression that results from the integration over cloud thickness H, $L=AH^2/2$, two further expressions of $\overline{R_{ea}}$ and τ_a that depend upon cloud thickness may be obtained :

$$\overline{R_{ea}} = K(d)\left(\frac{3}{4}\right)\left(\frac{9A^2}{16\pi^2\rho_l^2\overline{\rho_A}N_a^2}\right)^{1/6} H^{1/3} \qquad (3)$$

$$\tau_a = K(d)^{-1}\frac{9}{10\rho_l}\left(\frac{16\pi^2\overline{\rho_A}\rho_l^2 N_a^2 A^4}{9}\right)^{1/6} H^{5/3} \qquad (4)$$

The use of a « standard » droplet concentration valid for maritime clouds and of mean climatological values for K(d), $\overline{\rho_A}$ and A (Pontikis, 1996) leads to two expressions that do not explicitely contain N_a :

$$\overline{R_{ea}} = 1.42H^{1/3} \qquad (5)$$

$$\tau_a = 0.000976H^{5/3} \qquad (6)$$

3. CLOUD DROPLET EFFECTIVE RADIUS AND CLOUD OPTICAL THICKNESS ALGORITHMS

The method used in order to determine the algorithms relating R_e and τ to the brightness temperature of the SSM/I channels is illustrated on the example of the 24 April 1994. Figures 1(a,b) correspond respectively to the SSM/I 19GHz channel composite image and to the 18.00 h TU IR Meteosat 3 high resolution image. These images have been simultaneously analyzed in order to determine temporally and spatially collocated regions over the tropical Atlantic. Since the resolution of the SSM/I images is different from the IR image resolution, the IR images have been processed in order to establish a pixel to pixel correspondance with each one of the seven SSM/I channel images. The analysis has been made in terms of correlation between the brightness temperature of the pixels of the seven SSM/I channels and the radiances of the IR image for layer clouds. The region for which the best correlation has been found (R=0.63) is delimited (white rectangle in fig. 1a). Further, for this selected region and for each pixel of the IR image, the mean cloud thickness value has been deduced, thus allowing the calculation of the corresponding mean cloud droplet effective radius and cloud optical thickness values by using respectively expressions (5) and (6). The algorithms relating R_e and τ to the corresponding

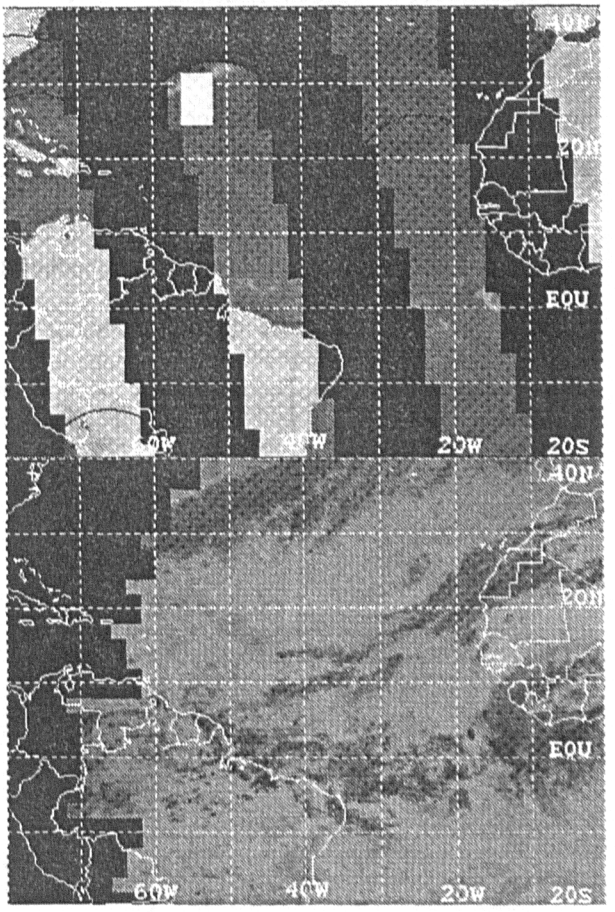

Figures 1(a, b) : SSM/I 19GHz channel composite and Meteosat 3, 18h00 TU infrared images obtained on the 24/04/94.

SSM/I brightness temperatures have then been determined by using multiregressional techniques. They may be written as follows:

$$R_e=r_0+r_1T_{H19}+r_2T_{H37}+r_3T_{H85}+r_4T_{V19}+r_5T_{V22}+r_6T_{V37}+r_7T_{V85} \quad (7)$$

$$\tau=t_0+t_1T_{H19}+t_2T_{H37}+t_3T_{H85}+t_4T_{V19}+t_5T_{V22}+t_6T_{V37}+t_7T_{V85} \quad (8)$$

where T_H and T_V represent respectively the horizontal and vertical polarisation SSM/I channel brightness

TABLE 1 : Linear multiregression coefficient values for R_e and τ.

i	r_i(correlation cefficient= 0.62)	t_i(correlation coefficient=0.62)
0	236.867630	2235.567311
1	0.415142	2.167483
2	0.634689	7.118068
3	0.029184	0.393547
4	- 0.262527	- 3.300510
5	- 0.099238	- 0.907697
6	- 0.801707	- 6.738409
7	- 0.535067	- 5.277226

temperatures. Table 1 contains the r and t linear correlation coefficient values. Figure 2 presents the comparison between the R_e values obtained from expression (5) and the algorithm predicted R_e values for the studied region.

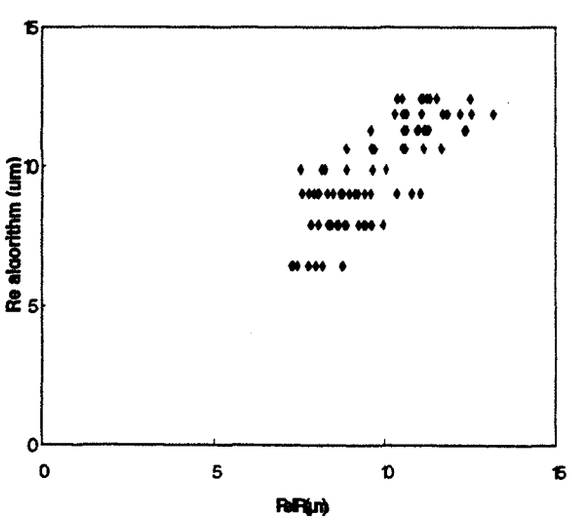

Figure 2 : R_e values determined from the IR image plotted respectively against the R_e values determined bu using algorithm (7).

4. OCEANIC EFFECTIVE RADIUS VALUES

Algorithm (7) has been used in order to determine the mean cloud effective radius for the Atlantic regions contained in all SSM/I images (ascending and descending) available for the 24 April 1994. These values vary between 8μm and 15μm. The mean R_e value is 11.5μm and it is in very good agreement with the 11.6μm value determined by Han et al. (1994) for the northern hemisphere oceanic regions, thus giving further confidence to the presented R_e algorithm. The R_e values have also been calculated by using Petty's (1990) and Alishouse and al. (1990) SSM/I liquid water path algorithms and the liquid water path dependent R_e expression (R_e=4.19$L^{1/6}$) derived by Pontikis and Hicks (1996). Note that this expression is not only valid for layer clouds (adiabatic) but also for convective clouds. As an example, Fig. 3 presents the R_e values calculated by using the liquid water paths obtained from Petty's (1990) algorithm plotted against the Re values obtained by using algorithm (7). The R_e values determined by using the SSM/I liquid water paths are systematically lower than the values determined by using algorithm (7). The corresponding mean oceanic R_e value is 8.4μm. This low effective radius value is most probably due to an underestimation of the liquid water path .

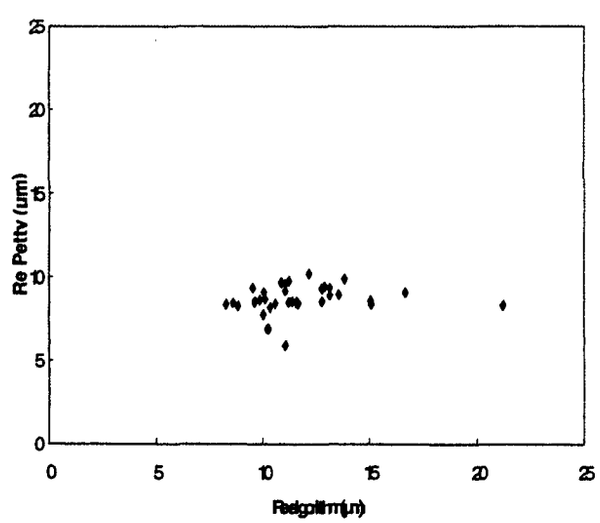

Figure 3 : R_e values calculated by using the SSM/I determined liquid water paths (Petty's liquid water path algorithm) plotted against the corresponding R_e values determined by using algorithm (7).

5. CONCLUSION

Two algorithms allowing respectively the estimation of the cloud droplet effective radius and the cloud optical thickness of oceanic cloud fields have been developed by comparing SSM/I brightness temperatures to the R_e and τ values extracted from the corresponding collocated IR image. The R_e algorithm has been used in order to determine the mean R_e value for the oceanic northern Atlantic region. This value is in good agreement with the values resulting from the analysis of ISCCP data presented by Han et al. (1994). The comparison between the R_e values obtained by using the R_e algorithm and the values resulting from the SSM/I liquid water paths leads to underestimated R_e values, thus suggesting an underestimation of the L values obtained from current SSM/I liquid water path algorithms.

REFERENCES

Alishouse, J. C., J. B. Snider, E. R. Westwater, C. T. Swift,. S. Ruf, S. A. Snyder, J. Vongsathorn, and R. R. Ferraro, 1990 :Determination of cloud liquid water content using the SSM/I. IEEE Trans. Geosci. Remote Sensing, 28, 817-822.

Bower, K. N., and T. W. Choularton, 1992 : A parameterization of the effective radius of ice-free clouds for use in global climate models. Atmos. Res., 27, 305-339.

Drusch, M., E. Ruprecht, and C. Simmer, 1994 : Relation between ISCCP C1 cloud optical thickness and SSM/I derived cloud liquid water path. 7th Conference on Satellite Meteorology and Oceanography, June 6-10, Monterrey, California, p.p. 148-151.

Fouquart, Y., J. C. Buriez and H. Herman, 1989 : The influence of boundary layer clouds on radiation : A review. Atmos. Res., 23, 203- 228.

Han, Q. W.B. Rossow, and A.A. Lacis, 1994 : Near global ISCCP data. J. Climate, 7, 445-497.

Kiehl, J. T., 1994 : Sensitivity of a GCM climate simulation to differences in continental versus maritime cloud drop size. J. Geoph. Res., 99, 23,107-23,115.

Liu, G., and J. A. Curry, 1993 : Determination of characteristic features of cloud liquid water from satellite microwave measurements. J. Geoph.Res., 98, 5069-5092.

Martin, G. M., D. W. Johnson, and A. Spice, 1994: The measurement and the parameterization of effective radius of droplets in warm stratocumulus clouds. J. Atmos. Sci., 51, 1823-1842.

Nakajima, T., M. D. King, J. D. Spinhirne, and L. F. Radke, 1991 : Determination of the optical thickness and effective particle radius of clouds from reflected solar radiation measurements. Part II : Marine stratocumulus observations. J. Atmos. Sci., 48, 728-750.

Petty, G. W., 1990 : On the response of the special sensor microwave / imager to the marine environment. Implications for atmospheric parameter retrievals. Ph. D. dissertation, 291 pp., University of Washington, Seattle.

Pontikis, C.A. , and E. M. Hicks, : 1992 : Contribution to the cloud droplet effective radius parameterization. Geoph. Res. Letters, 19, 2227-2230.

Pontikis, C. A., and E. M. Hicks, 1993 : The influence of clear air entrainment on the droplet effective radius of warm maritime convective clouds. J. Atmos. Sci., 50, 2889-2900.

Pontikis, C., 1993 : Parameterization of the cloud optical thickness : Influence of clear air entrainment. Geoph. Res. Letters, 20, 2655-2658.

Pontikis, C. A., 1995 : Contribution to the droplet effective radius parameterization of warm convective clouds : Clear air entrainment effects, 22, 795-798.

Pontikis, C., P. Dandin, and E. Hicks, 1995 : Etude du comportement physique des caractéristiques optiques des nuages stratiformes chauds et paramétrisations pertinentes associées. Atelier de Modélisation de l'Atmosphère, Toulouse, 28-30 Novembre, 159-163.

Pontikis, C. A., 1996 : Parameterization of the droplet effective radius of warm layer clouds. Geoph. Res. Letters, 23, 2629-2632.

Pontikis, C.A., and E. Hicks, 1996 : Parameterization of the droplet effective radius of warm clouds. Proceedings of the 12th International Conference on Clouds and Precipitation, 1220-1223.

Stephens, G. L., 1978b : Radiation profiles in extended waters clouds. II : Parameterizations schemes. J. Atmos. Sci., 35, 2123-2132.

Stephens, G. L., and C. M. R. Platt, 1987 : Aircraft observations of the radiative and microphysical properties of stratocumulus and cumulus cloud fields, J. Clim. and Appl. Met., 1243-1269.

P2.22B

USING SSM/I DATA AND COMPUTER VISION TO ESTIMATE TROPICAL CYCLONE INTENSITY

Richard L. Bankert*
Paul M. Tag
Naval Research Laboratory, Monterey,CA

1. INTRODUCTION

Satellite imagery and other remote sensing products often provide the only observational data of tropical cyclones. This is especially true in the western Pacific where aircraft reconnaissance missions stopped in 1987. Manual estimate procedures using satellite imagery (Dvorak, 1984) provide valuable assistance in determining tropical cyclone intensity. An objective Dvorak technique (Velden, et al., 1998) is currently being studied to enhance the manual method. In an effort to take advantage of the unique characteristics (Hawkins, et al., 1998) of Special Sensor Microwave/Imager (SSM/I) data, one Naval Research Laboratory effort (outside the scope of this paper) involves the computation of empirical orthogonal functions of SSM/I tropical cyclone data and presenting those values as inputs to a neural network to estimate the tropical cyclone intensity at a given imagery time (May, et al., 1997).

The algorithm applied in the research described here also uses SSM/I data, specifically the 85 GHz (H-pol) channel and a derived rain rate product. The 512x512 pixel imagery is cyclone-centered and image characteristics (computer vision features) are computed from the imagery data. A subset of these features is presented to a pattern recognition algorithm (k-nearest neighbor) and an intensity estimate is provided as output.

A description of the imagery characteristics (including available data and computer vision features) and feature selection methodology is provided in section two. Section three is a discussion of the algorithm used to automate the tropical cyclone intensity estimate and the current evaluation results. A summary follows in section four.

* *Corresponding author address:* Richard L. Bankert, Naval Research Laboratory, 7 Grace Hopper Ave, Monterey, CA 93943-5502;
e-mail: bankert@nrlmry.navy.mil

2. IMAGERY CHARACTERISTICS

For any supervised learning algorithm, "ground truth" data is needed to train and test the classifier or identification algorithm. To satisfy this requirement, 583 SSM/I images (512x512 pixels; cyclone-centered) and the associated best track intensity (in knots) are taken from 114 cyclones (from 1988 to 1997) in both the Atlantic (includes Caribbean Sea and Gulf of Mexico) and Pacific (eastern and western) basins. An example 85 GHz image is shown in Figure 1. To automate the tropical cyclone intensity estimation, characteristic features need to be computed. Using the 85 GHz (H-pol) channel and a derived rain rate product, 150 computer vision features are computed for each image. An example rain rate image is shown in Figure 2. See Figure 3 for a distribution of the 583 images according to intensity.

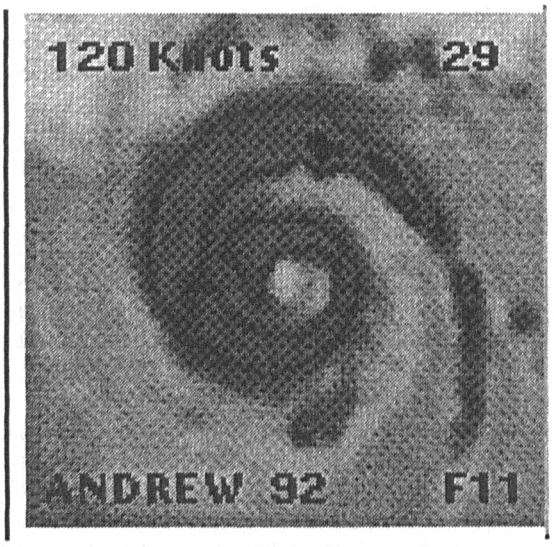

Figure 1. SSM/I 85 GHz (H-pol) image of Hurricane Andrew on 25 Aug 92 at 2252 UTC.

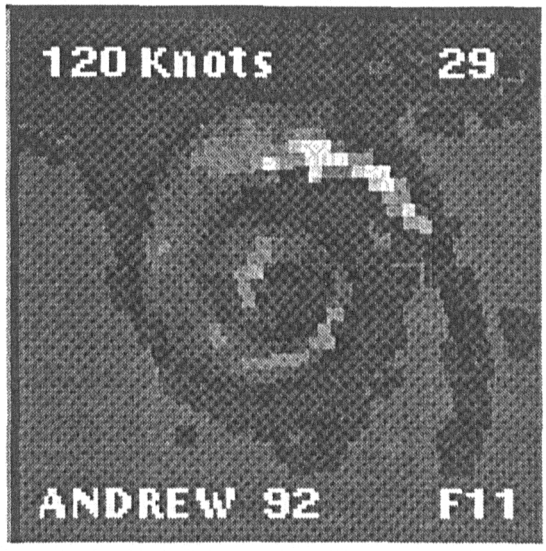

Figure 2. Derived rain rate image (using various SSM/I channels) of Hurricane Andrew on 25 Aug 92 at 2252 UTC (same as Figure 1).

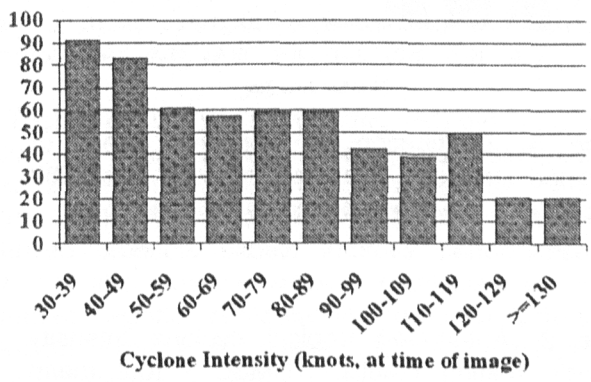

Figure 3. Distribution (by number) of the 583 training images, according to intensity.

The characteristic image features include computer vision attributes that can be described as size, shape, texture, and spectral measurements. Tropical cyclone-specific features include, among others, existence (yes/no) and size of an enclosed eye at a specific brightness temperature threshold (255K), the range of temperature thresholds for which an enclosed eye exists, and various rain rate measurements. Other features include latitude, longitude, date, time, etc.

Presenting redundant and irrelevant features to a pattern recognition algorithm will degrade its performance. To avoid this problem a feature selection algorithm is applied to the current data set. The selected feature subset is used as the input vector for the pattern recognition algorithm. For additional information on feature selection algorithms see Aha and Bankert (1995).

While previous uses of feature selection algorithms required the data to be organized in discrete classes, for this study the algorithm has been modified to make use of the actual intensity associated with each image (i.e, continuous data). Instead of searching for a feature subset that maximizes classfication accuracy, the search is for a subset that minimizes the root-mean-square error (measured in knots).

3. AUTOMATED INTENSITY ESTIMATE

A k-nearest neighbor classifier is used as the evaluation function in the feature selection algorithm and will serve as the automated tropical cyclone intensity estimate algorithm. This classification routine computes the similarity distances in feature space between the testing sample and each training sample. Using the single nearest neighbor distance as the standard for inclusion, those training samples within a distance factor (1.5 * nearest-neighbor distance) are used to estimate the testing sample intensity. A simple averaging technique is performed on those k-nearest neighbor intensities.

After a search and evaluation process within the feature selection algorithm, 18 characteristic features (listed in Table 1) were selected as the feature subset to represent each tropical cyclone at the time of the imagery. A leave-one-out cross validation test was applied to the entire data set. In this test, each sample (represented by the 18 selected features) is presented to the k-nearest neighbor algorithm, with the similarity distance to each of the remaining 582 samples computed. The feature selection and testing procedure is illustrated in Figure 4. The distribution of absolute error among 10 knot bins can be found in Figure 5; the average absolute error (AAE) for the 583 samples is 11.6 knots and the root mean square error (RMSE) is 15.8 knots.

Although the leave-one-out cross validation is considered a measure of the algorithm performance on unseen instances, two additional tests were performed on unseen cases. For each test, the data were divided into two parts: one to serve as the samples for feature selection and training and the other as testing. The first test was

a random selection (approx. 75% training, 25% testing). Twelve features were selected using 444 samples in the feature selection algorithm. Leave-one-out cross validation testing on these training samples resulted in an RMSE of 16.4 kts and an AAE of 12.5 kts (distance factor = 2.5). For the independent testing set (139 samples) the RMSE is 17.1 kts with an AAE of 13.5 kts (distance factor = 2.25).

Table 1. Selected features (583 samples).

1. # pixels > 0 rain rate
2. # TC (<255 K) pixels in NE quadrant
3. Max segmented region size / Total TC pixels
4. Latitude
5. Standard Dev. of TC pixels (inner 100x100)
6. Gray Level Diff. Vector contrast (N-S direction)
7. Sum and Diff. Hist. correlation (E-W direction)
8. Std. Dev. of quadrant sizes (inner 200x200)
9. Mean pixel value (inner 100x100)
10. Total rain rate (inner 150x150)
11. # pixels >0 rain rate (inner 150x150)
12. Median pixel value (> 255K pixels only)
13. # TC pixels (< 255K)
14. | Month - 9|
15. Minimum pixel value (inner 200x200)
16. Minimum pixel value (inner 100x100)
17. # TC pixels in SE quad / Total TC pixels
18. Highest enclosed eye threshold temperature - Lowest enclosed eye threshold temperature

The second test divided the samples by cyclone, with no images from a particular cyclone in both the training and testing sets. For example, all Andrew images are training samples and all Linda images are testing samples. Twelve features were selected using 439 training samples (103 tropical cyclones). Leave-one-out testing of these samples (distance factor = 1.5) resulted in an RMSE of 15.4 kts and AAE of 11.6 kts. For the independent testing set (144 samples; 11 tropical cyclones) the RMSE is 23.1 kts and the AAE is 18.5 kts (distance factor = 2.5).

All testing results are summarized in Table 2. Four of the five tests have very similar results. These results are very encouraging especially considering the fact that the best track intensity (used as ground truth) is recognized as being an approximation and not necessarily exact. The

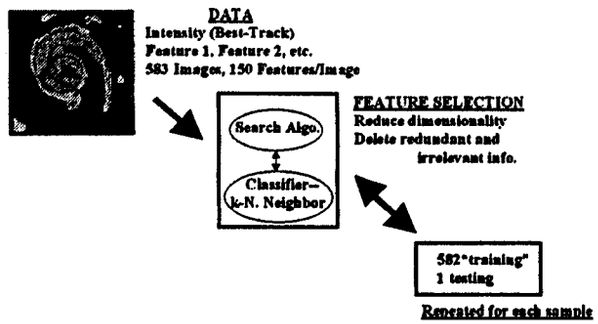

Figure 4. Procedural steps for extracting and selecting features with the imbedded leave-one-out cross validation test.

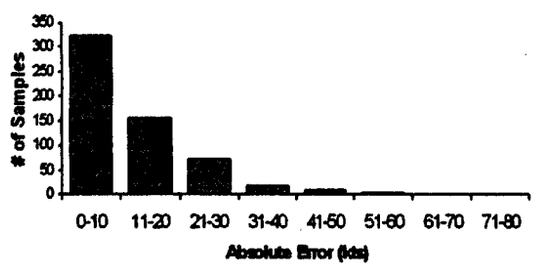

Figure 5. Distribution of absolute errors of estimated tropical cyclone intensity for 583 samples in a leave-one-out cross validation test.

Table 2. Automated tropical cyclone intensity estimate testing results. RMSE - root mean square error; AAE - average absolute error

TEST	*RMSE (kts)*	*AAE (kts)*
Leave-one-out (583 samples)	15.4	11.6
Leave-one-out (Random-444 samples)	16.4	12.5
Random Unseen (139 samples)	17.1	13.5
Leave-one-out (Cyclone-439 samples)	15.4	11.6
Cyclone Unseen (144 samples)	23.1	18.5

higher error statistics that resulted from the remaining test (cyclone unseen) can be explained in part to the fact that there were no images in the

training set that were taken from the same cyclone as the test sample. Therefore, there was no possibility of the k-nearest neighbor calculation being influenced by a training sample that is close in time (and image characteristic features) to the testing sample. What this result clearly shows is that there are many variations in tropical cyclone characteristics, as related to intensity, and that the training database needs to be as large and as inclusive as possible.

4. SUMMARY

An algorithm to estimate tropical cyclone intensity from SSM/I imagery using computer vision is demonstrated. A feature selection algorithm is applied to the data to reduce the dimension of the input vector and enhance the performance of the pattern recognition algorithm. A k-nearest neighbor algorithm is used to output a tropical cyclone intensity estimate at a particular SSM/I image time by calculating similarity distances (in the selected feature space) between the unknown sample and the stored training samples.

Testing results, while promising, indicate there is room for improvement. Adding more samples, examining other feature characteristics, and computing features from other SSM/I channels and derived products should improve performance. We will also examine ways to manipulate the k-nearest neighbor computations (distance factors, median instead of mean, etc.) to maximize performance on unseen samples.

5. ACKNOWLEDGMENT

The support of the sponsor, the Office of Naval Research, under Program Element 0602435N is gratefully acknowledged. The assistance of Jeff Hawkins (NRL Monterey) and Marla Helveston (Analysis and Technology) in supplying the data and offering technical advice is greatly appreciated. David Aha (NRL AI Center) is thanked for providing the feature selection algorithm and offering guidance.

6. REFERENCES

Aha, D.W., and R.L. Bankert, , 1995: A comparative evaluation of sequential feature selection algorithms. Proceedings of the Fifth International Workshop on AI and Statistics, Ft. Lauderdale, FL, 1-7.

Dvorak, V.F., 1984: Tropical cyclone intensity analysis using satellite data. NOAA Tech. Rep. NESDIS 11. U.S. Dept. of Commerce, 47 pp.

Hawkins, J.D., D.A. May, J. Sandidge, R. Holyer, and M.J. Heleveston, 1998: SSM/I-based tropical cyclone structural observations. Preprints 9th Conference on Satellite Meteorology and Oceanography, Amer. Meteor. Soc., 45 Beacon St., Boston, MA 02108, pages unknown.

May, D.A., J. Sandidge, R. Holyer, and J.D. Hawkins, 1997: SSM/I derived tropical cyclone intensities. Preprints 22nd Conference on Hurricanes and Tropical Meteorology, Amer. Meteor. Soc., 45 Beacon St., Boston, MA 02108, 27-28.

Velden, C.S., T.L. Olander, and R.M. Zehr, 1998: Development of an objective scheme to estimate tropical cyclone intensity from digital geostationary satellite infrared imagery. Accepted by *Weather and Forecasting*.

P2.23A SSM/I-BASED TROPICAL CYCLONE STRUCTURAL OBSERVATIONS

Jeffrey D. Hawkins*
Naval Research Laboratory
Monterey, CA 93943

Douglas A. May
Juanita Sandidge
Ron Holyer
Naval Research Laboratory
Stennis Space Center, MS 39529

Marla J. Helveston
Analysis & Technology
Bay St. Louis, MS, 39520

1. INTRODUCTION

Accurate monitoring of tropical cyclone (TC) intensities depends on the ability to map the internal storm structure. This can be accomplished in several ways with varying degrees of success. The methods employed to accomplish this task are largely ocean basin dependent.

Aircraft reconnaissance is routinely used in the Atlantic basin to directly measure the following critical parameters: a) location, b) central pressure, c) flight level winds, d) dropsonde derived profiles of wind, temperature and humidity, and e) radar maps of rain and 3-D wind fields. This vital information is made available to the National Hurricane Center (NHC) in near real-time and greatly assists the hurricane specialists during the preparation of warnings. Accurate knowledge of the location, intensity and radius of gale force winds is critical for public advisories and the data sets are assimilated into numerical weather forecast models.

The Atlantic basin (includes Caribbean Sea and Gulf of Mexico) is the only region where aircraft routinely are called upon to penetrate and map TC structure, typically well before potential landfall. Some storms impacting the eastern Pacific and Hawaiian Islands are also sampled via these instrumented planes. However, aircraft ceased to carry out reconnaissance missions in the western Pacific in the summer of 1987. Thus, remote sensing methods have been the major component to TC structure monitoring for over 10 years within this large domain.

* Corresponding author address: Jeffrey D. Hawkins, Naval Research Laboratory, 7 Grace Hopper Ave, Monterey, CA, 93943; e-mail: hawkins@nrlmry.navy.mil

TC intensity derivations are thus almost solely dependent on analysis of visible and infrared (vis/IR) imagery (both geostationary and polar orbiter) via the Dvorak technique (Dvorak, 1984). This subjective pattern recognition method has proven to be invaluable to operational TC centers. The Dvorak technique has numerous advantages/limitations and Velden, et.al. (1998) are now addressing some significant improvements via an enhanced objective scheme.

However, any vis/IR-based analysis scheme has restrictions due to the simple fact that the analysts can often not see the middle and lower-level cloud fields that are vital in understanding tropical cyclone structure. Upper-level cloud obscuration and the inability to accurately analyze nighttime IR cloud structures often frustrate analysts who wish to see inside the storm for additional information.

Section 2 will detail how passive microwave sensors can permit one to see inside TCs, section 3 will detail specific SSM/I observations and structure changes with time, and section 4 will discuss the findings of automated objective methods.

2. APPROACH

The Defense Meteorological Satellite Program (DMSP) series of polar orbiting platforms has carried a Special Sensor Microwave/Imager (SSM/I) since June 1987 (Hollinger, 1989). The suite of passive microwave channels at 19, 22, 37 and 85 GHz, permits the sensor to "see through" most upper-level cloud decks. At 85 GHz, brightness temperatures react strongly to hydrometers and ice particles. Brightness temperatures are significantly decreased in regions of heavy rain, thus permitting the sensor

to map rainbands within and around tropical cyclones, even when vis/IR imagery is totally obscured by upper-level clouds.

Examples of the advantage of SSM/I data versus vis/IR imagery can be found in Hawkins, et. al., 1998. Care must be used when mapping the 12-15 km resolution 85 GHz imagery to extract the wealth of inherent data. The technique of Poe (1990) has been successfully incorporated for TC applications and is illustrated in Figure 1 below.

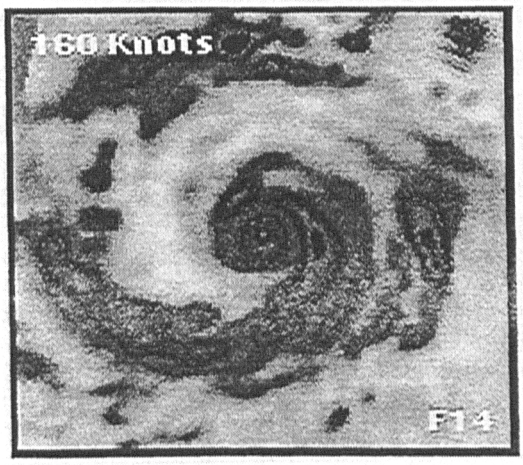

Figure 1. SSM/I 85 GHz image of Hurricane Linda at 1545Z on September 12, 1997. Darker gray shades represent colder brightness temperatures (Tb) associated with rainbands and eyewall features. Storm intensity is estimated at 160 kts (~ 80 ms^{-1}).

The ~ 500 km domain encompassed in Fig. 1 begins to demonstrate (although poorly in a black and white format) the structure evident in 85 GHz imagery. This horizontal polarized image clearly reveals the presence of a very small, compact eye, encircled by a relatively thin band of intense convection as depicted by the dark (low Tb) shading. These conditions are typical of very strong hurricanes where the eye has shrunk to a diameter near 20 km and has reached peak intensity.

Additional structural detail is manifested by the significant rainband that begins to the NE of the eye and wraps around to the south and then SW. This band is well organized and dominated by heavy precipitation. The location, size and shape of this band provide important information about the inflow present during this storm structure snapshot. Some heavy convection is located just NW of the eye and hints at the possibility of a 2nd eyewall forming. Additional heavy convection is found to the north and verifies the large extent of this storm and the excellent circulation. Note: Hurricane Linda obtained the highest estimated maximum sustained wind speed on record for a storm in the eastern Pacific basin (160 kts, ~ 80 ms^{-1}).

The fact the SSM/I 85 GHz data can capture the compact eye in Figure 1 bodes well for the sensor's capability to detect small, but high contrast features such as eyes, eyewalls and raincells. Thus, features that are smaller than the inherent 12-15 km resolution of the 85 GHz footprint may be mapped and analyzed with care.

This snapshot of TC structure in Fig. 1 is crucial to understanding the inner workings of a TC, since vis/IR imagery often preclude the extraction of this amount of detail due to upper-level cloud obscuration. The point to address next is whether or not the SSM/Is can provide the frequency of coverage necessary to map structure over the lifetime of a given system.

3. SSM/I TIMES SERIES

The chances that one SSM/I will pass over a given storm on one day is low, but is increased significantly when two operational sensors are available (Velden, et. al., 1989). This fact is dictated by the ~ 1400 km swath of the SSM/I sensor. However, since December 1990, at least two SSM/Is have been operational simultaneously and since November 1991 three SSM/Is have frequently been available (four sensors were in orbit during the summer of 1997).

Multiple SSM/Is clearly have a major impact on TC sampling intervals. Figure 2 is an example of how Hurricane Linda was sampled by the four SSM/I's available in 1997 [F10, F-11, F-13, F-14]. 85 GHz imagery varies from an "excellent " four/day (not showing partial hits in this display) to sometimes none (not the case for this storm period). These 512-km by 512-km browse images permit the viewer to grasp the basic storm structure from 9 Sept to 14 Sept. The best-track storm intensity at the time of the SSM/I image is displayed in the upper left hand corner (kts), the satellite ID# is in the bottom right and the date/time are along the bottom banner of each image.

Convection and banding are weak in the first image at 1746Z on 9 September with estimated maximum winds at 30 kts (15 ms^{-1}). Imagery on 10 September reveals a concentration in the convection that is then followed by a large flare-up in convection and banding later in the day. September 11th SSM/I data focuses on the development of an eye and the eye shrinks in

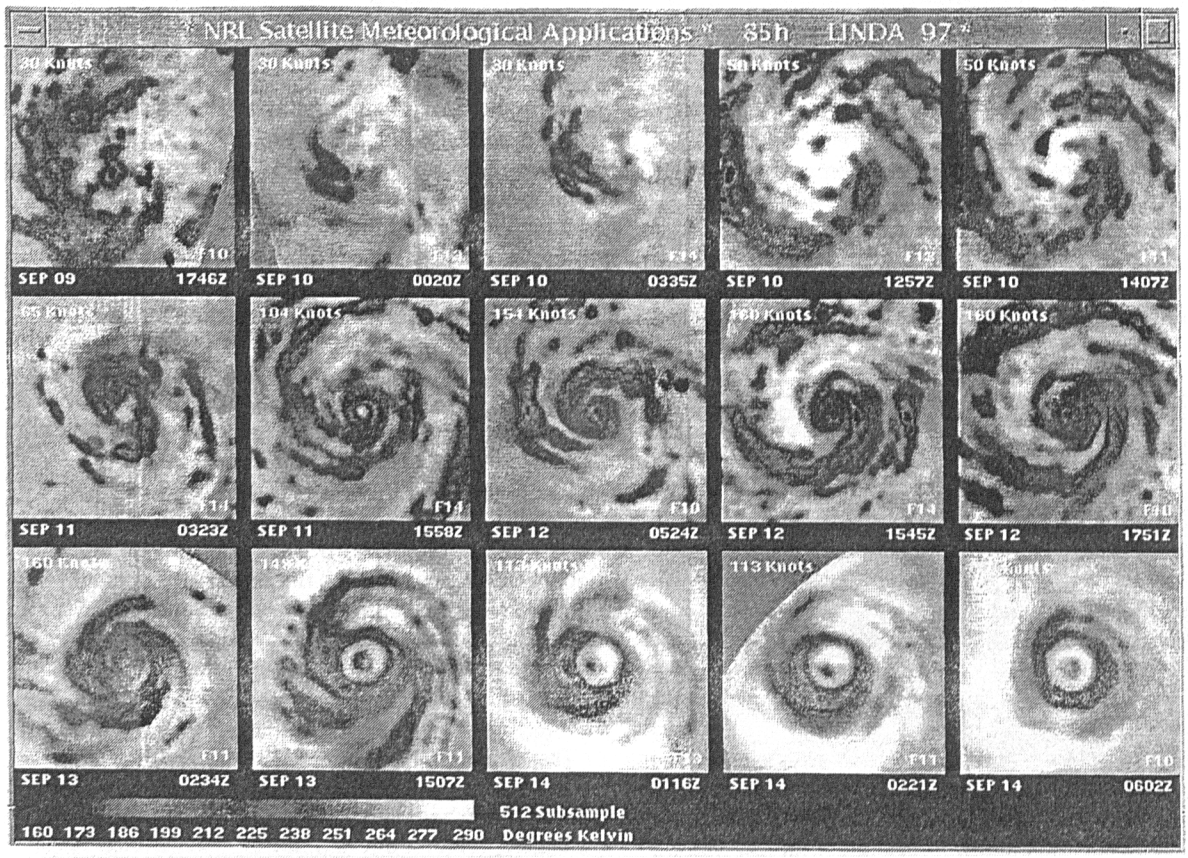

Figure 2. Time series of SSM/I 85 GHz imagery for Hurricane Linda from 9-14 September 1997. Each image represents ~ 500 km x 500 km domain. Darker brightness temperatures (Tb) represent cold values associated with precipitation and/or ice particles and delineate TC rainbands and eyewalls.

size until a very tightly coiled eyewall is clearly evident on the 12th. This development timetable is unusually fast and atypical for tropical cyclones in general and especially so for storms in the eastern Pacific.

Fig. 2 denotes the formation of a double or concentric eyewall pattern on 13 September. A secondary outer eyewall forms and then takes over dominance from the inner eyewall as evidenced by the dark gray shades (very low Tb) and associated scattering due to rain and ice particles in the intense convection. The inner eye weakens during the day as the outer eye cuts off the inflow.

Imagery on the 14th reveals the outer eye continues as the main circulation feature and the inner eye slowly weakens during the course of the day. In addition, the outer rainbands are weakening as the storm moves over colder water and convection in these bands slackens with time and the maximum sustained winds decrease.

Figure 2 has demonstrated the time series approach for mapping structure change within TCs. The level of detail in the SSM/I imagery is vitally important to the satellite analyst when faced with the ever-present prospect of upper-level clouds obscuring vis/IR imagery interpretation. This is especially important at night when IR-only data has forced the analyst to follow cold-cloud targets that often end up becoming separated from an exposed low-level circulation that is only discovered with the first good morning visible image.

Note that Fig. 2 has been purposely restricted to SSM/I passes that are "excellent" in coverage and map the entire storm system. Additional passes are available that cover portions of the storm and can provide structure details that would assist the TC analyst. Average hits/storm are typically 3-5 at latitudes of 15-30 degrees.

This frequency is now at a level high enough for operational use and the Joint Typhoon Warning Center has led the world tropical cyclone centers in utilizing this valuable tool in real-time TC analysis. Warning discussions routinely include input from SSM/I data pertaining to center locations, structure information, and concentric eyewalls.

4. TROPICAL CYCLONE INTENSITY ESTIMATES

The SSM/I 85 GHz imagery reveals important TC structure detail that is highly correlated with storm intensity. Hawkins, et. al., (1996, 1998) and May, et. al., (1997) have applied a neural network based approach to find an objective method to extract accurate intensities from SSM/I imagery. The 85 GHz imagery is represented by Empirical Orthogonal Functions (EOF) that contain the patterns of convection, rainbands, eyewalls, etc. that are present in SSM/I imagery.

A dependent data set of over 500 storms is used to "train" the neural net (NN). Intensity estimates for each storm pass are extracted from the "best-track" file created by the operational centers at the end of each season when all data can be re-evaluated and the "best" estimate of maximum sustained winds is determined.

Neural network results using no a priori intensity information have gone from outright bad to poor. Application of the neural network to a sequence of storm images such as displayed in Fig. 2 reveal that the NN captures the intensity trend correctly, but the absolute value has too much variability for operational use at this time.

Several efforts have been used to improve upon these results. A priori information in the form of 6 and 12-hour-old best-track intensities were used to train the NN. A test on an independent data set revealed that significant progress had been made in tuning the accuracy of the overall technique. Additional imagery is now being added to the training and verification data sets and NN configurations are being studied for new ways to reduce the variability from image to image. Note that no time averaging is done currently, though averaging is applied to both the Dvorak (1984) and Velden, et. al., (1998) techniques.

Joint efforts at NRL using computer vision techniques to extract TC intensity from SSM/I imagery/products is now showing real progress (Bankert and Tag, 1997). Thus, the combination of neural network and computer vision methods applied to SSM/I data and an objective Dvorak technique mean that TC forecasters will soon have additional tools to monitor storm intensity.

Acknowledgments. Special thanks are given to Gene Poe, Al Uliana and Beverly Gardiner at NRL-DC who assisted in creating the SSM/I TC database. We gratefully acknowledge the support of our research sponsors, the Office of Naval Research, Program Element (PE-060243N) and the Oceanographer of the Navy through the program office at the Space and Naval Warfare Systems Command, PMW-185 (PE-0603207N).

5. REFERENCES

Bankert, R.L., P.M. Tag, 1997: Automating the subjective analysis of satellite-observed tropical cyclone intensity, Preprints, AMS 22nd Conf. on Hurricanes and Tropical Meteorology, pp.37-38

Dvorak, V.F., 1984: Tropical cyclone intensity analysis using satellite data. NOAA Tech. Rep. NESDIS 11. US Dept. of Commerce, 47 pp.

Hawkins, J.D., J. Sandidge, R. Holyer, D.A. May, G. Poe, 1996: Tropical cyclone characterization via satellite remotely sensed techniques, Preprints, AMS 8th Conf. on Satellite Meteorology and Oceanography, pp. 200-203.

Hawkins, J.D., D.A. May, J. Sandidge, R. Holyer, and M.J. Helveston, 1998: Satellite tools for monitoring tropical cyclone intensity change, AMS Symposium on Tropical Cyclone Intensity Change, pp. 51-55.

Hollinger, J., 1989: DMSP Special Sensor Microwave/Imager Calibration/Validation, Final Report, Vol. 1, Naval Research Laboratory, Washington, D.C.

May, D.A., J. Sandidge, R. Holyer and J.D. Hawkins, 1997: SSM/I derived tropical cyclone intensities, 22nd AMS Conf. on Hurricanes and Tropical Meteorology, pp. 27-28.

Poe, G., 1990: Optimum interpolation of imaging microwave radiometer data, IEEE Trans. on Geosci. and Remote Sensing., GE-28, 800-810.

Velden, C.S., W.S. Olsen, B.A. Roth, 1989: Tropical cyclone center fixing using DMSP SSM/I data, 4th AMS Conf. on Satellite Meteorology, pp. J36-J38.

Velden, C.S., T.L. Olander, and R.M. Zehr, 1998: Development of an objective scheme to estimate tropical cyclone intensity from digital geostationary satellite infrared imagery, Accepted by Weather & Forecasting.

P2.24B

TOTAL WATER VAPOR FROM DMSP SSM/I AND NOAA TOVS: NORTH PACIFIC HIGH AND ITS INFLUENCES ON THE EAST ASIAN SUMMER MONSOON

Byung-Ju Sohn* and Do-Hyeong Kim
Department of Earth Science, Seoul National University
E-mail : sohnbj@plaza.snu.ac.kr

Hyo-Sang Chung
METRI, Korean Meteorological Administration

1. INTRODUCTION

Water vapor and its temporal and spatial variations are essential for understanding the earth's climate system. Oceans are major source regions of water vapor, but conventional radiosonde observations provide data only over small portion of huge oceans. Therefore measurements of water vapor covering all oceans must be achieved by satellite remote sensing.

Two primary methods to retrieve water vapor from satellites are the infrared (IR) and microwave (MW) methods. The retrievals in IR methods based on the High Infrared Resolution Sounder (HIRS/2) water vapor channels, provide global coverage at three atmospheric layers on both land and ocean. However, IR method has limitation over cloudy regions (Smith et al., 1979). MW can penetrate deep cloud layer, and thus it can give information on water vapor even in the cloudy region. But, MW method is unable to retrieve water vapor over land because of near unity emissivity of land surface. To obtain the global distribution of total water vapor it should be beneficial to use both NOAA TOVS and DMSP SSM/I water vapor data by compensating their deficiencies each other.

In this research, we focus on the features of water vapor distributions obtained from the combined NOAA TOVS and DMSP SSM/I data, examining the evolution of the East Asian summer monsoon viewed from the location and movement of the North Pacific high. In doing so we choose two summers of 1994 and 1995. That is because the year 1994 was extremely hot and dry over East Asia (Park and Schubert, 1997) whereas the year 1995 showed normal monsoon activities. Basic assumption is that the development of North Pacific high is one of the most important elements regulating monsoon activities over East Asia.

2. DATA AND METHODOLOGY

The SSM/I instrument is a passive MW radiometer that measures MW emission from the earth's surface and the atmosphere. The SSM/I instrument has 7 channels with 4 different frequencies at 19.35, 22.235, 37.0, 85.5 GHz. Each has both horizontal and vertical polarization channels except 22.235 GHz that has only vertical polarization. Wentz (1995) developed a statistical method to retrieve total water vapor (TWV) based on 19.35 (TB19V) and 22.235 (TB22V) brightness temperatures, i.e.:

$$TWV = 88.76 + 43.289\, ln(290\text{-}TB_{19v}) - 62.217\, ln(290\text{-}TB_{22v}) \quad (1)$$

where the subscript 'V' represents vertical polarization.

The water vapor data from IR method are obtained from the operational processing by NOAA NESDIS, commonly known as the TOVS data. The operational TOVS data product archived by NESDIS is composed of sets of meteorological parameters. Here we use layer precipitable water in three lowest layers (surface-850, 850-700, and 700-500 hPa). Daily maps of TOVS TWV were produced by integrating precipitable water at all three layers.

We blended two sets of TWV derived from two satellites to produce a new data set which covers both land and ocean area by keeping microwave measurements of TWV when both are available. From the combined TWV data we examine the characteristics of monsoon activities over East Asia during the summer seasons (June, July and August) of 1994 and 1995.

3. RESULTS

Geographical distributions TWV of 1994 and 1995 (not shown in this paper) indicate similar features to each other. Areas greater than 45 kg m^{-2} of TWV expand to higher latitude with respect to time. During June, the northern boundary of 45 kg m^{-2} is located near 20°N latitude, and then it moves to 30°N and 140°E, exhibiting a sudden northward jump of moist area. In contrast to the similar patterns found during June and August between 1994 and 1995, July distributions exhibit noticeable differences that are linked to locations of the North Pacific high.

In order to examine the role of the North Pacific high in the intensity or evolution of the East Asian summer monsoon, time-longitude diagrams are presented for the latitudinal band of 20°-30°N -- see Figure 1. Comparisons are made for 1994 and 1995, based on the assumption that subtropical high area holds less total water vapor because of dominant descending motion.

Normal monsoon year (summer of 1995) shows periodic westward movement of dry air from the western edge of the subtropical high to China, with period of about 20 days. This type of westward movement of dry area is very similar to the westward propagation of intraseasonal convective anomalies along off-equatorial 10°-20°N latitudes (Murakami, 1980; Nitta, 1987). Recent study of Wang and Xie (1997) further suggest that the emanation of Rossby wave from the Kelvin-Rossby wave due to the suppression of equatorial convection.

The importance of this westward propagation

*Corresponding Author's Address: Dr. B.J. Sohn, Department of Earth Sciences, Rm 24-303, Seoul National University, Seoul, 151-742, Korea.
E-mail: sohnbj@plaza.snu.ac.kr

implied in the monsoon development stems from the fact that the movement eventually induces the westward expansion of subtropical high. Consequently, the expansion of subtropical high establishes the environment providing confluence of the moist anticyclonic flow along the edge of the high with the humid air flow from Southeast Asia and thus more moisture supply to monsoon frontal area.

By contrast, there is not clear indication of the westward movement in the moisture field during July of 1994, compared to 1995, leading to the failure of the development of moisture confluence zone in the East Asian monsoon region and thus severe drought over North China, Korea, and Japan.

Such contrasts found in the moisture field is clearer in the NCEP streamline field given in Figure 2. Considering that moisture supply is critically dependent upon the location of the subtropical high, we postulate that the westward propagating signal should be the essential factor controlling or modulating monsoon activities over East Asia.

4. ACKNOWLEDGEMENTS

This research has been supported by Korean Science and Engineering Foundation (961-0405-017-2).

5. REFERENCES

Murakami, T., 1980: Empirical orthogonal function analysis of satellite-observed outgoing longwave radiation during summer. *Mon. Wea. Rev.*, **108**, 205-222.

Nitta, T., 1987: Convective activities in the tropical western Pacific and their impact on the Northern Hemisphere summer monsoon. *J. Meteor. Soc. Japan*, **65**, 373-390.

Park, C. K., and Schubert S. D., 1997: On the nature of the 1994 East Asian summer drought, *J. Climate*, **10**, 1056-1070.

Smith et al., 1979: The TIROS-N Operational Vertical Sounder. *Bull. Amer. Meteor. Soc.*, **58**, 1177-1187.

Wang, B., and X. Xie, 1997: A model for the boreal summer interseasonal oscillation, *J. Atmos. Sci.*, **54**, 72-86.

Wentz, F.J., 1995: A well calibrated ocean algorithm for SSM/I, RSS Tech. Rpt. 101395, Remote Sensing System, Santa Rosa, Ca.

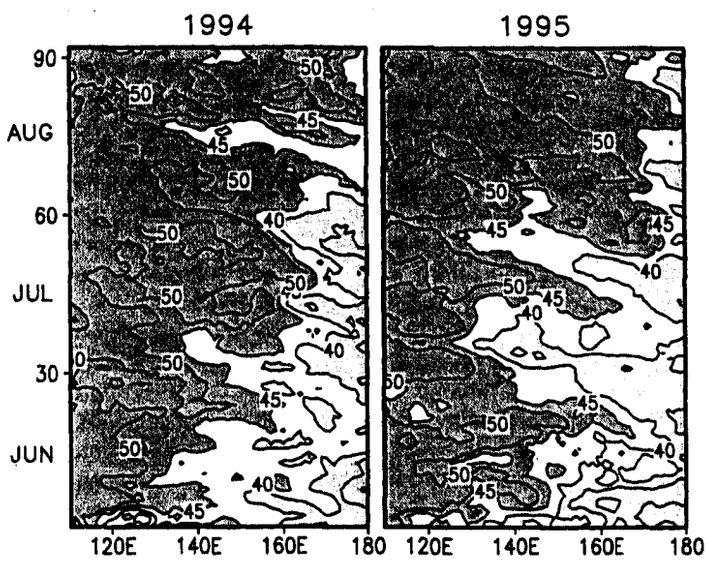

Fig. 1: Hovmoller diagram for total water vapor averaged over 20°-30°N latitude band for the summer (June, July, and August) of 1994 and 1995. Units are in kg m^{-2}

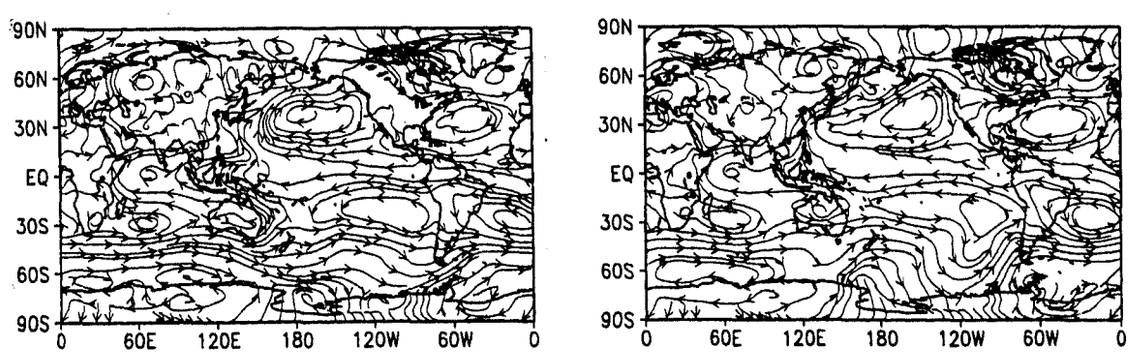

Fig. 2: Geographical distributions of NCEP streamline for July 1994 (left) and 1995 (right).

P2.25A VARIABILITY IN ATMOSPHERIC MOISTURE OVER THE TROPICAL EAST PACIFIC FROM MULTISPECTRAL SATELLITE OBSERVATIONS

Wesley Berg*, Merritt Deeter, and Don Anderson

CIRES, University of Colorado, Boulder, CO

1. INTRODUCTION

The use of satellite observations is critical to understanding the hydrology of the east Pacific. Due to a lack of in-situ observations, the hydrology of this region and the dynamics involving the transport of moisture between the east Pacific and the Americas is poorly understood. Traditional outgoing longwave radiation (OLR) observations are insufficient for understanding low-level moisture transport converging into the ITCZ and subsidence and drying of the upper troposphere above the ITCZ. The transport of moisture and development of convection along the east Pacific ITCZ is distinctly different than over the warm pool region. This in turn has given rise to large discrepancies in estimates of precipitation and hence latent heat release and the resultant seasonal to interannual circulation anomalies.

A comparison of annual average rainfall from various satellite techniques shows poor agreement over the east Pacific ITCZ. Large variations exist between climate rainfall estimates based on microwave and infrared satellite observations [Berg and Avery, 1995; Janowiak et al., 1993]. Janowiak et al. [1993] has suggested that this discrepancy is the result of shallow convection in this region, which results in lower warmer cloud tops in the IR and thus less rainfall estimated by the IR-based techniques.

A previous study by Berg [1994], has shown that for precipitating clouds (as determined by SSM/I), the ratio of cloud top temperatures below 235 K to the total is much greater over the warm pool region than over the east Pacific. In the warm pool region this ratio is close to 60%, while the value is closer to 20% over the east Pacific. This means that infrared-based satellite estimates validated over the west Pacific will tend to underestimate the total rainfall in the east Pacific by almost a factor of three, a fact which is consistent with the results of Berg and Avery [1995].

*Corresponding author address:: Wesley Berg, Cooperative Institute for Research in Environmental Sciences, University of Colorado, Campus Box 449, Boulder, CO 80309-0449; e-mail: wkb@cdc.noaa.gov

2. SATELLITE MONITORING OF MOISTURE

A variety of currently operational satellite instruments can help provide a much more comprehensive view of the distribution and variability of moisture in the atmosphere than traditional data sets such as outgoing longwave radiation (OLR) alone. This is an especially important issue of the tropical east Pacific where radiosonde and other in-situ data sets are unavailable for validation and/or assimilation into models.

2.1. Water vapor and cloud monitoring

Observations of clear- and all-sky brightness temperatures are available from the special sensor microwave moisture sounder (SSM/T2) from 1993 through the present, which are sensitive to moisture at several levels in the middle and upper troposphere. Combined with estimates of total column water vapor available from the special sensor microwave/imager (SSM/I) beginning in 1987, these instruments can be used to provide information on the vertical stratification of water vapor in the atmosphere. Both of these instruments are flown operationally on the defense meteorological satellite program (DMSP) satellite series. In addition, high frequency (every 3 hours) upper-tropospheric water vapor channel measurements from the GOES-8 and GOES-9 imagers are available along with the traditional IR window channel and visible images. In addition to water vapor sensors, data from SSM/I can be used to estimate cloud properties including liquid water content, ice content, and rainfall. Combined with visible and infrared cloud observations from GOES-9, information on the vertical and spatial distributions of moisture for both clear and cloudy scenes can be used to provide a better understanding of dynamical processes over the data sparse eastern Pacific.

2.2. UTWV from SSM/T2

Currently almost 5 years of upper tropospheric water vapor (UTWV) brightness temperature data is available from the SSM/T2 sensors. Figure 1a shows a time versus longitude plot over the equatorial band (10°N to 10°S) for this period. The first 3 harmonics of the annual cycle have been removed to highlight variability over intraseasonal to interannual time scales. The strong moisture signal corresponding to the 1997/98 El Niño is the most

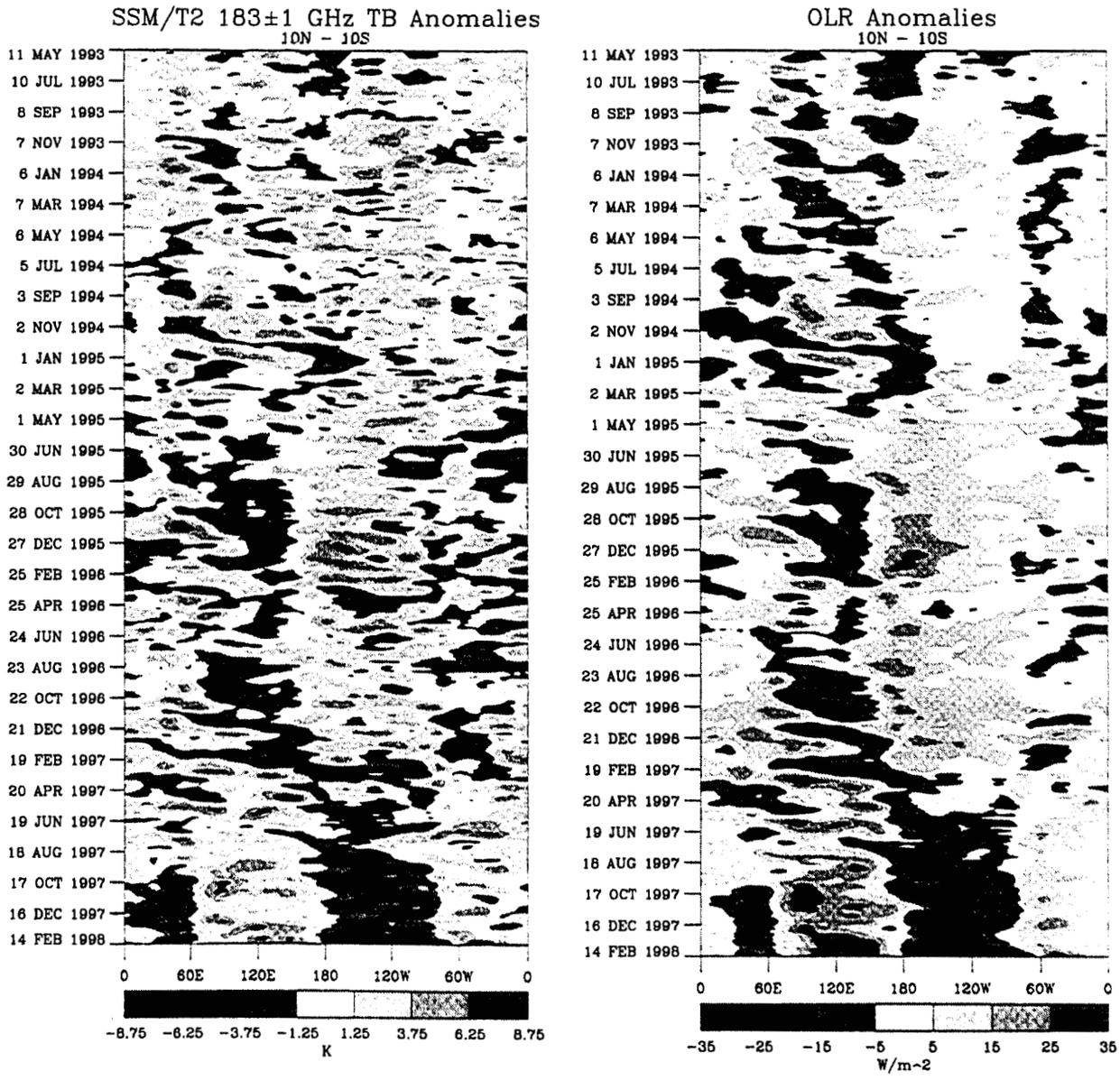

Figure 1: Time versus longitude plots averaged between 10°N and 10°S for a) SSM/T2 upper-tropospheric water vapor (UTWV) brightness temperature anomalies (183±1 Ghz), and b) outgoing longware radiation (OLR) anomalies. The first 3 harmonics of the annual cycle have been removed.

dominant feature. This shift in the center of convection from the west to the east Pacific is very similar to that of the OLR, which is shown in Figure 1b. The UTWV, however, is more sensitive to regions with strong subsidence as well as water vapor signals which are not evident in the OLR. As a result, the UTWV Tbs show evidence of possible westward propagating moisture anomalies into the eastern tropical Pacific over intraseasonal time scales. This signal is clearer in the 30-90 day band pass filtered UTWV time series. Further comparisons of these data sets with respect to the 1997/98 El Niño are discussed in the following section.

3. MONITORING OF THE 1997/98 EL NIÑO

Figure 2 shows a comparison of OLR, rainfall, integrated water vapor, and UTWV brightnes temperatures averaged for the months of January 1997 and January 1998. The effects of the 1997/98 El Niño are clearly evident in this figure as significantly more moisture in terms of both water vapor and cloud water is evident during the El Niño year. A very weak rainfall band along the east Pacific ITCZ is present in 1997 compared to intense activity during January of 1998. The southward shift of the ITCZ in 1998 is also evident in Figure 2. A strong band of water vapor at low levels extends all the

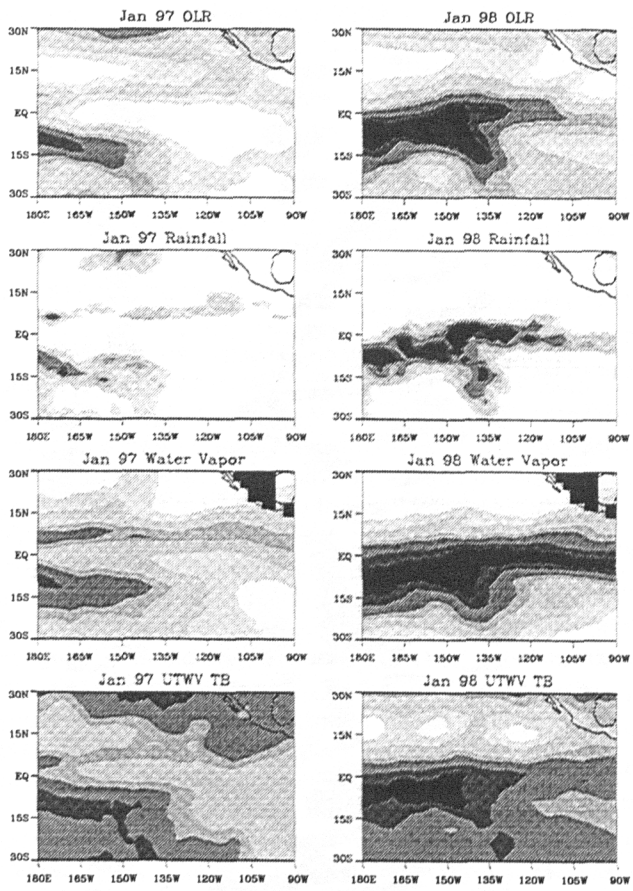

Figure 2: A comparison of satellite-derived observations between January 1997 and January 1998 of a) outgoing longwave radiation, b) rainfall derived from SSM/I, c) integrated water vapor from SSM/I, and d) upper-tropospheric water vapor (UTWV) brightness temperatures from SSM/T2. The range of values is consistant between the two years for each field.

way to the South American coast in 1998, although the intense precipitation is primarily west of 110° W.

The UTWV Tbs shown in the lower panels of Figure 2 indicate the presense of deep clouds and/or moisture at high levels over the convergence zones similar to the OLR. Unlike the OLR, however, strong subsidence at high levels is evident in the UTWV fields. This suggests an enhanced Hadley cell associated with the convection along the ITCZ resulting in extremely dry air in the upper troposphere around 15° - 20° N during the 1997/98 El Niño. This effect is even more evident in Figure 3, which shows a comparison of the OLR and UTWV TB anomalies for January of 1998. With the annual cycle removed, the anomalous drying of the upper troposphere is clearly evident. This demonstrates the utility of satellite observations of UTWV in conjunction with OLR because of the ability to detect both the ascending and descending branches of the atmospheric circulation.

Bates et al. [1996] found similar evidence of an extremely dry subsiding branch of the tropical circulation just southeast of Hawaii during the 1982/33 El Niño using UTWV brightness temperatures data from the

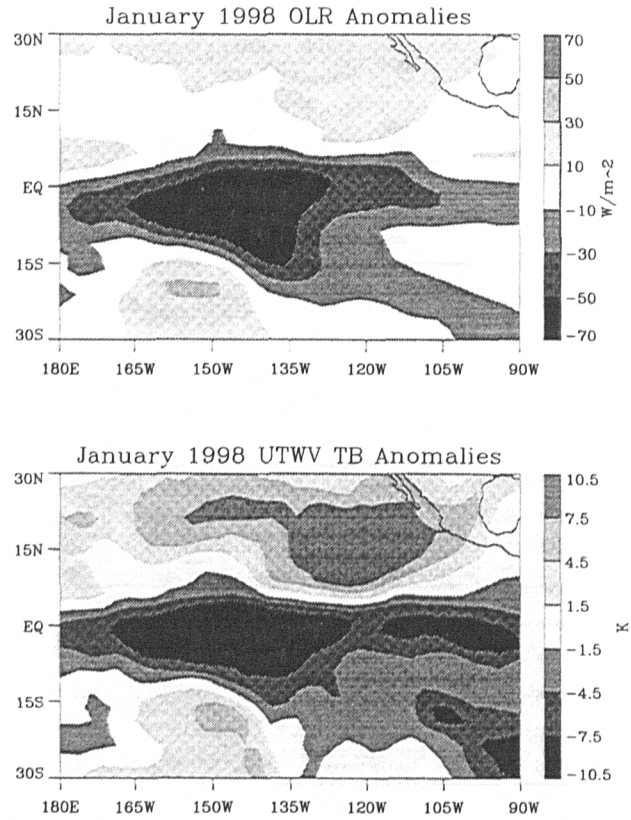

Figure 3: Anomalies of a) OLR and b) UTWV TBs for January 1998 over the eastern tropical Pacific. The first 3 harmonics of the annual cycle have been removed.

high-resolution infrared sounder (HIRS). Although the HIRS data extends back to 1979, providing a much longer time series of UTWV observations, it is far more sensitive to cloud contamination than the microwave SSM/T2. A comparison of these two data sets is given by Berg et al. [1998].

4. CONCLUSIONS

Satellite observations of moisture fields are critical to understanding atmospheric circulations over the tropical east Pacific due to the lack of in-situ observations over the tropical east Pacific and differences in the vertical distribution of rainfall and water vapor when compared with the warm pool region. The use of UTWV data provides information into the descending branches of the Hadley cell which are complementary to OLR observations. For example, there is strong evidence of a region of extremely dry air in the upper troposphere southeast of Hawaii during the 1997/98 El Niño. The availability of UTWV data from HIRS, SSM/T2, and GOES, therefore, provides an excellent source for climate studies of the tropical atmospheric circulations.

5. REFERENCES

Bates, J. J., X. Wu, and D. L. Jackson, 1996: Interannual variability of upper-troposphere water vapor band brightess temperatures, *J. Climate*, **9**, 427-438.

Berg, W. and S. K. Avery, 1995: An evaluation of monthly rainfall estimates derived from SSM/I over the tropical Pacific, *J. Geophys. Res.*, **100**, 1295-1315.

Berg, W., and S. K. Avery, 1994: Rainfall variability over the tropical Pacific from July 1987 through December 1991 as inferred via monthly estimates from SSM/I, *J. Appl. Meteor.*, **33**, 1468-1485.

Berg, W., J. J. Bates, D. L. Jackson, and M. Deeter, 1998: Analysis of upper tropospheric water vapor brightness temperatures from SSM/T2 and HIRS, in proceedings of the *9th Conference on Satellite Meteorology and Oceanography*, this issue.

Janowiak, J. E., P. A. Arkin, and P. Xie, 1993: An examination of rainfall variability in the eastern tropical Pacific, in *Proceedings of the eighteenth annual climate diagnostics workshop*, U.S. Dept. of Commerce, Nat. Oceanographic and Atmos. Admin., Washington, D.C., 216-219.

P2.27A

ABSOLUTE LIMITS FOR UPPER-TROPOSPHERIC HUMIDITY IN SUBTROPICAL HIGHS BASED ON SSM/T-2 OBSERVATIONS

Clay B. Blankenship*
Thomas T. Wilheit
Texas A&M University, College Station, Texas

1. INTRODUCTION

Water vapor plays an important role in the Earth's radiative balance. The subtropics are among the driest places in the atmosphere. These regions are important because they lose a large amount of radiation to space. The goal of this experiment is to establish absolute maxima for humidity near the 5-6 km level of the driest subtropical regions. This level is chosen because it can be very dry and because it is near the peak of the sensitivity function for the 183.31±1 GHz channel.

Observations from the Special Sensor Microwave Temperature-2 (SSM/T-2) radiometer have been used to retrieve profiles of water vapor in the atmosphere. Since many different profiles of water vapor can give the same set of observed brightness temperatures, there is some uncertainty in the retrieved profiles. A physical relaxation water vapor profile retrieval algorithm is used to establish strict limits on the humidity near the 5-6 km level of the subtropical high regions by finding the maximum humidity at that level for which a profile which can be found satisfying the observations. Maximum relative humidities of 3% and lower have been observed.

2. THE PHYSICAL RELAXATION ALGORITHM

A physical relaxation algorithm based on Blankenship (1997) is used to produce a humidity profile. This algorithm solves for RH starting with a known temperature profile (from the ECMWF analysis) and a first guess humidity profile. Four SSM/T-2 channels are used: 150 GHz and the three 183.3 GHz channels. The retrieved brightness temperature is computed using a forward radiative transfer model based on those of Wilheit (1990) and Al-Khalaf (1995). New profiles are computed iteratively, fitting to the observed brightness temperatures and climatological mean RH profile. A covariance matrix is used as a smoothness constraint on the retrieved humidity profile. After 25 iterations or when the normalized brightness temperature error, C_j, is less than 0.1, the RH profile with the lowest C_j is taken as correct, provided $C_j<1$. For a given pixel or set of observations, if no $C_j<1$, the algorithm has failed to produce a humidity profile matching the observations.

* *Corresponding author address:* Clay B. Blankenship, Texas A&M Univ., Dept. of Meteorology, College Station, TX 77843-3150; e-mail: cblanke@h2o.met.tamu.edu.

3. ESTABLISHING A LIMIT ON THE 5-6 km HUMIDITY

We are interested in the maximum water vapor content of the layer near 5.5 km ($RH_{5.5km}$) which satisfies the SSM/T-2 observations. The algorithm described in section 2 gives RH at 10 levels (1, 2, 3, 4, 5, 6, 7, 8, 10, and 12 km). Let RH_n be the value of RH at an altitude of *n* km and $RH_{n,0}$ be the initially retrieved value. The 5 and 6 km RH values are held fixed at some perturbation times their initial values (i.e., $RH_5=f\,RH_{5,0}$ and $RH_6=f\,RH_{6,0}$) and the retrieval is run again, allowing RH at the other eight levels to vary. These subsequent retrievals are run for values of f ranging from 1 to 2 in increments of 1/32. Since we are only interested in the driest areas, pixels with clouds or with an initial retrieved $RH_{5.5km}>50\%$ are ignored.

For each value of f, the new retrieved profile is checked with a forward radiative transfer model to see if

$$\frac{1}{M}\sum_{i=1}^{M}\left(\frac{T_i^{ret}-T_i^{obs}}{NE\Delta T_i}\right)^2 < 1 \text{ and} \qquad (1)$$

$$\left(\frac{T_i^{ret}-T_i^{obs}}{NE\Delta T_i}\right) < 2 \text{ for each i} \qquad (2)$$

(where T_i^{ret} and T_i^{obs} are the retrieved and observed brightness temperatures for the i'th channel, $NE\Delta T_i$ is the noise equivalent temperature uncertainty of each channel, and M is the total number of channels used). Condition (1) ensures that the rms of the difference between observed and retrieved brightness temperatures is less than the instrument noise level. Condition (2) ensures that no individual channel has a brightness temperature difference greater than twice the standard deviation of the measurement. This condition helps limit profiles which are too wet at one level and too dry at another. As a third condition, all levels must have a retrieved RH between 0% and 100%. This condition prevents unphysical profiles. The largest f which satisfies the above conditions gives a value for the maximum RH averaged over the layer from 4.5 to 6.5 km:

$$RH_{5.5km}^{\max} = f\,\frac{RH_{5,0}+RH_{6,0}}{2}.$$

4. RESULTS

Results from this experiment are presented in Figure 1. The left panel shows the retrieved 5-6 km relative humidity for a region west of southern Africa. The right panel shows the maximum 5-6 km relative humidity satisfying the stated constraints. Figure 2 shows the zonal averages of both variables for the pictured swath.

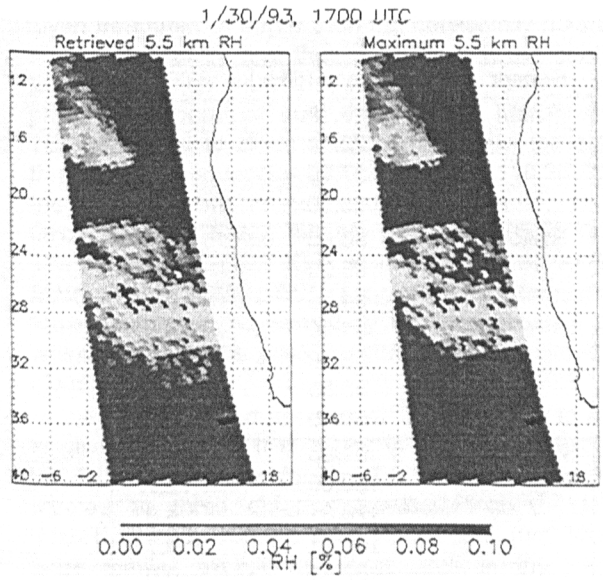

Figure 1. Retrieved 5.5±1 km RH (left panel) and maximum 5-6 km RH (right panel) for a region west of southern Africa. Black pixels indicate the algorithm was unable to determine the RH with certainty. The dynamic range was chosen to highlight the driest regions.

The lowest value of retrieved RH zonally averaged over one degree bands shown in Figure 2 is about 1.54% with a corresponding maximum RH of 2.66%. A parcel at 267 K (a typical value for these data) with a 3% RH has a water vapor density of .095 g m^{-3}. This parcel, assuming undiluted descent from saturation, would have been saturated at a temperature of 225 K. In a typical tropical atmosphere, this temperature occurs at 220 mb. For comparison, the tropopause is at about 100 mb (AFCRL, 1965).

5. CONCLUSIONS

Accurate humidity measurements in these regions are needed for climate models, but the few radiosondes from these regions often do not report RH below 20%. We have established a method for finding the maximum RH a given layer can have based on the SSM/T-2 observations. This method shows that humidities in the subsidence zones can be as low as 3%.

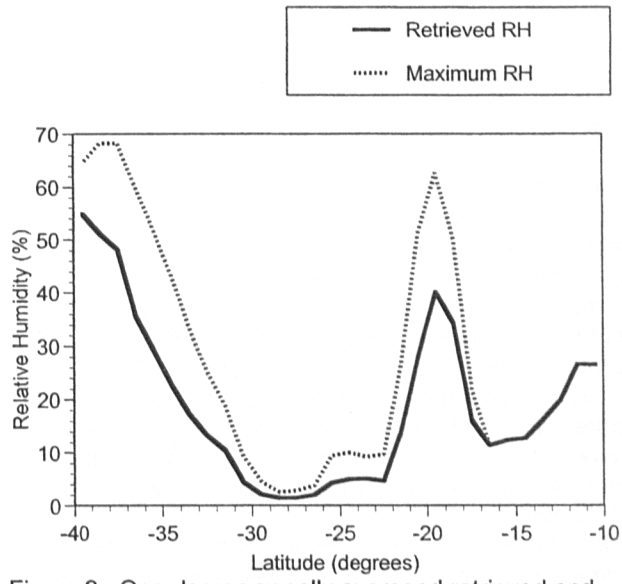

Figure 2. One degree zonally averaged retrieved and maximum RH at 5.5±1 km for the data in Figure 1.

6. REFERENCES

Air Force Cambridge Research Laboratory, 1965: *Handbook of Geophysics and Space Environments.* McGraw-Hill.

Al-Khalaf, A. K., Retrieval of atmospheric water vapor profiles from the special sensor microwave temperature-2 (SSM/T-2), 1995. *Ph.D Dissertation*, Texas A&M University, 145 pp.

Blankenship, C. B., Retrieval of Water Vapor Profiles Over Ocean Using SSM/I and SSM/T-2, 1997. *M.S. Thesis,* Texas A&M University, 76 pp.

Wilheit, T. T., 1990: An algorithm for retrieving water vapor profiles in clear and cloudy atmospheres from 183 GHz radiometric measurements: Simulation studies. *J. Appl. Meteor.*, **29**, 508-515.

P2.28B

CLOUD SENSITIVITY OF PASSIVE MICROWAVE OBSERVATIONS

Gerald W. Felde

Space Vehicles Directorate, Air Force Research Laboratory
Hanscom Air Force Base, Massachusetts

1. INTRODUCTION

Recently, Greenwald et al. (1997) developed a technique to retrieve integrated cloud liquid water content of nonprecipitating clouds over land surfaces using Special Sensor Microwave/Imager (SSM/I) 85.5 GHz measurements. Their method makes use of a normalized difference between the vertically and horizontally polarized brightness temperatures (TBs) at 85.5 GHz. This study is a preliminary exploration for the potential use of passive microwave TBs at several frequencies to extract information on the vertical structure of liquid water clouds over land backgrounds. The frequencies examined are listed in Table 1. They include those of the three DMSP (Defense Meteorological Satellite Program) passive microwave instruments, SSM/I, SSM/T (Temperature Sounder), and SSM/T-2 (Water Vapor Sounder); as well as, the frequencies in the 118 GHz sounder band of the NAST [NPOESS (National Polar-Orbiting Operational Environmental Satellite System) Airborne Sounder Testbed] aircraft instrument.

2. SIMULATIONS

A sensitivity analysis of vertically and horizontally polarized brightness temperatures (TB_v and TB_h) to liquid water clouds over land backgrounds was performed. It was based on TBs at each of the frequencies listed in Table 1 at a zenith angle of 55° calculated from the RADTRAN microwave atmospheric model (Isaacs et al., 1989). This model was modified to include the Liebe (1989) cloud attenuation module and the Bauer and Grody (1995) land surface emissivity module.

The SSM/I has a conical scan which results in a constant zenith angle of 53.1° while the SSM/T, SSM/T-2, and NAST have cross-track scans which results in variation in zenith angle from 0° at nadir to about 50° at scan edges. Two TB measurements are taken at each SSM/I frequency, one which is vertically polarized and the other which is horizontally polarized. For the cross-track scanners, the polarization rotates with scan angle and is all vertical at nadir but is a combination of vertical and horizontal at the other scan positions.

Corresponding author address: Gerald W. Felde, AFRL/VSBE, 29 Randolph Rd, Hanscom AFB, MA 01731-3010.

Table 1. Channel frequencies of passive microwave sensors and their TB_v sensitivity to 1.5 km thick cloud (total water = 1000 g/m^2) with top at 4.5 km.

Sensor	Frequency (GHz)	ΔTB (K)
SSM/I	19.35	1.8
	22.24	2.6
	37.00	5.3
	85.50	11.9
SSM/T	50.50	6.5
	53.20	2.1
	54.35	0.2
	54.90	0.0
	58.40	0.0
	58.83	0.0
	59.40	0.0
SSM/T-2	91.65	12.5
	150.00	12.7
	176.31	4.8
	180.31	0.7
	182.31	0.0
NAST (118 GHz Band)	113.25	12.7
	115.25	11.7
	116.20	10.3
	116.70	8.9
	117.15	6.7
	117.55	3.9
	117.95	1.0
	118.30	0.0
	118.53	0.0
	118.64	0.0
	118.69	0.0
	118.72	0.0

The atmospheric conditions used in the simulations were based on an Albany, NY summer radiosonde-measured profile. Cloud conditions were no cloud and a 1.5 km thick cloud layer with cloud top located at 1.5, 3.0, and 4.5 km with integrated liquid water values of 200, 400, 600, 800, or 1000 g/m^2. The liquid water concentration increased linearly from zero at cloud base to a maximum value at 0.5 km above cloud base and then remained constant throughout the rest of the cloud. Below 4.5 km, the relative humidity (RH) was set to 0.96 in the cloud layer and to 0.50 elsewhere. Above 4.5 km, the RH profile was not varied.

The difference between the model calculated TB for cloud-free conditions and for cloud conditions, ΔTB, was used as a metric for the sensitivity to a particular set of cloud conditions. The largest ΔTB values were found for vertically polarized TBs for the cloud layer at the highest altitude (tops at 4.5 km) having the maximum total cloud water (1000 g/m^2). These values are listed in Table 1. For all ΔTB values in this table which are greater than 5 K, the corresponding ΔTB values for horizontal polarization (not shown in the table) are smaller by amounts up to 1.6 K. This is because the vertically polarized surface emissivity at a given frequency is larger than the horizontally polarized surface emissivity and thus provides a better contrast to the emission from the cloud which has a colder physical temperature than the surface. The greatest TB_v sensitivity to cloud (ΔTB > 10 K) are the NAST three lowest frequencies (113.25, 115.25, 116.25 GHz), the SSM/T-2 two lowest frequencies (91.65, 150.00 GHz), and the SSM/I highest frequency (85.50 GHz). The largest ΔTB (12.7 K) is at 113.25 and 150.00 GHz. Many of the SSM/T, SSM/T-2, and NAST frequencies have minimal or no sensitivity to cloud because their weighting functions peak at atmospheric levels above cloud.

A more detailed analysis of TB_v sensitivity to cloud is given in Fig. 1. It is a plot of the 113.25 GHz TB_v vs. total cloud water for the 1.5 km thick cloud layer located at three different levels. Plots at 115.25, 116.20, 91.65, 150.00, and 85.50 GHz (not shown) were similar except for some shift in the vertical position of the set of curves. This figure indicates that for a cloud layer at a particular altitude, TB_v sensitivity to total cloud water increases with altitude. Also, it shows for constant total cloud water, the difference in TB_v among the three cloud layers increases as cloud water increases.

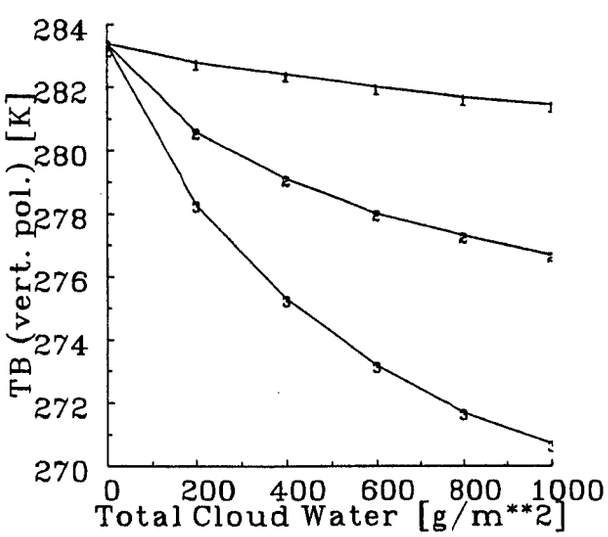

Fig. 1. TB_v sensitivity to total cloud water for a 1.5 km thick cloud layer with tops at: 1) 1.5 km, 2) 3.0 km, and 3) 4.5 km.

3. CONCLUSIONS

Simulations show for a 1.5 km thick water cloud over land background, TB_v has good sensitivity to total cloud water and cloud layer altitude for some of the SSM/I, SSM/T-2, and NAST frequencies. This study shows the potential of using microwave TBs for cloud parameter retrieval but additional sensitivity analysis needs to be done for cloud layers of varying thickness, for a range of different land surfaces, and for other atmospheric temperature and RH profiles.

REFERENCES

Bauer, P. and N. C. Grody, 1995: The potential of combining SSM/I and SSM/T2 measurements to improve the identification of snowcover and precipitation. *IEEE Trans. Geosci. and Remote Sensing*, **33**, 252–261.

Greenwald, T. J., C. L. Combs, A. S. Jones, D. L. Randel, and T. H. Vonder Haar, 1997: Further developments in estimating cloud liquid water over land using microwave and infrared satellite measurements. *J. Appl. Meteo.*, **6**, 389–405.

Isaacs, R. G., R. D. Worsham, and B. L. Lindner, 1989: Characterizing Microwave Propagation Using the AFGL Microwave Attenuation/Transmittance/Brightness Temperature Code. *GL-TR-89-0188*, Hanscom AFB, MA, 87 pp.

Liebe, H. J., 1989: MPM - An atmospheric millimeter wave propagation model. *Int. J. Infrared Millimeter Waves*, **10**, 631–650.

P2.29A CLOUD BASE HEIGHT RETRIEVAL FROM DMSP MICROWAVE DATA AND *a priori* CLOUD TOP TEMPERATURES

Thomas T. Wilheit*
Texas A&M University; College Station, Texas
and
Keith D. Hutchison
Center for Remote Environmental Sensing Technology (CREST)
Lockheed/Martin Missiles & Space; Sunnyvale, California

The retrieval of cloud base heights from spaceborne microwave measurements has been listed among the requirements for the CMIS sensor on the future NPOESS satellite. Technically this is a very daunting challenge. However, the water vapor profile algorithm reported by Wilheit and Hutchison, 1997 does yield a cloud base as a by-product of the water vapor retrieval under cloudy circumstances. The liquid cloud case reported by W&H, 1997, while hardly definitive, provides some basis for hope. While it is likely that any adequate algorithm will be highly tuned for local circumstances, if there is no physical basis for the retrieval imbedded in the signal then success is unlikely. Accordingly, we have examined the cloud base signal inherent in water vapor sounding channels.

For demonstration purposes, we have chosen the relevant channels on the current DMSP satellite. To examine the signals, an idealized atmosphere with 5 degrees of freedom has been used. It assumes a surface temperature of 288K and a lapse rate of 6.5K/km. The degrees of freedom are the top and bottom height of the cloud, the cloud liquid water content and the relative humidities above and below the cloud, each assumed to be constant. The relative humidity is fixed at 100% within the cloud.

A skeleton algorithm is assumed which minimizes a penalty function consisting of the normalized squares of the departures of observed brightness temperatures from the computed brightness and similar departures for ancillary information. A locally linear expansion about an assumed state is computed numerically and inverted to derive the retrieval algorithm. The coefficients of this algorithm are used with the assumed uncertainty in the measurement channels to derive a cloud base uncertainty. An uncertainty computed in this way is optimistic due to departures of a real atmosphere from the idealized assumptions but is pessimistic in that it does not account for non-linear constraints in the problem such as the cloud base cannot be below the surface nor above the cloud top.

The upper solid curve in each group in Figure 1 gives the uncertainty so calculated as a function of cloud top height for a 1 km thick cloud with 10 mg $(cm)^{-1}$ liquid water content. The baseline assumes 50% relative humidity above and below the cloud. The algorithm uses 6 channels out of the SSM/I-SSM/T2 combination (22.2 V, 37H, 150, 183 ±1, 183±3 and 183±7) with an assumed NEΔT of 0.6K in all channels to derive the cloud base in a

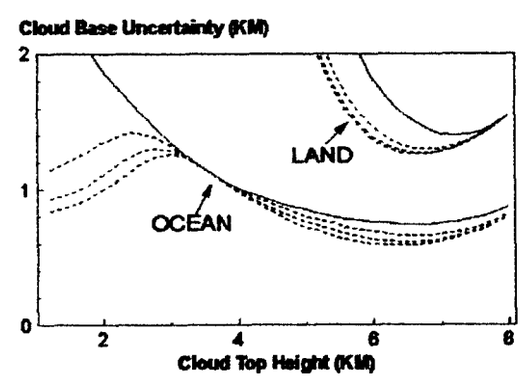

Figure 1

Uncertainty in retrieved cloud base height as a function of cloud top height for various cloud top temperature uncertainties

* Corresponding Author address: Thomas T. Wilheit, Department of Meteorology, Texas A&M University, College Station, TX 77845-3150
e-mail: wilheit@tamu.edu

slightly overdetermined retrieval. Computations were carried out for both ocean and land backgrounds.

The ocean case certainly suggests a reasonable possibility of retrieving cloud bases at least for clouds above 3 km or so. The results over land are much less encouraging.

We have tested the impact of knowledge of the cloud top temperature on the retrieval. We have used cloud top temperature uncertainties of 6, 3 and 0.3K. These are shown as the sets three dashed curves below the solid curves. It is clear CTT information with even a 6K uncertainty makes a major impact at low altitudes over the oceans; further improvements in the CTT contribute only modest improvements in the net uncertainties. Even with the CTT constraint, the results over land remain discouraging.

The model has been run with a variety of different baseline assumptions. Other assumed instrumental configurations can likewise be simulated. The results presented here may be translated to other assumed noise uncertainties by appropriate scaling.

This represents only the propagation of the measurement uncertainty in the brightness temperatures and not any departure of the real atmosphere from the assumed idealized atmosphere. On the other hand, some help may be gained by tuning the algorithm locally. Some of this tuning will be possible by using explicit constraints derived from local data such as relative humidity covariance matrices. Eventually a useful level of accuracy is only likely to be obtained by empirical tuning methods such as regressions and/or neural nets.

References

Wilhelt, T.T. and K.D. Hutchison, 1997; Water Vapour Profile Retrievals from SSM/T-2 Data Constrained by Infrared-based Cloud Parameters. *Int. J. Remote Sensing* **18**, 3263-3277

Acknowledgment

The authors gratefully acknowledge funding support from Lockheed/Martin Missiles & Space Company, Advanced Technology Center.

P 2.30B DEVELOPMENTS ON SST RETRIEVAL OVER THE ATLANTIC USING GEOSTATIONARY AND POLAR ORBITER SATELLITE DATA IN THE FRAME OF EUMETSAT OCEAN AND SEA ICE SATELLITE APPLICATION FACILITY.

Soren Andersen+, Alain Brisson++, Steinar Eastwood+++, Pierre Le Borgne*++, Anne Marsouin++
+ DMI, Copenhagen, Denmark, ++ Météo-France, Lannion, France, +++DNMI, Oslo, Norway

1. Introduction

A routine production of SST fields will be made in the preoperational phase (1997-2001) of the EUMETSAT Ocean and Sea Ice Satellite Application Facility (O&SI SAF). This production will be done by the O&SI SAF "Low and Mid Latitudes" at Météo-France/CMS in Lannion and by the O&SI SAF "High Latitudes" which includes the Norwegian and Danish Meteorological Institutes (DNMI and DMI).This project includes:

1- The calculation of SST over the North-East Atlantic at a 2 km resolution from the NOAA AVHRR data for each pass available over the North-East Atlantic.

2- The calculation of SST over the Northern and Southern areas of the Atlantic (above 50N and below 50S) at a 10 km resolution from the NOAA AVHRR data.

3- The calculation of GOES-8 and MSG derived SST fields on a hourly basis at a 10 km resolution from 50N to 50S.

The implementation of these processings will follow the following steps : algorithm development, prototyping, preoperational implementation, and preoperational experiment.

The algorithm development is based on the following principle : definition of algorithms on simulated brightness temperatures, validation against in situ measurements when they are already available. The present paper describes the status of the algorithm development step and its first results.

2. Simulated ir brightness temperature data base

The simulations have been performed on TIGR and will be soon performed on dedicated radio sounding sets collected at DNMI.

TIGR (Tovs Initial Guess Retrieval database), has been made at LMD Paris (Chedin et al 1985). We have been provided with the version of TIGR used in the frame of this project by V. Achard (Achard 1991) from ONERA.

A "global maritime" subset of TIGR has been made by selecting the maritime or coastal radio soundings.

A "geostationary" subset has been built out of the "global maritime" file by extracting data corresponding to the 60N 60S latitude band

Similarly, a radio sounding database has been built for latitudes north of 50N (65W-65E) containing only cloud free soundings over sea (NORA). The soundings have been collected from ships and small islands in the North Atlantic from 1993 up to today. These data will be used together with the NCEP/NCAR Arctic Marine Rawinsonde Archive received from NSIDC.

The main characteristics of the radio sounding databases are shown in table 1.

MODTRAN (Bernstein et al.,1995) has been used to compute the brightness temperatures on each radio sounding of the TIGR "global maritime" and "geostationary" subsets, under the following conditions:

-No aerosols have been considered.

-Four values of the secant of the satellite zenith angles have been retained

-Three surface temperatures have been assigned to each radio sounding: Ta1000 (1000 mb air temperature), Ta1000+3C, Ta1000-3C.

-Radiances have been simulated with emissivity values derived from the tables of Masuda 1988 with a moderate wind speed of 5 ms-1.

RS data bases	TIGR gl.maritime	TIGR geost.	NORA	NCEP/ NCAR
nb of cases	485	327	94	27
Ts (C) (st.dev.)	11.9 (8.7)	14.8 (8.2)	8.8 (5.7)	7.2 (5.5)
W_0 (g/cm2) (st.dev.)	1.89 (1.23)	2.18 (1.30)	1.15 (0.54)	1.24 (0.54)

Table 1. Main characteristics of the radio sounding data bases. Ts: mean surface temperature ; W_0: mean total water vapour content at nadir.

3. Match Up Data bases

Four main matchup data bases, gathering satellite data extracted at the time and location of in situ measurements of SST have been made in the frame of the O&SI SAF or adapted from those of the

*Corresponding author address : Pierre Le Borgne Météo-France/SCEM/CMS, BP 147, 22302 Lannion, FRANCE ; e-mail : Pierre.LeBorgne@meteo.fr

NOAA/NASA Pathfinder project. They will be referred to as the "n14pathfinder", "n14cms" and "g08cms" matchup databases. In order to avoid dawn or dusk conditions nighttime cases have been defined for sun zenith angles over 110 degrees, daytime cases for sun zenith angles below 70 degrees.

Global MDBs: Such bases have been build on the world ocean from AVHRR GAC data (Podesta et al, 1997) in the frame of the NOAA/NASA Pathfinder programme. "n14pathfinder" is representative of the year 1995. Oort (1983) climatological water vapour contents have been added to this data base.

High latitudes: A MDB is being built at DMI and DNMI. It covers the North Atlantic north of 65N between 70E and 70W and the Baltic Sea. It will include NOAA-12 and 14 data since November 1993.

Mid latitudes: Validation files have been built on a routine basis at CMS over the european seas since 1989. NB: channel 3 data are not included into the MDB in the present version of the processings. "n14cms" has been made with data from September 1996 till September 1997. It includes nighttime data only.

Geostationary: Satellite and in situ data have been extracted inside the GOES-8 Northern Hemisphere sector. Three hourly GOES-8 data acquired at CMS have been used. A provisional cloud masking scheme, inspired from that of the AVHRR, has been applied for every pixel. "g08cms" has been build following this processing from January 1997 till January 1998. Total water vapour contents derived from NWP model outputs (ARPEGE) are included in the CMS MDBs.

A summary of the MDB main characteristics is shown in table 2. The comparison of tables 1 and 2 shows that the TIGR based simulation files are biased towards dry and cold cases. This is due to a too small number of low latitude radio soundings.

MDB:	n14path finder	n14cms night	g08cms
box size (km)	12 *12	22*22	20*20
number of cases	9249	1044	26403
Ts (C) (st.dev.)	22.2 (6.4)	15.3 (4.8)	23.9 (6.1)
W_0 (g/cm2) (st.dev.)	3.00 (1.08)	1.63 (0.63)	3.46 (1.33)

Table 2. Main characteristics of the Matchup Data Bases

4. ALGORITHMS

The method we chose, based on the use of simulations (and not on regressions applied on bulk SST measurements) allows the determination of skin temperature algorithms. The skin to bulk temperature conversion problem will be studied at DMI. If needed, the bulk SST may be calculated by correcting the theoretical algorithms from the biases observed between calculated temperatures and measurements on MDBs.

Two cases have been considered:

-The derivation of SST from the two "split window" channels centred on 11 (AVHRR channel 4) and 12 microns (AVHRR channel 5) respectively. Split window algorithms allow the calculation of SST under night and day conditions. Three main approaches correspond to the latest developments in that field (Barton 1995): algorithms depending explicitely on water vapour content (Sobrino et al 1993, 1996, Emery et al 1994, Arbelo et al 1996, François and Ottlé 1996), temperature dependent algorithms, and quadratic algorithms (Emery et al 1994 and François and Ottlé 1996).

-The use of the channels centred on 3.7µm (AVHRR channel 3) or 3.9 µm (GOES-8 channel 2). These channels are potentially interesting since they show a minimum of atmospheric absorption. They are however affected by solar radiation and cannot be used by day.

Preliminary tests showed that quadratic algorithms are not as accurate the other proposed split window algorithms. Furthermore algorithms based on the use of 3.7/3.9 µm brightness temperature have shown the best results when all three IR channels are used. In consequence the formalisms selected in the frame of the project are the following :

Water vapour algorithms (WV):

$$Ts = D\,T11 + (a_0 + a_1 W + a_2 W^2)(T11 - T12) + c_0 + c_1 W + c_2 W^2$$

Temperature dependent algorithms (NL)

$$Ts = DT11 + (a_t T_{guess} + a_s S)\,(T11 - T12) + C$$

In that case the climatological SST, Ts_{clim}, has been chosen as the first guess SST.

T3.7 centred algorithms (T3.7, resp. T3.9)

$$Ts = E\,T3.7 + F(T11 - T12) + G$$

Simple triple window algorithms (TRI)

$$Ts = HT11 + J(T3.7 - T12) + K$$

All coefficients may depend linearly on S.

(Ts is the calculated SST, T3.7, T11 and T12 are the brightness temperatures at 3.7, 11 and 12 µm respectively; .$S = \sec(\theta) - 1$ and $W = W_0/\cos(\theta)$ with θ: satellite zenith angle ; W_0: total water vapour content at nadir ; all temperatures are in Celsius).

5. NOAA-14 RESULTS

Regression on TIGR (global maritime) produced the following coefficients :

NLN14: D = 0.979 ; A = $0.064Ts_{clim} + 1.227S$; C = 1.097

WVN14: D = 1.02 ; A = 0.972 + 0.328 W ; C = 0.466 + 0.909 S - 0.070 W - 0.040 W^2

T3.7N14: E= 1.003 + 0.019S ; F = 0.723 + 0.305S ; G= 1.175 + 0.998S

TRIN14: H = 1.004 + 0.020S ; J =0.888 + 0.135S ; K = 1.020 + 1.146S

These algorithms and the operational NOAA algorithms (MCSST and NLSST) have been applied on the simulation file and on the NOAA-14 MDBs.

The results of the validation are shown in table 3.

The main conclusions of the tests on the NOAA-14 case are the following:

-The simulation derived algorithms (NL and WV) show reasonable results on the global and mid latitude MDBs when compared to the operational ones. The WV algorithm presents however the best results on the simulation files.

-The results obtained when using T3.7 do not depend on the formalism retained. They are excellent, both on the simulation file and on the MDB (night).

6. GOES-8 RESULTS

GOES-8 algorithms have been determined on the geostationary subset of TIGR. They have the following coefficients:

NLG08: D = 0.981 ; A = $0.063Ts_{clim} + 1.143S$; C = 1.085

WVG08: D = 1.02 ; A = 0.946 + 0.307 W ; C = 0.518 + 0.860S - 0.1W - 0.033W^2

T3.9G08: E = 1.006 + 0.011S ; F = 0.408 + 0.299S ; G = 1.636 + 1.534S

TRIG08: H = 1.005 + 0.018S ; J = 0.784 + 0.115S ; K = 1.252 + 1.551S

The results of these algorithms applied on the simulation files and the MDBS are shown in table4. Since the results obtained on g08cms at night were questionable due to a defect of the cloud mask (this mask has been defined as "provisional" and will be soon upgraded, the algorithms have been applied also on Dr. X. Wu's MDB (g08wis) from CIMSS, University of Wisconsin. The results of the Legeckis and Zhu (1997) algorithm (L&Z) have been added for comparison. The overall conclusions are similar to those obtained for the NOAA14 case. However, the results of the simulation derived algorithms presents quite a small bias on the MDB (day), and a larger one (by about 0.5 C) on the MDB (night). This could be due to the diurnal thermocline effect, however such a difference was not observed on the pathfinder MDB.

validation files	n14pathfinder day&night		n14pathfinder day		n14pathfinder night		n14cms		global maritime TIGR	
nb cases	9249		4720		4137		1044		4948	
results	bias	st dev.	bias	st. dev	bias	st. dev.	bias	st. dev.	bias	st. dev.
MCSST	-0.10	0.70	-0.06	0.67	-0.13	0.70	-0.25	0.63	-0.68	0.54
NLSST	0.02	0.59	0.06	0.57	-0.03	0.61	-0.11	0.57	-0.13	0.60
NLN14	0.22	0.67	0.20	0.64	0.24	0.68	0.01	0.56	0.00	0.51
WVN14	0.27	0.71	0.22	0.71	0.33	0.70	0.20	0.58	-0.03	0.36
T3.7N14	/	/	/	/	0.21	0.55	/	/	0.0	0.17
TRIN14	/	/	/	/	0.21	0.55	/	/	0.0	0.17

Table 3. Results of the NOAA-14 algorithms

validation files	g08cms (day)		g08wis (day)		g08wis (night)		geostationary TIGR	
nb cases	2363		4048		2859		3612	
results	bias	st. dev.	bias	st. dev.	bias	st. dev.	bias	st. dev.
L&Z	-0.42	0.85	-0.15	0.80	-0.47	0.78	-0.29	0.45
NLG08	-0.38	0.74	-0.11	0.69	-0.53	0.72	0.0	0.53
WVG08	-0.21	0.86	0.10	0.73	-0.43	0.77	-0.11	0.42
T3.9G08	/	/	/	/	-0.55	0.68	0.0	0.27
TRIG08	/	/	/	/	-0.49	0.67	0.0	0.25

Table 4. Results of the GOES-8 algorithms.

7. SUMMARY AND CONCLUSION

For night and day processing, two split window algorithms showing reasonable results on the MDBs have been retained, one (NL), with temperature dependent coefficients, and an other (WV) whose coefficients depend on the total water vapour content. WV presents better results than NL on the simulation files but is more sensitive to the noise in the input brightness temperatures, due to larger D and A coefficients. This induces worst results on the validation files.

For night processing only, algorithms using the channel 3.7 µm temperatures show significantly better results, both on simulation files and on MDBs. The TRI and T3.7 algorithms gave the same results, due to the similar weight of T3.7 and T11 in both algorithms.

The final choice of operational algorithms will depend on:

- the level of instrumental noise reduction on the atmospheric correction which can be achieved by smoothing T11-T12 or T3.7-T12.
- the results of the specific studies led by DNMI on the high latitudes, since a good continuity should be guaranteed between low and mid latitude processing and high latitude processing.
- practical considerations that will be raised during the prototyping phase.

The method described in this paper is a basic tool which will be used to define algorithms for NOAA-K and for MSG. However some problems were pointed out, which requires more detailed studies:

- Reduction of the instrumental noise.
- Study of the mid to high latitude transition.
- Adding low latitude radio soundings to TIGR.
- Analysis of the effect of aerosols.

ACKNOWLEGMENTS

The authors wish to thank Dr. X. Wu from CIMSS, University of Wisconsin, for his help and fruitful discussions.

REFERENCES

Achard, V.,1991: "Trois problemes clés de l'analyse 3D de la structure thermodynamique de l'atmosphère par satellite: Mesure du contenu en ozone, classification des masses d'air, modélisation "hyper" rapide du transfer radiatif", Thèse, Université de Paris 7, Paris, France, 1991, pp. 44-58.

Arbelo, M., F. Herrera, F.J. Exposito, V. Caselles, and C. Coll, 1996: Determination of sea surface temperature using combined TOVS and AVHRR data. Application to the Canary Islands area, Spain, *Int. J. Remote Sensing*, **17**, 359-371.

Barton, I., 1995: Satellite derived sea surface temperatures: Current status, *J. Geophys. Res.*, **100**, 8777-8790.

Bernstein L.S., A. Berk., P.K. Acharya, D.C. Robertson, G.P. Anderson, J.H. Chetwynd, L.M. Kimball, 1996, Very Narrow Band Model Calculations of Atmospheric Fluxes and Cooling Rates Using the MODTRAN Code, *J. Atmos. Sci.*, **53**, 2887-2904.

Chedin, A, N.A. Scott, C. Wahiche, and P. Moulinier, 1985: " The improved initialization inversion method: A high resolution physical method for temperature retrievals from TIROS N series", *J. Clim. Appl. Meteor.*, **24**, 128-143.

Emery , W.J., Y. Yunyue, G.A. Wick, P.Schluessel, and R.W. Reynolds, 1994: Correcting infrared satellite estimates of sea surface temperature for atmospheric water vapor attenuation. *J. Geophys. Res.*, **99**, 5219-5236.

François, C. and C. Ottlé, 1996: Atmospheric corrections in the thermal infrared: Global and water vapor dependent split window algorithms-Applications to ATSR and AVHRR data *IEEE Trans. Geosci. Remote Sensing*, **34**, 457-470.

Legeckis R. and T. Zhu, 1997: Sea surface temperature from the GOES-8 geostationary satellite, *Bull Amer. Meteor. Soc.*, **78**, 1971-1983.

Masuda, K., T. Takashima and Y. Takayama, 1988: Emissivity of pure and sea waters for the model sea surface in the infrared window regions, *Remote Sens. Environ.*, **24**, 313-329.

Oort, A.H. 1983: Global atmospheric circulation statistics, 1958-1973. NOAA professional paper #14.

Podesta G.P., S. Shenoi, J. W. Brown and R. H. Evans, 1997: AVHRR Pathfinder Oceans Matchup database 1985-1995 version 19.0, http://www.rsmas.miami.edu/~gui/matchups.html.

Sobrino, J. A., Z.-L. Li, and M.P. Stoll, 1993: Impact of the atmospheric transmittance and total water vapor content in the algorithms for estimating satellite sea surface temperatures, *IEEE Trans. Geosci. Remote Sensing*, **31**, 946--952.

FIVE YEARS OPERATIONAL DERIVATION OF MULTICHANNEL SEA SURFACE TEMERATURES AT THE GERMAN REMOTE SENSING DATA CENTER

P2.33A

Stefan W. Dech*, P. Tungalagsaikhan, Andrea Holz & Robert E. Meisner
Deutsches Zentrum für Luft- und Raumfahrt (DLR), Oberpfaffenhofen, Germany

1. INTRODUCTION

The derivation of geophysical parameters is a key issue in remote sensing and earth sciences. However, too many scientific algorithms have been published in the last decade dealing with only a few data sets under well known "test" conditions, and less efforts were put into research for adapting and optimizing these algorithms for operational application. Particularly, AVHRR data provide an excellent and continuous information base for many atmosphere and surface-related parameters, such as temperatures, vegetation index, and follow-on products as climatologies, time series, Leaf Area Index (LAI), land cover, etc.. Keeping this in mind, DLR's German Remote Sensing Data Center (DFD) started in 1993 with the definition and generation of AVHRR-based value-added products in 1 km resolution, and the first operational "pathfinder" data sets available to the user community were Multichannel Sea Surface Temperature (MCSST) maps of the Mediterranean Sea and the Black Sea. Special emphasis was put from the beginning on accurate registering and cloud detection to ensure precise generation of time synthesis products, e.g. decade composites, weekly, and monthly averages. As of today, MCSST products in three different map projections, NDVI maps since 1994 and since March 1998 also Land Surface Temperatures (LST) derived from AVHRR data are accessible on-line with one day delay in full resolution through DLR's electronic user interface ISIS (http://isis.dlr.de). Alone in 1997, more than 10,000 digital data transfers were recorded, proving that DFD's data product philosophy is meanwhile widely accepted by the international user community and the resulting thematic information was put into scientific research.

In this paper, a brief summary of the major processing steps applied is given, and the value of the MCSST time series for many oceanographic and climatological issues is outlined by giving one example for the North Atlantic.

2. DERIVATION OF MCSST

MCSST products derived from NOAA AVHRR data were the first results of DLR's AVHRR pathfinder activities. The goal of the overall product palette is to provide the user with thematic information layers of highest possible reliability and quality that are at the same time easy to access via ISIS and WWW. Essential part of this philosophy includes the improvement of algorithms and standard products whenever necessary. After a phase of definition, the operational production chain based on SeaSpace's TeraScan software was launched in March 1993 covering the entire Mediterranean and Black Seas. Since then, daily, weekly, and monthly data synthesis maps have been generated in near real time and are accessible typically with a one day delay. MCSST maps covering the northeastern Atlantic including the Baltic and North Seas and the region around the Island of Madeira have been added since August 1994. The most important aspects of the MCSST maps from the user's viewpoint are precise image navigation respectively registration and sophisticated cloud screening procedures to ensure the best possible geometrical accuracy and cloud clearing. It is then guaranteed that only cloud-free pixels are taken for the later MCSST time composition [2]. After five years of operational MCSST production, more than 5.500 data granules are available to the user community allowing to analyze oceanographic features, to study eddies and currents, to serve during scientific campaigns and cruises, and to perform first analysis on temperature changes in the European Seas. However, in times of public fund cuts for remote sensing technologies, this AVHRR value-adding chain will only "survive" if people continue to make use of this offer.

2.1 Navigation

Automatic navigation of the satellite data is performed using an orbit model and timely orbital information. Appropriate coastline areas with significant features are selected in 1deg x 1deg boxes and tested for cloudiness. For the cloudfree boxes a cross correlation algorithm between the "real" coastline in the satellite image and the coastline of the reference data set (WDB-II) is run. Based on the yielding vector array, the satellite's yaw, pitch, and roll angles are corrected. The complete procedure is first done unsupervised, then the results are checked interactively and if necessary corrected manually. This is done for each scene before the remapping procedure is applied and ensures best possible quality.

*Corresponding author address: Dr habil Stefan W. Dech
Deutsches Zentrum für Luft- und Raumfahrt e.V. (DLR)
Deutsches Fernerkundungsdatenzentrum (DFD)
82234 Wessling, Germany, email: Stefan.Dech@dlr.de

2.2 Calibration

The solar AVHRR channels 1 (0.58 µm - 0.68 µm) and 2 (0.725 µm - 1.1 µm) are calibrated into technical albedo values as described by NOAA [3]. These channels are not taken into account for the generation of the MCSST, but are needed for the cloud detection procedure. The thermal channels 3 (3.55 µm - 3.93 µm), 4 (11.3 µm - 12.3 µm) and 5 (11.5 µm - 12.5 µm) are calibrated into radiances with reference temperature data from the internal blackbody on board and the cold space (in-flight calibration). These are then converted into brightness temperatures (or equivalent blackbody temperatures) using the inverse of Planck's radiation equation. The non-linearity between counts and radiances is considered. The resulting radiometric resolution is 0.1 degrees Celsius.

2.3 Cloud Screening and Clearing

To ensure that MCSST values are derived for cloud-free water surfaces only, several cloud tests are performed which are based on the principal characteristics of water bodies. The tests consider typical spectral and textural parameters of a cloud-free water body (e.g. dark, warm, and homogenous surface) and thresholds are adapted from case to case depending on the specific characteristics of the individual scene [1]. A WDB-II-based land/sea mask in 1 km geometrical resolution is used to mask remaining MCSST values over land areas.

2.4 MCSST Algorithm

The formula applied to obtain the Multichannel Sea Surface Temperature is based on the brightness temperatures of AVHRR channels 4 and 5 (T4 and T5). The method is known as the "Split Window Technique" and contains a correction for water vapor in the atmosphere that could otherwise lead to a significant drop in derived brightness temperatures, depending on the climatic region down to several degrees Celsius. The formula applied is according to [4]:

$$MCSST = A*T4 + B*(T4-T5) + C*(T4-T5)*(SEC(sza)-1) + D*(SEC(sza)-1) + E$$

Coefficients A, B, C, D and E are day/night specific for every AVHRR instrument. They are obtained from empirical buoy measurements and are provided by NOAA. SEC(sza) is the secant of the satellite zenith angle and corrects for different viewing conditions.

2.5 Geographical resolution and coverage

The data sets are remapped into three different standard Mercator projections with a geometrical resolution of 1.1132 km each at the center of the satellite maps. Figures 1 to 4 show the area of coverage for the MCSST products of the Mediterranean Sea, for example.

2.6 Synthesis

Three daily MCSST maps are composed containing up to six daily NOAA acquisitions. They are calculated using the maximum temperature value given at each pixel's position in order to minimize remaining cloud influences, as contamination of clouds leads to lower MCSST estimates. Weekly and monthly products are based on the daily maximum images using the average MCSST value at each pixel's position. Currently, only NOAA-14 data is used from each tree subsequent night and afternoon passages. In addition, pure night synthesis maps can be obtained on request.

3. DATA ACCESS

Data access is possible via ISIS, the "Intelligent Satellite Information System" of DLR. The data is currently free of charge except for the transmittal costs, and can be accessed via the following options:

Telephone Line: (login: isis, no password)
Modem (8 data bits, no parity, 1 stop-bit, CTS/RTS):
+49 (0)8153 28 1860
+49 (0)3981 480 186
ISDN: +49 (0)8153 930 050

Packet-Switching Networks: (login: isis, no password)

Datex-P X.25 +49 (0)1853 91926
WIN X.25 +49 (0)262 45 050 984011

Telnet (user: dlrpid) isis.dlr.de
WWW http://isis.dlr.de

For further help, please contact DFD's "Helpdesk": Tel: +49 (0)8153 28 2802, Fax: +49 (0)8153 1343, email: helpdesk@dfd.dlr.de.

4. APPLICATION EXAMPLES

4.1 Campaign Support

The MCSST data provided includes the regular support of oceanographic research and measurement campaigns providing near-real-time access to optimized data products. This enables scientists e.g. on board of research vessels to identify areas showing potentially interesting phenomena visible in SST data (e.g. eddies). One example for a campaign supported in 1997/1998 include the "Eddies and Leddies Interdisciplinary Study in the Algerian basin (ELISA)" where information on the current SST distribution transferred to the vessel assisted in navigating the ship to potential areas of interest. For the first ELISA cruise in July and August

1997 every overflight of NOAA AVHRR covering the Area between 40° 37' N and 36° 34' N and between 2° 45' E and 9° 38' E at least twice daily with a spatial resolution of 1 km. The data sets are made available on DFD's ftp server within approx. 30 minutes after reception and contain customer-requested information for the investigation area. Fig. 1 shows an image from July 30th 1997 with interesting eddy structures developing in that time.

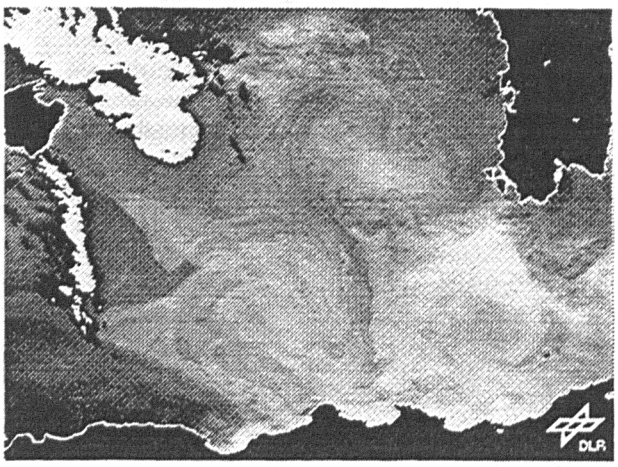

Fig. 1: Campaign-optimized MCSST product showing "ELISA" investigation area

The main objectives of the interdisciplinary project ELISA are to study, in the eastern part of the Algerian basin, the general circulation of the water masses (Modified Atlantic Water, Winter Intermediate Water, Levantine Intermediate Water, Tyrrhenian Dense Water, and Western Mediterranean Deep Water), the mesoscale dynamics and its consequences on the biological phenomena, and hence the ecosystem response. A specific aim will be to determine the structure, the origin and the trajectory of the various kinds of mesoscale eddies. Indeed, we have now demonstrated that Algerian Current- induced "eddies" can entrain LIW lenses from the Sardinian-slope flowing vein. But we cannot exclude either the possibility that the instability of the LIW vein, when going round the southwestern corner of Sardinia, generates intermediate eddies of LIW that would then be called "leddies", by analogy with the formation of "meddies".

4.2 North Atlantic Product: Oscillation of the Arctic Front

The second example (Fig. 2) demonstrates clearly the oscillating south-eastern Arctic front of the cold East Greenland current near Iceland. The subsets are specially processed as they are mean temperature values of the winter periods (November to April) of the years 1994-95, 95-96 and 96-97. Isolines of sea surface temperature are superimposed for easier comparison. The temperature range from 0 to 14 degrees Celsius is coded from white to black indicating cold to warm respectively. For additional analysis, temperature differences between the winter terms were calculated (Fig. 8-9). Warm anomalies are dark, cold ones are white, isolines are superimposed as well. Temperature differences of up to 4 degrees Celsius between two successive winters are observed in certain areas. Remarkable is the fact that in the winter of 95-96 the cold East Greenland current (Arctic front) went further south than in the other two winter terms. At the same time the Gulf stream transported warmer water much further north (see the 9 degrees isoline) so that the temperature gradient between cold and warm water masses rose. The 12 degree isoline in this subset is also visible only in that winter term. At the same time the North (and Baltic) Seas cooled down more than during the other two winters.

Observations like these are interesting for scientists in oceanography, marine biology, climatology, meteorology and other related sciences, since ocean currents like the ones shown here have an important influence on regional and global scales as they affect both regional weather systems and overall climate.

ACKNOWLEDGEMENTS

Our special thanks are expressed to Mr. T. "Thommi" Ruppert, who did all the sophisticated programming with high continuous engagement which made this production chain possible, to Isabelle Taupier-Letage from IFREMER for a fruitful cooperation, and to Mrs. S. Giegerich for editing assistance.

REFERENCES

[1] Bernstein, R. L., 1982: Sea Surface Temperature Estimation Using the NOAA-6 Satellite AVHRR. J. Geophys. Res., Vol. 87, No. C12, 9455-9465.

[2] Dech, S. W., 1995: Operational AVHRR-Based Derivation of MCSST and NDVI Products at the German Remote Sensing Data Center. Proceedings of "The Meteorological Satellite Data Users' Conference", Winchester, UK (4-8 Sept. 1995) EUMETSAT-Publications EUM P 17, Darmstadt, 595-599.

[3] Lauritson, L. N., G. J. Porto, W. Frank, 1979: Data Extraction and Calibration of TIROS-N/NOAA Radiometers. NOAA Technical Memorandum NESS 107.

[4] McClain, P. E., W. G. Pichel, C. C. Walton, 1985: Comparative Performance of AVHRR-Based Multichannel Sea Surface Temperatures. Journal of Geophysical Research, Vol. 90, C6, 11587-11601.

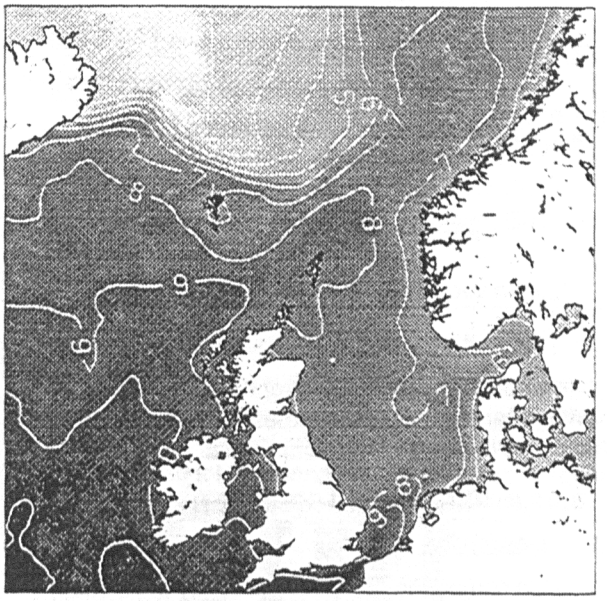

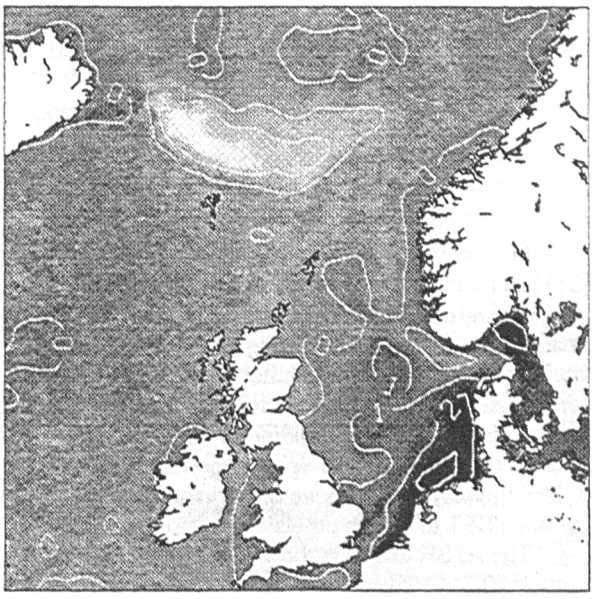

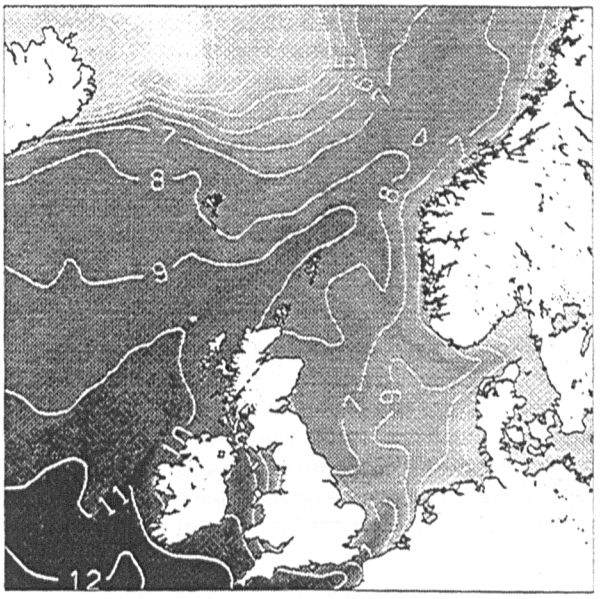

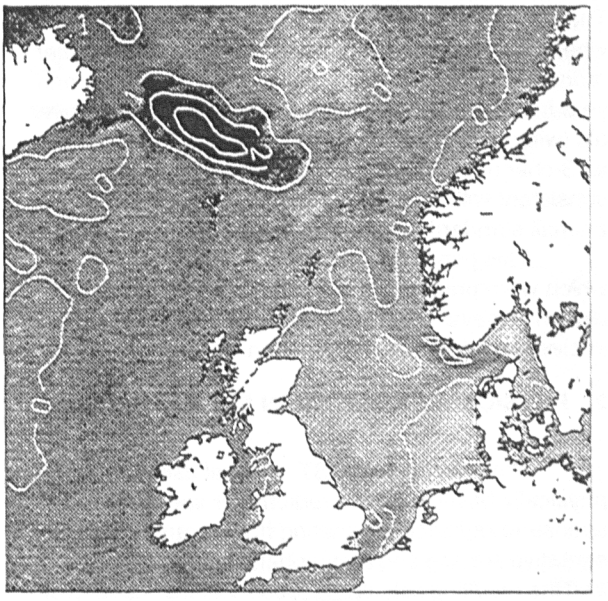

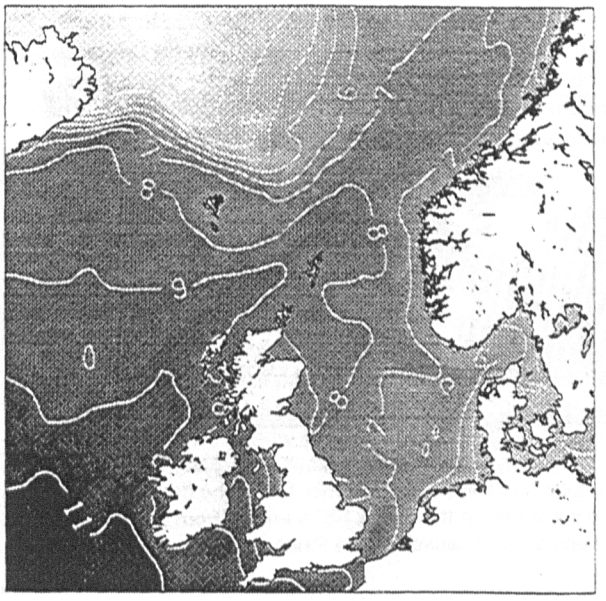

Fig.2: MCSST examples in the Northern Atlantic

Upper left:	Mean MCSST for winter 1994/1995
Middle left:	Mean MCSST for winter 1995/1996
Lower left:	Mean MCSST for winter 1996/1997
Upper right:	Differences between 94/95 and 95/96
Middle right:	Differences between 95/96 and 96/97

P2.35A HIGHLY ACCURATE RETRIEVAL OF SKIN SEA SURFACE TEMPERATURE

Christopher J Merchant*
University College London, UK

1. INTRODUCTION

Measurements of sea surface temperature (SST) are important for various oceanographic, meteorological and climatological purposes—from studying global surface fluxes to montoring ENSO events. The retrieval of SST from remote satellite measurements offers the advantage of global coverage. In July 1991, the along-track scanning radiometer (ATSR) was launched on the European Space Agency's ERS-1 satellite, the principal purpose of the instrument being to retrieve SST to a high precision, namely, 0.25 K.

The ATSR employs three infrared wavelength channels (3.7, 11 and 12 μm) to observe the sea surface at two view angles (forward ~55° and nadir ~0°). The 3.7 μm channel is not useful for SST retrieval when viewing daylit scenes because of reflected solar radiation. Moreover, this channel failed less than one year into the ATSR mission. Whilst 2-channel retrievals (without 3.7 channel) cannot yield SST as precise as 3-channel retrievals, it is necessary that they be consistent with each other: that is, unbiased and with a small standard deviation between them.

This paper describes the inconsistencies which were present in SST retrievals using the pre-launch retrieval scheme, the origin of those inconsistencies, and their near-elimination.

2. PHYSICALLY BASED SKIN SST RETRIEVALS

The approach to SST retrieval using ATSR is physically based—ie, the radiometer spectral response to radiance emanating from a range of representative surface and atmospheric states is modelled, and the resulting calculated "observations" used to define the retrieval scheme. This contrasts with the traditional AVHRR approach, where real observations are regressed to *in situ* measurements. There are pros and cons to both physical and statistical approaches. One implication that is worth highlighting is that ATSR SST retrievals are retrievals of *skin* SST, since it is the top layer (< 1 mm) of the sea surface from which thermal radiation is emitted and that is modelled for ATSR, whereas the AVHRR regression is to sub-surface (bulk) SSTs. The skin-bulk difference varies with wind speed and net surface flux, and is of order tenths of kelvin.

The equation used to derive the estimate of SST, $\hat{x}$, is:

$$SST_{algorithm} = a_0 + \sum_{channels} a_i T_i$$

or, in vector-matrix notation:

$$\hat{x} = a_0 + \mathbf{a}^T \mathbf{y}$$

where the summation over the product of coefficients (**a**) and observed brightness temperatures (**y**) is achieved by the inner vector product.

3. BIAS IN PRE-LAUNCH SCHEME RETRIEVALS

3.1 Description

On comparing pre-launch (Zavody et al, 1995) dual-view 2-channel SST retrievals (hereafter 'dual-2 SSTs') from ATSR with dual-3 SSTs, using night time data from the first nine months of the mission, an unacceptably large relative bias is apparent of -0.7 K globally (dual-2 SSTs cold relative to dual-3 SSTs), with up to -2 K biases in equatorial regions (Fig. 1). The standard deviation (SD) of dual-2 minus dual-3 SSTs is likewise large: 0.6 K. This inter-algorithm inconsistency points to absolute biases in the retrievals, with the largest biases actually present in the dual-2 SSTs.

3.2 Principal cause: Pinatubo aerosol

The eruption of Mount Pinatubo shorlty before ERS-1 launch injected ~2 x 10^{10} kg of SO_2 gas into the stratosphere. The stratospheric aerosols which formed as a result rendered invalid the pre-launch assumption that the stratosphere could be characterised as aerosol free. This was the most significant cause of SST bias (up to -1.5 K) in the first year of the ERS-1 mission.

3.3 Secondary cause: Water vapour continuum

The greatest incertainty in the radiative transfer modelling used to derive the pre-launch retrieval scheme was in the strength of the water vapour continuum absorption in the 11/12 μm window region. The inadequacies of the parameterisation adopted lead to

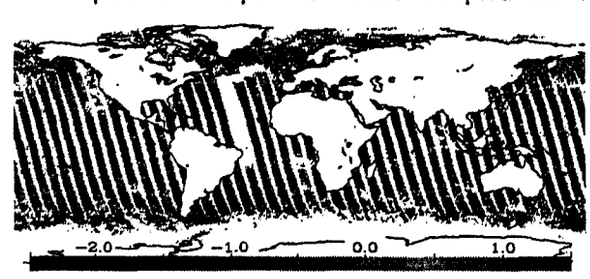

Fig. 1. Mean of dual-2 minus dual-3 SSTs for night time data from September-October 1991. The dark equatorial band is the bias in the dual-2 SSTs arising from the stratospheric aerosol caused by the Pinatubo eruption

*Corresponding author address: Chris Merchant, Mullard Space Science Laboratory, Holmbury St Mary, Dorking, Surrey, RH5 6NT, UK
e-mail: cjm@mssl.ucl.ac.uk

dual-2 SST bias in wet tropical atmospheres of -0.4 K.

3.4 Potential tertiary causes

Other possible causes of minor (<0.1 K) bias were: sea surface emissivity parameterisation (in particular at high wind speeds), inappropriate CO_2 concentration, and use of a not fully representative set of atmospheric and surface states.

4. SOLUTIONS

4.1 Aerosol robust coefficients

The effect of stratospheric aerosol of optical depth δ on ATSR brightness temperature observations is to change **y** to **y** + cδ**k**, where c is a negative constant, and **k** is a normalised vector describing the mode of brightness temperature variation (Fig 2).

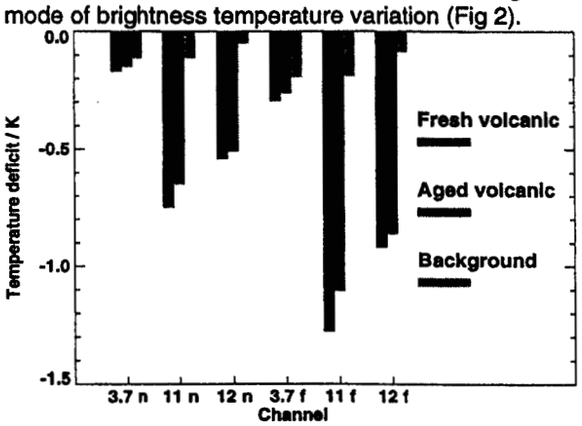

Fig. 2. Modes of variation introduced into brightness temperature by stratospheric aerosols —equals cδk for three types, with δ=0.01 for fresh (<1 month old) and aged (up to 1 yr) and δ=0.001 for background (in between major eruptions).

The solution is to choose coefficients **a** which are orthogonal to the aerosol modes. The equation to achieve this is:

$$\mathbf{a} = \mathbf{S}'^{-1}_{yy}\left[\mathbf{s}_{xy} - \mathbf{K}\left(\mathbf{K}^T\mathbf{S}'^{-1}_{yy}\mathbf{K}\right)^{-1}\left(\mathbf{K}^T\mathbf{S}'^{-1}_{yy}\mathbf{s}_{xy}\right)\right]$$

where $\mathbf{S}'_{yy}$ is the covariance matrix of observations (without aerosol present), $\mathbf{s}_{xy}$ is the covariance of observations and skin SST, and **K** the matrix comprised of the chosed aerosol modes, $\mathbf{k}_i$.

It turns out that using two aerosol modes (i = 'aged' and 'background') gives good results.

4.2 Updated water vapour continuum

Use of the recently updated continuum parameterisation reported in Han et al (1997) improves the residual dual-2 minus dual-3 bias in wet tropical regions. The change of parameterisation mainly has the effect of reducing the absorption in the 12 µm channel compared to the pre-launch assumption. Despite this being an improvemement, the observed distribution of 11 and 12 µm channel observations are not yet perfectly accounted for by the new parameterisation.

4.3 Others

The emissivity parameterisation of Watts (1996) has been adopted, and a global set of 1358 atmosperhic profiles and associated surface variables from the ECMWF Re-Analysis project used.

5. RESULTS

The effect of these improvements in the physical basis of the retrieval scheme has been to reduce the global dual-2 minus dual-3 SST bias from -0.67 K to +0.02 K for September-October 1991, and the SD from 0.57 K to 0.22 K (Fig. 3 and Fig. 4).

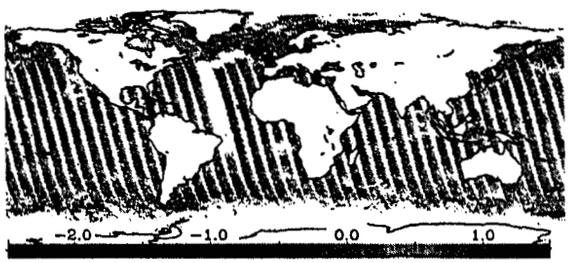

Fig. 3. As Fig. 1 but using new retrieval scheme

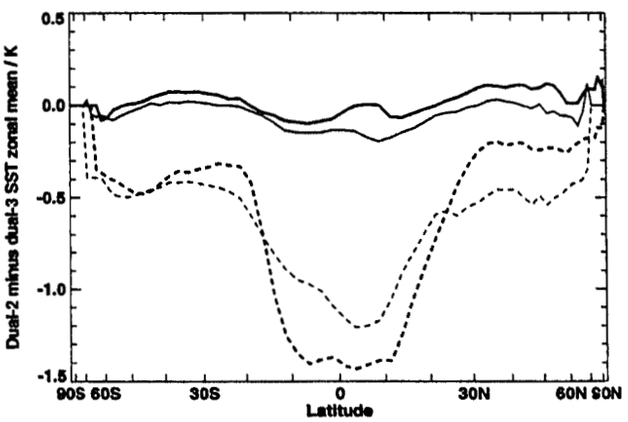

Fig. 4. Zonal relative SST biases for new (solid) and pre-launch (dashed) schemes for October 1991 (thick) and May 1992 (narrow).

As can be seen in Fig. 4, the new SST retrieval scheme gives improved consistency at all latitudes. Good results are also obtained for April-May 1992. Validation studies are underway to assess the corresponding improvement expected in the absolute SST retrieval accuracy.

Han, Shaw, Churnside, Brown & Clough, *J. Geophys. Res., 102,* 4353-4356, 1997.

Watts, Allen & Nightingale, *J. Atmos. Oceanic Technol., 13,* 126-141, 1996.

Zavody, Mutlow & Llewellyn-Jones, *J. Geophys. Res., 100,* 937-952, 1995.

Sensor Design Considerations for the Retrieval of Sea Surface Temperatures in the NPOESS Era

Keith D. Hutchison, Steve Marusa, William G. Uplinger, and John A. Twomey
Lockheed Martin Missiles & Space
Center for Remote Environmental Sensing Technology (CREST)
Sunnyvale, California
Tele: 408-756-2328; Fax: 408-743-1795; E-mail: keith.hutchison@lmco.com

ABSTRACT

The National Polar-Orbiting Operational Environmental Satellite System (NPOESS) requires improved accuracy in the retrieval of sea surface skin temperature (SST_S) from its Visible Infrared Imager Radiometer Suite (VIIRS) sensor over the current capability to retrieve bulk sea surface temperature (SST_B) with the operational NOAA satellites carrying the AVHRR sensor. Statistics show an existing capability to retrieve SST_B with a 1-σ accuracy of about 0.8 K in the daytime and 0.6 K with nighttime data. During the NPOESS era, a minimum 1-σ SST_S measurement uncertainty of 0.5 K is required during daytime and nighttime conditions while 0.1 K is desired. End-to-end simulations have been performed, using PACEOS™ to understand the implications of this more stringent requirement on algorithm retrieval methodologies and sensor design concepts.

INTRODUCTION

While satellite infrared sensors measure radiation from the ocean's surface skin, operational satellite-based sea surface temperature analyses are computed by regression of brightness temperatures against bulk ocean temperatures (SST_B) measured by buoys which sense the sub-surface region (McClain et al., 1985). Studies have estimated average differences between buoy and skin temperatures at about 0.1 K during the daytime and 0.3 K during the night but they may be as large as $^{+}/_{-}$ 1.0 degree (Schluessel et al., 1990). This means that differences between these reference temperatures can cause discrepancies that are nearly as large as the NPOESS SST_S accuracy requirement. Since in situ observations of sea surface skin temperature are only sporadically collected by research vessels, reliable regression coefficients are not yet available for the retrieval of SST_S from satellite observations. Thus, simulations become essential for evaluating the potential impact of these new requirements on sensor designs.

PACEOS™ SIMULATION SOFTWARE

End-to-end analyses of sensor design concepts on SST_S retrieval accuracy have been evaluated using a Lockheed Martin proprietary software package known as PACEOS™, an acronym for **P**erformance and **A**nalysis **C**apability for **E**arth **O**bservation **S**ystems (Marusa et al., 1997). An overview of the PACEOS™ architecture is shown in Figure 1.

PACEOS™ consists of two major functional areas: (1) the generation of space-based elements shown in the top of the figure and (2) a ground-based processing system seen in the lower half. The space-based elements functional area is divided into three sub-sections: (1) a Scene Generation Module which calculates upwelling radiance arriving at the sensor aperture, (2) the Sensor Performance Module where the energy (a) may be taken through a variety of optical parameters, (b) converted to electrical signals at the focal plane, and (c) processed, prior to (3) entering the Space Data Stream Formation Module which packages the sensor data into the satellite data stream for transmission to the ground. Corresponding modules in the ground-based elements functional area contain advanced science algorithms

to analyze data created in each module of the space-based elements. A short overview of each module provides insight into the capabilities for end-to-end simulations of SST_s and other environmental data products.

Figure 1. Architecture of the PACEOS™ software simulation environment.

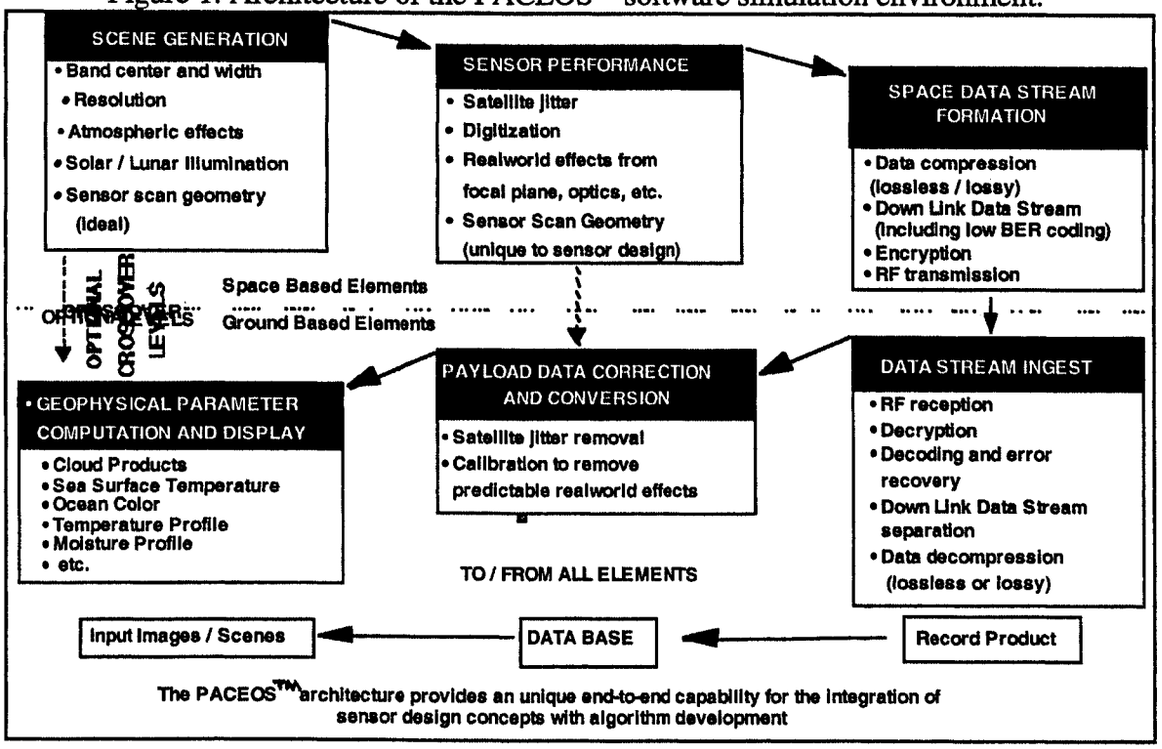

1. Scene Generation Module

Analysts employ simulation software to predict the utility of future remote sensing systems using either a completely new sensor design or a modification to an existing sensor concept. The Scene Generation Module permits an analyst to initiate PACEOS™ with either imagery acquired from space-based (or airborne) sensors or imagery synthesized from a materials data base which first associates surface classification with emissivity and reflectivity characteristics and then defines sensor bandpasses along with atmospheric conditions and external energy (solar or lunar) sources. Upwelling radiances are generated at satellite altitudes using a variety of atmospheric transmission codes that have been integrated into the PACEOS™ architecture. The output from the Scene Generation Module is a two-dimensional file of radiances arriving at the sensor aperture.

In addition, the Scene Generation Module provides the capability to specify a wide variety of conditions and vary each across the scene including: atmospheric profiles of all relevant meteorological conditions, cloud cover and cloud distributions, solar and/or lunar illumination, sensor scan or viewing angles, and surface material parameters such as temperature, emissivity, and topography.

To support development of ground processing systems, PACEOS™ permits the transfer of information from the scene generation module directly into the algorithms in the ground based elements function. This process allows an early evaluation of the feasibility of meeting product requirements from a "perfect" or idealized sensor. In such cases, failure of an optimized retrieval algorithm to meet minimum accuracy requirements, or meeting

them with small margins, is a clear indication that a major sensor design modification or new algorithm retrieval approach may be necessary.

2. Sensor Performance Module

The Sensor Performance Module supports sensor concept studies from two data sources: (1) a library containing the characteristics of numerous operational environmental satellite sensors and (2) sensor parameters created for a new design. This module uses information on satellite altitude, scan angle, and instantaneous field-of-view to calculate pixel along-track and cross-track resolution. Modulation transform functions (MTFs) are used to account for image degradation due to optical, motion, and atmospheric effects. The various MTFs may be input directly or calculated by PACEOS™ from design specifications. Additionally, optical and detector losses, radiation and electrical noise, and detector noise can be specified along with individual spectral response functions. Finally, it is also possible to include the effects of relative focal plane displacement due to phenomena such as thermal effects and jitter induced from either the satellite or the sensor. The output from this module is a file of digitized sensor data, up to 16-bits per pixel. The pixel data are then calibrated and Earth-located in the corresponding Payload Data Correction and Conversion Module of the corresponding ground processing system.

3. Space Data Stream Formation Module

The Space Data Stream Formation Module simulates the on-board processor functions necessary to prepare the sensor data for transmission to the ground processing system. Sub-system effects that can be simulated in the Data Stream Formation module include such features as the fidelity of RF transmission and data compression, if needed. This module is currently configured to run lossy or lossless data compression routines either internal or external to PACEOS™ and to accept data stream formations and downlink effects calculated off-line. Effects simulated in this module are removed in the Data Stream Ingest Module of the ground processing system.

RESULTS

The focus of these initial simulations is to understand how the basic components of algorithm or modeling errors and sensor hardware errors are related to total system error in an end-to-end simulation environment using sea surface temperature as the target algorithm. Simulated radiances were generated for a sensor in a nominal near-polar, sun-synchronous orbit of 850 km. The sensor viewed a cloud-free, 100x100 pixel array (10,000 pixels in total) in spectral bands centered near 3.7-, 10.8-, and 12.0-μm with ocean surface emissivity values assumed as 0.96, 1.0, and 0.99 respectively. Since NEΔT has its greatest impact on the coldest temperature in the required NPOESS measurement range, i.e. 271 - 313 K, only the minimum sea surface skin temperature was used in the simulations, i.e. each pixel was assigned an initial value of 271 K. Upwelling radiances were generated with MODTRAN-3, assuming a nadir scan position, a mid-latitude winter atmospheric profile, and a surface visibility of 23 km.

Once upwelling radiances were computed in the three spectral bands, instrument noise was added randomly to each set of simulations corresponding to NEΔT having a mean of 0.0 and 1-σ values of 0.0, 0.05, 0.1, and 0.3 K. This resulted in a total of 120,000 data points for the complete simulation. For simplicity, the NEΔT values in each spectral band were assumed to be identical. Furthermore, the response function of each channel in the notional sensor was assumed to be a step-function. Energy recorded by the detectors was calibrated and SST_s values were retrieved from the derived brightness temperatures using the MCSST algorithms (McClain et al., 1985). The retrieval of SST_s from daytime

imagery employed channels centered at 10.8- and 12.0-μm while SST_s retrieved from nighttime imagery also included data in the 3.7-μm band.

Results of the end-to-end simulations are shown in Figure 2. Upon inspection it appears that a sensor NEΔT value of ~ 0.08 K is required to meet the NPOESS SST_s EDR threshold requirement if only 10.8- and 12.0-μm data are used in the retrieval, based upon the standard (daytime) 2-channel MCSST algorithm. On the other hand, the requirements appear to be satisfied with an NEΔT as large as ~ 0.12 K if the additional 3.7-μm channel is included in the analysis, based upon the standard 3-channel (nighttime) MCSST algorithm.

Figure 2. Measurement uncertainty (1-σ) in retrieved sea surface skin temperatures (SST_s) as a function of NEΔT for a notional sensor with bandpasses centered at 3.7-, 10.8-, and 12.0-μm using NOAA's MCSST daytime and nighttime algorithms.

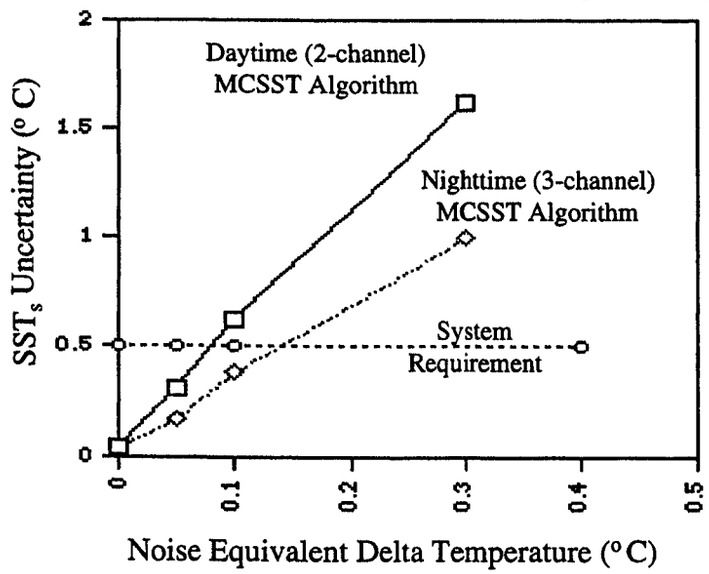

The results imply that an optimal sensor design might use 3-channels of infrared imagery during daytime and nighttime conditions in order to satisfy the SST_s measurement uncertainty EDR requirement in the NPOESS era using the current MCSST algorithms. Thus, it appears that a value of these simulations would be to determine whether an additional VIIRS channel might be used with the daytime algorithm. An alternative approach might keep the NEΔT at ~ 0.12 K and employ an enhanced retrieval algorithm that uses only two channels of daytime imagery with information from another NPOESS sensor, e.g. precipitable water. To further examine which option is better, more detailed analyses of the 2-channel daytime and 3-channel nighttime algorithms are needed and will be presented in a longer paper that is currently under review.

REFERENCES

Marusa, S. Rivera, R. A., Hutchison, K. D., and W. Uplinger, 1997: "Use of MODTRAN Software in Performance and Analysis Capability for Earth Observation Systems (PACEOS™) Software," Proc. 20th Conf. on Atmospheric Radiance and Transmission Modeling, Hanscom AFB, MA.

McClain, E. P., Pichel, W. G., and C. C. Walton, 1985: "Comparative performance of AVHRR-based multichannel sea surface temperatures," J. Geophys. Res., **90(C6)**, pp. 11,587 - 11,601.

Schluessel, P., Emery, W. J., Grassl, H., and T. Mammen, 1990: "On the bulk-skin temperature difference and its impact on satellite remote sensing of sea surface temperature," J. Geophys. Res., **95(C8)**, pp. 13,341-13,356.

P2.39A

DEVELOPMENT OF A MULTI-SENSOR ICE PRODUCT

Lars-Anders Breivik*, Øystein Godøy and Harald Schyberg
Norwegian Meteorological Institute, Oslo
Søren Andersen
Danish Meteorological Institute, Copenhagen

1 INTRODUCTION

Parts of the EUMETSAT satellite ground segments will within year 2001 be distributed to several Satellite Application Facilities (SAF) located and co-sponsored by national meteorological centres. A SAF dedicated to Sea Ice will be developed by the Norwegian (coordinator), the Danish and the Swedish Meteorological Institutes. The aim of the SAF is to produce a gridded multi-sensor sea ice product based on satellite observations from passive and active microwave measurements and from additional information from optical sensors. The product will contain: ice edge, estimations of ice cover and ice type that distinguish between multi year and first year ice. The objective of horizontal resolution is 10 km, and the product will be provided once per day. AVHRR is the only instrument that is able to provide information on such resolution. SSM/I and scatterometer will provide weather independent ice information of from 15 to 50 km resolution, however overlapping observations will make enhancement of the resolution possible.

2 SEA ICE RETRIEVAL FROM PASSIVE MICRO-WAVE RADIOMETRY

Microwave radiation from the earth's surface, as well as from the atmosphere and space, contribute to the antenna temperatures measured by the spaceborne sensors. Sea ice retrieval algorithms attempt to relate antenna temperatures at different wavelengths to sea ice parameters, making use of atmospheric and ocean surface radiative models.

There is a large contrast in terms of radiation in the microwave range between an ice covered and ice free ocean. Furthermore the radiation from different types of ice varies, e.g. first year ice is generally brighter than multi year ice. Where visual and infrared radiation is severely absorbed and scattered by clouds, microwave radiation penetrates most types of cloud cover. The main absorption of microwave radiation in the atmosphere is due to oxygen and water. The oxygen influence is fairly constant and well known. The atmospheric water content however constitutes an ever changing influence on the signal.

Some commonly used sea ice retrieval algorithms derived for SSM/I data will be considered for use in the SAF e.g. the NASA/TEAM algorithm (Gloersen and Cavalieri, 1986) and the Cosimo bootstrap algorithm (Comiso,1986). Also algorithms exploiting the high resolution information in the 85 GHz channels of the SSM/I (e.g. Markus and Burns, 1995) will be taken into account. The algorithms are not equally sensitive to the influence of different types of geophysical noise. In the ongoing work it must be determined if a combination of several algorithms can form an optimal solution. A large archive of brightness temperatures obtained from the SSM/I will be used as calibration data sets.

Spurious ice concentrations caused by wind and/ or clouds are traditionally dealt with by the use of threshold techniques known as weather filters. In the SAF processing chain data from NWP models, e.g. atmospheric profiles and surface wind speed will be used to improve the quality of weather filtering as well as ice parameter estimates.

3 SEA ICE RETRIEVAL FROM AVHRR DATA

The AVHRR instrument is capable of delivering products at 1.1x1.1 km at nadir and approximately 3x6 km towards the maximum viewing angle. Towards high latitudes the polar orbiting satellites usually covers each part of the area of interest approximately 10 times a day. As the primary purpose of the AVHRR instrument is cloud detection and identification, none of the channels can observe the surface through a cloud cover. Thus in periods of extensive and persistent cloud cover, the sea ice product can not rely on AVHRR data. An AVHRR based cloud mask will thus be an integrated part of the SAF processing chain.

The main physical problems encountered are connected to whether reflected solar light is available or not. At present, no algorithms identifying sea ice from thermal data alone is known. As much of the areas of interest for sea ice monitoring are at high latitudes, the lack of solar light during the winter season will reduce the benefit of existing algorithms much of the year. How much of the year AVHRR data is useful is still to be determined.

The most likely technique to be used by the SAF for image classification is the multispectral threshold technique. The method performs a sequence of threshold tests on each pixel. The general principle for solving the problem of detecting, classifying and quantifying sea ice is to use all the spectral information available as well as e.g. SYNOP data and NWP output. The foundation for this principle is that both reflectance and emissivity varies with wavelength for different surfaces. Each pixel is treated individually and tested in a multispectral feature space. The technique is used by several objective classification systems for satellite data, and e.g described by Karlsson and Liljas,1990.

4 SEA ICE RETRIEVAL FROM WIND SCATTER-OMETER DATA

Currently scatterometer data from the European Remote Sensing satellite, ERS-2 is available. The ERS scatterometer is a microwave radar sequentially illuminating the sea surface measuring the backscattered signal. The power of the reflected signal is dependent on the sea surface roughness and vary with incidence angle and azimuth angle. Over sea ice,

* *Corresponding author adress: Lars-Anders Breivik, Norwegian Meteorological Institute, P.O. Box 43, Blindern, N-0313 Oslo, Norway*
e-mail: l.a.breivik@dnmi.no

following Cavanie et al. 1994, two properties of the backscattering over ice can be used to derive sea ice information. Firstly, backscattering is relatively isotropic over sea ice compared to the strong anisotropic behaviour, which is the basic for wind direction retrieval, over water. Secondly, the change of backscatter with incidence angle shows larger variation over water than over sea ice. In addition the difference between expected backscatter over water and the measured one can be used. From these parameters algorithms for sea ice detection are designed. Furthermore, the change of backscatter with incidence angle over sea ice can be linked to ice types and used for sea ice classification.

As a part of the METOP program data from the Advanced SCATerometeter, ASCAT, will be available for ice analysis from 2001. This scatterometer is quite similar to the ERS scatterometer in specifications.

5 THE MULTI-SENSOR ICE PRODUCT

The scientific challenge in making a combined product from the available sensors, AVHRR, SSM/I and scatterometer, is to obtain a single reliable ice product from the various observations involving different and possibly contradicting information. For doing this, it is necessary to use an algorithm which takes into account the uncertainties in the ice classification of the various instruments. It is therefore essential not only with an ice estimate, but also with knowledge of the uncertainty or degree of accuracy involved. For example, there are uncertainties in AVHRR caused by possible cloud contamination and there are instrumental noise affecting all instruments. A good general tool for combining various data sources containing uncertain information is given by the Bayesian (inverse method) approach. Using this approach, several measured parameters can be combined to yield an optimal estimate. Combining independent information in this way will enable production of ice maps with much improved temporal and spatial resolution.

The approach is based on knowledge of the averaged relationship between ice properties and the measured quantity together with knowledge of the scatter of the expected measurement value for a given ice type. This knowledge can be expressed as a probability distribution for the measurement variable given the ice type. Assume e.g. that the satellite has measured a parameter A. From calibration data sets we can find the response of this parameter on an ice type I_k in terms of the probability distribution $p(A|I_k)$, the probability of doing an observation near A given that the ice type is I_k. This can be used to obtain an estimate of the probability of the ice type being I_k given the measurement, $p(I_k|A)$. Using Bayes theorem, we have

$$p(I_k|A) = \frac{p(A|I_k)}{\sum_j p(A|I_j)\, p(I_j)}\, p(I_k). \qquad (1)$$

The summation is performed over all possible, mutually exclusive ice types I_j. Thus, knowing the probability distribution for a measured parameter $p(A|I_j)$ for all possible ice types I_j we have a powerful tool for estimating the probability of each ice type. An estimate of the prior probability for the ice type, $p(I_j)$, is also needed. A simple algorithm for ice edge detection can be made by allowing I to have two values, "ice" and "water". The equation then gives a probability estimate for ice given the measurements. Setting both the prior probabilities for ice and water, p(ice) and p(water) equal to 50%, we get

$$p(\text{ice}|A) = \frac{p(A|\text{ice})}{p(A|\text{ice}) + p(A|\text{water})}. \qquad (2)$$

This framework can be generalized to a method for combining several satellite measured parameters to an optimal ice property estimate. It must be stressed that the method requires more than just thresholds on the measured parameter indicating an ice class. Such thresholds just give information on the relation between I and the most probable value of A. Here we use the full probability distribution of the measurement given the ice property. The method works in such a way that the measured parameters which the statistics shows to be most secure in distinguishing between ice properties, are the ones that alter the probability. Another advantage is that we not only obtain estimates of the most probable value of the ice parameters, but also the certainty of the estimate.

6 CONCLUSIONS

The aim of the sea ice SAF is to produce a daily sea ice analyse on a 10 km resolution grid. The challenge is to do this on basis of information from very different sensors, the passive and the active microwave sensors and the optical sensors with variations in resolution as well as in geophysical and instrumental uncertainties. In the SAF this analysis will be done by the Bayesian approach. Pre-knowledge of probability distributions of measured quantities given ice properties is used to design weights for the analysis. The final analysis will be the optimal result with the given information and include estimates of the uncertainty of the product.

REFERENCES

Cavanie, A., F. Gohin, Y. Quilfen and P. Lecomte, 1994, Identification of Sea Ice Zones using the AMI Wind: Physical Bases and Applications to the FDP and CERSAT Processing Chains. In: Proceedings Second ERS-1 Symposium, Hamburg 11 - 14 October 1993.

Comiso, J.C., 1986, Characteristics of arctic winter sea ice from satellite multispectral microwave observations. J. Geophys. Res., 91, C1, 975-994.

Gloersen, P.; Cavalieri, D.J., 1986, Reduction of weather effects in the calculation of sea ice concentration from microwave radiances. J. Geophys. Res., 91, C3, 3913-3919, 1986.

Karlsson, K.-G. and E. Liljas, 1990, The SMHI model for cloud and precipitation analysis from multispectral AVHRR data. SMHI Promis-Reports, No. 10.

Markus, T., B.A. Burns, 1995, A method to estimate subpixel-scale coastal polynyas with satellite passive microwave data, J. Geophys. Res., 100, C3, 4473-4487

INTERPRETATION OF SAR IMAGERY OF VESTFJORDEN, NORWAY

E. G. Mitchelson-Jacob* and B. Jones
University of Wales Bangor, Menai Bridge, Anglesey, UK

1. INTRODUCTION

The Norwegian coastline is very irregular and intersected by numerous fjords over 1000 m deep and with steep side-walls rising to more than 2000 m. Innumerable rocks and islands protect the coastline, the largest group of which are the Lofoten Islands. These form the seaward boundary of the region known as Vestfjorden (Fig. 1).

The oceanography of Vestfjorden is dominated by the Norwegian Coastal Current flowing northwards along the mainland coast and the Norwegian Atlantic Current following the shelf break further offshore. Whilst there is some freshwater and tidal influence in Vestfjorden itself, the surface circulation patterns are largely wind-driven. Meteorological and satellite data (AVHRR) have been studied from 1982-1995, with SAR imagery from 1993 complementing this time series. However, the meteorological observations were obtained from coastal stations and exhibit large spatial variations. It is therefore difficult to infer the wind field over the water using these data.

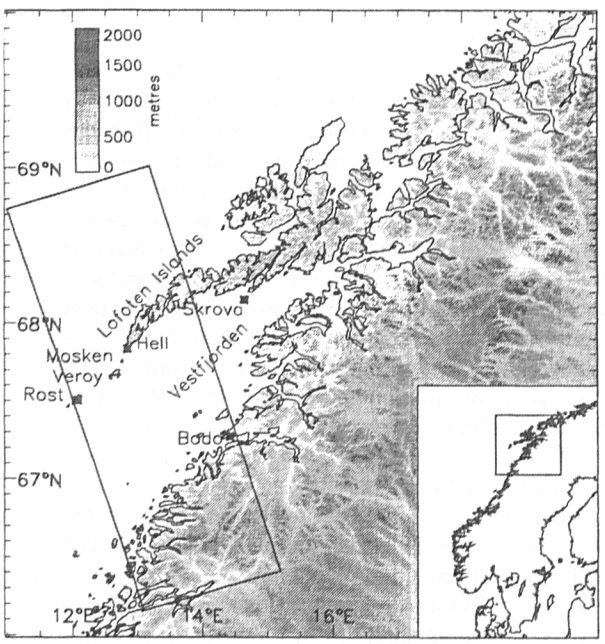

Figure 1. Vestfjorden, Norway showing land elevations and the location of the SAR imagery.

SAR imagery of Vestfjorden show both small and large scale variations in sea surface roughness. The interpretation of the imagery is dependent on the ability to determine the origin of the features. There is particular difficulty in the interpretation of areas of reduced surface roughness in regions of complex topography. A simple wind model has been developed to diagnose the effects of topography on the local wind field and hence on the patterns seen in SAR imagery.

In this paper we present some results from the wind model and their use in simulating and interpreting SAR imagery from 29 June 1993. A near-coincident AVHRR IR image was available to examine the effects of air-sea temperature difference on the signal.

2. SAR IMAGERY

Figure 2 shows a compilation of ERS-1 SAR images taken around 2041 on 29 June 1993. To the north-west of the Lofoten Islands, backscatter decreases north-eastwards, largely as a result of increasing radar beam incidence angle. Within

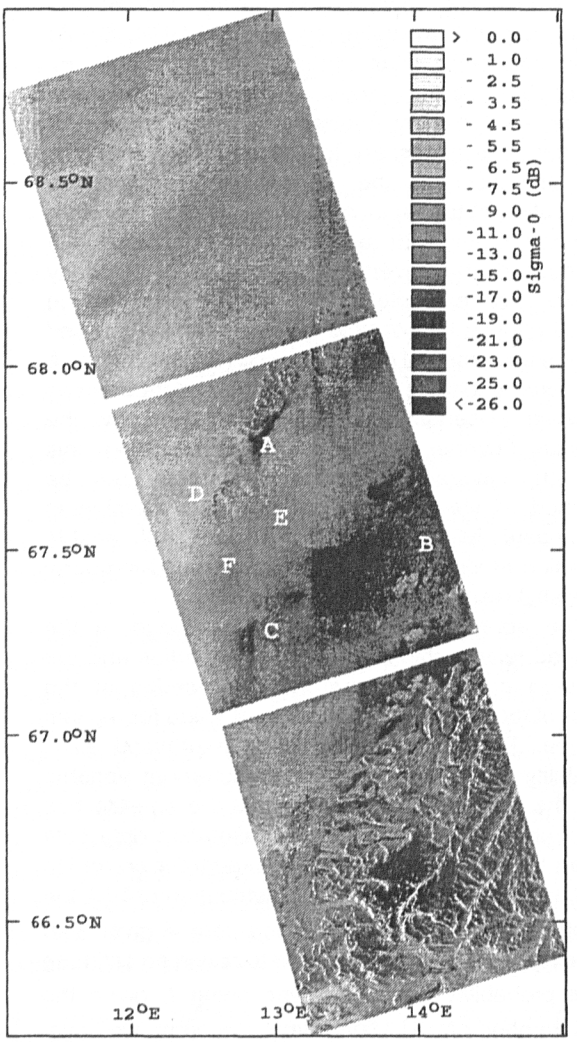

Figure 2. Calibrated SAR image from 2041, 29 June 1993.

*Corresponding author address: E.G. Mitchelson-Jacob, Unit for Coastal and Estuarine Science, Marine Science Laboratories, Menai Bridge, Anglesey, LL59 5EY, UK;
e-mail: egm@uces.bangor.ac.uk

Vestfjorden, the variability in the SAR signal increases. Backscatter is markedly reduced at Hell (denoted A in Fig. 2), in a broad swath running along the mainland coast (B) and in the mouth of the fjord (C). The signal increases south-westwards along the mainland coast, and is also enhanced along the seaward side of Mosken and Værøy (D). A sharp boundary feature (E) runs south-eastwards from Hell, and a more diffuse boundary (F) runs southwards from Værøy.

3. WIND OBSERVATIONS AND MODELLING

Mass and Dempsey (1985) proposed the use of a simple one level model to diagnose the effects of topographic steering and differential surface friction on the low level wind field in complex coastal regions. The model is forced by specifying the geopotential height and temperature on a reference pressure level lying above the planetary boundary layer *e.g.* 850 mb, and the atmospheric lapse rate.

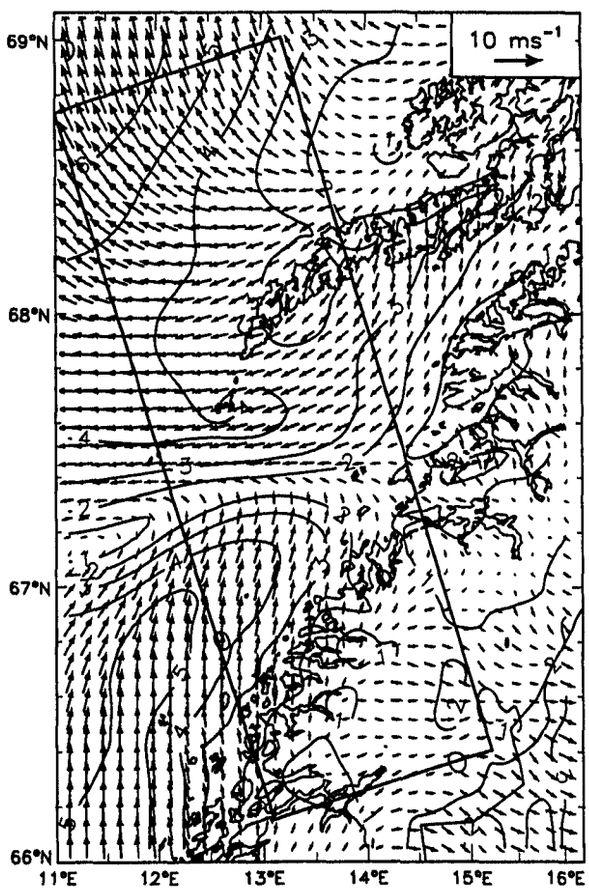

Figure 3. Modelled wind field for 0000, 30 June 1993. The box shows the location of the SAR imagery.

The synoptic situation on 29 June 1993 was complex, with weak pressure gradients and variable wind speeds and directions. To diagnose the wind field at the time of the SAR image, the model was forced with analysed pressure level data from the ECMWF global meteorological model. These data were available at 6-hourly intervals and therefore analyses from 1800, 29 June 1993 and 0000, 30 June 1993 were used. Figure 3 shows the diagnosed wind field for 0000, 30 June. The wind is generally north-easterly within Vestfjorden and veers towards south-easterly over the open ocean. There is a convergence zone lying at the mouth of the fjord. Wind speeds are generally weak, increasing to moderate over the open ocean, but decreasing in the convergence zone. For 0000, 30 June, the only available observations showed northerly winds of 3 knots at Skrova and Bodø (Fig. 1). The simulated wind is 4 knots from the north at Skrova and 2 knots from the south-east at Bodø. However, Bodø lies close to the convergence zone, and model points just to the north of the station have northerly winds. However, given the sparsity of observations at this time, validation of the model results relies on previous simulations of the wind field within Vestfjorden.

4. SAR SIMULATION

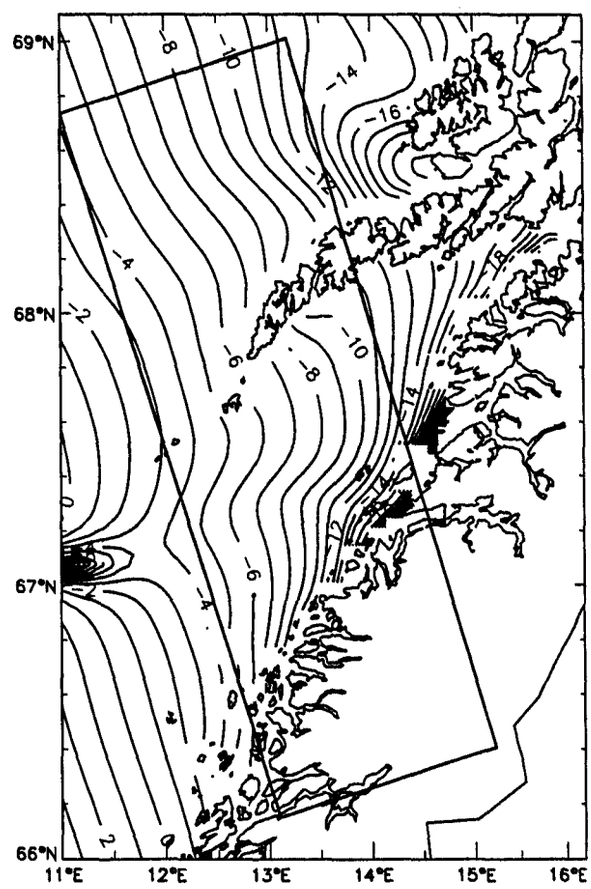

Figure 4. Simulated SAR signal for 2041, 29 June 1993. Contours show backscatter cross-section at 1 dB intervals. The box denotes the location of the SAR imagery.

The wind field at the time of the SAR image (2041) was estimated using a linear interpolation of the modelled wind field components between 1800 and 0000 on 29-30 June 1993. Figure 4 shows the simulated wind-driven SAR signal for 29 June 1993. The signal was calculated by generating the spectrum of gravity-capillary waves (Liu and Yan, 1996) at each wind model grid point. The wave spectra and the pass details for the ERS-1 SAR *i.e.* instrument polarization, look-angle and incidence angle range, were then substituted into a model for radar backscatter (Jones and Mitchelson-Jacob, 1998). This simulation should be compared with Figure 5, which shows the SAR imagery, smoothed using a boxcar filter of width 2 km.

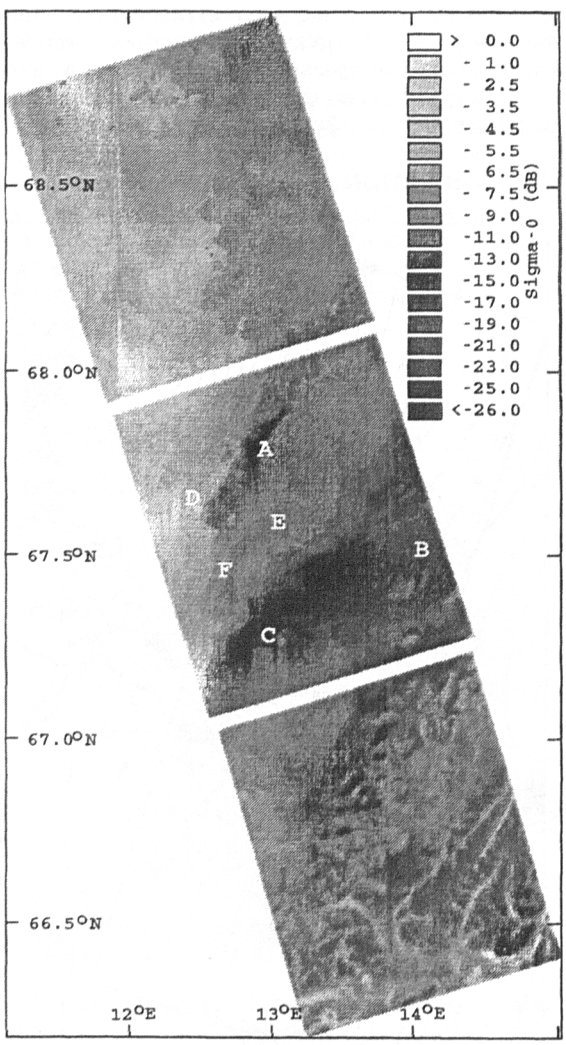

Figure 5. Calibrated SAR image from 2041, 29 June 1993, smoothed using a boxcar filter of width 2 km.

To the north of the Lofoten Islands, the simulated and observed signals show a general decrease in backscatter cross-section with increasing incidence angle, although the decrease is overestimated in the simulation. Within Vestfjorden, the simulation shows a decrease in backscatter towards Bodø and in the mouth of the fjord and, as observed, the backscatter contours become oriented along the axis of the fjord. However, the observed decrease is underestimated, and the feature towards the south of Hell (A in Fig. 2) is not evident.

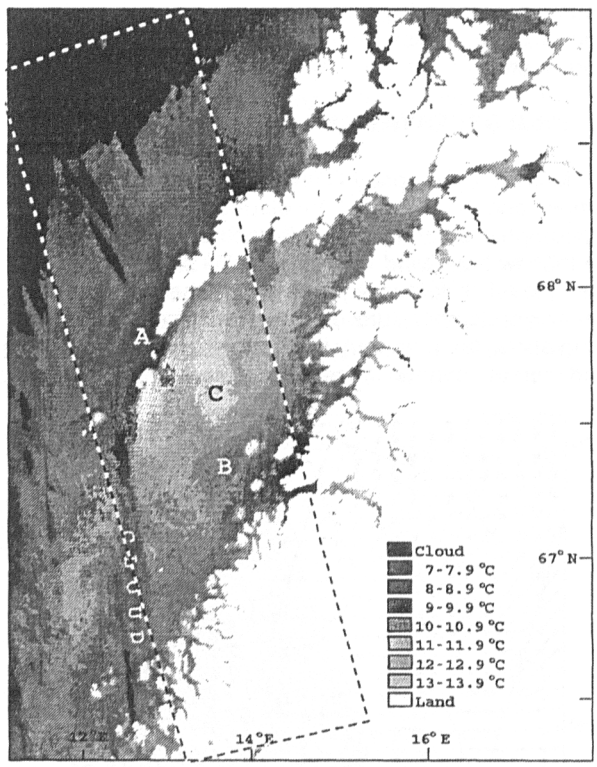

Figure 6. AVHRR infrared image taken at 1347, 29 June 1993, calibrated to sea-surface temperature. The box denotes the location of the SAR imagery.

5. EFFECTS OF SEA-SURFACE TEMPERATURE

Figure 6 shows an AVHRR infra-red image from 1347, 29 June 1993. There is a large, warm core, eddy within Vestfjorden (C), and a smaller warm eddy at its mouth. The water off Bodø is markedly colder (B) and cold, upwelled, water is also present on the seaward side of the southern Lofoten islands (A). Whilst the AVHRR and SAR images are not co-incident, these sea-surface features have been shown to be persistent (Mitchelson-Jacob, 1997).

The wave spectrum model assumes a neutrally stratified atmospheric boundary layer to relate the 10 m wind to surface stress. As a result, wave energy will be under- and overestimated, when the boundary layer is unstable and stable respectively. Air-sea temperature difference has therefore been parametrized in the backscatter model by using similarity theory (Monin and Obukhov, 1954) to generate a 'neutral-equivalent' 10 m wind from the model wind field. The Monin-Obukhov length scale is estimated using the charts of Hasse and Weber (1985), which relate air-sea temperature difference to

stability and the roughness length scale is assumed to be 1 mm. The observed air temperature was around 10°C at 1800 and 0000 and the sea temperature was taken from the AVHRR imagery. (Cloud was removed from the image by manual interpolation.) The model winds are enhanced where the air is colder than the sea, and reduced where the air is warmer than the sea. It must be noted, however, that this parametrization does not include the non-linear feedbacks between the air-sea temperature difference and the low level wind field.

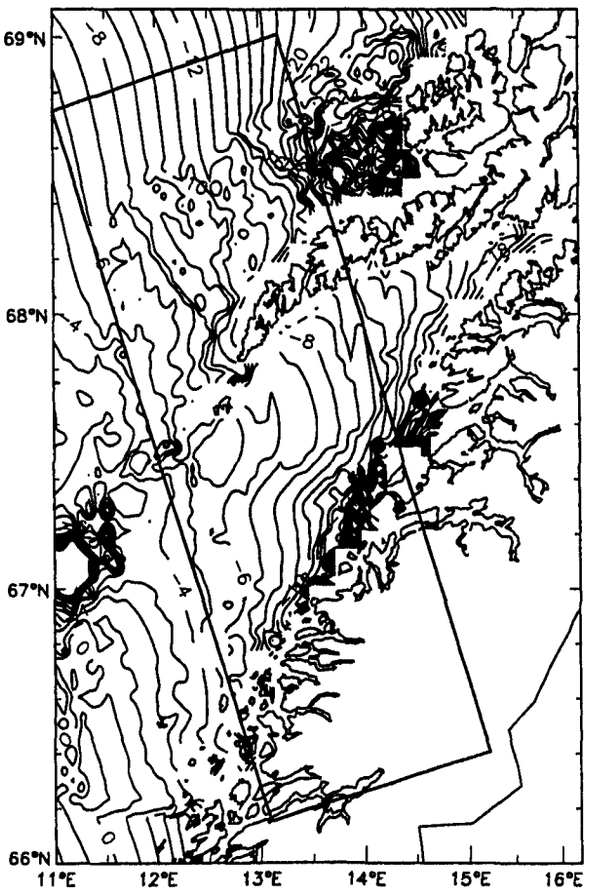

Figure 7. Simulated SAR signal for 2041, 29 June 1993, including the effects of air-sea temperature differences. Contours show backscatter cross-section at 1 dB intervals. The box denotes the location of the SAR imagery.

Figure 7 shows the simulated SAR signal, including the effects of air-sea temperature difference. Backscatter is enhanced above the warm core eddies (C in Fig. 6) and markedly decreased around Hell (A), as seen in Figure 2. However, backscatter is also reduced along the seaward boundary of the southern tip of the Lofoten Islands where an actual enhancement of the signal was observed. Whilst the model backscatter at Bodø is further decreased in this simulation, the observed decrease remains underestimated.

6. DISCUSSION

A simple wind model, including a parametrization of boundary layer stability effects, is of use in the interpretation of SAR imagery in a region of complex topography. At the time of the imagery, there was high spatial variability in the wind field. Many of the gross features in the imagery can be related directly to the wind field *e.g.* the low backscatter around Bodø and offshore towards the west (B and C in Figs. 2 and 5). The dark feature at Hell (A) and the enhanced backscatter within Vestfjorden are also influenced by atmospheric stability effects. The backscatter reduction in low winds is underpredicted by the backscatter model; the model does not make an allowance for the rapid decrease in SAR signals seen as drop-out occurs. Wind speeds at the time of the imagery were weak, often less than 3 ms^{-1}, and therefore signal drop-out is likely to have occurred.

The simulations do not capture the boundaries at E and F, nor the enhanced backscatter at D. E and F correspond to the locations of *in situ* observations of current boundaries associated with warm core eddies (Mitchelson-Jacob, 1997). D corresponds to a region of shallow water and strong tidal currents. A more sophisticated backscatter model, including wave-current interactions, will be required to simulate these effects.

ACKNOWLEDGEMENTS

This work was supported by the Procurement Executive (Ministry of Defence) through the Defence Evaluation and Research Agency, Winfrith, UK.

REFERENCES

Hasse, L. and H. Weber, 1985: On the conversion of Pasquill categories for use over the sea. *Bound.-Layer Meteor.*, **31**, 177-185.

Jones, B., and E.G. Mitchelson-Jacob, 1998: The analysis of SAR Imagery from the Sea Empress oil spill. *Int. J. Remote Sens.*, **19**, (in press).

Liu, Y., and X.-H. Yan, 1996: The wind-induced wave growth rate and the spectrum of the gravity-capillary waves. *J. Phys. Oceanogr.*, **25**, 3196-3218.

Mass, C.F., and D. Dempsey, 1985: A one-level, mesoscale model for diagnosing surface winds in mountainous and coastal regions. *Mon. Wea. Rev.*, **113**, 1211-1227.

Mitchelson-Jacob, E.G., 1997: The oceanography of Vestfjorden, Norway, from AVHRR imagery coincident with Rocky Water cruises (1993-1995). *Unit for Coastal and Estuarine Studies*, Report **U97-3**, 193pp.

Monin, A.S., and A.M. Obukhov, 1954: Basic laws of turbulent mixing in the atmosphere near the ground. *Tr. Akad. Nauk. SSSR Geofiz Inst.*, **24**, 163-187.

P2.41A

CONTRAIL COVERAGE OVER WESTERN EUROPE DERIVED FROM 2 YEARS OF NOAA-AVHRR-DATA

Richard Meyer*, Hermann Mannstein
Institut für Physik der Atmosphäre, DLR Oberpfaffenhofen

1 INTRODUCTION

High and optically thin ice clouds reduce the outgoing longwave flux at top of atmosphere mostly stronger than they decrease the downward solar radiative flux [13]. Thus an increase of thin ice clouds may lead to warmer surface temperatures [6].

Under certain atmospheric conditions aircraft form condensation trails [11] that can persist covering large proportions of the sky. In regions where these conditions for formation of persistent contrails are frequent and air traffic is dense the regional climate is affected. Due to the rapid growth of air traffic - fuel consumption is increasing 3 % per year [10] - its possible effects need further study.

To model the regional and global climatic effect of contrails we need to know their temporal and spatial distribution as well as their optical properties. Optical properties can be derived from in-situ measurements [4] and by remote sensing techniques [2, 5, 9]. Frequency can be obtained from synoptic observations of contrails as it was made by Minnis et al. [8] for the US, but to acquire their mean coverage of the sky areal measurements have to be taken. For this task we need remote sensing data with a high repetition rate and reasonable spatial resolution. Up to now only a few studies on regional contrail coverage have been performed. Mostly AVHRR data was used due to the availability of long time-series which is needed for proper means. Schumann and Wendling [12] estimate an average contrail coverage of 1.5 % from AVHRR-data for Southern Germany and the Alps. Bakan et al. [1] analyzed the biggest data set so far. Through visual inspection of daily AVHRR hard-copies from 52 months an average contrail coverage of 1 % over Central Europe and 2 % over the eastern part of the North Atlantic was obtained.

All these observations suffered from the subjectivity introduced by visual interpretation. Therefore there was a strong need for a fully automated scheme that detects contrails in satellite data. Engelstad et al. [3] created the first algorithm which was able to find contrails in AVHRR data, but had the tendency to misinterpret linear streaks of natural cirrus as contrails. The algorithm used here [7] was designed to have a low false alarm rate at a constant detection rate. This for the first time enables to analyze a large number of AVHRR-scenes operationally.

2 DETECTING CONTRAILS

With passive remote sensing methods ice clouds are recognized mainly by their low brightness temperatures in the thermal infrared. Due to originally smaller crystal sizes contrails [4] tend to show higher transmissivity in the AVHRR-channel 4 ($T4$: 10.3 to 11.3 μm) than in channel 5 ($T5$: 11.5 to 12.5 μm). This mostly causes contrails to appear bright on temperature difference images $TD = T4 - T5$.

The algorithm used here is described en detail by Mannstein et al. [7]. It takes advantage of both the mostly bright ridges contrails show in the TD-images and in the inverted temperature image $T5i$.

Unfortunately contrails often appear as very fuzzy structures hard to distinguish from background. Other objects like cloud edges, coast lines, mountain ridges etc. also form linear ridge structures of comparable scale and amplitude.

Therefore we take a scheme that combines different tests to avoid misdetections. Those tests are mainly based on spatial patterns - the way a human observer recognizes contrails in satellite images. Important for the derivation of climatological values is a constant detection efficiency for all scenes and viewing angles. To make the data independent from the individual scenery both images get normalized with their local standard deviation in a 5 x 5 surrounding $(\overline{SDTD}, \overline{SDT5})$. Within these normalized images the contrast is evenly distributed and independent from size and content of the actual scene. Therefore we can use global thresholds without loosing much sensitivity.

In the next step we use the sum of the normalized images N to avoid the interpretation of boundary layer cloud streets as contrails. To derive linear elements N is convolved with a line filter of 19 x 19 pixels in 16 different directions.

Because of the normalization of the input data, a single threshold is sufficient to isolate connected regions. These regions are treated as separate objects which might be contrails. Each of these objects is now checked against a binary mask which combines the following criteria:

$$N > 1.5, \quad (1)$$

$$TD > 0.2\text{K}. \quad (2)$$

$$\overline{G5} < 2 \cdot \overline{SDT5} + 1\text{K}, \quad (3)$$

where $\overline{G5}$ is the large scale maximum gradient for $T5$ calculated in a 15 x 15 pixel vicinity. Afterwards we recombine elongated structures disrupted by this check

*Corresponding author address: Deutsches Zentrum für Luft- und Raumfahrt e.V. (DLR), Institut für Physik der Atmosphäre, D-82234 Wessling; Tel +49 8153 28 2571, e-mail: Richard.Meyer@dlr.de

using morphological functions.

To be regarded as contrails, the resulting objects additionally have to consist of more than 10 pixels, must be longer than 15 pixels and must fit to the actual filter direction applied.

The filtering and testing procedures are repeated for 16 directions and the results are added to a binary contrail array. The proposed scheme mainly marks contrails of a width of 1 or 2 pixels. To detect wider contrails the whole algorithm is then applied to images reduced by a factor of 2. The results of this step are again added to the final binary contrail mask.

The performance of this scheme was tested against interactive interpretations of 60 satellite images by two observers. Greatest errors are found at the off-nadir scene borders due to the reduced horizontal pixel resolution there. To diminish this effect only a scan-angle of ± 50°is used.

Accurate visual inspection by zooming and optimizing the contrast confirms the assumption that many actual contrails still are undiscovered by the algorithm. In spite of the normalization the automatic scheme with its fixed parameters is inferior to the human eye in adapting to the specific contrasts in parts of the image. Thus the observer is able to recognize many more mostly weak contrails. But contrail coverage from AVHRR-images derived by the trained observers differed by a factor of 2, which shows that visual inspection is highly subjective. With the used algorithm we reach a detection efficiency defined as the ratio of correct contrail detections to the amount of all visually recognized contrails of 30 % to 50 %.

3 Results

The contrail detection algorithm is applied to AVHRR-images of NOAA-14 covering Central Europe (Fig. 1). We processed 660 daily noon scenes from April 1995 to February 1997. In Fig. 1) all remapped noon (1230 UTC ± 45 min) contrail masks are superimposed. It can be seen that the observed contrails accumulate mainly close to and in direction of the major flight routes.

Fig. 1) indicates that the algorithm is robust against misdetections of surface features. As you see coastlines and mountain ridges are almost never misclassified. Only Lake Balaton in Hungary seems to get falsely classified as contrail a few times. Therefore misdetections of static surface features and sensor line failures that are avoided through skillful parameter setting can be neglected for regional contrail cloud coverage.

To calculate the regional AVHRR-derived contrail coverage we divide the counts of the stacked contrail masks (Fig. 1) by the number of possible detections and filter the data with a circular gauss-kernel of 50 pixels. We have chosen this radius to represent the visibility range of a ground-based observer. Additionally the derived contrail cloudiness is corrected for yearly averaged inhomogeneity of the background. Like described by Mannstein et al. [7] this procedure adapts the reduced contrail detectivity to values which could be obtained above a thermally homogeneous background. Especially above more heterogeneous surfaces like land the AVHRR-derived corrected contrail coverage *ccc* gets enforced. This strong dependence of detection efficiency on $\overline{SDT5}$ is caused by normalizing the data.

Looking at the Alps in Fig. 1) we recognize that obviously above a certain value of $\overline{SDT5}$ we hardly can detect any contrails. As we cannot avoid this effect we exclude all pixels where $\overline{SDT5}$ exceeds 0.85 K (Fig. 2) from further considerations.

The average for the corrected daytime contrail coverage *ccc* in the whole dataset (Fig. 2) amounts to 0.5 % ± 0.25 %. The spatial pattern of the algorithm-derived contrail coverage agrees with the contrail observations by Bakan et al. [1]. They also obtained the maxima in the North-Atlantic flight corridor with declining contrail cloudiness to the Eastern and Southern parts of Europe. The absolute value for contrail cloudiness observed by Bakan et al. [1] is on the average 1.6 times higher than the annual mean of *ccc* we derived. This may be an effect of analyzing different years, but we also assume, that the deviations of absolute values may arise from the applications of two different methods. Again, this comparison indicates that trained human observers are more effective in contrail detection.

An advantage over the analysis of Bakan et al. [1] is the higher spatial resolution. Some heavily flown air traffic routes can still be recognized in Fig. 2). Maxima of contrail coverage of 1.0 % and higher are found over Wales, The Channel and in the Balaton region. The latter is as mentioned before partly caused by some misdetections occurring over Lake Balaton, but affects *ccc* just locally in a moderate way.

Fig. 3 shows the daily variation of the average contrail coverage in the area between 0°E and 20°E, 48°N and 55°N. To derive values comparable to Fig. 2) we applied the heterogeneity-correction using the annual average of $\overline{SDT5}$ for this box. Thereafter, the daily contrail coverage *ccc* varied from 0.0 % up to 5.7 % with a standard deviation of 0.6 %. Because contrails themselves lead to enhanced heterogeneity in the temperature images, we did not take into account the actual $\overline{SDT5}$ of the analyzed scene for heterogeneity-correction. But, avoiding this positive feedback on *ccc* we do neglect reduced detection efficiency caused by other image features.

As the 30-d floating average in Fig. 3 suggests, there are remarkable annual variations with a *ccc*-minimum below 0.2 % during summer and a *ccc*-maximum close to 0.9 % during winter and spring. But annual variations of detection efficiency might have influenced the results.

Additionally we analyzed NOAA-14 night scenes (0145 UTC ± 50 min) for the midseason months. With regard to the higher detection efficiency during night we used the nocturnal $\overline{SDT5}$-images for the heterogeneity correction. We found a mean nighttime contrail coverage *ccc* of 0.24 %, while *ccc* for the same period on daytime was 0.70 % (Fig. 3). Thus contrail coverage at night is about one third of the daytime noon coverage.

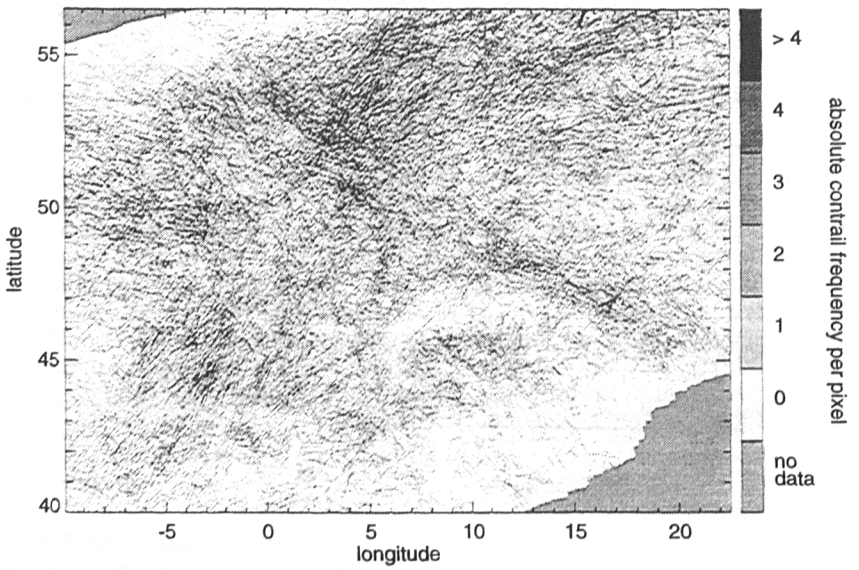

Figure 1: *Superimposed contrail masks for the period March 1995 to February 1997 (derived from 660 AVHRR passages 1230 UTC ± 45 min, pixels with less than 50 passages marked as "no data").*

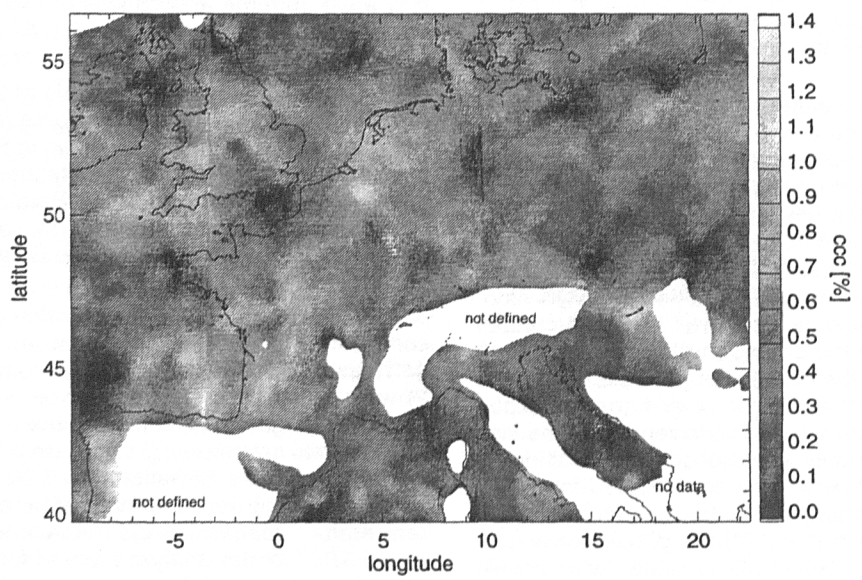

Figure 2: *Annual AVHRR-derived heterogeneity-corrected contrail coverage* ccc *derived from Fig. 1 ("not defined" are pixels with* $\overline{SDT5} > 0.85$ *K).*

4 Conclusions

The mean of the heterogeneity-corrected AVHRR-derived contrail coverage ccc reached 0.5 % ± 0.25 % over Western Europe. We recognize strong temporal and spatial variations in contrail coverage which match those derived by Bakan et al. [1]. Absolute values derived here are smaller by a factor of 1.6 which is of low significance due to analysis of different time-periods. Large differences of the two investigations can also be explained by an overestimation of the visual interpretations, but also by the poor detection efficiency of the automated scheme.

For the midseason month within this period we derive a nighttime contrail coverage of 0.2 % which has to be compared to 0.7 % for the same period from AVHRR-noon-passages. The observed annual cycle has its maxima during winter and spring, but might still be influenced by a differing detection efficiency.

Beyond this the scheme is not able to detect atypical contrails such as very wide spread and fuzzy ones, which are hard to distinguish from natural cirrus. The approach used also cannot recognize cases where

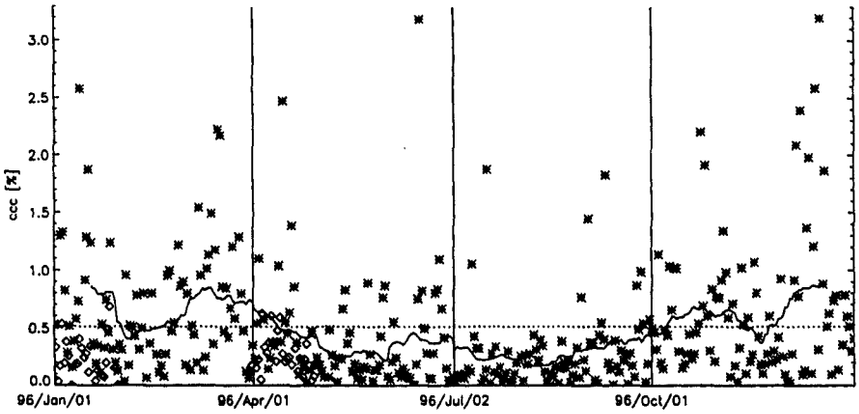

Figure 3: *Average AVHRR-derived corrected contrail coverage ccc for the box 0°E to 20°E, 48°N to 55°N. Asterisks are noon passages, diamonds nighttime passages. The solid line shows the 30-d floating average, the dotted line marks the annual average for daytime. Plotted are all values where data coverage was higher than 70 %. Not shown: absolute maximum of 5.6 % at January 14th 1996.*

contrails cover a large proportion of the sky destroying their individual line pattern.

Automated contrail recognition gives the opportunity to derive contrails' optical properties and their cloud forcing which should be further investigated to clearly define what kind of contrail are recognized by the automatic scheme.

Acknowledgments: This work was supported by BMBF (German Fed. Min. for Education, Science, Research and Technology) and the Bavarian State Min. for Reg. Development and Environmental Affairs.

References

[1] S. Bakan, M. Betancor, V. Gayler, and H. Grassl. Contrail frequency over Europe from NOAA-satellite images. *Ann. Geophys.*, 12:962–968, 1994.

[2] M. Betancor Gothe and H. Grassl. Satellite remote sensing of the optical depth and mean crystal size of thin cirrus and contrails. *Theor. Appl. Clim.*, 48:101–113, 1993.

[3] M. Engelstad, S. K. Sengupta, T. Lee, and R. M. Welch. Automated detection of jet contrails using the AVHRR split window. *Int. J. Remote Sensing*, 13(8):1391–1412, 1992.

[4] J.-F. Gayet, G. Febvre, G. Brogniez, H. Chepfer, W. Renger, and P. Wendling. Microphysical and optical properties of cirrus and contrails: cloud field study on 13 october 1989. *J. Atmos. Sci.*, 53:126–138, 1996.

[5] M. Kästner, K. Kriebel, R. Meerkötter, W. Renger, G. Ruppersberg, and P. Wendling. Comparison of cirrus height and optical depth derived from satellite and aircraft measurements. *Mon. Wea. Rev.*, 121:2708–2717, 1993.

[6] K. N. Liou. Influence of cirrus clouds on weather and climate processes: a global perspective. *Mon. Wea. Rev.*, 114:1167–1198, 1986.

[7] H. Mannstein, R. Meyer, and P. Wendling. Operational detection of contrails from NOAA-AVHRR-data. *Int. J. Remote Sensing*, submitted, 1998.

[8] P. Minnis, J. K. Kirk Ayers, and S. P. Weaver. Surface-based observations of contrail occurrence frequency over the U.S., April 1993 - April 1994. Ref. Pub. 1404, NASA, June 1997.

[9] P. Minnis, D. Young, L. Nguyen, D. Garber, J. Smith, W.L., and R. Palikonda. Transformation of contrails into cirrus during success. *Geophys. Res. Lett.*, SUCCESS Special Issue, submitted June 1997, 1998.

[10] U. Schumann. On the effect of emissions from aircraft engines on the state of the atmosphere. *Ann. Geophys.*, 12:365–384, 1994.

[11] U. Schumann. On conditions for contrail formation from aircraft exhausts. *Meteor. Z.*, 5(3):4–23, 1996.

[12] U. Schumann and P. Wendling. Determination of contrails from satellite data and observational results. In U. Schumann, editor, *Lecture notes in engeneering: Air traffic and the environment - background, tendencies and potential, DLR international colloquium, Bonn, Germany, November 15/16, 1990, 140-153*, volume 60, 1990.

[13] B. Strauss, R. Meerkoetter, B. Wissinger, P. Wendling, and M. Hess. On the regional climatic impact of contrails – microphysical and radiative properties of contrails and natural cirrus clouds. *Ann. Geophys.*, in press, 1997.

P2.42B

FOG DETECTION AND FORECAST OF FOG DISSIPATION USING BOTH AVHRR AND METEOSAT DATA

A.I. Anthis[1]
Hellenic National Meteorological Service

A.P. Cracknell[2]
University of Dundee, Dundee, Scotland, U.K.

1. Introduction

During winter months, low clouds and fog constitute one of the serious problems affecting human activities, especially driving on the roads and aviation. In Greece, fog is observed during winter months mainly in certain areas of Central and Northern Greece. The most usual fog area is lowland Thessalia. Due to the fact that lowland Thessalia is surrounded by high mountains, fog and stratus are formed by radiational cooling. In that area, fog can persist for many hours into daytime and in some cases it can last continuously for the whole day.

Fog detection is very important for aviation but fog dissipation forecast is a very difficult task for forecasters since fog duration is a marginal situation depending on small changes of specific meteorological parameters.

2. Detection of fog in daytime

Fog and stratus top temperature is usually not very different from the surface temperature. Moreover, fog and stratus can appear as warmer surfaces than land in winter, when there is a temperature inversion. During daytime, the most appropriate channels for fog detection are the visible channels of meteorological satellite imagery. In infrared satellite imagery, it is difficult to detect fog and low clouds, especially during the time of its formation. However, once the Sun has heated the ground sufficiently in surrounding areas, fog will appear colder than the surrounded areas.

Fog detection during daytime is relatively straightforward using conventional visible and infrared images. However, in contrast to other types of clouds, fog and low stratus appear relatively warm on infrared images especially if the fog layer is not too thick, since their temperature is close to that of the underlying land or sea surface. Because of the later characteristic, detection of fog on satellite images is difficult at night when there is no sunlight and therefore no visible channel data exist.

3. Detection of fog at night

The difficulties for fog detection at night on infrared satellite imagery arise from the fact that the temperatures of the fog and of the underlying surface are similar (Scorer, 1986). Moreover in some cases, fog top has a higher temperature than the surrounding area due to temperature inversion.

In the absence of visible channel data, the property of fog (and other water cloud) of the variation of its emissivity with wavelength is used (Eyre *et al.* 1984). At around 11μm, opaque water clouds emit radiation as though they were black bodies ($\varepsilon \approx 1$). Therefore, the equivalent 'black body' temperature (brightness temperature) will be almost equal to the physical temperature of the cloud top. At around 3.7μm, opaque water clouds have an emissivity of 0.8-0.9 (Eyre *et al.*, 1984). Therefore, the measured brightness temperature will be significantly lower than the physical temperature of the cloud tops. This property is not exhibited by land or sea surfaces to the same degree (Eyre et al., 1984). Thus the difference between the brightness temperature from the two channels (CH4 - CH3)

[1] Anastassios I. Anthis, Dept.of Weather Satellites and Radars, Hellenic National Meteorological Service, Hellinikon, 16777, Athens, GR; e-mail: anthis@hnms.gr.
[2] A.. P. Cracknell, Department of Applied Physics and Electronic & Mechanical Engineering, University of Dundee, Dundee, DD1 4HN, Scotland, U.K.

of the AVHRR is sensitive to the presence of fog or low clouds.

As in most cases it is impossible to separate low stratus clouds from fog, the term "fog" would indicate fog or stratus or simultaneous existence of both.

In this work, the data used are both AVHRR and METEOSAT. AVHRR data are used for fog detection at night and METEOSAT data are used for fog observation and fog dissipation forecast during the day over Thessalia lowland area, located in the mainland of Central Greece.

The typical indications for possible fog formation are :

a. Low-level moisture: The presence of significant amounts of low-level moisture can sometimes be inferred by a reduced rate of land cooling on night-time infrared images. The Earth's surface appears warmer under low-level moist air prior to fog formation, than where the air is drier. Such areas are an indication of fog formation.

b. Cloud cover. Areas with cloud cover during the day, followed by clear skies at night are likely locations for radiation fog formation.

c. Snow cover. Snow cover can be a source of cooling that leads to fog formation, if the dew-point is above freezing.

d. Precipitation. Precipitation during the late afternoon and evening hours followed by clearing skies, often leads to fog formation.

4. Prediction of fog dissipation

It has been proved (Gurka 1974, 1978) that there is a correlation between fog reflectivity as it is measured from the visible channel of meteorological satellites and fog duration.

Fog is dissipated according to the layer thickness after certain hours as the day goes on. Radiation fog and stratus dissipate from their outer edges inwards due to differential heating. Since fog generally diminishes from the outer edges inward, referring to aviation forecasting, it is important for the forecaster to consider for the dissipation time the location of the airport of interest with respect to the fog boundary. It has been shown (Gurka 1974) that high resolution satellite images can be used for fog dissipation determination as there is a strong relation between fog reflectivity as it is recorded from satellite sensors and the tendency for the remaining or dissipation of the fog. The time of fog dissipation is a function of :

a. Reflectivity of the fog layer.

b. The existence or not of any clouds above the fog layer.

c. Fog extent.

d. Time of the day.

For the prediction of fog dissipation time, a quantitative measure of fog brightness should be used. For this purpose, a graph is created of fog duration time in hours after sunrise, versus fog - land difference from the visible channel which is normalised according to the vertical Sun viewing angle as introduced by Gurka (1978).

5. A case study

An area of 10x6 pixels over the city of Larissa (located inside lowland Thessalia) has been selected, where there are traditional meteorological observations.

The estimation of factor parameters (a), (b) and (c) of paragraph 4 from traditional weather observations, is very difficult or even impossible. As far as local forecast is concerned, experienced meteorologists can estimate the thickness of fog cloud from its transparency. However fog can be transferred slowly towards that area and that estimation cannot be forecasted easily. In the case of an area where there is not any weather observation station, then the estimation of fog dissipation is not based on any real observations. In this case it is important to examine the land surface characteristics and topography since those are important factors for the area where fog could cover. In both cases it is clear that satellite remote sensing makes a positive contribution to the prediction of fog dissipation.

6. Approach to the problem

For fog detection at night, the technique presented by *Eyre et. al.*, (1984) is applied. In this technique, only the three IR AVHRR channels are used. The difference of CH4-CH3 is used to distinguish fog or low stratus from land or sea (*Eyre et. al.*, 1984).

In figure 1, the image of AVHRR Ch4-CH3 difference is presented. The fog and low cloud area is very well defined as white. Middle and high clouds are presented as dark areas in the image.

7. Fog reflectivity versus fog duration

For fog dissipation detection the visible channels of METEOSAT are used, normalised according to the vertical Sun viewing angle. A normalised visible satellite image offers the user several advantages over conventional visible images. For avoiding a false effect of the very low Sun viewing angle during the early morning

hours, the images are selected after 1 hour after sunrise.

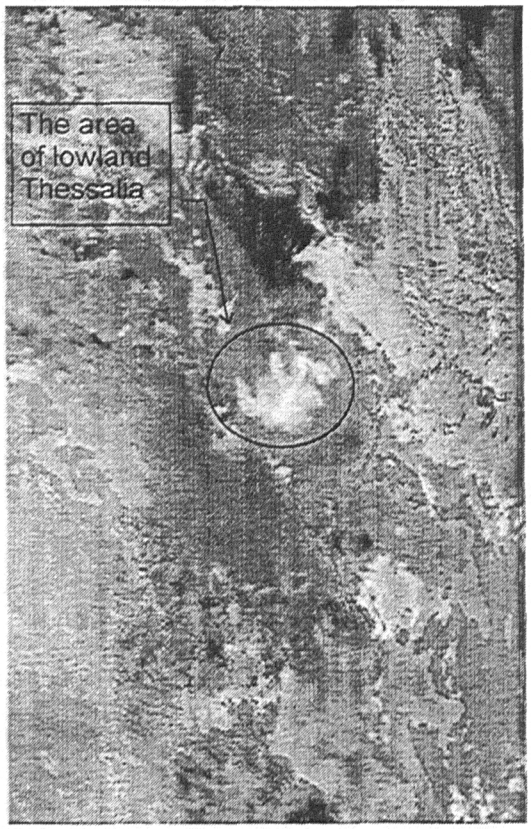

Figure 1: AVHRR CH4 - CH3. The fog and low clouds area is very well defined as white. Middle and high clouds are presented as dark.

For the study of fog detection over the area of Thessalia lowland, Greece, the case study of 14 November 1996 was examined.

For removing the atmospheric effect from the measured reflectivity value recorded from satellite, the difference (fog reflectivity normalised) - (land reflectivity normalised for clear land) has been calculated for every VIS METEOSAT image.

According to the diagram in figure 2, the relation of fog reflectivity versus fog duration is linear until two hours before fog dissipation (where fog duration is between 2 and 6 hours). Below the limit of 2 hours, according to the diagram, there is no-linearity. Since in Mediterranean countries, fog in most cases lasts only a few hours after sunrise even in the winter, more precise prediction is necessary in order to increase the accuracy of fog dissipation prediction.

In order to obtain even better results for radiation fog created in an area where land morphology favours fog development, a method is used which involves considering the topography of the area of interest as follows:

a. A mask of the area of Thessalia lowland is created.

b. The area covered by fog is determined from the first available VIS METEOSAT image.

c. The percentage of the above area covered by fog for the next few hours of the day is calculated.

d. A diagram is created, taking into account the fog persistence after the first morning calculations, and the percentage of the same area affected by fog in the following hours, versus fog duration (figure 3).

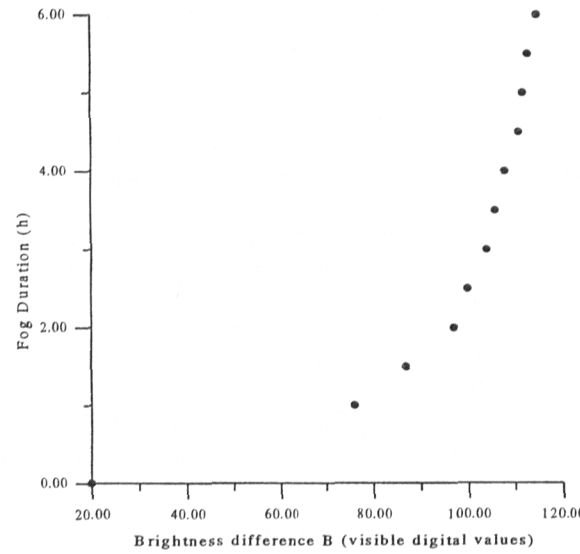

Figure 2: Fog duration time in hours origin from dawn, when the first visible image showing the area covered by fog is available, versus fog - land difference of visible channel which is normalised according to the vertical Sun viewing angle. The relation is linear until two hours before fog dissipation. It can be seen that dissipation occurs two hours after the linearity is broken.

8. Discussion

Apart from the use of remote sensing data to estimate fog dissipation time, it is also important to introduce, if possible, the current and forecast parameter values (i.e. wind speed and direction, surface temperature and dew point, 850 hPa wind speed and direction, 850 hPa temperature and dew point) which would affect fog duration or fog dissipation.

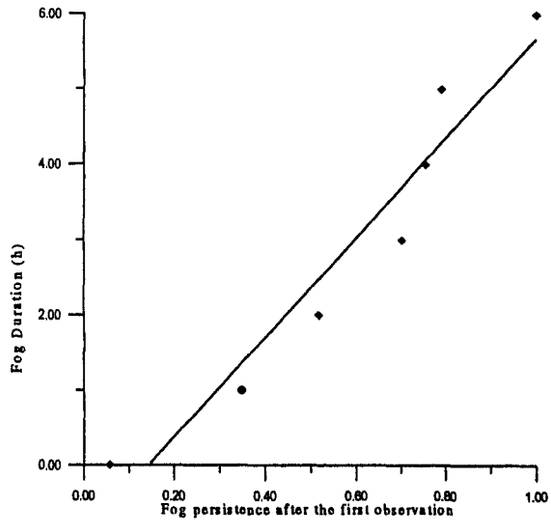

Figure 3: Coverage of the area affected by fog early in the morning in a specific area of Thessalia lowland, and the percentage of the same area affected by fog in the following hours, versus fog duration.

9. References

Anderson, R.K., Ashman, J.P., Bittner, F., Farr G.R., Ferguson, E.W., Oliver V.J. and Smith, A.H. (1973). Application of meteorological satellite data in analysis and forecasting. ESSA tech. report 51 (Washington D.C., Air Weather Service).

Anthis, I.A., (1993), Approaches to multispectral cloud classification of AVHRR images. MSc Thesis, Department of Applied Physics and Electronic & Mechanical Engineering, University of Dundee, Scotland, U.K.

Anthis, I.A., Hayes, L.W.B., Vaughan, R.A. and Cracknell, A.P., (1996): Classification of cloud complexity in severe weather conditions over the Ionian sea and the south-east Dodecanese using METEOSAT data. *International Journal of Remote Sensing, 17, 2857-2867.*

Bader, M.J., Forbes, G.S., Grant, J.R., Lilley, R.B.E. and Waters, A.J., (1995), Images in Weather Forecasting. Cambridge University Press, 499 pages.

Derrien,M; Le Gleau,H; Harang,L; Noyalet,A; Piriou,JL (1989): An automatic cloud classification using AVHRR at night. 4th AVHRR Data Users' Meeting, Rothenbourg, 5-8 September 1989, EUMETSAT, Darmstadt, Germany, 69-72.

Dybbroe, A. (1993): Autiomatic detection of fog at night using AVHRR data. 6th AVHRR Data Users' Meeting, Belgirate, Italy, EUMETSAT, Darmstadt, Germany, 245-252.

Eyre,JR; Brownscombe,JL and Allam,RJ (1984): Detection of fog at night using Advanced Very High Resolution Radiometer (AVHRR) imagery. Meteorological Magazine 113, 266-271.

Hunt,GE (1973): Radiative properties of terrestrial clouds at visible and infra-red thermal window wavelengths. Quarterly Journal of Royal Meteorological Society 99, 346-369.

Gurka,JJ (1974): Using Satellite Data for forecasting fog and stratus dissipation. 5th Conference on Weather Forecasting and Analysis, 54-57, 4-7 March 1974, St Louis, Mo, NOAA, Washington, DC, USA.

Gurka,JJ (1978): The use of enhanced visible imagery for predicting the time of fog dissipation. Conference on Weather Forecasting and Analysis and Aviation Meteorology, 343-346, NOAA, Washington, DC, USA.

Karlsson, K.G., (1989), Development of an operational cloud classification model. *International Journal of Remote Sensing,* 10, 687-693.

Liljas, E., (1982), *Automated Techniques for the Analysis of Satellite Cloud Imagery.* Nowcasting (Ed: K.A. Browning,Ed,Academic Press Inc.(London) Ltd.), 167-176.

Liljas,E (1987): Multispectral Classification of Cloud, Fog and Haze. (Remote Sensing Applications in Meteorology and Climatology, Ed: R.A.Vaughan, Kluwer Academic Publishers), 301-319.

Parikh, J., (1977), A Comparative Study of Cloud Classification Techniques. *Remote Sensing of Environment,* 6, 67-81.

Scorer, R.S. (1986): Cloud investigation by satellite. Ellis Horwood Limited, Chichester.

Thomas, I.L., Benning, V.M. and Ching, N.P., (1987),Classification of Remotely Sensed Images. IOP, Bristol.

P2.43A

FOG DETECTION IN OPERATIONAL MODE

Astrid Clausen*
University of Hannover, Hannover, Germany

Hans Roozekrans
Royal Netherlands Meteorological Institute, KNMI, De Bilt, The Netherlands

Peter Scheidgen
VCS Nachrichtentechnik GmbH, Bochum, Germany

1. INTRODUCTION

There is a need at KNMI to obtain information on the occurrence and areal coverage of fog at the ground for operational purposes (traffic, aviation, shipping). For that reason, an automatic fog detection algorithm based on NOAA/AVHRR data is implemented in an operational running HRPT-receiving system.

2. FOG ALGORITHM

The fog detection is based on the brightness temperature differences of Channel 3 and Channel 4 of NOAA/AVHRR data due to varying emissivities of fog in the spectral region of Channel 3 (3.7 µm) and Channel 4 (11.5 µm). This is pointed out by several authors (e.g. Eyre *et al.*, 1984; Bendix and Bachmann, 1991a). The algorithm as it is put into practice is given by Bendix and Bachmann (1991b) including threshold values of the temperature differences for fog detection at night and day situations. As Channel 3 temperatures are erroneous at day especially at low sun elevations, correcting factors for Channel 3 temperatures to a sun elevation of 30° of horizon are given. This enables a fog detection in dependence on scan time and sun elevation and submits a fast image processing which is mandatory for use in an operational mode.

3. OPERATIONAL MODE

The brightness temperature difference of Channel 3 and Channel 4 provides an indication of the occurrence of low cloud, either fog or stratus. Hence, additional information is needed to identify fog on the ground. This is realised by displaying „fog/stratus indication" maps on a Meteorological Work Station (MWS) enabling the overlay of synoptic ground observations on top of the map. The „fog /stratus indication" maps show Channel 4 data together with marked pixels where low clouds (fog or stratus) have been detected (Fig. 1, Fig. 2). Thereby the map provides information about the presence and types of cloud and the extension of fog.

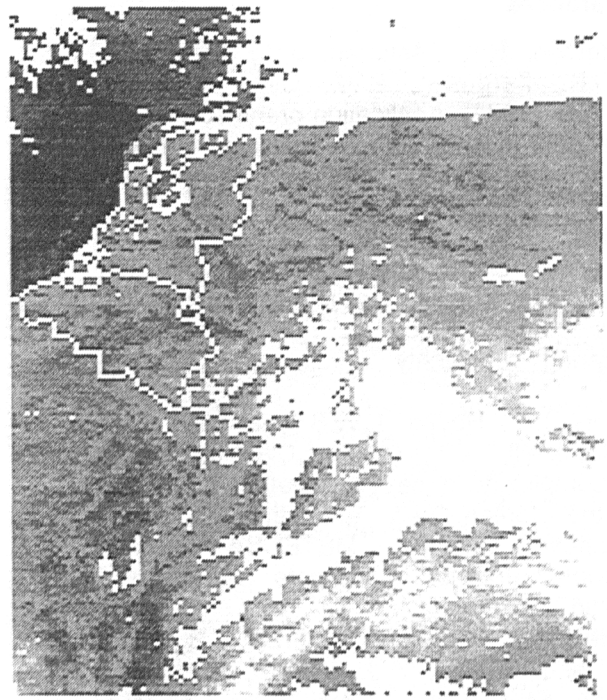

Fig. 1: NOAA 12 from 19th October 1997, 07:08 UTC. Fog detection at night.

* *Corresponding author address*: Astrid Clausen, Institute of Meteorology and Climatology, University of Hannover, Hannover, Germany, e-mail: ac@vcs.de

The ground observations ensure the forecaster if fog is present (and how thick). Another handle enabling the forecaster to discriminate between fog and stratus is the pattern of the fog/stratus marked areas. Sharp edges of areas point to fog and diffuse edges point to stratus.
The algorithm is controlled by a set of editable parameters like threshold values and correcting factors for Channel 3 temperatures as defined by Bendix and Bachmann (1991a, 1991b). Thus the algorithm and the threshold values, originally evaluated for the Alpine region, can be refined and adapted to the Netherlands.

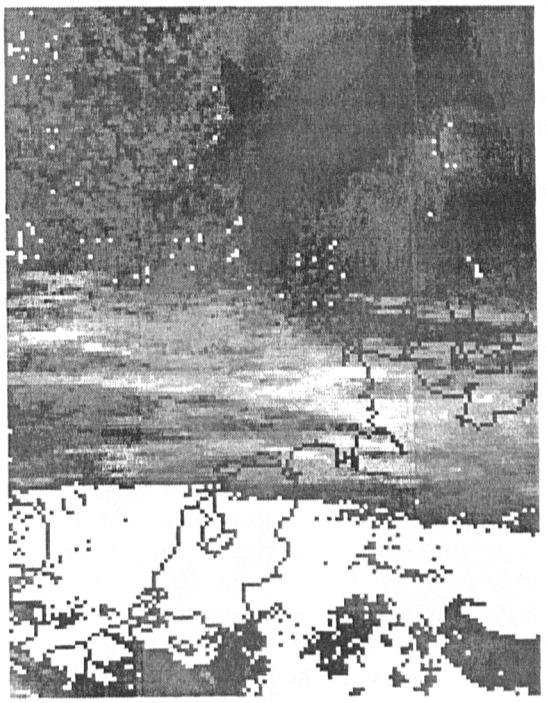

Fig. 2: NOAA 14 from 20th October 1997, 03:29 UTC. Fog detection at night.

4. STATUS

Up to now the algorithm works and gives good results at night. One situation from 19th of October 1997 is shown in Fig. 1. The northern part of Germany is influenced by maritime moist air resulting in advection fog in contrast to radiation fog in the southern part of Germany. Different mountains as the Alps , Blackwood or Voges can clearly be identified by sticking out of the foggy region. Another example is the situation from the following day (20th of October 1997) shown in Fig. 2. The moist air has moved southwards followed by a striking line in east-west direction dividing foggy and non foggy regions caused by a cold front. By checking synoptic data for these situations a good match can be found regarding the margins of the foggy regions.
At day the normalisation of Channel 3 temperature works in principle. However, the correction of radiance at low sun elevations often leads to overall foggy situations. By varying the parameters of the fog algorithm an improvement of this algorithm is to be expected. The actual work is focused on this part.

5. OUTLOOK

Due to the fog algorithm in operational mode an adaptation of the editable parameters for different areas becomes possible. This leads to more detailed information about spatial fog distribution and enables climatological investigations about fog distribution in space and time.

6. REFERENCES

Bendix, J., and Bachmann, M., 1991a: Ein operationell einsetzbares Verfahren zur Nebelerkennung auf der Basis von AVHRR-Daten der NOAA-Satelliten. *Meteorol. Rdsch.* **43**, 169 - 178.

Bendix, J. and Bachmann, M., 1991b: Operational detection of fog in the Alpine region by means of advanced very high radiometer (AVHRR) imagery of NOAA-satellites. *Proc. 5th AVHRR Data Users' Meeting*, 25-28 June 1991b, Tromsö, Norway, EUM P09.

Eyre, J.R., Brownscombe, J.L. and Allam, R.J., 1984: Detection of fog at night using Advanced Very High Resolution Radiometer (AVHRR) imagery. *Met. Mag.* **113**, 266 - 271.

P2.44B

RETRIEVAL OF AEROSOL PROPERTIES FROM MERIS

Th. Heinemann*, J, Fischer
Freie Universität Berlin, Berlin, Germany

1. Introduction

Aerosols play an important role in the climate system. The direct radiative forcing by aerosol as well as the effect of aerosol on cloud formation and cloud albedo influence significantly the global and local radiation budget. Information about the global distribution of atmospheric aerosol is one of the largest uncertainties in present climate models. A global monitoring of aerosol amount and aerosol type is necessary. The new generation of ocean colour sensors like SeaWiFS, MERIS and MOS have the capability to derive global aerosol distribution with a high temporal and spatial coverage over the oceans.

2. MERIS and MOS

The Medium Resolution Imaging Spectrometer MERIS willl be launched in 1999 by the European Space Agency (ESA) on ENVISAT. Detailed information about the sensor and its application are given by ESA and Fischer (ESA, 1996) and (Fischer, 1998). Three channels of MERIS are dedicated to aerosol remote sensing and atmospheric correction of ocean colour imagery. The Modular Optoelectronic Scanner (MOS) developed by the German Aerospace Center (DLR) is flying on the Indian Research Satelite (IRS) since October 1996. Its band specification and spatial resolution is comparable to MERIS but the swath is much smaller. Two channels in the near infrared are used to test aerosol remote sensing algorithms for MERIS with MOS data. Table 1. shows the aerosol channels of MERIS and MOS-B.

3. Database for algorithm development

The algorithms for the determination of aerosol optical depth and aerosol type from MERIS radiance measurements are developed and verified by means of radiative transfer calculations for the wavelength as given in Table 1.

*Corresponding author address: Thomas Heinemann, Freie Universität Berlin, Institut für Weltraumwissenschaften, Fabeckstr, 69, 14195 Berlin, Germany, e-mail: tom@zedat.fu-berlin.de

The radiative transfer model MOMO is described by Fell and Fischer, 1995. 1100 cases with different atmospheric conditions over a rough ocean surface were simulated. Four different aerosol types, maritime, continental (WCP, 1986), clean maritime and a tropospheric background aerosol were included in the simulations. The aerosol optical depth was varied between 0.0 and 0.5. Different aerosol vertical profiles were also considered.

Table 1: MERIS and MOS-B channels for aerosol remote sensing

MERIS		MOS-B	
Centre	Width	Centre	Width
705nm	10nm		
775nm	15nm	750nm	10nm
865nm	20nm	870nm	10nm

4. Retrieval of aerosol optical depth

The algorithm for the retrieval of the aerosol optical depth is based on a linear regression of the radiances measured in two or three of the aerosol channels of MERIS or MOS. The regression parameters are determined from 800 simulated data sets for 1700 different combinations of sun zenith angle, viewing zenith angle and azimuth difference. The remaining 300 cases were used to test the algorithm itself. The average root mean square error (RMSE) of derived aerosol optical depth at 550nm is 0.026 for moderate viewing and sun zenith angles (<70°) out of the sunglint region. Figure 1 shows the RMSE of the aerosol optical depth projected on the swath of MERIS on ENVISAT. The sunglint area is not suitable for the retrieval due to the strong and very variable signal from the surface. Simulations with ocean roughness according to different wind speeds show that the sunglint influences the retrieval in the whole swath. An accuracy of the wind speed of 3m/s is necessary to ensure reliable results for the tropical regions (near the sunglint). This aspect will be discussed in more details on the poster. The average RMSE of the retrieval scheme increases to 0.03 if 1% sensor noise is added to the data. Simulations with other marine aerosol types (Shettle+Fenn, 1979) showed similar results. The algorithm has already been applied to MOS-data. A detailed validation is planned.

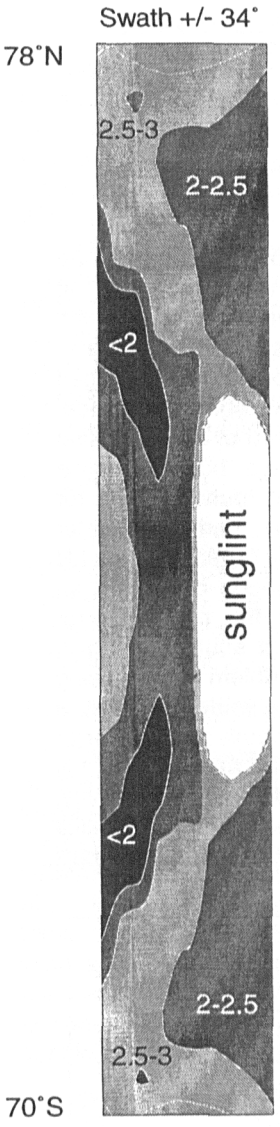

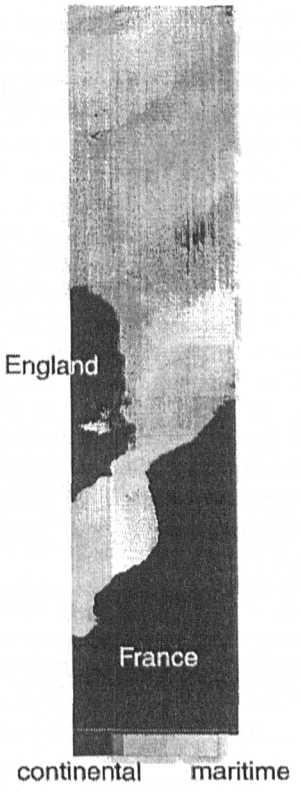

Figure 1 (left): RMSE of optical depth *100 projected on the swath of MERIS

Figure 2 (right): Aerosol classification for a MOS-B scene (southern North Sea)

5. Aerosol type estimation

The determination of the aerosol type from multispectral measurements is an ill posed problem. However the spectral information is sufficient to discriminate between larger and smaller aerosol particles. The relation ε between the aerosol path radiances in two channels depends only slightly on the aerosol concentration but can be related to the aerosol type . The aerosol path radiance itself can be obtained by subtracting the Rayleigh path radiance from the measured radiance. Our algorithm for the aerosol type estimation is based on this relation. Larger (more oceanic) aerosol particles are distinguished from smaller (more continental) ones. A discrimination in 5 size-classes is possible. Figure 2 shows the aerosol type as derived from MOS-B data over the southern North Sea on April 1st 1997. A comparison with the meteorological situation of this day allows the interpretation of the results. The aerosol particles in the southern part are larger due to the high humidity in this area. At the English coast large sediment loads are transported to the North Sea by several rivers. The non negligible water leaving radiance contaminates the results of the aerosol retrieval. In the northern part of the scene easterly wind from The Netherlands transports polluted air with smaller particles over the ocean.

6. Conclusions

The ocean colour sensors MERIS and MOS are suitable for the remote sensing of aerosol optical depth and aerosol type. The RMSE of the aerosol optical depth retrieval is between 0.2 and 0.3 depending on the observation geometry. Aerosol type can be estimated within 5 size-classes ranging from maritime to continental. The strongest limitations of the algorithms are uncertainties in the estimation of the ocean roughness and the water leaving radiance.

ESA, 1996: The Medium Resolution Imaging Spectrometer. Report of the MERIS Scientific Advisory Group, ESA-SP-1184, ESA Publications Division, ESTEC, Nordwiijk, The Netherlands.

Fischer, J., R. Bennartz, T. Heinemann, L. Schüller, R. Preusker, 1998: Retrieval of atmospheric parameters from ENVISAT's MERIS, this issue, P4.47A

Fell, F. and J. Fischer, 1995: Validation of the FU Berlin radiative transfer model. Final report of the EC-Contract MAS2-VT92-0020. Available via Institute for Space Sciences, Free University of Berlin, Germany.

WCP (World climate research program), 1986: A preliminary cloudless standard atmosphere for radiation computation, WCP-112, WMO/TD-No.24

Shettle, E.P. and R.W. Fenn, 1979: Models for the aerosols of the lower atmosphere and the effects of humidity variations on their optical parameters, AFGL-TR-79-0214. Env. Res. Papers No. 676.

P2.45A DIRECT RETRIEVAL OF THE SURFACE LATENT HEAT FLUX FROM SATELLITE DATA; COMPARISON TO LIU ET AL. (1984) METHOD ON DATA OF THE SEMAPHORE EXPERIMENT

Denis Bourras*, Laurence Eymard*
Centre d'Etude des Environnements terrestre et Planétaires, VELIZY, FRANCE

1. INTRODUCTION

The latent heat flux values over oceans are required for a wide range of studies such as coupling of global circulation and atmosphere models. The latent heat flux (LEF) is proportional to the evaporation flux which is the vertical transport of humidity:

$$E = < w.q > \quad (1)$$

Few surface LEF values are available over oceans, at a global scale. The most reliable flux data come from scientific ships during the large experiments which combine ship, buoy, and aircraft measurements. In this paper, we use data from the SEMAPHORE (Structure des Echanges Mer-Atmosphère, Propriétés des hétérogénéités Océaniques: Recherche Expérimentale) experiment (Eymard et al., 1996) which took place in 1993 near the Azores Islands.

The most direct way to obtain surface turbulent fluxes from many sorts of data is to apply the bulk method. This method is based on the Monin and Obukhov (1954) similarity theory. In the bulk parametrization method, (1) is developed into a function of retrievable geophysical parameters :

$$L_E = \rho.E.C_E.(U_S - U_A).(Q_S - Q_A) \quad (2)$$

The subscript A corresponds to a reference altitude, S stands for surface quantities, CE is the bulk transfer coefficient, Q is the specific humidity, U the scalar wind, and ρ.E a constant. The transfer coefficient parametrizations needed in the bulk flux calculation are selected among the numerous existing models (e.g. Large and Pond, 1982).

Few LEF measures are available at a global scale. A solution to get a real-time global coverage should consist in the use of spaceborne sensors, insofar as they already provide operational measurements for geophysical parameters related to the LEF such as the sea surface temperature (SST), the columnar water vapour or the near surface wind.

Liu and Niiler (1984) propose to apply a bulk formula to retrieve the surface LEF using near surface parameters derived from satellite. In this method -hereafter referred as the LN method-, the geophysical parameters such as wind, sea surface specific humidity or humidity above the surface are first retrieved from a sensor which operates at microwave wavelengths by means of algorithms; then, the bulk flux is computed, as shown on figure 1.

When applying the LN method to data averaged over one month and two square degrees in space, Esbensen et al. (1993), and Eymard et al. (1989) find errors close to 30 W/m^2 in average, but they notice that 100 W.m^{-2} errors can be found locally for particular climate locations, or bad radiometer calibration zones. Schlüessel et al. (1995) use the LN method succesfully on instantaneous data, with an error of 30 W.m^{-2}. In any case the retrieval error found is high. Among the different sources of error, the wind retrieval is still a problem when using satellites such as SSM/I, and the retrieval of QA is noisy. At least one part of the bulk retrieval error could be reduced since the application of the LN method implies too many calculation stages: namely, the retrieval of the bulk parameters from satellite measurements and the application of the bulk formula.

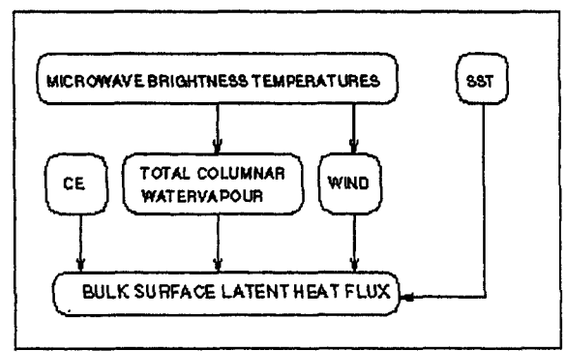

FIG. 1. Use of the bulk method to derive latent heat fluxes from SSM/I.

In this paper, we propose a simpler approach in which we relate directly the LEF to different frequency brightness temperatures (Tb) and to the SST through a multilinear regression. The direct method is established in two stages: a construction stage to create the regressive algorithm, and a validation stage consisting in comparing the LEF retrieved by the algorithm (applied on SSM/I brightness temperatures) with known surface LEF values. For these both stages, we use two independent datasets. The construction dataset is a global marine atmosphere database representative for annual global meteorology based on ECMWF

* CETP/UVSQ, 78140 VELIZY VILLACOUBLAY FRANCE
e-mail : dbs@cetp.ipsl.fr

(European Centre for Medium Range Weather Forecast) analyses in which brightness temperatures are simulated with a radiative transfer model. The validation dataset gathers real spaceborne information, and corresponding surface data from the ARPEGE model.

After a description of the datasets used -in section 2-, we evaluate the LN method on the SEMAPHORE experiment. Then, we study the sensitivity of different brightness temperatures to the latent heat flux. In section 3, we establish the direct method and the results of the two methods are compared for instantaneous data.

2. DATASETS

They consist of a simulation dataset intended to establish the sensitivity of the microwave brightness temperatures to the latent heat flux, a creation dataset to build the flux retrieval methods, and a validation dataset to apply them.

2.1 The simulation dataset

This first dataset is used to study the sensitivity of the microwave brightness temperatures to the latent heat flux. Typical humidity and wind profiles are modelled from radiosoundings obtained during SEMAPHORE. A radiative transfer model (Prigent et al., 1997) is used to simulate brightness temperatures at the SSM/I frequencies. SST and wind ranges are selected among the real variations measured during SEMAPHORE. The latent heat flux is computed with a bulk method using the transfer coefficient parametrization of Dupuis et al. (1997).

2.2 The creation dataset

The second dataset is required to derive the statistical relationship between the surface fluxes and the brightness temperatures. To get a large database representative of the natural atmospheric variations at any place on the earth, we use ECMWF global prediction fields, distributed over one year (between 1992 and 1993). The fields consist of 36 hour predictions, to optimize the balance of the hydrological cycle. We calculate the fluxes from the model fields using a bulk formula, and the brightness temperatures are simulated using the radiative transfer model (same algorithms as in section 2.1).

The database is split in two databases which are respectively the GLOBAL database, and SEMA (the SEMAPHORE zone of GLOBAL). These two creation datasets are sampled in terms of latent heat flux to get a constant histogram of the situations *represented for each* LEF value.

2.3 The validation dataset

The SEMAPHORE experiment took place in a subtropical midlatitude square zone from -30 to -15 longitude degrees, and from +15 to +30 degrees in latitude. The meteorological situations are mainly anticyclonic on this region, in all seasons. The characteristic water vapour profile from radiosoundings presents a strong inversion. We used data from the 15th october to the 15th November 1993. On the selected period, the scalar wind speed magnitude is about 6 $m.s^{-1}$, the average vertical humidity gradient is equal to 9 $g.kg^{-1}$, and the LEF ranges from 10 to more than 300 $W.m^{-2}$, with an average of 110 $W.m^{-2}$.

Because the in-situ measurements were performed on one ship only, it is not possible to validate the algorithms statistically. However, data from surface buoys and radiosoundings were available from two ships most of the time, and were assimilated in the ARPEGE model (operational model of METEO FRANCE) after the experiment (Giordani et al., 1997). In the following, we will take the reanalyzed output fields as the reference 'in-situ' data. The ARPEGE fields are model predictions obtained 6 hours after real data have been assimilated. This choice is a compromise between having data close to observations, and waiting for a balanced energy budget in the model.

The reference fluxes are computed with the algorithm presented in section 2.1. When comparing the results obtained with this algorithm to the LEF predicted by ARPEGE, we find a deviation as large as 20 $W.m^{-2}$. It accounts for the in-situ LEF determination error. On another dataset, Weare (1989) find an average error of 30 $W.m^{-2}$, in a complete study about the accuracy of LEF measures over oceans.

The satellite data used are SSM/I brightness temperatures which are available at the following frequencies: 19.35, 22.235, 37.0, and 85.5 GHz. A correction is applied to the SSM/I brightness temperatures to avoid a known bias between the real and the simulated brightness temperatures (Ellison et al., 1996). The SSM/I has a sampling footprint of 25 km for the low frequencies.

No other satellite data are used in this paper, since we use instantaneous data, and that satellites like AVHRR or ERS1 overpass the SEMAPHORE zone at times too different from SSM/I to use instantaneous data.

SST are available from METEOSAT satellite, but SST does not vary at all at short time and space scales on SEMAPHORE. As the SST are only available for cloud free locations (i.e., too few locations during the campaign), we choose to use the ARPEGE SST in the following of this study. We must take into account a SST retrieval error of 1°C on our algorithms.

Data preconditioning:

The ARPEGE model has been validated both in columnar water vapour (W) by comparison of the

fields to the structures shown by the Alishouse et al. (1990) algorithm, and in terms of wind (U) by comparison to the SSM/I algorithm of Goodberlet et al. (1990). The structures observed on the W and U ARPEGE predicted fields are most of the time shifted compared with the fields sensed by the satellite. As the aim of this paper is only the vertical retrieval of the LEF, we choose to retrieve the flux only on locations where the error between the model and SSM/I is less than 0.3 g/cm2 for W and 2 m/s for U.

As the brightness temperatures are polluted by cloud liquid water and important W, the two following pixel selection criteria were adopted: L<0.3 g/cm2, and W<3 g/cm2. Moreoever, we avoid situations where U is greater than 15 $m.s^{-1}$ since wind is not retrieved correctly beyond this value.

Finally, 54 different coupled images are available on the SEMAPHORE zone. The SSM/I data are projected on the ARPEGE zone, and interpolated at the ARPEGE maximum resolution of 0.16 square degrees.

3. COMPARISON FOR INSTANTANEOUS DATA

3.1 The LN method: description and application

In the LN method, the bulk formula (2) is used with spaceborne data. Unlike in the case of ground based instrumentation, only few geophysical parameters -useful for the latent heat flux calculation- can be retrieved from present spaceborne sensors such as SSM/I.

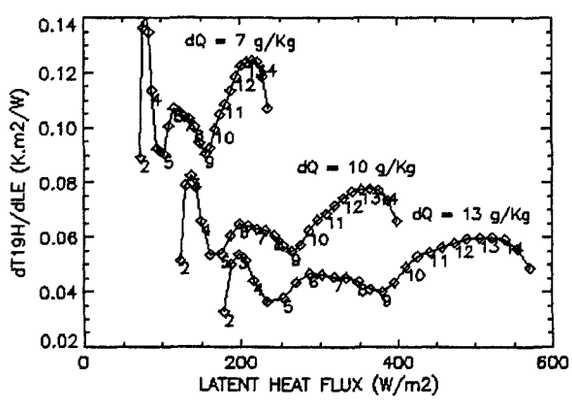

FIG. 2a. Sensitivity of the horizontally polarized brightness temperature at 19 GHz to the Latent heat flux, as a function of scalar wind intensity. Figure computed from the simulation dataset, with dT=5° and SST=22°C.

The wind is retrieved by using the Goodberlet algorithm. On the SEMAPHORE zone, the standard deviation of wind is close to 2 $m.s^{-1}$; i.e. an equivalent uncertainty as important as 45 $W.m^{-2}$ for a LEF value of 150 $W.m^{-2}$.

The QA retrieval error is a problem in the LN method. Liu et al. (1986) suggest to calculate QA from W by using a polynomial relationship, whereas W is retrieved by an algorithm applied on microwave brightness temperatures. Schultz et al. (1993) relate the brightness temperatures to the columnar water vapour content under 500 m using a linear algorithm. However, they relate W500m to QA by a linear relationship. No enhancement can be obtained, since Liu and Schulz use multilinear functions (at least on the SEMAPHORE area). Moreover a single relationship between Tb and QA should be more efficient. In order to proove this assertion, we build one algorithm on the creation dataset on the SEMAPHORE zone only, and another on the whole database and we compare the QA founds to the other methods. The application of these two algorithms to the SEMAPHORE instantaneous validation dataset leads to better results, as reported on table 1.

Method	correl.	σ (g/Kg)	bias (g/Kg)
Liu et al. (1986) -global-	**0.824**	**1.48**	**0.58**
Shulz et al. (1991) -global-	**0.73**	**1.22**	**1.14**
Bourras et al. (1998) -global-	**0.63**	**1.19**	**1.12**
Bourras et al. (1998) -local-	**0.7**	**1.08**	**0.71**

TABLE 1. Comparison of different authors' near surface specific humidity retrieval error.

To apply the LN method to the validation dataset, data should be averaged over one month and two square degrees, but we evaluate this method performance on the validation dataset without any time and space average. The Goodberlet algorithm is used to retrieve the wind, and Liu's method is used to obtain QA. QS is deduced from the ARPEGE SST, and CE equals 1.2. The application of the LN method to the validation dataset leads to a good mean behaviour but the standard deviation of error equals 56 $W.m^{-2}$, with a 17 $W.m^{-2}$ bias. As explained above, the uncertainties are mainly related to the wind and the QA retrieval error. The LN method is not very efficient for instantaneous data because of its form. A scatterplot between the ARPEGE latent heat flux and a bulk flux computed from equation (2) with CE=1.2, and U, QA, and QS deduced from ARPEGE shows a deviation of error of 30 $W.m^{-2}$. This is the result we would have if there was no retrieval error.

3.2 The direct method: principle, brightness temperature sensitivity to the LEF:

As shown on figure 1, the LN method uses microwave brightness temperatures and a SST information (if it is not also retrieved from brightness temperatures). One can easily show that the different functions of figure 1 are multilinear, or almost

multilinear. This way, by relating directly the input parameters (SST, Tb) to the surface LEF, we expect to reduce the uncertainties in the flux retrieval. In fact, with a simple mutilinear regression, the different stages of the LN method are bypassed (particularly, the direct method avoids the multiplication between the wind and the surface level humidity gradient). To our knowledge, one similar attempt had been made by Draper and Smith in 1981, as an illustration of multivariate regression analysis (see a figure in Liu, 1990). The data were monthly averaged and gave results comparable to the LN method results.

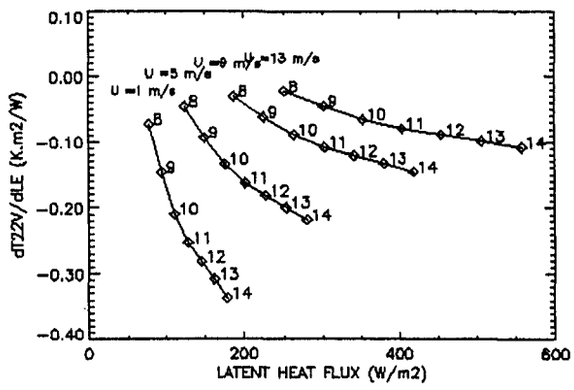

FIG. 2b. Same figure as FIG. 3a. for the 22 GHz channel (vertical polarization). The sensitivity is computed as a function of the vertical humidity gradient. Constant values are: dT=5° and SST=22°C.

The simulation database is used to simulate the sensitivity of the SSM/I brightness temperatures to the latent heat flux according to the bulk latent heat flux dependant variables, i.e. U,ΔQ,ΔT,SST.

On figure 2a-2b, we lay the emphasis on the sensitivity of the T19H channel to the LEF in terms of U variations, and of the T22V channel in terms of ΔQ. Different interesting aspects of the sensitivity such as the increasing sensitivity for decreasing ΔQ, or the nonlinear behaviour of the sensitivity will not be discussed here and are the object of another study. Anyway, according to these curves a statistical algorithm using brightness temperatures as inputs should be sensitive to the LEF.

Input parameters selected:

To build our algorithms, the input parameters are selected to maximize the sensitivity to water vapour and near surface wind. Different attempts have been made. Among the different configurations tested, we finally selected the algorithms which use the five following parameters: T19V/T19H (a polarization ratio sensitive to the surface scalar wind), T22V (which corresponds to a water vapour absorption ray), ln(280-T37V) and ln(280-T37H) (polarization ratio sensitive to surface and clouds), and Qs (instead of the SST).

3.3 Direct method results and comparison to the LN method

First, the algorithm coefficients are calculated from the creation dataset, then the algorithm is applied on the validation dataset.

We make regressions on the two sampled databases SEMA, and GLOBAL (see section 2.1). The brightness temperatures and SST combination used are those presented in section 3.2. On figure 3, we show that the obtained algorithms are sensitive to the LEF in each case. The standard deviations found are 25, and 45 W.m^{-2} respectively for the SEMA, and the GLOBAL datasets. We notice that when the database covers a greater area, the standard deviation of the retrieval is greater. On figure 3, we show that saturation occurs beyond 200 W.m^{-2}, which leads to flux underestimation, and that the regression is noisy for low flux values.

On figure 4, we show the application of the GLOBAL algorithm to the validation dataset. The standard deviation of error is about 32 W.m^{-2} and the sensitivity is close to that found with simulated data. As expected, the behaviour is the same as for the creation dataset.

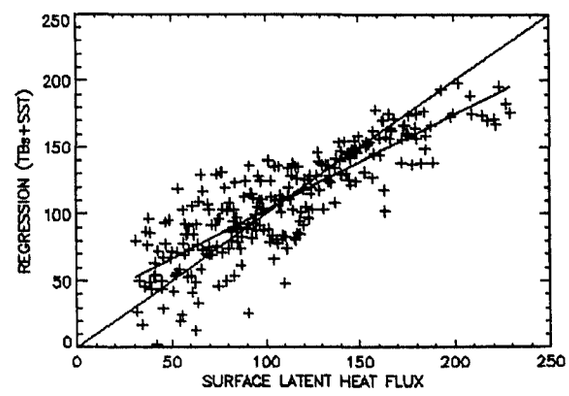

FIG. 3. Scatterplot of the Latent heat flux retrieval algorithm vs the reference latent heat flux, on the SEMAPHORE zone of the creation dataset.
Correlation coefficient: 0.86, σ=25.4 W.m^{-2}.

Despite the important error, we show that the uncertainties are lower than with the LN method (see section 3.1). The bias is equal to 18 W.m^{-2}, which is negligible if we take into account the uncertainty on the reference LEF (i.e. 20 W.m^{-2}, see section 2.1). When we apply the SEMA and the GLOBAL algorithms, we notice that the sensitivity is not really affected by the use of these algorithms, but the bias may differ significantly. It shows the importance of having corresponding climatic zones for the creation and the validation dataset, when trying to relate the brightness temperatures to the surface LEF because the average LEF differs from one region to another.

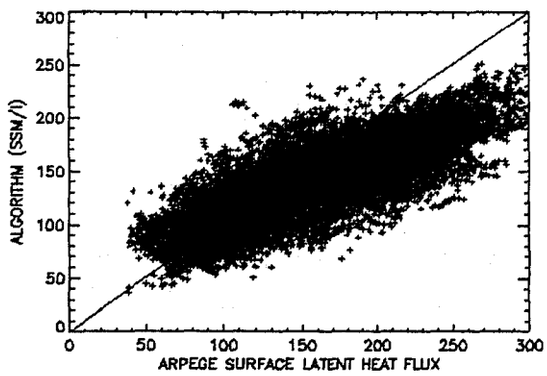

FIG. 4. Scatterplot of the application of the GLOBAL algorithm to the validation dataset vs the ARPEGE reference bulk flux.

On a scatterplot of the LEF error versus the scalar wind intensity, and on a scatterplot of the wind retrieval error versus the scalar wind intensity, we show that the LEF retrieval error is correlated to the scalar wind value, which is itself correlated to its retrieval error. Thus, we confirm that there is a lack of sensitivity of SSM/I to the near surface scalar wind.

Method	correl.	σ (W/m²)	bias (W/m²)
Liu et al. (1984) -global-	**0.53**	**56.0**	**+17.4**
Bourras et al. (1998) -global-	**0.8**	**32.4**	**-18.6**

TABLE 2. Latent heat flux retrieval error on the validation dataset for the two approaches.

Hence, we can relate directly the brightness temperatures and the SST to the LEF for instantaneous data, whereas the LN method applied to these data tends to amplify the retrieval error mainly in terms of bias.

4. CONCLUSION

We show that it is possible to use a statistical algorithm to relate directly microwave brightness temperatures and a SST information to the surface latent heat flux.

Simulations predict the sensitivity of the brightness temperatures to the latent heat flux; the created algorithm, applied to our validation dataset has the same characteristics as predicted by the creation dataset, and induces less noise than the LN method. The standard deviation of error found for instantaneous data is lower than 35 $W.m^{-2}$. The bias may differ significantly following the area selected for the creation of the algorithm.

REFERENCES

Alishouse, J. C., S. Snyder, J. Vongsathorn, and R. R. Ferraro, 1990: Determination of oceanic total precipitable water from the SSM/I, *IEEE Trans. Geosci. Remote Sens.*, **28**, 811-822.

Dupuis, H., P. K. Taylor, A. Weill, and K. Katsaros, 1997: Inertial dissipation method applied to derive turbulent fluxes over the ocean during the SOFIA/ASTEX and SEMAPHORE experiments with low to moderate wind speeds, *J. Geophys. Res.*, **21**,115-21,129.

Esbensen, S. K., D. B. Chelton, D. Vickers, and J. Sun, 1993: An analysis of errors in Special Sensor Microwave Imager evaporation estimates over the global oceans, *J. Geophys. Res.*, **98**, C4, 7081-7101.

Eymard, L., C. Klapisz, and R. Bernard, 1989: Comparison between Nimbus-7 SMMR and ECMWF model analyses: the problem of surface latent heat flux, *J. Atmos. Oceanic Technol.*, **6**, 866-881.

Eymard, L., et al., 1996: Study of the air-sea interactions at the mesoscale: the SEMAPHORE experiment, *Ann. Geophysicae*, **14**, 986-1015.

Goodberlet, M. A., C. T. Swift, J. C. Wilkerson, 1990: Ocean surface wind speed from the Special Sensor Microwave/Imager (SSM/I), *IEEE Trans. Geosci. Remote Sens.*, **28**, 5, 823-828.

Giordani, H., S. Planton, B. Bénech, and B.H. Kwon, 1997: Atmospheric Boundary Layer Response to Sea Surface Temperatures during the SEMAPHORE Experiment, Accepted *J. Geophys. Res.*, SEMAPHORE special edition.

Ellison, W. J., A. Balana, G. Delbos, K. Lamkaouchi, L. Eymard, C. Guillou, C. Prigent, 1996: Study and measurement of the dielectric properties of sea water, *European space Agency report*, 11197/94/NL/CN.

Large, W. G., and S. Pond, 1982: Open ocean momentum flux measurements in moderate to strong winds, *J. Phys. Oceanogr.*, **11**, 324-336.

Liu, W. T., and P. P. Niiler, 1984: Determination of monthly mean humidity in the atmospheric surface layer over oceans from satellite data, *J. Phys. Oceanogr.*, **14**, 1451-1457.

Liu, W.T., 1986: Statistical relation between monthly mean precipitable water and surface-level humidity over global oceans, *Mon. Wea. Rev.*, **114**, 1591-1602.

Liu, W. T., 1988: Moisture and latent heat flux variabilites in the tropical Pacific derived from satellite data, *J. Geophys. Res.*, **93**, 6749-6760, and 6965-6968.

Liu, W. T., 1990: Remote sensing of surface turbulent heat flux, *Surface Waves and Fluxes*, G. C. Geernaert and W. J. Plant, **2**, Kluwer Academic Publishers, 293-309.

Liu, W. T., W. Tang, and P. P. Niiler, 1991: Humidity profiles over the ocean, *J. Climate*, **4**, 1023-1034.

Monin, A.S., and A. M. Obukhov, 1954: Basic laws of turbulent mixing in the ground layer of the atmosphere, *Akad. Nauk SSSR Geofiz. Inst Tr.*, **151**, 163-187.

Prigent, C., L. Phalippou, and S. English, 1997: Variational inversion of the SSM/I observations during the ASTEX campaign, *J. Appl. Meteor.*, **36**, 5, 493-507.

Schulz, J., P. Schlüessel, and H. Grassl, 1993: Water vapour in the atmospheric boundary layer over oceans from SSM/I measurements, *Int. J. Remote Sensing*, **14**, 15, 2773-2789.

Schlüessel, P., L. Schanz, and G. Englisch, 1995: Retrieval of latent heat flux and longwave irradiance at the sea surface from SSM/I and AVHRR measurements, *Adv. Space Res.*, **16**, 10, 107-116.

Weare, B. C., 1989: Uncertainties in estimates of surface heat fluxes derived from marine reports over the tropical and subtropical oceans, *Tellus*, **41A**, 357-370.

P2.46B SOLAR RADIATION BUDGETS FOR MAGS AND BALTEX

J. Feng[1], R. Hollmann[2], J. Müller[2], R. Stuhlmann[2] and H.G. Leighton[1]*

[1]Department of Atmospheric and Oceanic Sciences, McGill University, Montreal, Canada
[2]Institut für Atmosphärenphysik, GKSS Forschungszentrum, Geesthacht, Germany

1. Introduction

The Mackenzie Gewex study (MAGS) and the Baltic Sea Experiment (BALTEX) are two of the GEWEX regional experiments. One of the goals of these experiments is to improve understanding of the energy and water cycles of these regions and specifically to improve the capability of modelling these cycles. An important component of the models is the solar radiation absorbed at the surface since it has a direct impact on the hydrology of these regions through its influence on melting of snow and on evaporation. Apart from being able to reproduce surface radiation fluxes correctly, the ability of the models to reproduce measured top-of-the-atmosphere (TOA) fluxes provides an indirect measure of how realistically the models are able to simulate clouds in these regions.
The ScaRaB instrument on the Meteor-3 satellite measured narrowband and broadband radiances during the period March 1994 to February, 1995. These data can be combined with AVHRR data from the NOAA polar orbiting satellites to provide much better temporal coverage of the TOA radiation budgets over the MAGS and BALTEX regions than is obtained from ScaRaB alone.

In this paper we show solar radiation budgets at the top of the atmosphere for the MAGS and BALTEX regions that are deduced from ScaRaB broadband and narrowband radiance measurements. The net solar fluxes at the surface are calculated from the top-of-the-atmosphere budgets using the algorithm of Li et al. (1993).

2. Method

A new narrowband-to-broadband conversion algorithm was developed using the A2 data from the well calibrated ScaRaB narrowband (0.5-0.7 μm) and the broadband (0.2-4.0 μm) SW channels. The algorithm considers the effect of scene type and viewing geometry on the conversion. As with ERBE, the surface is classified into five geotypes: land, ocean, snow, desert, and land-ocean mix. Cloud cover is grouped into four classes: clear (less than 5% cloud cover), partly cloudy (between 5% and 50% cloud), mostly cloudy (between 50% and 95% cloud), and overcast (more than 95% cloudy). The cosines of the solar zenith angle and the viewing zenith angles are each divided into 10 bins. For each scene type, cloud cover, cosine solar zenith angle bin, and cosine viewing zenith angle bin, a linear expression $L_{bb} = aL_{nb} + b$ is derived from correlations between the broadband radiance and ScaRaB ch1 narrowband radiance. Examples of such correlations are shown for land with different geometries and cloud cover in Fig. 1. The values of the coefficients a and b were recorded in a look-up table.

Relationships between the ScaRaB narrowband reflectance and AVHRR narrowband reflectance were derived from MODTRAN calculations for a range of geometries and scene types. Fig. 2 shows the normalized spectral response function of ScaRaB channel and NOAA-12 AVHRR channel 1.
The TOA reflectance of ScaRab ch1 is defined as :

$$\alpha_{ScaRab} = \frac{\pi \int_{0.5}^{0.7} R_{ScaRab}(\lambda) L_{TOA}(\lambda) d\lambda}{\int_{0.5}^{0.7} R_{ScaRab}(\lambda) S_0(\lambda) \cos(\theta) d\lambda}$$

The TOA reflectance of AVHRR ch1 is defined as:

$$\alpha_{AVHRR} = \frac{\pi \int_{0}^{\infty} R_{AVHRR}(\lambda) L_{TOA}(\lambda) d\lambda}{\int_{0}^{\infty} R_{AVHRR}(\lambda) S_0(\lambda) \cos(\theta) d\lambda}$$

R_{ScaRab} and R_{AVHRR} are the spectral response function of ScaRab channel 1 and AVHRR channel 1 separately. $S_0(\lambda)$ is the solar irradiance at TOA. θ is the solar zenith angle. The simulations are carried out for 5 scene types: ocean, vegetation land, desert and snow under clear sky, and stratus cloud. Fig. 3 shows the surface spectral reflectivities (Bowker et al. 1985) used in these calculations. The solar zenith angles range from 10 to 80°, viewing zenith angles

* *Corresponding author address:* Henry Leighton, Dept. of Atmos. and Oceanic Sci., McGill University, 805 Sherbrooke St. W., Montreal, QC, Canada, H3A 2K6; e-mail: henry@zephyr.meteo.mcgill.ca

are 0, 30, and 60°, and the azimuth angle is 60°. Fig. 4 shows the results of calculated reflectances over ocean and snow surfaces under clear skies. These results, and other similar calculations show that for any particular scene type, the relationship between the ScaRab and AVHRR reflectances are independent of geometry. To a good approximation, the relationship for a particular scene type can be expressed in the form $\alpha_{AVHRR} = \alpha_{ScaRab} + b$ over the range of geometries considered.

The table gives the values of b for the scene types considered.

Surface type	Ocean	Land	Desert	Snow	Cloud
b	0.001	0.027	0.054	0.042	0.034

3. Results

As an example of the above procedures, the narrowband-to-broadband algorithm is applied to an overpass of ScaRab over MAGS region on August 22, 1994 21.61 UT. Fig 5a shows the outgoing SW flux at the TOA from the ScaRab broadband channel while Fig 5b shows the outgoing SW flux at the TOA calculated from the ScaRab narrowband radiance. In both cases the ERBE angular distribution models Suttles et al., 1988) have been used for the radiance to flux conversions. Clearly, the flux pattern of these two figures is very similar. Figs 5c,d show the SW fluxes absorbed at surface obtained by applying the Li et al. (1993) algorithm to the results in Figs 5a and b respectively. Fig 5e is the difference field from these two figures. The differences are between -10 to 10 W/m^2 over most of the area. The overall average of the difference is -0.48 W/m^2 and the σ is 14.7 W/m^2. Fig 6 shows the average differences in the flux absorbed at the surface from all passes of ScaRaB over the MAGS region in July, 1994 deduced from the broadband measurements and the narrowband measurements. The differences are between -5 to 5 W/m^2 over most of MAGS area., although regions of greater systematic differences over the lakes, the coastal region and the south-east portion of the MAGS region do occur.

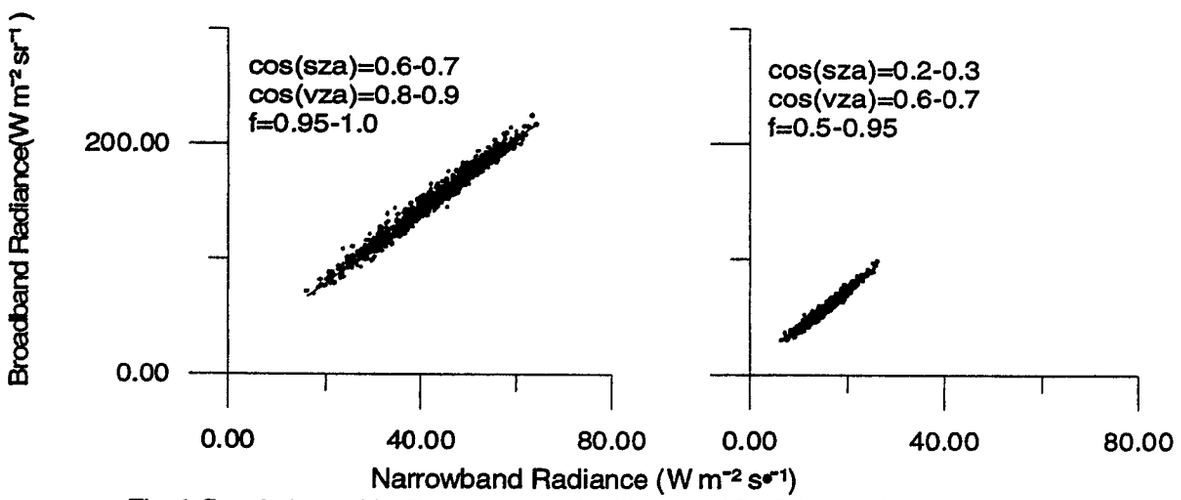

Fig. 1 Correlations of ScaRab narrowband radiance and ScaRab broadband radiance

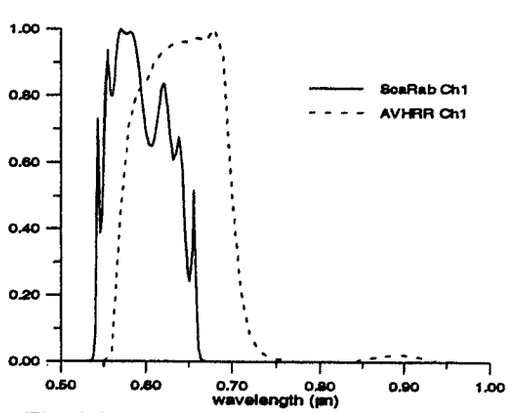

Fig. 2 Spectral response function of ScaRab channel 1 and AVHRR channel 1

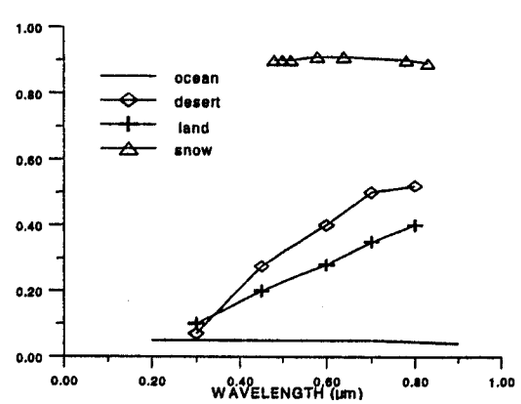

Fig. 3 Surface spectral reflectivity

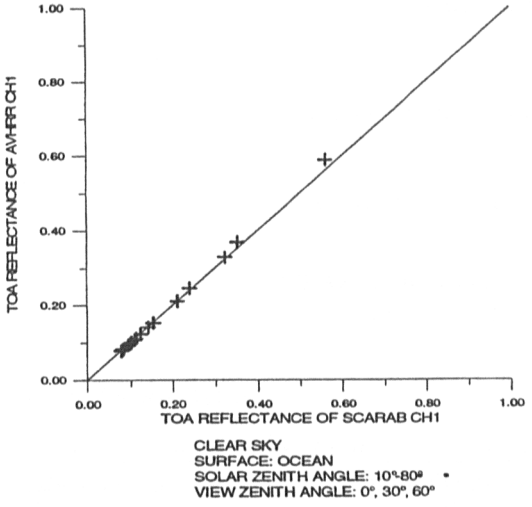

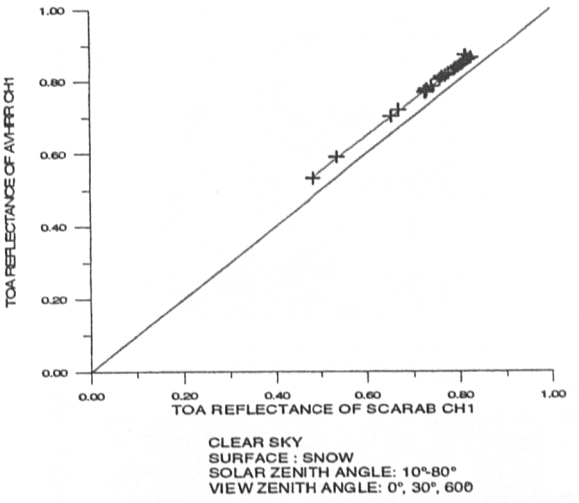

Fig. 4 Correlations of TOA reflectance of AVHRR ch1 and TOA reflectance of ScaRab ch1

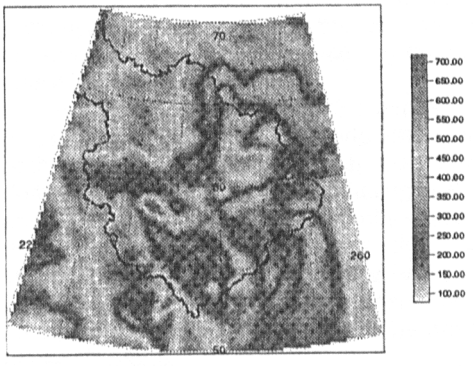

Fig. 5.a Outgoing SW flux at TOA, August 22, 1994, 21.61 UT

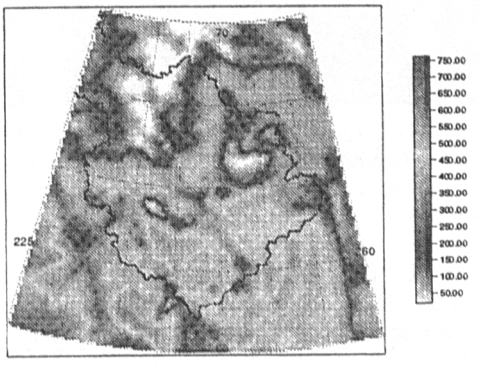

Fig. 5c. Net SW flux at surface from broadband TOA flux, August 22, 1994, 21.61 UT

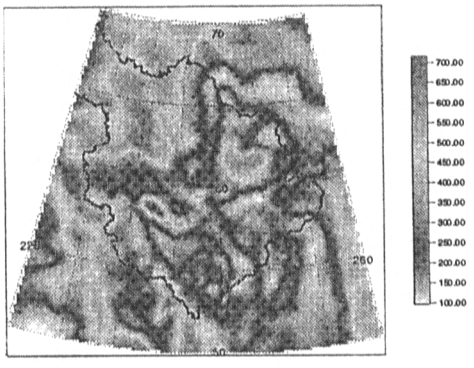

Fig. 5b. Outgoing SW flux at TOA from narrowband TOA radiance, August 22, 1994, 21.61 UT

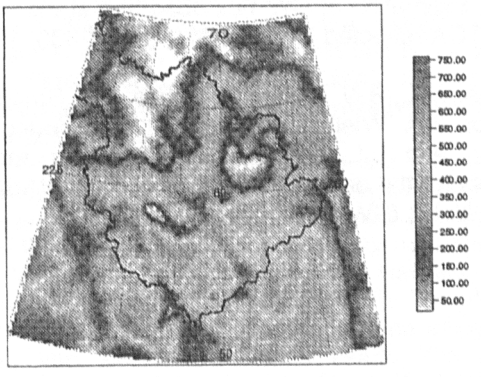

Fig. 5d Net SW flux at surface from narrowband TOA radiance, August 22, 1994, 21.61 UT

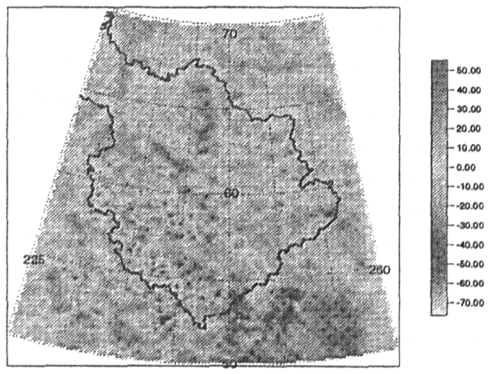

Fig. 5e. Difference between the net SW flux at surface from narrowband radiance and the net SW flux at surface from broadband flux, August 22, 1994, 21.61 UT

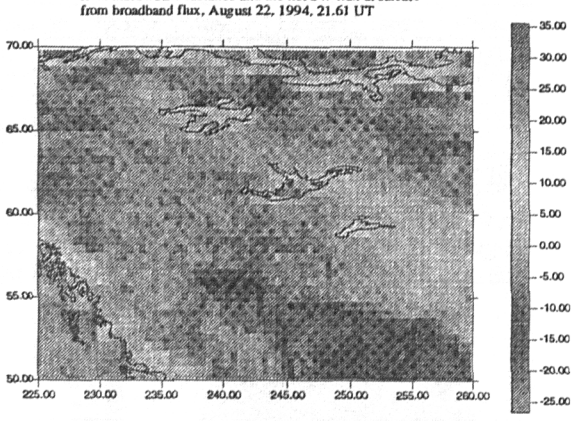

Fig. 6. Mean difference for July

References

Bowker, D. E., R.E. Davis, D.L. Myrick, K. Stacy and W.T. Jones, 1985: Spectral reflectances of natural targets for use in remote sensing studies, NASA RP-1139, 1985.

Li, Z., H.G. Leighton, K. Masuda, and T. Takashima, 1993: Estimation of SW flux absorbed at the surface from TOA reflected flux, J. Clim., 6, 317-330, 1993.

Suttles, J. T., R.N. Green, P. Minnis, G.L. Smith, W.F. Staylor, B.A. Wielicki, I.J. Walker, D.F. Young, V.R. Taylor, and L.L. Stowe, 1988: Angular radiation models for the earth-atmosphere system, NASA RP-1194, Vol. 1 (SW radiation)

P2.49A

A RADAR-SATELLITE RAINFALL ESTIMATION TECHNIQUE FOR HYDROLOGICAL APPLICATIONS

Federico Porcú*
FISBAT-CNR, Clouds and Precipitation Group, Bologna, Italy

Marco Borga
DTeSAF, University of Padua, Agripolis, Legnaro (PD), Italy

Franco Prodi
FISBAT-CNR, Clouds and Precipitation Group, Bologna, Italy, and
Physics Dept., University of Ferrara, Ferrara, Italy

1. INTRODUCTION

The use of METEOSAT IR data for precipitation estimation is investigated for three rainfall events in Northern Italy, driven by autumnal cold fronts. Satellite-based analysis of this kind of events is made difficult due to their stratified characteristics, prone to lower level forcing (e.g. topography) that is not easy to catch from the satellite IR. However, an improved understanding of these events is mandatory because such systems deeply affect the autumnal climatology of Europe and often cause hydrometeorological disasters.

Successful satellite rainfall estimation techniques (Lovejoy and Austin, 1979 among others) make use of both infrared and visible data, in order to improve the definition of the cloud types causing rain. Bi-spectral and IR techniques have recently been compared (King et al., 1995), showing that considerable improvement can be obtained by using visible data. However, due to the requirement of monitoring precipitation also during the night, we are forced here to use IR alone.

The utility of radar data to calibrate the Negri-Adler-Wetzel technique (NAW, Negri et al., 1984), to improve quantitative rainfall estimates is evaluated. The proposed Run Time Calibration technique (RTC) makes use of simultaneous NAW and radar estimate adjusting the NAW rainfall coefficients for every satellite slot. RTC requires the satellite and radar estimates to be matched on a calibration area, located inside the radar domain. Areas of different sizes are tested in this work, for calibration and validation, to maintain consistency with typical sizes of hydrological basins in Southern Europe. Considerable improvement of the satellite estimates for medium integration areas ($\approx$ 1000 km^2) are obtained.

2. DATA

The analysis was performed for three events, occurring on 2-4/10/1992, 7-9/10/1993 and 14-15/11/1996 over Northern Italy. The 1992 and 1993 events were characterized by moderate/high rainrates, while in 1996 mainly light rain was detected. For these events METEOSAT and radar data were available. A raingauge network was also used for radar data adjustment.

The meteorology of the western Mediterranean is often controlled in autumnal months by cold fronts induced by low pressure fields in the Lion Gulf or surrounding areas: most of the mesoscale precipitating systems are related to these events. Mediterranean regions are prone to hydrometeorological hazard, with particular reference to the Tyrrhenian coasts of Italy and France. In these regions cold fronts carry humid warm air from S and/or SW which develops pre-frontal convective clouds and frontal, stratified clouds. The successive occurrence of high intensity, convective and long-lasting, stratified precipitation is an highly favorable combination for flooding.

2.1 *IR data processing*

METEOSAT IR (10.5–12.5 μm) data, from the FISBAT Institute archive, were used for this study. The temporal resolution of the satellite data is 30 minutes, and the spatial resolution of the pixel is about 7.5 (to the North) by 5 km over Northern Italy. During the first two events the satellite was in autumnal eclipse, so the first and last two slots were not disseminated. The METEOSAT IR data were processed using NAW for quantitative comparison and calibration with the radar data.

NAW first defines clouds in the IR image by means of the 253 °K isotherm. The coldest 10%, of the area defined as cloud is assigned a rainrate R_{10}, and the next 40% is assigned a lower rainrate of R_{40}. To the remaining cloud fraction (the warmest 50%) is assigned a rainrate R_{50}, equal to zero. Therefore, the threshold for high and low precipitation assignments may vary for each different cloud. The nominal rainrates were determined by Negri et al (1984) for tropical thunderstorm events as follows: $R_{50} = 0$, $R_{40} = 2$ and $R_{10} = 8$ mm h^{-1}.

For satellite-radar comparison, radar images were remapped, after parallax correction, onto the METEOSAT grid. Since the radar domain is scanned by the satellite approximately at the 22th and 52th minute each hour, radar-based reference rainrate was obtained by averaging appropriately radar maps taken

*Corresponding author address: Federico Porcú, FISBAT-CNR, via Gobetti 101, I-40129 Bologna, Italy; e-mail F.Porcu@fisbat.bo.cnr.it.

from the 15th to the 30th minute, and from the 45th to the 60th minute, respectively.

Validation of satellite rainfall estimation is a critical issue. The main difficulty is that there are no well established standards to measure and/or estimate rainfall at the space-time scales of interest. Satellite estimation cannot be evaluated with confidence unless the validation data set is itself known to be very well calibrated in an absolute sense. In the context of IR rainrate evaluation, radar observations of rainfall are generally most useful, though radar is itself a remote sensing technique with its own unique error sources and calibration problems.

2.2 Radar data processing

The radar derived data were provided by the C-band Doppler radar located in Northern Italy on Monte Grande hill. The complex topography of the mountain area presents so drastic shielding problems that they cannot be overlooked: radar rainfall error sources are magnified when the rainfall estimation is required over mountainous terrain.

Radar volume scans were performed every 15 minutes and complementary data from 30 raingauges were available in the range of the radar rainfall coverage. The use of accumulation maps as reference fields requires that careful processing of radar data is performed. The following preprocessing steps were performed:

1. attenuation correction, carried out using an iterative procedure due to Hildebrand (1978);
2. correction for effects due to the vertical variations in reflectivity caused by melting layer (bright band): the algorithm developed by Andrieu and Creutin (1995) was used;
3. correction of the beam blocking error.

Reflectivity measurements were related to the radar rainfall rate through the Marshall-Palmer relation and mapped onto a Cartesian coordinate system with a grid spacing of 1 km by 1 km. Finally, the mean field bias adjustment due to various error sources was carried out by using concurrent radar and raingauges data.

3. AREAL PRECIPITATION MEASUREMENTS

Instantaneous, satellite mean areal precipitation values were computed using NAW and compared with the corresponding radar values for the considered precipitation events over a study area S, 180x140 km^2 wide, centered on the radar position, at 45.34N, 11.68E.

To investigate the sensitivity of NAW to the reduction of the integration area, we introduced a further subdivision. The study area is divided in two equal sub-areas, symmetrically with respect to the radar site, H_{west} and H_{east} (≈12600 km^2 each). In each of them, areas $A1_{west}$ and $A1_{east}$ (≈8000 km^2 each) are defined in terms of Meteosat pixel as a rectangular region 16 lines by 12 pixels; each A1 area is divided into four areas 8 by 6 (areas A4, 2000 km^2 each) and sixteen areas 4 by 3 pixels (areas A16, 500 km^2 each).

Radar-satellite errors are summarized by using the Root Mean Square Difference (RMSD) between radar and satellite areal rainfall estimates:

$$RMSD = \frac{1}{N_A}\sum_{A=1}^{N_A}\left(\frac{1}{N_t}\sum_{i=1}^{N_t}(R_i^r - R_i^s)^2\right)_A^{1/2}$$

where N_t is the total number of satellite slots considered, N_A is the number of areas where the parameters are computed (1 for S, A1 and H, 4 for A4, 16 for A16), R^s_i is the areal mean satellite-based rainrate at time i and R^r_i is the corresponding areal mean reference radar rainrate.

Figure 1 plots RMSD values between satellite NAW estimation and radar measurements integrated over the different areas previously defined, as a function of the area sizes.

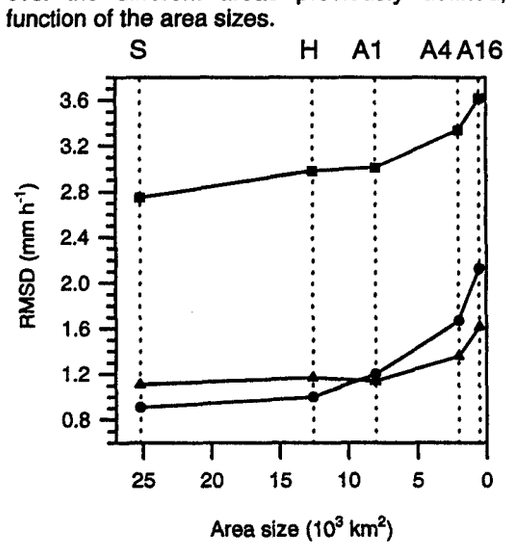

Figure 1. RMSD values between NAW and radar averaged, as a function of the validation areas, for the three cases: 92 (triangle), 93 (square) and 96 (circle).

Inspection of fig 1 shows that RMSD increases with decreasing the size of the integration areas, especially between A1 and A16. This points out that this type of IR-based estimation are of limited use for monitoring precipitation over medium size basins.

A deeper analysis of NAW performance, preliminary to the setup of a radar-based calibration technique for satellite estimates, is carried out in the next paragraphs.

NAW basically works following a 2 steps procedure: it first detects in each cloud areas with no rain, light and heavy rain, and then assigns accordingly nominal rainrate to the selected areas. There is evidence that a change of the nominal rainrate would improve the NAW performances at mid-latitude (Levizzani et al, 1990, Marroccu et al, 1993). The aim of this work is to generalize and validate this statement and delineate a strategy for an automatic reassignment of the nominal coefficients.

Assessment of quantitative precipitation estimates obtained through NAW was performed on

the study area. Analysis of results from this technique in delineating light-moderate and heavy rain areas was performed by computing a set of quantitative parameters. The three level precipitation satellite derived images (R_{10}, R_{40} and R_{50}) were compared with corresponding radar maps. The following parameters were computed (see tab 1) for each satellite rain class (C_k, where k=10, 40, 50 refers to the corresponding NAW areas): mean radar rainrate (m_k); mean radar rainfall over the wet pixels (mz_k).

TABLE 1

Year	m_{50}	m_{40}	m_{10}	mz_{50}	mz_{40}	mz_{10}
92	0.7	2.4	3.1	2.3	3.3	3.4
93	0.2	1.1	2.6	1.1	2.1	3.6
96	0.3	0.6	1.9	1.3	1.8	3.0

Table 1. Parameters for evaluation of the NAW rain classes over the study area; *m* and *mz* in mm h^{-1}.

The results show that the delineation in no-rain, light-moderate and heavy rain areas obtained using NAW is somehow confirmed by the radar measurements, although a very high variance affects these mean values. Both m and mz increase in a similar way along the different rain classes (from C_{50} to C_{10}). This suggests that the number of dry pixels decreases moving from C_{50} to C_{10}, and rainrate mean values of the wet pixels increase. Relatively high values are found for m_{50}, especially for 92 (0.7). This result indicates that a significant rainfall underestimation affects IR estimates. Nonetheless this result can be considered as acceptable, given that wet pixels inside the no-rain satellite class have lower mean values ($mz_{50} < mz_{40}, mz_{10}$).

Differences among the events are found in the numerical values of m coefficients, ranging from 1.9 (96) to 3.1 (92) for m_{10}, and from 0.6 (96) to 2.4 (92) for m_{40}. These values are also quite far from the ones assigned in the original version of NAW, and this is the main reason for the high RMSD values: in particular, the amount of precipitation to be assigned to class C_{10} is much lower in our cases, and this can be easily understood because of the different dynamics of the precipitating systems with respect to the ones observed by Negri et al (1984) for the original set up of the technique. Nevertheless, the reassignment of nominal rainrate with general applicability is thus not possible as far as these events are considered.

The ranking of m and mz values among the NAW rainfall classes is observed also reducing the target area (results not reported). This confirms that the partition scheme used by NAW to discriminate inside different cloud areas performs well, if we integrate over large areas (≈8000 km^2). In cloud areas assigned by the satellite to high rainrate, radar usually detects higher values of areal averaged precipitation.

4.SATELLITE CALIBRATION BY RADAR

We pointed out in the previous section that the partition scheme used by NAW to divide cloudy areas into three precipitation classes is still valid if we integrate precipitation over some large areas. The way we choose to calibrate NAW is therefore to work on the nominal rainrate values leaving the original partition scheme, by means of radar measurements. Previous NAW applications at mid-latitude (Levizzani et al, 1990, Marroccu et al, 1993) increased the performance by a reassignment of nominal rainrate: these authors made a-posteriori changes in rainrate values, for the particular events they studied. In this work we propose a technique to provide a continuous and automatic calibration of the NAW coefficients without a-posteriori knowledge of the ongoing event, and thus suitable for operational applications. The specific purpose of such a technique is to improve, for nowcasting purposes satellite IR-based rainfall estimation at the medium basin space scale (≈ 1000 km^2)

4.1 *The calibration technique*

We propose the RTC to improve the NAW performances over basin of some hydrological interest. The technique requires that a calibration area is defined inside the radar domain: it has to be selected where a good rainfall measure is operationally available. In this work we choose a flat area near the radar site (within 80 km) and adjusted the radar estimates by a dense raingauge network. RTC includes the following steps:

1. for each satellite slot NAW processing is carried out on the calibration area, obtaining cloud partition in three classes C_{50}, C_{40} and C_{10};
2. m_{50}, m_{40} and m_{10} are computed in the calibration area;
3. these values are used as nominal rainrates for the target area;
4. m_{50}, m_{40} and m_{10} are updated every satellite slot.

Assessment of the RTC performances is carried out by comparing calibrated satellite data and radar data on an independent validation area, which is not included in the calibration area.

4.2 *RTC application over areas of different sizes*

In figure 2 the results for RMSD are shown as a function of target areas size. The use of RTC reduces the RMSD for all the three cases, although for 92 and 96 the improvement is not marked as it is for 93. NAW and RTC show similar behavior by decreasing the target area size. The sensitivity of RTC with respect to the increase of calibration area is quite low, although a larger calibration area insures lower RMSD for the three cases. The use of a large calibration area provides lower values of the m_k coefficients, often precipitation peaks are smoothed: in the case of a simultaneous high peak over the target area the rainfall will be very likely underestimated. On the contrary, the use of a small calibration area will make m_k too sensitive to local features of the precipitation fields, that may often not be correlated with the rainfall pattern on the target area, especially if the two areas are not close to each other.

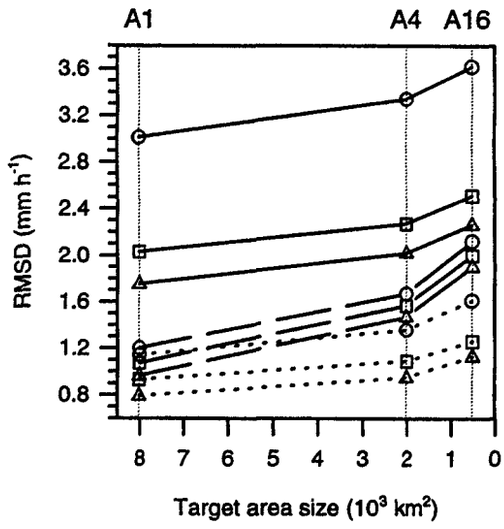

Figure 2. RMSD values between NAW and radar (circle), RTC calibrated over A1 and radar (square) and RTC calibrated over H and radar (triangle) as a function of the different target area sizes, for the three cases: 92 (dashed), 93 (solid) and 96 (dotted)

5. CONCLUSIONS

Radar rainfall maps and IR satellite rainfall estimations have been compared for three cyclonic precipitating events over Northern Italy. The comparison between radar and satellite rain maps were carried out over a study area, where radar data were corrected and adjusted by means of a dense raingauge network.

Quantitative analysis of the NAW results has been carried out to test the performances of the technique with respect to the size of the areas. The results show that discrepancies in terms of RMSD between radar and satellite even if we average rainfall over larger areas. Large overestimate in the 93 case leads to RMSD around 3 mm h^{-1}, while for 92 and 96, RMSD is around 1 mm h^{-1}, if integrated over the whole study area: for 92 this could be satisfactory, given the higher mean precipitation values, but it is not for 96 where lower rainfall was measured. These RMSD values increase as we decrease the test area, and below 2000 km^2 also for 92 case the RMSD is very high (1.7 mm h^{-1}). Based on comparison results, it is argued that the quantitative use of IR precipitation data as input to rainfall-runoff models has to be limited to large basins (some ten-thousand km^2), characterized by large response time.

A deeper analysis of the NAW precipitation patterns shows that the cloud partition scheme used by this technique performs no/low/high rain area partition in acceptable agreement with calibrated radar rainfall, considered as ground-truth. Therefore the main source of error in the NAW procedure, applied to stratified, mid-latitude cloud systems, is in the choice of numerical values for the nominal rainrates to be assigned to the different areas.

We introduced a calibration technique (RTC) that make use of radar data over a defined calibration area to compute, for every satellite slot, actual rainrates, to be used in the NAW scheme. RTC computes mean areal rainrates in the calibration area within the three satellite classes and uses these value to compute satellite derived estimates in regions where adjusted radar data are not available.

The use of this technique markedly reduced the overestimation of the NAW in the three cases. The relative error of the satellite estimates with respect to adjusted radar measurements is about 30% for the precipitation peaks: this means that via the satellite, the radar estimate can be "extended" outside the domain in order to monitor larger or remote areas and to track longer cloud systems. Better performances of the RTC are achieved when the same cloud system covers both calibration and target areas, and this is often the case if we consider large cloud bands related to autumnal cold fronts. For this reason an application of RTC to smaller scale, convective cloud systems is not envisaged.

6. REFERENCES

Andrieu, H., and J.D. Creutin, 1995: Identification of vertical profiles of radar reflectivities for hydrological applications using an inverse method. Part 1: Formulation. *J. Appl. Meteor.*, **34**, 225-239.

Bellon, A., S. Lovejoy and G.L.Austin, 1980: Combining satellite and radar data for the short-range forecasting of precipitation. *Mon. Wea. Rev.*, **108**, 1554-1566.

Hildebrand, P.H., 1978: Iterative correction for attenuation of 5 cm radar in rain. *J. Appl. Mteor.*, **17**, 508-513.

King, P.W.S, W.D.Hogg and P.A.Arkin (1995) The role of visible data in improving satellite rain-rate estimates. *J. Appl. Meteor.*, **34**, pp 1608-1621.

Levizzani, V., F.Porcú and F.Prodi, 1990: Operational rainfall estimation using METEOSAT infrared imagery: an application in Italy's Arno river basin. Its potential and drawbacks. *ESA J.*, **14**, 313-323.

Marroccu, M., A.Pompei, G.Dalu, G.L.Liberti and A.J.Negri, 1993: Precipitation estimation over Sardinia from satellite infrared data. *Int. J. Remote Sensing*, **14**, 1, 115-134.

Negri, A.J., R.F.Adler and P.J.Wetzel, 1984: Rain estimation from satellite: an examination of the Griffith-Woodley technique. *J. Climate Appl. Meteor.*, **23**, 102-116.

7.AKNOWLEDGEMENTS

This work has been funded by the Commission of the European Communities, DGXII, Environment and Climate Program (Climatology and Natural Hazards Unit Contracts ENV-CT96-0281 and ENV4-CT96-0290), and by the Italian National Research Council grant 93.02975.PF42. CSIM (Regione Veneto) provided radar data and is gratefully acknowledged.

P2.55A

RAPID COLLAPSE OF A GULF WINTER SHEMAL

Joe Parsons*
Department of Civil Aviation, Dubai UAE

1. ABSTRACT

Meteorological factors which resulted in the occurrence of sandstorms over Baluchistan and influenced the rapid collapse of a Gulf Winter Shemal are presented. These factors significantly reduced visibility over the Arabian Sea and subsequently the occurrence of extremely low overnight temperatures over the Northern United Arab Emirates (UAE).

An event on 8 December 1994 is presented with the support of primary data satellite imagery, upper air soundings and surface observations. The presence of a low level convergence field which moved into the eastern Gulf opposing the northwesterly to westerly surface flow is revealed.

Examination of historical records suggest similar occurrences to the December 1994 event. Common factors are suggested for the Meteorological mechanisms producing these events as aids to nowcasting and forecasting future occurrences using primary data imagery from Geostationary satellites and prognostic model products.

2. BACKGROUND

The Gulf Shemal is a well documented phenomena which affects the region. Its prediction and its effects *(Perrone)* on especially marine activities are of importance to operational planning. This paper identifies the rapid Shemal collapse over the lower Gulf and its replacement by cold low level air. To support this investigation MARF EUMETSAT were approached for images stored in their archives. These were manipulated to give animated loops. These images not only showed the principal changes that occurred on 8 December but that these changes were ancillary to the presence of duststorms over Baluchistan and poor visibility over the Arabian Sea induced by strong northerly winds.

There were two events of cold dry air incursion in December 1994. The principal event on 7/8 December on which this paper is based and a second event on 25/26 December. The Shemal between the 5 and 7 of December which was followed by cold low level air incursion showed identifiable changes in cloud, humidity wind speed and direction.

Corresponding Author address:
Joe Parsons Serco IAL, PO Box 1897, Dubai, UAE. Fax +9714 245461, towen@emirates.net.ae

The second event resulted in bringing about record low overnight December minimum temperatures over the northern UAE and the lowest December minimum at Dubai since records began in 1974. This event was more difficult to identify from satellite imagery but its occurrence within 3 weeks of the first event appeared to be induced by similar meteorological mechanisms.

3 .OBSERVATIONS

3.1.Surface Charts

Surface meteorological charts (not shown but refer to map 3.1.1) for the 8 December show the progressive change in wind speed and direction associated with the cold air. At 0300 UTC (0700 local time) the Shemal was well established over the lower Gulf with northwesterly winds of Force 5 to 7. At Bandar Abbas and Khassab northeasterly winds of Force 4 were reported. At 0600 UTC the observation from Bandar Abbas gave a visibility of 1000 metres in dust with a Force 4 east-northeasterly wind. At South West Fateh (SWF) the wind was northwesterly Force 4. By 0900 UTC the surface wind at South West Fateh had changed to northeasterly Force 6 and at Bandar Abbas had increased to Force 7 with a surface visibility of 1200 metres. The 1200 UTC observations identify the demarcation between the two airstreams with a northerly wind at Dubai Airport of Force 3 and a Force 4 westerly wind at the Dubai Jebel Ali Port of Force 4. The mean speed of movement of the northeasterly airstream being 10-15 knots.

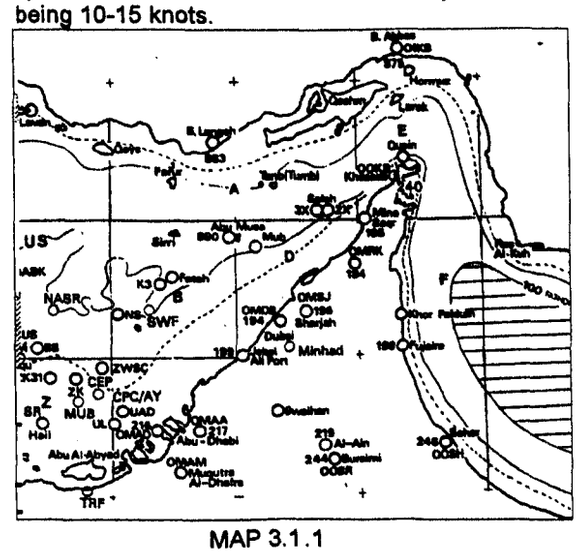

MAP 3.1.1

3.2 Surface Temperatures

The graphs of absolute maximum and minimum temperatures for Dubai and Ras Al Khaimah (OMRK) (Fig 3.2.1 and 3.2.2) show the decrease of around 10°C in day maximum temperatures between 5th and 8th December as a consequence of the Shemal with overnight minimum temperatures between 16 and 20°C. After the cold dry air incursion and Shemal collapse the absolute minimum temperatures over the Northern UAE fell to between 7°C and 13°C (After the second Shemal the overnight minimum temperatures fell from broad means of 17° C. to 7° C.. At Ras Al Khaimah and Sharjah the overnight minimum temperatures were close to 5° C.).

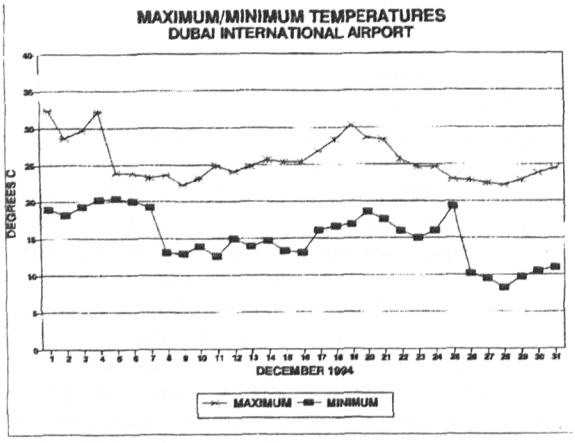

Fig 3.2.1.

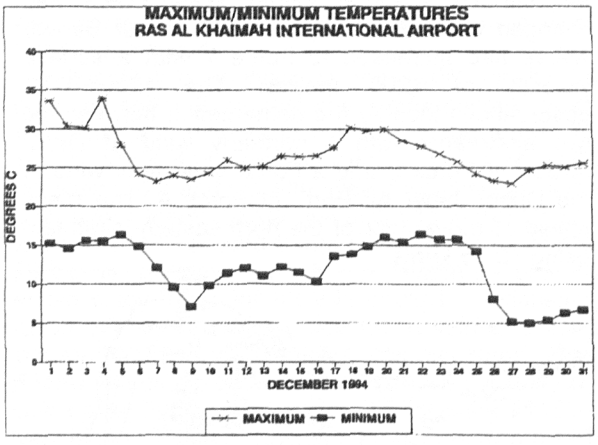

Fig 3.2.2.

3.3 Satellite Images

Meteosat satellite images from MARF EUMETSAT in the Vis (08/0600, 0900, 1200 UTC) and in the IR (08/0000 and 1200 UTC) are respectively presented. These show an area of dust/sand being advected into the Arabian sea especially noticeable in the Visible spectrum. The images in the IR/Vis indicate the progressive movement of a boundary of low cloud with dust haze which moved in a line steadily southwestwards from near Bandar Lengeh / Mina Saqr at 0000 UTC to near Qeys Island/Abu Dhabi by 1800 UTC. The low level cumuliform stratocumulus stream from the mid Gulf can be seen to retreat north and west in this sequence. Later images show that this displacement was reversed. This is supported by the observation from South West Fateh where the wind changed from northeasterly Force 2-3 to northwesterly Force 4 between 09/0300 and 09/0600 UTC.

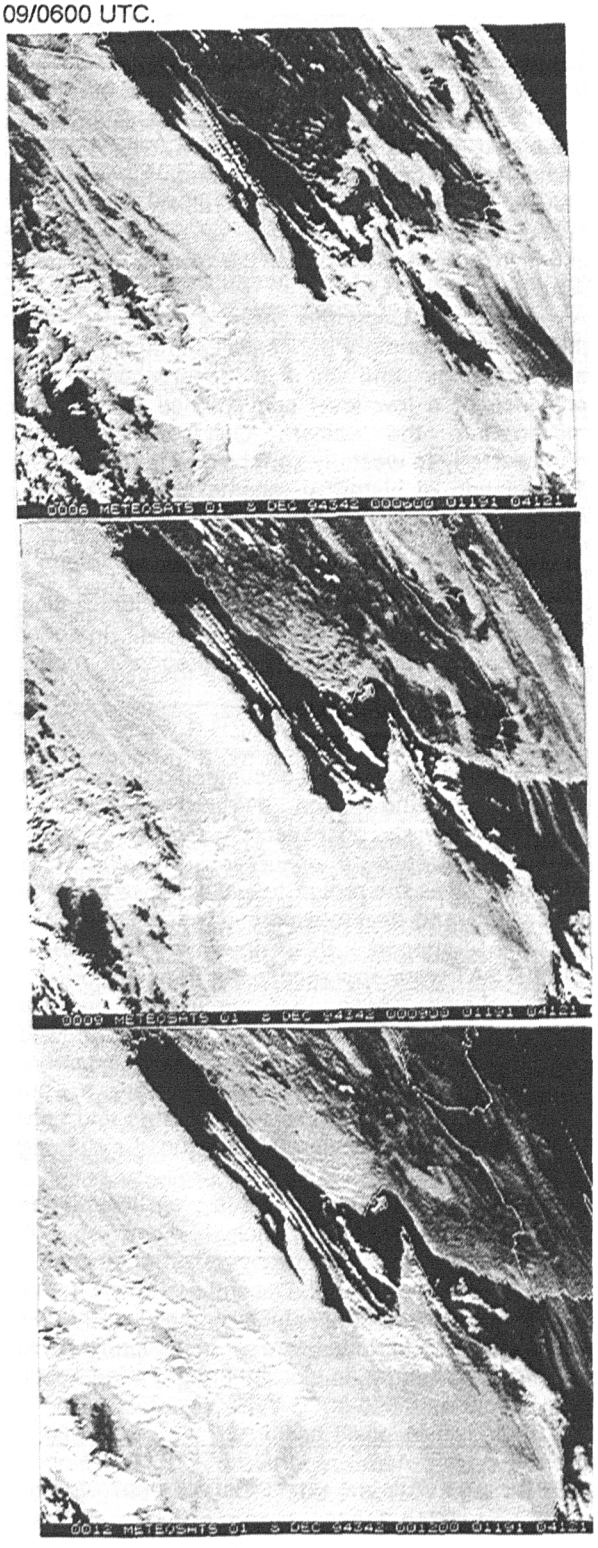

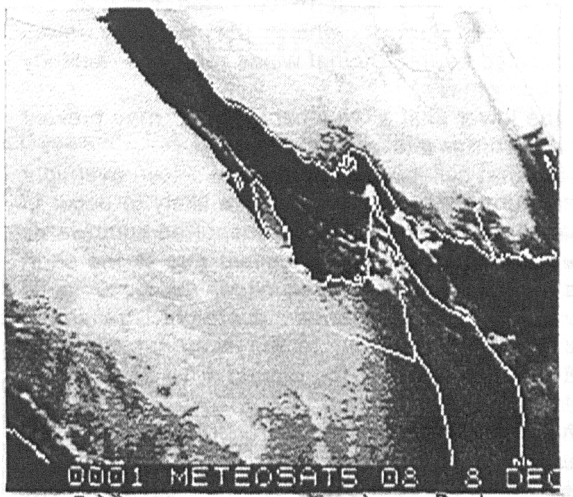

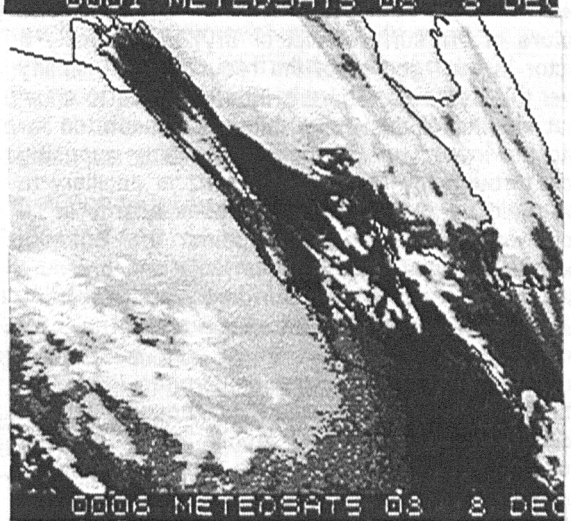

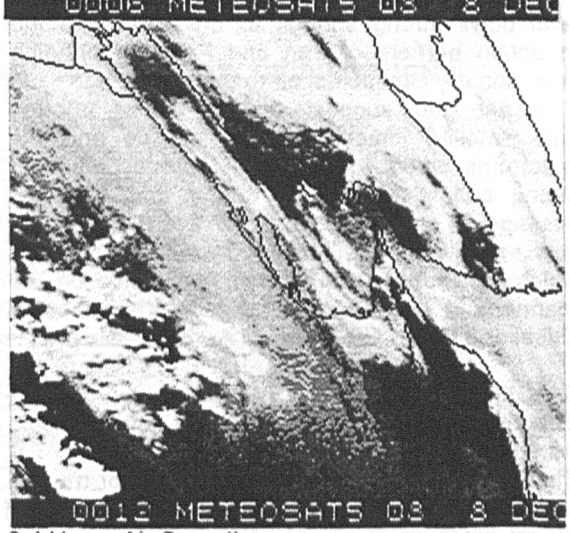

3.4 Upper Air Soundings

The upper air soundings taken at Abu Dhabi between 08/0000 UTC and 09/0000 UTC show the general cooling in the lower atmosphere below 800 HPa. resulting from the northwesterly winds in that layer of between 15 and 30 knots. Comparison of these soundings (See Low Level T/ Phi-grams) show a slightly deeper layer of cooler air between the surface and 500 feet with the low level winds having veered north to northeasterly up to 3,000 feet. Subsequently the sounding at 09/1200 UTC shows the winds having backed again to northwesterly.

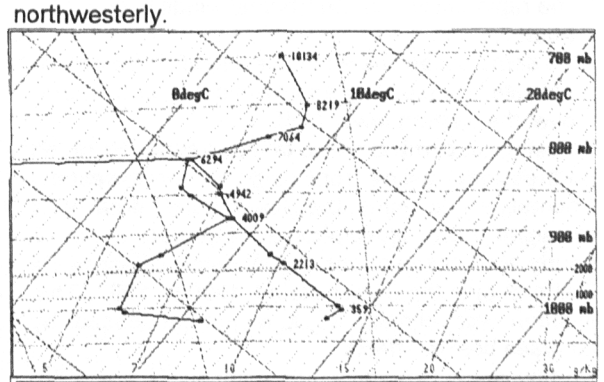

surface	500	1000	1500	2000	2500	3000	3500	4000	4500	5000 ft
29011	30520	30518		31020		31023		31020		30020kt
1018	1000	982	965	947	930	914	897	880	864	848 mb

41217 00 Z 00 DEC 94 a = Hyatt (360 ft)

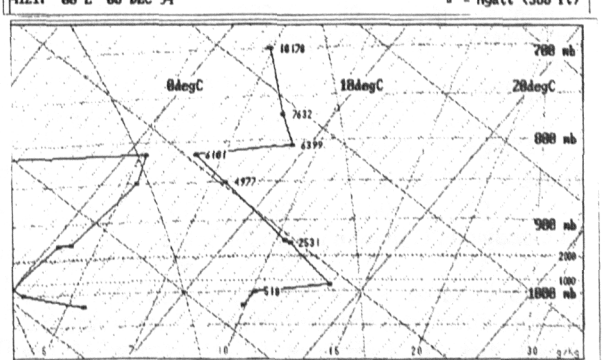

surface	500	1000	1500	2000	2500	3000	3500	4000	4500	5000 ft
00006	03516	03516		02015		00515		35015		33016kt
1019	1001	983	966	948	931	915	898	882	866	849 mb

41217 00 Z 09 DEC 94 a = Hyatt (360 ft)

Low Level T/Phi-grams

3.5 Upper Air Patterns

The upper air patterns associated with this and similar events showed a succession of troughs transiting the region from west to east at or near 30 degrees North. Examination of the troughs and their nature indicated that they became markedly confluent with diffluence in the upstream ridges. Classically these patterns producing significant pressure rises at the surface over Iran and Pakistan.

4. HISTORY AND COMMON FEATURES

Following the identification of the mechanisms for the December events the climatological records at Dubai Airport for a 20 year period were re-examined using the basic parameters of a 5° C. decrease or more in overnight minimum temperature to seek to identify similar occurrences. These events were then compared with the surface wind reports. On a number of occasions during the winter months absolute minimum temperatures were recorded following the breakdown of the Shemal. The common features prior to these occurrences were:

* Strong pressure rises over Iran.
* Strong eastnortheasterly surface winds reported at Bandar Abbas usually accompanied by dust or or sandstorms
* The rapid decline of the Shemal winds within 24 hours .
* On some occasions a tell tale line of cloud on satellite images lying approximately North South over the eastern lower Gulf.

To establish commonalties in the occurrence of the northeasterly winds replacing the northwesterly Shemal winds over the lower Gulf data was extracted from November to February from 3 hourly wind observations at SW Fateh Offshore Oil Platform over the 8 year period 1990 to 1997. This location was chosen as it is not influenced by land/sea breeze effects..

Northwesterly Shemal winds (defined as > = 20kt) which were replaced within 24 hours or less by northeasterly winds of = >05kt and = > 10kt and compared with all occasions when the northwesterly winds collapsed.

Table

	Nov	Dec	Jan	Feb	All
To NE > = 05 knots					
	05	16	11	06	38
To NE > = 10 knots					
	01	08	06	03	18
All Occasions Collapse within 24 hours.					
	17	32	29	36	114

The above table, which must be treated with some caution, due to the limited number of observations, shows that the frequency of occurrence of the collapse of northwesterly winds to northeasterly winds is 49% (33% from NE > = 05 knots and 16% from NE > = 10 knots) compared with the collapse of the Shemal winds to other wind directions.

5.. CONCLUSIONS

It is probable that the westward penetration of the cold and dry continental surface air is dependent on a number of other factors in addition to the build of pressure over Iran during and after the passage of an upper trough. The strength of the opposing Shemal flow and its decrease due to the movement and development of further disturbances upstream is also important factors. However there does appear to be ample evidence to support the establishment of a contrary easterly flow through the Straits of Hormuz following a winter Shemal on some occasions when strong northerly surface flows occur over Iran and Pakistan. On such occasions the main body of the northwesterly Shemal winds near the surface converge with the northeasterly winds over the eastern lower Gulf and are thereafter diverted southwards over the Rub Al Khali. (Empty Quarter) of Saudi Arabia.

The collapse of the Shemal and the opposing northeasterly flows such as those described may lead at the very least to confused seas at the Straits of Hormuz where the westerly swell generated by the Shemal winds meet the easterly surface winds.

In the lower Gulf a "weather window" may present itself at times after a strong Shemal.

After the collapse of a Shemal low overnight minimum temperatures are more likely to occur in the low humidity air that is transported southwards from Iran which is less modified due to the short sea track. As a consequence, there is good evidence for extreme overnight minimum temperatures to occur in the Northern Emirates after a Shemal and for ground frost to occur in inland sheltered areas.

This case study and past records suggest that duststorms and sandstorms can affect the Arabian Sea when the strong northerly flow develops. The nature of the surface (wet or dry) is obviously a factor in the degree of the reduction of visibility over this sea area. There is little evidence to show that significant dust and sand is transported far into the lower Gulf as the northeasterly opposing flow through the Straits of Hormuz is ancillary to the main event and the flow looses energy in its southwestward penetration against the Shemal. However, if upstream developments and pressure falls which cause a reduction in the northwesterly Shemal flow are coincident with a strong north or northeasterly low level flow, dust haze from southeast Iran and Pakistan could affect the UAE.

The mechanisms suggested for these events to occur are the passage of mobile, relaxing upper troughs which by their nature induce significant pressure rises over Iran and establish northerly low level flows strong enough to break through the mountain barriers of Iran and Pakistan bringing cold and dry continental air to the region.

This case study suggests that the use of primary data satellite images in both the IR and Vis spectrums when global model products predict strong builds of pressure during and after the passage of upper troughs can assist greatly in nowcasting and forecasting weather changes which can impact with some significance on the marine and other weather sensitive activities of Dubai and the Northern United Arab Emirates.

6. ACKNOWLEDGEMENTS

The author wishes to acknowledge the following with grateful thanks.
The Department of Civil Aviation Dubai for making available their comprehensive weather records.
Mr. W J H Owen Senior Met Officer Dubai
MARF EUMETSAT

7. REFERENCES

1. Winter Shemal over the Gulf - Thomas J Perrone 1979 (Naval Environmental Prediction Research Facility).

P2.59A

SATELLITE-BASED PRODUCTS FOR MONITORING OF WEATHER IN SOUTH AMERICA

J.C. Ceballos*, L.A.T. Machado**, J. Sakuragi***, G.B. França*, R. Hallak*, R.C.G. Pereira* and C.A. Nobre*
Instituto Nacional de Pesquisas Espaciais - INPE - Brazil

1. INTRODUCTION

The brazilian Center for Weather Forecasting and Climate Studies performs operational NWP, running a GCM (CPTEC/COLA). Meteorological data are presently ingested from GTS and NCEO analyses. Nevertheless, measured data are excessively sparse over Southern Hemisphere so that additional data sets are recommended in order to enhance quality of results and monitoring over South America, in particular its tropical sector.

Full resolution satellite imagery from GOES-8 and NOAA-12 and -14 is currently detected and processed by brazilian Institute for Space Research (INPE). Since January 1997, several products are developed and/or tested, in order to provide operational data for general users and for circulation models. Multispectral imagery for South America and selected subregions is currently released through internet at site http://www.cptec.inpe.br.

2. SOME PRODUCTS IN DEVELOPMENT

Wind fields between 90W and 30W, 20N and 45S are assessed for low, middle and high level cloud displacements. A procedure originally applied to Meteosat images (Sakuragi *et al.* 1996) has been adapted for GOES-8, including possibility of altitude correction for semi-transparency of high clouds. Data assimilation in CPTEC/COLA GCM run at CPTEC is being analysed, especially in which concerns the impact of these new data sets on weather forecasting.

* CPTEC-INPE, Rodovia Presidente Dutra km 40 - 12630 Cachoeira Paulista (SP) - Brazil. E-mail: juanc @cptec.inpe.br ** Centro Técnico Aeroespacial, S.J. dos Campos, SP. *** Universidade do Valo do Paraíba, S.J. dos Campos, SP. ****Universidade Federal do Rio de Janeiro, RJ.

Vertical profiles and horizontal fields of thermodynamic variables are obtained by TOVS/ITPP5 for NOAA satellites passages over the region. The analysis of profiles shows that "anchorage" to surface temperature together with regression method produces the best fit to regional soundings (Hallak and Sakuragi 1996).

Time series of sounding at Alcantara, Northeast Brazil, are being collected and compared with TOVS soundings. Preliminary results suggest that the mean deviation of temperature is about ±2K and lower for lower troposphere data. Data assimilation in CPTEC/COLA GCM model and the analysis of impact on forecast are in advance.

Sea Surface Temperature (SST) is being processed for NOAA-AVHRR (França *et al.* 1994), providing daily, weekly and monthly charts for brazilian atlantic coast released through internet. Regional calibration is in process, in collaboration with brazilian buoys programme. The use of navigation techniques is being additionally used for studies of vegetation indices, as well as for cross-comparison of cloudiness as detected by TOVS-HIRS and AVHRR pixels.

Solar radiation monitoring is supported by a model formerly developed for Meteosat imagery (Ceballos and Moura 1997; see also Ceballos *et al* in these Proceedings). The accuracy of the model is being tested by comparison with ground truth; preliminary results show satisfactory results, with standard deviations (related to ground truth) of 800 Wh/m^2 for daily irradiation and 3% of m.s.e. for monthly means.

3. RESULTS

A growing data set of full resolution files GOES-8 and NOAA TOVS and AVHRR at CPTEC/ INPE is coordinated by a Group of Meteorological Satellite Applications. This Group includes the presence of scientists of several universities and other brazilian

institutions, allowing to profit the the multiple possibilities of analysis provided by this data set.

The lines described above provide operational information (released though internet at the site http://www.cptec.inpe.br), as well as generate research lines with estrategic impact on South American region. Numerical results are illustrated in poster session.

REFERENCES

Ceballos, J.C. e G.B.A. Moura (1997). Solar radiation assessment using Meteosat 4-VIS imagery. Solar Energy 60,209-219.

França, G.B.; A.P. Cracknell (1994). Retrieval of land and sea temperature using NOAA11 AVHRR data in north-eastern Brazil. Int. J. of remote sensing 15: 1695-1712.

Hallak, R. ; Sakuragi, J. ; A previsão do CPTEC como estimativa inicial para a inferência dos perfis verticais de TOVS [The CPTEC forecasts as first guess for TOVS vertical profiles]. Anais IX Congresso Brasileiro de Meteorologia , V. 1 , pp(582) - (586) , Campos do Jordão - SP , 1996 .

Sakuragi, J. ; Machado, L. A. T. ; Sakamoto, M. S. Comparação entre o vento estimado via satélite e as radiossondagens [A comparison of wind estimation by means of satellite an radiosoundings]. , Anais IX Congresso Brasileiro de Meteorologia , V. 2 , pp(1472) -(1476) , Campos do Jordão - SP , 1996 .

P2.60B IDENTIFICATION OF WARM ADVECTION ON SATELLITE DATA

N. Fedorova *, L. Bakst

Meteorological Research Center
Federal University of Pelotas
Rio Grande do Sul, BRAZIL

ABSTRACT

The paper presents a study of the cloudiness with the typical structure: the anticyclone curvature of cloud's mass and great quantity of the clouds *Ci* on the cloudiness' boundary. The conventional and satellite data joint analysis showed: this cloudiness structure is observed in a synoptic situations with the warm air advection; this cloudiness was localized in northerly and northwesterly periphery of the anticyclone, in the trough of the cyclone or in the diffuse pressure field; generally a lines of the instability are indetified in the synoptic map. Sometimes in this cloudiness some new cyclone was formed or the old cyclone was regenerated at after 24 - 48 h. The satellite data enable to estimate the warm air advection regions some earlier, than the synoptic maps.

1. INTRODDUCTION

The thermal advection estimate the principal change of the weather, because it is the principal component in the frontogenesis, cyclogenesis and other process and also it govern by these process very often (Chakina, 1985, Bluestein, 1993). The satellite data enable to estimate the cold advection (Rao et al.1990), but any methods for the identification of the warm advection didn't exist before. The main purposes of this investigation are the identification of the warm advection, using the satellite data, and also the analysis of the synoptic process, which have the warm advection signs.

2. DATA AND METODOLOGY

The thermal IR images at intervals of 3 h. taken by GOES and METEOSAT over the South America were used for 8 months of 1995-1996.

* Corresponding author address: Natalia Fedorova
Centro de Pesquisas Meteorologicas / UFPel
Av. Ildefonso Simoes Lopes, 2751
CEP: 96060-290 Pelotas-RS
Brazil
e-mail: natalia@cpmet.ufpel.tche.br

The following conventional data have been used in the present study:

- temperature at 700 hPa level obtained from National Meteorological Center, Washington for 00 UTC one time por day;

- Surface charts at 12 h. UTC. These charts were plotted and analyzed by the Marine Ministry of Brazil.

- Surface continuous data of the temperature at the University Meteorological Station in Pelotas and in Meteorological Station in Porto Alegre.

The advection was calculated using the following equation:

$$\left(\frac{\partial T}{\partial T}\right)_{adv_g} = \frac{g}{f}\left(\frac{\partial H}{\partial x}\frac{\partial T}{\partial y} - \frac{\partial H}{\partial y}\frac{\partial T}{\partial x}\right)$$

where T - temperature at 700 hPa level, H - geopotencial at 700 hPa level.

The cloudiness in the IR images with the typical structure (the anticyclone curvature of cloud's mass and great quantity of the clouds *Ci* on the cloudiness' boundary) was observed during two-three days and was analyzed together with the conventional data and with the calculation result of the thermal advection.

3. RESULTS

The cloudiness with the typical structure (figure 1) have been associated with following synoptic process (figures 2 and 3):

- *Frontogenesis (for exempla the figures for 11 August 1995).* The typical cloudiness appeared in the diffuse pressure field near the jet stream (figure 1a.); the synoptic charts didn't show any frontal zone. The surface temperature rise at the average by 7°C/12 h.; the temperature field at 700 hPa level show the warm air and the thermal advection at the average by 2 °C/12 h. The cyclone with the frontal zones formed after 48 h. in that cloudiness.

• *Cyclogenesis (for exempla the figures for 22 September 1995).* The cloudiness with the anticyclone curvature had the biggest dimension. Two or three cloud's mass of that type were appeared. The biggest area with the warm advection (the average by 3 °C/12 h. and maximal 6 °C/12 h.) was observed in the cloud's mass area. The surface temperature increase by12°C/12 h. This cloud's mass formed in the north or north-east parts of the anticyclone, but after 24 or 48 h. the first closed isobar around a low pressure was observed on surface charts and cyclone was developed.

• *Cyclone regeneration (for exempla the figures for 22November 1995).* The typical cloudiness appeared on the cold front periphery in the thermal trough. The warm air advection was observed in this cloudiness in the frontal side of the cold or occlusion front. The warm air penetrated into the cyclone and it became deeper again. The surface temperature increase by 2-3 °C/12 h.

• *Mesoscale cloud's mass formation (for exempla the figures for 14 February 1996).* This cloudiness in the north or north-east part of the anticyclone was formed. The minimal surface temperature increase by8 °C/12 h. and the maximal surface temperature was elevated by 2 °C/12 h. The thermal advection (1 °C/12 h) was observed in small area.

The results of a verification during 5 months of 1996 shown that all cloud's mass with the structure, described above, were associated with the thermal advection. The maximal warm advection was 13.8°C/12h. and the minimal one was 2.2°C/12h.

4. CONCLUSION

The typical cloudiness structure on the thermal IR images with thermal advection was following: the anticyclone curvature of the cloud's mass and great quantity of the clouds *Ci* on the cloudiness' boundary.

The principal synoptic processes with this cloudiness type were following: frontogenesis, cyclogenesis, cyclone regeneration and mesoscale cloud's mass formation.

This cloudiness type was observed on the diffuse pressure field, in the trough and on the north or north-east periphery of the anticyclone; the synoptic charts didn't show any frontal zone.

The thermal advection decreased or finished, when the anticyclone curvature of cloud's mass reduced.

The satellite data enable to estimate the warm air advection regions some earlier, than the synoptic maps.

5. REFERENCES

Bluestein H.B., 1993: Synoptic-Dynamic Meteorology in Midlatitudes. Oxford University Press. Vol. I, II. 431, 594pp.

Chakina, N. P., 1985: The dynamics of the atmospheric fronts and cyclones. Hydrometeoisdat, Leningrad, 263 pp. (in Russian).

Rao, P.K., S.J Holmes, R.K. Anderson, J.S.Winston, P.E. Lehr, 1990: Weather Satellites: Systems, Data, and Environmental Applications. American Meteorologocal Society, Boston, 503pp.

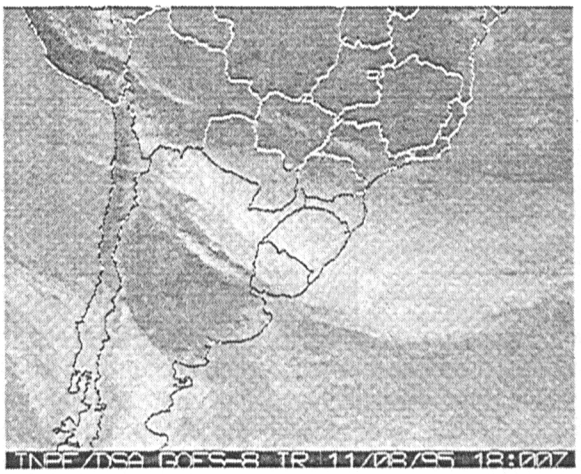

11 August 1995

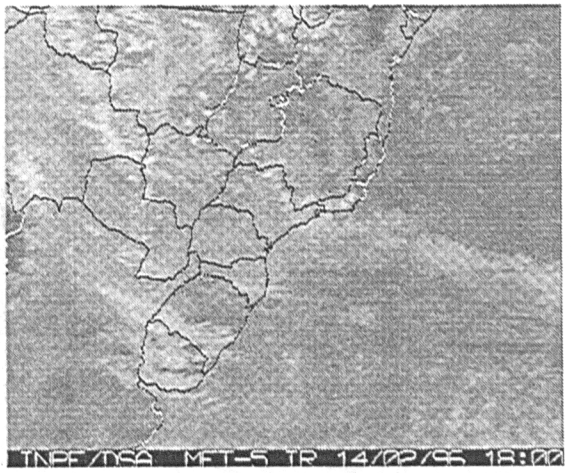

14 February 1996

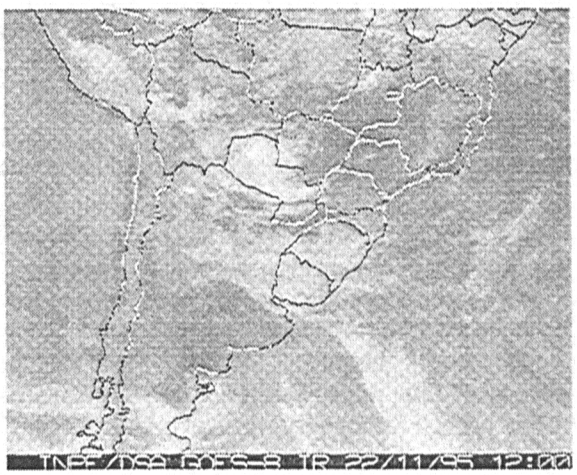

22 November 1995

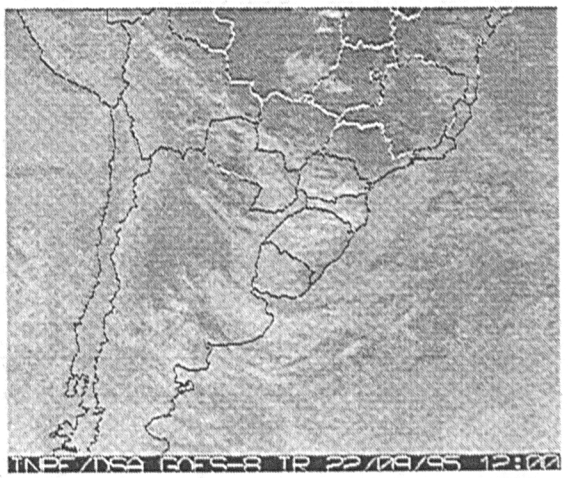

22 September 1995

Figure 1. The thermal IR images taken by GOES with four types of the warm advection.

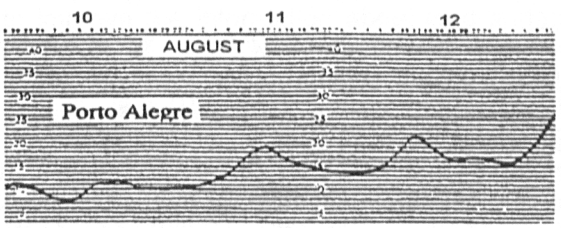

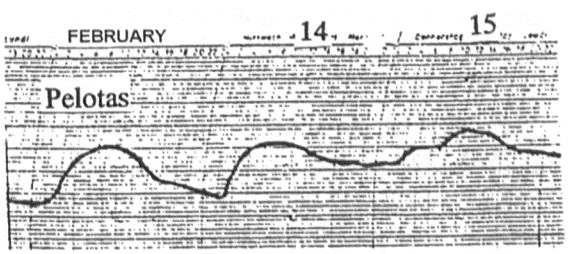

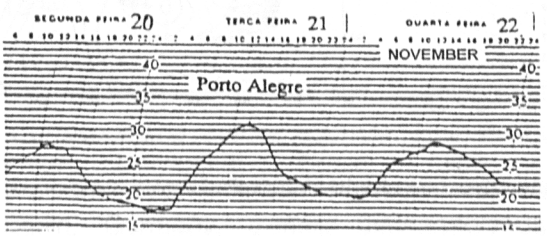

Figure 2. Surface variation of the temperature.

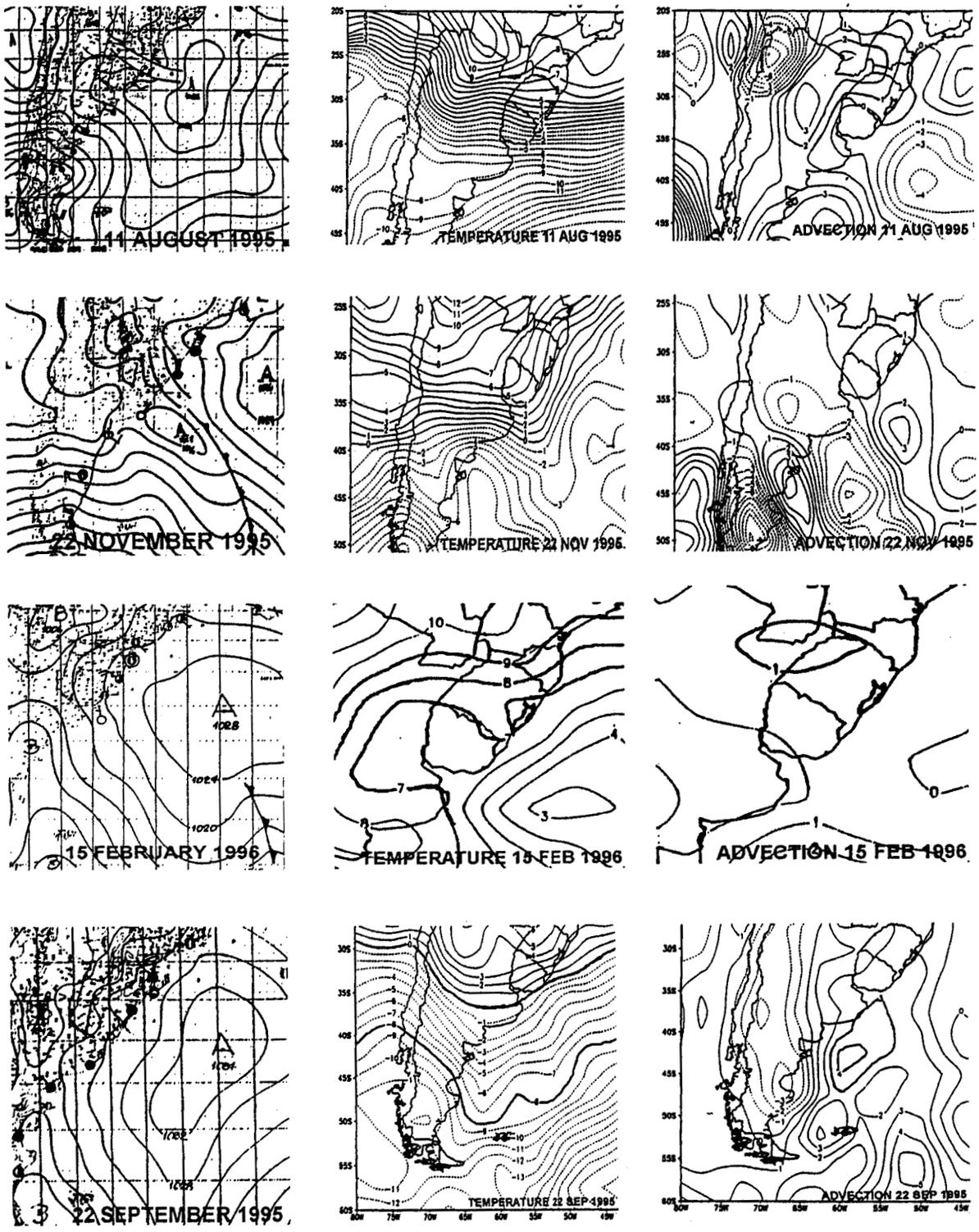

Figure 3. Surface synoptic, temperature and advection charts at 700hPa level.

P2.67A

GLOBAL LAND SURFACE PROPERTIES INFERRED FROM COMBINED PASSIVE MICROWAVE AND VISIBLE/NEAR-INFRARED SATELLITE DATA

Ralf Bennartz*
Free University of Berlin, Berlin, Germany
G.Garik Gutman,
NOAA-NESDIS/ORA, Washington D.C., USA

1 Introduction

The characterization of land surfaces by means of satellite data has been an extensive area of research in recent years (e.g. Grody, 1988; Neale et al., 1990; Tarpley, 1991, Gutman et al., 1995). Information about land surface characteristics on a global scale is typically obtained utilising data from two different spectral regions. First, from the Advanced Very High Resolution Radiometer's (AVHRR) visible and near infrared channels (Channel 1 and 2), the Normalized Difference Vegetation Index (NDVI) may be obtained. The NDVI is sensitive to photosynthetically active vegetation and varies strongly in densely vegetated areas (Choudhury and Tucker, 1987; Teng et al., 1995). Second, information from the microwave spectral range is utilised. Here, most studies focus on the Microwave Polarization Difference Index (MPDI) which is typically derived from passive microwave radiometers such as the Special Sensor Microwave/Imager (SSM/I). The MPDI is mainly influenced by surface roughness, plant water content and, if not covered by vegetation, by soil moisture. In contrast to the NDVI, the MPDI was found to be more sensitive in sparsely vegetated areas (Teng et al., 1995).
The synergy of MPDI and NDVI has been found to improve the information about land surfaces (Teng et al., 1995; van de Griend and Owe, 1994). However, these studies are restricted to special climatic regions, except Choudhury and Tucker (1987), who used global SMMR data. The global combination of MPDI derived from the Special Sensor Microwave/Imager (SSM/I) and NDVI data is addressed in this paper. The period covered in this investigation is April 1993- March 1994.

*Corresponding author address: Ralf Bennartz, Freie Universität Berlin, Institut für Weltraumwissenschaften, Fabeckstr, 69, 14195 Berlin, Germany, e-mail: bennartz@zedat.fu-berlin.de

2 Data preprocessing

2.1 NDVI-data

The AVHRR onboard the NOAA-satellites provides two channels to measure the NDVI. AVHRR channel one is located at 570-700 nm, channel two at 720-980 nm. Although other sensors with a higher spectral and spatial resolution exist, the AVHRR is the unique sensor that allows to derive global, long-term NDVI datasets. At NOAA-NESDIS, global NDVI datasets (second generation Global Vegetation Index (GVI)) have been derived for more than 11 years (Tarpley, 1991; Gutman et al., 1995).
Clouds contaminating the AVHRR's field of view have to be rejected when deriving the NDVI. This is done by deriving monthly maximum composites. This simple algorithm will provide accurate results unless persistent clouds occur. Introducing an additional AVHRR channel 4 (11μm) cloud detection threshold lead to a more accurate treatment of those persistent clouds (Gutman et al., 1994).
The measured NDVI is further dependent on the observation geometry. The effects of observation geometry on surface reflectivity can be described by means of Bi-directional Reflection Functions (BRDF). The reflection depends on the solar and satellite zenith angle and the relative azimuth between both. Since the NOAA-satellites show a significant orbit drift, artificial trends would be found, if the data were not corrected for these variations in sun-target-sensor geometry. An empirical method to account for these variations is described in Gutman (1994).

2.2 Microwave Data

The response of microwave radiation to land surface parameters can be expressed in terms of emissivity. The response of microwave measurements to vegetation is affected by several other surface parameters, like soil and plant water content, or surface type.

Since the horizontally and vertically polarized emissivities show significant differences, most previous studies focused on the use of polarization differences to obtain land surface information. The advantage using polarization differences is, that it is almost independent from the land surface temperature. The most common variable to determine land surface characteristics is the Microwave Polarization Difference Index (MPDI). MPDI has been shown to work as a separator for different land surface types (e.g.Neale et al., 1990). It is in general defined as the difference of the vertically and horizontally polarized brightness temperatures normalized by their sum.

Global remote sensing of land surface characteristics is in practice restricted to data obtained from SSM/I. This instrument has been flown continuously since August 1987 and provides an almost daily coverage of the whole earth. It provides seven channels at the four frequencies 19, 22, 37, and 85.5 GHz (both polarizations at each frequency except 22 GHz, where only the vertically polarized channel is available). MPDI is in this study derived from the 37 GHz channels of the SSM/I. Daily SSM/I data were pre-processed to allow an easy combination with the NOAA-GVI dataset. The following two steps were performed.

First, rain events and thick clouds were rejected from the dataset. The precipitation screening algorithms over land typically make use of the combination of the 85.5 GHz channels. Due to scattering of precipitation-sized ice particles the measurements at 85.5 GHz get depressed and fall below the brightness temperatures observed at 37 or 19 GHz. Thin clouds and other atmospheric constituents only have a small influence on the measurements below 50 GHz and may to first order be neglected.

In a second step, the SSM/I data were mapped to the same grid as the NOAA-GVI data and monthly mean values, standard deviations, minima, and maxima of MPDI and additionally of each SSM/I channel were calculated for the entire period.

The above outlined procedure allows to combine the NDVI dataset and the derived microwave dataset in an optimal way. Both datasets are on similar levels of data processing. The exclusion of clouds (AVHRR) and precipitation (SSM/I) leads to datasets describing the variability of land surfaces with only minor contamination due to atmospheric/angular effects.

3 Results

3.1 The impact of open water surfaces on MPDI

Due to the low spatial resolution of spaceborne passive microwave radiometers (in the order of 30 km for the SSM/I's 37 GHz channel) microwave derived land surface parameters generally represent an average of many distinct surface features. In particular, small open water surfaces within the field of view tend to decrease the horizontally polarized brightness temperatures and therefore increase the polarization differences. To further evaluate the response of MPDI to subscale water surfaces, a high resolution global land/sea mask (550m x 550m) was convolved to the resolution of the combined NDVI/MPDI dataset. The land/sea

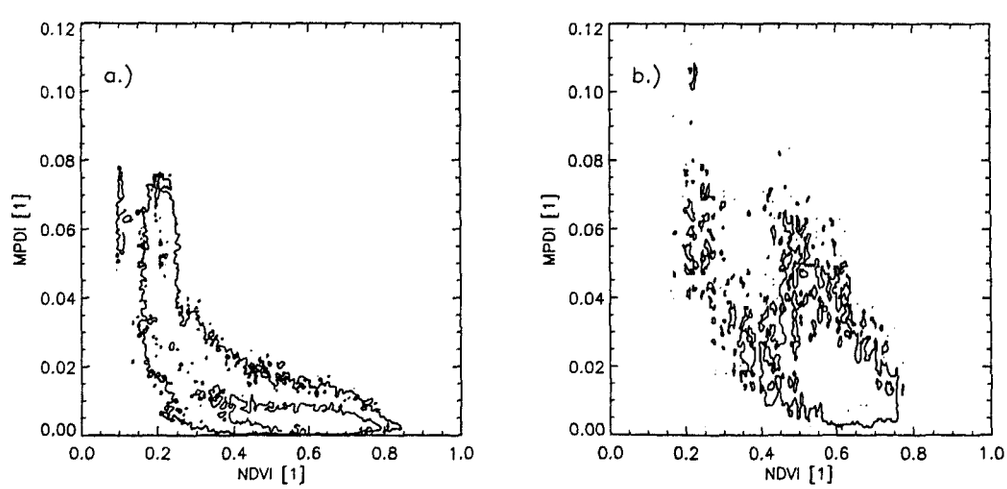

Figure 1 Two-dimensional histograms of global MPDI/NDVI data. The left histogram was calculated from land pixels alone, while the right one was taken from mixed land/water pixels.

mask includes all great river systems as well as major lakes. However, small rivers and lakes are not included. Further, the area covered by lakes and rivers varies strongly in time, so the land/sea mask only allows to derive a crude estimate of land/water distribution in July 1993. After convolution the value of each pixel was the relative amount of open water within the $0.3^{\circ}x0.3^{\circ}$ area.

Figure 2 shows two-dimensional histograms of the data-distribution of NDVI and MPDI for water-free (a.) pixels and pixels with sub-scale water surfaces between 50% and 99%. (with regard to the convolved land/sea mask). The histogram for the water-free pixels shows an inverse relationship between NDVI and MPDI (as e.g. reported by Choudhury and Tucker, 1987). The mixed land/water pixels (b.) show a more linear relation between MPDI and NDVI. The combination of MPDI > 0.02 and NDVI > 0.3 does only appear for the mixed pixels. Based on this preliminary investigations, it appears to be possible to distinguish land pixels from mixed pixels and to use combined MPDI data and NDVI data e. g. for flood detection on a scale smaller than the scale of the SSM/I footprints.

4 Literature

Bauer, P., and N.C.Grody, 1995: The potential of combining SSM/I and SSM/T2 measurements to improve the identification of snowcover and precipitation. IEEE Trans.Geosci.Remote Sensing, 33, No.2, 252- 261.

Bauer, P., and P. Schluessel, 1993: Rainfall, Total Water, Ice Water and Water Vapour over Sea from Polarized Microwave Simulations and SSM/I Data, J.Geophys.Res., 98, 2757-2765.

Choudhury, B.J., and C.J.Tucker 1987: Monitoring global vegetation using Nimbus-7 37 GHz data, some empirical relations. Int.J.Rem.Sens., 8, No.3, 1085-1090.

Grody N.C., 1988: Surface Identification using satellite microwave radiometers. IEEE Trans.Geosci.Remote Sensing, 26, No.6, 850-859.

Gutman, G.G., 1994 : Global data on land surface parameters from NOAA AVHRR for use in numerical climate models. J.Climate, 7, 669-680.

Gutman, G.G., A.M.Ignatov, and S.Olson, 1994: : Towards better quality of AVHRR composite images over land: Reduction of cloud contamination. Rem. Sens.Env., 50, 134-148.

Gutman, G.G., D.Tarpley, A.M.Ignatov, and S.Olson, 1995 : The enhanced NOAA global land data set from the Advanced Very High Resolution Radiometer, Bul.Am.Met.Soc., 76, No.7, 1141-1156.

Neale, C.M.U., J.Marshall, MacFarland, and K.Chang, 1990: Land-Surface-Type Classification using Microwave Brightness Temperatures from the Special Sensor Microwave/Imager. IEEE Trans. Geosci. Rem.Sens., 28, No.5, 829-837.

Tarpley, J.D., 1991: The NOAA Global Vegetation Index product- A review. Palaeogeogr., Paleoclimatol., Paleoecol. (Global and Planetary Change Session)., 90, 189-194.

Teng, W.L., P.C. Doraiswamy, and, J.R.Wang, 1995: Temporal variations of the microwave polarization difference index and its relationship to the normalized difference vegetation index in a densely cropped area. Photogrammetric Engeneering, 61, No.8, 1033-1039.

van de Griend, A.A., and Owe, M., 1993: Determination of microwave vegetation optical depth and single scattering albedo from large scale soil moisture and Nimbus/SMMR satellite observations. Int.J.Rem.Sens., 14, No.10, 1875-1886.

van de Griend, A.A., and Owe, M., 1994: Microwave vegetation optical depth and inverse modelling of soil emissivity using Nimbus/SMMR satellite observations. Meteorol.Atmos.Phys. , 54, 225-239

LAND SURFACE TEMPERATURES AND LEAF AREA INDEX DERIVED FROM AVHRR/NDVI TIME SERIES

P2.69A

P. Tungalagsaikhan*, Stefan W. Dech, Robert E. Meisner
Deutsches Zentrum für Luft- und Raumfahrt (DLR), Oberpfaffenhofen, Germany
Christina Preusser
Katholische Universität Eichstätt, Eichstätt, Germany

1. INTRODUCTION

In order to analyze the interactions between land and atmosphere, accurate knowledge of parameters describing the land surface, including its vegetation cover, is required. Important climate parameters such as Land Surface Temperature (LST) and Leaf Area Index (LAI) are widely requested as inputs for simulation models of energy fluxes, water balance dynamics and net primary production. This information can be derived from AVHRR data, but is not regularly available so far. The overall goal of this work is therefore not the development of new methods to derive these quantities, but to define algorithms to operationally generate European maps containing LST and LAI information on a daily basis for further application and analysis.

In this study, a time series of Normalized Difference Vegetation Index (NDVI) value-adding products operationally generated at DLR's German Remote Sensing Data Center (DFD) serves as input data base. Providing information on photosynthetic activity, density and phenological status of the vegetation canopy, the NDVI offers an effective means of estimating LAI and surface emissivity, which are strongly related to land cover properties. LST can then be derived from thermal infrared channels and surface emissivity. Operational derivation of LAI is based on a procedure developed by Sellers (1996) [6], whereas LST is calculated according to a split window technique of Becker (1990) [1]. Data processing steps for operational usage are shown, first results are presented and validations are discussed.

2. DATA BASE

The German Remote Sensing Data Center (DFD) of the German Aerospace Center (DLR) has been operationally generating AVHRR based "value added" data products such as Sea Surface Temperatures (SST) and NDVI, since March 1993.

The AVHRR input data is calibrated, navigated and cloud screened. NDVI is then calculated from channels 1 and 2 albedo values. At the moment no corrections are performed on the NDVI data, but an operational atmospheric corrections scheme using ERS-2 GOME and NOAA/TOVS data for ozone and water vapor correction is in preparation. For operational derivation of LAI and LST, an NDVI 10 day rolling MVC serves as input. Additionally, channel 4 and 5 IR data are required for LST calculation.

Another important input parameter for LAI and LST derivation is information on land cover properties. It is provided by a land cover classification over central Europe based on modeled NDVI time series and NDVI monthly composites, which was generated within a master thesis by N.-B. Hermann, University of Mainz.

3. OPERATIONAL DERIVATION OF LAI

A simple empirical procedure suitable for large scale LAI derivation developed by Sellers [6] provides the algorithms for operational processing. It allows estimation of LAI from NDVI derived Fraction of Absorbed Photosynthetically Active Radiation (FAPAR).

3.1 Data preprocessing

The LAI calculation procedure requires the determination of statistical quantities. In order to enable later operational processing, these quantities as well as FAPAR and LAI are calculated using an NDVI time series from 1996 covering the area of Germany with a spatial resolution of 1 km and the above mentioned land cover classification.

Since no corrections had been performed, the NDVI data must be improved. Thus, daily NDVI products are synthesized to nine and ten day maximum value composites considering similar satellite viewing angle conditions [3]. In order to avoid negative influences caused by variations in atmospheric conditions and cloud contamination, a spectral analysis method is applied to reduce such effects. From the resulting data set in connection with the land cover classification, 98 and 2 percentiles of NDVI distributions per vegetation class, representing fully active, dense vegetation and no vegetation, respectively, are computed. These statistical quantities are necessary for the derivation of a solar zenith angle correction [6], accounting for varying illumination geometry throughout the year. The effects of the corrections are illustrated in Fig. 1.

* Corresponding author address: P. Tungalagsaikhan
Deutsches Zentrum für Luft-und Raumfahrt e.V. (DLR)
Deutsches Fernerkundungsdatenzentrum (DFD)
82234 Wessling, Germany, email: tunga@dfd.dlr.de

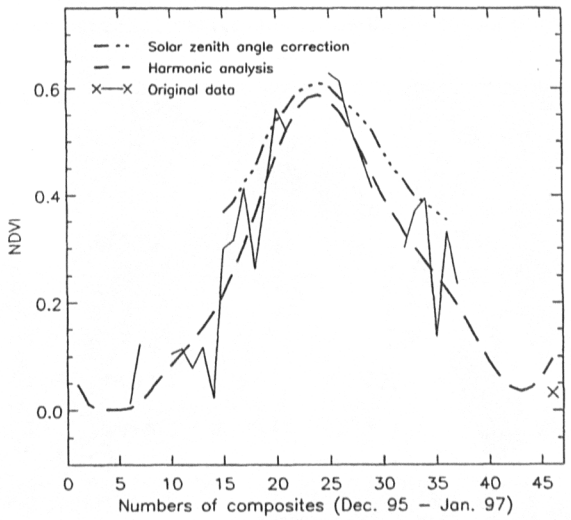

Fig. 1: Effects of spectral analysis and solar zenith angle correction of NDVI data

3.2 Processing scheme

The corrected NDVI composites representing the growing period of 1996 are used to estimate FAPAR. The formerly determined $NDVI_{98\%}$ and $NDVI_{2\%}$ values can be used for estimating FAPAR from NDVI [6]. For the determination of LAI from FAPAR a differentiation between vegetation morphologies is essential. Homogenous vegetation canopies like pastures and deciduous forests are best represented by an exponential equation [4], whereas for clustered vegetation, for example coniferous forests, a linear relationship can be applied [2]. By introducing the parameter F_{cl} (fraction of clumped vegetation in the grid) these differences in vegetation morphology are accounted for. Another important factor is $LAI_{max,i}$ the maximum leaf area index for vegetation type i as obtained from a survey of ecological literature. The equation for estimating LAI from FAPAR [6] is given by

$$LAI = (1 - Fcl)LA\,\mathrm{Im}\,ax,i \frac{\log(1 - FAPAR)}{\log(1 - FAPAR\ \max)} + Fcl \frac{LA\,\mathrm{Im}\,ax,iFAPAR}{fAPAR\ \max} \quad (1)$$

where

$LAI_{max,i}$ = Maximum LAI for vegetation type i

F_{cl} = Fraction of clumped vegetation in one pixel

In operational use the values determined from the exemplary calculation of LAI are applied to an NDVI 10-day rolling composite instead of the corrected time series.

3.3 Results and validation

The spatial distribution of LAI around the beginning of June 1996 is illustrated in *Fig. 2*. Maximum LAI (up to 8) can be observed for coniferous forests. Deciduous forests reach more moderate values of about 3 to 4, not having fully developed their foliage yet. Pastures and grasslands as well as agricultural areas tend to have the lowest LAI due to their relatively low canopy height compared to forests. Mean LAI values for both vegetation classes range from 1.0 to 2.0. Urban areas and bare soil are by definition set to zero LAI.

According to this visual approach the LAI calculation algorithm seems to produce reasonable estimates. The relations between different vegetation classes correspond to the $LAI_{max,i}$ values used, which indicates the need for accurate information on that item.

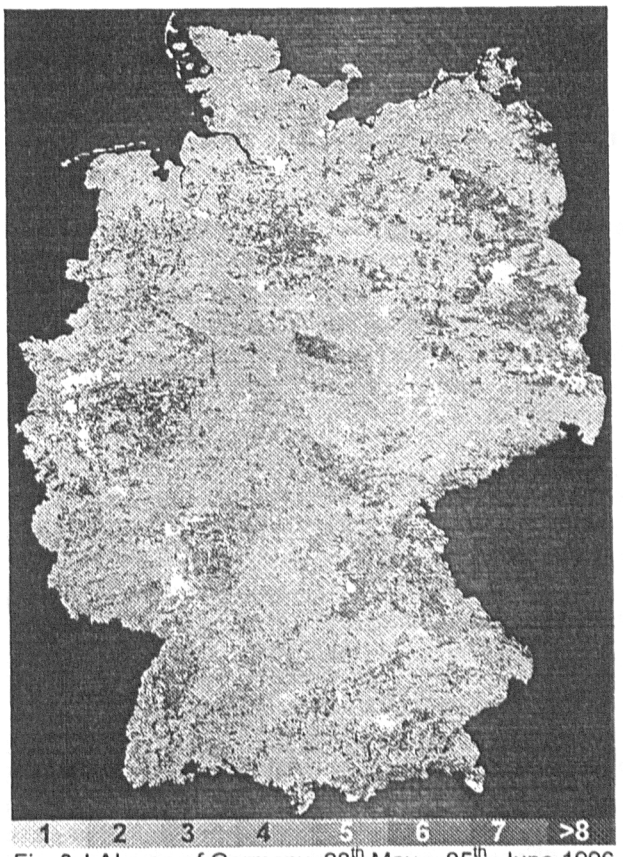

Fig. 2: LAI map of Germany, 28th.May – 05th. June 1996. Cities and nonvegetated areas are white, and lakes are black.

Therefore, the derivation of the statistical LAI percentiles is highly determined by the quality of the land cover classification. In general, a quantitative validation of the 1 km LAI products is hardly possible, though, because extensive ground measurements are lacking. However, a first validation with data from the Deutscher Wetterdienst (DWD) at a test site in Eastern

Germany showed reasonable results with maximum differences of 0.5.

4. OPERATIONAL DERIVATION OF LST

4.1 Processing scheme

In order to define an operational LST pathfinder product, different existing LST algorithms based on split-window techniques were compared [5]. The Becker and Li model [1] was found to be the most suitable for LST generation over Europe:

$$T_{Becker\&Li} = 1.274 + \frac{T_4 + T_5}{2}[1 + 0.15616\frac{1-\varepsilon}{\varepsilon} - 0.482\frac{\Delta\varepsilon}{\varepsilon^2}] \quad (2)$$
$$+ \frac{T_4 - T_5}{2}[6.26 + 3.98\frac{1-\varepsilon}{\varepsilon} + 38.33\frac{\Delta\varepsilon}{\varepsilon^2}]$$

where

$$\varepsilon = \frac{\varepsilon_4 + \varepsilon_5}{2} \qquad \Delta\varepsilon = \varepsilon_4 - \varepsilon_5 \quad (3)$$

For estimating the surface emissivity (ε) the relationship given by

$$\varepsilon_4 = 1.0094 + 0.047 \ln(NDVI)$$
$$\Delta\varepsilon = (\varepsilon_4 - \varepsilon_5) = 0.01 \quad (4)$$

is applied [7]. A "rolling" NDVI maximum value composite over the last 10 days is used as input data. In case of missing data in this rolling composite, a constant emissivity value derived from the land cover classification is set.

4.2 Results and validation

An LST composite from three consecutive afternoon overpasses is illustrated in *Fig. 3*. The LST varies from 8 °C up to more than 32 °C (Northern Africa). Lakes (in black) and clouds (in white) are masked. Snow in the high mountains (in white) are masked, too.

A series of tests under "same atmospheric conditions" were made to validate the AVHRR-derived LST by comparison with ground temperatures at 5 cm and 2 m height, and at 5 cm depth, measured at more than 120 meteorological stations randomly distributed over Germany. *Fig. 4* shows typical temperature curves in comparison with AVHRR-based LST for 5th June 1996. Generally, it was observed that the LST calculated with all the algorithms used here did not differ much.

All models showed a tendency to "overestimate" the LST from morning and noon passages during summer and spring, and "underestimate" morning values during winter. This effect can be explained by different processes of the "skin", the subterranean, and air temperatures associated to the solar irradiation, the penetration of the thermal energy, and air resistance.

Fig. 3: Southern Part from first LST map, European coverage, 20th. February 1998.
Clouds and snow are white, and lakes are black.

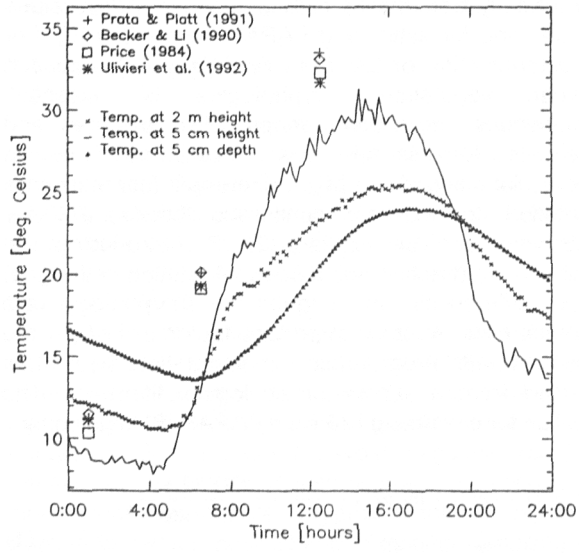

Fig. 4: Comparison between the satellite-derived LST (01:01, 06:32 and 12:32 UTC) and ground temperatures (51° 15′ N / 7° 39′ E).

The dynamics of temperature dependency on height could also be confirmed by the results of a field experiment in Sinai, Egypt (*Fig. 5*), where the calculated LST were very well coincident with measurements.

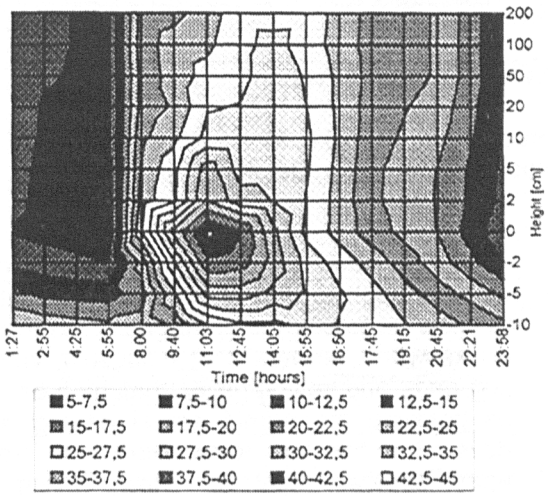

Fig. 5: Vertical profiles of temperatures (time axis is not equidistant), 18 October 1995, Egypt (29°37'15"N / 35°28'40" E).

An additional error source is the difference between spatially integrated satellite pixel measurements and exactly registered station data. Despite the above mentioned considerations, a high correlation between in situ measurements and calculated LST was observed. Such a plot is presented in *Fig. 6*. The calculated LST are clearly higher than air temperatures at midday. The linear fit curve is well acceptable with a root mean square deviation (RMSD) of 2.89 °C.

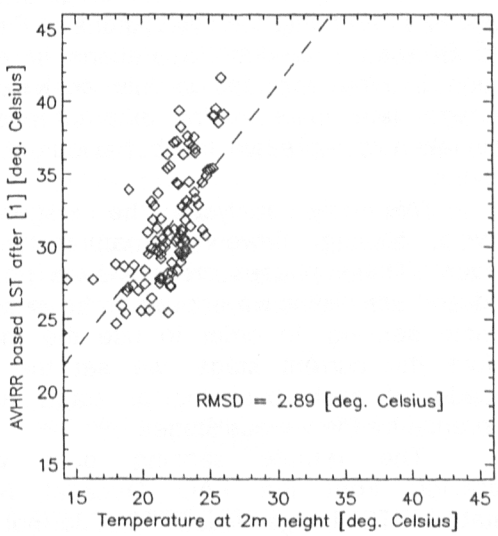

Fig. 6: Scatterplot of the temperature at 2 m height with AVHRR derived LST ,05 June 1996, 12:32 UTC.

5. DATA ACCESS

Since March 1998, LST products have been operationally generated on a daily basis and are accessible through DFD's electronic interface ISIS (http://isis.dlr.de). An operational LAI product is in preparation and will be available by the end of this year.

ACKNOWLEDGEMENTS

The authors express their appreciation to Andreas Lippert from the University Munich, and DWD for providing ground temperature data. Thanks also to M. Bittner, T. Erbertseder, N. Hermann and T. Ruppert for their valuable contributions to this paper. Thanks also to R. Steinbrecher, T. Schoenemeyer and G. Smiatek from IfU in Garmisch for the fruitful cooperation and many discussions. Thanks also to Susan Giegerich for her help with English expression.

REFERENCES

[1] Becker, F. and Z.L. Li, 1990: Towards a local split window method over land surface. *Int. J. Rem. Sens.*, **3**, 369-393.

[2] Huemmrich, K.F. and S.N. Goward, 1992: Spectral vegetation indexes and the remote sensing of biophysical parameters *Proc. Int. Geosci. Remote Sens. Symp. (IGARSS)*, Houston , TX, Institute of Electrical and Electronics Engineers, 1017 – 1019.

[3] Gutman, G.G., 1991: Vegetation indices from AVHRR: An update and future prospects *Remote Sens. Environ.*, **35**, 121-136.

[4] Monteith, J.L. and M.H. Unsworth, 1990: Principles of environmental physics

[5] Prata, A.J., Caselles, V., Coill, C.,Sobrino, J.A. and Ottle C., 1995: Thermal remote sensing of land surface temperature from satellites: Current status and future prospects *Remote Sens. Reviews*, **12**, 175-224.

[6] Sellers, P.J., et al., 1996: A revised land surface parameterization (SiB2) for atmospheric GCM's. Part II: The generation of global fields of terrestrial biophysical parameters from satellite data *J. Climate*, **9**, 706-737.

[7] Van de Griend, A.A. and M. Owe, 1993: On the relationship between thermal emissivity and the normalized difference vegetation index for natural surfaces *Int. J. Rem. Sens.*, **14**, 1119-1137.

P2.75A

MONTORING PHENOLOGICAL STAGES OF CULTIVATED CROPS BY REMOTE SENSING IN MALI

DIALLO Mamadou Adama* and BERNARD Tychon*

Direction Nationale de la Météorologie, Bamako, Mali
Fondation Universitaire Luxembourgeoise, Arlon, Belgium

1. INTRODUCTION

Meteorological conditions constitute dominating factors in crops production in Sahel, particularly because of droughts which characterize the climate at those latitudes.

Estimation of optimal sowing date and prediction of phenological stages are essential data for agricultural campain monitoring.

The main objective of this work is to develop a methodology to monitor, from space, the conditions favorable to sowing and phenological stages of cultivated plants in a given area using normalized difference vegetation index data (NDVI) from the Advanced Very High Resolution Radiometer (AVHRR) of the U.S. National Oceanic Atmospheric Administration (NOAA) satellite.

2. METHODOLOGY

We investigated millet and sorghum growing in the regions of Segou (sahelien zone) and Sikasso (soudanian zone) in Mali (West Africa).

The study is based on a reference agricultural season supposed to be normal (1995). The relationships between remote and field data are fixed and calibrated for the year 1995. 1996, the following year serve then as a validation period. In a later research, a new reference year will be established by averaging several years.

The methodology is centred on the working hypothesis and preliminary treatments allowing a modelisation of phenological stages. First of all, we considered that millet and sorghum plants mime natural vegetation, that is to say millet and sorghum start growing when natural vegetation is regaining strength ; its various phenological stages last all over the vegetation period. Finally the harvest period corresponds to the senescence period.

* *Orresponding authors adresses:* DIALLO M. A. Direct. Nat. Météorologie, BP 237 Bamako Mali; fax: (223) 22.21.01. TYCHON B. FUL, 185 avenue de longwy;Arlon Belgique;e-mail:tychon@ful.ac.be

In other words, these plants cycle is close enough to that of the natural vegetation to allow us to study them together. In this part of the word, farmers start cultivation with the first rains and sow varieties matching as mush as possible the humid period ending a few days after the last rains. Moreover, from a morphological point of view, millet and sorghum heights range from values close to natural herbaceous and bushes vegetation.

At last, at the national level, the millet and sorghum cultivation area is increasing from year to year, say an increase of 41% from 1991 to 1994.

3. ANALYSIS

We used the field data from the form 01 (Agrhymet Program) which contains decadal observations of the phenological stages of cultivated plants in control parcels spread all over Mali (date of sowing and phenological stages of millet and sorghum). All stations surrounding the two regions of Segou and Sikasso (around 25 stations in each region). Were included in this analysis an average date value for the different phases was taken to represent the behaviour of two regions.

We only analysed the stages of sowing, tillering, flowering, maturation and harvest. These phases are observed on the field and are distinctive enough to be seen by remote sensing. In order to use the model before the current stage, we set the first decade of each phenological stage as a reference for the various stages.

The remote sensing data were extracted from the FAO Decadal NDVI database. The image file is in "IDA" format and the file name respect FAO conventions (ex: dv95083.af). The pixel dimensions are 7.6X7.6 km. The NDVI is formulated like that: NDVI=(IR-R)/(IR+R) where IR and R are respectively infrared and red radiations.

A one degree size square centred on the two main stations was used to calculate a average NDVI value during the decades of the growing period.

Three remote sensing indicators were proposed to be compared with field data:

- the average decadal value of NDVI (figure 1)
- the cumulated decadal value of NDVI starting the first decade of May (figure 2)
- the smoothed tangent of average decadal value of NDVI.
- the smoothed tangent of average decadal value of NDVI.

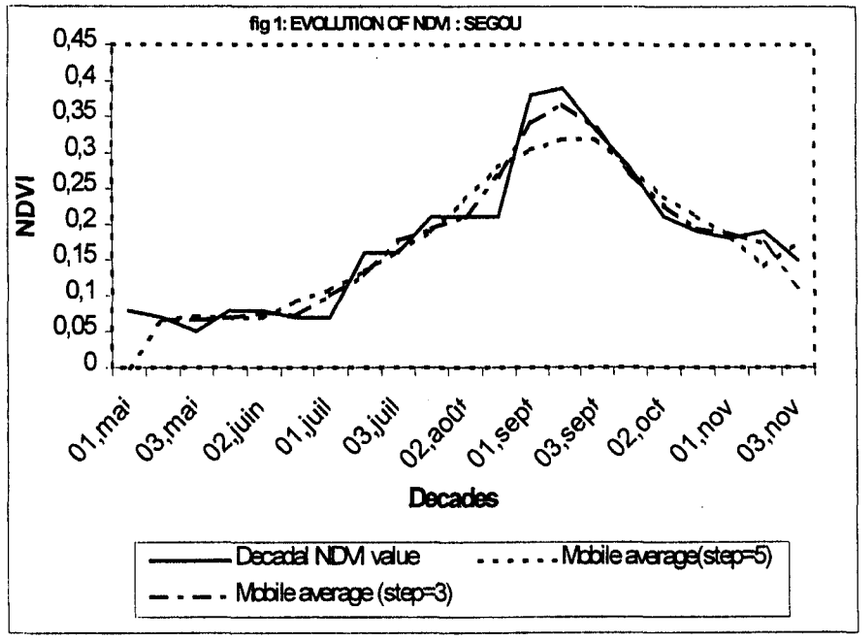

4. RESULTS

The first results of this approach to estimate plants growing by the normalized difference index show some interesting characteristics:

As mentioned by JUSTICE and AL, 1985, the index value 0.05 is confirmed to be threshold of minimum vegetation presence ; threshold 0.07 for sowing and zero tangent at flowering stage are useful criteria in the Segou's region (table 1).

The examination of there indicators or parameters (table 1) : the decadal NDVI, cumulation NDVT and tangent show that some indicators are more sensitive than others according to the stages. This means an interest for combination of several indicators in the monitoring of vegetation.

The cumulated value of NDVI seems to be very promising.

The correlation coefficient of the linear regression between this parameter and phenological stages is 0.996 in Segou's region and 0.997 in Sikasso's region (figures 2 & 3).

The degree of uncertainty between the model set up and calibrated from 1995 data and the real observed values in 1996 lies between 0 and 16% according to the various stages in the two regions, excepted for sowing stage at Sikasso, where it reaches 31.8 %.

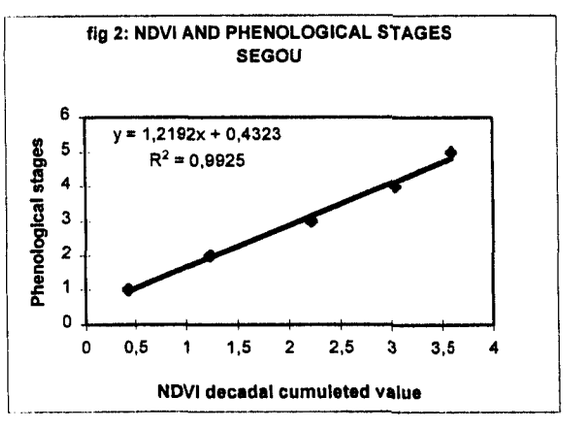

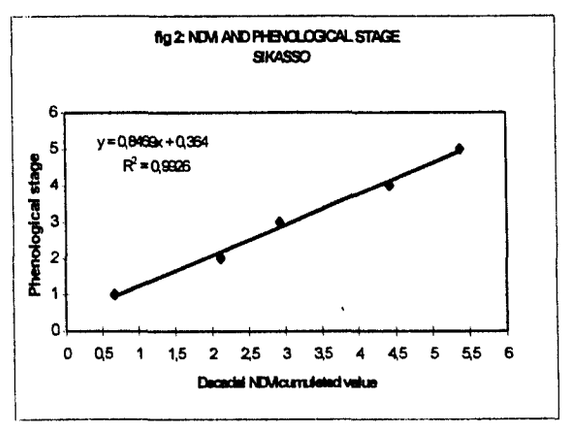

Table 1: comparaison of 1995 data to1996 data

	SEGOU					
	Decadal NDVI	Cumulated decadal NDVI			Tangent	
	$\frac{val96 - val95}{val_{max}95 - val_{min}95}(\%)$	Modèle	Val.96	$\frac{val96 - val95}{val95}(\%$	Val.95	Val.96
Sowing	18	0.47	0.41	-4.7	0.01	0.02
Tillering	-3	1.29	1.29	4	0.04	0.05
Flowering	0	2.11	2.33	5	0.00	0.02
Maturation	50	2.93	3.49	15	-0.04	-0.03
harvest	12	3.75	4.37	21	-0.04	-0.03

5. CONCLUSION

This result is a first exploratory contribution toward the evaluation of the optimum date of sowing and phenological stages of millet and sorghum through the use of satellite informations.

We could retain the index value 0.07 as the threshold of decadal NDVI for starting in Segou region and concerning the tangent zero at flowering, the value 0.04 for tillering and – 0.04 for maturation. The equation which result from linear regression between X (cumulated decadal value of NDVI) and Y (phenological stages) are:

SEGOU: Y = 1.21X+0.43

SIKASSO: Y = 0.85X+0.36

Ideally, it would be convenient to:

- define the cultivated area for millet and sorghum in each zone and calculate the NDVI value for those same cultivated area,
- work on a long period not less than 10 years,
- make sure available field data are reliable and accurate.

The study must be improved and completed by a more elaborated analysis applying others approch and statistics methods on time series data (field and satellite) for several years. We intend to implement an operational system adapted to the whole sahelian area.

REFERENCE

-ACHEHBOUNI J.R., HUETE A.R.,KERR Y.H. and SOROOSHLAN S. (1994). A Modified Soil Adjusted Vegetation Index. Remote Sens. Environ, 48, pp. 119-126.

- A.S. and VALENZUELA C.R. (1991). Remote Sensing and Geographical Information Systems for Ressource Manegement in Developing Countries. ECSE, EEC, EAEC.

-HIERNAUX P.H.Y. et JUSTICE C.O. (1986) Suivi du développement végétal au cours de l'été 1984 dans le sahel malien. Int. J. Remonte Sensing.

-JUSTICO. And HIERNAUX P.H.Y. (1986) Monitoring the grasslands of the Sahel using NOAA AVHRR data. Niger 1983, Int Journal remote Sensing. Vol. 7, n°11, pp. 1475-1497.

-MILLINGTON A.C., WELLENS J., SETTLE J.J. and SAUL R.J. (1991). Explaining and montoring land cover dynamics in drylands using multi-temoral analysis of NOOA AVHRR imagery. Remote Sensing for Regioal to Global Seales.

-VAKSMAN M. et TRAORE S. (1991) Adéquation entre risque climatique et choix variétal du mil. Cas de la zone de Bankass au Mali. Communication présentée au Séminaire International, Bamako, 9-13 décembre 1991 sur le bilan Hydrique Agricole et Secheresses en Afrique Tropicale.

P2.82B

LAND SURFACE RESPONSE TO NON-PERIODIC HYDROMETEOROLOGICAL EVENTS APPLYING WAVELET TRANSFORM ANALYSIS TO AVHRR AND SMMR TIME SERIES DATA

Saturnino Leguizamón *, Universidad de Mendoza, Mendoza, Argentina
Massimo Menenti, SC-DLO, Wageningen, The Netherlands
Bhaskar Choudhury, NASA/GSFC, Greenbelt, MD, USA

1. INTRODUCTION

For many years Menenti et al. (1991, 1993) have been carrying out a study of natural and cultivated areas in South America and Africa using the information provided by Fourier analysis of Normalized Difference Vegetation Index (NDVI) time series

Although Fourier transform (FT) has contributed to understand many of dynamical features present in a NDVI time-series, this transform has the limitation that it is only applicable to stationary and periodical data. Furthermore, it has a good frequency localization but it is unable to localize some phenomena occurring in the time domain.

The present work intends to demonstrate the practical usefulness of wavelet transform (WT), as an alternative to the traditional FT, to locate non periodical events in the time series data provided by the Advanced Very High Resolution Radiometer (AVHRR) and by the Scanning Multichannel Microwave Radiometer (SMMR) on board the NOAA and Nimbus satellites.

The present study is an extension of previous works (S. Leguizamón, 1996) facing the problem of locate and mapping areas of similar dynamical behaviour of the vegetation in South America aiming at a better knowledge of the bioclimatic phenomena in this region.

2. MATERIALS AND METHODOLOGY

2.1 *Data*

The input data for these studies are 114 NDVI (AVHRR/GAC) images of South America corresponding to 9.5 years (Jan. to Dec. of years 1982-1990, ..., and Jan. to June 1991) and 108 SMMR Polarization Difference (PD) images, covering the central region of the Province of Buenos Aires in Argentina. The latter are monthly average PD values obtained during the years 1979 to 1987.

The NDVI time series gives us information on the dynamical behaviour of the vegetation along the period considered. On the other hand, the SMMR time series provides information on land surface hydrological conditions.

* *Corresponding author address:* Saturnino Leguizamón, Universidad de Mendoza-CIS, Arístides Villanueva 776, 5500 Mendoza- Argentina. Fax.: +54-61-201100.
e-mail: sleguiza @lanet .losandes.com.ar

The purpose of adding microwave data provided by the SMMR sensor to the dynamical analysis of the vegetation aims at looking for some correlation between a given non-periodic behaviour in the NDVI series and the hydrological conditions of the terrain under study. The polarization difference data used in this work was taken in the 37 GHz channel of the SMMR sensor.

The NDVI and SMMR time-series were obtained by chosen specific geographic locations in the series of images provided by both sensors.

2.2 *Wavelet Transform*

Wavelet analysis has evolved in the last few years as a powerful method to describe signals at different resolutions. The wavelet transform (WT) is performed using translated and dilated versions of a single signal function called wavelet. The basic idea of the WT is to represent any arbitrary function f as a superposition of wavelets and at different scale levels. This leads to the concept of multiresolution analysis in which a signal is decomposed into coarser approximations and the so called "details", which are signals obtained from the differences between two approximations.

The continuous wavelet transform (CWT) of a function $f \in L^2$ is defined as $W_{a,b}(f) = |a|^{-1/2} \int f(t)\, \psi[(t-b)/a)]\, dt$, where the function $\psi_{a,b}(t)=|a|^{-1/2}\, \psi[(t-b)/a]$ is the wavelet function. The parameters a ($a \neq 0$) and b are used to control the dilation and translation of the wavelet, respectively. The wavelet function used in our study is expressed as $\psi(t) = (1 - t^2) \exp(-t^2/2)$ and is called the "Mexican hat".

When the WT operation, above described, is applied to a function f, the results can be graphically represented in a *scalogram* or *phase plane*. This plane has time and time-scale as coordinates.

2.3 *Methodology*

The scalogram is a bidimensional graphic in which the evolution of the phenomenon under study, at different time scales (or time resolutions) is plotted vs. time. The magnitude of the wavelet coefficients is represented by means of a gray scale or colours. Fast events (in which high frequencies are envolved) appear in the small scale region of the graphic. Periodic events can also be observed by the periodical behaviour of the gray levels along a given scale. Slow events occupy the large scale region of the scalogram. In this way, owing to the time

localization property of the WT, it is possible to observe in which part of the time axis a given phenomenon takes place.

3. EXPERIENCES AND RESULTS

For the application of the proposed methodology several geographical locations were chosen. In the NDVI images, 1024 x 1280 pixels in size, 20 geographical sectors located in selected points of South America were chosen. The geographic regions regarded in this experience were determined by the availability of ancillary data, or areas already covered by previous studies for comparisons.

Consequently, for this study we obtained 20 NDVI time series with 108 points in length. Before applying CWT to the series, these were "cleaned up" removing some outliers due to the presence of evident irregularities. The sequences were also detrended in order to avoid the appeareance of "end effects" in the transformed series.

When the FT is applied to a given time-series one is able to observe the dynamical characteristics of the series in graphics of magnitude and phase plotted against frequency.

In the case of the CWT the "earlyness" or lag of a crop, as well as periodicity of a signal, can be directly visualized in the scalogram or phase-plane. The information provided by the phase plane in the time-scale axis is closely related with frequency of a given phenomena. Large time-scale values correspond to low frequencies (low resolution) and small time-scale values are related to high frequencies (high resolution).

In the case of SMMR data the time-series were obtained by using the same criterium used in NDVI data. Some geographical locations were selected from the SMMR images which are 32 x 24 pixels in size. The length of the microwave time-series was of 108 values corresponding to the monthly information obtained from 1979 to 1987.

Each point in the phase plane represents the magnitude of the wavelet coefficient corresponding to the respective time and scale. Wavelet coefficients are a measure of the intensity of the local variations of the signal for the scale under consideration. The value of a coefficient will be large when the dilated wavelet is close to the scale of the heterogeneity in the signal. The value of a coefficient is small when the local signal is smooth for that particular scale. Hence the value of a coefficient for a particular location and at any scale can be understood as a characterization of the dynamical behaviour of the signal at that time and for a given time-scale (or time resolution).

Fig. 1 shows the contour lines of a scalogram corresponding to a non-periodical time-series. In ordinates we have the scale (or frequency) of the original signal. In abscissas we have time.

In a stationary and periodic time-series the peaks and valleys (closed lines) should appear aligned in a constant coordinate (in the same scale). This is not the case for Fig. 1. The most important feature of the scalogram is that one can see where some "anomaly" of the time-series takes place.

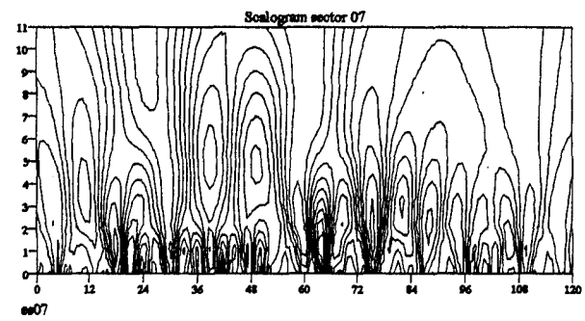

Fig. 1.- Scalogram of cuasi-periodic time-series

4. CONCLUSIONS

The present work intends to demonstrate the practical usefulness of wavelet transform, as an alternative to the traditional Fourier transform, to locate non periodical events in the time series data provided by the AVHRR and SMMR sensors.

The application of continuous wavelet transform to the time-series of interest allows the obtention of a graphic, called the scalogram, in which it is possible to observe the "discontinuities" or "anomalies" present in the signal.

We conclude that CWT is an excelent tool in the search of non periodical events in long time series.

REFERENCES

Leguizamón, S. 1996: Unsupervised Fuzzy C-Means Classification for the Determination of Dynamically Homogeneous Areas. *Proceedings of the VIII Simposio Brasileiro de Sensoramiento Remoto,* Salvador, BA, Brasil.

Menenti, M., S. Azzali, W. Verhoef, R. van Swol, 1991: Mapping agroecological zones and time lag in vegetation growth by means of Fourier analysis of time series of NDVI images, *MARS Report 32, DLO* The Winand Staring Centre, Wageningen, The Netherlands.

Menenti, M., S. Azzali, A. de Vries, D. Fuller and S. Prince, 1993: Vegetation Monitoring in Southern Africa using Temporal Fourier Analysis of AVHHR/NDVI Observations, *Proc. of Intern. Symposium on Remote Sensing in Arid & Semi-Arid Regions*, Lanzhou, P R. of China.

P2.84B

IMPROVED LONG-TERM AVHRR REFLECTANCE AND NDVI TIME SERIES USING EMPIRICALLY DERIVED NADIR CORRECTION FACTORS

Dirk Koslowsky *
Freie Universität, Berlin, Germany

1. INTRODUCTION

Attempts to generate spectral as well as broadband albedo maps of the whole Mediterranean lead to two basic conclusion: i) Compositing and mosaicing spectral as well as broadband reflectances from AVHRR data without normalization to nadir viewing conditions for such a large area is not meaningfull; ii) The application of mean Nadir Correction Functions (NCF), gathered for the Iberian Peninsula to remove the main contribution of the Bidirectional Reflectance Distribution Function (BRDF), to the whole Merditerranean area already results in a considerable improvement of the reflectance maps. The widely used maximum NDVI composite technique to get cloud free maps of the vegetation index prefer data according to extreme off-nadir observation conditions due to the different BRDF of land surfaces for the two shortwave channels CH1 and CH2 of the AVHRR instrument. If first guess NCF are applied previously to the reflectance data this disadvantage can be removed to a large exctent. Corrections to nadir observation conditions not only remove the variations of the anisotropy of the land surface, but also result in data which are comparable to other sources with higher resolution like Landsat and SPOT data, which gather data only under near- nadir conditions

2. SURFACE ANISOTROPY

Land surfaces show considerable anisotropy in reflectance in CH1 and CH2. The physical resolution of the AVHRR instrument given by the instantaneous field of view (IFOV) is varying over the scan angle range from 1.0 km^2 at the nadir to 12.4 km^2 for extreme off-nadir observation conditions. The structure of the surface together with the illumination by the sun and the viewing conditions of the instrument result in various amounts of shadows in the IFOV and cause differences in the directional spectral albedos in the magnitude of up to +/-50% of the nadir values. One main structure element of the surface is the existence of vegetation, its type and development state. Thus the BRDF of a surface element is a function of the vegetation cycle and is not invariant in time. Rapid changes in the state of vegetation in the spring or at harvest time will force strong changes in the BRDF within only few days. Land use maps cannot reflect this feature. Thus the state of surface anisotropy has to be monitored by remote sensing tenchiques, too (i.e. Barnsley et al., 1994).

The AVHRR instrument on the NOAA satellites is the only source of temporal high resolution data with global coverage. The disadvantage of the necessity of a large scan angle range of +/- 55^0 can be used to overcome this problem. To achieve sun-synchronous orbits some prerequisits are necessary, which result in periodic variations of the local observation conditions with a period of about 9 days. In this period the radiation geometry changes from off- nadir backscattering over nadir to off-nadir forward scattering conditions. If no clouds are present, it is possible to get samples of intersections of the BRDF. For sun synchronous orbits the local observation time and accordingly the sun height and azimuth is directly related to the sample number and therefore the local zenith distance of the satellite and the day of the year. The orbital drift towards later observation time from year to year change this conditions only very slowly and is depicted in Fig. 1.

3. EXTRACTION OF EMPIRICAL NADIR CORRECTION FUNCTIONS

Daily 3-dimensional plots can be generated for each year of operation with the date as the x-axis, the nadir distance of the satellite as the y-axis, and the reflectances as z-axis (Fig. 2). Missing values due to data losses or cloudy conditions can be interpolated by a Delauny-triangulation combined with a low pass filtering of the data. In case of a complete data set for one year a cross section through such a distribution at nadir results in a nadir corrected course of the reflectance data of the whole year. A cross section at a specific date provides the actual reflection function, and its reciprocal can be used as a Nadir Correction Function (NCF) to get estimates for nadir conditions for a given satellite zenith distance.

Fig. 2 show examples of such 3-dimensional plots of reflectances of CH1 and CH2 respectively over the area of the EFEDA (Bolle et al., 1993) test site Belmonte in the Castilia La Mancha in Spain. At the left hand side the pronounced anisotropy of the surface can be seen as well as its variation not only in the course of the year, but also from year to year, mainly caused by the different illumination conditions due to the shift in local observation time. If the inferred NCF are apllied to the data set the result is shown on the right hand side is obtained. The anisotropy is widely removed and the remaining changes in the reflectances show the influence of the vegetation cycle of the year, that is accompanied by low reflectance in CH1 and high values in CH2 at high vegetation activity.

Even though the NCF are only valid for a specific land surface type and vegetation cover for which the distribution was generated, an average for the whole Iberian Pensinsula was applied successfully as a first order correction for surface anisotropy.

* *Corresponding author adress:* Dirk Koslowsky, Free Univ., Inst. of Meteorology, D-12165 Berlin;
e-mail kosze@zedat.fu-berlin.de.

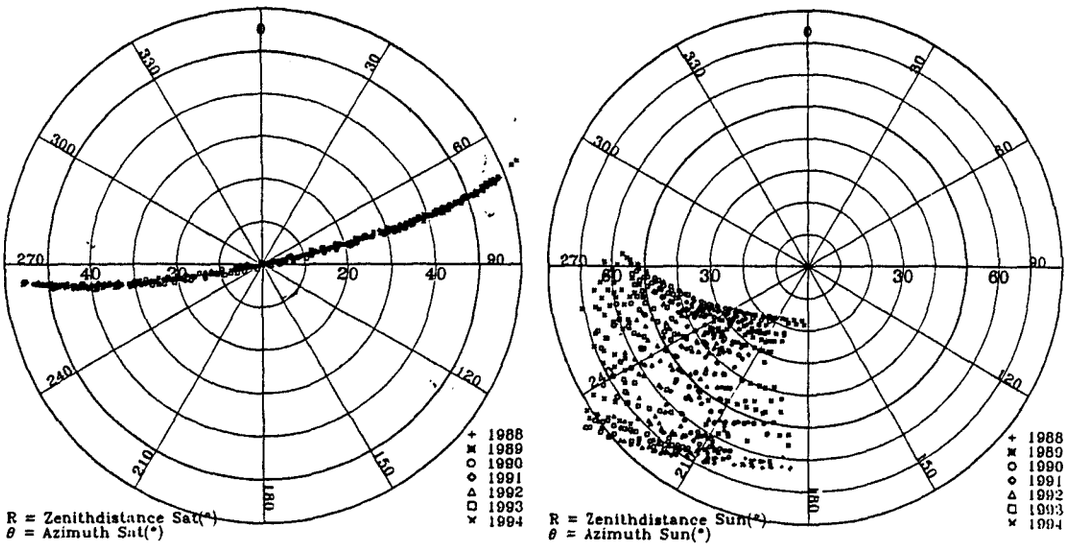

Fig. 1: Zenithdistance of satellite (left) and sun (right) as a function of its azimuth for the whole mission of NOAA 11

4. NADIR CORRECTED TIME SERIES

By applying such a normalization technique to TOA reflectances data the combined influence of both the surface anisotropy and the variable view through the atmosphere averaged over the short period of about 10 days is included. To infer from these TOA data the surface refectances it is only necessary to perform radiance tranfer calculations for the nadir viewing conditions with atmopsheric quantities referring to the mean conditions of such a period and will represent the actual situation better than climatological data. Measurements of the optical depth are normally done only for limited field measurement campaigns, as long as no anchor stations are installed and working in the region of interest. Thus the uncertainty in the distribution of the main atmospheric constituents affecting the shortwave channels of the AVHRR, the aerosol and water wapor, is quite large and probably higher than the error due to the sampling period for the NCF. Desirable in this context would be methods to determine the optical depth directly from remote sensing data. This could be possible over small water bodies or even by careful evaluation of the ratio of reflectances of illuminated and shadowed surfaces.

Mean conditions for the whole Iberian Peninsula including RMS values of the NCF are shown in Fig. 3 for the month of June. Even the use of such mean correction functions considerably reduces the scattering caused by the changing viewing geometry of the daily data sets. The resulting corrected yearly courses of reflectances and NDVI are better suited for evaluation of characteristic differences from year to year than time series only smoothed by statistical methods.

Fig. 4 shows 9 year data sets of daily uncorrected and nadir corrected reflectances for three test site without any filtering. The time series of NOAA 11 ended in September 1994 and is extended by NOAA 14 data since January 1995. The data of this two satellites are carefully intercalibrated by a RMS fit of the nadir corrected data (Koslowsky, 1997). The regression lines for the desert target show no slope and this indicates, that the influences by sensor degradation and by changing observation time are corrected sufficiently.

5. CONCLUSIONS

The use of empirically derived Nadir Correction Functions improves long-term data sets of the shortwave channels of the AVHRR. If they are previously applied the obtained maximum NDVI composites avoid the preference of the less meaningful data with extreme off-nadir observation conditions.

REFERENCES

Barnsley, M.J., Strahler, A.H., Morris, K.P., and Muller, J.-P. ,1994: Sampling the surface bidirectional reflectance distribution function (BRDF): 1. Evaluation of current and future satellite sensors.
Rem. Sens. Rev. **8**:271-311.

Bolle, H.-J., André, J.-C., Arrue, J.L., et al. ,1993: EFEDA: European Field Experiment in a Desertification-threatened Area. *Ann. Geophys.* II:173-189.

Koslowsky, D., 1996: Mehrjährige validierte und homogenisierte Reihen des Reflexionsgrades und des Vegetationsindexes von Landoberflächen aus täglichen AVHRR-Daten hoher Auflösung. Met.Abh.,A, **9**(1), Freie Univers. Berlin, Inst. f. Meteor.

Koslowsky, D.: Signal degradation of the AVHRR shortwave channels of NOAA 11 and NOAA 14 by daily monitoring of desert targets. *Adv. Space Res.* **19**(1), 1355-1358.

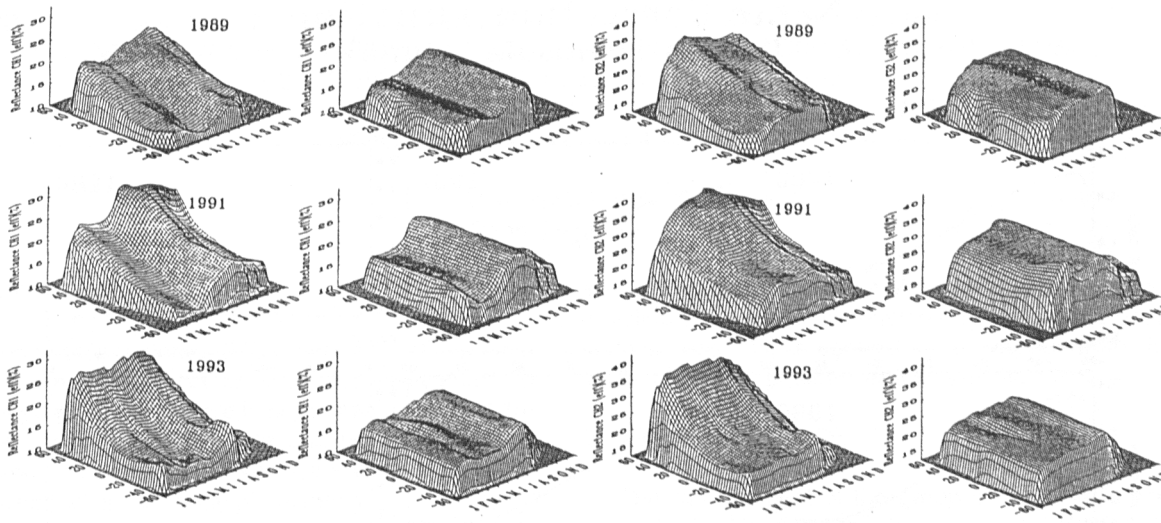

Fig. 2: Three-dimensional plots of reflectances (TOA) for the EFEDA test site Belmonte for selected years with respect to date and observation angle before and after nadir normalization for AVHRR-CH1 and -CH2.

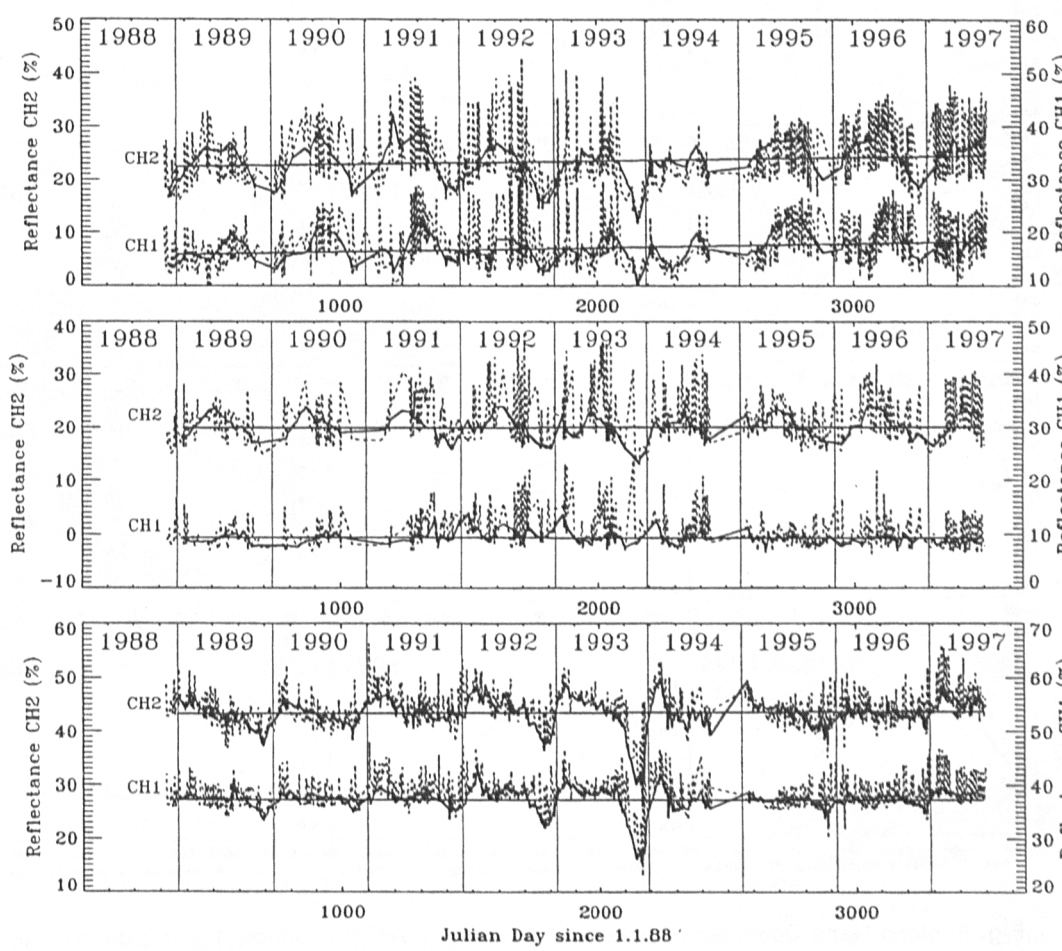

Fig. 3: 9 year time series of daily reflectances for the test sites Belmonte (upper graph), Tuscany (middle graph), and a desert test site in the Sahara (lower graph), before (dashed) and after (solid) nadir normalization.

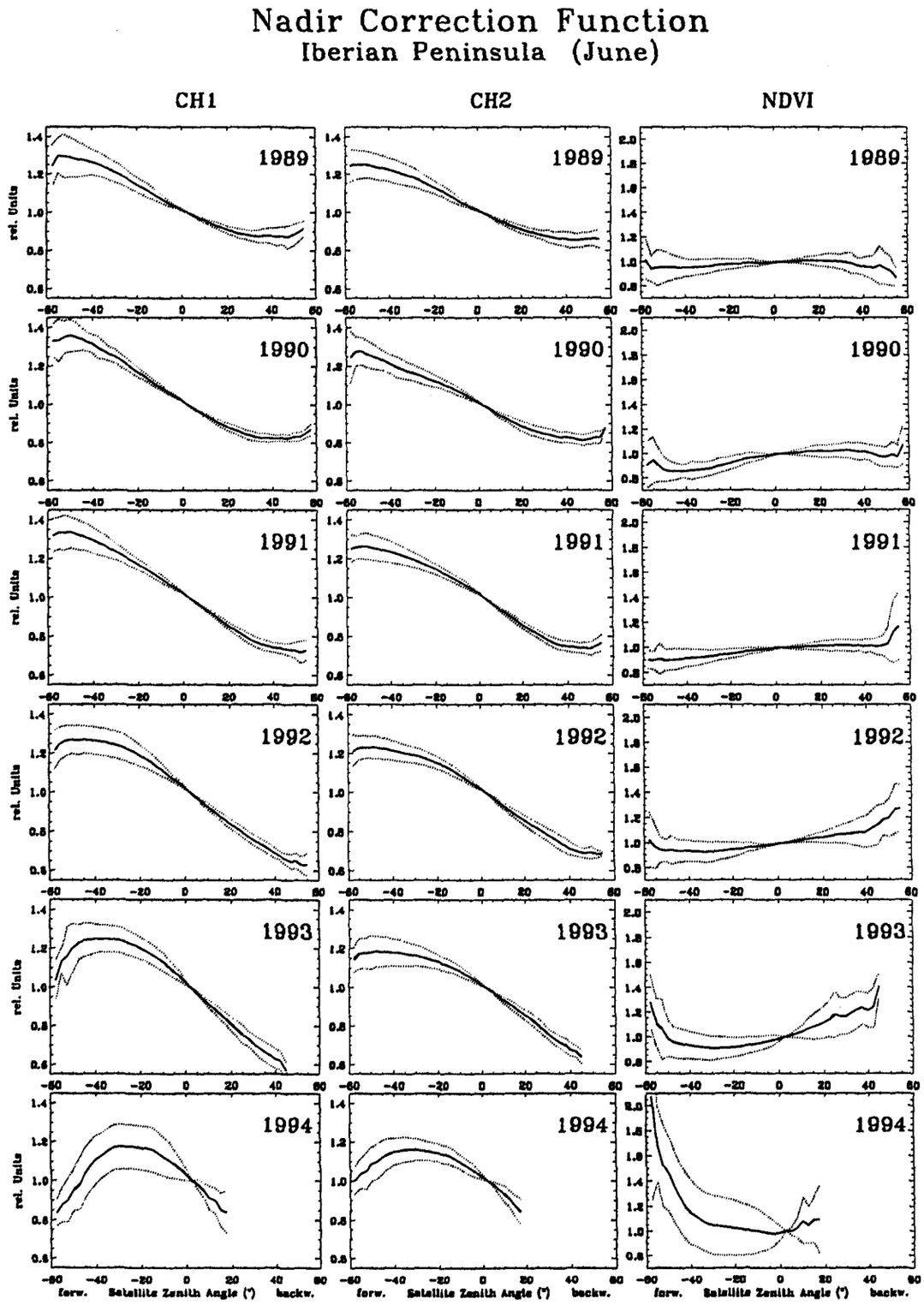

Fig. 4: Mean Nadir Correction Functions of Spain for AVHRR channels 1 and 2 as well as the NDVI for the month of June from 1989 to 1994. The functions are composed of 25 areas of 100 km^2 each. The dotted lines indicates the scatter of the data.

P2.88B ANTARCTIC MESOCYCLONE EVENTS OVER THE SOUTHERN PACIFIC DURING FROST SOP1 AND SOP3 : A MESO-SCALE ANALYSIS USING AVHRR, SSM/I, ERS-SCATTEROMETER AND NUMERICAL MODEL DATA

Michael Lieder and Günther Heinemann*

Universität Bonn
Bonn, Germany

1. INTRODUCTION

Meso-scale cyclones (MCs) over Antarctic oceans have been the subject of several investigations in recent years. Since Antarctic MCs often occur in data-sparse regions, satellite data and simulations using meso-scale numerical models are important tools for the investigations of these phenomena.

The current paper investigates two MC events occurring during July 1994 and January 1995 over the Antarctic region of the Southern Pacific, i.e. over the northern Amundsen and Bellingshausen Sea. Both months are special observing periods (SOPs) of the Antarctic First Regional Observing Study of the Troposphere (FROST, Turner et al., 1996). For the SOPs comprehensive datasets containing in-situ and satellite observations, model fields and manual analyses (surface and upper air) exist. The goal of the present study is to use multi-sensor satellite data of the FROST data set in conjunction with meso-scale model simulations for the investigation of Antarctic MCs. Satellite imagery and retrievals are used for synoptic and sub-synoptic description of the MCs, but also serve to validate the model simulations by comparing near-surface wind and integrated water vapour from the model fields with satellite-retrieved fields.

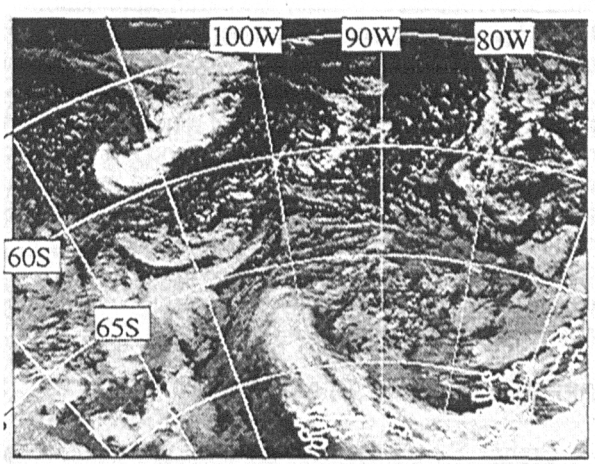

Fig.1: AVHRR infrared image for 14 UTC 11 January 1995 (reduced resolution, polarstereographic projection) showing the three MCs M1, M2 and M3 at 58°S/112°W, 59°S/95°W and 60°S/83°W, respectively, and parts of large-scale cyclone with its center at 67°S/90°W.

* *Corresponding author address*: G. Heinemann, Meteorologisches Institut der Universität Bonn, Auf dem Hügel 20, D53121 Bonn, Germany. (email: gheinemann@uni-bonn.de)

2. SUMMERTIME CASE

The development of the group of three MCs was studied (Fig.1). Satellite data from AVHRR, ERS scatterometer and SSM/I, and the sparse data of the two buoys in this area were used. A distinct signal of

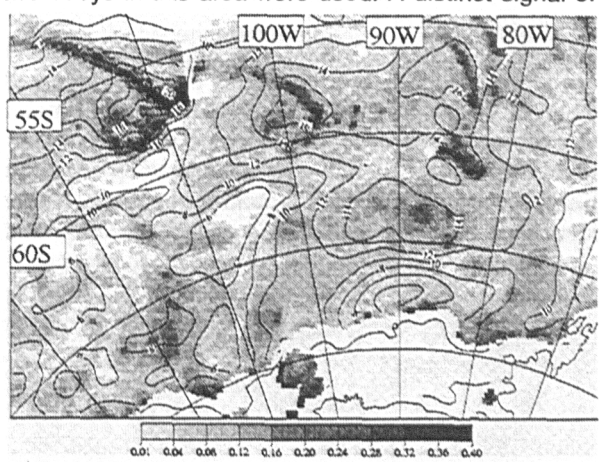

Fig.2: SSM/I-derived cloud liquid water (greyshaded, scale in kg/m²) and near-surface wind speed (contour interval 2 m/s) for 10-13 UTC 11 January 1995.

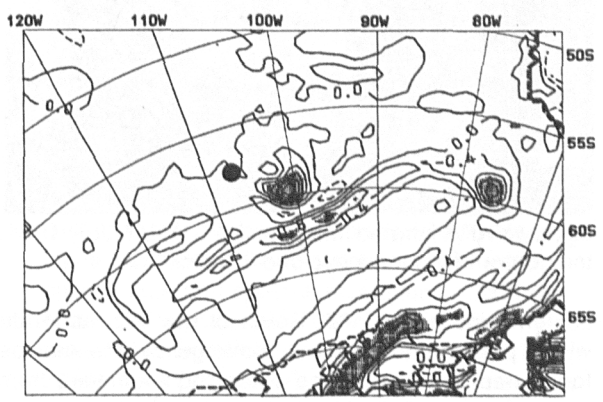

Fig.3: NORLAM forecasts (50 km grid) of the relative vorticity at 950 hPa (contour interval $0.4 \cdot 10^{-4}$ s^{-1}, shaded for values lower than $-1.0 \cdot 10^{-4}$ s^{-1}) after 18 h simulation time (valid at 18 UTC 11 January). The centre of M3 at 18 UTC 11 January obtained from satellite images is marked by the full circle.

the MCs in the infrared imagery and the SSM/I-retrieved near-surface wind speed, integrated water vapour (IWV) and cloud liquid water (CLW) can be found (Fig.2).

Numerical simulations were performed using the meso-scale model NORLAM (for model details see Heinemann, 1997; Grønås et al., 1987). The numerical model results showing two of the MCs as pronounced cyclonic vorticity maxima (Fig.3) being shortwave baroclinic developments triggered by an upper-level trough.

3. WINTERTIME CASE

Fig.4 shows an AVHRR infrared image for 6 July 1994 1220 UTC. A MC with a diameter of about 1000 km can be observed at 123°W/51°S, east of the MC the cloud bands of a front associated with a synoptic low at 110°W/70°S can be seen. The development of the MC started in the early morning of 5 July in the area around 150°W/42°S. After approximately 60 hours lifetime the MC decays in the Bellingshausen Sea (100°W/62°S) on the afternoon of 7 July.

A detailed view of the MC and the prevailing winds are shown in Fig.5, that combines the SSM/I-derived CLW of 6 July 07 UTC and the ERS scatterometer winds for 08 UTC. This rare example of the 500 km narrow ERS swath fully hitting a MC shows the cyclonic rotation of the strong winds around the center with very low wind speeds, especially on the northern and

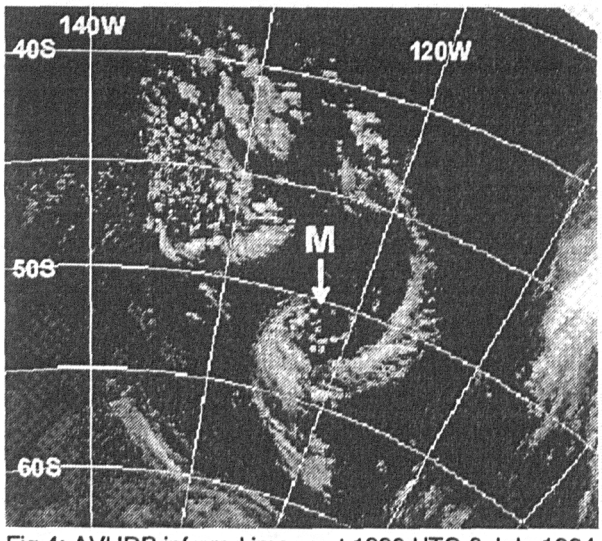

Fig.4: AVHRR infrared image at 1220 UTC 6 July 1994, the center of the mesocyclone is indicated.

eastern side of the MC. South of the MC moderate winds prevail and a sharp convergence line can be found near the cloud band extending southward from the center of the MC with winds turning from westerly to northerly directions.

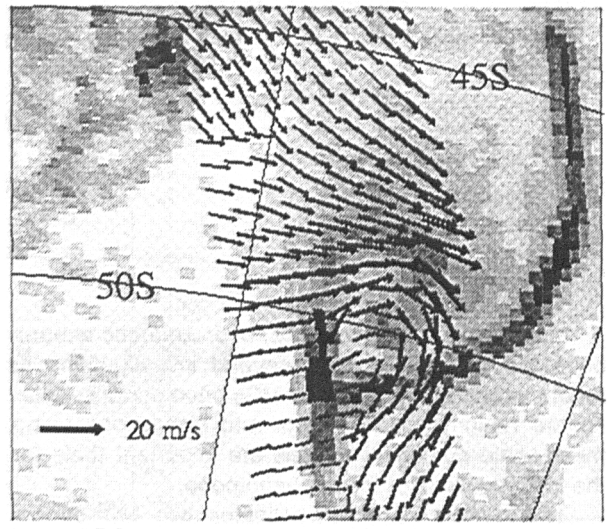

Fig.5: ERS-1 scatterometer wind vectors for 08 UTC 6 July 1994 superimposed on SSM/I-retrieved CLW at 07 UTC.

4. INTERCOMPARISONS

Intercomparisons have been performed between numerical model results, ERS and SSM/I retrievals for 10-12 January 1995 in order to assess the quality of the simulation results. Especially the parameters near-surface wind and IWV show good agreement allowing to use the model results with confidence for the study of processes not retrievable from satellite data. The differences between ERS and NORLAM wind vectors is 1.1 m/s and -3.2 deg for the mean bias, and the standard deviation is 2.5 m/s and 25 deg for wind speed and direction, respectively. The difference between ERS and SSM/I wind speed retrievals has values of 1.1 m/s (bias) and 1.2 m/s (standard deviation). The higher values SSM/I retrievals may be due to different reference heights of the satellite retrievals.

REFERENCES

Grønås, S., A. Foss and M.Lystad, 1987: Numerical simulations of polar lows over the Norwegian Sea. *Tellus,* 39A, 334-353.

Heinemann, G., 1997: Idealized simulations of the Antarctic katabatic wind system with a three-dimensional meso-scale model. *J. of Geophys. Res.,* 102, 13825-13834.

Turner, J., D. Bromwich, S. Colwell, S. Dixon, T. Gibson, T. Hart, G. Heinemann, H. Hutchinson, K. Jacka, S. Leonard, M. Lieder, L. Marsh, S. Pendlebury, H. Phillpot, M. Pook and I. Simmonds, 1996: The Antarctic First Regional Observing Study of the Troposphere (FROST) Project. *Bull. Am. Meteorol. Soc.*, 77, 2007-2032.

P2.90B

THE SATELLITE APPLICATION FACILITY -SAF- OF EUMETSAT TO SUPPORT NOWCASTING: AN INTRODUCTION

Nowcasting SAF Consortium:
José Miguel Fernández*,
INM, Madrid, Spain
Hervé Legléau,
Météo-France, CMS-Lannion, France
Veronika Zwatz-Meise,
ZAMG, Vienna, Austria
Adam Dybbroe,
SMHI, Norrköping, Sweden

ABSTRACT

In the Application Ground Segment of Eumetsat for operational product generation in the 2000's, will exist a central element -MPEF- and de-centralised, finality oriented ones -SAF-. The SAF on 'Support to Nowcasting and Very Short-range Forecasting will provide the product extraction from the Meteosat Second Generation -MSG- data flux for near real time needs. Activities are started in 1997 a consortium of Meteorological institutes, hosted by Spain and also integrated by Austria, France and Sweden. Agreed products to be developed include analyses of cloudiness, clear-air and cloud patterns, precipitation and wind information. The presentation introduces possibilities of MSG in relation to needs and aims in nowcasting starting from the current status, some basic assumptions for the SAF, and justification and important features of the selected products.

1. NOWCASTING AS A SATELLITE APPLICATION

Nowcasting combines the continuous monitoring of atmospheric features on a horizontal scale

between tens and hundreds of kilometres, with the prediction of their development over the next two or three hours, for local use. It today relies heavily on the display of images and on their interpretation by the forecaster, and as only geoestationary satellite and radar networks are capable of satisfying the time-scale requirement at achievable cost, it can be objectively considered a rather new discipline in operational meteorology, particularly for the use of derived

satellite imagery products or the development of fully objective techniques. On the other hand Short range forecasting extends the time scale of predictions to 3 to 12 hours, mainly on a national or regional scale, and will add techniques such as local and mesoscale model computations using numerical data (for example calibrated radiances or derived geophysical parameters), and expert systems, although both are subject to further development.

The following phenomena are the most relevant in nowcasting and short range forecasting activities:

- frontal disturbances and related cloud and wind patterns,
- Convective patterns within unstable air masses,
- clouds and fog within the atmospheric boundary layer.

In these applications area there is at present a lack of detailed information on the thermodynamic characteristics of the atmosphere. Furthermore spatial, time and spectral resolutions of current Meteosat operational -MOP- imagery has revealed as insufficient, offering only 2.5 to 5km, 30min, and the lone WV channel, while need for

* *Corresponding first author address*: José Miguel Fernández Serdán, Servicio de Teledetección, Instituto Nacional de Meteorología, Ap. 285, 28071 Madrid, Spain; e-mail: serdan@inm.es

1 to 3km, 5 to 15min, and a set of absortion channels are put forward.

2. THE METEOSAT SECOND GENERATION - MSG- MISSIONS RELATED TO NOWCASTING

The MSG Programme represents an important evolution from MOP; the final choice has been to develop a 12-channel Spinning-Enhanced Visible and InfraRed Instrument -SEVIRI, coping with the following missions:

Multi-spectral imaging mission mainly devoted to cloud and land/sea surface. Channels similar to well known AVHRR/3 to be flown on NOAA next series from 1998 and the addition of IR8.7μm largely will cover this mission.

High resolution imaging mission to monitor small scale and local weather features (such as convective cloud evolution, fog, etc..) in support of nowcasting. A HRVIS channel fills this mission for the enlarged European sector with 1km spatial resolution.

Air mass analysis mission to monitor the thermodynamic and other characteristics of the atmosphere. This missions suffered from relaxations, being discarded first the sounding instruments then some of the absortion channels selected for SEVIRI which nevertheless keeps 4 of these (2 absortion Water Vapor, one CO_2, one O_3). To be noted, for any channel the time and spatial resolutions will be the same, 15min and 3km (except HRVIS).

Product E'xtraction Mission of MSG to derive meteorological and other products from the basic SEVIRI data, to be carried out by different elements of the Eumetsat Ground Segment: by Eumetsat directly at the Meteosat Products Extraction Facility -

MPEF-, or relying on the existing expertise, means and projects within EUMETSAT Member States, through the strategy of a de-centralised network of Satellite Applications Facilities -SAFs-, 3 of these are now launched ('pilot' SAFs), others are being defined.

SAF structure is also for the Eumetsat Polar System -EPS- programmes, but the SAF in Support to Nowcasting and Very Short-range Forecasting - Nowcasting SAF here-after, apart from being the earliest one is with the MPEF the element clearly related to the MSG Product extraction mission.

3. THE NOWCASTING SAF

Following a long clarification procedure started in 1994 within Eumetsat with different member

states (Meteorological Institutes) as contributors, the Nowcasting SAF has resulted from the convergence and re-definition of 3 activity areas dealing with Cloud and precipitation, Severe weather, and feature Synoptic analysis. Once signed the agreements (December 1996), INM is assuming a host role and is responsible *vis-a-vis* Eumetsat, other contributors being Météo France, SMHI (Sweden), and ZAMG (Austria); contribution of other Meteorological Services or Institutes is here as for other SAF foreseen through an strategy of visiting or cooperating scientists.

The purpose is the development, and distribution to Eumetsat members, of software packages for the calculation of a series of products on the state and recent evolution of the atmosphere, mostly from the MSG data flow as acquired through a High data-Rate User Station -HRUS. This products are to be integrated with other diverse source of data in the work routines for Diagnostic, Nowcasting and Very short-range forecasting in the Meteorological Institutes . The modules will allow calculations at the highest spatial and time resolution (generally 3km and 15min) for any region inside the geographical area of relevance for Eumetsat members (i.e. similar to current Meteosat B-format).

The project schedule covers 5 years roughly as follows: 1997 has been for detailed definition, 1998-1999 is to be for the major development of the products, 1999-2000 will be for the validation and final modules preparations, and 2001 will regard the final validation, integration and testing, and delivery. The plan is also considering the submision of a proposal for operations or next phases. As no real MSG data will be available before end 2000 or 2001, it is to be noted that the product development will need to rely on existing data (other satelites including GOES, NOAA, MOP), radiative simulations from Numerical modelled atmospheres (and the real SEVIRI validation will be short); other conventional and remote sensing meteorological data will server for training,, tuning and validation.

4. NOWCASTING SAF PRODUCTS

4.1. Basic considerations

12 products have been selected considering MSG and SEVIRI possibilities, the nowcasting needs on products, those expected from other SAF or MPEF, etc.. The description of products and algorithms is not yet concluded (some very new will certainly need refinement or confirmation at an ulterior step), nor the interaction with products users who will still contribute to the refinement and validation. Only a brief product description is intended here, the detailed plans will certainly be made reachable through the INM server *http://www.inm.es*, once revised in Eumetsat.

4.2. SAF products to be developed by SMHI and Météo-France

Cloud flag and amount CMa, Cloud type (including fog): The basis for extraction proposed for both are thresholding algorithms (including updating of threshold calculation, and texture) using window channels, well known for the AVHRR data from NOAA- TIROS/N (e.g. Derrien et al., 1993): a basic mask for free clear pixels detection -even free of aerosol, fractional or semitransparent cloud; a second of visual cloud classes for diagnostics.

Cloud top temperature/height: Corrected black-body window temperatures, with more than one channel combination tested for semitransparent or fractional clouds (e.g. experience for GOES, Menzel et al. 1982). To be used for Aviation and other products (height assignment).

Precipitating clouds (SMHI): Improvement of cloud type with the main purpose to determine areas of extensive precipitation in a few classes (at its probability)with a few classes (and its likelihood); information from numerical models will be an optional but important feature. For precipitation analysis.

Special development subjects are the aerosol identification and separation of similar clouds, the channel combination for non-opaque or filled pixels, and the precipitation product. SMHI and Météo-France are cooperating (except for the last) assuming geographical criteria, SMHI will prepare for high latitudes and the optional AVHRR modules (including or mainly from microwave AMSU data in the case of precipitation).

4.3. SAF products from ZAMG

Automatic satellite image interpretation: A fast interpretation of images and even product maps in terms of conceptual models in synoptic and meso scale, the first step being the image segmentation and pattern recognition techniques (Zwatz-Meise et al., 1996). For improvement the use of satellite motion winds and numerical model fields is considered as part of the method. This products eases and adds objectiveness to the first approach to the diagnostics, as usually done on MOP images at many operational centres.

Air mass advection: This product was understood as an extrapolation (using satellite motion winds) of channel data and other products; as a result of the detailed definition of the SAF it will probably move to become "Air mass classification" for the identification (and perhaps extrapolation) of air mass boundaries and characteristics found more realistic, and which assumes some ideas from the former.

Special subjects for the next phases are the complete definition and development of the second product, and for both to gain in the objective validation criteria.

4.4. SAF products from INM

Convective Rainfall Rate: A more sophisticated cloud classification of precipitating clouds for identified convective pixels, adding corrections related to the evolution and local environment, known to affect precipitation in convective cases. Based on the GOES experience (Scofield, 1987), should provide quantitative estimates useful even if not highly accurate, to monitor the evolution of convective systems.

Total Precipitable Water: To be performed in areas with no cloud, on the basis on a physically-based channel combination like the split-window correction (Dalu, 1986).

Layer Precipitable Water: Also in clear areas, use of semi-empirical methods to add information on a -coarse- vertical moisture distribution: 2 (3 as more unlikely) layer-values in the troposphere (2 or 3 absortion WV-sensitive channels are in SEVIRI). This will complete the description of the Water vapor content in the atmosphere (the most interesting is a to get information for medium and low levels but it is more easy for the high).

Stability Analysis Imagery: Aiming to reproduce, in no cloud areas through a combination of channels (regression and neural networks methods are being studied) an atmospheric thermodynamic index to be determined (as a result of an Eumetsat funded preliminar study, indices as SK and MSK seem good candidates, but LI should also be considered following existing GOES experience, Mostek et al., 1986). The development should estimate the channel or channel combination sensitivity to relevant changes influencing stability. Even if not very accurate because no real sounding capabilities in MSG, high resolution frequently updated maps should help the analysis of the preconvective atmosphere.

High Resolution Wind Vectors from HRVIS: The method will assume existing techniques for cloud tracking (e.g. Schmetz et al., 1996), and develop optimization for areas of interest for nowcasting to get resolution better than 25 to 30 pixels particularly for land cloud structures; a HRVIS analysis is also considered. These winds are intended to provide information on dynamical features in the atmosphere.

Rapid Developing Thunderstorms Product: Determination and coding of "object" properties (e.g. Adler et al., 1988) for convective systems (storm to meso-scales), from the analysis of a few channels (temperature or temperature difference thresholding), the evolution, and optional numerical models information.

The clear-air products (Layer precipitable and Stability analysis in particular) require important development at least for the MSG context; Convective Rainfall and Rapid developing products will need to put together different techniques, whose final result needs to be proven, as well as the ability to actually get High resolution winds useful for the nowcasting.

5. CONCLUSIONS

Nowcasting SAF aims to produce modules for the extraction of 12 products from MSG data, as final deliverables. Important development is neded at the involved Meteorological Institutes (INM, Météo France, SMHI, ZAMG), to reach optimal results, in particular because of the newness of the data (Meteosat Second Generation -MSG- data are not yet available before 2001, and no complete equivalence exists earlier). The user requirements, guidance, implication, etc, is also needed along the phases to get the best products for the intended application.

References

Adler, R.F. and Negri, A. J. , 1988: A satellite infrared technique to estimate tropical convective and stratiform rainfall. J. Appl. Meteor., 27, 30-51.

Dalu G., 1986. Satellite remote sensing of atmospheric Water vapor. Int. J. Remote Sensing, 7, 9 1089-1097.

Derrien M., B.Farki, L.Harang, H.Le Gléau, A.Noyalet, D.Pochic, A.Sairouni, 1993. Automatic cloud detection applied to NOAA-11/AVHRR imagery. Remote Sensing of Env., 46, pp 246-267.

Menzel W.P., Smith W.L., and Stewart T.R., 1982. Improved Cloud Motion Wind Vector and Altitude Assignment Using VAS. Journ. Clim. and Appl. Met., 22, pp 377-384.

Mostek, A., Uccellini L.W., Petersen R.A. and Chesters, D., 1986. Assesment of VAS soundings in the analysis of a preconvective environment. Mon. Wea. Rev., 114, pp 62-87.

Scofield, R.A., 1987. The NESDIS operational convective precipitation Technique. Mon. Wea. Rev., 115, No.8, pp 1773-1792.

Schmetz J., K. Holmlund, A. Ottenbacher, 1996. Low level Winds from High-Resolution Visible Imagery, EUM P 18, pp. 71-79.

Zwatz-Meise, V., Scheiber, J., Zobl, Z., 1996. Towards Automatic Meteosat Image Interpretation. Procs. 1996 Met. Sat. Data Users' Conf., pp 97-104.

Neural network approaches to ocean parameter retrievals : application to the ERS1 scatterometer wind and to phytoplancton content from ocean color measurements.

By

M. Crepon, C. Mejia, S. Thiria, L. Gross, N. Tran
(LODYC, UPMC, 4 Place Jussieu, 75005, Paris, France),

P. Richaume, H. Roquet
(Meteo France, SCEM/PREVI/MAR
42, Av. G. Coriolis
31057 TOULOUSE CEDEX)

F. Badran
(Conservatoire National des Arts et Metiers
Departement d'Informatique
292 rue Saint Martin, 75003, Paris, France)

R. Frouin
(Scripps Institution of Oceanography
University of California San Diego
9500 Gilman Drive
La Jolla, CA 92093-0221, USA)

Corresponding author
(mc@lodyc.jussieu.fr)

Introduction

Inversion of satellite remote data often may be difficult due to the non linearity of the problem or to the fact that the relationship between the measured quantities and the geophysical parameters are empirical. As shown in Thiria et al. (1993), Neural networks provide an efficient methodology to overcome these difficulties. Besides they can deal with noisy data. In the present study inversion is considered as the determination of an invert transfer function. The observed quantities are associated to the geophysical parameters through of a Neural Network. The Neural Network is calibrated on a specific data set (learning) and then can be generalized to other situations. This methodology was applied with success for retrieving the wind vectors from the scatterometer ERS1 measurements and for determining chlorophyll content from Seawifs.

1)ERS1 scatterometer wind retrieval

The transfer function giving the wind vector from the radar measurements (sigma-0) is a very complex multivalued function. The wind speed is a non linear function with respect to the sigma-0 and several solutions can be obtained for the wind direction. A neural network methodology has employed for retrieving the wind vectors from the ERS1 measurements. The data set consists in ERS1 scatterometer sigma-0 collocated with ECMWF N.W.P. model analyzed wind vectors onto the North Atlantic Ocean for the year 1994-1996. In order to improve the confidence of the ERS1 measurements we used a space window of 13 sigma-0 triplets for the input arguing that the wind vectors must present some space coherency. A first neural network computes the velocity and a second one taking into account the wind velocity estimates the direction. This second neural networks is used as a classifier. The output is divided in 36 classes of 10 degree interval representing the whole azimuth range of the wind vector ; the neural network is trained to gives the probability for the direction to belong to some classes. This allows us to determine several ambiguities ranked by their probabilities. The performances for the wind retrieval (both for modulus and direction) are very good when compared to classical method.

In order to check the quality and the homogeneity of NN-inverse we give the performances for each track and for wind speed (**Table 1**) and wind direction (**Table 2**).

track	0	1	2	3	4	5	6	7	8	9
bias (m/s)	-0.2	0.0	-0.1	-0.1	-0.1	-0.1	-0.1	-0.1	0.0	0.0
rms (m/s)	1.6	1.6	1.5	1.6	1.6	1.6	1.6	1.6	1.6	1.7

Table 1 : *performances of NN-inverse when approximating the wind speed : the first row gives the bias with respect to the track and the second gives the rms.*

The bias and the RMS. are very low and not dependent of the track, which proves the good quality and the homogeneity of NN-inverse methodology since each track is inverted by using a specific NN model.

track	0	1	2	3	4	5	6	7	8	9
1-alias	78.4	77.9	79.3	79.5	78.1	73.1	73.7	65.9	71.4	66.3
2-alias	85.1	85.0	86.9	87.7	87.5	87.8	87.6	88.0	88.2	86.9
3-alias	86.1	85.9	87.6	88.6	88.4	88.8	88.4	88.8	88.8	87.6
4-alias	86.5	86.4	88.0	89.0	88.7	89.1	88.7	89.1	89.1	87.9

Table 2 : *Performances of the wind direction retrieval. Each row displays, for each track i and for different number of possible solutions (alias) allowed, the performances. A given direction is considered correct if the computed direction differs by less than ±20° from the ECMWF direction.*

These very good results show :

1. the existence of a good solution among all the aliases ; about 88 % of the directions are consistent with I-ECMWF and for the remaining 12 % we can not state without further investigation since I-ECMWF is not an error-free reference.
2. the quality of the first rank solution ; the first alias (the wind direction having the highest probability) given by the NN-inverse is correlated at ±20° with ECMWF wind direction in 75% of the collocations which is better than the theoretical limit of 72% and for the first and second alias in 85% of the collocations.

The first point is mainly linked to the overall neural networks abilities in non-linear modelling whereas the second is mainly due the spatial context used in the input. We can thus expect to remove the ambiguity without any external information.

2) Phytoplancton content retrieval from ocean color measurements

We used Neural Networks to compute phytoplankton pigment concentration (chlorophyll-a plus phaeopigments) from satellite-derived marine reflectances. We made an academic study by simulating two types of spectral reflectance at the sea surface level with respect to pigment concentration C (0.03-30 mg) by using the model of Morel (1988) : TEST1 data are free of noise, TEST2 data take into account realistic radiometric noise. These data are used to calibrate two different Neural Networks, denoted NN-1 and NN-2. We chose a particular ocean color

radiometer, the Sea-Viewing-Wide-Field-of-View-Sensor (Seawifs) which provides five ocean-color channels: 412, 443, 490, 510 and 555 nm.
We made several experiments which are summarized in **Table 3** :

	NN-1	NN-2	
TEST1'	0.024 mg m^{-3} 0.14 % 99.99 %	0.014 mg m^{-3} 0.10 % 99.99 %	RMS (mg m^{-3}) relative RMS (%) Corr.(%)
TEST2'	2.138 mg m^{-3} 59.02 % 95.81 %	0.014 mg m^{-3} 0.14 % 99.99 %	RMS (mg m^{-3}) relative RMS (%) Corr.(%)

Table 3 : *Performances of the different neural models NN-1 and NN-2 tested on the different test sets TEST1' and TEST2'. The test sets are data extracted of TEST1 and TEST2 which have been used in the learning procedure*

It is seen that NN-1 presents good performances on free noise data but quite bad performances on noisy data while NN-2 presents good performances onto the two cases. It is concluded that that the Neural Network is able to learn the noise and extract information from noisy data.
When compared to classical polynomial inversion it is found that the Neural Network gives better performances with noisy data

Conclusion

Adding to their ability to model complex functions, the major advantages of Neural networks are the following : NN are complex and stable function's approximator able to deal white noise measurement and very adaptive systems, the accuracy of the inversion can be enhanced by using spatial windows which increases the information (ERS1 scatterometer wind retrieval), multivaluate function can be determined by using neural networks as classifier (direction of the scatterometer wind), information is not frozen a-priori (in the determination of chlorophyll content from ocean color observations, Neural Network uses reflectance instead of reflectance ratio).

References :

S. THIRIA, F. BADRAN, C. MEJIA and M. CREPON, .- A Neural Network Approach for modelling Non Linear Transfer functions : Application for Wind Retrieval from Spaceborne Scatterometer Data. *J. Geophys. Res. 98, 22,827-22841,* 1993

Check out the AMS Journals Online now on the AMS Web site

AMS Journals Online

Now the complete contents of the AMS journals and Bulletin articles are available on the Web!

All users can view titles and abstracts of articles from the AMS journals (starting with the January 1997 issues), while subscribers will have the added ability to view the complete articles delivered in two forms–as HTML, optimized for on-screen viewing, and as Adobe Acrobat PDF files, for printing a precise "reprint" of the article as it appeared in the journal. The full text of *Bulletin* articles will be available free of charge to all users of the site.

- Flexible full-text and fielded search capability
- Journal contents available online *prior* to the print journal

- *Journal of the Atmospheric Sciences*
- *Journal of Climate*
- *Journal of Atmospheric and Oceanic Technology*
- *Monthly Weather Review*
- *Weather and Forecasting*
- *Journal of Applied Meteorology*
- *Journal of Physical Oceanography*

Access the AMS Journals Online from the AMS Web site:
http://www.ametsoc.org/AMS

Subscriptions are available in the form of institutional network site licenses or individual subscriptions. See the AMS Web site for details, or write to the American Meteorological Society, 45 Beacon St., Boston, MA 02108.

SPECIAL INTRODUCTORY OFFER

Subscribe to the 1998 volume year now for any journal online and receive 1997 volume year of that journal online at no extra charge.